

AJNR

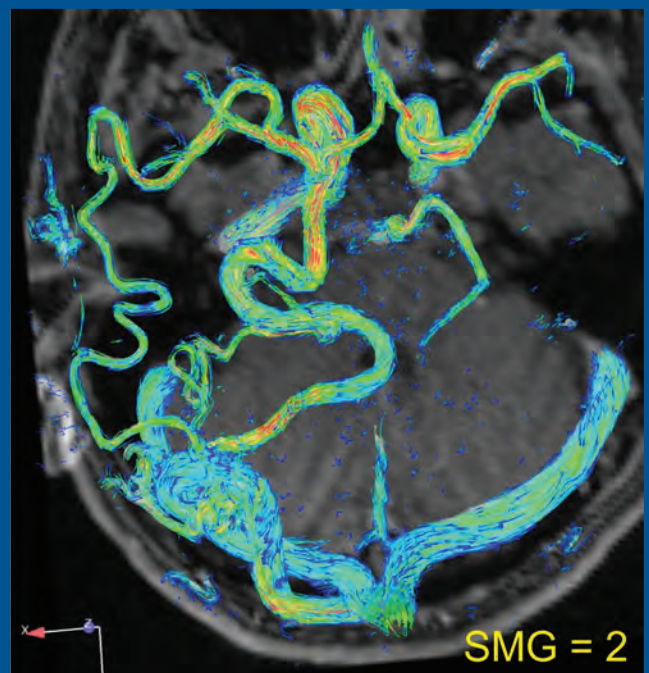
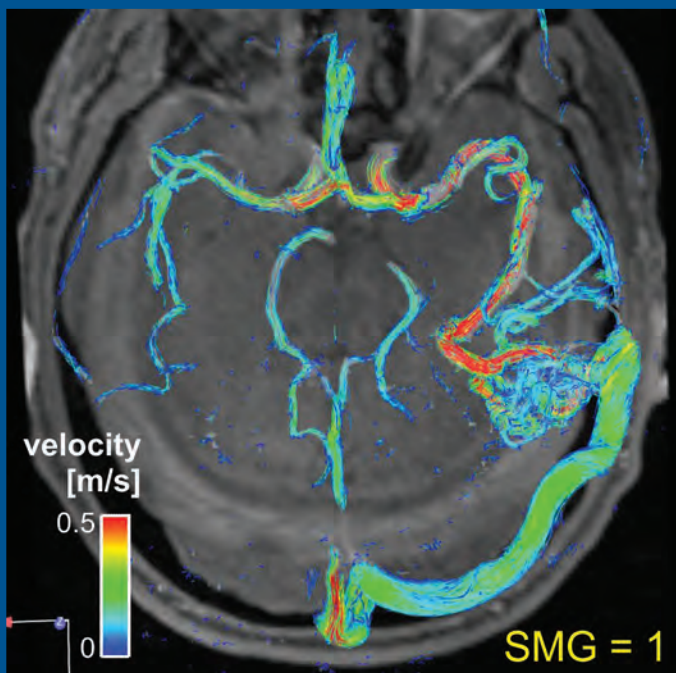
AMERICAN JOURNAL OF NEURORADIOLOGY

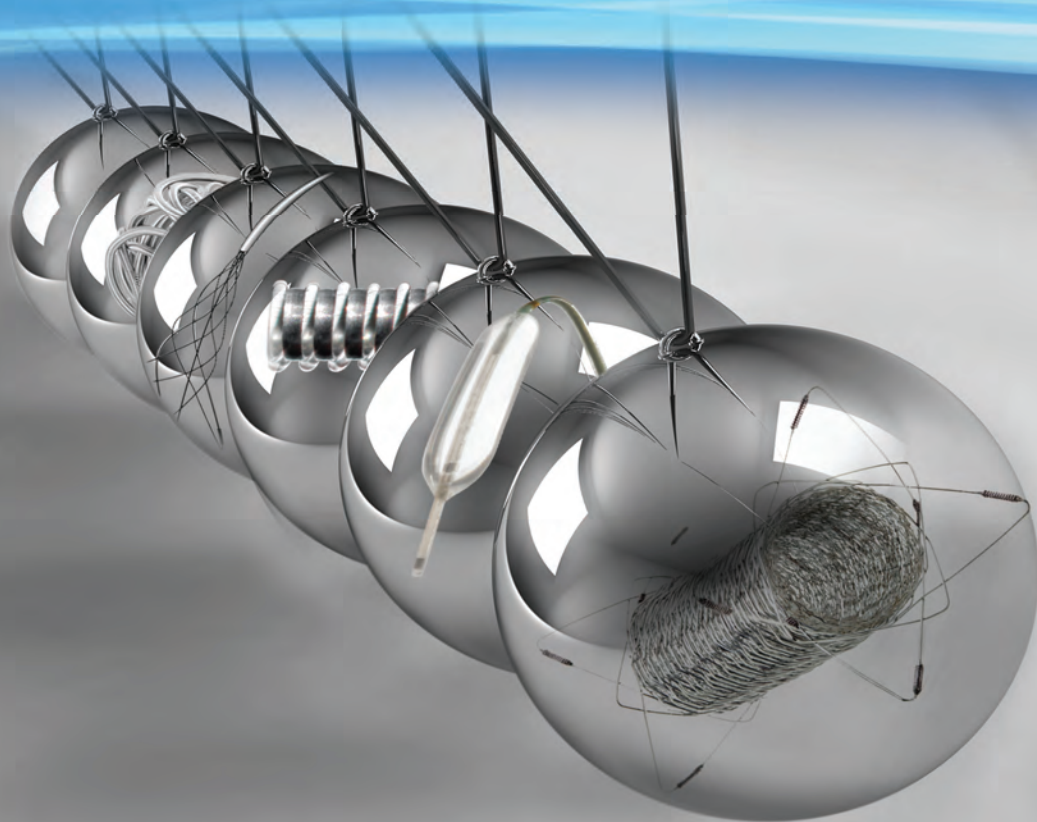
OCTOBER 2013
VOLUME 34
NUMBER 10
WWW.AJNR.ORG

THE JOURNAL OF DIAGNOSTIC AND
INTERVENTIONAL NEURORADIOLOGY

CTA in face transplantation candidates
Implementation and feasibility of cerebral
4D DSA
Imaging features of HPV-positive oropharyngeal
cancers

Official Journal ASNR • ASFNR • ASHNR • ASPNR • ASSR





As a research and clinical leader in their industry,
MicroVention continues to lead the way in endovascular therapies.

Collaboration with industry leaders allows them to be on the pulse of the latest
innovations and deliver essential state-of-the-art products to their customers.

- MicroVention products are easy to use
- MicroVention is the leader in Clinical Trials and Registries
- MicroVention listens to their customers to continually
introduce innovative products
- MicroVention is a technology leader and is *On the Pulse of Innovation*

For more information or a product demonstration,
contact your local MicroVention representative:

MicroVention, Inc.

Worldwide Headquarters

1311 Valencia Avenue
Tustin, California 92780, USA

MicroVention UK Limited

MicroVention Europe, S.A.R.L.

MicroVention Deutschland GmbH

Web



PH +1.714.247.8000

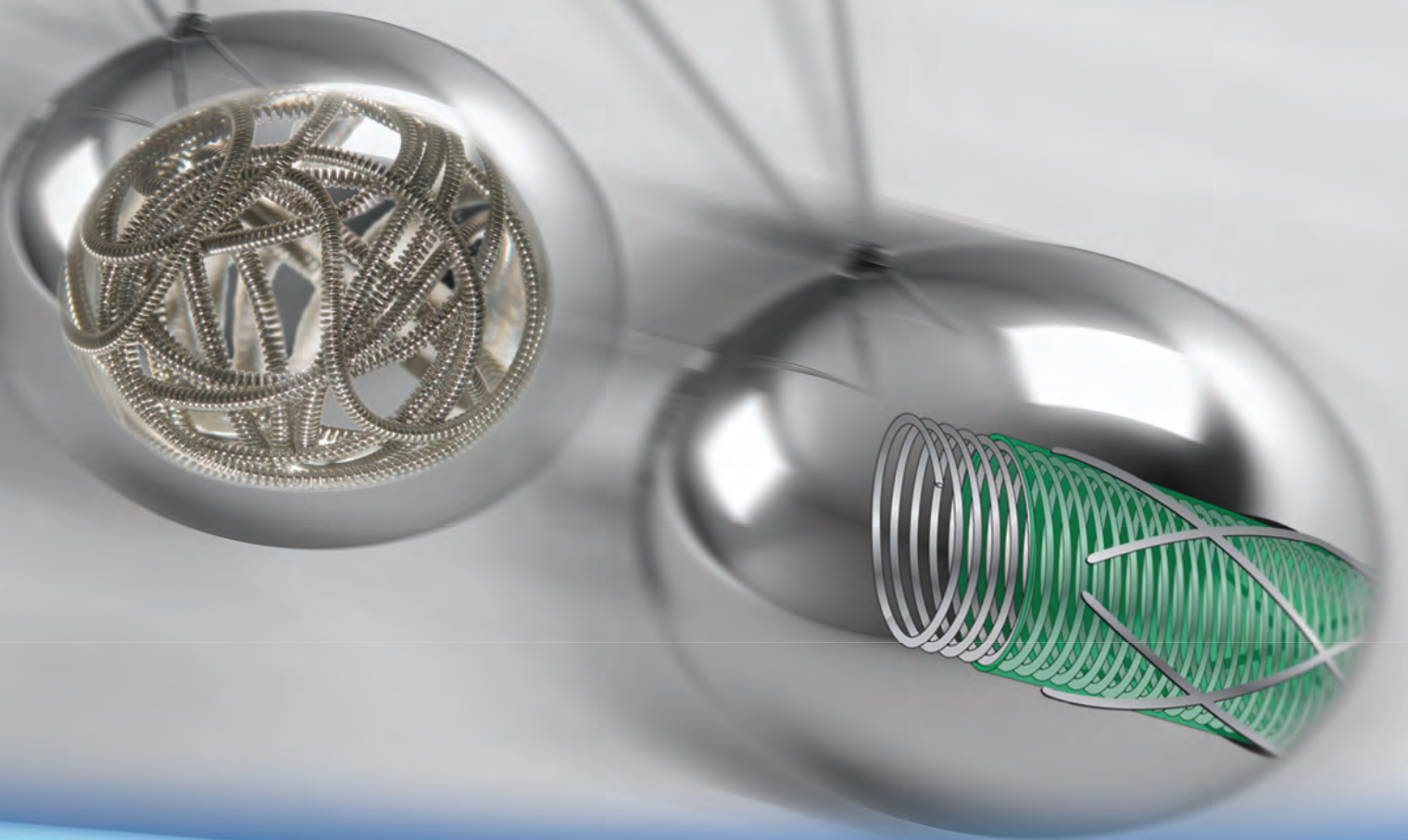
PH +44 (0) 191 258 6777

PH +33 (1) 39 21 77 46

PH +49 211 210 798-0

microvention.com

Perpetual motion keeps
MicroVention
On the Pulse of Innovation



 **MicroVention[®]**
TERUMO

CE
0297

MICROVENTION, Headway Duo, HydroFrame, HydroFill, and Cosmos are registered trademarks of MicroVention, Inc. FRED, Scepter C and LVIS are trademarks of MicroVention, Inc. Scientific and clinical data related to this document are on file at MicroVention, Inc. Refer to Instructions for Use for additional information. *Caution: the FRED[™], LVIS[™] and LVIS[™] Jr. devices are investigational devices limited by U.S. law to investigational use. © 2013 MicroVention, Inc. 7/13

A TERUMO Group Company

ASNR 52ND ANNUAL MEETING & THE FOUNDATION OF THE ASNR SYMPOSIUM 2014

MAY 17-22 | Montreal ■ Palais des congrés de Montreal

ASNR 2014 PROGRAM CHAIR/PRESIDENT-ELECT - Gordon K. Sze, MD, FACR

THE FOUNDATION OF THE ASNR



The Foundation of the ASNR Symposium 2014: Inflammatory and Infectious Diseases of the CNS

SYMPOSIUM 2014:

- The Role of Inflammation and Infections in Stroke, Seizures, White Matter Diseases, etc.
- Advanced Imaging Techniques in the Evaluation of Inflammatory CNS Diseases
- Infectious Agents for Human Good: Oncolytic Viruses, Viral Vector Gene Therapy and Advanced Imaging

ADDITIONAL NEW EDUCATIONAL COURSE PROGRAM IN 2014 (concurrent program with the Symposium 2014)

EDUCATIONAL COURSE 2014: with world class speakers including

- Anne G. Osborn, MD, Thomas P. Naidich, MD, Donald Resnick, MD, James G. Smirniotopoulos, MD, Jeffrey S. Ross, MD, Howard A. Rowley, MD, David M. Yousem, MD, MBA, Laurie A. Loevner, MD, Peter M. Som, MD, Patricia A. Hudgins, MD, Robert D. Zimmerman MD, FACR, Hugh D. Curtin, MD, M. Judith Donovan Post, MD, FACR, and More...

ANNUAL MEETING:

- One-day **MINI SYMPOSIUM** on **STROKE** - Organized by Pina C. Sanelli, MD, MPH and Max Wintermark, MD
- One-day **MINI SYMPOSIUM** on **TUMORS** - Organized by Girish M. Fatterpekar, MD, MBBS, DNB, Whitney B. Pope, MD, PhD and Gordon K. Sze, MD, FACR
- Nobel Prize Laureate, Stanley Prusiner, MD, Keynote Speaker, on Prions and Alzheimer's Disease, Parkinson's Disease, and Other Neurodegenerative Disorders
- More "Hands-On" Experience Applicable to Your Practices
- Young Professionals Programming
- Expanded Self-Assessment Module (SAM) Session Programming Throughout the Week

PROGRAMMING DEVELOPED IN COOPERATION WITH THE...

- American Society of Functional Neuroradiology (ASFNR) David J. Mikulis, MD
- American Society of Head and Neck Radiology (ASHNR) Yoshimi Anzai, MD, MPH
- American Society of Pediatric Neuroradiology (ASPNR) Richard L. Robertson, MD
- American Society of Spine Radiology (ASSR) Meng Law, MD, MBBS, FRACR
- Society of NeuroInterventional Surgery (SNIS) Peter A. Rasmussen, MD



ASFNR ASHNR ASPNR ASSR SNIS

Abstract Deadline:

Friday, December 13, 2013!

Abstract submission site will be available late September. Please visit www.asnr.org/2014 for more information.

TO REQUEST PROGRAMMING AND REGISTRATION MATERIALS FOR THE ASNR 52ND ANNUAL MEETING, CONTACT:

ASNR 52ND ANNUAL MEETING

c/o American Society of Neuroradiology
800 Enterprise Drive, Suite 205
Oak Brook, Illinois 60523-4216

Phone: 630-574-0220
Fax: 630-574-0661
Email: meetings@asnr.org
Website: www.asnr.org/2014



Scan Now
to visit our website

AJNR

AMERICAN JOURNAL OF NEURORADIOLOGY

OCTOBER 2013
VOLUME 34
NUMBER 10
WWW.AJNR.ORG

Publication Preview at www.ajnr.org features articles released in advance of print. Visit www.ajnrblog.org to comment on AJNR content and chat with colleagues and AJNR's News Digest at <http://ajnrdigest.org> to read the stories behind the latest research in neuroimaging.

EDITORIAL

PERSPECTIVES

- 1863 **The Wisdom of Crowds** *M. Castillo*

REVIEW ARTICLES

- 1866 **Resting-State fMRI: A Review of Methods and Clinical Applications**
M.H. Lee, C.D. Smyser, and J.S. Shimony
- 1873 **CT Angiography for Surgical Planning in Face Transplantation Candidates**
S. Soga, B. Pomahac, N. Wake, K. Schultz, R.F. Prior, K. Kumamaru, M.L. Steigner, D. Mitsouras, J. Signorelli, E.M. Bueno, D.S. Enterline, and F.J. Rybicki

PATIENT SAFETY

- 1882 **Radiation Dose for 345 CT-Guided Interlaminar Lumbar Epidural Steroid Injections** *A.L. Chang, A.H. Schoenfeld, A.L. Brook, and T.S. Miller*

HEALTH CARE REFORM VIGNETTE

- 1887 **Alphabet Soup: Our Government "In-Action"** *J.A. Hirsch, W.D. Donovan, G.N. Nicola, R.M. Barr, P.W. Schaefer, and E. Silva III*

BRAIN

- 1890 **Geniculocalcarine Tract Disintegration after Ischemic Stroke: A Diffusion Tensor Imaging Study** *Y. Zhang, S. Wan, and X. Zhang*

- 1895 **Association of CT Perfusion Parameters with Hemorrhagic Transformation in Acute Ischemic Stroke** *A.R. Jain, M. Jain, A.R. Kanthala, D. Damania, L.G. Stead, H.Z. Wang, and B.S. Jahromi*

- 1901 **Stroke Mismatch Volume with the Use of ABC/2 Is Equivalent to Planimetric Stroke Mismatch Volume** *M. Luby, J. Hong, J.G. Merino, J.K. Lynch, A.W. Hsia, A. Magadán, S.S. Song, L.L. Latour, and S. Warach*

- 1908 **4D CT Angiography More Closely Defines Intracranial Thrombus Burden Than Single-Phase CT Angiography** *A.M.J. Frölich, D. Schrader, E. Klotz, R. Schramm, K. Wasser, M. Knauth, and P. Schramm*

- 1914 **4D Digital Subtraction Angiography: Implementation and Demonstration of Feasibility** *B. Davis, K. Royalty, M. Kowarschik, C. Rohkohl, E. Oberstar, B. Aagaard-Kienitz, D. Niemann, O. Ozkan, C. Strother, and C. Mistretta*

- 1922 **Intracranial 4D Flow MRI: Toward Individualized Assessment of Arteriovenous Malformation Hemodynamics and Treatment-Induced Changes** *S.A. Ansari, S. Schnell, T. Carroll, P. Vakil, M.C. Hurley, C. Wu, J. Carr, B.R. Bendok, H. Batjer, and M. Markl*

COMMENTARY

- 1929 **Fast 4D Flow MRI Re-Emerges as a Potential Clinical Tool for Neuroradiology** *P. Turski, M. Edjlali, and C. Oppenheim*

★ Indicates Editor's Choices selection

🔑 Indicates Fellows' Journal Club selection

🔑 Indicates open access to non-subscribers at www.ajnr.org

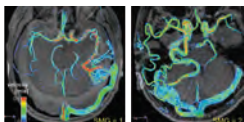
☰ Indicates article with supplemental on-line table

📷 Indicates article with supplemental on-line photo

📺 Indicates article with supplemental on-line video

EBM 1 Indicates Evidence-Based Medicine Level 1

EBM 2 Indicates Evidence-Based Medicine Level 2



Time-integrated 3D images of AVM show velocity of blood flow from highest (red) to lowest (blue).

 **1931 Evolution of Cortical and Thalamus Atrophy and Disability Progression in Early Relapsing-Remitting MS during 5 Years** *R. Zivadinov, N. Bergsland, O. Dolezal, S. Hussein, Z. Seidl, M.G. Dwyer, M. Vaneckova, J. Krasensky, J.A. Potts, T. Kalincik, E. Havrdová, and D. Horáková*

 **1940 Parenchymal Hypointense Foci Associated with Developmental Venous Anomalies: Evaluation by Phase-Sensitive MR Imaging at 3T** *M. Takasugi, S. Fujii, Y. Shinohara, T. Kaminou, T. Watanabe, and T. Ogawa*

 **1945 Widespread White Matter Alterations in Patients with End-Stage Renal Disease: A Voxelwise Diffusion Tensor Imaging Study** *M.-C. Chou, T.-J. Hsieh, Y.-L. Lin, Y.-T. Hsieh, W.-Z. Li, J.-M. Chang, C.-H. Ko, E.-F. Kao, T.-S. Jaw, and G.-C. Liu*

 **1952 Assessment of Whole-Brain White Matter by DTI in Autosomal Recessive Spastic Ataxia of Charlevoix-Saguenay** *K.K. Oguz, G. Haliloglu, C. Temucin, R. Gocmen, A.C. Has, K. Doerschner, A. Dolgun, and M. Alikasifoglu*

 **1958 MR Imaging Features of Amyloid-Related Imaging Abnormalities** *J. Barakos, R. Sperling, S. Salloway, C. Jack, A. Gass, J.B. Fiebach, D. Tampieri, D. Melançon, Y. Miaux, G. Rippon, R. Black, Y. Lu, H.R. Brashear, H.M. Arrighi, K.A. Morris, and M. Grundman*

FUNCTIONAL

1966 Role of Semantic Paradigms for Optimization of Language Mapping in Clinical fMRI Studies *D. Zacà, S. Jarso, and J.J. Pillai*

COMMENTARY

1972 Improving Clinical fMRI: Better Paradigms or Higher Field Strength? *R. Beisteiner*

INTERVENTIONAL *Published in collaboration with Interventional Neuroradiology*

 **1974 Spinal Dural Arteriovenous Fistulas: Clinical Experience with Endovascular Treatment as a Primary Therapy at 2 Academic Referral Centers** *J.J. Gemmete, N. Chaudhary, A.E. Elias, A.K. Toma, A.S. Pandey, R.A. Parker, I. Davagnanam, C.O. Maher, S. Brew, and F. Robertson*

  **1980 Hemodynamics of 8 Different Configurations of Stenting for Bifurcation Aneurysms** *K. Kono and T. Terada*

1987 Stent-Assisted Coiling Versus Balloon Remodeling of Wide-Neck Aneurysms: Comparison of Angiographic Outcomes *N. Chalouhi, R.M. Starke, M.T. Koltz, P.M. Jabbour, S.I. Tjoumakaris, A.S. Dumont, R.H. Rosenwasser, S. Singhal, and L.F. Gonzalez*

COMMENTARY

1993 Does Stent-Assisted Coiling Still Have a Place in the Management of Intracranial Aneurysms? *L. Pierot and C. Cognard*

1996 Stent Retriever Use for Retrieval of Displaced Microcoils: A Consecutive Case Series *T.M. Leslie-Mazwi, M. Heddier, H. Nordmeyer, M. Stauder, A. Velasco, P.J. Mosimann, and R. Chapot*

EXTRACRANIAL VASCULAR

2000 Differences between Internal Jugular Vein and Vertebral Vein Flow Examined in Real Time with the Use of Multigate Ultrasound Color Doppler *G. Ciuti, D. Righi, L. Forzoni, A. Fabbri, and A. Moggi Pignone*

HEAD & NECK

  **2005 Differences in Imaging Characteristics of HPV-Positive and HPV-Negative Oropharyngeal Cancers: A Blinded Matched-Pair Analysis** *S.C. Cantrell, B.W. Peck, G. Li, Q. Wei, E.M. Sturgis, and L.E. Ginsberg*

2010 Morning Glory Disc Anomaly: Characteristic MR Imaging Findings *S. Ellika, C.D. Robson, G. Heidary, and M.J. Paldino*

PEDIATRICS

-  **2015 Early White Matter Changes in Childhood Multiple Sclerosis: A Diffusion Tensor Imaging Study** *A. Blaschek, D. Keeser, S. Müller, I.K. Koerte, A. Sebastian Schröder, W. Müller-Felber, F. Heinen, and B. Ertl-Wagner*
-  **2021 Incidental Findings in Youths Volunteering for Brain MRI Research** *R.E. Gur, D. Kaltman, E.R. Melhem, K. Ruparel, K. Prabhakaran, M. Riley, E. Yodh, H. Hakonarson, T. Satterthwaite, and R.C. Gur*
-  **2026 Abnormal Cerebral Microstructure in Premature Neonates with Congenital Heart Disease** *L.B. Paquette, J.L. Wisnowski, R. Ceschin, J.D. Pruetz, J.A. Detterich, S. Del Castillo, A.C. Nagasunder, R. Kim, M.J. Painter, F.H. Gilles, M.D. Nelson, R.G. Williams, S. Blüml, and A. Panigrahy*
-  **2034 Neuroradiologic Features in X-linked α -Thalassemia/Mental Retardation Syndrome** *T. Wada, H. Ban, M. Matsufuji, N. Okamoto, K. Enomoto, K. Kurosawa, and N. Aida*
-  **2039 Bone Involvement in Atypical Teratoid/Rhabdoid Tumors of the CNS** *M. Warmuth-Metz, B. Bison, N.U. Gerber, T. Pietsch, M. Hasselblatt, and M.C. Frühwald*

SPINE

-  **2043 Intramedullary Spinal Cord Metastases: MRI and Relevant Clinical Features from a 13-Year Institutional Case Series** *J.B. Rykken, F.E. Diehn, C.H. Hunt, K.M. Schwartz, L.J. Eckel, C.P. Wood, T.J. Kaufmann, R.K. Lingineni, R.E. Carter, and J.T. Wald*

ONLINE FEATURES (www.ajnr.org)

LETTERS

- E113 Differentiation of Skull Base Chordomas from Chondrosarcomas by Diffusion-Weighted MRI** *B.S. Freeze and C.M. Glastonbury*
- E114 Manual Hippocampal Volumetry Is a Better Detector of Hippocampal Sclerosis than Current Automated Hippocampal Volumetric Methods** *H.R. Pardoe and G.D. Jackson*
- E116 Reply** *A.C. Coan and F. Cendes*

BOOK REVIEWS *R.M. Quencer, Section Editor*

Please visit www.ajnrblog.org to read and comment on Book Reviews.

Official Journal:

American Society of Neuroradiology
American Society of Functional Neuroradiology
American Society of Head and Neck Radiology
American Society of Pediatric Neuroradiology
American Society of Spine Radiology

EDITOR-IN-CHIEF

Mauricio Castillo, MD

Professor of Radiology and Chief, Division of Neuroradiology, University of North Carolina, School of Medicine, Chapel Hill, North Carolina

SENIOR EDITORS

Harry J. Cloft, MD, PhD

Professor of Radiology and Neurosurgery, Department of Radiology, Mayo Clinic College of Medicine, Rochester, Minnesota

Nancy J. Fischbein, MD

Professor of Radiology, Otolaryngology-Head and Neck Surgery, Neurology, and Neurosurgery and Chief, Head and Neck Radiology, Department of Radiology, Stanford University Medical Center, Stanford, California

Lucien M. Levy, MD, PhD

Professor of Radiology, Chief and Program Director of Neuroradiology, George Washington University Medical Center, Washington, DC

Jeffrey S. Ross, MD

Staff Neuroradiologist, Barrow Neurological Institute, St. Joseph's Hospital, Phoenix, Arizona

Pamela W. Schaefer, MD

Clinical Director of MRI and Associate Director of Neuroradiology, Massachusetts General Hospital, Boston, Massachusetts, and Associate Professor, Radiology, Harvard Medical School, Cambridge, Massachusetts

Charles M. Strother, MD

Professor of Radiology, Emeritus, University of Wisconsin, Madison, Wisconsin

EDITORIAL BOARD

Ashley H. Aiken, Atlanta, Georgia
A. James Barkovich, San Francisco, California
Walter S. Bartynski, Charleston, South Carolina
Barton F. Branstetter IV, Pittsburgh, Pennsylvania
Jonathan L. Brisman, Lake Success, New York
Julie Bykowski, San Diego, California
Donald W. Chakeres, Columbus, Ohio
Alessandro Cianfoni, Lugano, Switzerland
Colin Derdeyn, St. Louis, Missouri
Rahul S. Desikan, San Diego, California
Richard du Mesnil de Rochemont, Frankfurt, Germany
Clifford J. Eskey, Hanover, New Hampshire
Massimo Filippi, Milan, Italy
David Fiorella, Cleveland, Ohio
Allan J. Fox, Toronto, Ontario, Canada
Christine M. Glastonbury, San Francisco, California

John L. Go, Los Angeles, California
Wan-Yuo Guo, Taipei, Taiwan
Rakesh K. Gupta, Lucknow, India
Lotfi Hacein-Bey, Sacramento, California
David B. Hackney, Boston, Massachusetts
Christopher P. Hess, San Francisco, California
Andrei Holodny, New York, New York
Benjamin Huang, Chapel Hill, North Carolina
Thierry A.G.M. Huisman, Baltimore, Maryland
George J. Hunter, Boston, Massachusetts
Mahesh V. Jayaraman, Providence, Rhode Island
Valerie Jewells, Chapel Hill, North Carolina
Timothy J. Kaufmann, Rochester, Minnesota
Kenneth F. Layton, Dallas, Texas
Ting-Yim Lee, London, Ontario, Canada
Michael M. Lell, Erlangen, Germany
Michael Lev, Boston, Massachusetts
Karl-Olof Lovblad, Geneva, Switzerland
Lisa H. Lowe, Kansas City, Missouri
Franklin A. Marden, Chicago, Illinois
M. Gisele Matheus, Charleston, South Carolina
Joseph C. McGowan, Merion Station, Pennsylvania
Kevin R. Moore, Salt Lake City, Utah
Christopher J. Moran, St. Louis, Missouri
Takahisa Mori, Kamakura City, Japan

Suresh Mukherji, Ann Arbor, Michigan
Amanda Murphy, Toronto, Ontario, Canada
Alexander J. Nemeth, Chicago, Illinois
Laurent Pierot, Reims, France
Jay J. Pillai, Baltimore, Maryland
Whitney B. Pope, Los Angeles, California
M. Judith Donovan Post, Miami, Florida
Tina Young Poussaint, Boston, Massachusetts
Joana Ramalho, Lisbon, Portugal
Otto Rapalino, Boston, Massachusetts
Álex Rovira-Cañellas, Barcelona, Spain
Paul M. Ruggieri, Cleveland, Ohio
Zoran Rumboldt, Charleston, South Carolina
Amit M. Saindane, Atlanta, Georgia
Erin Simon Schwartz, Philadelphia, Pennsylvania
Aseem Sharma, St. Louis, Missouri
J. Keith Smith, Chapel Hill, North Carolina
Maria Vittoria Spampinato, Charleston, South Carolina
Gordon K. Sze, New Haven, Connecticut
Krishnamoorthy Thamburaj, Hershey, Pennsylvania
Kent R. Thielen, Rochester, Minnesota
Cheng Hong Toh, Taipei, Taiwan
Thomas A. Tomsick, Cincinnati, Ohio
Aquila S. Turk, Charleston, South Carolina
Willem Jan van Rooij, Tilburg, Netherlands
Arastoo Vossough, Philadelphia, Pennsylvania
Elysa Widjaja, Toronto, Ontario, Canada
Max Wintermark, Charlottesville, Virginia
Ronald L. Wolf, Philadelphia, Pennsylvania
Kei Yamada, Kyoto, Japan

EDITORIAL FELLOW

Falgun H. Chokshi, Atlanta, Georgia

YOUNG PROFESSIONALS ADVISORY COMMITTEE

Asim K. Bag, Birmingham, Alabama
Anna E. Nidecker, Sacramento, California
Peter Yi Shen, Sacramento, California

HEALTH CARE AND SOCIOECONOMICS EDITOR

Pina C. Sanelli, New York, New York

Founding Editor

Juan M. Taveras

Editors Emeriti

Robert I. Grossman, Michael S. Huckman,
Robert M. Quencer

Special Consultants to the Editor

Sandy Cheng-Yu Chen, Girish Fatterpekar,
Ryan Fitzgerald, Yvonne Lui,
Louise M. Henderson, Greg Zaharchuk

INR Liaisons

Timo Krings, Karel terBrugge

Managing Editor

Karen Halm

Electronic Publications Manager

Jason Gantenberg

Editorial Assistant

Mary Harder

Executive Director, ASNR

James B. Gantenberg

Director of Communications, ASNR

Angelo Artemakis

AJNR (Am J Neuroradiol ISSN 0195-6108) is a journal published monthly, owned and published by the American Society of Neuroradiology (ASNR), 800 Enterprise Drive, Suite 205, Oak Brook, IL 60523. Annual dues for the ASNR include \$170.00 for journal subscription. The journal is printed by Cadmus Journal Services, 5457 Twin Knolls Road, Suite 200, Columbia, MD 21045; Periodicals postage paid at Oak Brook, IL and additional mailing offices. Printed in the U.S.A. POSTMASTER: Please send address changes to American Journal of Neuroradiology, P.O. Box 3000, Denville, NJ 07834, U.S.A. Subscription rates: nonmember \$370 (\$440 foreign) print and online, \$300 online only; institutions \$430 (\$495 foreign) print and basic online, \$850 (\$915 foreign) print and extended online, \$355 online only (basic), extended online \$770; single copies are \$35 each (\$40 foreign). Indexed by PubMed/Medline, BIOSIS Previews, Current Contents (Clinical Medicine and Life Sciences), EMBASE, Google Scholar, HighWire Press, Q-Sensei, RefSeek, Science Citation Index, and SCI Expanded. Copyright © American Society of Neuroradiology.



The Wisdom of Crowds

M. Castillo, *Editor-in-Chief*

When we talk about “outsourcing,” we mean asking a well-defined and select group of individuals, generally receiving a salary, to solve a task.¹ This activity is a cornerstone of the business world and has become extremely common in the last 20 years. “Offshoring” is a different process because, unlike outsourcing, in it, the functions of a company or business are relocated to a different country. Not surprising, offshoring can be a political hot potato, while outsourcing rarely raises eyebrows. In our profession, one can view the interpretation of images done at night elsewhere as outsourcing because the process of obtaining them and the equipment remains with us. We are simply buying a service to make our lives easier.

However, when India and South American countries begin building “medical cities” and our patients go there to obtain imaging studies, offshoring of radiology occurs. When both of these activities become a threat to our economic well-being, the opposite (“insourcing”) may occur—that is, we hire more radiologists or pay extra to some already working in our departments to stay overnight and interpret studies. Insourcing is a great way of controlling costs because it tends to use existing infrastructure or adds to it relatively cheaply. The most extreme way of insourcing is “backsourcing,” which happens when all activities that were once done outside (or offshore) are brought back in-house. In addition, of course, if one does backsourcing at a national level, then it becomes “onshoring.” One aspect that defines all these activities is the people doing them. Professionals who do work via outsourcing, offshoring, insourcing, and onshoring are groups of paid employees specifically hired to work at a task and many times are experts (or least, have some experience) at what they do.

Lately, a very different outsourcing model has become popular: crowdsourcing. In crowdsourcing, a nonspecific group of individuals, most unpaid, are given the chance to solve a task. If we can string a long line of computers to make work faster and more exact, the same idea can be applied to humans. In crowdsourcing, the “crowd” part refers to the users, and most are volunteers who are not paid for their services but receive some type of recognition. The entity that looks for the answers is the “crowdsourcer,” and when the issue is solved, it will own the solution.² It would be entirely possible to ask neuroradiologists to capture images from patients with aneurysms, perform computer-flow analysis via freeware, interpret the data obtained, and post their results on the Web site of the project. This would be an example of “community science” or crowdsourcing in which no one would be paid but all would contribute to the understanding of why aneurysms grow and rupture.

The first ever use of crowdsourcing is said to have been the

Oxford English Dictionary (Oxford University Press, 1928), in which the entire British community contributed to index and define all words in the English language, a fascinating story told by Simon Winchester in *The Professor and the Madman*.³ However, crowdsourcing did not become truly efficient until the advent of Web 2.0. Because of its reach and instantaneous nature, Web crowdsourcing has become popular. The appeal of crowdsourcing is the concept that collective intelligence is better than individual, and this forms the basis of the “wisdom of the crowd” principle. Dr Sarah Fortune, an Associate Professor of Immunology and Infectious Diseases at the Harvard School of Public Health, used crowdsourcing to identify cells resistant to tuberculosis drugs.⁴ The only way she could have expedited her research was by hiring 100 graduate students or crowdsourcing it via the Web; she chose the latter. Using a specific computer program (Crowdfunder; <http://crowdfunder.com>), Dr Fortune was able to recruit 1000 on-line workers who looked at her cell images (costing her only a few pennies per image).⁵ She used Crowdfunder, a crowdsourcing service that, as of this writing, had already done more than 775 million tasks (you can watch the number of tasks being performed in real-time at their Web site).

Crowdsourcing is bound to become an important way of doing research in the future (a search of the term “crowdsourcing in medicine” using Google Scholar yielded almost 2000 related items). When data produced by crowdsourcing are evaluated, most experts express high levels of confidence in the results.⁶ The pharmaceutical industry is looking into crowdsourcing as a means of encouraging alternative models of drug discovery.⁷ Using this model, drug companies are poised to save billions of dollars. Eli Lilly and Dupont have already used it to solve vexing research and development problems.⁸ Although these 2 companies offered money to those who solved their issues, the rise of crowdsourcing is based on the fact that everyday folks do it in their “spare cycles” (techie parlance for “free time”), and they represent an enormous new pool of cheap or free labor.⁹ Eli Lilly funded InnoCentive, a crowdsourcing platform now used by Boeing and Proctor and Gamble among others, with incredible results: Thirty percent of problems found on their Web site have been solved by no other than hobbyists! These collaborators are paid somewhere between US \$10,000 and \$25,000 when they solve a problem, which is cheaper than hiring a scientist to do it. As sales of many products decrease, research and development departments become too expensive to run and are no longer affordable, and crowdsourcing their functions becomes an attractive solution.

It seems to me that imaging research would be an ideal platform for crowdsourcing. Images can be cheaply and rapidly transmitted, exchanged, and analyzed, and data could be entered into an open Web site and modified as needed once it is there (Wikipedia works this way). In my experience, radiologists are always willing to give their opinions, contribute with their own cases, and have a good fund of knowledge of computers. In an interesting

<http://dx.doi.org/10.3174/ajnr.A3417>

study, virtual colonoscopy studies were assessed with computer-aided detection and also made available to 228 “knowledge workers” via a crowdsourcing platform.¹⁰ When it came to identifying polyps, both systems produced similar results (about 85% each). In this study, the so-called “knowledge workers” (euphemism for laypeople) received only minimal training while the computer-aided detection was highly specialized. The corresponding author noted that radiologists may be too busy to participate in this type of experiment despite the fact that these tasks generally take less than 1 minute to complete. Money may have something to do with this. If one looks at the different pay schemes in several crowdsourcing platforms, it is obvious that one cannot make a living from them, and as an example, users of Mechanical Turk (<http://aws.amazon.com/mturk/>; the for-pay crowdsourcing Amazon platform that has over 400,000 registered workers) make less than the minimum wage.¹¹

As the financial situations of our governments continue to deteriorate, it seems logical to look for research funding elsewhere, perhaps in the general public. President Obama funded most of his first campaign with small contributions from a multitude of people. This is what is called “crowdfunding,” and the government is not too happy with it. Regulation of crowdfunding is a nightmare for the US Securities and Exchange Commission; and as of this writing, it had not been able to enact laws to define and regulate it.¹² In reality, if no more than \$1 million is raised in this way, regulations are still pretty loose. Nevertheless, big brother is watching, and the US government has established 3 organizations related to crowdfunding (National Crowdfunding Association, Crowdfunding Professional Association, and CrowdFund Intermediary Regulatory Advocates).

Kickstarter is the largest crowdfunding Web platform and has raised over US \$100 million for the funding of creative projects.¹³ Kickstarter posts a “daily project” and attempts to get donations for it from everyone. None of its projects involve the medical field, and these vary from workshops for science fiction and fantasy writers (106% funded) to making better marshmallows (1501% funded). If you click on a project, you can see its number of backers, the pledge goal, total collected money, and the days left to fund it. Crowdfunding seems to work well for disaster relief, support of artists, political campaigns, software development, and even scientific research. Unlike the traditional fundraising events that most universities and institutions hold, crowdfunding occurs outside the geographic boundaries. Most of the typical funding events are meant to bring the donor and recipient together with the idea that personal contact will entice donors to offer financial support. It seems that crowdfunding erases this aspect because the average distance between donors and recipient in crowdfunding platforms is, on average, 3000 miles.¹⁴ This may work for small-amount donors, however not for those who give us millions of dollars. Patients have also started using crowdfunding to pay their medical bills.¹⁵

There are 2 general crowdfunding platforms for science projects. The first one established was the Science Fund Challenge with a current rate for funding projects of 135% versus 20% for the federal government.¹⁶ This site is part of another larger one, RocketHub, that attempts to collect money for soft and hard sciences.¹⁷ Petridish (<http://www.petridish.org>) is perhaps one of

the most serious enterprises that entices donors to “explore the world with renowned researchers,” and Healthtechhatch (<https://www.healthtechhatch.com>) was, as of the time of this writing, beta-testing its site dedicated to crowdfunding in medicine. It seems that the number of crowdfunding platforms for medicine projects is exploding. GiveForward (www.giveforward.com) labels itself as the “The #1 Medical Fundraising Site,” a claim that is probably true because they have raised over US \$22 million since its recent inception. Other sites include www.medstarttr.com and www.iamscientist.com. As expected, levels of suggested donations are higher on these than on RocketHub, and donors have the chance to give their money to respected institutions and researchers (on the homepage of Petridish, one can find projects from the Cold Spring Harbor Laboratory, State University of New York, California State University, and many more). There, one can also access the biographies and curricula of the investigators. Some are PhD candidates looking for funds to complete their dissertations.

Rather than just getting money for research, these crowdfunding sites have a more complex and perhaps positive societal influence: outreach—that is, they let the general public know what is going on with the sciences. Additionally, researchers must exactly detail on the Web what the money is used for, creating a greater transparency in the public eye than that seen with grants given by the government. Obviously, crowdfunding is not the solution for the ever-dwindling federal funding for research, but it is clearly an alternative on a smaller scale. Crowdfunding supports the concept of “open notebook science,” in which all data generated in experiments are made available on-line and, thus, are completely transparent. As the expense of delivering and advancing medicine continues to increase, participation by all involved, including patients, may be one answer to understanding the real costs and complexity of research. The Society for Participatory Medicine (and its journal) encourages this type of activity.¹⁸ Maybe it is time to allow the lay public and our patients to participate in our academic activities so that they can see what we do (because we do it so well). Our research has always been hampered by the small amount of patients whom we are able to reach for donations, and crowdsourcing projects may be an answer to this problem. Additionally, our professional societies could begin to explore the possibility of crowdfunding, or at least we should post some of our projects on Web sites dedicated to this activity.

REFERENCES

1. Outsourcing. Wikipedia. <http://en.wikipedia.org/wiki/Outsourcing>. Accessed October 10, 2012
2. Crowdsourcing. Wikipedia. <http://en.wikipedia.org/wiki/Crowdsourcing>. Accessed October 10, 2012
3. Winchester S. *The Professor and the Madman*. London, UK: Penguin; 1998
4. Sarah Fortune. <http://www.hsph.harvard.edu/faculty/sarah-fortune/index.html>. Accessed October 10, 2012
5. Burke A. Crowdsourcing scientific progress: how Crowdfunder's hordes help Harvard researchers study TB. *Forbes*. October 16, 2011. <http://www.forbes.com/sites/teconomy/2011/10/26/crowdsourcing-scientific-progress-how-crowdfunders-hordes-help-harvard-researchers-study-tb>. Accessed October 10, 2012
6. Oprea TI, Bologna CG, Boyer S, et al. **A crowdsourcing evaluation of the NIH chemical probes.** *Nat Chem Biol* 2009;5:441–47
7. Norman TC, Bountra C, Edwards AM, et al. **Leveraging crowdsourc-**

- ing to facilitate discovery of new medicines. *Sci Transl Med* 2011;3:1–3
8. Alsever J. What is crowdsourcing? CBS Money Watch. March 7, 2007. http://www.cbsnews.com/8301-505125_162-51052961/what-is-crowdsourcing. Accessed October 10, 2012
 9. Howe J. The rise of crowdsourcing. *Wired*. <http://www.wired.com/wired/archive/14.06/crowds.html>. Accessed October 10, 2012
 10. Nguyen TB, Want S, Anugu V, et al. **Distributed human intelligence for colonic polyp classification in computer-aided detection for CT colonography.** *Radiology* 2012;262:824–33
 11. amazon web services. <http://aws.amazon.com>. Accessed October 10, 2012
 12. Barnett C. First SEC rulings launch crowdfunding with accredited. *Forbes*. August 20, 2012. <http://www.forbes.com/sites/chancebarnett/2012/08/30/first-s-e-c-rulings-launch-crowdfunding-with-accredited>. Accessed October 10, 2012
 13. Fund and Follow Creativity. www.kickstarter.com. Accessed October 10, 2012
 14. Agrawal A, Catalini C, Goldfarg A. The geography of crowdfunding. http://papers.ssrn.com/sol3/papers.cfm?abstract_id=1692661. Accessed October 10, 2012
 15. www.youcaring.com. Accessed October 10, 2012
 16. SciFund Challenge. <http://scifundchallenge.org>. Accessed October 10, 2012
 17. The Worlds Crowdfunding Machine. <http://www.rockethub.com/projects/scifund>. Accessed October 10, 2012
 18. Society for Participatory Medicine. www.participatorymedicine.org. Accessed on October 10, 2012

Resting-State fMRI: A Review of Methods and Clinical Applications

M.H. Lee, C.D. Smyser, and J.S. Shimony



ABSTRACT

SUMMARY: Resting-state fMRI measures spontaneous low-frequency fluctuations in the BOLD signal to investigate the functional architecture of the brain. Application of this technique has allowed the identification of various RSNs, or spatially distinct areas of the brain that demonstrate synchronous BOLD fluctuations at rest. Various methods exist for analyzing resting-state data, including seed-based approaches, independent component analysis, graph methods, clustering algorithms, neural networks, and pattern classifiers. Clinical applications of resting-state fMRI are at an early stage of development. However, its use in presurgical planning for patients with brain tumor and epilepsy demonstrates early promise, and the technique may have a future role in providing diagnostic and prognostic information for neurologic and psychiatric diseases.

ABBREVIATIONS: BOLD = blood oxygen level–dependent; DMN = default mode network; ICA = independent component analysis; RS-fMRI = resting-state fMRI; RSN = resting-state network

fMRI using task-based or stimulus-driven paradigms has been critical to our current understanding of brain function. Using the relative changes from baseline in the BOLD signal during the performance of a task or in response to a stimulus, one infers that certain areas of the brain are activated. In recent years, there has been an increase in interest in the application of the technique at rest, termed resting-state fMRI or functional connectivity MR imaging. RS-fMRI investigates synchronous activations between regions that are spatially distinct, occurring in the absence of a task or stimulus, to identify RSNs. In this review, we provide a discussion of RS-fMRI studies and analysis techniques and present potential clinical applications from the literature.

Background on RS-fMRI

RS-fMRI focuses on spontaneous low frequency fluctuations (<0.1 Hz) in the BOLD signal. The functional significance of these fluctuations was first presented by Biswal et al in 1995.¹ In this study, subjects were told not to perform any cognitive, language, or motor tasks. The authors identified a seed region in the

left somatosensory cortex on the basis of traditional block design fMRI, during which the same subjects performed bilateral finger tapping. After determining the correlation between the BOLD time course of the seed region and that of all other areas in the brain, the authors found that the left somatosensory cortex was highly correlated with homologous areas in the contralateral hemisphere. The existence of synchronous spontaneous fluctuations between primary and higher order somatosensory areas was further confirmed by later studies.^{2–6}

Perhaps the most fundamental RSN is the DMN (Fig 1A), first identified from PET data by Raichle et al⁷ (for further discussion, see Gusnard et al⁸). In this study, the authors analyzed data from healthy volunteers resting quietly with their eyes closed. They found that consistent regions of the brain were active at rest but decreased their activity when cognitive tasks were performed. The default mode network was identified by Greicius et al⁹ by using fMRI and was confirmed in many studies by using a variety of analysis methods.^{2–6,10,11} Studies have hypothesized that there are 2 large opposing systems in the brain, one including the DMN and the other composed of attentional or task-based systems, such as somatosensory, visual, or attention RSNs. Terms used to refer to these systems include “task-positive” and “task-negative”^{4,12,13} and “intrinsic” and “extrinsic.”^{14,15}

Several other RSNs have been identified. The somatosensory network, studied first by Biswal et al,¹ includes primary and higher order motor and sensory areas (Fig 1B). The visual network is highly consistent across various studies and spans much of the occipital cortex (Fig 1C).^{2–6} An auditory network consisting of

From the Mallinckrodt Institute of Radiology (M.H.L., J.S.S.) and Departments of Neurology and Pediatrics (C.D.S.), Washington University School of Medicine, St. Louis, Missouri.

This work was supported by grant NIH R21 CA159470 (J.S.S.).

Please address correspondence to Joshua S. Shimony, MD, Mallinckrodt Institute of Radiology, Washington University School of Medicine, Campus Box 8131, 510 S Kingshighway Blvd, St. Louis, Missouri 63110; e-mail: shimonyj@wustl.edu

Indicates open access to non-subscribers at www.ajnr.org

<http://dx.doi.org/10.3174/ajnr.A3263>

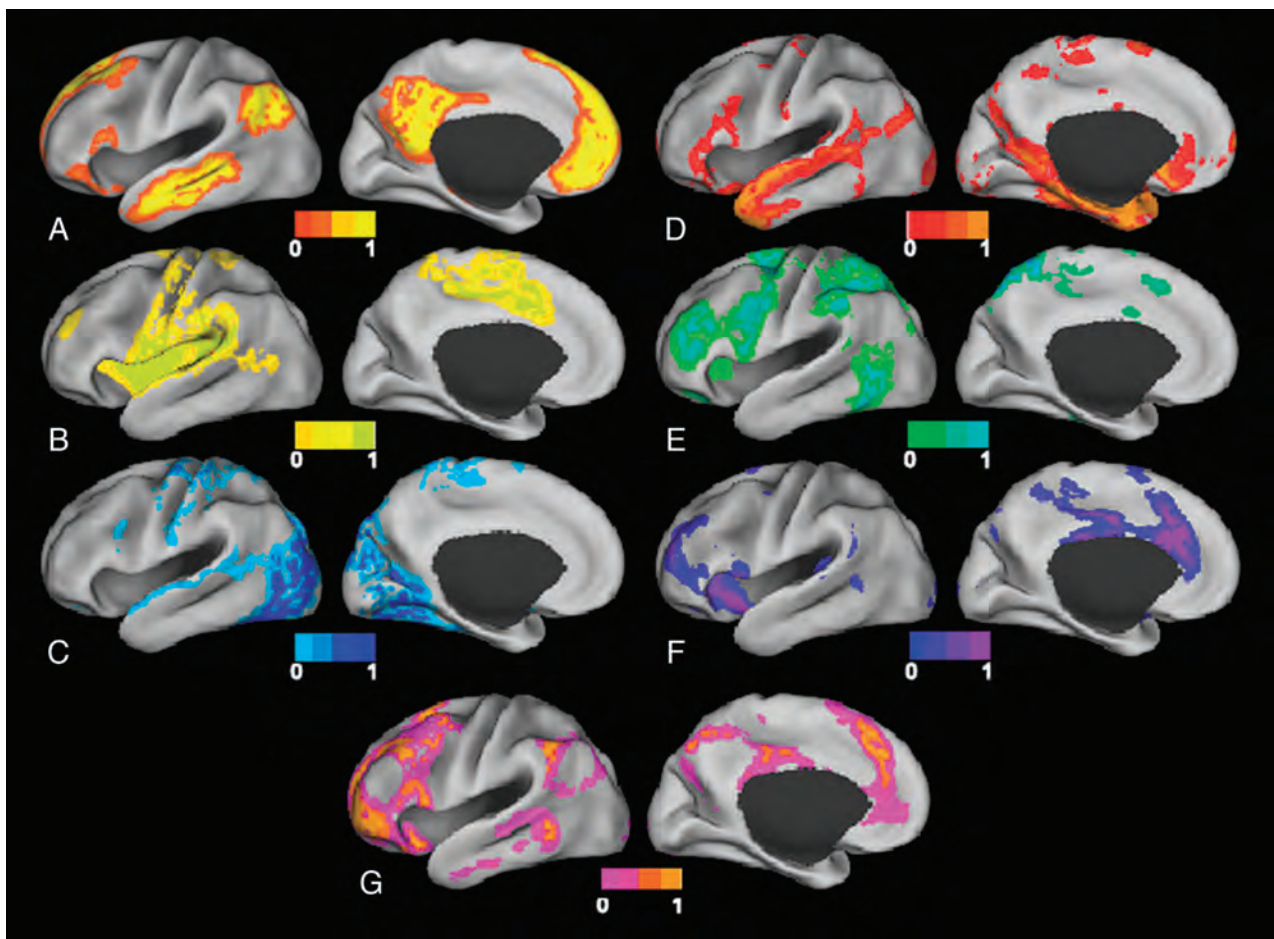


FIG 1. Surface plots of RSNs. *A*, Default mode network. *B*, Somatomotor network. *C*, Visual network. *D*, Language network. *E*, Dorsal attention network. *F*, ventral attention network. *G*, Frontoparietal control network.

the Heschl gyrus, the superior temporal gyrus, and the posterior insula has been identified.⁵ A language network that includes Broca and Wernicke areas but also extends to prefrontal, temporal, parietal, and subcortical regions has been described by using RS-fMRI (Fig 1D).¹⁶

RSNs involved in attentional modulation and cognitive control have also been identified. Two networks identified by using both RS-fMRI and task-based fMRI include the dorsal and ventral attention networks.^{4,6,17,18} The dorsal attention network (Fig 1E) includes the intraparietal sulcus and the frontal eye field and is involved in the executive control of attention. The ventral attention network (Fig 1F), which includes the temporoparietal junction and ventral frontal cortex, is involved in the detection of salient cues (those that stand out from their environment).¹⁷ The frontoparietal control network (Fig 1G), which includes the lateral prefrontal cortex and the inferior parietal lobule, is thought to be involved in decision-making processes.¹⁹ Finally, the cingulo-opercular network, which includes the medial superior frontal cortex, anterior insula, and anterior prefrontal cortex, is thought to play a role in performing goal-directed task sets.^{4,20}

Analysis Methods

BOLD signal preprocessing generally includes correction for section-dependent time shifts and intensity differences. This is followed by regression of head motion and other nuisance regressors.

Nuisance regressors include the signal time courses for regions of interest located in the ventricles and white matter, which are thought to include high proportions of noise related to cardiac and respiratory signals.²¹⁻²⁴ Spatial smoothing and low-pass filtering to retain frequencies <0.1 Hz help to remove signal from non-neuronal causes and improve the signal-to-noise ratio.^{24,25} Images are then registered to atlas space to achieve spatial concordance with coordinate systems and between subjects.

Controversial topics in data preprocessing include whole-brain regression and head-motion correction. Whole-brain regression, which regresses out the average time course of the entire brain, has been proposed as a method of improving the specificity of correlations and reducing noise.²⁶ The whole-brain signal has also been found to correlate with the effects of carbon dioxide partial pressure variation.²⁷ However, some believe that by shifting the distribution of correlations, whole-brain regression produces spurious negative correlations that have no physiologic significance.^{28,29} Head-motion correction has also recently become a matter of debate because it has been shown that inadequate correction for head motion can result in spurious correlations in RS-fMRI analysis.³⁰⁻³² Although head motion is less concerning in healthy young adults, it poses significant challenges for the analysis of data acquired from children, older adults, and patients.

After these preprocessing steps, a number of methods can be

used to analyze the data, each with its own inherent advantages and disadvantages. In this section, we provide a brief overview of some of the statistical and mathematic approaches previously applied to RS-fMRI data.

The first¹ method used was seed-based analysis, which has been applied in numerous studies.^{1,7,17,19} This method entails selecting ROIs and correlating the average BOLD time course of voxels within these ROIs with each other and with the time courses of all other voxels in the brain. Typically, a threshold is determined to identify voxels significantly correlated with the region of interest. However, this approach requires a priori selection of ROIs.

Another popular approach is ICA,^{2,10} a mathematic technique that maximizes statistical independence among its components. For RS-fMRI data, ICA can be used to spatially identify distinct RSNs. Compared with seed-based methods, ICA has the advantage of requiring few a priori assumptions but does compel the user to manually select the important components and distinguish noise from physiologic signals. Some studies have aimed to automate this process and use ICA as a method for identifying noise within the BOLD signal.³³⁻³⁶ Despite the differences in the 2 approaches, Rosazza et al³⁷ showed that the results of seed-based analysis and ICA are significantly similar in a group of healthy subjects.

Graph methods provide a distinct alternative to seed-based analyses and ICA.^{4,38-44} This approach views RSNs as a collection of nodes connected by edges. With RS-fMRI data, ROIs can be represented as nodes, and correlation between the ROIs, as the connectivity of the edges. Connectional characteristics of the graph can then be computed.⁴⁴ Examples of measures of interest include the average path length, a measure of global connectedness, which is the average length of the shortest connection between all pairs of nodes.⁴⁴ Another measure of interest is the clustering coefficient, which is related to the connectedness of neighboring nodes and reflects the presence of smaller subgraphs.⁴⁴ Using these techniques, several studies have demonstrated that the brain exhibits a small world topology. Small world topology, which was first described in social networks, allows each node to have a relatively low number of connections while still being connected to all other nodes with a short distance. This is achieved through the existence of hubs, which are critical nodes with large numbers of connections, that allow high levels of local connectivity.^{39,45} Small world networks have high clustering coefficients implying high levels of local connections (ie, cliques or groups) and an overall short distance between any 2 nodes, or a small average path length.⁴⁰⁻⁴²

Another method used to analyze RS-fMRI data is clustering algorithms. Clustering algorithms attempt to group items that are alike on the basis of a set of relevant characteristics to the problem of interest. When analyzing RS-fMRI data, one may want to group a collection of voxels or ROIs on the basis of similarities in their BOLD time courses by using some distance metric, such as a Pearson correlation. One example of a clustering algorithm is hierarchical clustering,^{42,46} which builds a dendrogram (a treelike structure) of all members. Other examples of clustering algorithms are the K-means¹⁵ and *c*-means⁴⁷ clustering algorithms. In these algorithms, all voxels are assigned membership to 1 of sev-

eral clusters on the basis of their distances from the cluster centers, which, in turn, are calculated from an average of their members. The algorithm iterates to update memberships and cluster centers until convergence is achieved.⁴⁷ Other variations on clustering include spectral-based clustering⁴⁸ and graph-based clustering.¹¹

Multivariate pattern classification is another method that can be used for analysis of RS-fMRI data.⁴⁹ This approach uses patterns in the data that were previously deemed important in a training dataset to classify a new dataset. As an example, one might identify specific sets of patterns or features for each RSN and use them to identify the networks in a new dataset.⁵⁰ In another example, Dosenbach et al⁵¹ used RS-fMRI to predict individual brain maturity. Temporal correlations were computed between the BOLD time courses of various regions throughout the brain. Some of these functional connections were more informative than others in predicting brain maturity and could be used in a classifier to predict the brain maturity of an individual.

Reliability of RS-fMRI

Important issues to consider in regard to RS-fMRI are the test-retest reproducibility and intersubject variability. Studies suggest that RSNs can be detected reliably across imaging sessions^{52,53} and across different subjects,^{10,53} though there may be some loci of variability between subjects.⁵² In particular, Chou et al⁵⁴ examined the reproducibility of RS-fMRI during 1 year and found an intraclass correlation of >0.60 for >70% of the functional networks examined.

Clinical Applications

RS-fMRI has provided many interesting insights on RSNs in the healthy brain and in multiple disease states.⁵⁵ However, practical application of RS-fMRI in the clinical setting requires the ability to establish conclusions on the basis of analysis of data from individual patients. In this section, we focus on studies that have demonstrated potential clinical applications at the single subject level. Group-level studies were included in the pediatric applications section due to the more limited literature in this cohort.

Presurgical Localization of Eloquent Cortex

RS-fMRI has been applied to identify specific brain RSNs for presurgical planning in patients with brain tumor (Fig 2). Compared with existing task-based methods, RS-fMRI is less demanding and can be performed on patients who may not otherwise be able to cooperate with task-based paradigms, such as young children, patients with altered mental status, sedated patients, and those who are parietic or aphasic,⁵⁶⁻⁵⁸ especially because BOLD activity seen in RS-fMRI has also been seen during sleep⁵⁹ and anesthesia.^{60,61} Another advantage of RS-fMRI over task-based fMRI is the ability to identify many networks simultaneously, thus saving scanning time if information from multiple networks is required.

Several studies have reported the application of RS-fMRI for preoperative planning. Zhang et al⁶² reported the successful localization of motor areas in 4 patients with tumors distorting sensorimotor regions. Using a seed-based approach, they used an ROI placed in the contralateral undistorted sensorimotor cortex to identify the sensorimotor area in the distorted ipsilateral hemisphere. A study by Kokkonen et al⁵⁷ illustrated the convergence

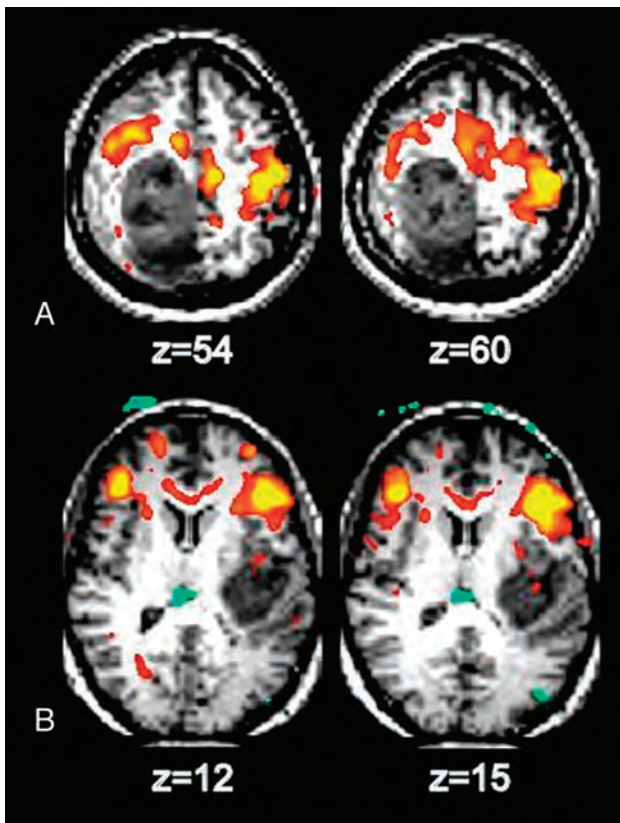


FIG 2. Identification of motor and language areas by using RS-fMRI in 2 patients with glioblastoma multiforme. *A*, The somatosensory area is displaced anterior to the tumor. *B*, Broca area is displaced anterior to the tumor.

between ICA analysis of RS-fMRI and task-based fMRI in identifying sensorimotor areas in 8 patients with tumor and 10 controls. An additional study by Kokkonen et al,⁶³ comparing RS-fMRI pre- and postresection in patients with glioma, suggested that edema affects the BOLD response on the side ipsilateral to the tumor and that auditory and motor cortices are easier to detect postoperatively by using the BOLD signal.

A more challenging problem is the identification of language areas, which are known to be more variable in location⁶⁴ and which can also be distorted by tumor. In particular, this presents a challenge to the seed-based approach but may be more tractable with other analysis methods.

Surgical Planning in Patients with Epilepsy

RS-fMRI may also be used for presurgical planning in patients with epilepsy. The higher spatial resolution afforded by RS-fMRI over electroencephalography could provide a distinct advantage in mapping epileptic foci or networks. Seed-based methods were used by Liu et al⁵⁶ to successfully locate sensorimotor areas by using RS-fMRI in patients with tumors or epileptic foci close to sensorimotor areas. They found agreement between RS-fMRI, task-based fMRI, and intraoperative cortical stimulation data. In another study from the same laboratory, Stufflebeam et al⁶⁵ were able to localize areas of increased connectivity in 5 of 6 patients that overlapped with epileptogenic areas identified by invasive electroencephalography. Zhang et al⁶⁶ used graph methods and a pattern classifier to identify regions involved in the epileptogenic net-

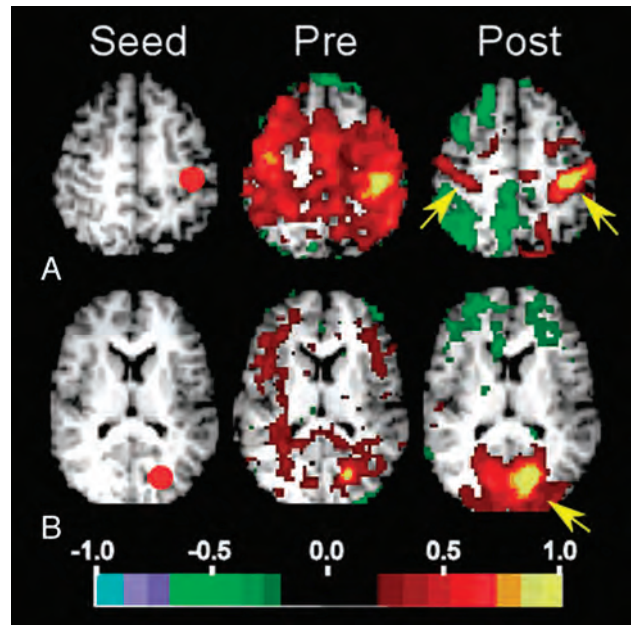


FIG 3. Selected seed-based correlation maps. Columns show the seeds (left), preoperative maps (middle), and postoperative maps (right). The map quantity illustrated is the Fisher z-transformed correlation coefficient thresholded at ± 0.2 . *A*, Left somatomotor cortex seed ($-39 -26 51$). Postoperatively, the somatomotor RSN is improved and involves primary somatosensory areas (arrows). *B*, Visual cortex seed ($-20 -75 12$). Postoperatively, the visual RSN is improved and involves the occipital lobe (arrow).

work. Using RS-fMRI data from 16 patients with intractable medial temporal lobe epilepsy, they achieved an average sensitivity of 77.2% and a specificity of 83.86%. Bettus et al⁶⁷ reported that increases in basal functional connectivity were a specific marker of the location of the epileptogenic zone in 22 patients with mesial temporal lobe epilepsy.

In the future, RS-fMRI may also be of benefit in selecting patients for epilepsy surgery and in evaluating their outcomes. In a study of a 5-year-old patient with severe epileptic encephalopathy, a normal pattern of RSNs returned following corpus callosotomy (Fig 3).⁶⁸ The change from abnormal to normal RSNs was accompanied by the resolution of behavioral regression that had preceded the surgery and the resumption of new skill development. The implications of this study extend beyond the benefit to the practice of epilepsy surgery by providing evidence that RSNs may be essential to the development and maintenance of the functional organization of the brain.

Identification of Patients with Alzheimer Disease

Several studies have demonstrated the potential utility of RS-fMRI in identifying patients with Alzheimer disease. A graph analysis of fMRI data from patients with Alzheimer disease and controls showed that clustering coefficients for the hippocampus were significantly lower in patients compared with controls, and that this measure could separate patients from controls with a sensitivity of 72% and a specificity of 78%.⁶⁹ Koch et al⁷⁰ studied 15 patients with Alzheimer disease and investigated differences in the default mode network as a marker for Alzheimer disease. They used both ICA and the correlations between 2 ROIs within the DMN. With a multivariate model including both methods, they

achieved an accuracy of 97%. The authors of another study used parameters from both structural MR imaging and RS-fMRI and were also able to distinguish patients with Alzheimer disease from healthy controls with an accuracy of 89%.⁷¹ Interestingly, this study also found that several default mode regions were most important in the classification.

Chen et al⁷² studied patients with Alzheimer disease, patients with amnesic mild cognitive impairment, and controls and used seed-based methods to determine correlations between pairs of 116 regions. Using linear regression analysis and a leave-one-out cross-validation, the authors showed that RSN characteristics could identify patients with Alzheimer disease and distinguish patients with mild cognitive impairment from controls.

RS-fMRI may also be able to distinguish different types of dementia. In a study of behavioral-variant frontotemporal dementia, Alzheimer disease, and controls, reciprocal changes were seen between the frontotemporal and Alzheimer dementia groups.⁷³ The frontotemporal dementia group demonstrated decreased connectivity in the salience network but increased connectivity in the default mode network. Conversely, patients with Alzheimer disease demonstrated decreased connectivity in the default mode network but increased connectivity in the salience network. A linear discriminant analysis by using these divergent characteristics was able to distinguish frontotemporal dementia from Alzheimer disease in all cases and achieved an overall 92% accuracy.

Other Applications

Recent work has demonstrated the ability of RS-fMRI to assist in the diagnosis of disorders of consciousness, demonstrating a negative correlation between the connectivity of the DMN and the level of consciousness impairment.⁷⁴ Pattern classification of RS-fMRI has been applied to distinguish patients with psychiatric diseases from controls, including major depressive disorder⁷⁵ and schizophrenia.^{76,77} RS-fMRI has also been used to identify patients with autism⁷⁸ and attention deficit/hyperactivity disorder.⁷⁹

Pediatric Applications

RS-fMRI can also be applied to study pediatric populations. Recent work has used RS-fMRI in infants to demonstrate immature forms of RSNs incorporating regions similar to those identified in older children and adults. Smyser et al⁸⁰ performed longitudinal analysis of network development in a cohort of very preterm infants during the neonatal period. Multiple RSNs were identified as early as 26 weeks' gestation, with characteristic patterns of neural network development reported. Interestingly, differences in RSNs were identified between term infants and those born prematurely, a finding also reported by using other neuroimaging modalities. Doria et al⁸¹ reported a similar collection of RSNs during the neonatal period in a cohort of preterm infants. Other investigators have applied RS-fMRI to define early forms of RSNs during infancy in former preterm and healthy term-born subjects.⁸²⁻⁸⁵

RS-fMRI of healthy subjects during early and middle childhood has established the patterns of normative functional cerebral development during this period.⁸⁶⁻⁸⁹ Although many RSNs are similar to those recognized in adults, consistent differences reported in pediatric subjects include decreased long-range

and increased short-range correlations. The clinical significance of these differences remains undetermined. Most recently, RS-fMRI has been applied to investigate differences in RSN development across pediatric disease states. Investigations in older populations have demonstrated disparities in neural networks for many disease states, including Tourette syndrome, attention deficit/hyperactivity disorder, and autism spectrum disorder.⁹⁰⁻⁹²

Future Directions

Although studies to date are promising, much work is needed before RS-fMRI can be used routinely in the clinical setting. Further work is needed to compare the various analysis methods and their efficacy in detecting different disease states both in groups and especially in individual subjects. The Human Connectome Project,⁹³ which is currently in progress, will aid in furthering our understanding of the relationships between functional connectivity and structural connectivity by using advanced MR imaging methods with behavioral and genetic factors.

CONCLUSIONS

RS-fMRI has provided new insights on the functional architecture of the healthy brain. Various RSNs, or collections of regions that have synchronous spontaneous BOLD fluctuations, have been identified, including the DMN and sensorimotor, visual, and attentional networks. While clinical applications of RS-fMRI are still limited, many potential clinical applications are currently being investigated and include presurgical planning for patients with brain tumor and epilepsy. Because it is noninvasive and does not require patient cooperation, RS-fMRI may be particularly useful in patients who are not able to undergo currently available methods for lesion localization. Other potential clinical applications include the identification of patients with Alzheimer disease and various other neurologic and psychiatric diseases.

REFERENCES

1. Biswal B, Yetkin FZ, Haughton VM, et al. **Functional connectivity in the motor cortex of resting human brain using echo-planar MRI.** *Magn Reson Med* 1995;34:537-41
2. Beckmann CF, DeLuca M, Devlin JT, et al. **Investigations into resting-state connectivity using independent component analysis.** *Philos Trans R Soc Lond B Biol Sci* 2005;360:1001-13
3. De Luca M, Beckmann CF, De Stefano N, et al. **fMRI resting state networks define distinct modes of long-distance interactions in the human brain.** *Neuroimage* 2006;29:1359-67
4. Power JD, Cohen AL, Nelson SM, et al. **Functional network organization of the human brain.** *Neuron* 2011;72:665-78
5. Smith SM, Fox PT, Miller KL, et al. **Correspondence of the brain's functional architecture during activation and rest.** *Proc Natl Acad Sci U S A* 2009;106:13040-45
6. Yeo BT, Krienen FM, Sepulcre J, et al. **The organization of the human cerebral cortex estimated by intrinsic functional connectivity.** *J Neurophysiol* 2011;106:1125-65
7. Raichle ME, MacLeod AM, Snyder AZ, et al. **A default mode of brain function.** *Natl Acad Sci U S A* 2001;98:676-82
8. Gusnard DA, Raichle ME, Raichle ME. **Searching for a baseline: functional imaging and the resting human brain.** *Nat Rev Neurosci* 2001;2:685-94
9. Greicius MD, Krasnow B, Reiss AL, et al. **Functional connectivity in the resting brain: a network analysis of the default mode hypothesis.** *Proc Natl Acad Sci U S A* 2003;100:253-58
10. Damoiseaux JS, Rombouts SA, Barkhof F, et al. **Consistent resting-**

- state networks across healthy subjects. *Proc Natl Acad Sci U S A* 2006;103:13848–53
11. van den Heuvel M, Mandl R, and Hulshoff Pol H. **Normalized cut group clustering of resting-state fMRI data.** *PLoS One* 2008;3:e2001
 12. Chai XJ, Castanon AN, Ongur D, et al. **Anticorrelations in resting state networks without global signal regression.** *Neuroimage* 2012;59:1420–28
 13. Zhang Z, Liao W, Zuo XN, et al. **Resting-state brain organization revealed by functional covariance networks.** *PLoS One* 2011;6:e28817
 14. Doucet G, Naveau M, Petit L, et al. **Brain activity at rest: a multiscale hierarchical functional organization.** *J Neurophysiol* 2011;105:2753–63
 15. Golland Y, Golland P, Bentin S, et al. **Data-driven clustering reveals a fundamental subdivision of the human cortex into two global systems.** *Neuropsychologia* 2008;46:540–53
 16. Tomasi D, Volkow ND. **Resting functional connectivity of language networks: characterization and reproducibility.** *Mol Psychiatry* 2012;17:841–54
 17. Fox MD, Corbetta M, Snyder AZ, et al. **Spontaneous neuronal activity distinguishes human dorsal and ventral attention systems.** *Proc Natl Acad Sci U S A* 2006;103:10046–51
 18. Seeley WW, Menon V, Schatzberg AF, et al. **Dissociable intrinsic connectivity networks for salience processing and executive control.** *J Neurosci* 2007;27:2349–56
 19. Vincent JL, Kahn I, Snyder AZ, et al. **Evidence for a frontoparietal control system revealed by intrinsic functional connectivity.** *J Neurophysiol* 2008;100:3328–42
 20. Dosenbach NU, Visscher KM, Palmer ED, et al. **A core system for the implementation of task sets.** *Neuron* 2006;50:799–812
 21. Dagi MS, Ingeholm JE, and Haxby JV. **Localization of cardiac-induced signal change in fMRI.** *Neuroimage* 1999;9:407–15
 22. de Munck JC, Goncalves SI, Faes TJ, et al. **A study of the brain's resting state based on alpha band power, heart rate and fMRI.** *Neuroimage* 2008;42:112–21
 23. Lund TE, Madsen KH, Sidaros K, et al. **Non-white noise in fMRI: does modelling have an impact?** *Neuroimage* 2006;29:54–66
 24. Van Dijk KR, Hedden T, Venkataraman A, et al. **Intrinsic functional connectivity as a tool for human connectomics: theory, properties, and optimization.** *J Neurophysiol* 2010;103:297–321
 25. Uddin LQ, Mooshagian E, Zaidel E, et al. **Residual functional connectivity in the split-brain revealed with resting-state functional MRI.** *Neuroreport* 2008;19:703–09
 26. Fox MD, Zhang D, Snyder AZ, et al. **The global signal and observed anticorrelated resting state brain networks.** *J Neurophysiol* 2009;101:3270–83
 27. Chang C, Glover GH. **Effects of model-based physiological noise correction on default mode network anti-correlations and correlations.** *Neuroimage* 2009;47:1448–59
 28. Anderson JS, Druzgal TJ, Lopez-Larson M, et al. **Network anticorrelations, global regression, and phase-shifted soft tissue correction.** *Hum Brain Mapp* 2011;32:919–34
 29. Murphy K, Birn RM, Handwerker DA, et al. **The impact of global signal regression on resting state correlations: are anti-correlated networks introduced?** *Neuroimage* 2009;44:893–905
 30. Power JD, Barnes KA, Snyder AZ, et al. **Spurious but systematic correlations in functional connectivity MRI networks arise from subject motion.** *Neuroimage* 2012;59:2142–54
 31. Satterthwaite TD, Wolf DH, Loughhead J, et al. **Impact of in-scanner head motion on multiple measures of functional connectivity: relevance for studies of neurodevelopment in youth.** *Neuroimage* 2012;60:623–32
 32. Van Dijk KR, Sabuncu MR, and Buckner RL. **The influence of head motion on intrinsic functional connectivity MRI.** *Neuroimage* 2012;59:431–38
 33. Kundu P, Inati SJ, Evans JW, et al. **Differentiating BOLD and non-BOLD signals in fMRI time series using multi-echo EPI.** *Neuroimage* 2012;60:1759–70
 34. Starck T, Remes J, Nikkinen J, et al. **Correction of low-frequency physiological noise from the resting state BOLD fMRI: effect on ICA default mode analysis at 1.5 T.** *J Neurosci Methods* 2010;186:179–85
 35. Thomas CG, Harshman RA, Menon RS. **Noise reduction in BOLD-based fMRI using component analysis.** *Neuroimage* 2002;17:1521–37
 36. Tohka J, Foerde K, Aron AR, et al. **Automatic independent component labeling for artifact removal in fMRI.** *Neuroimage* 2008;39:1227–45
 37. Rosazza C, Minati L, Ghielmetti F, et al. **Functional connectivity during resting-state functional MR imaging: study of the correspondence between independent component analysis and region-of-interest-based methods.** *AJNR Am J Neuroradiol* 2012;33:180–87
 38. Behrens TE, Sporns O. **Human connectomics.** *Curr Opin Neurobiol* 2012;22:144–53
 39. Bullmore E, Sporns O. **Complex brain networks: graph theoretical analysis of structural and functional systems.** *Nat Rev Neurosci* 2009;10:186–98
 40. Eguiluz VM, Chialvo DR, Cecchi GA, et al. **Scale-free brain functional networks.** *Phys Rev Lett* 2005;94:018102
 41. Fair DA, Cohen AL, Power JD, et al. **Functional brain networks develop from a “local to distributed” organization.** *PLoS Comput Biol* 2009;5:e1000381
 42. Salvador R, Suckling J, Coleman MR, et al. **Neurophysiological architecture of functional magnetic resonance images of human brain.** *Cereb Cortex* 2005;15:1332–42
 43. Salvador R, Suckling J, Schwarzbauer C, et al. **Undirected graphs of frequency-dependent functional connectivity in whole brain networks.** *Philos Trans R Soc Lond B Biol Sci* 2005;360:937–46
 44. van den Heuvel MP, Stam CJ, Boersma M, et al. **Small-world and scale-free organization of voxel-based resting-state functional connectivity in the human brain.** *Neuroimage* 2008;43:528–39
 45. Sporns O, Honey CJ, Kotter R. **Identification and classification of hubs in brain networks.** *PLoS One* 2007;2:e1049
 46. Cordes D, Haughton V, Carew JD, et al. **Hierarchical clustering to measure connectivity in fMRI resting-state data.** *Magn Reson Imaging* 2002;20:305–17
 47. Lee MH, Hacker CD, Snyder AZ, et al. **Clustering of resting state networks.** *PLoS One* 2012;7:e40370
 48. Bellec P, Rosa-Neto P, Lyttelton OC, et al. **Multi-level bootstrap analysis of stable clusters in resting-state fMRI.** *Neuroimage* 2010;51:1126–39
 49. Pereira F, Mitchell T, Botvinick M. **Machine learning classifiers and fMRI: a tutorial overview.** *Neuroimage* 2009;45:S199–209
 50. Hacker CD, Laumann TO, Szrama NP, et al. **Multi-layer neural network classification of resting state networks.** In: *Proceedings of the Annual Meeting of the Society for Neuroscience*. Washington, DC. November 12–16, 2011
 51. Dosenbach NU, Nardos B, Cohen AL, et al. **Prediction of individual brain maturity using fMRI.** *Science* 2010;329:1358–61
 52. Biswal BB, Mennes M, Zuo XN, et al. **Toward discovery science of human brain function.** *Proc Natl Acad Sci U S A* 2010;107:4734–39
 53. Shehzad Z, Kelly AM, Reiss PT, et al. **The resting brain: unconstrained yet reliable.** *Cereb Cortex* 2009;19:2209–29
 54. Chou YH, Panych LP, Dickey CC, et al. **Investigation of long-term reproducibility of intrinsic connectivity network mapping: a resting-state fMRI study.** *AJNR Am J Neuroradiol* 2012;33:833–38
 55. Zhang D, Raichle ME. **Disease and the brain's dark energy.** *Nat Rev Neurol* 2010;6:15–28
 56. Liu H, Buckner RL, Talukdar T, et al. **Task-free presurgical mapping using functional magnetic resonance imaging intrinsic activity.** *J Neurosurg* 2009;111:746–54
 57. Kokkonen SM, Nikkinen J, Remes J, et al. **Preoperative localization of the sensorimotor area using independent component analysis of resting-state fMRI.** *Magn Reson Imaging* 2009;27:733–40
 58. Shimony JS, Zhang D, Johnston JM, et al. **Resting-state spontaneous**

- fluctuations in brain activity: a new paradigm for presurgical planning using fMRI. *Acad Radiol* 2009;16:578–83
59. Fukunaga M, Horovitz SG, van Gelderen P, et al. Large-amplitude, spatially correlated fluctuations in BOLD fMRI signals during extended rest and early sleep stages. *Magn Reson Imaging* 2006;24:979–92
 60. Kiviniemi V, Kantola JH, Jauhiainen J, et al. Independent component analysis of nondeterministic fMRI signal sources. *Neuroimage* 2003;19:253–60
 61. Peltier SJ, Kerssens C, Hamann SB, et al. Functional connectivity changes with concentration of sevoflurane anesthesia. *Neuroreport* 2005;16:285–88
 62. Zhang D, Johnston JM, Fox MD, et al. Preoperative sensorimotor mapping in brain tumor patients using spontaneous fluctuations in neuronal activity imaged with functional magnetic resonance imaging: initial experience. *Neurosurgery* 2009;65:226–36
 63. Kokkonen SM, Kiviniemi V, Makiranta M, et al. Effect of brain surgery on auditory and motor cortex activation: a preliminary functional magnetic resonance imaging study. *Neurosurgery* 2005;57:249–56, discussion 249–56
 64. Sanai N, Mirzadeh Z, Berger MS. Functional outcome after language mapping for glioma resection. *N Engl J Med* 2008;358:18–27
 65. Stufflebeam SM, Liu H, Sepulcre J, et al. Localization of focal epileptic discharges using functional connectivity magnetic resonance imaging. *J Neurosurg* 2011;114:1693–97
 66. Zhang X, Tokoglu F, Negishi M, et al. Social network theory applied to resting-state fMRI connectivity data in the identification of epilepsy networks with iterative feature selection. *J Neurosci Methods* 2011;199:129–39
 67. Bettus G, Bartolomei F, Confort-Gouny S, et al. Role of resting state functional connectivity MRI in presurgical investigation of mesial temporal lobe epilepsy. *J Neurol Neurosurg Psychiatry* 2010;81:1147–54
 68. Pizoli CE, Shah MN, Snyder AZ, et al. Resting-state activity in development and maintenance of normal brain function. *Proc Natl Acad Sci U S A* 2011;108:11638–43
 69. Supekar K, Menon V, Rubin D, et al. Network analysis of intrinsic functional brain connectivity in Alzheimer's disease. *PLoS Comput Biol* 2008;4:e1000100
 70. Koch W, Teipel S, Mueller S, et al. Diagnostic power of default mode network resting state fMRI in the detection of Alzheimer's disease. *Neurobiol Aging* 2012;33:466–78
 71. Dai Z, Yan C, Wang Z, et al. Discriminative analysis of early Alzheimer's disease using multi-modal imaging and multi-level characterization with multi-classifier (M3). *Neuroimage* 2012;59:2187–95
 72. Chen G, Ward BD, Xie C, et al. Classification of Alzheimer disease, mild cognitive impairment, and normal cognitive status with large-scale network analysis based on resting-state functional MR imaging. *Radiology* 2011;259:213–21
 73. Zhou J, Greicius MD, Gennatas ED, et al. Divergent network connectivity changes in behavioural variant frontotemporal dementia and Alzheimer's disease. *Brain* 2010;133:1352–67
 74. Vanhaudenhuyse A, Noirhomme Q, Tshibanda LJ, et al. Default network connectivity reflects the level of consciousness in non-communicative brain-damaged patients. *Brain* 2010;133:161–71
 75. Craddock RC, Holtzheimer PE 3rd, Hu XP, et al. Disease state prediction from resting state functional connectivity. *Magn Reson Med* 2009;62:1619–28
 76. Bassett DS, Nelson BG, Mueller BA, et al. Altered resting state complexity in schizophrenia. *Neuroimage* 2012;59:2196–207
 77. Shen H, Wang L, Liu Y, et al. Discriminative analysis of resting-state functional connectivity patterns of schizophrenia using low dimensional embedding of fMRI. *Neuroimage* 2010;49:3110–21
 78. Anderson JS, Nielsen JA, Froehlich AL, et al. Functional connectivity magnetic resonance imaging classification of autism. *Brain* 2011;134:3742–54
 79. Zhu CZ, Zang YF, Cao QJ, et al. Fisher discriminative analysis of resting-state brain function for attention-deficit/hyperactivity disorder. *Neuroimage* 2008;40:110–20
 80. Smyser CD, Inder TE, Shimony JS, et al. Longitudinal analysis of neural network development in preterm infants. *Cereb Cortex* 2010;20:2852–62
 81. Doria V, Beckmann CF, Arichi T, et al. Emergence of resting state networks in the preterm human brain. *Proc Natl Acad Sci U S A* 2010;107:20015–20
 82. Damaraju E, Phillips JR, Lowe JR, et al. Resting-state functional connectivity differences in premature children. *Front Syst Neurosci* 2010;4:pii:23
 83. Fransson P, Aden U, Blennow M, et al. The functional architecture of the infant brain as revealed by resting-state fMRI. *Cereb Cortex* 2011;21:145–54
 84. Gao W, Zhu H, Giovanello KS, et al. Evidence on the emergence of the brain's default network from 2-week-old to 2-year-old healthy pediatric subjects. *Proc Natl Acad Sci U S A* 2009;106:6790–95
 85. Lin W, Zhu Q, Gao W, et al. Functional connectivity MR imaging reveals cortical functional connectivity in the developing brain. *AJNR Am J Neuroradiol* 2008;29:1883–89
 86. Fair DA, Cohen AL, Dosenbach NU, et al. The maturing architecture of the brain's default network. *Proc Natl Acad Sci U S A* 2008;105:4028–32
 87. Fair DA, Dosenbach NU, Church JA, et al. Development of distinct control networks through segregation and integration. *Proc Natl Acad Sci U S A* 2007;104:13507–12
 88. Kelly AM, Di Martino A, Uddin LQ, et al. Development of anterior cingulate functional connectivity from late childhood to early adulthood. *Cereb Cortex* 2009;19:640–57
 89. Thomason ME, Chang CE, Glover GH, et al. Default-mode function and task-induced deactivation have overlapping brain substrates in children. *Neuroimage* 2008;41:1493–503
 90. Church JA, Fair DA, Dosenbach NU, et al. Control networks in paediatric Tourette syndrome show immature and anomalous patterns of functional connectivity. *Brain* 2009;132:225–38
 91. Fair DA, Posner J, Nagel BJ, et al. Atypical default network connectivity in youth with attention-deficit/hyperactivity disorder. *Biol Psychiatry* 2010;68:1084–91
 92. Jones TB, Bandettini PA, Kenworthy L, et al. Sources of group differences in functional connectivity: an investigation applied to autism spectrum disorder. *Neuroimage* 2010;49:401–14
 93. Van Essen DC, Ugurbil K, Auerbach E, et al. The Human Connectome Project: a data acquisition perspective. *Neuroimage* 2012;62:2222–31

CT Angiography for Surgical Planning in Face Transplantation Candidates

S. Soga, B. Pomahac, N. Wake, K. Schultz, R.F. Prior, K. Kumamaru, M.L. Steigner, D. Mitsouras, J. Signorelli, E.M. Bueno, D.S. Enterline, and F.J. Rybicki



ABSTRACT

SUMMARY: Facial allotransplantation replaces missing facial structures with anatomically identical tissues, providing desired functional, esthetic, and psychosocial benefits far superior to those of conventional methods. On the basis of very encouraging initial results, it is likely that more procedures will be performed in the near future. Typical candidates have extremely complex vascular anatomy due to severe injury and/or multiple prior reconstructive attempts; thus, each procedure is uniquely determined by the defects and vascular anatomy of the candidate. We detail CT angiography vascular mapping, noting the clinical relevance of the imaging, the angiosome concept and noninvasive delineation of the key vessels, and current controversies related to the vascular anastomoses.

Restoring complex facial components such as eyelid and/or lip function is nearly impossible (Figs 1A and 2A) with conventional reconstructive techniques.^{1,2} Allotransplantation is accepted as the only option for the most complex craniofacial reconstruction (Fig 1A, -B). On the basis of the large population of patients with facial defects and encouraging initial results,³ it is likely that face transplantation will become a more common procedure. This underscores the need for radiologists to recognize the need for vascular mapping in these patients and to learn key aspects of the surgery that are important for image acquisition and reporting.

There have been approximately 20 face transplantations performed to date; 4 of these patients, including 3 from the United States,³ had “full” face transplantation,⁴ defined as restoration of the forehead, eyelids, nose, lips, chin, and cheeks, with or without bone. Patients with smaller defects can undergo so-called “partial” transplantation (Fig 1). Although candidate screening in-

cludes patients with malignancy and congenital etiologies, most patients to date have had severe trauma. For our patients, suitable brain dead, sex-, and skin color–matched donors are identified from our regional organ bank.

The intricacy of facial transplantation includes vascular preparation of both the recipient site and donor allograft. Long (15–22 hours) operation times^{5,6} and massive (up to 35 units) blood loss⁷ have been reported. The vascular anastomoses are the most critical part of the operation. Although 1 arterial and venous anastomosis appears adequate for perfusion of facial tissues, additional vessels are typically connected to ensure adequate facial blood flow.^{8,9}

Open dialogue between surgeons and radiologists is critical to assess potential anastomoses and 3D relationships between vessels and other structures (eg, shrapnel, bone fragments) and to minimize the risk of critical blood loss and ischemia time.

The radiologist is charged with preoperative identification of the best target arteries. The risk of vascular anastomotic complications can be reduced if vessels with unfavorable anatomy are excluded from anastomoses. Preoperative knowledge of vascular anatomy allows the surgeons to plan ahead and prepare backup options such as vein grafts. We have observed that the elimination of vascular “unknowns” has led to more timely operations.

Face transplantation surgery is highly variable, and surgical planning for each case is unique. For the allograft, the recipient’s tissue deficits determine the design, ranging from partial to full facial transplantation. The allograft includes not only the skin but also the underlying soft tissues, cartilage, and bone, depending on the defect of the recipient. This article focuses on the importance of the blood vessels. High-quality noninvasive image acquisition and postprocessing are essential because there is variation in subject anatomies, common sources for arterial and venous anasto-

From the Department of Radiology (S.S., N.W., R.F.P., K.K., M.L.S., D.M., J.S., F.J.R.), Applied Imaging Science Laboratory; and Division of Plastic and Reconstructive Surgery (B.P., E.M.B.), Brigham and Women’s Hospital, Boston, Massachusetts; Toshiba Medical Research Institute (K.S.), Vernon Hills, Illinois; and Department of Radiology (D.S.E.), Duke University Medical Center, Durham, North Carolina. Dr Soga is currently affiliated with Department of Radiology, National Defense Medical College, Tokorozawa, Saitama, Japan.

Paper previously presented in part and awarded a Radiological Society of North America 2010 Certificate of Merit, a Radiological Society of North America 2011 Excellence in Design Award, and an Excellent Educational Poster Award at: 71st Annual Meeting of the Japan Radiological Society, April 12–15, 2012; Yokohama, Japan.

Please address correspondence to Frank J. Rybicki, MD, Applied Imaging Science Laboratory, Department of Radiology, Brigham and Women’s Hospital, 75 Francis St, Boston, MA, 02115; e-mail: frybicki@partners.org

Indicates open access to non-subscribers at www.ajnr.org

<http://dx.doi.org/10.3174/ajnr.A3268>



FIG 1. A 59-year-old man who underwent partial face transplantation. *A*, Severe disfigurement of the midface caused by a high-voltage burn injury is demonstrated, despite multiple conventional reconstructive attempts. *B*, Two-year postoperative follow-up illustrates restoration of form and function.

moses are often depleted by previous reconstructive efforts or injury, and the surgical dissection can be very difficult due to scarring and fibrosis.

Literature supports CT vascular mapping for living hepatic and renal donors,^{10,11} considering it fundamental for safety and surgical outcomes.^{12,13} One distinction for facial transplantation imaging is that selection of donor vessels is affected by both allograft design and the recipient's vascular anatomy as a result of extensive defects or prior interventions. Moreover, head and neck vascular anatomy has higher patient-to-patient variability, particularly with respect to venous outflow, emphasizing the importance of preoperative mapping for reliable microvascular anastomoses and minimizing the risk of venous congestion and thrombosis in anastomotic vessels, the most common complications of microsurgery.

This article illustrates vascular CT for surgical planning. The angiosome concept is presented with respect to its influence on the donor vessel selection. Relevant controversies for vessel anastomoses are discussed, and current CT protocols are emphasized.

VASCULAR CONSIDERATIONS IN FACIAL TRANSPLANTATION

Donor Vessels and Angiosomes

The allograft design is determined by the recipient's defect (Figs 1A, 2A, and 3A). The vascular pedicles or donor vessels are chosen by using the angiosome (Fig 3D) concept,^{14,15} to optimize adequate perfusion. Each angiosome has a source artery that supplies 3D composite blocks of skin and underlying tissues (muscles, nerves, and bones).¹⁶ This concept suggests that multiple arteries are needed for perfusion of the facial skin and most of the facial skin is supplied by the superficial temporal, facial, and ophthal-

mic arteries.¹⁶ However, several anastomotic networks allow perfusion of multiple adjacent territories¹⁷⁻²⁰ or across the midline.^{8,9} Thus, a source artery can also perfuse neighboring angiosomes when connecting potential vessels, called "choke vessels," open, and subsequently develop into collateral vessels.¹⁵ For example, the source artery for the ophthalmic angiosome of the central forehead is typically a branch of the internal carotid artery. However, this angiosome can be supplied by reversed flow from the adjacent superficial temporal and facial artery territories.¹⁷

Selection of Recipient Vessels

Although the head and neck have a rich and often redundant vascular network,²¹ in our experience, it is common that the typical target vessels are depleted from either massive defects or multiple surgeries (Figs 2B, -C and 4). When it is available for surgery, CTA mapping of the course, caliber, contour, and 3D relationship to metal from the injury or prior surgeries is the most important preoperative step. CTA preoperatively identifies alternative recipient vessels when more suitable vessels are depleted. The usual strategy²² is to identify adjacent small vessels by CTA.²³ When small neighboring vessels are not available, major neck vessels, such as the internal jugular system, can be used.²²

Another critical element of surgical planning is the identification of anatomic variants (Table and Fig 5).²⁴ Both arteries and veins can have a common trunk, leading to larger caliber vessels compared with the smaller individual vessels. Larger caliber trunks are considered more favorable because the anastomosis is simpler and safer. Duplications are also common, and in general, these are considered advantageous because of increased options for anastomoses. Seventeen percent of individuals have dupli-

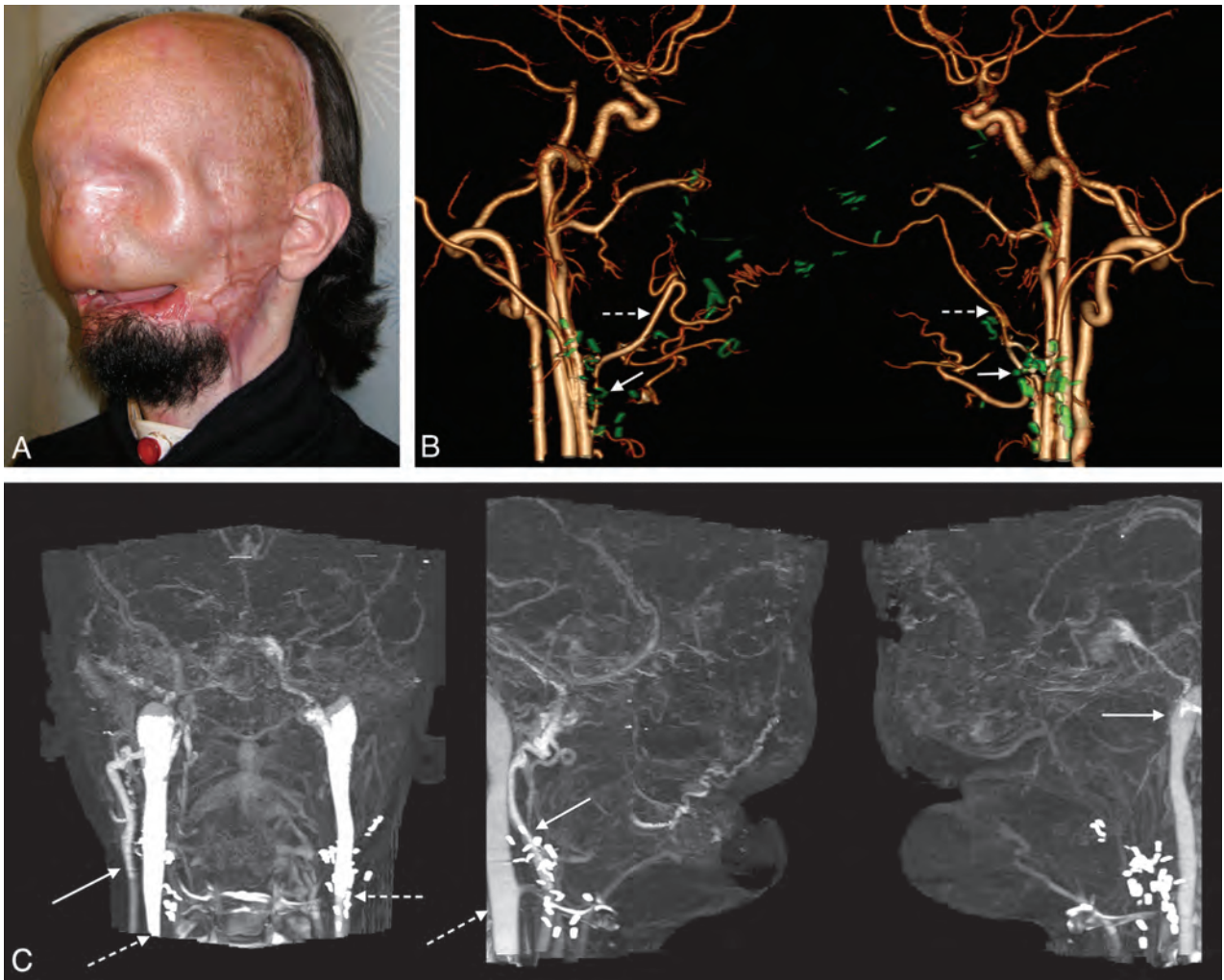


FIG 2. Candidate for full face transplantation. *A*, After catastrophic loss of facial tissues, muscle flaps and skin grafts placed during >20 surgeries rendered the patient's face featureless. *B*, Surgical-planning volume-rendered CT angiography depicts residual arteries after previous reconstructions using bilateral free latissimus muscle and serratus muscle flap arteries (*dashed arrows*), which are anastomosed end-to-end to the bilateral facial artery stumps (*arrows*). While not ideal, those facial and/or flap arteries are technically available and considered for microsurgical anastomoses. Prior surgical clips are rendered in green using the multiobject segmentation described in the text. *C*, Venous images from the same CT acquisition show occluded or absent bilateral anterior, posterior facial, and left external jugular veins. Patency of the right external jugular vein (*arrow*) and bilateral internal jugular veins (*dashed arrows*) is confirmed.

cated external jugular veins, and 30% of individuals have duplicated anterior jugular veins.²⁴

As a general rule, 2 venous anastomoses are used to maintain sufficient outflow. Conventional thinking is that compared with the corresponding arteries, selection of drainage veins is considered less critical.²⁵ However, it is essential to maintain sufficient drainage because venous congestion and thrombosis are the most common cause of flap failure.^{26,27} Additionally, there is a high incidence of venous thrombosis after neck dissection, up to 30% in the internal jugular vein.²⁸⁻³⁰

Planning Vascular Anastomoses

Once all vessels are identified, planning the vascular anastomoses considers the following: 1) optimal size match between donor and recipient vessels, 2) sufficient length between the allograft pedicle and donor vessel, and 3) surgical accessibility of the pedicle. Communication between the radiologist and surgeon by using the postprocessing methods described below is essential to portray the spatial relationships.

Surgical planning meticulously considers and matches the caliber and length of recipient and donor vessels. When these are highly compatible, it is possible to perform end-to-end anastomoses; the technique is simple and easily performed with less blood flow turbulence. However, other techniques are often required, usually from large-diameter discrepancies that increase the technical difficulty of the anastomoses and the reliability of the final conduit. Moreover, abrupt caliber changes are also undesirable because these induce turbulence and predispose to platelet aggregation.³¹ In related interventions, artery size discrepancy³² and/or intricate anastomoses³³ have been shown to have higher complication rates.

In our experience, 3-fold diameter discrepancies between donor and recipient vessels have been encountered and are accommodated for by end-to-side anastomoses. Other options would include sleeve and so-called "fishmouth" anastomoses for the management of size discrepancies in microvascular anastomosis.³¹ Practically, an end-to-side anastomosis is often the only

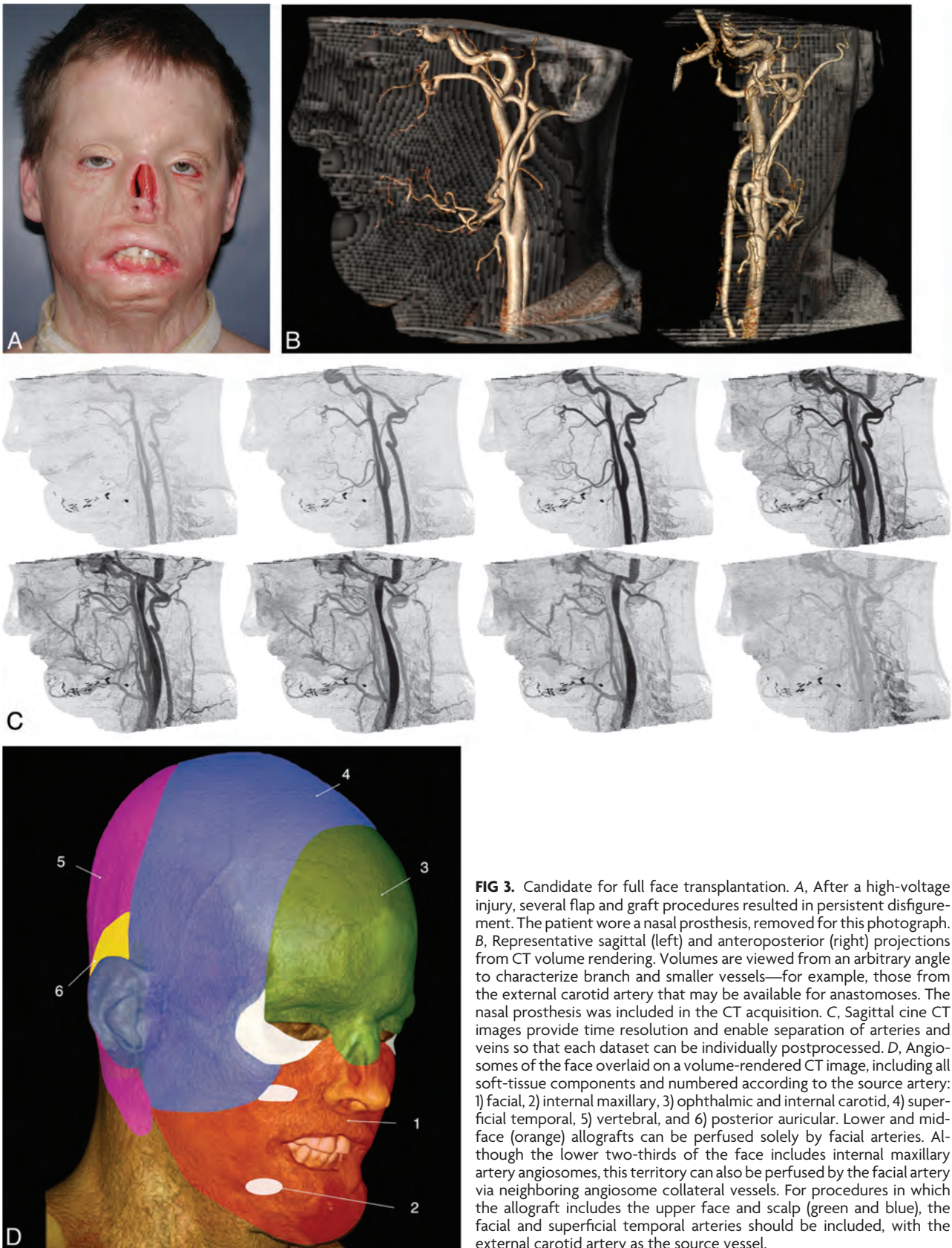


FIG 3. Candidate for full face transplantation. *A*, After a high-voltage injury, several flap and graft procedures resulted in persistent disfigurement. The patient wore a nasal prosthesis, removed for this photograph. *B*, Representative sagittal (left) and anteroposterior (right) projections from CT volume rendering. Volumes are viewed from an arbitrary angle to characterize branch and smaller vessels—for example, those from the external carotid artery that may be available for anastomoses. The nasal prosthesis was included in the CT acquisition. *C*, Sagittal cine CT images provide time resolution and enable separation of arteries and veins so that each dataset can be individually postprocessed. *D*, Angiosomes of the face overlaid on a volume-rendered CT image, including all soft-tissue components and numbered according to the source artery: 1) facial, 2) internal maxillary, 3) ophthalmic and internal carotid, 4) superficial temporal, 5) vertebral, and 6) posterior auricular. Lower and mid-face (orange) allografts can be perfused solely by facial arteries. Although the lower two-thirds of the face includes internal maxillary artery angiosomes, this territory can also be perfused by the facial artery via neighboring angiosome collateral vessels. For procedures in which the allograft includes the upper face and scalp (green and blue), the facial and superficial temporal arteries should be included, with the external carotid artery as the source vessel.

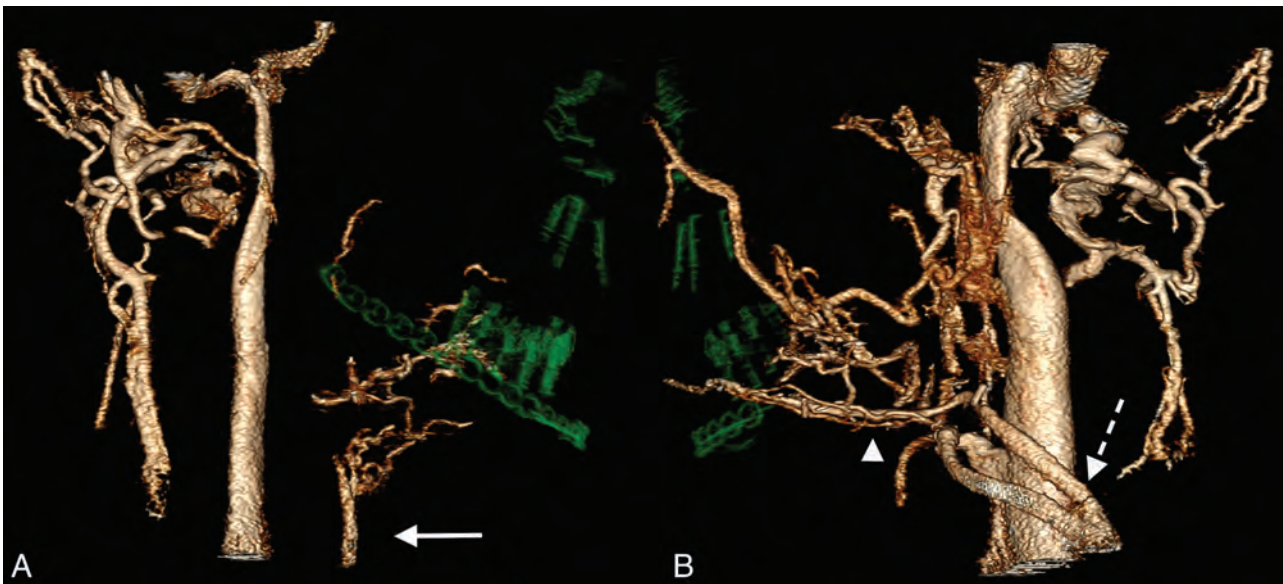


FIG 4. Volume-rendered venous-only reformatted images from a candidate who had a blast injury. *A*, Anterior and posterior facial veins and the external jugular vein are absent on the right, presumably from the injury. Imaging confirms the patency of the anterior jugular vein (*arrow*), a potential alternative for flap drainage. *B*, On the left, the external jugular vein (*dashed arrow*) and anterior facial vein (*arrowhead*) are available for flap drainage.

Major variations in branching patterns of the external carotid artery (3 types) and variations in the confluence of the facial, lingual, and superior thyroid veins with internal jugular vein (5 types)

Variant Type	Description
Arterial	
Noncommon trunk	Facial, lingual, and superior thyroid arteries arise separately from the ECA
Truncus linguofacialis	Facial and lingual arteries arise from the ECA in a common trunk
Truncus thyrolingualis	Superior thyroid and lingual arteries arise from the ECA in a common trunk
Venous	
Thyrolinguofacialis	Facial, lingual, and superior thyroid veins form a thyrolinguofacialis vein
Linguofacialis	Facial and lingual veins form a venous stem
Thyrofacialis	Facial and superior thyroid veins join together, and separate lingual vein joins into the IJV
Nonfacial vein	Superior thyroid and lingual veins join together into the IJV
Separation	Lingual and superior thyroid veins fuse independently with the IJV

Note:—ECA indicates external carotid artery; IJV, internal jugular vein.

available option. Both rat microsurgery studies and human vascular surgery studies have shown no differences in patency rates between end-to-end and end-to-side anastomoses.³⁴⁻³⁶ As the number of procedures and surgical approaches evolve, selection criteria will vary among surgeons, based on personal preferences and complex patient and donor presentations.

Surgical Controversies

There are 3 main controversies in face transplantation that influence preoperative CT acquisition and interpretation.

1) Is One Arterial Anastomosis Sufficient for Perfusion of a Full Face Allograft?

Increasing evidence suggests that 1 arterial anastomosis may be sufficient for tissue perfusion.^{8,9,37} However, bilateral single arterial anastomoses are prudent to minimize the risk of flap ischemia due possible anastomotic complications (blood clot, stenosis, and vascular compression from head rotation). Thus, as noted in the image

reformation section below, arterial maps should include all potential major branches from the external carotid system because of scar tissue and the potential for unexpected vascular findings at surgery.

2) Can the Facial Artery Alone Perfuse the Maxilla?

Cadaveric studies have suggested that the facial artery cannot adequately perfuse the maxilla.^{9,17} However, there is accumulating evidence that the facial artery can adequately perfuse both the entire maxilla and the mandible anteriorly from the insertion of the masseter muscle.^{37,38} A successful, defined by improved esthetic and functional outcome after surgery, facial transplantation suggests that the facial artery alone can perfuse a mid-facial allograft that includes the maxilla.⁸

3) Should Bilateral External Carotid Artery Anastomoses Be Performed?

We are cautious regarding bilateral end-to-end anastomoses because there is a presumed increased risk of ischemia in certain external carotid territories such as the hypopharynx.⁸ On the other hand, Meningaud et al⁹ have reported bilateral end-to-end external carotid artery anastomoses,⁷ suggesting that this is often the best option because of sufficient arterial length for cervical connections and the large diameter that is safer for anastomosis. Of note, these reports^{7,9} did not specify the exact location of the anastomoses, and the relationship to the lingual artery (ie, proximal or distal) was not clear. Although experience to date with bilateral external carotid artery anastomoses is largely anecdotal, there is a recognized risk of catastrophic ocular ischemia from

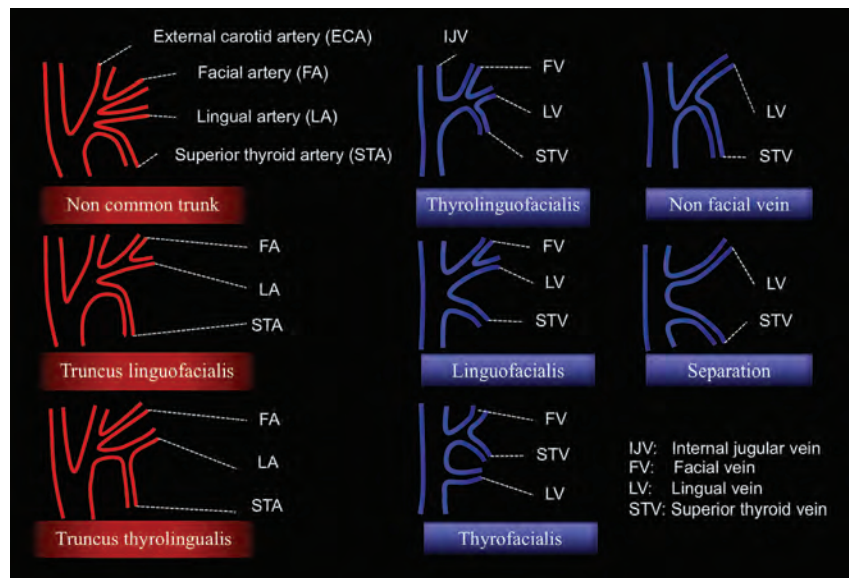


FIG 5. Major variations in branching patterns of the external carotid artery (3 types) and variations of the confluence of the facial, lingual, and superior thyroid veins with the internal jugular vein (5 types), described by Shima et al.²⁴ Descriptions of each variation are found in the Table.

anastomosis between the external carotid and the ophthalmic arteries.³⁹ Alizai et al⁴⁰ reported 2 cases of ocular ischemic syndrome due to bilateral external carotid artery occlusion.

IMAGING FOR PREOPERATIVE SURGICAL PLANNING

Rationale

We hypothesize that meticulous vascular mapping can reduce the procedure time, similar to results in breast reconstruction, by using abdominal perforator flaps⁴¹ and anterolateral thigh flaps.⁴² We also postulate that catastrophic iatrogenic vascular injury can be avoided with CTA and careful surgical planning. Of note, Liu et al⁴² demonstrated that preoperative CTA for patients undergoing an anterolateral thigh flap was associated with a significant reduction in major surgical complications, as well as the length of surgery and the need for a secondary debulking procedure. A shortened operation time enhances patient safety. Finally, although details regarding imaging and surgery related to bone allografts or prostheses are beyond the scope of this review, 3D and 2D reformatted CT is the best technique⁴³ to provide accurate assessment of severe bone defects,^{37,38} facilitating 3D understanding of skeletal stability, rotation, and displacement of bony fragments. Volumetric CT also enables 3D cephalometric measurements and creation of physical models of bones, which can be used for designing or improving bone allografts or prostheses.

CT Image Acquisition

Presurgical vascular mapping is challenging because the vessels are small, the FOV must be large enough to include the full extent of the external carotid artery and those branches that could be used for anastomoses, and there may be substantial metal artifacts (implants and shrapnel). In addition, patients are generally young, and thus cumulative radiation doses are a concern, particularly because both arterial and venous maps are needed.

At our institution, all surgical-planning CT images²³ are acquired axially with 320 × 0.5 mm detector row CT (Aquilion One; Toshiba Medical Systems, Tochigi-ken, Japan), which covers the

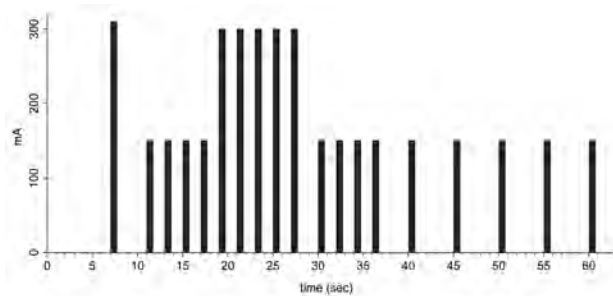


FIG 6. Timing diagram for a 320–detector row CT acquisition for face transplantation candidates. Each bar refers to 1 phase of the multiphase axial acquisition; each volume includes the entire anatomy required for surgical planning.

entire FOV,⁴⁴ to enable multiple phases by using intermittent dynamic volumes with a 0.75-second gantry rotation. The protocol (Fig 6), initially developed⁴⁵ for brain perfusion, includes pure arterial and venous volumes for input to postprocessing software. For patients with at least partial vision, the gantry is angulated to limit radiation to the orbits; and regarding the inferior aspect of the FOV, care is taken to limit radiation to the thyroid,⁴⁶ usually by limiting the craniocaudal coverage to 14 cm (280 × 0.5 mm detector row acquisition).

The contrast injection is timed by using a 20-mL test bolus to time the dual (EmpowerCTA; ACIST Medical, New York, New York) main injection (60-mL iopamidol, 370 mg I/mL, Isovue-370; Bracco Diagnostics, Princeton, New Jersey), followed by 40-mL normal saline.

CT Image Postprocessing

Volume rendering illustrates the spatial relationships between skin, soft tissues, vessels, and bones (Fig 7). Vascular overlays show the presurgical orientation of different facial structures (Fig 8) that are important for planning the dissection.

There are several considerations related to the anastomoses.

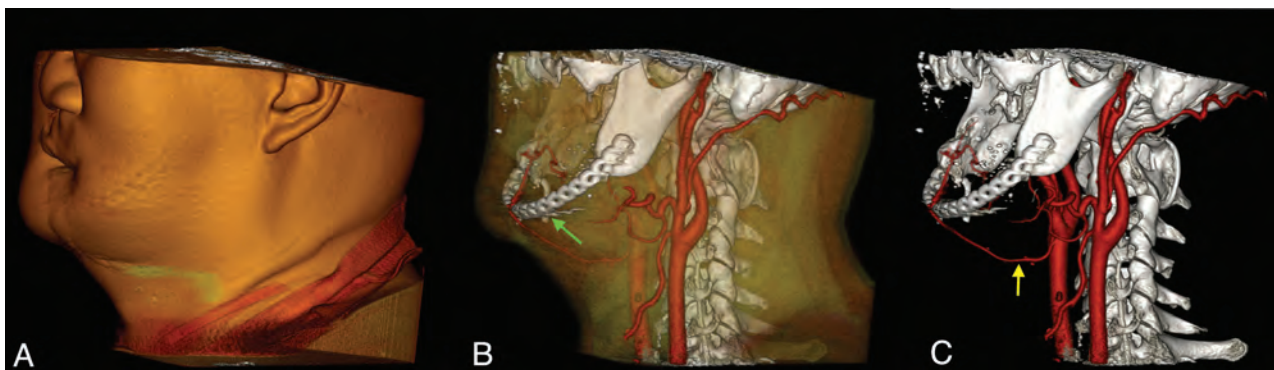


FIG 7. Candidate for full face transplantation. *A*, Volume-rendered image including full soft tissues. *B*, Skin and superficial soft tissues have been shadowed. This view depicts the relationship of the bones, postsurgical hardware (green arrow), and segmented arteries. *C*, Volume rendering that exclusively shows the bones, postsurgical hardware, and arteries. The superior thyroid artery (yellow arrow) is used for the anastomosis of free flap, and its surgically altered course is demonstrated.



FIG 8. Face transplantation candidate shown with fusion of the preoperative photograph and CT venography images. Meticulous CT segmentation and feature mapping are used to depict preoperative structures critical for rapid, precise, surgical dissection.

The course and branches of the external carotid artery should be documented. In our experience, it is important to map and annotate the facial, superior thyroid, lingual, and superficial temporal arteries (Fig 3*B*) because these are common targets for recipient vessels. Although there is often a close correlation between arteries and veins, venous drainage does not always parallel arterial territories.¹⁶ While the use of the external jugular and facial veins has been reported, there is a rich venous network, and preoperative imaging should include venous enhancement to identify all veins, including the anterior jugular vein, internal jugular vein, and vein grafts from prior procedures. Imaging characterization

includes patency, diameter, and variation. Vascular diameters are essential for surgical planning, and manual correction of vessel segmentation is required. Specifically, caliber changes and specific branching patterns must be meticulously illustrated to minimize the risk of complications and provide secondary and tertiary surgical options.

Regarding shrapnel, metal implants from prior reconstruction, and bone fragments from initial trauma, postprocessing considerations include the 3D spatial relationships of blood vessels and neighboring structures and the presence of artifacts. Multiplanar reformation, maximum intensity projections, and volume rendering define the 3D spatial relationships of blood vessels and neighboring structures. We routinely use multiobject segmentation (Vitrea fX 6.0; Vital Images, A Toshiba Medical Systems Group Company, Minnetonka, Minnesota) to portray the spatial relationships (Fig 9*B*). Metal artifacts can limit the assessment of blood vessels, though these artifacts are generally less severe than those in corresponding MR images.⁴⁷

4D volumes (3 spatial planes plus time) enable cine (Fig 3*C*) assessment of small-caliber vessels similar to that described in the lower extremity.⁴⁸ The drawback of multiphase CT is increased radiation exposure in comparison with fewer phases that could, in theory, give the same static information. However, preoperative acquisition of multiple phases largely ensures that essential pure arterial and venous images are available for postprocessing and interpretation. As in other high-flow body parts,⁴⁸ the timing for separation of small arteries versus veins can be challenging, particularly if there are unexpected findings such as a postinjury or postoperative fistula or asymmetric blood flow from injury or previous reconstructive surgeries. Thus, we advocate multiphase imaging, keeping in mind that the risks associated with life-long immunosuppression and the operation itself are far greater than those from surgical planning vascular CTA.

Future Directions

For most vascular mapping applications before transplantation,^{49,50} CT angiography has replaced invasive conventional angiography. The challenges for CT, namely small-caliber vessels, rapid transit time, and metal artifacts, also pose challenges for advanced MR imaging acquisitions. For face transplantation candidates, initial comparisons between time-resolved imaging^{51,52}

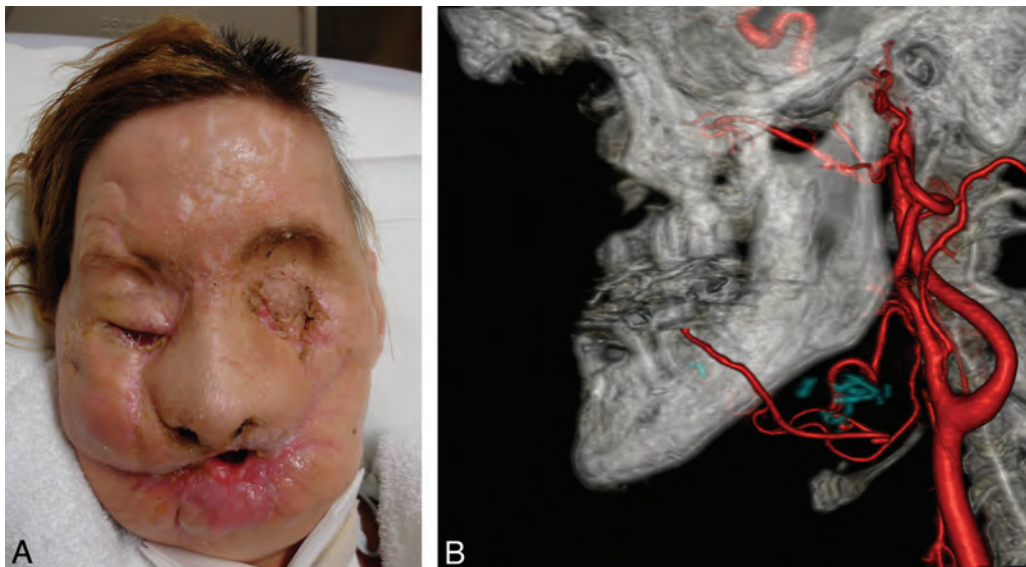


FIG 9. Candidate for full face transplantation who was attacked by a chimpanzee. *A*, Photograph of the victim after multiple conventional reconstructive surgeries for catastrophic facial injury, demonstrating the limitation of conventional surgical options. *B*, Volume-rendered reformations of CT images by using multiobject segmentation to rapidly communicate information to the surgical team. In red, the arteries, including the course of right facial artery, are clearly demonstrated. The facial artery was used for the anterolateral thigh flap immediately after the injury. The anastomosis can be identified via surgical clips rendered in green.

suggested the superiority of CT when compared to MR.⁴⁷ Moreover, axial wide-area-detector CT protocols provide datasets amenable for future studies of tissue perfusion after surgery and in the clinical setting of tissue rejection.

MR angiography is an attractive alternative for follow-up studies, particularly in patients with few metallic implants and thus relatively low susceptibility artifacts. For suspected complications, specialized imaging such as diffusion-weighted sequences for allograft function⁵³ and high-resolution vessel wall sequences^{54,55} for rejection can be performed. These can be complementary to 3D high-spatial-resolution MR angiography and time-resolved sequences for arterial and venous separation.

CONCLUSIONS

Face transplantation is now accepted as the only option for the most complex craniofacial reconstruction. With initial technical successes, the number of patients will continue to increase, emphasizing the need for radiologists to understand the surgical relevance, preoperative arterial and venous mapping, and current controversies regarding vascular anastomoses. Face transplantation candidates require complex CT protocols to depict arterial and venous imaging of the external carotid arteries and veins, their branches, and changes from severe facial injuries and prior attempts at reconstruction. The complexity of this process is reflected in the technical challenges of image acquisition and interpretation in patients with unexpected anatomy from severe deformity and prior surgical reconstructions. Meticulous communication between radiologists and surgeons related to vascular anastomoses will facilitate preoperative planning and optimization of the surgical technique.

Disclosures: Ericka Bueno—RELATED: Department of Defense,* Comments: U.S. Department of Defense research contract with my institution (Contract W911QY-09-C-021). David Enterline—UNRELATED: Consultancy: Bayer Healthcare, Dfine Inc, Grants/Grants Pending: Siemens Healthcare,* Guerbet Group,* Payment for Lec-

tures (including service on Speakers Bureaus): Bayer Healthcare, Bracco Diagnostics, Stock/Stock Options: Pioneer Surgical Technology, Medical Simulation Corp. Frank Rybicki—RELATED: Grant: United States Department of Defense,* Contract W911QY-09-C-021; grant support to the institution from Toshiba Medical Systems Corp. and Bracco Diagnostics. *Money paid to the institution.

REFERENCES

1. Spinelli HM, Jelks GW. **Periocular reconstruction: a systematic approach.** *Plast Reconstr Surg* 1993;91:1017–24, discussion 1025–26
2. Langstein HN, Robb GL. **Lip and perioral reconstruction.** *Clin Plast Surg* 2005;32:431–45, viii
3. Pomahac B, Pribaz J, Eriksson E, et al. **Three patients with full facial transplantation.** *N Engl J Med* 2012;366:715–22
4. Lengelé BG. **Current concepts and future challenges in facial transplantation.** *Clin Plast Surg* 2009;36:507–21
5. Meningaud JP, Paraskevas A, Ingallina F, et al. **Face transplant graft procurement: a preclinical and clinical study.** *Plast Reconstr Surg* 2008;122:1383–89
6. Siemionow MZ, Papay F, Djohan R, et al. **First US near-total human face transplantation: a paradigm shift for massive complex injuries.** *Plast Reconstr Surg* 2010;125:111–22
7. Lantieri L, Meningaud J, Grimbert P, et al. **Repair of the lower and middle parts of the face by composite tissue allotransplantation in a patient with massive plexiform neurofibroma: a 1-year follow-up study.** *Lancet* 2008;372:639–45
8. Pomahac B, Lengele B, Ridgway EB, et al. **Vascular considerations in composite midfacial allotransplantation.** *Plast Reconstr Surg* 2010;125:517–22
9. Meningaud JP, Benjoar MD, Hivelin M, et al. **Procurement of total human face graft for allotransplantation: a preclinical study and the first clinical case.** *Plast Reconstr Surg* 2010;126:1181–90
10. Rankin SC, Jan W, Koffman CG. **Noninvasive imaging of living related kidney donors: evaluation with CT angiography and gadolinium-enhanced MR angiography.** *AJR Am J Roentgenol* 2001;177:349–55
11. Kamel IR, Kruskal JB, Pomfret EA, et al. **Impact of multidetector CT on donor selection and surgical planning before living adult right lobe liver transplantation.** *AJR Am J Roentgenol* 2001;176:193–200
12. Caruso S. **Imaging in liver transplantation.** *World J Gastroenterol* 2009;15:675

13. Singh A, Sahani D. **Imaging of the renal donor and transplant recipient.** *Radiol Clin North Am* 2008;46:79–93, vi
14. Taylor GI, Palmer JH. “**Angiosome theory.**” *Br J Plast Surg* 1992;45:327–28
15. Taylor GI, Palmer JH. **The vascular territories (angiosomes) of the body: experimental study and clinical applications.** *Br J Plast Surg* 1987;40:113–41
16. Houseman ND, Taylor GI, Pan WR. **The angiosomes of the head and neck: anatomic study and clinical applications.** *Plast Reconstr Surg* 2000;105:2287–313
17. Banks ND, Hui-Chou HG, Tripathi S, et al. **An anatomical study of external carotid artery vascular territories in face and midface flaps for transplantation.** *Plast Reconstr Surg* 2009;123:1677–87
18. Jeng SF, Wei FC, Noordhoff MS. **Replantation of amputated facial tissues with microvascular anastomosis.** *Microsurgery* 1994;15:327–33
19. Hammond DC, Bouwense CL, Hankins WT, et al. **Microsurgical replantation of the amputated nose.** *Plast Reconstr Surg* 2000;105:2133–36, quiz 2137, discussion 2138
20. Blanco-Dávila F, Arrendondo G, De La Garza O, et al. **Anatomical study of the blood supply to the skin in rhytidectomy.** *Aesthetic Plast Surg* 1995;19:175–81
21. Yazar S. **Selection of recipient vessels in microsurgical free tissue reconstruction of head and neck defects.** *Microsurgery* 2007;27:588–94
22. Takamatsu A, Harashina T, Inoue T. **Selection of appropriate recipient vessels in difficult, microsurgical head and neck reconstruction.** *J Reconstr Microsurg* 1996;12:499–507; discussion 508–13
23. Soga S, Ersoy H, Mitsouras D, et al. **Surgical planning for composite tissue allotransplantation of the face using 320-detector row computed tomography.** *J Comput Assist Tomogr* 2010;34:766–69
24. Shima H, von Luedinghausen M, Ohno K, et al. **Anatomy of microvascular anastomosis in the neck.** *Plast Reconstr Surg* 1998;101:33–41
25. Taylor GI, Caddy CM, Watterson PA, et al. **The venous territories (venosomes) of the human body: experimental study and clinical implications.** *Plast Reconstr Surg* 1990;86:185–213
26. Nahabedian MY, Momen B, Manson PN. **Factors associated with anastomotic failure after microvascular reconstruction of the breast.** *Plast Reconstr Surg* 2004;114:74–82
27. Kubo T, Yano K, Hosokawa K. **Management of flaps with compromised venous outflow in head and neck microsurgical reconstruction.** *Microsurgery* 2002;22:391–95
28. Fisher CB, Mattox DE, Zinreich JS. **Patency of the internal jugular vein after functional neck dissection.** *Laryngoscope* 1988;98:923–27
29. Leontsinis TG, Currie AR, Mannell A. **Internal jugular vein thrombosis following functional neck dissection.** *Laryngoscope* 1995;105:169–74
30. Brown DH, Mulholland S, Yoo JH, et al. **Internal jugular vein thrombosis following modified neck dissection: implications for head and neck flap reconstruction.** *Head Neck* 1998;20:169–74
31. López-Monjardin H, de la Pena-Salcedo JA. **Techniques for management of size discrepancies in microvascular anastomosis.** *Microsurgery* 2000;20:162–66
32. Chuang DC, Jeng SF, Chen HT, et al. **Experience of 73 free groin flaps.** *Br J Plast Surg* 1992;45:81–85
33. Ploteau S, Rogez JM, Donnez J, et al. **Which are the ideal donor and recipient vessels for a whole ovarian transplantation?** *Fertil Steril* 2011;95:751–55
34. Miyamoto S, Takushima A, Okazaki M, et al. **Comparative study of different combinations of microvascular anastomosis types in a rat vasospasm model: versatility of end-to-side venous anastomosis in free tissue transfer for extremity reconstruction.** *J Trauma* 2009;66:831–34
35. Dotson RJ, Bishop AT, Wood MB, et al. **End-to-end versus end-to-side arterial anastomosis patency in microvascular surgery.** *Microsurgery* 1998;18:125–28
36. Schouten O, Hoedt MT, Wittens CH, et al. **End-to-end versus end-to-side distal anastomosis in femoropopliteal bypasses; results of a randomized multicenter trial.** *Eur J Vasc Endovasc Surg* 2005;29:457–62
37. Guo S, Han Y, Zhang X, et al. **Human facial allotransplantation: a 2-year follow-up study.** *Lancet* 2008;372:631–38
38. Siemionow M, Papay F, Alam D, et al. **Near-total human face transplantation for a severely disfigured patient in the USA.** *Lancet* 2009;374:203–09
39. Geibprasert S, Pongpech S, Armstrong D, et al. **Dangerous extracranial-intracranial anastomoses and supply to the cranial nerves: vessels the neurointerventionalist needs to know.** *AJNR Am J Neuroradiol* 2009;30:1459–68
40. Alizai AM, Trobe JD, Thompson BG, et al. **Ocular ischemic syndrome after occlusion of both external carotid arteries.** *J Neuroophthalmol* 2005;25:268–72
41. Masia J, Larranaga J, Clavero JA, et al. **The value of the multidetector row computed tomography for the preoperative planning of deep inferior epigastric artery perforator flap: our experience in 162 cases.** *Ann Plast Surg* 2008;60:29–36
42. Liu SC, Chiu WK, Chen SY, et al. **Comparison of surgical result of anterolateral thigh flap in reconstruction of through-and-through cheek defect with/without CT angiography guidance.** *J Craniomaxillofac Surg* 2011;39:633–38
43. Avery LL, Susarla SM, Novelline RA. **Multidetector and three-dimensional CT evaluation of the patient with maxillofacial injury.** *Radiol Clin N Am* 2011;49:183–203
44. Rybicki FJ, Otero HJ, Steigner ML, et al. **Initial evaluation of coronary images from 320-detector row computed tomography.** *Int J Cardiovasc Imaging* 2008;24:535–46
45. Yahyavi-Firouz-Abadi N, Wynn BL, Rybicki FJ, et al. **Steroid-responsive large vessel vasculitis: application of whole-brain 320-detector row dynamic volume CT angiography and perfusion.** *AJNR Am J Neuroradiol* 2009;30:1409–11
46. Shu KM, MacKenzie JD, Smith JB, et al. **Lowering the thyroid dose in screening examinations of the cervical spine.** *Emerg Radiol* 2006;12:133–36
47. Soga S, Pomahac B, Mitsouras D, et al. **Preoperative vascular mapping for facial allotransplantation: four-dimensional computed tomographic angiography versus magnetic resonance angiography.** *Plast Reconstr Surg* 2011;128:883–91
48. Sommer WH, Helck A, Bamberg F, et al. **Diagnostic value of time-resolved CT angiography for the lower leg.** *Eur Radiol* 2010;20:2876–81
49. Bueschen AJ, Lockhart ME. **Evolution of urological imaging.** *Int J Urol* 2011;18:102–12
50. Chen YS, Cheng YF, De Villa VH, et al. **Evaluation of living liver donors.** *Transplantation* 2003;75:516–19
51. Korosec FR, Frayne R, Grist TM, et al. **Time-resolved contrast-enhanced 3D MR angiography.** *Magn Reson Med* 1996;36:345–51
52. Ersoy H, Goldhaber SZ, Cai T, et al. **Time-resolved MR angiography: a primary screening examination of patients with suspected pulmonary embolism and contraindications to administration of iodinated contrast material.** *AJR Am J Roentgenol* 2007;188:1246–54
53. Eisenberger U, Thoeny HC, Binsler T, et al. **Evaluation of renal allograft function early after transplantation with diffusion-weighted MR imaging.** *Eur Radiol* 2010;20:1374–83
54. Mitsouras D, Owens CD, Conte MS, et al. **In vivo differentiation of two vessel wall layers in lower extremity peripheral vein bypass grafts: application of high-resolution inner-volume black blood 3D FSE.** *Magn Reson Med* 2009;62:607–15
55. Rybicki FJ, Mitsouras D, Owens CD, et al. **Multi-contrast high spatial resolution black blood inner volume three-dimensional fast spin echo MR imaging in peripheral vein bypass grafts.** *Int J Cardiovasc Imaging* 2010;26:683–91

Radiation Dose for 345 CT-Guided Interlaminar Lumbar Epidural Steroid Injections

A.L. Chang, A.H. Schoenfeld, A.L. Brook, and T.S. Miller

ABSTRACT

BACKGROUND AND PURPOSE: CT guidance is increasingly being used to localize the epidural space during epidural steroid injections. A common concern is that CT may be associated with significantly higher radiation doses compared with conventional fluoroscopy. The goal of this retrospective study was to determine the average dose-length product and effective dose delivered while interlaminar epidural steroid injections are performed and allow comparison with other modalities.

MATERIALS AND METHODS: A total of 281 patients who had undergone 345 consecutive CT-guided epidural steroid injections of the lumbar spine were evaluated for radiation exposure. The dose-length product for each scan was derived from the CT dose index volume and scan length. Effective dose was then calculated from the dose-length product and a κ coefficient of 0.015. Procedure time was calculated from the PACS time stamp on the scout image to the last CT image of the last image series.

RESULTS: The average dose-length product across all procedures was 89.6 ± 3.33 mGy·cm, which represents an effective dose of 1.34 ± 0.05 mSv. No complications from the procedure were observed, and average procedure time was 8 minutes.

CONCLUSIONS: The use of a stationary table and an intermittent scanning technique allow for short procedures and doses that are significantly lower than those of conventional diagnostic CT scans. Furthermore, because CT dose index overestimates radiation dose in stationary table procedures, the actual radiation dose may be even lower than stated here.

ABBREVIATIONS: CTDI = CT dose index; CTDI_{vol} = CTDI volume; DLP = dose-length product; ED = effective dose; ESI = epidural steroid injection

CT guidance has been increasingly adopted for use in interventional procedures of the spine, including epidural steroid injections (ESIs). ESIs are performed by injection of a corticosteroid solution, often with a local anesthetic, into the epidural space of the spine. This procedure is frequently used to treat radicular pain from herniated disks and spinal stenosis. CT offers several advantages versus traditional fluoroscopy, including the ability to visualize the soft tissues and provide higher anatomic precision and more accurate needle placements, and the option of using air instead of contrast medium to localize the epidural space.¹ Accurate localization of the epidural space and needle position during ESIs is crucial, as it facilitates precise delivery of medications and reduces the risks for needle misplacement and subsequent complications. Previous reports on blind injections have shown incor-

rect placement in up to 25% of cases, even when performed by experienced providers.² We recently reported our experience of safely performing 1000 procedures with CT guidance and air contrast to localize the epidural space.¹ The goal of this study was to analyze a cohort of similar patients to evaluate the dose-length product (DLP) and effective dose (ED) delivered while interlaminar ESI was being performed.

Review of CT Dose Index, Dose-Length Product, and Effective Dose

CT dose index (CTDI) is a commonly used measure of dose in CT dosimetry. It is defined by the formula

$$CTDI = \frac{1}{NT} \int_{-\infty}^{\infty} D(z) dz,$$

where N is the number of sections in a single axial scan, T is equivalent to the width of sections imaged by 1 channel of a multidetector row CT, and $D(z)$ represents the radiation dose profile along the z -axis of the scanner. CTDI is an estimate of the average dose to a central volume receiving contiguous scans along the z -axis

Received November 11, 2012; accepted after revision January 22, 2013.

From the Department of Radiology (A.L.C., A.H.S., A.L.B., T.S.M.), Montefiore Medical Center, Albert Einstein College of Medicine, Bronx, New York; and Department of Radiological Sciences (A.L.C.), University of California, Irvine, California.

Please address correspondence to Todd Miller, MD, Montefiore Medical Center Department of Radiology, 111 East 210th St, Bronx, New York, 10467; e-mail: tmiller@montefiore.org

<http://dx.doi.org/10.3174/ajnr.A3540>

and includes the contribution to the dose from overlap of dose tails.^{3,4} The measurement of CTDI is made with a pencil-shaped ionization chamber with a standard length of 100 mm in an acrylic cylindrical phantom, which gives rise to the definition of

$$CTDI_{100} = \frac{1}{NT} \int_{-50\text{ mm}}^{50\text{ mm}} D(z) dz.$$

Within the cylindrical phantom, the dose is higher at the periphery of a given section compared with the center, and a weighted version of $CTDI_{100}$ is defined as

$$CTDI_w = \frac{1}{3} CTDI_{100\text{ center}} + \frac{2}{3} CTDI_{100\text{ edge}},$$

which averages the dose over the field of view. A 16-cm diameter cylinder is used to measure $CTDI_w$ for head examinations, whereas a diameter of 32 cm is used for body examinations.

The most commonly used form of CTDI in dosimetry is $CTDI_{vol}$, which also incorporates the scanner's pitch into the dose estimate:

$$CTDI_{vol} = \frac{1}{pitch} CTDI_w$$

where

$$pitch = \frac{1}{NT}$$

and I represents the table increment in millimeters (mm) per axial scan. $CTDI_{vol}$ is easily calculated and is available in most scanner output dose tables. The SI unit of measurement of the dose is the milligray (mGy).

Because scans of greater physical length increase with the proportion of the body exposed to radiation and thus affect the radiation dose, the DLP was developed to incorporate scan length into the dose calculation: $DLP = CTDI_{vol} \times scan\ length\ (cm)$. The units of DLP are in milligray centimeters (mGy-cm) and represent the total energy absorbed in the scanned volume.

Lastly, one other common index in dosimetry is ED (measured in millisievert [mSv]), which takes into account that a given radiation dose has different effects on tissues with different sensitivities to radiation. The ED is defined as the summation of the dose to a series of organs multiplied by their weighting factors. However, in CT examinations, the ED can be approximated by the simplified relationship, $ED = \kappa \times DLP$, where κ is the conversion coefficient from DLP to ED. The value of the coefficient κ depends on the region of the body being scanned. Effective dose is most useful when used as a parameter to compare relative exposure/risk between different types of imaging studies.⁵

MATERIALS AND METHODS

Study Design

After receiving approval from the institutional review board, we conducted a retrospective review on 281 consecutive patients undergoing 345 CT-guided interlaminar ESIs in the lumbar spine at a single institution during an 8-month period. All procedures were performed by 1 of 3 interventional neuroradiologists who perform at least 500 CT-guided procedures annually. Patients were seen in an office consultation before the procedure, moni-

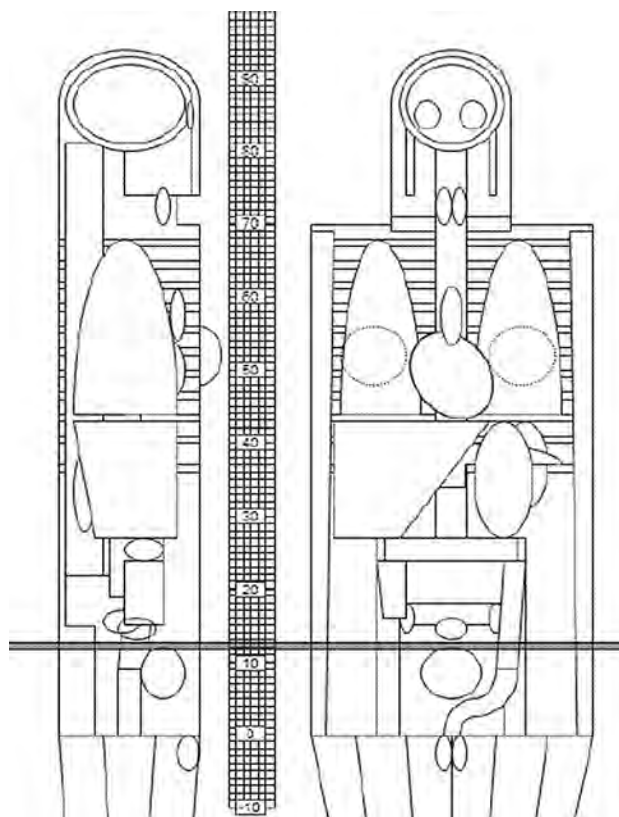


FIG 1. Approximate anatomic region used in ImPACT dosimetry software.

tored for 1 hour immediately after the procedure, contacted by phone at 24 hours, and seen in the office 1 month later.

There are several different modes possible with CT; one option is to use CT in a fluoroscopic mode, which provides continuous real-time image collection in a manner similar to traditional fluoroscopy. Another option is to use intermittent scans, where single images are taken serially, either with a foot pedal or remotely at the control station. These scans all occur on a stationary table, so that the same cross section is continually acquired. In our study, images were obtained by use of an intermittent scanning mode. The procedures were conducted at 120 kVp and 50 mA; in a few instances, the milliampere needed to be increased to provide better resolution in patients with a large body habitus.

$CTDI_{vol}$ and DLP displayed in the CT scanner dose report were recorded for each patient. The $CTDI_{vol}$ was also measured under standard conditions with acrylic phantoms and compared with the displayed value to verify its accuracy. The mean deviation of measured versus reported dose was +1.9% (range, -6% to +12% across scanners). The images for each patient were individually reviewed to ensure that each procedure was correctly categorized. We obtained procedure time by comparing the scout image with the last CT image.

Dose Calculations

Once the DLP had been collected for each individual case, an ED/DLP conversion coefficient was calculated from the ImPACT CT Patient Dosimetry Calculator version 1.0.2 (ImPACT, London, United Kingdom), a widely available spreadsheet in the ra-

List of all outliers at 2 SDs above the mean, and their causes

Patient No.	DLP (mGy·cm)	Scan Parameter	Cause
1	826.91	120 kVp 460 mA	Technical error, patient morbidly obese
2	551.78	120 kVp 150 mA	Patient morbidly obese
3	362.39	120 kVp 150 mA	Patient morbidly obese
4	319.39	120 kVp 100 mA	Patient morbidly obese
5	306.79	120 kVp 200 mA	Patient morbidly obese
6	257.26	120 kVp 100 mA	Patient morbidly obese, long procedure time
7	216.66	120 kVp 50 mA	Patient morbidly obese, technically difficult, long procedure time

radiation dosimetry community, and by using ICRP 103 weighting factors (Fig 1).⁶ By taking into account the affected organs and their specific weighting factors, we estimated the ED/DLP coefficient to be approximately 15 $\mu\text{Sv}/\text{mGy}\cdot\text{cm}$.^{7,8}

Technique

All procedures were performed with intermittent CT guidance by use of LightSpeed RT 16/LightSpeed Xtra scanners (GE Healthcare, Milwaukee, Wisconsin), with 120 kVp, 50 mA, and 0.8-second rotation time. Patients were placed in a prone position. The patient's back was then marked, prepped, and draped in the usual sterile manner. Several helical images through the target level were then performed to plan trajectory and identify an interruption between the laminae to allow the needle to reach the target epidural space from a posterior (dorsal interlaminar) approach. Lidocaine 2% was used to anesthetize the area, and a 22-gauge spinal needle was then advanced into the epidural space by use of an interlaminar approach. A 3-mL Luer-slip syringe with either 1 mL of air or contrast medium (iohexol 180 mg/mL) was attached to the spinal needle, and a loss-of-resistance technique was used to guide the needle past the ligamentum flavum, and air or iohexol was injected to identify the epidural space.¹ Additional axial images were then obtained to confirm correct placement of the needle. This was repeated until the epidural space was demonstrated with the injection. A steroid/anesthetic mixture of betamethasone sodium phosphate and betamethasone acetate (12–18 mg) and bupivacaine hydrochloride 0.5% (1–3 mL) was injected into the epidural space, and the needle was withdrawn ending the procedure. Any potential complications were recorded and reported according to Society of Interventional Radiology guidelines.⁹

RESULTS

A total of 281 patients underwent 345 CT-guided lumbar ESIs via an interlaminar approach. The average patient age was 59.7 years, 206 (59.7%) were women, and 139 (40.2%) were men. The mean DLP for all procedures was 89.6 ± 3.33 mGy·cm, and the median value was 78.34 mGy·cm. By use of the above-stated ED/DLP conversion factor (also known as the coefficient) of 15 $\mu\text{Sv}/\text{mGy}\cdot\text{cm}$, the obtained mean DLP converts to an estimated ED of 1.34 ± 0.05 mSv. Average procedure time was 8.4 ± 0.4 minutes, beginning from scout image acquisition to the last axial image acquired. No complications were observed during the procedure or at 1-month office follow-up.

DISCUSSION

The use of CT as a guidance technique for minimally invasive procedures has brought many advantages and innovations.

The traditional drawback to CT use has been its association with increased risk from higher radiation exposures than fluoroscopy.^{10,11} There are several reasons to quantify radiation exposure in lumbar ESIs. Multiple ESIs are not uncommon for pain relief in some patients, some of whom present at a relatively young age. Repeated radiation exposure over the same anatomic area can increase both deterministic and stochastic radiation-related risks, which makes the determination of exposure from any diagnostic or therapeutic study important.

In our study, the average DLP from use of an interlaminar approach for ESIs was 89.6 ± 3.33 mGy·cm while using an intermittent scanning mode. The conversion of our average DLP to ED by an ED/DLP factor of 15 $\mu\text{Sv}/\text{mGy}\cdot\text{cm}$ yields a value of 1.34 ± 0.05 mSv. By comparison, the average background radiation dose per person in the United States is approximately 3.11 mSv per year, and a regular CT of the abdomen/pelvis is approximately 10 mSv.¹² Intermittent scans also have the advantage of decreasing radiation exposure to the patient and operator,¹³ with the potential to completely eliminate exposure to the operator when image acquisition is initiated from within the shielded control station.

Our value compares favorably to lumbar radiographs in the lumbar spine, with an estimated 1–1.5 mSv in studies done in the United Kingdom, by the NRC, and by the UNSCEAR.^{12,14–16} Schmid et al¹⁷ conducted simulations by using Rando phantoms (The Phantom Library, Salem, New York) and estimated that the ED from 4–10 intermittent CT scans ranged from 1.51–3.53 mSv, with 4 scans estimated to be the average number necessary. Thus, our results are near the general predicted range. Schmid et al¹⁷ also found that 1–3 minutes of conventional fluoroscopy yielded an ED of 0.41–1.25 mSv, respectively, with 1 minute being the estimated average fluoroscopy time necessary. Kim et al¹⁸ also performed a study using phantoms to estimate ESI dose with conventional fluoroscopy and found an estimated ED of 0.93 mSv from a mean clinical procedure time of 40.7 seconds (range, 14.3–95.9 seconds).

Limited work has previously been done on the dose from CT fluoroscopy in ESI; however, Hoang et al¹⁹ recently compared CT fluoroscopy with conventional fluoroscopy in lumbar ESIs. They found that conventional fluoroscopy yielded 0.85 mSv from a mean exposure time of 37 seconds, whereas CT fluoroscopy yielded 0.45 mSv with exposure time of 4.7 seconds, though they also performed preliminary planning CTs, which added 2.90 mSv to produce a total dose of 3.35 mSv per procedure.¹⁹

A limitation of any study measuring radiation exposure involves the differences between studies in machine types, settings, and even operator skill, which can all affect the exposure time and dose. However, these studies do provide a useful context for understanding and comparing our results with known data on predicted doses for intermittent scans and conventional fluoroscopy.

A few values in our data were found to be causing a positive

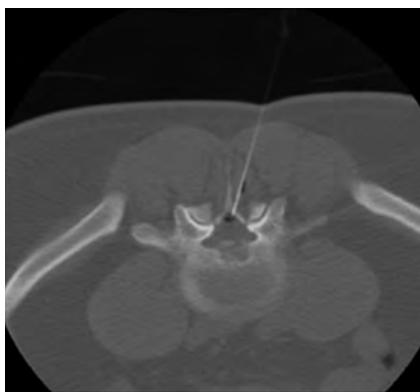


FIG 2. CT guidance used to localize the epidural space with adequate visualization by use of air contrast.

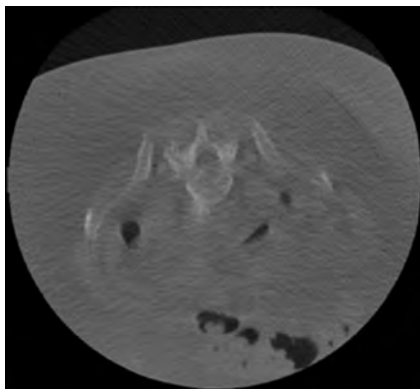


FIG 3. Limited resolution with 50 mA on a patient with a very large body habitus.

skew in our DLP; although the mean was 89.6 mGy·cm, the median value was 78.34 mGy·cm, and the DLP ranged from 11.67–826.91. When evaluating all cases both above and below 2 SDs of the mean, we found 6 outliers, all of which were greater than the mean. After reviewing these cases individually (Table), we determined that in most cases of high DLP, the tube current had been increased to improve poor resolution in images because of excessive soft tissue mass in obese patients. In other cases, technically difficult studies contributed to long procedure times and greater CT usage. In a single case, the tube current had been incorrectly set to a higher value used in diagnostic imaging. Any of these factors can increase the received dosage.

We observed several limitations to our study. First, it is important to note that the CT machines used in our study did not use the currently available iterative reconstruction techniques that may reduce the dose by 40%–70% without loss of image quality.²⁰

In addition, multiple factors could have caused overestimation of dose. High dose and time outliers typically occur in patients with a very large body habitus, where a higher milliamperage is required to maintain adequate image resolution (Figs 2 and 3).^{21,22} This also underscores that ED data should not be used to estimate any given person's individual risk as age and body habitus significantly alter their radiation exposure, but rather as a parameter to compare exposures across different studies and procedures.

A factor that can cause an overestimation of ED stems from how CTDI is defined. The definition of CTDI assumes that the table is incrementally advanced through a scan length, which does not apply to interventional procedures utilizing a stationary table. CTDI includes the dose tails resulting from scatter in the integration of the dose, and these dose tails are reduced when a stationary table is used. Several groups have measured the peak skin dose to be only 50%–65% of the stated $CTDI_{100}$.^{3,23,24} In fact, Leng et al²³ used a correction factor of $0.6 \times CTDI_{vol}$ to correct for the dose in interventional intermittent stationary table scans. This finding implies that the intermittent CT dose is potentially even lower than the result reported here. Without very thin thermoluminescent or solid-state dosimeters, it is difficult to know how much lower the actual dose is than when estimated by the CTDI, and doing so would be a next logical step for further research.

The future of CT guidance for procedures in the spine is promising. The ability of CT to provide precise 3D needle localization combined with the radiation exposure results seen here, along with ongoing research currently being conducted on dose reduction methods for CT guidance,²⁵ provides great future potential for the use of CT in spinal procedures.

CONCLUSIONS

The use of an intermittent scan mode can provide the advantages of CT guidance without necessarily subjecting the patient to excessive radiation; our study found an average ED of 1.34 ± 0.05 mSv per interlaminar ESI in the lumbar spine while using an intermittent scanning mode.

REFERENCES

1. Chang A, Pochert S, Romano C, et al. **Safety of 1000 CT-guided steroid injections with air used to localize the epidural space.** *AJNR Am J Neuroradiol* 2011;32:E175–177
2. White AH, Derby R, Wynne G. **Epidural injections for the diagnosis and treatment of low-back pain.** *Spine* 1980;5:78–86
3. Bauhs JA, Vrieze TJ, Primak AN, et al. **CT dosimetry: comparison of measurement techniques and devices.** *Radiographics* 2008;28:245–53
4. McCollough CH, Leng S, Yu L, et al. **CT dose index and patient dose: they are not the same thing.** *Radiology* 2011;259:311–16
5. American Association of Physicists in Medicine. *The Measurement, Reporting, and Management of Radiation Dose in CT.* College Park, MD: American Association of Physicists in Medicine; 2008. AAPM Report No. 96
6. **The 2007 Recommendations of the International Commission on Radiological Protection. ICRP publication 103.** *Ann ICRP* 2007;37:1–332
7. Miller TS, Fruauff K, Farinhas J, et al. **Lateral decubitus positioning for cervical nerve root block using CT image guidance minimizes effective radiation dose and procedural time.** *AJNR Am J Neuroradiol* 2013;34:23–28
8. Huda W, Ogden KM, Khorasani MR. **Converting dose-length product to effective dose at CT.** *Radiology* 2008;248:995–1003
9. Sacks D, McClenny TE, Cardella JF, et al. **Society of Interventional Radiology clinical practice guidelines.** *J Vasc Interv Radiol* 2003;14:S199–S202
10. Brenner DJ, Hall EJ. **Computed tomography—an increasing source of radiation exposure.** *N Engl J Med* 2007;357:2277–84
11. Mahesh M. **Fluoroscopy: patient radiation exposure issues.** *Radiographics* 2001;21:1033–45
12. National Council on Radiation Protection and Measurements. Report No. 160—Ionizing Radiation Exposure of the Population of the

United States (2009). Bethesda, MD: National Council on Radiation Protection and Measurements; 2009

13. Paulson EK, Sheafor DH, Enterline DS, et al. **CT fluoroscopy-guided interventional procedures: techniques and radiation dose to radiologists.** *Radiology* 2001;220:161–67
14. Alexander MD, Oliff MC, Olorunsola OG, et al. **Patient radiation exposure during diagnostic and therapeutic interventional neuro-radiology procedures.** *J Neurointerv Surg* 2010;2:6–10
15. Hart D, Wall BF. *Radiation Exposure of the UK Population from Medical and Dental X-Ray Examinations.* Chilton, UK: National Radiological Protection Board; 2002. Publication no. NRPB-W4
16. Simpson AK, Whang PG, Jonisch A, et al. **The radiation exposure associated with cervical and lumbar spine radiographs.** *J Spinal Disord Tech* 2008;21:409–12
17. Schmid G, Schmitz A, Borhardt D, et al. **Effective dose of CT- and fluoroscopy-guided perineural/epidural injections of the lumbar spine: a comparative study.** *Cardiovasc Intervent Radiol* 2006;29:84–91
18. Kim S, Toncheva G, Anderson-Evans C, et al. **Kerma area product method for effective dose estimation during lumbar epidural steroid injection procedures: phantom study.** *AJR Am J Roentgenol* 2009;192:1726–30
19. Hoang JK, Yoshizumi TT, Toncheva G, et al. **Radiation dose exposure for lumbar spine epidural steroid injections: a comparison of conventional fluoroscopy data and CT fluoroscopy techniques.** *AJR Am J Roentgenol* 2011;197:778–82
20. Schindera ST, Diedrichsen L, Müller HC, et al. **Iterative reconstruction algorithm for abdominal multidetector CT at different tube voltages: assessment of diagnostic accuracy, image quality, and radiation dose in a phantom study.** *Radiology* 2011;260:454–62
21. Uppot RN, Sahani DV, Hahn PF, et al. **Effect of obesity on image quality: fifteen-year longitudinal study for evaluation of dictated radiology reports.** *Radiology* 2006;240:435–39
22. Uppot RN, Sahani DV, Hahn PF, et al. **Impact of obesity on medical imaging and image-guided intervention.** *AJR Am J Roentgenol* 2007;188:433–40
23. Leng S, Christner JA, Carlson SK, et al. **Radiation dose levels for interventional CT procedures.** *AJR Am J Roentgenol* 2011;197:W97–103
24. Leng SV, Vrieze TJ, Lu Y, et al. **A direct skin dose calculation method in CT scans without table motion: influence of patient size and beam collimation.** *Med Phys* 2010;37:3110
25. Shepherd TM, Hess CP, Chin CT, et al. **Reducing patient radiation dose during CT-guided procedures: demonstration in spinal injections for pain.** *AJNR Am J Neuroradiol* 2011;32:1776–82

Alphabet Soup: Our Government “In-Action”

J.A. Hirsch, W.D. Donovan, G.N. Nicola, R.M. Barr, P.W. Schaefer, and E. Silva III

For radiology payment policy aficionados, a fascinating interplay of government agencies occurred this past year. Surprisingly, published discussions of these events are scant.¹ In this vignette, we will review a recent US Government Accountability Office (GAO) report, the subsequent Health and Human Services (HHS) response, and the role of several key government agencies.

In September 2012, the GAO presented Congress with a report titled “Higher Use of Advanced Imaging Services by Providers Who Self-Refer Costing Medicare Millions.”²

What Did the GAO Find?

The GAO report concluded the following:

1) Some factor or factors other than the health status of patients, provider practice size, or specialty or geographic location (ie, rural or urban) helped drive the higher advanced imaging referral rates among self-referring providers compared with non-self-referring providers.

2) Providers who began to self-refer advanced imaging services after purchasing or leasing imaging equipment or joining practices that self-referred substantially increased their referrals for MR imaging and CT services relative to other providers.

3) Financial incentives for self-referring providers may be a major factor driving the increase in referrals.

4) To the extent that these additional referrals are unnecessary, they pose an unacceptable risk for beneficiaries, particularly in the case of CT services, which involve the use of ionizing radiation.²

What Were the GAO Recommendations for Executive Action?

The GAO recommended that the administrator of the Centers for Medicare and Medicaid Services (CMS) take the following actions:

1) Insert a self-referral flag on its Medicare Part B claim form and require providers to indicate whether the advanced imaging services for which a provider bills Medicare are self-referred.

2) Determine and implement a payment reduction for self-referred advanced imaging services to recognize efficiencies when the same provider refers and performs a service.

3) Determine and implement an approach to ensure the appropriateness of advanced imaging services referred by self-referring providers.²

Given the degree of scrutiny directed toward health care costs in general and imaging volumes in particular, these recommendations would be expected to generate considerable interest. The problem of financially motivated self-referral has been previously documented across multiple modalities.³⁻⁵ As with these earlier published studies, the report supports the thesis that financially motivated self-referral is problematic. This report states that it costs the Medicare program millions in unnecessary costs and is harmful to Medicare beneficiaries.

How, in Fact, Did the Department of Health and Human Services Respond?

The US Department of Health and Human Services was provided the opportunity to respond to the GAO report before its formal publication. The GAO report stated, “HHS did not comment on our findings that self-referring providers referred substantially more advanced imaging services than nonself-referring providers or our conclusion that financial incentives for self-referring providers may be a major factor driving the increase in referrals for advanced imaging services.”²

The GAO further stated, “We are concerned that neither HHS nor CMS appears to recognize the need to monitor the self-referral of advanced imaging services on an ongoing basis and determine those services that may be inappropriate, unnecessary, or potentially harmful to beneficiaries.”²

Of the 3 GAO recommendations for executive action, HHS agreed only to “consider” the third GAO recommendation re-

Received April 23, 2013; accepted after revision May 7.

From the Neurovascular Program (J.A.H.), Massachusetts General Hospital, Harvard Medical School, Boston, Massachusetts; Norwich Diagnostic Imaging Associates (W.D.D.), Norwich, Connecticut; Hackensack University Medical Center (G.N.N.), Hackensack, New Jersey; Mecklenburg Radiology Associates (R.M.B.), Charlotte, North Carolina; Neuroradiology Division (P.W.S.), Massachusetts General Hospital, Boston, Massachusetts; and South Texas Radiology Group (E.S.), University of Texas at San Antonio, San Antonio, Texas.

Please address correspondence to Joshua A. Hirsch, Neuroendovascular Program, Massachusetts General Hospital, Harvard Medical School, Boston, MA 02114; e-mail: Hirsch@snisonline.org

<http://dx.doi.org/10.3174/ajnr.A3672>

Imaging on the same day as the office visit: wide variation in how frequently different types of imaging services were performed on same day as a related office visit, 2008^a

Type of Imaging	Proportion of Services Performed on the Same Day as the Office Visit
Advanced imaging	
MRI: brain	8.4%
MRI: other	8.2%
CT: head	23.8%
CT: other	13.1%
Nuclear medicine	8.5%
Echocardiography	25.9%
Other echography	28.4%
Standard imaging	50.9%
All imaging	35.4%

^a All imaging services in the Table are considered designated health services under the Stark self-referral law. The Table excludes the professional component of imaging services (unless it is part of a global service) and imaging performed in hospitals. Office visits include evaluation and management and consultation services provided in physicians' offices.⁸

garding determining and implementing a methodology to ensure the appropriateness of advanced imaging studies. HHS formally disagreed with the other 2 recommendations.

CMS provided 4 reasons for not taking action:

1) HHS believes that other payment reforms such as accountable care organizations and value-based purchasing programs (such as the physician value-based modifier) will better address overuse.

2) HHS mentioned the technical and professional component Multiple Procedure Payment Reduction Policy as having already addressed the self-referral problem.^{6,7}

3) HHS lacks statutory authority to act. HHS indicates that reducing payment for self-referred studies is statutorily prohibited because the Medicare statute prohibits paying a differential by physician specialty for the same service.

4) HHS believes that a new checkbox on the claim form identifying self-referral would be complex to administer.

The GAO Is Not Alone

The Medicare Payment Advisory Commission (MedPAC) has also produced a very similar analysis but stopped short of making formal recommendations in a June 2010 report.⁸ In this report, MedPAC issued an extensive critique of in-office self-referred imaging and highlighted several mechanisms it said were contributing to the growth in imaging volume. MedPAC suggestions to restrain in-office self-referral of imaging services included preauthorization, lower payment rates for high-volume self-referrers, excluding tests not provided during an office visit, and bundled payments for services.

The MedPAC analysis also highlighted a key revelation about in-office self-referred imaging. MedPAC data showed that in-office advanced imaging studies are rarely performed on the same day as an office visit, debunking the myth that in-office imaging primarily serves to improve patient convenience (Table).⁸

The GAO and MedPAC analyses have recently found support in the current White House administration. President Barack Obama recently released his proposed budget for fiscal year (FY) 2014. The FY 2014 budget recommends the exclusion of certain services, specifically advanced diagnostic imaging, radiation therapy, and physical therapy, from the in-office ancillary service ex-

emption to the Stark self-referral law. Although certain exemptions remain under President Obama's FY 2014 budget proposal, the acknowledgment of the advanced imaging/self-referral conundrum certainly highlights the abuse of this current Stark Law exemption.

What Is the GAO?

Established as the General Accounting Office as part of the Budget and Accounting Act of 1921, the GAO is tasked to "investigate...all matters relating to the receipt, disbursement, and application of public funds, and shall make to the President...and to Congress...reports [and] recommendations looking to greater economy or efficiency in public expenditures."⁹

The General Accounting Office was renamed the "Government Accountability Office" in 2004. According to the current mission statement of the GAO, the agency exists to support the Congress in meeting its constitutional responsibilities and to help improve the performance and ensure the accountability of the federal government for the benefit of the American people. The GAO can be thought of as an advocate for taxpayers in that its investigations have uncovered inefficiency and frank waste in government.

What Is HHS?

President Warren G. Harding proposed a Department of Education and Welfare as early as 1923. The Department was created 30 years later as the Department of Health, Education, and Welfare (HEW).¹⁰ In 1979, it was renamed the Department of Health and Human Services, as we know it today. HHS is administered by the Secretary (a cabinet-level position), who is appointed by the President with the advice and consent of the Senate. The current Secretary of HHS is Kathleen Sebelius.

What Is CMS?

President Johnson signed the Social Security Act on July 30, 1965. Among other things, this act established both Medicare and Medicaid. The Social Security Administration would administer Medicare, and the Social and Rehabilitation Service would administer Medicaid. Both agencies were organized under what was then known as the HEW, the forerunner of the present day HHS.

In 1977, the Health Care Financing Administration was established and became responsible for the coordination of both Medicare and Medicaid and was subsequently renamed the Centers for Medicare and Medicaid Services in 2001. CMS is a federal agency within the HHS that administers the Medicare program. Additionally, it collaborates with state governments to administer Medicaid, the State Children's Health Insurance Program, and health insurance portability standards. The current Acting Director of CMS is Marilyn Tavenner.

Since 1992, the CMS has benefited from physician input regarding physician work and practice expense values through the Relative Value Scale Update Committee of the American Medical Association—commonly known as the RUC. There is evidence that the formerly high esteem of CMS for the RUC process may be evolving—see related articles for further discussion.¹¹⁻¹⁴ The American Society of Neuroradiology (ASNR) has formally advised the RUC on issues pertinent to neuroradiology since

close to the time of its inception. It works in close association with the American College of Radiology, the Society of Interventional Radiology, and various other professional radiology and neurosurgical societies.

What Is MedPAC?

The Medicare Payment Advisory Commission is an independent congressional agency established by the Balanced Budget Act of 1997 to advise Congress on issues affecting the Medicare program. In addition to advising Congress on payments to private health plans participating in Medicare and providers in the traditional fee-for-service program of Medicare, MedPAC is also tasked with analyzing access to care, quality of care, and other issues affecting Medicare.

The Commission is made up of 17 members. Commissioners are appointed to 3-year terms (subject to renewal) by the Comptroller General and serve part-time. There is usually a minority of physician members—currently 5. MedPAC meets publicly to discuss policy issues and formulate its recommendations to Congress. Commission members and staff also seek input on Medicare issues through frequent meetings with individuals interested in the program, including staff from congressional committees and the CMS, health care researchers, health care providers, and beneficiary advocates.

Two reports—issued in March and June each year—are the primary outlet for Commission recommendations. In addition to these reports and others on subjects requested by Congress, MedPAC advises Congress through other avenues, including comments on reports and proposed regulations issued by the Secretary of the Department of Health and Human Services, testimony, and briefings for congressional staff.¹⁵

The authors of this article were gratified to see the GAO take such a clear and forthright stand on the issue of self-referral. The radiology community has argued many of these same points for years, with limited success.

On the other hand, the tepid response of HHS—agreeing to only consider 1 of 3 calls for executive action—is disheartening. We are hard-pressed to understand how HHS and CMS could seem so cavalier toward the recommendations of the GAO, an impartial organization whose very mission is to formally advise the federal government on issues of improving economy and efficiency in taxpayer expenditures.

We urge HHS and CMS to re-examine their stance on this issue and on the GAO report; we urge the radiology community to continue its pressure on lawmakers to take the GAO recommendations to heart, on behalf of taxpayers, in the interest of improved government efficiency, for improving health care outcomes, and ultimately on behalf of the patients we all serve.

ACKNOWLEDGMENTS

We would like to thank Mike Morrow, ASNR staff, for his review of this manuscript.

Disclosures: Joshua Hirsch—UNRELATED: Consultancy: CareFusion, Comments: I received fees for more than 12 months and less than 36 months for work related to vertebral augmentation, Stock/Stock Options: N-Focus, Intratech.

REFERENCES

1. Silva E 3rd. **How Medicare views self-referral.** *J Am Coll Radiol* 2013;10:168–69
2. US Government Accountability Office. **Medicare: higher use of advanced imaging services by providers who self-refer costing Medicare millions.** <http://www.gao.gov/assets/650/648989.pdf>. Published September 2012. Accessed April 10, 2013
3. Levin DC, Rao VM, Parker L, et al. **Ownership or leasing of CT scanners by nonradiologist physicians: a rapidly growing trend that raises concern about self-referral.** *J Am Coll Radiol* 2008; 5:1206–09
4. Agarwal R, Levin DC, Parker L, et al. **Trends in PET scanner ownership and leasing by nonradiologist physicians.** *J Am Coll Radiol* 2010;7:187–91
5. Levin DC, Rao VM, Parker L, et al. **Ownership or leasing of MRI facilities by nonradiologist physicians is a rapidly growing trend.** *J Am Coll Radiol* 2008;5:105–09
6. Silva E 3rd. **The PC MPPR: implications for practices.** *J Am Coll Radiol* 2012;9:311–12
7. Allen B Jr, Donovan WD, McGinty G, et al. **Professional component payment reductions for diagnostic imaging examinations when more than one service is rendered by the same provider in the same session: an analysis of relevant payment policy.** *J Am Coll Radiol* 2011;8:610–16
8. The Medicare Payment Advisory Commission. Report to Congress: Aligning Incentives in Medicare. http://www.medpac.gov/documents/jun10_entirereport.pdf. Published June 2010. Accessed April 10, 2013
9. Budget and Accounting Act of 1921. Public-No. 13. 67th Congress. J. 1084
10. Woolley J, Peters G, Dwight D. Eisenhower: 28-Special Message to the Congress Transmitting Reorganization Plan of 1953 Creating the Department of Health, Education, and Welfare. March 12, 1953. <http://www.presidency.ucsb.edu/ws/?pid=9794>. Accessed April 10, 2013
11. Hirsch JA, Silva E 3rd, Nicola GN, et al. **The RUC: a primer for neurointerventionalists.** *J Neurointerv Surg* 2013 Jan 18. [Epub ahead of print]
12. Hirsch JA, Donovan WD, Leslie-Mazwi TM, et al. **Component coding and the neurointerventionalist: a tale with an end.** *J Neurointerv Surg* 2012 Dec 19. [Epub ahead of print]
13. Donovan WD. **The resource-based relative value scale and neuroradiology: ASNR's history at the RUC.** *Neuroimag Clin N Am* 2012;22:421–36
14. Donovan WD. **What is the RUC?** *AJNR Am J Neuroradiol* 2011;32:1583–84
15. The Medicare Payment Advisory Commission. About MedPAC. <http://www.medpac.gov/about.cfm>. Accessed April 10, 2013

Geniculocalcarine Tract Disintegration after Ischemic Stroke: A Diffusion Tensor Imaging Study

Y. Zhang, S. Wan, and X. Zhang

ABSTRACT

BACKGROUND AND PURPOSE: Our aim was to investigate the disintegration of the geniculocalcarine tract by using DTI-derived parameters in cases of unilateral occipital or temporal-occipital ischemic stroke with geniculocalcarine tract involvement and to determine whether geniculocalcarine tract fibers affected by infarction and unaffected ipsilateral geniculocalcarine tract fibers have different disintegration processes.

MATERIALS AND METHODS: Seventy-one patients underwent routine MR imaging and DTI of the brain. Fractional anisotropy and mean diffusivity of the geniculocalcarine tract fibers affected by infarction, ipsilateral unaffected GCT fibers, and the contralateral geniculocalcarine tract were measured and compared at 5 different time points (from <1 week to >1 year) poststroke.

RESULTS: The fractional anisotropy of geniculocalcarine tract fibers affected by infarction (0.27 ± 0.06) was lower than that of contralateral GCT fibers (0.49 ± 0.03). The fractional anisotropy of geniculocalcarine tract fibers affected by infarction was not different in the first 3 weeks ($P = .306$). The mean diffusivity of geniculocalcarine tract fibers affected by infarction (0.53 ± 0.14) was lower than that of the contralateral GCT fibers (0.79 ± 0.07) in the first week but higher after the second week (0.95 ± 0.20 to 0.79 ± 0.06). The mean diffusivity gradually increased until it was equal to the mean diffusivity of CSF after the eighth week (2.43 ± 0.26), at which time both the fractional anisotropy and mean diffusivity values stabilized. The fractional anisotropy (0.50 ± 0.04) and mean diffusivity (0.77 ± 0.06) of the ipsilateral unaffected GCT fibers were similar to those of the contralateral GCT fibers (0.50 ± 0.03 and 0.79 ± 0.07) during the first 3 weeks. The fractional anisotropy then gradually decreased (from 0.42 ± 0.03 to 0.27 ± 0.05), while the mean diffusivity increased (from 0.95 ± 0.09 to 1.35 ± 0.11), though to a lesser degree than in the corresponding geniculocalcarine tract fibers affected by infarction.

CONCLUSIONS: The geniculocalcarine tract fibers affected by infarction and the ipsilateral unaffected GCT fibers showed different disintegration processes. The progressive disintegration of geniculocalcarine tract fibers affected by infarction was stable until the eighth week poststroke. The ipsilateral unaffected GCT fibers began to disintegrate at the fourth week, but to a lesser degree than the geniculocalcarine tract fibers affected by infarction.

ABBREVIATIONS: GCT = geniculocalcarine tract; CGCT = contralateral GCT fibers; FA = fractional anisotropy; MD = mean diffusivity; UGCT = ipsilateral unaffected GCT fibers

Structural imaging studies have identified the size and location¹⁻⁶ of lesions due to ischemic stroke in conjunction with DTI.⁷ DTI-derived measures are valid markers of ischemic pyra-

midal tract damage.⁸ The degree of functional motor deficit after a stroke is highly dependent on the overlap of lesions with the corticospinal tract.⁹ DTI studies also have established the relationship between motor impairment in acute phases and damage to the descending motor tracts.¹⁰⁻¹⁵ The integrity of the pyramidal tract and all of its descending tracts accounts for recovery after stroke.⁸ However, research has primarily concentrated on the pyramidal tract.¹⁶⁻¹⁸ Although a case describing vision recovery after a perinatal stroke as evidenced by functional and diffusion MR imaging has been reported,¹⁹ there are no data regarding disintegration of the GCT after an infarction.²⁰⁻²³ Understanding ischemic damage to the GCT and probable plasticity is important in determining the prognosis of vision impairment and recovery.

We used DTI-derived parameters to measure the GCT in 71 patients with unilateral occipital or temporal-occipital ischemic

Received August 1, 2012; accepted after revision January 31, 2013.

From the Zhongshan Ophthalmic Center (Y.Z.), State Key Laboratory of Ophthalmology, Sun Yat-sen University, Guangzhou, Guangdong, China; Department of Radiology (S.W.), Lu Shan Sanatorium, Nanjing Military Region, Jiu Jiang, Jiang Xi, China; Department of Radiology (X.Z.), Nan Fang Hospital, Southern Medical University, Guangzhou, Guangdong, China; and Department of Radiology (X.Z.), Kang Huang Hospital, Dongguan, Guangdong, China.

This work was supported by the Fundamental Research Funds of the State Key Laboratory of Ophthalmology.

Please address correspondence to Xuelin Zhang, MD, Department of Radiology, Nan Fang Hospital, Southern Medical University, Guangzhou, Guangdong, China, 510515; E-mail: zxlfnfy@163.com

<http://dx.doi.org/10.3174/ajnr.A3535>

stroke with GCT involvement. We evaluated the time course of GCT disintegration and hypothesized that GCT fibers affected by infarction and ipsilateral unaffected GCT fibers have different disintegration processes.

MATERIALS AND METHODS

Subjects

The study group consisted of 71 patients (41 men and 30 women; right-handed; age range, 39–89 years; mean age, 63.3 years). Only 1 MR imaging examination was performed in each patient. The time of MR imaging evaluation poststroke was 1 week in 26 patients, 2–3 weeks in 7 patients, 4–8 weeks in 7 patients, 8 weeks to 1 year in 15 patients, and >1 year in 16 patients. Inclusion criteria were the following: 1) occurrence of the first unilateral occipital or temporal-occipital ischemic stroke; 2) a single infarction lesion that involved the ipsilateral GCT in T1WI, T2WI, and FLAIR sequences; 3) no previous or subsequent cerebral ischemia or hemorrhage; 4) standard physical and occupational therapy poststroke; and 5) absence of other diseases affecting the nervous system.

The research protocol was approved by the Human Ethics Committee for Clinical Research at Southern Medical University (Guangzhou, China). All of the procedures involving the participants were conducted following the Declaration of Helsinki and institutional guidelines in compliance with the stated regulations. Oral and written informed consent was obtained from all participants.

Data Acquisition

MRI was performed by using a 1.5T scanner (Signa Twin; GE Healthcare, Milwaukee, Wisconsin) with an 8-channel phased array head coil. Magnetic field gradients permit up to 40-mT/m/s amplitude and a magnetic field gradient switching rate of up to 120 mT/m/s. The baseline scan was in the axial plane by using a standard head coil. Before and during scanning, head movement was limited by vacuum fixation cushions. All subjects underwent routine brain MR imaging, which included T1WI, T2WI, and FLAIR sequences. Consecutive sections in identical locations for all sequences were acquired with a section thickness of 5 mm. The parameters of T1WI FLAIR included TR/TI/TE, 2500/750/11.9 ms; section thickness, 5 mm; intersection separation, 1.5 mm; matrix size, 320 × 256; FOV, 240 × 180 mm; and double collections. The parameters of T2WI included TR/TE, 4900/99.3 ms; section thickness, 5 mm; intersection separation, 1.5 mm; matrix size, 320 × 224; FOV, 240 × 180 mm; and double collections. The parameters of T2WI FLAIR included TR/TE, 8500/128 ms; section thickness, 5 mm; intersection separation, 1.5 mm; matrix size, 320 × 192; FOV, 240 × 240 mm; and single collection.

DTI was performed in the axial plane by using a spin-echo EPI diffusion tensor sequence after routine MR imaging (TR/TE, 6000/60.1 ms; FOV, 240 × 240 mm; $b=1000$ s/mm²; NEX, 2; diffusion-sensitive gradient direction, 13; matrix size, 128 × 128; section thickness, 3.5 mm; intersection separation, 0 mm).

Data Analysis

DTI datasets were processed by using Volume One 1.72 (GE Healthcare) and diffusion tensor Visualizer 1.72 software (Tokyo

University, Tokyo, Japan) to obtain directionally encoded color, FA, and ADC images.

The GCT is a fiber tract from the lateral geniculate body, or the subcortex visual center, to the calcarine fissure of the occipital lobe. The afferent nerve fibers of the anterior visual pathway (optic nerve and optic tract) terminate at the dorsal lateral geniculate body, which is the nucleus of the lateral geniculate body ganglion cells, and transform neurons to form the GCT. The GCT passes through the inferior back of the internal capsule and the lenticular nucleus, along the lateral sagittal plane adjacent to the lateral ventricle and is shaped like a convex lamina.^{24,25} The GCT contains the anterior visual pathway afferent fibers and efferent nerve fibers from the occipital lobe to the lateral geniculate body, thalamus, and oculomotor nucleus.^{26,27}

ROIs were drawn on the axial directionally encoded color images. The lateral ventricle triangular-region planes (Fig 1A, yellow triangle) in which the GCT fibers were completely displayed as green fiber tracts adjacent to the lateral ventricles were selected. The infarction lesions were defined in the same planes of the T1WI and T2WI (Fig 1A, -C, -E, -G, brown masses). The ROIs on GCT fibers affected by infarction consisted of GCT fibers overlapped by the infarction lesion (Fig 1B, -D, -F, -H, white arrows). The unaffected GCT ROIs consisted of ipsilateral GCT fibers outside the infarction lesion (Fig 1B, -D, -F, -H, white triangles). The contralateral GCT ROIs were defined as the entire GCT in the contralateral unaffected hemisphere (Fig 1B, yellow circle). The FA and MD of the ROIs were calculated in 3 continuous planes and 3 different regions in each plane by the same observer to obtain a mean value. Calculations were made independently by 3 different observers to obtain the mean value.

Statistical Analysis

One-way ANOVA was used to evaluate the differences between the FA and MD of the GCT fibers affected by infarction, UGCT, and CGCT on the basis of time points after stroke. The least-significant-difference *t* test was used to compare the FA and MD between 2 different time points poststroke in GCT fibers affected by infarction, UGCT, and CGCT. $P < .05$ was used to determine statistical significance. All analyses were performed by using the Statistical Package for the Social Sciences software, Version 11.0 (SPSS, Chicago, Illinois).

RESULTS

In the GCT fibers affected by infarction, the FA (0.27 ± 0.06) was lower than the FA in the CGCT (0.49 ± 0.03) after the first week poststroke (Table and Fig 2). The FA within the first week (0.27 ± 0.06) was not different from the FA in the second-to-third weeks (0.29 ± 0.05 , $P = .306$). The FA values stabilized at 8 weeks to 1 year ($P = .643$). The FA values were significantly different between the different time points poststroke ($F = 62.152$, $P = .000$). The MD of the GCT fibers affected by infarction (0.53 ± 0.14) was lower than the MD of the CGCT (0.79 ± 0.07) in the first week poststroke but was higher after the second week (0.95 ± 0.20 and 0.79 ± 0.06 , respectively). The MD gradually increased (2.43 ± 0.26) until it was equal to the MD in the CSF after the eighth week ($P = .643$). The MD stabilized at 8 weeks to 1 year ($P = .087$). The

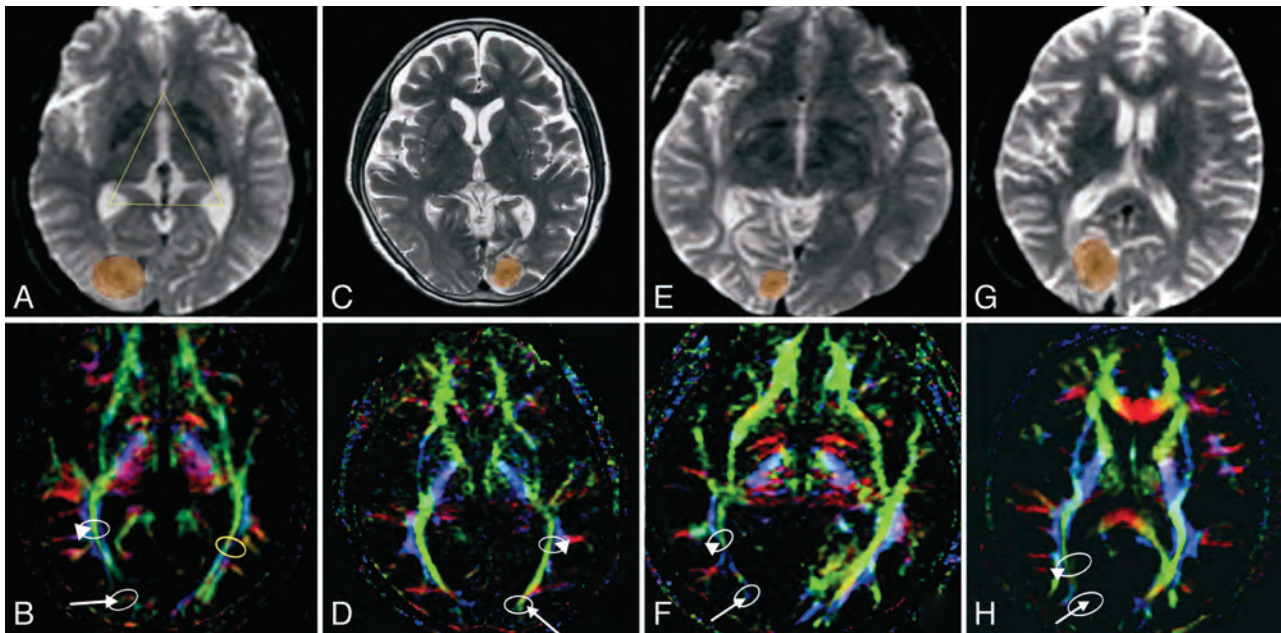


FIG 1. A and B, A 52-year-old man, 16 days postinfarction in the right occipital lobe. The infarcted GCT was hypointense (*arrow*), while the ipsilateral unaffected GCT (*triangle*) remained normal. C and D, A 68-year-old man, 6 weeks after infarction in the left occipital lobe. The infarcted GCT was hypointense (*arrow*), while the signal intensity of the unaffected GCT (*triangle*) decreased minimally. E and F, A 52-year-old man, 8 months after infarction in the right occipital lobe. The infarcted GCT (*arrow*) has vanished, while the ipsilateral unaffected GCT (*triangle*) is significantly hypointense. G and H, A 67-year-old woman, 5 years after infarction in the right occipital lobe. The infarcted GCT (*arrow*) has vanished. The ipsilateral unaffected GCT (*triangle*) is remarkably hypointense but complete.

Mean FA and MD values of GCT fibers affected by infarction, UGCT, and CGCT at different times after stroke^a

Time after Stroke	No.	Infarcted GCT Fibers		Unaffected GCT Fibers		Contralateral GCT Fibers	
		FA	MD	FA	MD	FA	MD
<1 Week	26	0.27 ± 0.06	0.53 ± 0.14	0.50 ± 0.03	0.78 ± 0.08	0.49 ± 0.03	0.79 ± 0.07
2~3 Weeks	7	0.29 ± 0.05	0.95 ± 0.20	0.49 ± 0.05	0.76 ± 0.04	0.50 ± 0.02	0.79 ± 0.06
4~8 Weeks	7	0.18 ± 0.07	1.88 ± 0.35	0.42 ± 0.03	0.95 ± 0.09	0.51 ± 0.02	0.77 ± 0.03
8 Weeks~1 year	15	0.08 ± 0.04	2.43 ± 0.26	0.31 ± 0.04	1.07 ± 0.11	0.49 ± 0.03	0.78 ± 0.08
>1 Year	16	0.08 ± 0.02	2.57 ± 0.24	0.27 ± 0.05	1.35 ± 0.11	0.49 ± 0.04	0.78 ± 0.09
F value		62.152	293.441	134.550	101.004	1.115	0.2222
P value		.000	.000	.000	.000	.357	.925

^a × 10⁻³ mm²/s.

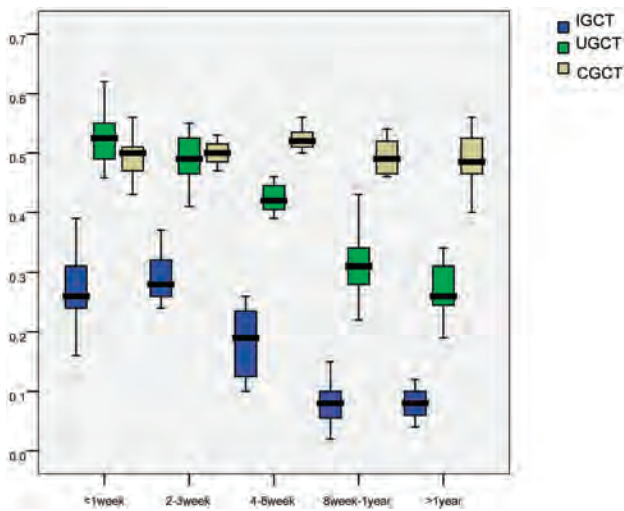


FIG 2. FA values of GCT fibers affected by infarction, UGCT, and CGCT at different times after stroke (× 10⁻³ mm²/s).

MD values were significantly different at the different time points poststroke ($F = 293.441, P = .000$).

In UGCT, the FA (0.50 ± 0.04) and MD (0.77 ± 0.06) were similar to the values in the CGCT (0.50 ± 0.03 and 0.79 ± 0.07 , respectively) during the first 3 weeks poststroke. From the fourth week, the FA gradually decreased (from 0.42 ± 0.03 to 0.27 ± 0.05), while the MD gradually increased (from 0.95 ± 0.09 to 1.35 ± 0.11) (Table and Fig 3). However, the ranges were lower compared with the GCT fibers affected by infarction at the corresponding time points. The FA and MD of the UGCT stabilized during the first 3 weeks ($P = .781, P = .686$, respectively). There were significant differences between the values at the different time points poststroke ($F = 134.550, P = .000; F = 101.004, P = .000$).

In the CGCT, there were no differences between the FA and MD values at the various time points poststroke ($F = 1.115, P = .357; F = 0.222, P = .925$, respectively).

In the first 3 weeks poststroke, the GCT fibers affected by infarction were significantly hypointense, while the UGCT had a

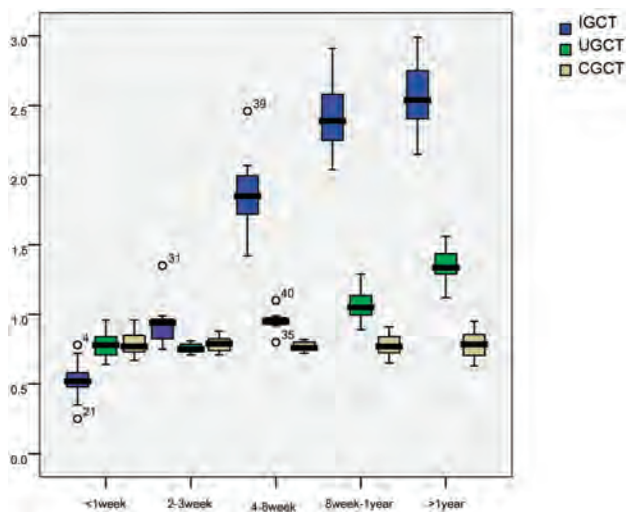


FIG 3. MD values of GCT fibers affected by infarction, UGCT, and CGCT at different times after stroke ($\times 10^{-3}$ mm²/s).

normal signal intensity and morphology (Fig 1A, -B). During the fourth-to-eighth weeks poststroke, the signal intensity of the UGCT gradually decreased, though their integrity remained intact (Fig 1C, -D). From the eighth week to 1 year poststroke, the GCT fibers affected by infarction had nearly disappeared, while the UGCT were significantly hypointense (Fig 1E, -F). The GCT fibers affected by infarction were absent after 1 year poststroke. The UGCT were remarkably hypointense but maintained their complete forms (Fig 1G, -H).

DISCUSSION

The FA of the GCT fibers affected by infarction was lower than that of the CGCT immediately after stroke onset (Table). Cells in the central infarcted area where blood flow is dramatically decreased die rapidly after ischemic occlusion. A series of delayed pathophysiologic reactions, including the ischemic cascade, reactions to inflammation, capillary dysfunction, blood-brain barrier damage, and ischemic reperfusion injuries cause necrosis and apoptosis of local neurons and astrocytes.²⁸ Degeneration initiates at the end of the distal axon and extends toward the neuron. The flow of information and substances terminates when the neuron is damaged. This phenomenon is known as Wallerian degeneration.²³ The GCT fibers in the infarction lesion develop Wallerian degeneration. Their axons degenerate and demyelinate at the same time. Reduced FA values in the GCT fibers affected by infarction suggest alterations in axonal attenuation and arrangement. The ordered axonal arrangements and the integrity of the myelin sheath are damaged in GCT fibers affected by infarction. With the disintegration of these barriers, the water molecules in the fiber tracts lose their directivity parallel to the fiber tract and present as a chaotic state.¹⁷ The FA values, which are significantly lower than the FA values of the CGCT, did not change during the first 3 weeks poststroke. This period may be an important phase of fiber disintegration and a critical time for intervention. The FA stabilized at 8 weeks to 1 year, suggesting that degeneration of the fibers ceased approximately 2 months after infarction.

During the first week poststroke, the GCT fibers affected by infarction had lower MD values than the CGCT. The MD reflects

changes in restrictive barriers of the fiber tracts, such as the axonal membrane, myelin sheath, and extracellular space.^{29,30} In the early stages of ischemic stroke, metabolic disorders in the cell induce an increase in intracellular osmotic pressure. Extracellular water enters the cell and causes edema. The volume of the cells increases, while the extracellular spaces decrease. The diffusion resistance increases, and the MD values are reduced. After the second week, the GCT fibers affected by infarction had higher MD values than the CGCT. The MD gradually increased and was equal to the MD of the CSF after the eighth week. During that time, the cellular structure disappeared when the swollen cells ruptured. The extracellular space and the water content of the tissues increased. The diffusion resistance decreased. The MD increased and was eventually equal to the MD of the CSF. This outcome suggests necrosis and tissue liquefaction.

There were no differences between the FA and MD of the UGCT and CGCT during the first 3 weeks. After the fourth week, the FA gradually decreased, while the MD gradually increased (Table). However, the ranges were lower compared with those of the GCT fibers affected by infarction. The degeneration and atrophy of the UGCT, including the disintegration, demyelination, and increased water content in the tissues, are a delayed minimal process compared with the GCT fibers affected by infarction. This suggests several approaches regarding the intervention and treatment of UGCT. First, the initial 3 weeks poststroke are a key phase for interventions because significant damage has not yet occurred. The degeneration of UGCT may be delayed or alleviated if effective interventions have been performed. Second, the FA and MD of the UGCT were not stabilized until 1 year after the infarction. Because the demyelination and degeneration of fibers in the unaffected GCT are chronic and continuous, the interventions and treatments for UGCT may last for a longer time. Third, additional research should focus on studying UGCT in the long term. Changes in the FA and MD may suggest possible modifications or plasticity of the fibers.

Diffusion indices may be valid markers of GCT integrity after ischemic stroke and predictors of vision prognosis.²⁰⁻²³ For example, MR tractography predicts visual field defects following temporal lobe resection.¹⁹ Vision recovery after perinatal stroke as evidenced by functional and diffusion MR imaging has also been shown.³¹ White matter reorganization is closely related to the status of axons, including axonal attenuation. The MR imaging diffusion entropy method primarily depends on axonal attenuation rather than axonal orientation and is a potentially useful measurement for detecting white matter reorganization.^{1,32} These techniques assist in investigating complex crossing fibers and white matter plasticity, which contributes to our ultimate goal of vision recovery after ischemic stroke.

CONCLUSIONS

In this study, we explored changes in GCT fiber integrity by investigating the mean FA and MD from 1 week until >1 year after stroke onset. Diffusion indices provide information on the underlying microanatomic or pathologic changes in white matter fiber bundles.^{25,26,33,34} The GCT fibers affected by infarction and UGCT undergo different processes of disintegration. The GCT fibers affected by infarction disintegrated from stroke onset until

the eighth week poststroke. The UGCT did not disintegrate until the fourth week poststroke, though to a lesser degree than the GCT fibers affected by infarction. DTI-derived measures are valid markers of geniculocalcarine tract integrity after ischemic stroke.

REFERENCES

- Mohr JP, Foulkes MA, Polis AT, et al. **Infarct topography and hemiparesis profiles with cerebral convexity infarction: the Stroke Data Bank.** *J Neurol Neurosurg Psychiatry* 1993;56:344–51
- Saver JL, Johnston KC, Homer D, et al. **Infarct volume as a surrogate or auxiliary outcome measure in ischemic stroke clinical trials.** *Stroke* 1999;30:293–98
- Binkofski F, Seitz RJ, Arnold S, et al. **Thalamic metabolism and corticospinal tract integrity determine motor recovery in stroke.** *Ann Neurol* 1996;39:460–70
- Crafton KR, Mark AN, Cramer SC. **Improved understanding of cortical injury by incorporating measures of functional anatomy.** *Brain* 2003;126:1650–59
- Schiemanck SK, Kwakkel G, Post MW, et al. **Impact of internal capsule lesions on outcome of motor hand function at one year post-stroke.** *J Rehabil Med* 2008;40:96–101
- Shelton FN, Reding MJ. **Effect of lesion location on upper limb motor recovery after stroke.** *Stroke* 2001;32:107–12
- Ciccarelli O, Catani M, Johansen-Berg H, et al. **Diffusion-based tractography in neurological disorders: concepts, applications, and future developments.** *Lancet Neurol* 2008;7:715–27
- Lindenberg R, Renga V, Zhu LL, et al. **Structural integrity of corticospinal motor fibers predicts motor impairment in chronic stroke.** *Neurology* 2010;74:280–87
- Zhu LL, Lindenberg R, Michael P, et al. **Lesion load of the corticospinal tract predicts motor impairment in chronic stroke.** *Stroke* 2010;41:910–15
- Jang SH, Bai D, Son SM, et al. **Motor outcome prediction using diffusion tensor tractography in pontine infarct.** *Ann Neurol* 2008;64:460–65
- Kunimatsu A, Aoki S, Masutani Y, et al. **Three-dimensional white matter tractography by diffusion tensor imaging in ischaemic stroke involving the corticospinal tract.** *Neuroradiology* 2003;45:532–35
- Yamada K, Mori S, Nakamura H, et al. **Fiber tracking method reveals sensor motor pathway involvement in stroke patients.** *Stroke* 2003;34:E159–62
- Konishi J, Yamada K, Kizu O, et al. **MR tractography for the evaluation of the functional recovery from lenticulostriate infarcts.** *Neurology* 2005;64:108–13
- Nelles M, Gieseke J, Flacke S, et al. **Diffusion tensor pyramidal tractography in patients with anterior choroidal artery infarcts.** *AJNR Am J Neuroradiol* 2008;29:488–93
- Kunimatsu A, Itoh D, Nakata Y, et al. **Utilization of diffusion tensor tractography in combination with spatial normalization to assess involvement of the corticospinal tract in capsular/pericapsular stroke.** *J Magn Reson Imaging* 2007;26:1399–404
- Puig J, Pedraza S, Blasco G, et al. **Acute damage to the posterior limb of the internal capsule on diffusion tensor tractography as an early imaging predictor of motor outcome after stroke.** *AJNR Am J Neuroradiol* 2011;32:857–63
- Radlinska B, Ghinani S, Leppert IR, et al. **Diffusion tensor imaging, permanent pyramidal tract damage, and outcome in subcortical stroke.** *Neurology* 2010;75:1048–54
- Schaechter JD, Fricker ZP, Perdue KL, et al. **Microstructural status of ipsilesional and contralesional corticospinal tract correlates with motor skill in chronic stroke patients.** *Hum Brain Mapp* 2009;30:3461–74
- Seghier ML, Lazeyras F, Zimine S, et al. **Visual recovery after perinatal stroke evidenced by functional and diffusion MRI: case report.** *BMC Neurol* 2005;26:5:17
- Wieshmann UC, Symms MR, Clark CA, et al. **Wallerian degeneration in the optic radiation after temporal lobectomy demonstrated in vivo with diffusion tensor imaging.** *Epilepsia* 1999;40:1155–58
- Werring DJ, Clark CA, Parker GJ, et al. **A direct demonstration of both structure and function in the visual system: combining diffusion tensor imaging with functional magnetic resonance imaging.** *Neuroimage* 1999;9:352–61
- Yamamoto A, Miki Y, Urayama S, et al. **Diffusion tensor fiber tractography of the optic radiation: analysis with 6-, 12-, 40-, and 81-directional motion-probing gradients, a preliminary study.** *AJNR Am J Neuroradiol* 2007;28:92–96
- Yamamoto T, Yamada K, Nishimura T, et al. **Tractography to depict three layers of visual field trajectories to the calcarine gyri.** *Am J Ophthalmol* 2005;140:781–85
- Miller NR. **Diffusion tensor imaging of the visual sensory pathway: are we there yet?** *Am J Ophthalmol* 2005;140:896–97
- Wan SH, Zhang XL, Xie XL. **The initial clinical application of MR- DTI and DTT in the adult optic radiation.** *J Clin Radiol* 2007;26:1076–79
- Tong Y. **Neuro-ophthalmology.** In: Ge J, ed. *Ophthalmology.* Beijing: People's Medical Publishing House; 2005:323–25
- Zeng LF. **Visual pathway and visual center.** In: Li FM, ed. *Chinese Ophthalmology.* Vol 1. 2nd ed. Beijing: People's Medical Publishing House; 2005:180–90
- Dong Q. **Atherosclerosis cerebral infarction.** In: Chen JZ, ed. *Practice of Internal Medicine.* Vol 2. 12th ed. Beijing: People's Medical Publishing House; 2007:2669–74
- Le Bihan D. **Looking into the functional architecture of the brain with diffusion MRI.** *Nat Rev Neurosci* 2003;4:469–80
- Pierpaoli C, Basser PJ. **Towards a quantitative assessment of diffusion anisotropy.** *Magn Reson Med* 1996;36:893–906
- Powell HW, Parker GJ, Alexander DC, et al. **MR tractography predicts visual field defects following temporal lobe resection.** *Neurology* 2005;65:596–99
- Jiang Q, Zhang ZG, Chopp M. **MRI evaluation of white matter recovery after brain injury.** *Stroke* 2010;41:S112–13
- Chanraud S, Zahr N, Sullivan EV, et al. **MR diffusion tensor imaging: a window into white matter integrity of the working brain.** *Neuropsychol Rev* 2010;20:209–25
- Parekh MB, Carney PR, Sepulveda H, et al. **Early MR diffusion and relaxation changes in the parahippocampal gyrus precede the onset of spontaneous seizures in an animal model of chronic limbic epilepsy.** *Exp Neurol* 2010;224:258–70

Association of CT Perfusion Parameters with Hemorrhagic Transformation in Acute Ischemic Stroke

A.R. Jain, M. Jain, A.R. Kanthala, D. Damania, L.G. Stead, H.Z. Wang, and B.S. Jahromi



ABSTRACT

BACKGROUND AND PURPOSE: Prediction of hemorrhagic transformation in acute ischemic stroke could help determine treatment and prognostication. With increasing numbers of patients with acute ischemic stroke undergoing multimodal CT imaging, we examined whether CT perfusion could predict hemorrhagic transformation in acute ischemic stroke.

MATERIALS AND METHODS: Patients with acute ischemic stroke who underwent CTP scanning within 12 hours of symptom onset were examined. Patients with and without hemorrhagic transformation were defined as cases and controls, respectively, and were matched as to IV rtPA administration and presentation NIHSS score (± 2). Relative mean transit time, relative CBF, and relative CBV values were calculated from CTP maps and normalized to the contralateral side. Receiver operating characteristic analysis curves were created, and threshold values for significant CTP parameters were obtained to predict hemorrhagic transformation.

RESULTS: Of 83 patients with acute ischemic stroke, 16 developed hemorrhagic transformation (19.28%). By matching, 38 controls were found for only 14 patients with hemorrhagic transformation. Among the matched patients with hemorrhagic transformation, 13 developed hemorrhagic infarction (6 hemorrhagic infarction 1 and 7 hemorrhagic infarction 2) and 1 developed parenchymal hematoma 2. There was no significant difference between cases and controls with respect to age, sex, time to presentation from symptom onset, and comorbidities. Cases had significantly lower median rCBV (8% lower) compared with controls (11% higher) ($P = .009$; odds ratio, 1.14 for a 0.1-U decrease in rCBV). There was no difference in median total volume of ischemia, rMTT, and rCBF among cases and controls. The area under the receiver operating characteristic was computed to be 0.83 (standard error, 0.08), with a cutoff point for rCBV of 1.09.

CONCLUSIONS: Of the examined CTP parameters, only lower rCBV was found to be significantly associated with a relatively higher chance of hemorrhagic transformation.

ABBREVIATIONS: AIS = acute ischemic stroke; rCBF = relative cerebral blood flow; rCBV = relative cerebral blood volume; HI = hemorrhagic infarction; HT = hemorrhagic transformation; IQR = interquartile range; rMTT = relative mean transit time; ROC = receiver operating characteristic analysis; PH = parenchymal hematoma

Stroke accounts for 1 in every 18 deaths in the United States,¹ leaving nearly 30% of patients permanently disabled.² Worldwide, stroke is a leading cause of disability and the fourth leading cause of mortality with 6.15 million deaths reported annually.³ In the United States alone, nearly 800,000 individuals have stroke each year, with a quarter of those being recurrent strokes.^{1,4}

Many advances have been made in stroke prevention, imag-

ing, and treatment during the past 20 years. The advent of IV rtPA for AIS in 1995 has improved outcomes for patients presenting within 3 hours,⁵ and with ongoing research, the time window for intravenous thrombolysis has been expanded.⁶⁻⁸ However, the use of IV rtPA at >3 hours also carries increased risk of hemorrhagic transformation,⁹ which remains a serious complication of ischemic stroke management and occurs in 4%–22% of patients with stroke.^{5,10,11} HT can be asymptomatic or symptomatic in 3%–25% of cases with resulting worsened outcome.¹² Ongoing effort to find predictors of HT has yielded various factors, including the etiology of stroke, extent of infarction on initial CT, increasing stroke severity (NIHSS score), increasing age, congestive heart failure, high glucose levels, and blood pressure on presentation.^{11,13-17} Serum markers such as matrix metalloproteinase-9 levels¹⁸; imaging modalities such as CT,¹⁹ SPECT,²⁰ MR imaging,²¹ diffusion- and perfusion-weighted

Received May 18, 2012; accepted after revision December 16.

From the Departments of Neurosurgery (A.R.J., M.J., A.R.K., D.D., B.S.J.) and Imaging Sciences (H.Z.W.), University of Rochester Medical Center, Rochester, New York; and Departments of Emergency Medicine and Neurological Surgery (L.G.S.), University of Florida College of Medicine, Gainesville, Florida.

Please address correspondence to Minal Jain, MBBS, MPH, Department of Neurosurgery, University of Rochester, 601 Elmwood Ave, Box 670, Rochester NY 14642; e-mail: minal_jain@urmc.rochester.edu

Indicates open access to non-subscribers at www.ajnr.org

<http://dx.doi.org/10.3174/ajnr.A3502>

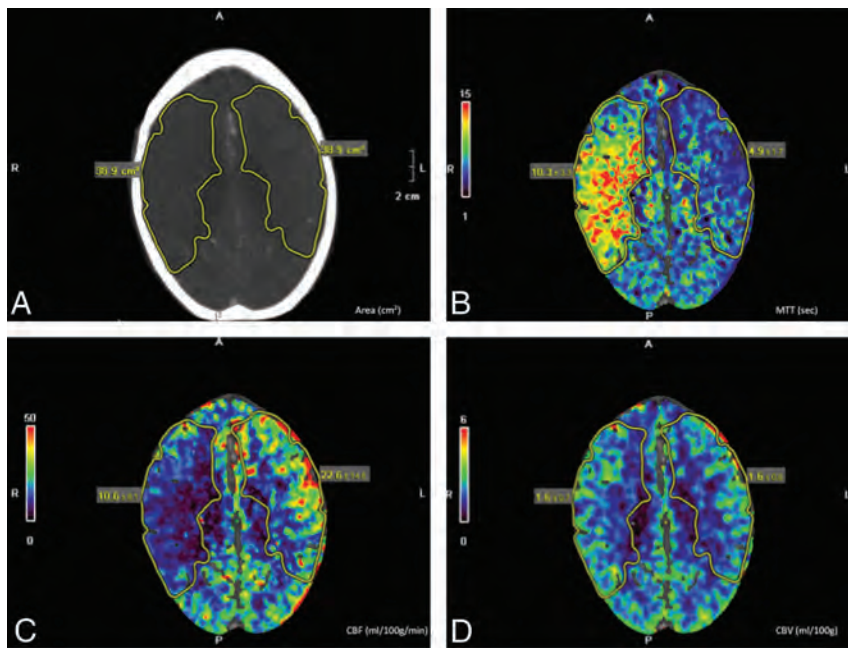


FIG 1. CTP maps. A, volume at risk of ischemia (volume computed from the area and thickness of each section [5 mm]). B, MTT. C, CBF. D, CBV. CTP images of a patient with AIS with right MCA occlusion. rMTT, rCBF, and rCBV are computed by normalizing MTT, CBF, and CBV of the ischemic area to the contralateral normal side. The outlined region of interest shows increased MTT, decreased CBF, and preserved CBV in each respective panel.

Table 1: Characteristics of study cohort

Characteristics	Total Patients (n = 83)
Female (No.) (%)	37 (44.6%)
Age (yr) (median) (IQR)	72 (61–80)
Time (min) to arrival (median) (IQR)	124 (64–314)
Stroke severity on arrival (NIHSS) (median) (IQR)	7 (3–15)
Medical history	
Hypertension	77.8%
Diabetes	26.8%
Dyslipidemia	52.4%
Stroke/TIA	34.9%
Coronary artery disease	24.4%
Medication history	
Antiplatelets	45.0%
Anticoagulants	10.1%
Thrombolysis done	27.7%
Functional outcome (mRS) at discharge (median) (IQR)	3 (1–5)
Duration (days) of hospital stay (median) (IQR)	5 (3–8)

MR imaging²²; and blood-brain barrier permeability measures on CTP²³ are also under investigation to formulate predictive models for HT.

In this study, we sought to investigate the hypothesis that there are inherent characteristics of ischemic brain tissue measurable by CTP that might predict hemorrhagic transformation. We evaluated the value of CBV, CBF, MTT, and volume of affected brain tissue toward prediction of HT in ischemic stroke.

MATERIALS AND METHODS

This was an institutional review board–approved study conducted at a single academic stroke center receiving >700 patients

with ischemic stroke/TIA annually. The study extended from July 2009 to February 2010, and a cohort of all adult patients presenting with symptoms consistent with stroke/TIA within 12 hours of onset who underwent emergent CTP imaging was selected. At our institution, all patients with stroke presenting within 12 hours of symptom onset undergo CTP imaging. Patients with contraindications to CTP (ie, anaphylactic reaction to contrast, patients with known poor kidney function) were excluded. In addition, patients with a final diagnosis of TIA and those with infratentorial/bilateral/lacunar strokes were excluded. In this study, only patients with a discharge diagnosis of AIS were included in the final cohort.

The medical records were reviewed to obtain age, sex, medical history (hypertension, diabetes, dyslipidemia, coronary artery disease, TIA, stroke), smoking history, medication use, signs and symptoms on arrival, stroke severity at presentation (NIHSS score), use of IV rtPA and endovascular therapy, in-hospital outcome, and functional status on discharge (measured by the mRS). Follow-up noncontrast CT or MR imaging or both were reviewed to document the development of hemorrhagic transformation. “HT” was defined according to the European Cooperative Acute Stroke Study on NCCT as an area of increased attenuation within an area of low attenuation in a typical vascular distribution.²⁴ On MR imaging, HT was identified by the presence of blood-product signal characteristics on T1, T2, and gradient-echo sequences. “Hemorrhagic transformation” was defined as per the European Cooperative Acute Stroke Study I and II trials and was classified as HI and PH.^{15,24,25} This was further subdivided into HI 1 and HI 2 and PH 1 and PH 2. “HI 1” was defined as small petechiae along the peripheral margins of infarct. Confluent petechiae within the infarcted region but without mass effect were classified as HI 2. “PH 1” was defined as hematoma with a mass effect of <30% of the infarcted volume, and a PH with a mass effect of >30% of infarct volume was classified as PH 2.

The CTP imaging studies of every research patient were analyzed. CTP images were processed by using Vitrea software (Vital Images, Minnetonka, Minnesota) by using a delay-insensitive algorithm (see “Imaging Protocol” below for further details). A freehand region of interest was used to outline the total brain tissue at risk of ischemia as defined by increased MTT and corresponding decreased CBF. A mirrored region of interest was automatically generated by the Vitrea software for measurement of CBF, CBV, and MTT within the contralateral normal brain and was used to normalize CBF, CBV, and MTT values derived for the affected hemisphere. This process is shown in Fig 1. Of note, we considered further subanalyses by breaking down each perfusion parameter measurement into 2 further values (for penumbral and

Table 2: Comparison of cases and controls (matched on IV rtPA and NIHSS \pm 2)

Characteristics	Cases (n = 14)	Controls (n = 38)	P Value
Age (yr) (median) (IQR)	71 (61–77)	75 (65–84)	.15
Female (No.) (%)	4 (28.6%)	19 (50.0%)	.22
Time (min) to arrival (median) (IQR)	127.5 (25–391)	134 (67–547)	.23
Arrival systolic BP (mm Hg) (median) (IQR)	146.5 (136–171)	153 (134–162)	.87
Arrival diastolic BP (mm Hg) (median) (IQR)	81.5 (75–98)	83 (66–102)	.74
Arrival glucose level (mg/dL) (median) (IQR)	123.5 (107–141)	120.5 (104–142)	.85
Arrival INR (median) (IQR)	1 (1–1.1)	1.1 (1–1.2)	.15
Medical history			
Hypertension	85.7%	75.0%	.71
Diabetes	21.4%	29.7%	.73
Dyslipidemia	57.1%	54.1%	.84
Stroke/TIA	35.7%	29.7%	.68
Coronary artery disease	42.9%	16.2%	.05
Antiplatelet use	50%	38.9%	.48
Smoking	43.2%	27.0%	.20

Note.—BP indicates blood pressure; INR, International Normalized Ratio.

Table 3: Comparison of CTP parameters for matched cases and controls after excluding patients having undergone endovascular therapy^a

Parameter	Cases (n = 7)	Controls (n = 24)	P Value
MTTv (median) (IQR)	209.6 (48.5–345.6)	147.6 (78.53–235.8)	.5548
Mean \pm SD	194.91 (136.98)	161.59 (115.19)	
rMTT (median) (IQR)	1.83 (1.42–2.23)	1.80 (1.50–2.16)	.8873
Mean \pm SD	1.87 (0.43)	2.20 (1.70)	
rCBF (median) (IQR)	0.54 (0.40–0.63)	0.58 (0.46–0.70)	.5079
Mean \pm SD	0.52 (0.14)	0.58 (0.15)	
rCBV (median) (IQR)	0.92 (0.83–1.07)	1.11 (1–1.29)	.0093 ^b
Mean \pm SD	0.93 (0.13)	1.19 (0.36)	

Note.—MTTv indicates volume at risk of ischemia.

^a Seven cases (accounting for 13 controls) and 1 additional control who received endovascular therapy were excluded.

^b Statistically significant ($P < .05$).

core infarct regions, based on the CBV).²⁶ However, our sample size limited our ability to make multiple comparisons, and we, therefore, chose to proceed with measurements encompassing the entire ischemic region, as was done by previous authors.²⁷

A matched case-control cohort was created. Any patient who had HT on follow-up imaging (CT or MR imaging) was considered a “case.” Corresponding controls (≤ 4) were selected for each of the cases by matching based on IV rtPA administration and presenting NIHSS score (± 2). The matching was performed by using SAS (SAS Institute, Cary, North Carolina) (percentage match, greedy method).

Nonparametric analysis was performed to compare cases and controls by using the Wilcoxon rank sum test. For the initial analysis, all patients with endovascular therapy were excluded. CTP parameters were compared for cases and controls by using the Wilcoxon rank sum test, and P values $< .05$ were considered significant. Analysis was then repeated, including endovascular patients as well, but excluding those with SAH or PH that might be interpreted as procedure-related (1 endovascular patient with PH was therefore excluded). Conditional logistic regression was used to analyze the effect of CTP parameters on the development of hemorrhagic transformation, and ROC curves were created. All analyses were performed in SAS 9.2/JMP 9 (SAS Institute).

Imaging Protocol

CTP imaging was performed on a 64-detector CT scanner (Brilliance; Philips Healthcare, Best, the Netherlands) following an initial noncontrast CT scan. This involved successive gantry rotations during IV administration of 50 mL of ioversol (Optiray 350; Mallinck-

rodt, St. Louis, Missouri) at 5 mL/s followed by a 40-mL saline push. Coverage of 40 mm was obtained, with 8×5 mm thick sections, 32×1.25 mm collimation, and standard reconstruction. Acquisition parameters were 80 kV(peak), 150 mAs; 2-second cycle time; 30 cycles; 0.4-second rotation; and FOV, 230.

Postprocessing of images was performed by using Vitrea software, Version 3.0.1 (Vital Images). We used whole values derived from each region of interest rather than threshold values, because we have found that data derived from our commercial CTP software is more semiquantitative in nature and we feared that choosing a set uniform threshold across all patients would not account for differences in cardiac output, anatomy, and timing of injections among individual patients. Visually matched areas of increased MTT and decreased CBF were, therefore, outlined as ischemic areas, and all values were then reported as relative to the contralateral hemisphere, to account for potential interpatient variability noted above. The Vitrea software automatically chooses the selected arterial input function and venous output function (typically a proximal A2 vessel and a large dural sinus, respectively). These are verified by the technologist to be anatomically accurate and to result in correct time-to-peak maps of arterial and venous time-intensity curves. In rare cases in which there are discrepancies in the automatic arterial input function and venous output function locations, the arterial input function and venous output function are manually selected by the technologist. We additionally verified each arterial input function and venous output function for all patients included in the study.

RESULTS

Characteristics of the Patient Population

Eighty-three patients with stroke were enrolled in the study. The characteristics of the cohort are presented in Table 1. Of the total cohort, 16 (19.3%) patients developed HT during their hospital stay. Of these, 37.5% had an early HT (HT within 36 hours of symptom onset). The median duration to the development of HT was 38.7 hours (IQR, 18.8–52.4 hours).

Characteristics of Matched Cases and Controls

After matching for IV rtPA administration and presenting NIHSS score (± 2), 38 controls were found for 14 cases (no controls were found for 2 patients with HT). There were no differences between cases and controls with respect to age, sex, vital parameters on presentation, history of disease or medication use, initial laboratory investigations, and smoking history (Table 2). Cases had a longer hospital stay (median, 8.5 days; IQR, 7–12 days) compared with controls (median, 5 days; IQR, 3–8 days; $P = .012$). There

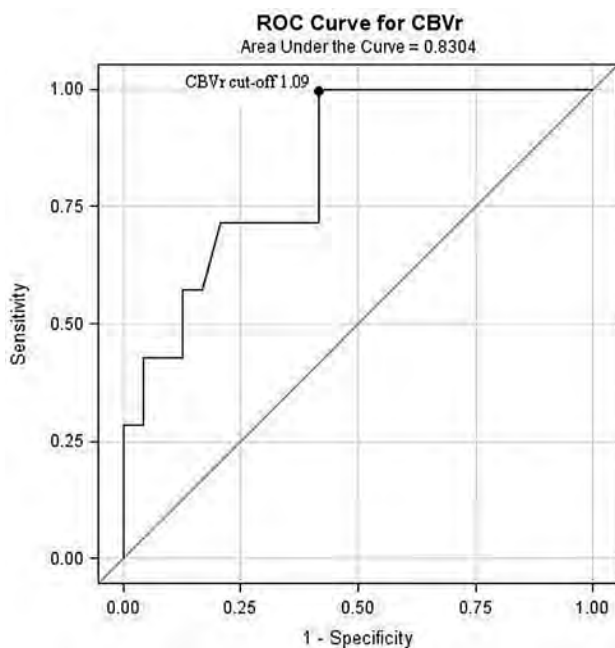


FIG 2. ROC curve of rCBV in patients with and without HT, excluding all patients receiving endovascular therapy (7 cases [accounting for 13 controls] and 1 additional control who received endovascular therapy were excluded). rCBV represents CBV of the ischemic area normalized to the contralateral side. The cutoff point indicates the threshold at which rCBV can predict HT with optimal sensitivity and specificity.

was a statistically nonsignificant difference between functional outcome assessed at discharge between cases (median mRS score, 5; IQR, 3–5) and controls (median mRS score, 3.5; IQR, 1–5; $P = .11$). Of the 14 cases, 13 had HI (7 HI 1 and 6 HI 2) and 1 case developed PH 2. Seven cases and 1 control were noted to have undergone endovascular therapy for acute ischemic stroke.

Comparison of Cases and Controls

All cases and controls who had undergone endovascular therapy were excluded (7 cases [accounting for 13 controls] and 1 additional control who received endovascular therapy were excluded). As seen in Table 3, these remnant cases had higher median total volume at risk of ischemia, longer median rMTT, and lower median rCBF compared with controls, though this did not reach statistical significance. Cases did have a significantly lower median rCBV compared with controls (median rCBV of cases, 0.92; IQR, 0.83–1.07 versus median rCBV of controls, 1.11; IQR, 1.0–1.29; $P = .01$). For each 0.1-U decrease in rCBV, the odds of developing an HT increased by 14% (OR, 1.14; 95% CI, 1.05–

1.25). The ROC curve for rCBV is shown in Fig 2. The area under the ROC curve was computed to be 0.83 (SE, 0.08; 95% CI, 0.67–0.99), with a cutoff point for rCBV of 1.09. The sensitivity for this cutoff value was 100%, and specificity was 58.3%.

Considering that only SAH or PH can truly be interpreted as being procedure-related hemorrhage after endovascular therapy, we repeated the above analysis (excluding cases with both endovascular therapy and SAH/PH [$n = 1$] and their corresponding controls [$n = 2$]). Repeat analysis depicted in Table 4 yielded similar results as before: Cases had higher volume at risk of ischemia, longer median rMTT, and lower median rCBF compared with controls. However, this again did not reach statistical significance. The median rCBV was significantly lower in cases compared with controls (median CBVr of cases, 0.92; IQR, 0.78–1.03 versus median rCBV of controls, 1.09; IQR, 0.97–1.17; $P = .004$). For each 0.1-U decrease in rCBV, the odds of developing an HT increased by 12% (OR, 1.12; 95% CI, 1.05–1.19). The ROC curve for rCBV is shown in Fig 3. The area under the ROC curve was computed to be 0.78 (SE, 0.08; 95% CI, 0.62–0.94), with a cutoff point for rCBV of 0.98. The sensitivity for a cutoff value of rCBV was 76.92% with a specificity of 72.22%.

DISCUSSION

The incidence of HT has been reported to vary between 2% and 44% of patients with ischemic stroke,^{5,11,24} and the 19.3% rate observed in our study falls within this range. Besides thrombolytic therapy, HT has been associated with age younger than 65 years,²⁸ hyperglycemia,²⁹ acute hypertension³⁰ and blood pressure variability,³¹ low levels of coated platelets,³² and cardioembolic stroke subtype.³³ As new avenues are explored to stretch the time window for beneficial therapy,³⁴ there is an increasingly acute need to accurately predict the likelihood of HT in every patient eligible for intervention to judiciously triage these patients to available therapies while reducing complications.

Prediction of HT by reduced pretherapeutic CBF, an inherent characteristic of the stroke itself, was first suggested by Ueda et al³⁵ by using SPECT. A reduction in CBF to <50% of normal was considered as the critical value for developing HT.³⁶ Gupta et al³⁷ in their study of 23 patients with symptomatic stroke or carotid stenosis concluded that mean ipsilateral CBF < 13 mL/100 g per minute was the cutoff for developing HT. In our cohort, we found that rCBV rather than rCBF was the strongest predictor of HT. This is similar to reports of rCBV (rather than rCBF) being a stronger predictor of penumbra viability in patients with AIS,²⁶ with similar³⁸ or even lower³⁹ values reported by authors for

rCBV in patients with HT. In other words, indicators of penumbra viability may also indirectly predict HT, which would be expected to occur more frequently in infarcted core rather than salvageable penumbra regions. We found in our patients that a cutoff rCBV of at least 0.98 could predict development of HT in patients with AIS with 72% specificity.

The role of imaging in acute stroke is ever-expanding.^{40,41} Many modalities

Table 4: Comparison of CTP parameters for matched cases and controls^a

Parameter	Cases ($n = 13$)	Controls ($n = 36$)	P Value
MTT _v (median) (IQR)	234.9 (178.2–326.15)	183.55 (84.83–265.83)	.1968
Mean \pm SD	233.32 (111.53)	186.61 (116.72)	
rMTT (median) (IQR)	2.06 (1.69–2.39)	1.8 (1.55–2.17)	.4020
Mean \pm SD	2.00 (0.40)	2.16 (1.42)	
rCBF (median) (IQR)	0.45 (0.39–0.59)	0.53 (0.42–0.70)	.2572
Mean \pm SD	0.48 (0.12)	0.54 (0.16)	
rCBV (median) (IQR)	0.92 (0.78–1.03)	1.09 (0.97–1.17)	.0037 ^b
Mean \pm SD	0.92 (0.17)	1.13 (0.33)	

Note:—MTT_v indicates volume at risk of ischemia.

^a Excluding cases with both endovascular therapy and SAH/PH ($n = 1$) and their corresponding controls ($n = 2$).

^b Statistically significant ($p < .05$).

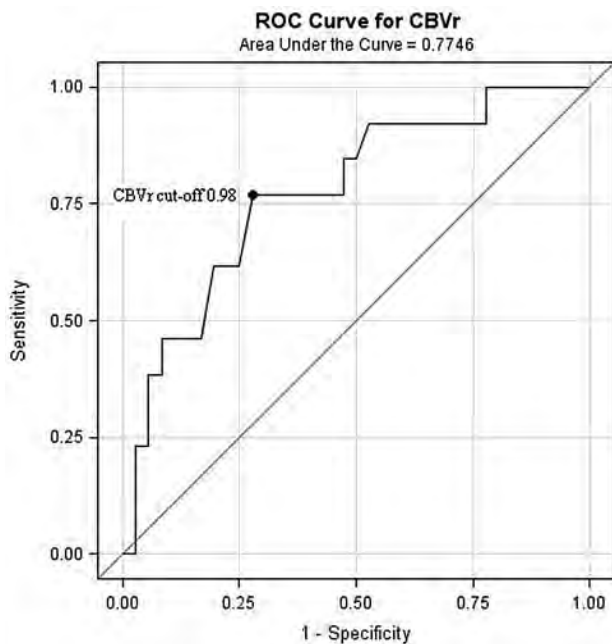


FIG 3. ROC curve of rCBV in patients with and without HT (excluding cases with both endovascular therapy and PH/SAH [$n = 1$] and their corresponding controls [$n = 2$]). rCBV represents CBV of the ischemic area normalized to the contralateral side. The cutoff point indicates the threshold at which rCBV can predict HT with optimal sensitivity and specificity.

have shown promise in delineating both the extent of viable brain tissue within the area at ischemic risk as well as in predicting HT. The high risk of HT was associated in the past with an M1 MCA occlusion and lack of collateral flow evaluated by transcranial Doppler, SPECT, and clinical criteria (Toronto Embolic Scale).²⁰ More recently, BBB permeability studies via MR and CTP imaging have been shown to have a high sensitivity for predicting symptomatic HT.^{23,42} The ROC for rCBV in our study suggests that CBV may also predict HT. The utility of this finding lies in the fact that CT imaging is already a part of the imaging protocol in a large number of tertiary care institutions. CTP as an add-on can be performed easily and quickly in an emergent setting, while providing information about tissue-level hemodynamics, extent of penumbra, and final infarct size.⁴³ Should our findings be replicated on a larger scale, an additional utility would be prediction of HT, which could further guide emergent treatment decisions for patients with acute stroke.

Limitations

There are several limitations to this study. This was a retrospective study. Effects of stroke severity at presentation and IV rtPA administration were controlled for by matching; however, this reduced the final cohort size. No adjustments were made for specific anatomic locations of perfusion parameters and region-specific risk of HT. Our results represent only a single-institution experience and have not been validated and may, therefore, not be representative of community practice.

CONCLUSIONS

Our data suggest that CTP imaging and, in particular, low rCBV can predict HT in patients with AIS. Should this exploratory anal-

ysis be validated in larger studies, initial multimodal CT imaging, including CTP, could be used to triage patients at high risk of HT to treatments less likely to further exacerbate their inherent risk of impending intracerebral hemorrhage.

REFERENCES

- Lloyd-Jones D, Adams RJ, Brown TM, et al. **Heart disease and stroke statistics: 2010 update—a report from the American Heart Association.** *Circulation* 2010;121:e46–e215
- Asplund K, Stegmayr B, Peltonen M. **From the twentieth to the twenty-first century: a public health perspective on stroke.** In: Ginsberg MD, Bogousslavsky J, eds. *Cerebrovascular Disease Pathophysiology, Diagnosis, and Management*. Vol 2. Malden, Massachusetts: Blackwell Science; 1998
- World Health Organization. The top 10 causes of death: updated 2011. <http://www.who.int/mediacentre/factsheets/fs310/en/index.html>. Accessed March 12, 2012
- Incidence and Prevalence: 2006 Chart Book on Cardiovascular and Lung Diseases.* Bethesda, Maryland: National Institutes of Health, National Heart Lung and Blood Institute; 2006
- Tissue plasminogen activator for acute ischemic stroke: the National Institute of Neurological Disorders and Stroke rt-PA Stroke Study Group.** *N Engl J Med* 1995;333:1581–87
- Hacke W, Kaste M, Bluhmki E, et al. **Thrombolysis with alteplase 3 to 4.5 hours after acute ischemic stroke.** *N Engl J Med* 2008;359:1317–29
- Wahlgren N, Ahmed N, Davalos A, et al. **Thrombolysis with alteplase 3–4.5 h after acute ischaemic stroke (SITS-ISTR): an observational study.** *Lancet* 2008;372:1303–09
- Ahmed N, Wahlgren N, Grund M, et al. **Implementation and outcome of thrombolysis with alteplase 3–4.5 h after an acute stroke: an updated analysis from SITS-ISTR.** *Lancet Neurol* 2010;9:866–74
- Lees KR, Bluhmki E, von Kummer R, et al. **Time to treatment with intravenous alteplase and outcome in stroke: an updated pooled analysis of ECASS, ATLANTIS, NINDS, and EPITHET trials.** *Lancet* 2010;375:1695–703
- Jaillard A, Cornu C, Durieux A, et al. **Hemorrhagic transformation in acute ischemic stroke: the MAST-E study—MAST-E Group.** *Stroke* 1999;30:1326–32
- Larrue V, von Kummer RR, Muller A, et al. **Risk factors for severe hemorrhagic transformation in ischemic stroke patients treated with recombinant tissue plasminogen activator: a secondary analysis of the European-Australasian Acute Stroke Study (ECASS II).** *Stroke* 2001;32:438–41
- Kerenyi L, Kardos L, Szasz J, et al. **Factors influencing hemorrhagic transformation in ischemic stroke: a clinicopathological comparison.** *Eur J Neurol* 2006;13:1251–55
- Kidwell CS, Saver JL, Carneado J, et al. **Predictors of hemorrhagic transformation in patients receiving intra-arterial thrombolysis.** *Stroke* 2002;33:717–24
- Dzialowski I, Pexman JH, Barber PA, et al. **Asymptomatic hemorrhage after thrombolysis may not be benign: prognosis by hemorrhage type in the Canadian alteplase for stroke effectiveness study registry.** *Stroke* 2007;38:75–79
- Fiorelli M, Bastianello S, von Kummer R, et al. **Hemorrhagic transformation within 36 hours of a cerebral infarct: relationships with early clinical deterioration and 3-month outcome in the European Cooperative Acute Stroke Study I (ECASS I) cohort.** *Stroke* 1999;30:2280–84
- Larrue V, von Kummer R, del Zoppo G, et al. **Hemorrhagic transformation in acute ischemic stroke: potential contributing factors in the European Cooperative Acute Stroke Study.** *Stroke* 1997;28:957–60
- Dowlathshahi D, O'Donnell M, Sharma M. **Possible influence of stroke etiology on hemorrhagic transformation following thrombolysis in warfarin-treated patients.** *Arch Neurol* 2010;67:1413, author reply 1414

18. Castellanos M, Leira R, Serena J, et al. **Plasma metalloproteinase-9 concentration predicts hemorrhagic transformation in acute ischemic stroke.** *Stroke* 2003;34:40–46
19. Toni D, Fiorelli M, Bastianello S, et al. **Hemorrhagic transformation of brain infarct: predictability in the first 5 hours from stroke onset and influence on clinical outcome.** *Neurology* 1996;46:341–45
20. Alexandrov AV, Black SE, Ehrlich LE, et al. **Predictors of hemorrhagic transformation occurring spontaneously and on anticoagulants in patients with acute ischemic stroke.** *Stroke* 1997;28:1198–202
21. Knight RA, Barker PB, Fagan SC, et al. **Prediction of impending hemorrhagic transformation in ischemic stroke using magnetic resonance imaging in rats.** *Stroke* 1998;29:144–51
22. Tong DC, Adami A, Moseley ME, et al. **Prediction of hemorrhagic transformation following acute stroke: role of diffusion- and perfusion-weighted magnetic resonance imaging.** *Arch Neurol* 2001;58:587–93
23. Hom J, Dankbaar JW, Soares BP, et al. **Blood-brain barrier permeability assessed by perfusion CT predicts symptomatic hemorrhagic transformation and malignant edema in acute ischemic stroke.** *AJNR Am J Neuroradiol* 2011;32:41–48
24. Hacke W, Kaste M, Fieschi C, et al. **Intravenous thrombolysis with recombinant tissue plasminogen activator for acute hemispheric stroke: the European Cooperative Acute Stroke Study (ECASS).** *JAMA* 1995;274:1017–25
25. Hacke W, Kaste M, Fieschi C, et al. **Randomised double-blind placebo-controlled trial of thrombolytic therapy with intravenous alteplase in acute ischaemic stroke (ECASS II): Second European-Australasian Acute Stroke Study Investigators.** *Lancet* 1998;352:1245–51
26. Parsons MW, Pepper EM, Bateman GA, et al. **Identification of the penumbra and infarct core on hyperacute noncontrast and perfusion CT.** *Neurology* 2007;68:730–36
27. Aviv RI, d'Este CD, Murphy BD, et al. **Hemorrhagic transformation of ischemic stroke: prediction with CT perfusion.** *Radiology* 2009;250:867–77
28. Saver JL. **Hemorrhage after thrombolytic therapy for stroke: the clinically relevant number needed to harm.** *Stroke* 2007;38:2279–83
29. Broderick JP, Hagen T, Brott T, et al. **Hyperglycemia and hemorrhagic transformation of cerebral infarcts.** *Stroke* 1995;26:484–87
30. Bowes MP, Zivin JA, Thomas GR, et al. **Acute hypertension, but not thrombolysis, increases the incidence and severity of hemorrhagic transformation following experimental stroke in rabbits.** *Exp Neurol* 1996;141:40–46
31. Ko Y, Park JH, Yang MH, et al. **The significance of blood pressure variability for the development of hemorrhagic transformation in acute ischemic stroke.** *Stroke* 2010;41:2512–18
32. Prodan CI, Stoner JA, Cowan LD, et al. **Lower coated-platelet levels are associated with early hemorrhagic transformation in patients with non-lacunar brain infarction.** *J Thromb Haemost* 2010;8:1185–90
33. Okada Y, Yamaguchi T, Minematsu K, et al. **Hemorrhagic transformation in cerebral embolism.** *Stroke* 1989;20:598–603
34. Rowley HA. **Extending the time window for thrombolysis: evidence from acute stroke trials.** *Neuroimaging Clin N Am* 2005;15:575–87, x
35. Ueda T, Hatakeyama T, Kumon Y, et al. **Evaluation of risk of hemorrhagic transformation in local intra-arterial thrombolysis in acute ischemic stroke by initial SPECT.** *Stroke* 1994;25:298–303
36. Seki H, Yoshimoto T, Ogawa A, et al. **Hemodynamics in hemorrhagic infarction: an experimental study.** *Stroke* 1985;16:647–51
37. Gupta R, Yonas H, Gebel J, et al. **Reduced pretreatment ipsilateral middle cerebral artery cerebral blood flow is predictive of symptomatic hemorrhage post-intra-arterial thrombolysis in patients with middle cerebral artery occlusion.** *Stroke* 2006;37:2526–30
38. Souza LC, Payabvash S, Wang Y, et al. **Admission CT perfusion is an independent predictor of hemorrhagic transformation in acute stroke with similar accuracy to DWI.** *Cerebrovasc Dis* 2012;33:8–15
39. Lin K, Zink WE, Tsiouris AJ, et al. **Risk assessment of hemorrhagic transformation of acute middle cerebral artery stroke using multimodal CT.** *J Neuroimaging* 2012;22:160–66
40. Sims J, Schwamm LH. **The evolving role of acute stroke imaging in intravenous thrombolytic therapy: patient selection and outcomes assessment.** *Neuroimaging Clin N Am* 2005;15:421–40, xii
41. Schellinger PD. **The evolving role of advanced MR imaging as a management tool for adult ischemic stroke: a Western-European perspective.** *Neuroimaging Clin N Am* 2005;15:245–58, ix
42. Thornhill RE, Chen S, Rammo W, et al. **Contrast-enhanced MR imaging in acute ischemic stroke: T2* measures of blood-brain barrier permeability and their relationship to T1 estimates and hemorrhagic transformation.** *AJNR Am J Neuroradiol* 2010;31:1015–22
43. Wintermark M, Reichhart M, Thiran JP, et al. **Prognostic accuracy of cerebral blood flow measurement by perfusion computed tomography, at the time of emergency room admission, in acute stroke patients.** *Ann Neurol* 2002;51:417–32

Stroke Mismatch Volume with the Use of ABC/2 Is Equivalent to Planimetric Stroke Mismatch Volume

M. Luby, J. Hong, J.G. Merino, J.K. Lynch, A.W. Hsia, A. Magadán, S.S. Song, L.L. Latour, and S. Warach



ABSTRACT

BACKGROUND AND PURPOSE: In the clinical setting, there is a need to perform mismatch measurements quickly and easily on the MR imaging scanner to determine the specific amount of treatable penumbra. The objective of this study was to quantify the agreement of the ABC/2 method with the established planimetric method.

MATERIALS AND METHODS: Patients ($n = 193$) were selected from the NINDS Natural History Stroke Registry if they 1) were treated with standard intravenous rtPA, 2) had a pretreatment MR imaging with evaluable DWI and PWI, and 3) had an acute ischemic stroke lesion. A rater placed the linear diameters to measure the largest DWI and MTT lesion areas in 3 perpendicular axes—A, B, and C—and then used the ABC/2 formula to calculate lesion volumes. A separate rater measured the planimetric volumes. Multiple mismatch thresholds were used, including MTT volume – DWI volume ≥ 50 mL versus ≥ 60 mL and (MTT volume – DWI volume)/MTT volume $\geq 20\%$ versus MTT/DWI = 1.8.

RESULTS: Compared with the planimetric method, the ABC/2 method had high sensitivity (0.91), specificity (0.90), accuracy (0.91), PPV (0.90), and NPV (0.91) to quantify mismatch by use of the ≥ 50 mL definition. The Spearman correlation coefficients were 0.846 and 0.876, respectively, for the DWI and MTT measurements. The inter-rater Bland-Altman plots demonstrated 95%, 95%, and 97% agreement for the DWI, MTT, and mismatch measurements.

CONCLUSIONS: The ABC/2 method is highly reliable and accurate for quantifying the specific amount of MR imaging–determined mismatch and therefore is a potential tool to quickly calculate a treatable mismatch pattern.

ABBREVIATIONS: CI = confidence interval; IQR = interquartile range; NPV = negative predictive value; PPV = positive predictive value; SD = standard deviation

In the clinical setting, there is a need to perform quantitative mismatch measurements quickly and easily to determine the specific amount of treatable penumbra. The ABC/2 method of measuring quantitative mismatch is a viable option because it can be performed immediately on the MR imaging scanner and has precedence in other diseases. Prior studies by use of the ABC/2

method to measure intracerebral hemorrhage or subdural hematoma volumes have been extensively applied and validated.¹⁻³ Kothari et al¹ demonstrated that the ABC/2 method had excellent correlation with the planimetric method when applied to the measurements of intracerebral hemorrhage volumes. Furthermore, they demonstrated excellent inter-rater and intrarater reliability for the ABC/2 method.¹ Gebel et al² adapted the ABC/2 method successively to measure subdural hematoma volumes and demonstrated excellent correlation with a computerized technique. Huttner et al³ applied the ABC/2 method to more complicated intracerebral hemorrhage patterns and found that modification of the formula to ABC/3 produced more accurate measurements. In acute ischemic stroke, automated mismatch measurements by use of postprocessing software are advantageous⁴ for quantifying mismatch but are not generally available. Quality or format limitations of some scans may prohibit automated software from producing usable mismatch results. The feasibility of qualitative evaluation of mismatch on MR imaging before thrombolysis has been presented.^{5,6} However, in recent

Received July 27, 2012; accepted after revision December 3.

From the National Institute of Neurological Disorders and Stroke (M.L., J.H., J.G.M., J.K.L., A.W.H., A.M., L.L.L., S.W.); Bethesda, Maryland; Johns Hopkins Community Physicians (J.G.M.), Bethesda, Maryland; Medstar Washington Hospital Center Stroke Center (A.W.H.), Washington, DC; Cedars Sinai Medical Center (S.S.S.), Los Angeles, California; and NINDS Natural History of Stroke Investigators (S.W.), Bethesda, Maryland.

This research was supported by the Division of Intramural Research of the National Institutes of Health and the National Institute of Neurological Disorders and Stroke.

Please address correspondence to Marie Luby, PhD, Section on Stroke Diagnostics and Therapeutics, 10 Center D, MSC 1063, Bldg 10, Room BID733, Bethesda, MD 20892-1063; e-mail: lubym@ninds.nih.gov

Indicates open access to non-subscribers at www.ajnr.org

<http://dx.doi.org/10.3174/ajnr.A3476>

stroke clinical trials, specific imaging thresholds for mismatch beyond visual confirmation were required to make enrollment decisions.⁷⁻¹² Optimization of thresholds including mismatch of $>20\%$ ^{10,11} and $\text{PWI/DWI} >1.8$,¹² have been investigated retrospectively by many investigators to apply these conditions prospectively for automated measurement.¹⁰⁻¹² Validation of the ABC/2 mismatch method may prove to be less challenging than validating the numeric methods for automated mismatch measurements. Furthermore, the ABC/2 method is a possible alternative to automated methods when image quality restricts their usage. However, the agreement of the ABC/2 method with the planimetric method has not been fully defined. Sims et al¹³ established that the ABC/2 method provided the best estimation of infarction and MTT volumes. The prior study demonstrated a high PPV of 92%; however, the results had a poor NPV of 33%.¹³ Pedraza et al¹⁴ recommended that a larger study looking at broader range of mismatch volumes and clinical outcomes ultimately should be performed. Vogt et al¹⁵ used the ABC/2 method mainly in CT scans in >1800 patients with ischemic stroke and hemorrhage but demonstrated in a subset of MR imaging scans that their infarct volume results were stable regardless of imaging technique. Warach et al¹⁶ demonstrated a difference in favorable clinical outcome in desmoteplase-treated patients versus placebo-treated patients in a post hoc analysis of the Desmoteplase in Acute Ischemic Stroke Trial-2 when applying a specific mismatch threshold of >60 mL. However, no study has compared these various mismatch definitions across both the ABC/2 and planimetric methods to quantify their agreement and feasibility for application in the clinical trial setting. Therefore, the primary focus of this study was to compare the agreement across definitions when quantifying the amount of mismatch by use of both the ABC/2 and planimetric methods.

The objectives of this study were to compare the ABC/2 and planimetric methods to determine the agreement between the mismatch volumes and resulting classifications. Our hypotheses were 1) the ABC/2 measurements were equivalent to the planimetric measurements and therefore the ABC/2 method was an accurate tool for quick quantification of treatable mismatch patterns, and 2) the ABC/2 mismatch classifications predicted the same clinical outcomes as the planimetric mismatch classifications.

MATERIALS AND METHODS

Patients

This is an analysis of data from the National Institute of Neurological Disorders and Stroke Natural History registry. The NINDS Natural History registry is a dataset formed from 2 acute stroke centers: Suburban Hospital in Bethesda, Maryland, and Medstar Washington Hospital Center in Washington, DC. The appropriate ethics and institutional review boards approved the study. For this study, all patients were treated with standard intravenous rtPA within 3 hours of time last known well between December 2000 and October 2009. Patients were included if they 1) were treated with standard intravenous rtPA, 2) had a pretreatment MR imaging with evaluable DWI and PWI, and 3) had an acute ischemic stroke lesion.

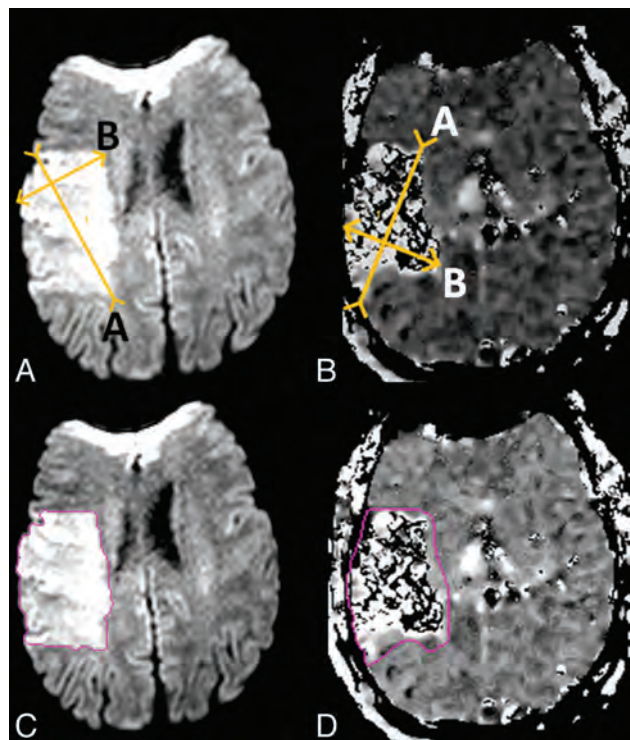


FIG 1. Corresponding measurements for the ABC/2 method (A, DWI = 116.1 mL; B, MTT = 194.7 mL) and planimetric method (C, DWI = 116.2 mL; D, MTT = 248.4 mL) on paired sections placed independently by 2 different readers.

Imaging Series

Imaging was performed by use of 1.5T (TwinSpeed; GE Healthcare, Milwaukee, Wisconsin) or 3T (Achieva; Philips, Best, the Netherlands) clinical MR imaging scanners. DWI and PWI series were acquired co-localized over the entire brain with a superior to inferior coverage of 14 cm. Typical imaging parameters for DWI spin-echo echo-planar series included either 40–3.5-mm- or 20–7-mm-thick contiguous axial oblique sections with $b = 0$ and $b = 1000$ seconds/mm², trace or isotropically weighted, TR/TE = 6000–7000/72–90 ms, acquisition matrix of 64×64 – 128×128 , and 22 cm FOV. The PWI was a dynamic susceptibility contrast series with the use of a single dose of 0.1 mmol/kg of gadolinium (Magnevist; Bayer Schering Pharma, Wayne, New Jersey). Typical imaging parameters for PWI gradient echo-planar series included 20 contiguous axial oblique sections with single-dose gadolinium contrast injection of 0.1 mmol/kg through a power injector by using 25–40 phase measurements, TR/TE = 2000–2200/45 ms, acquisition matrix of 64×64 – 128×128 , 7-mm section thickness, and 22-cm FOV.

Image Analysis

ABC/2 Volume Method for Quantitative Mismatch. A rater (J.H.) measured the ABC/2 volume of DWI and MTT lesions by using a DICOM image viewer. After optimizing the window level settings, the 2 longest perpendicular linear diameters (A and B) on the section where the abnormality on DWI appeared largest were measured (Fig 1A). The same process was repeated on the section with the largest area of MTT abnormality (Fig 1B). With the use of these diameters, the product of the section thickness, and the total

Table 1: Comparison of volume statistics between patients classified as mismatch versus no mismatch by use of the 50-mL mismatch definition for the ABC/2 and planimetric methods

Volume Statistics	ABC/2 Mismatch Yes (n = 94)	ABC/2 Mismatch No (n = 56)	Planimetric Mismatch Yes (n = 92)	Planimetric Mismatch No (n = 62)
Median DWI volume (IQR, 25–75), mL	26.1 (8.9–69.4)	10.2 (1.97–24.98)	26.4 (6.2–71.0)	8.7 (2.4–18.0)
Median MTT volume (IQR 25–75), mL	198.4 (134.3–287.2)	28.26 (11.58–59.35)	191.2 (137.6–276.8)	28.4 (11.4–44.3)
Median mismatch volume (IQR 25–75), mL	151.5 (86.1–225.5)	15.85 (5.78–30.3)	149.6 (89.8–208.9)	15.14 (3.2–30.5)
Median mismatch percentage (IQR 25–75), %	81% (62.8–95%)	57.5% (29.3–80.5%)	84% (59–96.8%)	53% (25.3–80%)

number of sections containing the lesion (C), the ABC/2 DWI and MTT volumes were calculated with the formula: volume = ABC/2. For discontinuous lesions, only the largest lesion area was measured. Multiple measurements were not performed across the discontinuous lesions. However, if the lesion was continuous and included multiple vascular territories, the measurement included the entire lesion area. For punctate lesions, the largest lesion area was measured.

Planimetric Volume Method for Quantitative Mismatch. A rater (M.L.) with extensive experience and established rater reliability statistics measured the lesion volumes on the DWI and MTT maps by using a semi-automated quantitative, planimetric method in Cheshire (Boulder, Colorado).¹⁷ The intrarater and inter-rater reliability of the planimetric measurements of DWI and MTT was validated as a highly consistent and repeatable method by use of Cheshire in the Luby et al study.¹⁷ Lesion areas were segmented on a section-by-section basis, with user-selected seed points followed by user-driven editing (Fig 1C, -D).

Thresholds for Quantitative Mismatch. Patients were classified as having a quantitative mismatch when the difference in the volumes on the MTT and the DWI was $\geq 50 \text{ mL}^2$ versus $\geq 60 \text{ mL}^2$ and $(\text{MTT volume} - \text{DWI volume})/\text{MTT volume} \geq 20\%$ ^{10,11} versus $\text{MTT}/\text{DWI} \geq 1.8$.¹²

Inter-Rater Reliability of ABC/2 Volume Method. For the purposes of determining inter-rater reliability of the ABC/2 method, the rater (M.L.) who performed the planimetric volume measurements independently measured the ABC/2 lesion volumes on DWI and MTT, blinded to the quantitative results already generated for the study.

Statistical Analysis

The following analyses were performed: 1) lesion volumes for the ABC/2 and planimetric methods and associated mismatch classifications, based on the $\text{MTT} - \text{DWI} \geq 50 \text{ mL}$ versus $\geq 60 \text{ mL}$ and $(\text{MTT volume} - \text{DWI volume})/\text{MTT volume} \geq 20\%$ versus $\text{MTT}/\text{DWI} \geq 1.8$ definitions, 2) agreement of mismatch classifications as determined by the ABC/2 and planimetric methods, 3) inter-rater reliability measures for the DWI and MTT and measurements by use of the ABC/2 method, and 4) functional outcome rates by use of modified Rankin Scale scores among individuals across the ABC/2 and planimetric methods. SPSS Statistics (v17.0; SPSS, Chicago, Illinois) was used for all statistical analyses.

For the lesion volume statistics, only cases with positive lesions, that is, $>0 \text{ mL}$ volumes, were included. Values are reported as mean ($\pm \text{SD}$) or median (IQR, 25–75) when appropriate. Agreement rates were defined as the number of cases agreed di-

vided by the total number of cases ($n = 193$) except as noted. Linear regression of volumes was performed to demonstrate the correlation between the ABC/2 and planimetric measurements. The Bland-Altman plots were generated to display the spread of the lesion volumes and the limits of agreement between the ABC/2 and planimetric measurements, specifically to illustrate how many of the measurements were within 2 SD from the mean volume difference. Inter-rater reliability of the lesion volumes was quantified by Spearman correlation coefficients and Bland-Altman plots. The Bland-Altman plots were generated to display the spread of the lesion volumes and the limits of agreement between the 2 independent sets of ABC/2 measurements. Cohen κ coefficients were calculated. The Bland-Altman and linear regression plots were on the logarithmic scale. Contingency (2×2) tables were used to calculate specificity, sensitivity, accuracy, PPV, and NPV of the ABC/2 method compared with the planimetric method.

RESULTS

Patients

From December 2000 through October 31, 2009, 385 patients were treated with standard intravenous rtPA. Of these, 234 patients had a pretreatment MR imaging. Forty-one patients were excluded because they did not include PWI ($n = 18$) or the DWI and MTT maps were not available or not evaluable ($n = 23$). The final sample in this study includes 193 patients. In 143 patients, the MR imaging was performed at 1.5T and in 50 at 3T. Fifty-two percent of the patients were women ($n = 102$). The mean age of the patients was 70.8 (± 15.7) years, and the median time from stroke onset to baseline MR imaging was 103 (IQR, 79–128) minutes. The median baseline NIHSS score in the 192 patients for whom these data are available was 9 (IQR, 4–18).

ABC/2 Volumes

Using the ABC/2 method, DWI ($n = 184$), MTT ($n = 170$), and mismatch ($\text{MTT} - \text{DWI}$, $n = 150$) median volumes were 18.9 mL (IQR, 3.1–60.0), 116.3 mL (IQR, 33.0–249.5), and 78.9 mL (IQR, 26.8–183.6), respectively. Overall, 48.7% of patients of the entire sample ($n = 94/193$) were classified as having a mismatch by the ABC/2 method by use of the $\text{MTT} - \text{DWI} \geq 50 \text{ mL}$ definition. Table 1 contains the volume statistics for the 94 patients with mismatch $\geq 50 \text{ mL}$ versus the 56 patients without measurable mismatch. Forty-four percent of patients ($n = 85/193$) were classified as having a mismatch by use of the $\text{MTT} - \text{DWI} \geq 60 \text{ mL}$ definition. Seventy-four percent of patients ($n = 142/193$) were classified as having a mismatch by use of the $\text{MTT} - \text{DWI} \geq 20\%$ definition versus 60% ($n = 116/193$) by use of the $\text{MTT}/\text{DWI} \geq 1.8$ definition.

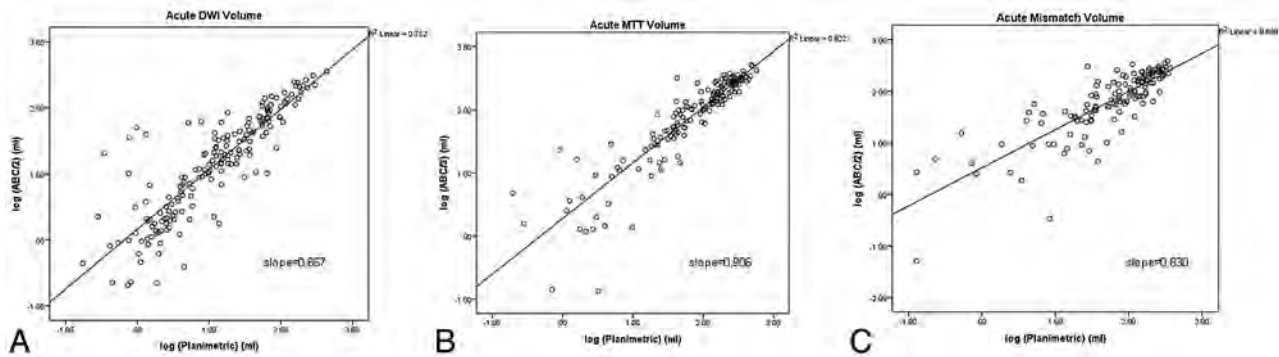


FIG 2. Linear regression plots of ABC/2 with planimetric measurements displaying the respective regression lines with R^2 and slope values for DWI (A), MTT (B), and mismatch (C). Plots are on the logarithmic scale.

Planimetric Volumes

With the use of the planimetric volume method, DWI ($n = 186$), MTT ($n = 167$), and mismatch (MTT-DWI, $n = 154$) median volumes were 12.4 mL (IQR, 2.6–51.8), 103.9 mL (IQR, 30.7–208.6), and 74.2 mL (IQR, 21.8–165.9), respectively. Overall, 48% of patients ($n = 92/193$) were classified as having a mismatch by the planimetric volume method by use of the MTT–DWI ≥ 50 mL definition. Table 1 contains the volume statistics for the 92 patients with mismatch ≥ 50 mL versus the 62 patients without measurable mismatch. Forty-five percent of patients ($n = 87/193$) were classified as having a mismatch by use of the MTT–DWI ≥ 60 mL definition. Seventy-four percent of patients ($n = 142/193$) were classified as having a mismatch by use of the MTT–DWI $\geq 20\%$ definition versus 60% ($n = 116/193$) by use of the MTT/DWI ≥ 1.8 definition.

Comparison of ABC/2 and Planimetric Measurements

The linear regression plots (Fig 2) of ABC/2 with planimetric measurements are displayed for DWI (Fig 2A), MTT (Fig 2B), and mismatch (Fig 2C). The plots are on the logarithmic scale. The R^2 , slope and confidence intervals for DWI, MTT, and mismatch are 0.752, 0.867 (CI, 0.83–0.99), 0.822, 0.906 (CI, 0.82–0.95), and 0.69, 0.83 (CI, 0.65–0.83), respectively. The Bland-Altman plots (Fig 3) of the ABC/2 versus planimetric measurements demonstrated that 93.4%, 94.9%, and 93.3% for the DWI, MTT, and mismatch measurements were within the thresholds defined by 2 SD from the mean differences. The Spearman correlation coefficients were 0.84 and 0.87 for the DWI and MTT measurements, respectively ($P < .01$), between the ABC/2 and planimetric methods. The sensitivity (0.91), specificity (0.90), accuracy (0.91), PPV (0.90), and NPV (0.91) were excellent for the ABC/2 method by use of the planimetric mismatch definition ≥ 50 mL. Volume statistics for the discrepant patients ($n = 17$) are included in Table 2. On the basis of the ABC/2 measurements of cases FN 6, FN 7, and FN 8, treatment decisions requiring a mismatch may have changed. However, there is a positive mismatch for the remaining 14 discrepant patients across both methods; therefore, changes in treatment decisions for thrombolysis are not likely.

Correlation Between Mismatch and Functional Outcome

Patients who were classified with a positive mismatch by visual or ABC/2 methods were more likely to have a good outcome as de-

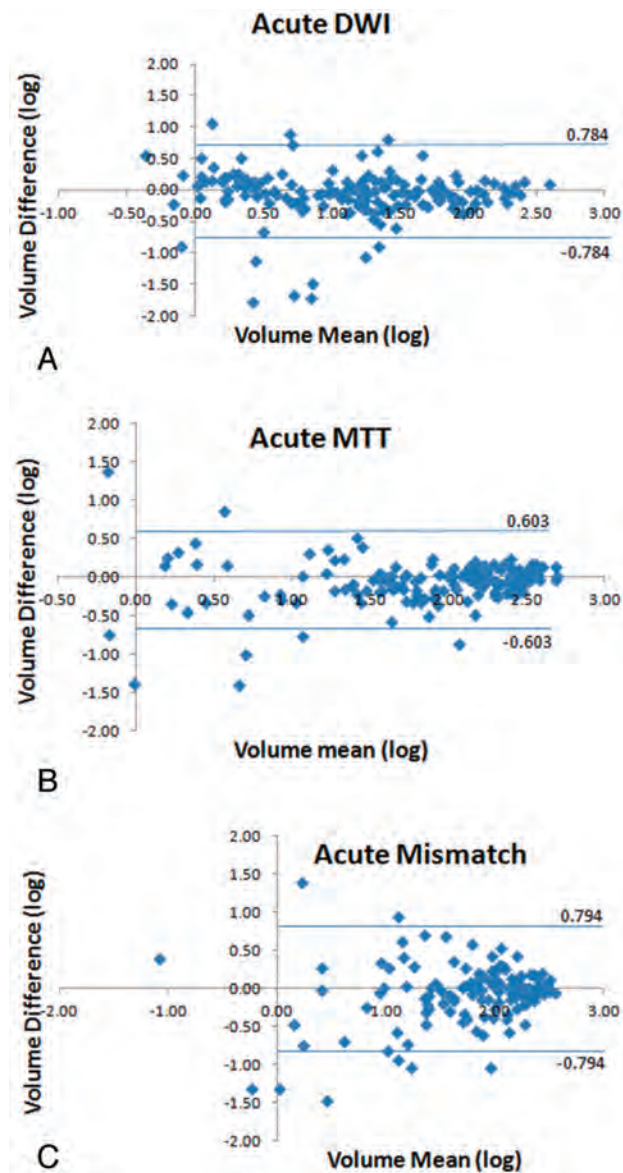


FIG 3. Bland-Altman plots of the ABC/2 and planimetric volume measurements demonstrate the difference between the log volume of the planimetric measurement and the log volume of the ABC/2 measurement over the mean for DWI (A), MTT (B), and mismatch (C). Threshold lines above and below plots represent values that are 2 SD from the mean difference. Plots are on the logarithmic scale.

Table 2: Volume statistics for discrepant patients (n = 17, nine false-positives and eight false-negatives) on the basis of the ABC/2 method compared with the planimetric method by use of the mismatch definition ≥ 50 mL

Case No.	ABC/2 DWI (mL)	ABC/2 MTT (mL)	ABC/2 Mismatch (mL)	ABC/2 Mismatch Percentage	Planimetric DWI (mL)	Planimetric MTT (mL)	Planimetric Mismatch (mL)	Planimetric Mismatch Percentage
FP 1	3.9	54.2	50.3	92.8	3.8	38.4	34.6	90.2
FP 2	32.3	86.8	54.5	62.8	13.5	40.4	26.9	66.7
FP 3	26.5	83.2	56.6	68.1	17.3	22.4	5.1	22.8
FP 4	20.4	97.3	76.9	79.0	9.0	45.0	36.0	80.0
FP 5	14.1	97.7	83.7	85.6	20.3	51.1	30.8	60.2
FP 6	23.0	110.6	87.6	79.2	26.1	61.3	35.2	57.5
FP 7	4.6	133.7	129.1	96.6	5.6	41.5	36.0	86.6
FP 8	357.9	513.3	155.4	30.3	436.5	474.3	37.9	8.00
FP 9	16.7	318.1	301.4	94.8	15.1	42.6	27.5	64.6
FN 1	111.3	121.4	10.1	8.3	72.2	122.5	50.3	41.1
FN 2	44.2	60.6	16.4	27.0	26.8	105.8	79.1	74.7
FN 3	91.7	119.7	28.1	23.4	71.1	133.7	62.6	46.8
FN 4	266.3	298.4	32.1	10.7	223.5	344.8	121.3	35.2
FN 5	207.5	247.2	39.6	16.0	180.5	254.6	74.1	29.1
FN 6	2.3	0.0	N/A	N/A	3.1	186.5	183.3	98.3
FN 7	311.0	291.0	N/A	N/A	279.2	354.1	74.9	21.2
FN 8	243.5	240.5	N/A	N/A	170.3	261.0	90.7	34.8

Note:—FP indicates false-positive; FN = false-negative.

Table 3: Summary of functional outcome (modified Rankin Scale) at follow-up of all patients on the basis of mismatch definition of ≥ 50 mL by use of the ABC/2 and planimetric methods

Functional Outcome (Modified Rankin Scale) at Follow-Up	Positive ABC/2 Quantitative Mismatch (n = 94)	Positive Planimetric Quantitative Mismatch (n = 92)
Favorable outcome (0,1): all patients with positive mismatch	28%	27%
Favorable outcome (0,1): patients ≤ 80 years of age with positive mismatch	39%	38%

defined by modified Rankin Scale score = 0 or 1 (Table 3). The median last follow-up modified Rankin Scale score was 3 (IQR, 1–5), on the basis of the available data (n = 177), with a total of 66 patients (37.3%) with a good outcome. Among patients classified with a mismatch ≥ 50 mL by either the ABC/2 or planimetric method, 27–28% had a favorable outcome (Table 3). Considering only patients with age ≤ 80 years, the favorable outcomes were still consistent and, as expected, higher (38–39%). The ABC/2 and planimetric methods demonstrated nearly identical favorable outcome rates on the basis of the presence of positive mismatch defined as ≥ 50 mL.

Inter-Rater Reliability of ABC/2 Volume Method

There was strong inter-rater correlation and agreement between the 2 independent sets of ABC/2 measurements. The Spearman correlation coefficients were 0.89, 0.91, and 0.82 for the DWI (n = 193), MTT (n = 180), and mismatch (n = 125) measurements, respectively (P < .01). The Bland-Altman plots (Fig 4) of the 2 independent ABC/2 measurements demonstrated that 95%, 95%, and 97% for the DWI, MTT, and mismatch measurements were within the thresholds defined by 2 SD from the mean differences.

DISCUSSION

Our study demonstrates that mismatch volume calculated by the ABC/2 quantitative method is equivalent to the planimetric method. This expands on our prior study that established the equivalence between the visual and planimetric methods.⁵ However, as used in prior clinical trials, it is likely that a specific amount of penumbra must be calculated beyond visual confirmation of mismatch only. The equivalence between the ABC/2 and planimetric methods was supported by 3 main results. The Bland-Altman analysis demonstrated that 93% of the 193 patients in this study had mismatch volumes consistent between the ABC/2 and planimetric methods. The Spearman correlation coefficients of the DWI and MTT measurements were both high between the ABC/2 and planimetric methods. The sensitivity (0.91), specificity (0.90), accuracy (0.91), PPV (0.90), and NPV (0.91) were excellent for the ABC/2 method by use of the planimetric mismatch definition ≥ 50 mL. The ABC/2 method had both high PPV and NPV for the measurement of mismatch compared with the planimetric method, both of which have not been previously demonstrated in similar studies by Sims et al¹³ and Pedraza et al.¹⁴ This is also the largest ischemic stroke study looking at MR imaging–determined mismatch by both ABC/2 and planimetric methods. This study provides a reference for selection of mismatch thresholds and the comparability across these methods for future stroke trial design.

The ABC/2 and planimetric measurements of DWI and MTT lesion volumes used in this study are highly dependent on the “eyeball” image interpretation by the raters. The “eyeball” approach has been used and generally agreed to approximate the 20% mismatch threshold.¹⁰ In most stroke centers, this visual confirmation of mismatch is the most commonly applied method. However, the mismatch definition ≥ 50 mL was the focus of this study, based on the prior study⁵ that demonstrated equivalence between the visual method, that is, the 20% eyeball method, and the planimetric method by use of this threshold. The intrarater and inter-rater reliability of these methods have been documented as highly reliable.^{5,6,13} ABC/2 measurements can be per-

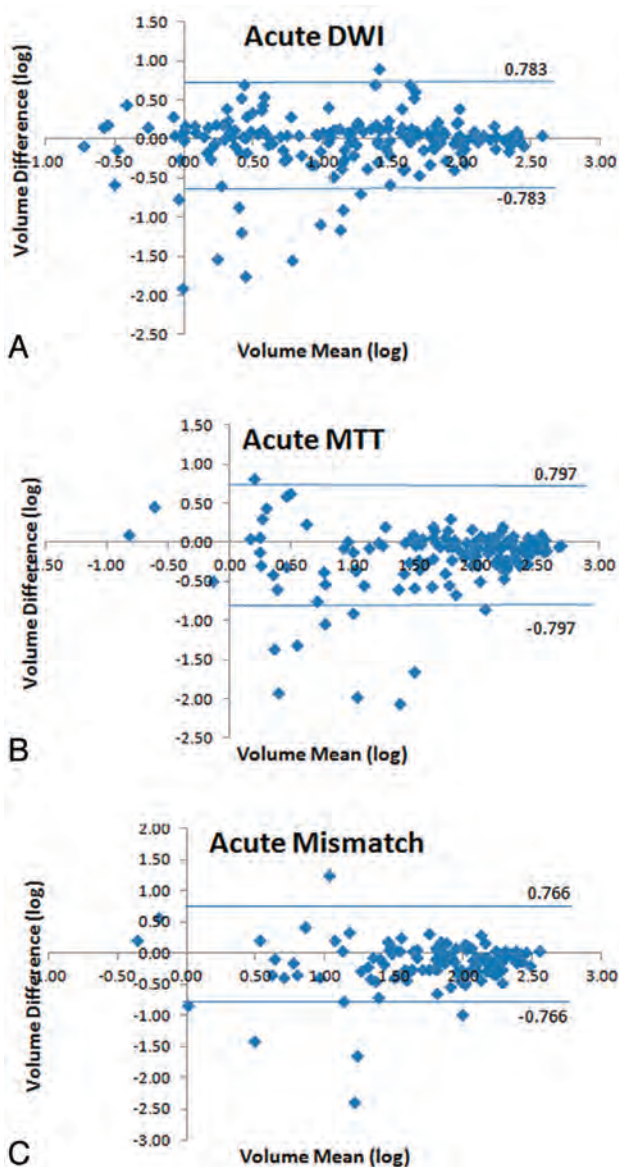


FIG 4. Bland-Altman plots of the 2 independent ABC/2 volume measurements demonstrate the difference between the log volume of the measurements over the average for DWI (A), MTT (B), and mismatch (C). Threshold lines above and below plots represent values that are 2 SD from the mean difference. Plots are on the logarithmic scale.

formed on any scanner, and, as shown in this study and others, are a reliable and accurate method to assess brain volumes.^{1-3,5,13} The ABC/2 has the advantage that it can be performed in real time by clinicians caring for patients with acute ischemic stroke. The average computation time of automated algorithms varies across centers; not all centers have access to automated algorithms, and not all centers acquire the images or format suitable for processing by these algorithms. If future clinical trials have inclusion criteria that are based on specific mismatch volumes, a valid, reliable, fast, and accessible method beyond visual confirmation will be required. Gómez-Mariño et al¹⁸ recommended that the ABC/2 method be applied routinely in acute stroke because it is a fast and low-cost method. We propose that the ABC/2 method is an alternative method when automated mismatch measurements are not available.

Our study has several limitations. We attempted to replicate the methods readily available on a MR imaging scanner; however, the measurements were not actually performed in an acute clinical setting. Image interpretation differences between the raters were a source of error, independent of the methods. Some of these differences probably were due to suboptimal diffusion and perfusion acquisitions compounded by the differences in the experience of the 2 raters in this study. As shown in Table 2, discrepancy case FN6 was identified as a negative perfusion case by the ABC/2 rater but was measured as a significant perfusion deficit by the planimetric rater. One specific limitation of the ABC/2 method was how discontinuous lesions were evaluated; only the largest lesion was measured rather than combining measurements across the multiple lesions. This probably contributed to some of the discrepancies seen between the ABC/2 and planimetric methods listed in Table 2.

We found that mismatch is common among thrombolytic-treated patients, whether visually confirmed (35%) or defined by mismatch ≥ 50 mL by use of the ABC/2 method (31%) and is associated with a favorable outcome. We conclude that the ABC/2 method is accurate for classifying the presence of MR imaging-determined quantitative mismatch in patients with acute stroke and therefore a potential tool to quickly determine a treatable mismatch pattern. One possible future study is to apply the ABC/2 method in the acute clinical setting to demonstrate the feasibility of the use of this method when making clinical trial inclusion decisions. Ideally, this study would be performed in conjunction with the application of an automated mismatch method to determine the agreement between these methods.

ACKNOWLEDGMENTS

The authors would like to acknowledge and thank the NIH Stroke Team and the patients for their valuable participation and cooperation.

REFERENCES

1. Kothari RU, Brott T, Broderick JP, et al. **The ABCs of measuring intracerebral hemorrhage volumes.** *Stroke* 1996;27:1304–05
2. Gebel JM, Sila CA, Sloan MA, et al. **Comparison of the ABC/2 estimation technique to computer-assisted volumetric analysis of intraparenchymal and subdural hematomas complicating the GUSTO-1 trial.** *Stroke* 1998;29:1799–801
3. Huttner HB, Steiner T, Hartmann M, et al. **Comparison of ABC/2 estimation technique to computer-assisted planimetric analysis in warfarin-related intracerebral parenchymal hemorrhage.** *Stroke* 2006;37:404–08
4. Straka M, Albers GW, Bammer R. **Real time diffusion-perfusion mismatch analysis in acute stroke.** *J Magn Reson Imaging* 2010;32:1024–37
5. Luby M, Ku KD, Latour LL, et al. **Visual perfusion-diffusion mismatch is equivalent to quantitative mismatch.** *Stroke* 2011;42:1010–14
6. Schellinger PD, Jansen O, Fiebich JB, et al. **Feasibility and practicality of MR imaging of stroke in the management of hyperacute cerebral ischemia.** *AJNR Am J Neuroradiol* 2000;21:1184–89
7. Hacke W, Albers G, Al-Rawi Y, et al, DIAS Study Group. **The Desmoteplase in Acute Ischemic Stroke Trial (DIAS): a phase II MRI-based 9-hour window acute stroke thrombolysis trial with intravenous desmoteplase.** *Stroke* 2005;36:66–73
8. Furlan AJ, Eyding D, Albers GW, et al. **Dose escalation of desmote-**

- plase for acute ischemic stroke (DEDAS): Evidence of safety and efficacy 3 to 9 hours after stroke onset. *Stroke* 2006;37:1227–31
9. Hacke W, Furlan AJ, Al-Rawi Y, et al. **Intravenous desmoteplase in patients with acute ischaemic stroke selected by MRI perfusion-diffusion weighted imaging or perfusion CT (DIAS-2): a prospective, randomised, double-blind, placebo-controlled study.** *Lancet Neurol* 2009;8:141–50
 10. Davis SM, Donnan GA, Parsons MW, et al, EPITHET Investigators. **Effects of alteplase beyond 3 h after stroke in the Echoplanar Imaging Thrombolytic Evaluation Trial (EPITHET): a placebo-controlled randomised trial.** *Lancet Neurol* 2008;7:299–309
 11. Butcher KS, Parsons M, MacGregor L, et al, EPITHET Investigators. **Refining the perfusion-diffusion mismatch hypothesis.** *Stroke* 2005;36:1153–59
 12. Albers GW, Thijs VN, Wechsler L, et al, DEFUSE Investigators. **Magnetic resonance imaging profiles predict clinical response to early reperfusion: the diffusion and perfusion imaging evaluation for understanding stroke evolution (DEFUSE) study.** *Ann Neurol* 2006;60:508–17
 13. Sims JR, Gharai LR, Schaefer PW, et al. **ABC/2 for rapid clinical estimate of infarct, perfusion, and mismatch volumes.** *Neurology* 2009;72:2104–10
 14. Pedraza S, Puig J, Blasco G, et al. **Reliability of the ABC/2 method in determining acute infarct volume.** *J Neuroimaging* 2012;22:155–59
 15. Vogt G, Laage R, Shuaib A, et al, VISTA Collaboration. **Initial lesion volume is an independent predictor of clinical stroke outcome at day 90: an analysis of the Virtual International Stroke Trials Archive (VISTA) database.** *Stroke* 2012;43:1266–72
 16. Warach S, Al-Rawi Y, Furlan AJ, et al. **Refinement of the magnetic resonance diffusion-perfusion mismatch concept for thrombolytic patient selection: insights from the desmoteplase in acute stroke trials.** *Stroke* 2012;43:2313–18
 17. Luby M, Bykowski JL, Schellinger PD, et al. **Intra- and interrater reliability of ischemic lesion volume measurements on diffusion-weighted, mean transit time and fluid-attenuated inversion recovery MRI.** *Stroke* 2006;37:2951–56
 18. Gómez-Mariño R, André C, Novis SA. **Volumetric determination of cerebral infarction in the acute phase using skull computed tomography without contrast: comparative study of 3 methods.** *Arq Neuropsiquiatr* 2001;59:380–83

4D CT Angiography More Closely Defines Intracranial Thrombus Burden Than Single-Phase CT Angiography

A.M.J. Frölich, D. Schrader, E. Klotz, R. Schramm, K. Wasser, M. Knauth, and P. Schramm



ABSTRACT

BACKGROUND AND PURPOSE: In patients with acute stroke, the location and extent of intravascular thrombi correlate with clinical and imaging outcomes and have been used to predict the success of intravenous thrombolysis. We hypothesized that 4D-CTA reconstructed from whole-brain CTP more closely outlines intracranial thrombi than conventional single-phase CTA.

MATERIALS AND METHODS: Sixty-seven patients with anterior circulation occlusion were retrospectively analyzed. For 4D-CTA, temporal maximum intensity projections were calculated that combine all 30 spiral scans of the CTP examination through temporal fusion. Thrombus extent was assessed by a semi-quantitative clot burden score (0–10; in which 0 = complete unilateral anterior circulation occlusion and 10 = patent vasculature). In patients with sufficient collateral flow, the length of the filling defect and corresponding hyperdense middle cerebral artery sign on NCCT were measured.

RESULTS: Clot burden on temporal maximum intensity projection (median clot burden score, 7.0; interquartile range, 5.1–8.0) was significantly lower than on single-phase CT angiography (median, 6.0; interquartile range, 4.5–7.0; $P < .0001$). The length of the hyperdense middle cerebral artery sign (14.30 ± 5.93 mm) showed excellent correlation with the filling defect in the middle cerebral artery on temporal maximum intensity projection (13.40 ± 6.40 mm); this filling defect was larger on single-phase CT angiography (18.08 ± 6.54 mm; $P = .043$).

CONCLUSIONS: As the result of an increased sensitivity for collateral flow, 4D-CTA temporal maximum intensity projection more closely outlines intracranial thrombi than conventional single-phase CT angiography. Our findings can be helpful when planning acute neurointervention. Further research is necessary to validate our data and assess the use of 4D-CTA in predicting response to different recanalization strategies.

ABBREVIATIONS: CBS = clot burden score; HMCAS = hyperdense middle cerebral artery sign; ICC = intraclass correlation coefficient; spCTA = single-phase CT angiography; tMIP = temporal maximum intensity projection

In patients with acute stroke with large-vessel occlusion, the location and extent of intracranial arterial thrombi has been shown to correlate with infarct size and clinical outcome.^{1–3} The length and location of clot has also been used to predict treatment response, suggesting that more proximal and longer clots may be resistant to intravenous thrombolysis.^{4,5} Thus, reliable depiction of thrombus

burden may provide important prognostic information and affect treatment decisions in the acute phase. Thin-section NCCT has been used for clot depiction. However, it has been shown that NCCT appearance of clot depends on thrombus composition,^{6–8} suggesting that some (low-attenuation) portions of clot could be less well discernible with this technique. NCCT may also be more challenging when vascular calcifications or a high hematocrit appear as intra-arterial hyperdensities. CTA is widely used for thrombus detection in patients with stroke. However, visibility of thrombus extent on CTA depends on the strength of collateral flow, particularly with current-generation fast acquisition protocols.⁹ Volumetric CTP examinations obtained as part of a multi-modal stroke CT protocol can be reconstructed to yield time-resolved 4D-CTA.^{10–12} Compared with standard spCTA, this technique provides a broad temporal coverage from nonenhanced through arterial to venous phases. We hypothesized that 4D-CTA is more sensitive to delayed contrast arrival and allows better approximation of intracranial clot burden than standard arterial-phase spCTA. Because there is no current criterion standard for thrombus imaging, we

Received December 4, 2012; accepted after revision January 17, 2013.

From the Departments of Neuroradiology (A.M.J.F., D.S., R.S., M.K., P.S.) and Neurology (K.W.), University Medical Center Göttingen, Göttingen, Germany; and Siemens AG (E.K.), Healthcare Sector, Computed Tomography, Forchheim, Germany.

Paper previously presented in part at: Annual Meeting of the American Society of Neuroradiology, April 23, 2012; New York, New York.

This work was supported by intradepartmental funding. The department has a research agreement with Siemens AG, Forchheim, Germany.

Please address correspondence to Andreas M.J. Frölich, MD, Department of Neuroradiology and Department of Neurology, University Medical Center Göttingen, Robert-Koch-Str 40, 37075 Göttingen, Germany; e-mail: a.froelich@gmail.com

Indicates open access to non-subscribers at www.ajnr.org

<http://dx.doi.org/10.3174/ajnr.A3533>

compared clot burden measured on 4D-CTA and spCTA. In patients with a clearly visible HMCAS, we used its length as a reference to assess the accuracy of filling defects observed on 4D-CTA and spCTA.

MATERIALS AND METHODS

Study Design

We retrospectively identified patients with acute ischemic stroke from an institutional review board–approved endovascular stroke data base who met the following inclusion criteria: 1) presence of a complete multi-modal CT examination (including NCCT of the head, spCTA of the head and neck, and thin-section 4D-CTA reconstructions from the CTP data set), 2) time of symptom onset <24 hours, 3) acute anterior circulation intracranial vessel occlusion, and 4) attempted endovascular recanalization. Patients with insufficient coverage of the intracranial arteries or severe motion artifacts on 4D-CTA were excluded. For all patients, CTP parameter maps were used to assess salvageable brain tissue and guide treatment decisions, whereas 4D-CTA was reviewed retrospectively.

Image Acquisition

CT images were obtained on a 128-section multi-detector CT scanner (Definition AS+; Siemens, Erlangen, Germany). Scanning order was NCCT of the head, near whole-brain CTP, and, last, craniocervical CTA. Volumetric CTP data were acquired by means of a periodic spiral approach consisting of 30 consecutive spiral scans of the brain¹⁰ (96 mm in z-axis, 2-second delay after start of contrast injection, 1.5-second mean temporal resolution, 45-second total scan duration, 80 kV, 200 mAs, rotation time 0.3 seconds, maximum pitch 0.5, collimation 2×64×0.6 mm). A 36-mL bolus of contrast (Imeron 400; Bracco, Konstanz, Germany) was used at a flow rate of 6 mL/s followed by a 30-mL saline chaser at 6 mL/s. For spCTA (120 kV, 120 reference mAs, rotation time 0.3 seconds, pitch 0.6, collimation 2×64×0.6 mm), 65 mL of contrast was injected with a biphasic protocol (45 mL at 6 mL/s, 15 mL at 3 mL/s) and was followed by a 30-mL saline chaser at 3 mL/s. To reduce the total number of images, CTP data were reconstructed with a section width of 1.5 mm every 1 mm (Kernel H20f, 512 Matrix) for 4D-CTA, resulting in 2850 single images. spCTA was acquired with automatic bolus triggering in the aortic arch (100 HU, 2-second delay), and data were reconstructed with a section width of 0.75 mm every 0.4 mm. The effective dose (calculated by multiplying dose-length products with published conversion factors) was 5.3 mSv for the CTP scan, 1.1 mSv for the craniocervical CTA portion (20 cm from vertex), and 2.1 mSv for the remaining more caudal CTA range (15 cm).¹⁰ Biplanar DSA was obtained during the endovascular procedure (Axiom Artis dBA; Siemens).

Demographic Data

Demographic and clinical data obtained from medical records included age, sex, time from symptom onset to CT examination, and application of intravenous or intra-arterial recombinant tissue plasminogen activator. NIHSS score at presentation was retrospectively assigned by a stroke neurologist with certification for the scale. In patients with wake-up stroke, time last seen well was used as a substitute. When the time last seen well was not docu-

mented, symptom onset was defined as midnight when presenting between midnight and noon and noon when presenting between noon and midnight.

Image Analysis

Four-dimensional CTA data were processed with the use of a commercial software package (Dynamic Angio, Siemens) that includes automatic motion correction and a dedicated noise reduction technique as previously described¹⁰ and creates 3D temporal maximum intensity projection data. tMIP images essentially depict the maximum enhancement over the 45-second scan time for every voxel and therefore they fuse contrast opacification from early arterial up to late venous phases of the CTP examination into 1 CT data set (processing time is <80 seconds). This technique has also been referred to as “timing-invariant CTA.”¹³ In addition to axial thin-section source images, maximum intensity projections in axial and coronal planes were reconstructed for both spCTA and tMIP (10-mm section thickness, 3-mm increment). Two readers (12 years and 2 years of experience in acute stroke imaging) blinded to clinical information assessed tMIP and spCTA in randomized order according to a previously validated, semi-quantitative clot burden score.¹ CBS (0–10) is calculated as a sum of all visible patent vascular segments including the proximal and distal M1 segments of the middle cerebral artery (2 points each); supraclinoid ICA (2 points); and M2 branches, A1 anterior cerebral artery segment, and infraclinoid ICA (1 point each).¹ A CBS of 0 thus means complete unilateral anterior circulation intracranial occlusion. Biplanar DSA images obtained at the beginning of the endovascular procedure were evaluated for early partial or complete recanalization of the occluded vessel in direct comparison to spCTA.

Thrombus length was measured in patients with M1 occlusion and an unequivocal HMCAS. Because thin-section NCCT was not routinely obtained, the presence of HMCAS was assessed by 2 raters in consensus on nonenhanced thin-section (1.5-mm) images reconstructed from the early phase of the CTP examination. For this purpose, the temporal average of 1–5 spiral scans before the arrival of the contrast bolus was calculated to reduce noise compared with the raw 1.5-mm CTP sections. To qualify as unequivocal HMCAS, the attenuation in a region of interest within the affected middle cerebral artery had to be at least 20% higher than on the unaffected side. HMCAS length was assessed by manually adjusting a semi-automatic, curved, 3D vessel analysis tool (InSpace, Siemens) to fit the intravascular hyperattenuation and measuring its length along the axis of the resulting curved vessel skeleton. On 4D-CTA and spCTA, the length of the filling defect within the middle cerebral artery was measured by connecting straight lines in axial or coronal planes at the discretion of the rater if at least 1 of the raters was able to define a proximal and distal clot end.

Statistical Analysis

Standard descriptive statistics are reported for baseline variables, means are reported ± standard deviation. Inter-rater reliability was assessed by the single-measures intraclass correlation coefficient for absolute agreement. Median CBSs for the 2 raters were calculated for spCTA and tMIP and then compared with the Wil-

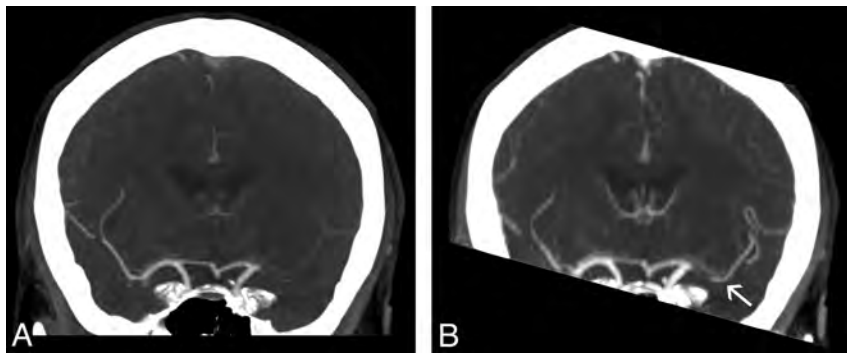


FIG 1. Assessment of clot burden. A, Coronal spCTA maximum intensity projection in a patient with left-sided middle cerebral artery occlusion shows lack of opacification of the entire M1 segment (4 points) as well as M2 segments (1 point each), resulting in a CBS of 4. B, The corresponding tMIP reveals delayed filling of the very distal M1 as well as M2 segments (arrow). Raters defined only the proximal M1 as occluded and assigned a CBS of 8.

coxon test. Spearman rank correlation and the Mann-Whitney test for independent samples were used to correlate CBS with clinical variables. The paired *t* test, Pearson correlation, and Bland-Altman analyses were used to assess mean clot length and filling defect measurements. $P < .05$ was considered statistically significant. All statistical analyses were performed with the use of MedCalc 12 (MedCalc Software, Mariakerke, Belgium).

RESULTS

Demographic and Clinical Data

Among 149 consecutive patients with acute stroke (January 2009 to February 2012) in our university hospital endovascular stroke treatment data base, thin-section 4D-CTA was available in 71 patients with anterior circulation vessel occlusion. After excluding patients with insufficient coverage of the basal intracranial arteries for CBS evaluation ($n = 2$) and severe motion artifacts ($n = 2$), 67 patients entered the final analysis. Mean age was 70 ± 14 years; 36 patients (54%) were women. Median NIHSS score on presentation was 17 (range, 4–26). Mean time between symptom onset and CT was 150 minutes (30–624 minutes). Mean time between CT and DSA was 88 minutes (31–179 minutes). The most proximal vessel occlusion was classified as common carotid artery ($n = 1$), cervical carotid artery ($n = 11$), terminal internal carotid artery ($n = 10$), as well as the M1 ($n = 42$) and M2 ($n = 3$) segments of the middle cerebral artery. Intravenous bridging thrombolysis was used in 55 patients (82%). Six of these patients (11%) showed early partial or complete recanalization on the initial DSA series.

Clot Burden

Median CBS on tMIP (7.0; range, 2.5–9.0; interquartile range, 5.1–8.0) was significantly higher than on spCTA (6.0; range, 1.0–9.0; interquartile range, 4.5–7.0; $P < .0001$; Fig 1). When looking at individual cases, median CBS was identical between tMIP and spCTA in 22 cases (33%). The largest difference in CBS was 4 points (higher on tMIP) and the lowest -1 point (lower on tMIP). In 23 patients (34%), median tMIP CBS was ≥ 1 point higher than spCTA; in 9 patients (13%), it was ≥ 2 points higher. Conversely, spCTA CBS was ≥ 1 point higher than tMIP in only 2 cases (3%). The distal thrombus end could be identified by both raters in 30 patients on spCTA (45%) versus 48 patients (72%) on tMIP. Inter-rater reliability between the 2 raters was substantial

for both spCTA (ICC: 0.74, 95% CI: 0.61–0.83) and tMIP (ICC: 0.74, 95% CI: 0.60–0.84).

CBS scores on spCTA tended to decrease with increasing presenting NIHSS score without reaching significance ($\rho = -0.197$; $P = .109$); this was less apparent for tMIP ($\rho = -0.135$; $P = .2771$). The presence of early recanalization after intravenous thrombolysis did not significantly correlate with CBS ($P = 1.0$ for spCTA; $P = .40$ for tMIP). Mean time from CT to DSA was similar for patients with and without early recanalization (78 versus 90 minutes, $P = .365$).

Thrombus Length

Among 42 patients with M1 occlusion, 31 had sufficient collateral flow for length analysis of the filling defect according to at least 1 rater. Mean length of the filling defect was significantly lower on tMIP (12.50 ± 5.81 mm) than on spCTA (14.44 ± 6.65 mm; $P = .036$). Among all M1 occlusions, 14 (33%) had an unequivocal HMCAS on thin-sectioned non-enhanced CTP reconstructions. Filling defects were measurable in 13 of these on tMIP versus 10 on spCTA. Mean HMCAS length for these 10 patients was 14.30 ± 5.93 mm. The mean corresponding filling defect on tMIP (13.40 ± 6.40 mm) was significantly shorter than on spCTA (18.08 ± 6.54 mm; $P = .043$). Length of the filling defect on tMIP showed excellent correlation with the length of the HMCAS ($n = 13$; $r = 0.94$; 95% CI: 0.83–0.98; $R^2 = 0.88$; $P < .0001$; Fig 2). There was no significant correlation for spCTA ($n = 10$; $r = 0.52$; 95% CI: -0.17 – 0.86 ; $R^2 = 0.27$; $P = .127$). Bland-Altman plots showed increased accuracy of tMIP for predicting HMCAS length (Fig 3).

DISCUSSION

Assessing Clot Burden and Thrombus Length

The present study shows that tMIP reconstructions from 4D-CTA more closely outline intracranial clot burden than conventional arterial-phase spCTA. Although the appearance of clot burden can be identical on spCTA and tMIP, the latter revealed significant additional information on clot extent in approximately one-third of our population. The distal thrombus end was identified more often on tMIP than on spCTA (both raters identified it in 72% versus 45% of cases). Because tMIP can be reconstructed from volumetric CTP examinations without additional contrast or radiation exposure, the presented approach can be easily integrated into existing CT stroke imaging protocols.

Importantly, it is conceivable that thrombi could also be more closely approximated by adjusting the speed and triggering delay of spCTA to reveal delayed collateral flow. However, intracranial bolus passage is difficult to predict, and delaying the scan too much may dramatically reduce arterial contrast. Adjustment of spCTA timing thus does not seem justified on the basis of our present results, especially considering that tMIP can be obtained simply by adding another reconstruction, without otherwise altering the multi-modal CT protocol.

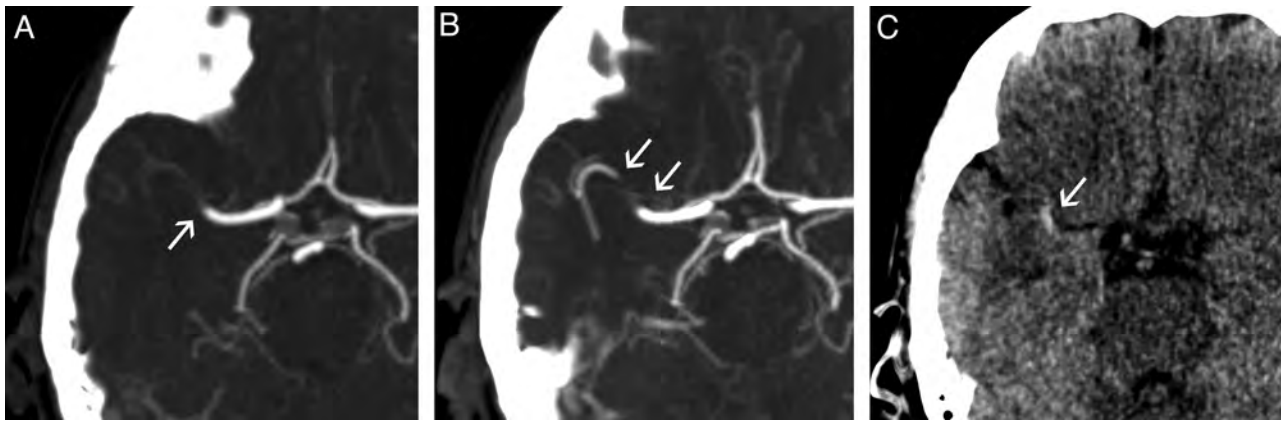


FIG 2. Filling defects and hyperattenuated clot. *A*, Axial spCTA maximum intensity projection shows a right-sided middle cerebral artery occlusion (*arrow*). *B*, On the corresponding tMIP, the occluding thrombus is well visualized as a filling defect. *C*, Axial thin-section image from the nonenhanced phase of the CTP scan shows an HMCAS matching this filling defect.

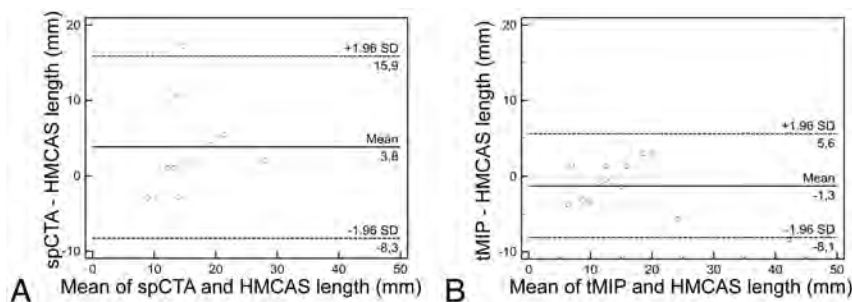


FIG 3. Measuring clot length. Bland-Altman plots illustrate the comparative precision of filling defects on spCTA (*A*) and on tMIP (*B*) in predicting the length of the HMCAS.

The overall observed difference in CBS between tMIP and spCTA was rather small (1 point difference of the median), in part because of patients with identical CBS on tMIP and spCTA ($n = 22$). When a difference was present, a commonly observed pattern was that tMIP showed patency of M2 branches not seen on spCTA. The difference in CBS is best explained by the increased sensitivity of tMIP for delayed collateral flow reaching the vasculature distal to the occlusion site. Indeed, in the initial description of the CBS it was pointed out that the score depends on delayed collateral flow.¹ The authors conclude that this may actually be a strength of the score, because decreased collateral flow (which in turn will decrease the CBS on spCTA) has been associated with larger infarcts and poorer outcome. The tMIP technique may thus weaken the prognostic power of the CBS because temporal fusion makes strong, early collateral flow virtually indistinguishable from delayed, weaker collaterals, leading to identical CBS despite different physiologic implications. Interestingly, we observed a (nonsignificant) trend toward a higher presenting NIHSS with lower CBS on spCTA; this correlation was less apparent on tMIP. Thus, we deem it possible that diminished collateral flow (leading to lower CBS scores on spCTA but not necessarily on tMIP) is accompanied by more severe clinical deficits on presentation.

To validate both spCTA and tMIP against a reference, we assessed clot length in patients with M1 occlusion who also had an unequivocal HMCAS and sufficient collateral flow according to at least 1 rater. Our results show an excellent correlation between the length of the filling defect on tMIP and the length of the HMCAS,

confirming that tMIP may adequately outline middle cerebral artery thrombi. Correlation of HMCAS with spCTA was not significant, probably because of inaccuracy in estimating the filling defect on spCTA, depending on collateral flow. Previous investigators have shown a strong correlation of the HMCAS and the spCTA filling defect, but they specifically selected patients with sufficient collateral flow and a filling defect matching the HMCAS,¹⁴

which may explain this discrepancy. In 2 patients with long (>20 mm) clots, the tMIP filling defect was measured >5 mm shorter than the HMCAS, which we tend to attribute to the slightly different measurement techniques used (curved analysis for HMCAS, orthogonal lines for filling defects).

Thin-section NCCT has previously been used elegantly to assess clot length (measured as HMCAS length) and predict response to intravenous thrombolysis.⁵ Compared with tMIP, this represents a technically less demanding approach to determine middle cerebral artery clot length. However, the technique may be affected by clot composition, because erythrocyte-rich thrombi have been shown to display higher attenuation values than platelet-rich thrombi.^{6,8} Furthermore, the presence of vascular calcifications or a high hematocrit may mimic the HMCAS and thus decrease specificity.¹⁴ Thus, tMIP could be helpful in quantifying thrombus length when an HMCAS is not unequivocally seen or when the longitudinal extent of the HMCAS is uncertain. In addition, it is conceivable that an erythrocyte-rich, high-attenuation, and hence well-visible thrombus may be accompanied by appositional, platelet-rich, low-attenuation thrombi, which would lead to discrepancies between the HMCAS and CTA imaging. This could hypothetically account for some of the presently observed differences between tMIP and HMCAS; however, this did not affect overall correlation of tMIP and HMCAS in our comparably small sample size. Particularly in patients with weak collateral flow, any arterial segment not opacified on tMIP could theoretically harbor thrombi or stagnant blood, potentially in different stages of the clotting process. Correlation with thin-section NCCT

could then reveal which parts correspond to high-attenuation thrombus. For these reasons, we propose that CT angiographic techniques may in some cases offer complementary information on clot physiology compared with the assessment of the HMCAS. The value of tMIP, then, lies in the ability to depict the complete extent of vessels perfused within the acquisition time.

One of our study's limitations is that thin-section NCCT was not routinely obtained. Instead, we used temporal average thin-section reconstructions from the early, nonenhanced phase of the CTP examination to assess the HMCAS, which may have affected sensitivity and comparability of our results. We observed an unequivocal HMCAS in 33% of patients with M1 occlusion, which is low compared with recently reported sensitivity and specificity values of the HMCAS on thin-section NCCT.¹⁵ Four-dimensional CTA was reconstructed with a higher section width and increment than spCTA (1.5/1.0 mm versus 0.75/0.4 mm), which was chosen as a compromise between a manageable number of images and acceptable image quality. Other limitations include the presence of more venous enhancement on tMIP than on spCTA, which may in some cases make evaluation of the arterial tree more difficult. However, this was not a limiting factor for arterial analysis in our patients. Slight venous contamination was also invariably present on spCTA images because of residual contrast material from the immediately preceding CTP examination. We also cannot exclude that additional vessel segments would become visible on tMIP if the acquisition time of the CTP examination would be increased beyond the presently used 45 seconds. Finally, the retrospective design of our study carries the risk of selection bias, particularly because we only assessed patients undergoing endovascular treatment. However, this allowed us to assess early recanalization on conventional angiography after bridging thrombolysis. We did not observe a clear relation between early recanalization and clot burden, which we tend to attribute to the low sample size of early recanalizers ($n = 6$). This low early recanalization rate (11%) emphasizes previous reports on this matter.⁴ It is important to note that recanalization was assessed relatively early in our study: Thrombolysis was initiated as soon as possible after interpretation of NCCT; the mean 88 minutes between CT and DSA can therefore be used to approximate the maximum duration between thrombolysis and assessment of early recanalization. This may have contributed to the relatively low recanalization rate observed. Assessing tMIP and other 4D-CTA reconstructions in predicting response to standard intravenous therapy seems desirable; however, this would require a different patient collective to compare outcomes after intravenous therapy only.

Clinical Implications

Accurate information on the extent of thrombus is important for adequate treatment planning. Previous studies have consistently shown that larger, more proximal clots often do not respond to intravenous thrombolysis and are associated with worse clinical outcome.¹⁻⁵ As a result, more aggressive endovascular recanalization procedures are often considered in these patients. With an increasing number of available neurovascular medical and device-assisted treatment options, precise definition of the target lesion, that is, the occluding thrombus, is desirable. Animal model

evidence has shown that longer clots (>10 mm) are associated with decreased procedural success and increased rates of complications such as distal embolization during mechanical thrombectomy.¹⁶ Evaluation of the patency of M2 branches may also be particularly helpful when mechanical thrombectomy is considered, further emphasizing the need for precise thrombus delineation from the interventionalist's perspective. With the recent halting of the Interventional Management of Stroke III trial, it is becoming increasingly clear that adequate selection of patients likely to benefit from a specific type of endovascular therapy is crucial in establishing evidence of clinical efficacy. Besides clinical variables and imaging strategies directed at defining salvageable brain tissue, clot characteristics such as length,⁵ location,^{17,18} composition,⁶⁻⁸ and degree of luminal occlusion¹⁹⁻²¹ should be considered as potential predictors of the clinical efficacy of different available medical and endovascular treatment modalities.

CONCLUSIONS

Because of an increased sensitivity for delayed collateral flow, 4D-CTA tMIP improves the definition of clot extent compared with standard spCTA, more frequently and more closely outlining thrombi occluding intracranial arteries. Precise assessment of clot burden may help in making treatment decisions, especially when endovascular therapy is considered. Clot characteristics such as size, composition, and location should be further assessed as potential predictors of the efficacy of available medical and endovascular stroke treatment modalities.

ACKNOWLEDGMENTS

We thank Hans-Joachim Helms from our university's department of medical statistics for reviewing the statistical analyses.

Disclosures: Andreas Frölich—RELATED: Grant: Research grant with Siemens Healthcare; * Consulting Fee or Honorarium: Speaker's honoraria from Siemens Healthcare; Support for Travel to Meetings for the Study or Other Purposes: Travel support from Siemens Healthcare. Ernst Klotz—UNRELATED: Employment: Full-time employee of Siemens Healthcare, Germany. Michael Knauth—RELATED: Support for Travel to Meetings for the Study or Other Purposes: Speaker's Bureau for Siemens Medical (not study-related); UNRELATED: Payment for Lectures (including service on speakers bureaus): Siemens Medical, Arcandis, Penumbra, Codman. Peter Schramm—RELATED: Support for Travel to Meetings for the Study or Other Purposes: Siemens AG (travel support); UNRELATED: Payment for Lectures (including service on speakers bureaus): Siemens AG (speakers honoraria) (*money paid to institution).

REFERENCES

1. Puetz V, Dzialowski I, Hill MD, et al. **Intracranial thrombus extent predicts clinical outcome, final infarct size and hemorrhagic transformation in ischemic stroke: the clot burden score.** *Int J Stroke* 2008;3:230–36
2. Sillanpaa N, Saarinen JT, Rusanen H, et al. **Location of the clot and outcome of perfusion defects in acute anterior circulation stroke treated with intravenous thrombolysis.** *AJNR Am J Neuroradiol* 2012;34:100–106
3. Tan IY, Demchuk AM, Hopyan J, et al. **CT angiography clot burden score and collateral score: correlation with clinical and radiologic outcomes in acute middle cerebral artery infarct.** *AJNR Am J Neuroradiol* 2009;30:525–31
4. Bhatia R, Hill MD, Shobha N, et al. **Low rates of acute recanalization with intravenous recombinant tissue plasminogen activator in ischemic stroke: real-world experience and a call for action.** *Stroke* 2010;41:2254–58
5. Riedel CH, Zimmermann P, Jensen-Kondering U, et al. **The importance of size: successful recanalization by intravenous thrombolysis**

- sis in acute anterior stroke depends on thrombus length. *Stroke* 2011;42:1775–77
6. Kim EY, Heo JH, Lee SK, et al. Prediction of thrombolytic efficacy in acute ischemic stroke using thin-section noncontrast CT. *Neurology* 2006;67:1846–48
 7. Liebeskind DS, Sanossian N, Yong WH, et al. CT and MRI early vessel signs reflect clot composition in acute stroke. *Stroke* 2011;42:1237–43
 8. Puig J, Pedraza S, Demchuk A, et al. Quantification of thrombus Hounsfield units on noncontrast CT predicts stroke subtype and early recanalization after intravenous recombinant tissue plasminogen activator. *AJNR Am J Neuroradiol* 2012;33:90–96
 9. Pulli B, Schaefer PW, Hakimelahi R, et al. Acute ischemic stroke: infarct core estimation on CT angiography source images depends on CT angiography protocol. *Radiology* 2012;262:593–604
 10. Frölich AM, Psychogios MN, Klotz E, et al. Angiographic reconstructions from whole-brain perfusion CT for the detection of large vessel occlusion in acute stroke. *Stroke* 2012;43:97–102
 11. Gratama van Andel HA, Venema HW, Majoie CB, et al. Intracranial CT angiography obtained from a cerebral CT perfusion examination. *Med Phys* 2009;36:1074–85
 12. Saake M, Goelitz P, Struffert T, et al. Comparison of conventional CTA and volume perfusion CTA in evaluation of cerebral arterial vasculature in acute stroke. *AJNR Am J Neuroradiol* 2012;33:2068–73
 13. Smit EJ, Vonken EJ, van der Schaaf IC, et al. Timing-invariant reconstruction for deriving high-quality CT angiographic data from cerebral CT perfusion data. *Radiology* 2012;263:216–25
 14. Riedel CH, Jensen U, Rohr A, et al. Assessment of thrombus in acute middle cerebral artery occlusion using thin-slice nonenhanced computed tomography reconstructions. *Stroke* 2010;41:1659–64
 15. Riedel CH, Zoubie J, Ulmer S, et al. Thin-slice reconstructions of nonenhanced CT images allow for detection of thrombus in acute stroke. *Stroke* 2012;43:2319–23
 16. Gralla J, Burkhardt M, Schroth G, et al. Occlusion length is a crucial determinant of efficiency and complication rate in thrombectomy for acute ischemic stroke. *AJNR Am J Neuroradiol* 2008;29:247–52
 17. Saarinen JT, Sillanpaa N, Rusanen H, et al. The mid-M1 segment of the middle cerebral artery is a cutoff clot location for good outcome in intravenous thrombolysis. *Eur J Neurol* 2012;19:1121–27
 18. Saqqur M, Uchino K, Demchuk AM, et al. Site of arterial occlusion identified by transcranial Doppler predicts the response to intravenous thrombolysis for stroke. *Stroke* 2007;38:948–54
 19. Christoforidis GA, Mohammad Y, Avutu B, et al. Arteriographic demonstration of slow antegrade opacification distal to a cerebrovascular thromboembolic occlusion site as a favorable indicator for intra-arterial thrombolysis. *AJNR Am J Neuroradiol* 2006;27:1528–31
 20. Frölich AM, Psychogios MN, Klotz E, et al. Antegrade flow across incomplete vessel occlusions can be distinguished from retrograde collateral flow using 4-dimensional computed tomographic angiography. *Stroke* 2012;43:2974–79
 21. Saqqur M, Tsvigoulis G, Molina CA, et al. Residual flow at the site of intracranial occlusion on transcranial Doppler predicts response to intravenous thrombolysis: a multi-center study. *Cerebrovasc Dis* 2009;27:5–12

4D Digital Subtraction Angiography: Implementation and Demonstration of Feasibility

B. Davis, K. Royalty, M. Kowarschik, C. Rohkohl, E. Oberstar, B. Aagaard-Kienitz, D. Niemann, O. Ozkan, C. Strother, and C. Mistretta

ABSTRACT

BACKGROUND AND PURPOSE: Conventional 3D-DSA volumes are reconstructed from a series of projections containing temporal information. It was our purpose to develop a technique which would generate fully time-resolved 3D-DSA vascular volumes having better spatial and temporal resolution than that which is available with CT or MR angiography.

MATERIALS AND METHODS: After a single contrast injection, projections from the mask and fill rotation are subtracted to create a series of vascular projections. With the use of these projections, a conventional conebeam CT reconstruction is generated (conventional 3D-DSA). This is used to constrain the reconstruction of individual 3D temporal volumes, which incorporate temporal information from the acquired projections (4D-DSA).

RESULTS: Typically, 30 temporal volumes per second are generated with the use of currently available flat detector systems, a factor of ~200 increase over that achievable with the use of multiple gantry rotations. Dynamic displays of the reconstructed volumes are viewable from any angle. Good results have been obtained by using both intra-arterial and intravenous injections.

CONCLUSIONS: It is feasible to generate time-resolved 3D-DSA vascular volumes with the use of commercially available flat detector angiographic systems and clinically practical injection protocols. The spatial resolution and signal-to-noise ratio of the time frames are largely determined by that of the conventional 3D-DSA constraining image and not by that of the projections used to generate the 3D reconstruction. The spatial resolution and temporal resolution exceed that of CTA and MRA, and the small vessel contrast is increased relative to that of conventional 2D-DSA due to the use of maximum intensity projections.

ABBREVIATIONS: II = image intensifier; IA = intra-arterial; TOA = time of arrival

In 1980, when DSA was introduced,¹⁻³ it was originally hoped that intravenous x-ray angiography would be feasible. However, the inability to clearly visualize vascular structures caused by vessel overlap as well as limited signal-to-noise ratio due to then available contrast medium and the image intensifier (II) detector technology quickly led to the adaption of techniques by use of small intra-arterial (IA) contrast injections in combination with the newly available real-time digital imaging capabilities. This capability greatly facilitated the development of the minimally invasive procedures by using x-ray angiography and the field of interventional radiology in general.

The feasibility of obtaining rotational volume acquisitions by using a C-arm angiographic system equipped with an II was initially simulated in 1988 and then by use of an II-based apparatus, implemented in 1996 by Ning and Kruger.^{4,5} In 1997, Fahrig et al^{6,7} extended this work showing both in vitro and in vivo results. These systems, as well as currently used systems with flat detectors, allow creation of 1 3D-DSA volume per gantry rotation. Since the introduction of commercial angiographic systems and software suitable for performing 3D-DSA in 1999, the assessment of vasculature in interventional x-ray suites has been done by using the combination of 3D-DSA volume reconstructions (non-time-resolved) and multiple conventional 2D-DSA acquisitions. Multiple 2D acquisitions have been necessary because of 1) the need to visualize the sequences of vascular filling and 2) the inability to clearly see anatomic details on the 3D reconstructions because of the resulting overlap of arterial and, in some instances, venous structures. The need to obtain multiple 2D temporal series at the desired view angle obviously contributes significantly to the radiation exposure and contrast medium dose associated with these examinations.

Received August 29, 2012; accepted after revision December 21.

From the University of Wisconsin School of Medicine and Public Health (B.D., E.O., B.A.-K., D.N., O.O., C.S., C.M.), Madison, Wisconsin; Siemens AG (K.R.), Healthcare Sector, Hoffman Estates, Illinois; and Siemens (M.K., C.R.), Research Collaborations, AX, Forchheim, Germany.

Please address correspondence to Charles Strother, MD, Department of Radiology, University of Wisconsin School of Medicine and Public Health, 600 North Highland Ave, Madison, WI 53792; e-mail: cstrother@uwhealth.org.

<http://dx.doi.org/10.3174/ajnr.A3529>

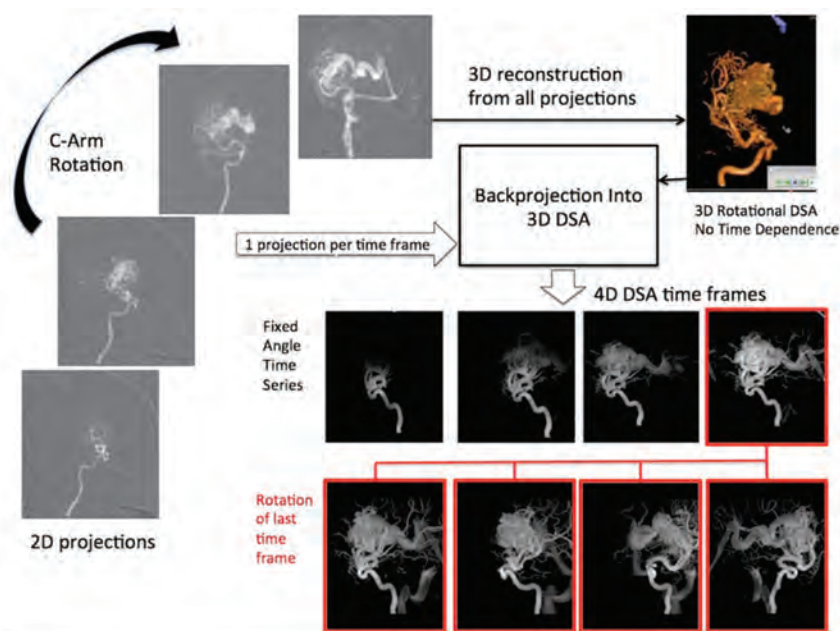


FIG 1. Schematic of 4D-DSA reconstruction. After creation of the 4D-DSA timeframes, each one may be viewed in a dynamic form showing the inflow and outflow of contrast from the vasculature, just as with a standard 2D-DSA series. As shown on the 2 series of 4 images at the bottom of the illustration, any selected time (in this case, the image framed in red in the top row of 4 images) may be viewed at any desired angle. Four possible views of the selected image are shown in the bottom row of 4 images.

The method that we describe involves the use of a 3D-DSA vascular volume as a constraining image. The proposed reconstruction method uses all, or most of, the projections obtained after a rotational acquisition done before (mask run) and after (fill run) the injection of contrast medium. This constraining volume is combined with the acquired projections to form a time-series of 3D volumes (4D-DSA). The 3D-DSA depicts an average of the vascular opacification present during the rotational acquisition. Each of the individual projections used to form the standard 3D-DSA volume contains temporal information. Although it must be understood that a CT volume cannot be reconstructed from a single projection, we do not propose a new 3D-DSA volume reconstruction technique. We have developed algorithms that permit 3D-DSA time-resolved volumes (4D-DSA) to be generated by use of the constraining volume and single x-ray projections. Rather than 1 vascular volume per gantry rotation, this technique typically generates 30 time-resolved 3D-DSA volumes per second (by use of a currently available flat detector angiographic system), a rate ~200 times faster than could be achieved by use of sequential gantry rotations, and at the same contrast and x-ray dose as used to obtain 1 standard 3D-DSA volume.

This capability allows for the viewing of the vasculature in a dynamic display, at any angle, for all time points at any desired angle. This largely eliminates the problem of vessel overlap. The availability of a “library” of time-resolved 3D timeframes thus facilitates diagnosis by providing the ability to view the anatomy not only in any desired view but also to do this at any desired phase of vascular filling, thus eliminating any confusion that might occur as the result of vascular overlap. An additional benefit is that it provides a library of vascular roadmaps at any stage of vascular filling for use in endovascular therapeutic procedures.

The purpose of the work was to investigate the feasibility of reconstructing time-resolved 3D vascular volumes (4D-DSA) from conventional 3D-DSA acquisitions.

MATERIALS AND METHODS

Data Acquisition

All images were acquired by use of either a biplane Artis dBA system or an Artis Zeego flat detector angiographic system (Siemens, Erlangen, Germany). All human and animal studies were performed under institutionally approved institutional review board and/or Animal Care and Use Committee protocols. Rotational images for subtracted 3D reconstructions were obtained by use of 5-, 8-, or 10-second acquisitions to capture the full cycle of contrast inflow and washout. To obtain a sufficient number of consistent projections for an accurate 3D reconstruction and to capture inflow and washout, the rotational acquisition must be long enough to follow a bolus through the vasculature. This may be

achieved by use of either multiple C-arm rotations or by use of C-arm rotations of an appropriate duration, for example, 5, 8, or 10 seconds. It seems likely that, depending on the dynamics of the circulation, that is, fast or slow, there will be particular acquisition protocols that are optimal for particular conditions, for example, a 5-second acquisition for evaluation of a patient with an aneurysm at the circle of Willis or a fast-flow carotid cavernous fistula or an 8- or 10-second acquisition for a patient with occlusive disease in which filling occurs by collaterals. More experience is required before definite recommendations can be given regarding choice of an optimal acquisition protocol. Intravenous studies were performed after injection of iohexol (300 mg I/mL) into a peripheral vein at the rate of 4 mL/s over 8–10 seconds followed by a 10-mL saline chase injected at the same rate. Intra-arterial studies were obtained by use of injection of 5–8 mL iohexol.

Image Processing and Reconstruction Process

Four-dimensional DSA reconstruction uses multiplicative projection processing to generate a series of time-resolved 3D volumes (4D-DSA) by embedding the time-resolved data from the standard projections of a rotational acquisition. Before back projection, the individual projections from the acquisition are spatially convolved to increase the SNR. They therefore form a low spatial frequency mask that basically enhances portions of the 3D constraining image that are present at each point in time. After a normalization step, this mask then provides proper projection weighting. As a result of the convolution process, the SNR of the individual timeframes is limited by the constraining image SNR ratio and not by the SNR of the individual projections. When the single projections are back-projected into the 3D volume, there is a tendency for the projection values from overlapping vessels to

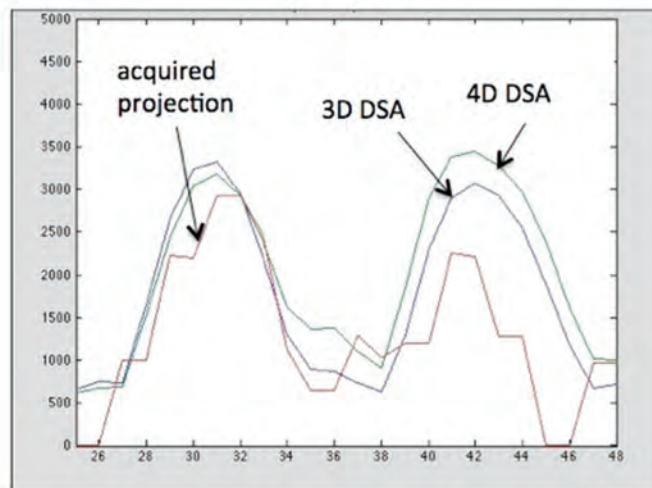
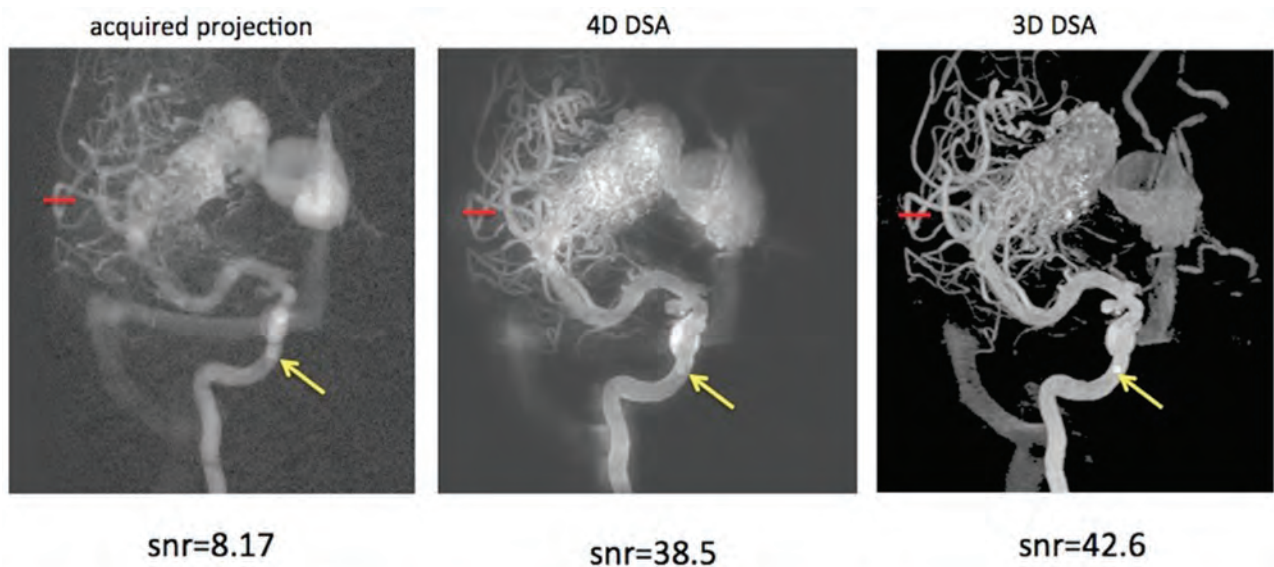


FIG 2. Images show a selected projection from a 3D-DSA rotational acquisition (*top left*), a 4D-DSA timeframe (*center*), and a standard 3D-DSA reconstruction (*right*). The SNRs of the 3 images at the region indicated by the yellow arrows are shown beneath each image. The single image at the bottom shows traces of the profile across the 2 arteries indicated by the red line. These images were obtained by use of an IA injection of contrast medium.

cause the deposition of erroneous signal (an opacity shadow from opacified vessel to nonopacified vessel) into vessels in the 3D volume. To reduce this effect, for each timeframe, an angular (temporal) search is performed, looking for a range of time before and after the frame that is being projected. After this search, the minimum signal for each voxel is assumed to be due to the ray with the minimum degree of overlap; that value is then assigned to the timeframe being processed. For voxels requiring an angle other than the current angle as a result of the search, the temporal resolution is lower than the typical 30/s rate, as data from a different timeframe are substituted. The frequency of this depends on the sparsity of the vessel configuration. However, overall volume frame rates of 6 frames/s are typical. Figure 1 illustrates the steps in this process. Any of the time-resolved 3D timeframes (3D volumes) can be rotated for viewing at whatever angle the user thinks gives the clearest depiction of the relevant vasculature. These 3D timeframes can be viewed with playback speed reduced or increased, paused, or replayed as desired. The user

interface provides for interactive 4D viewing of the 3D temporal volume timeframes and provides for a true interactive 4D viewing experience of the contrast-enhanced perfusion of a vascular network.

Estimate of Relative SNR

The SNR values for the acquired projections, for 3D-DSA and for 4D-DSA, were estimated by placing regions of interest in the images. Because variations of the signal selected by the maximum intensity projection process can contribute to the standard deviation in a region of interest, the statistical variations in the 4D-DSA image were measured from the difference between 2 successive 4D-DSA frames that were rotated to the same position. In the 3D-DSA, these variations were very small, so no subtraction was performed. It was not possible to subtract sequential acquired projections because they are not 3D-rotatable and cannot be registered for subtraction. Thus, the presence of these potential signal variations in the acquired

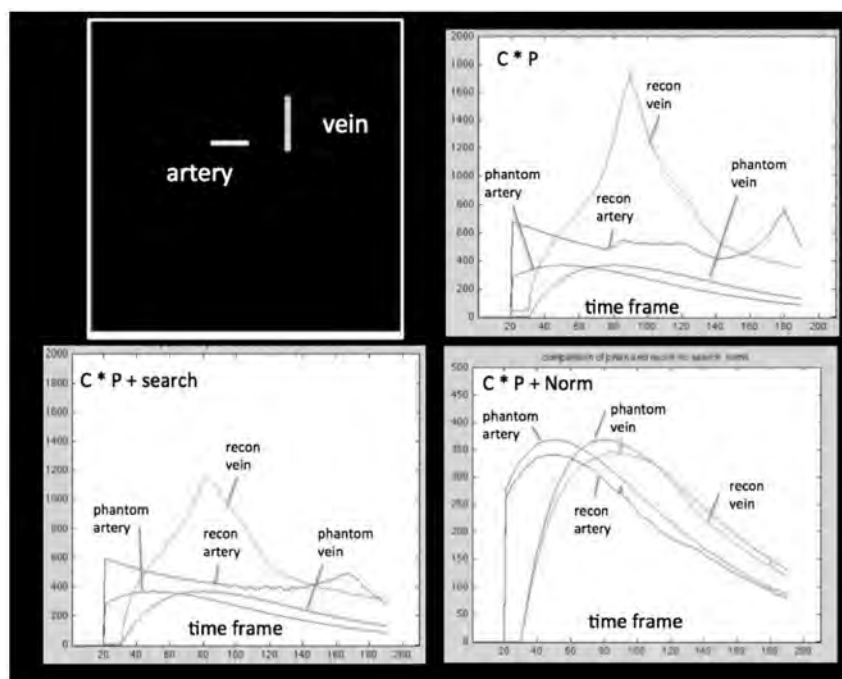


FIG 3. Demonstration of the effects of reconstruction elements on accuracy of reconstructed simulated vessel signal curves. The digital phantom is shown in the top frame on the left. The vessels in the phantom (phantom artery and phantom vein) had specified time dependence. These are considered to represent ground truth. The input time curves for these vessels are shown in each panel for comparison. C indicates constraining image; P, projections. The reconstructed wave forms are shown: 1) after multiplication (represented by $C \times P$) of the projections by a binary constraining image (top right); 2) multiplication of the projections by the binary constraining image plus an angular minimum search (represented by $C \times P + \text{search}$, bottom left); and 3) multiplication of the projections by the binary constraining image followed by normalization by the estimate of the numbers of projected ray voxels obtained from the constraining image ($C \times P + \text{Norm}$, bottom right). The y-axis shows arbitrary units of attenuation. The x-axis shows the projection number.

projection region of interest could have decreased the measured SNR shown in Fig 2.

Simulation of Flow Information From 4D-DSA

A digital phantom was constructed to simulate the various steps in signal curve generation. The phantom consisted of a vein and an artery running perpendicular to the vein. Each was assigned venous and arterial γ -variate time dependences. A 4D-DSA reconstruction was performed with the use of a constraining volume obtained from the reconstruction of the known vessel distribution. Signal curves were then generated from 2 selected regions of interest for different versions of the 4D-DSA reconstruction algorithm.

Quantitative Color-Coded 4D-DSA

Previous work has shown the ability to create color-coded parametric images from 2D-DSA series.^{8,9} Because the basic 4D-DSA images contain signal that is proportional to the contrast (iodine) concentration as a function of time, it is possible to also view these series as a color-coded display showing contrast time of arrival (TOA) in each pixel. TOA maps were created by first forming a volume showing the highest contrast concentration, that is, vessel opacification that occurred during the rotational acquisition (C_{max}) and noting the time to reach $C_{\text{max}}/4$ on a per-voxel basis. Color-coded 4D-DSA images were obtained by multiplying TOA maps by a binarized version of the 4D-DSA MIP timeframes.

A method for displaying regions of vascular anatomy with increasing times of the contrast bolus arrival can be achieved by multiplying the TOA image by a sliding window that sequentially reveals pixels within a TOA range defined by the window. We refer to this as a bolus arrival mode. For the results illustrating this capability, we used a Gaussian display window with full width at half maximum of 20 4D-DSA timeframes.

RESULTS

Simulation of Reconstruction Elements

The angular search results in some distortion of the signal waveforms. When it is desired to generate quantitative signal curves, the effect of this can be limited because it is possible to omit points from the waveform for which the search resulted in the choice of a projection that is too remote (in time) from the current frame. The signal curve then can be interpolated by use of points for which the search resulted in a suitable temporal displacement, for example, below a chosen threshold.

For the purpose of generating signal curves that correspond exactly to the signal curves in the acquired projections,

it is possible to modify the basic reconstruction algorithm to include a binary version of the constraining image. In this case, the projection values are directly deposited in the 3D vascular space and will reproduce the signal curves provided by the projections. This series of 3D volumes does not accurately represent the actual opacification of the vascular network because of vessel overlap and the use of the back-projection step used to create these volumes. However, for the purpose of generating individual voxel signal curves, there are several characteristics of the 4D-DSA reconstruction algorithm that affect the resultant curves that aim to correct the vessel overlap problem inherent in the 3D timeframe volumes. This is demonstrated in the simulations performed with the digital phantom.

As shown in Fig 3, after the basic back-projection step when the projections are multiplied by a binary constraining image (upper right), there are signal peaks caused by the alignment of the vessels with the projection direction. When these are present, they can occasionally give the impression of reversed flow. These peaks are somewhat reduced when the angular search is added to the reconstruction (Fig 3, lower left panel). Better results are obtained when the projections are normalized by dividing them by an estimate of the number of aligned voxels along the individual rays, obtained from the constraining image (Fig 3, lower right panel). These normalizing projection images (1 per projection) are created by forward projections of the thresholded and binarized con-

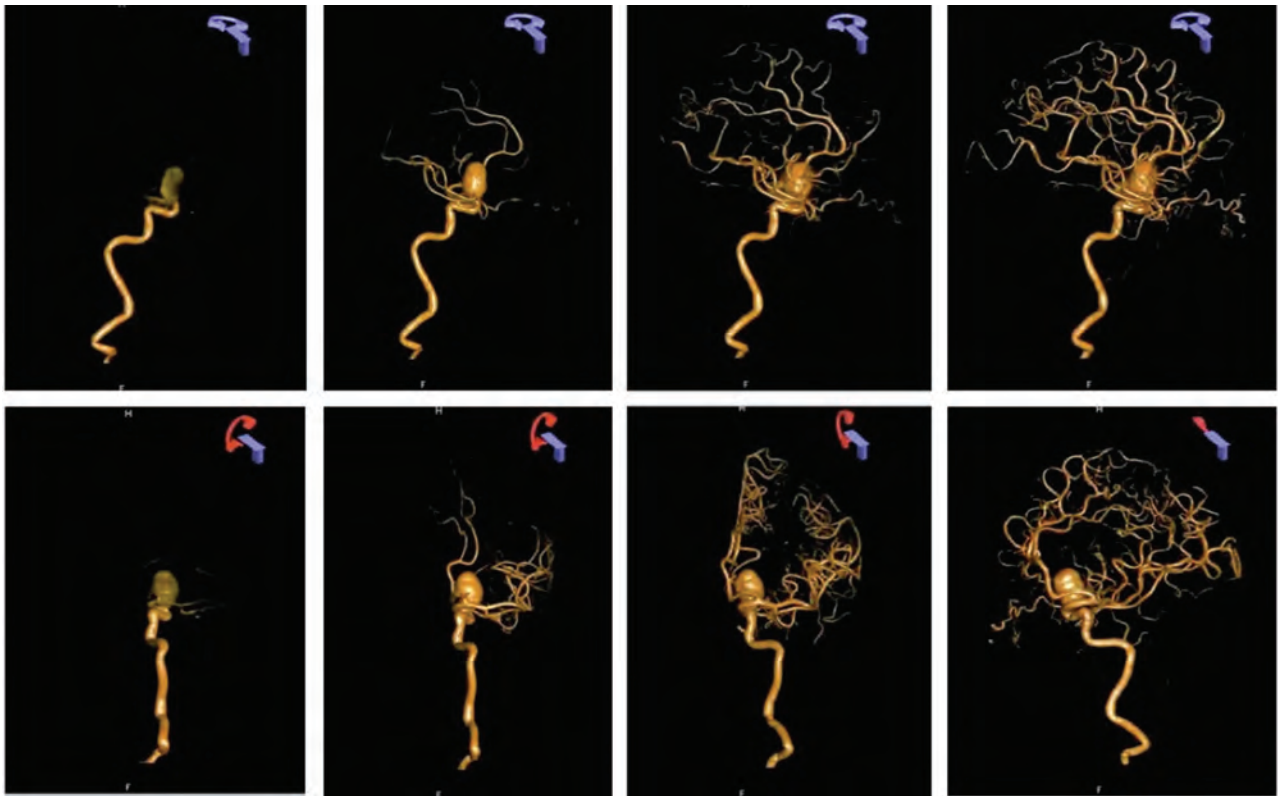


FIG 4. Four-dimensional DSA reconstruction from a 3D-DSA reconstruction performed for evaluation of an unruptured paraclinoid aneurysm. An IA injection of contrast was used for this examination. The *top row* shows selected timeframes viewed at the rate of 6 frames per second at a fixed viewing angle. The *bottom row* shows the same timeframes viewed at 4 different angles, which would have not been obtainable in a biplane acquisition because of the mechanical inability to position the A-plane gantry (red icon).

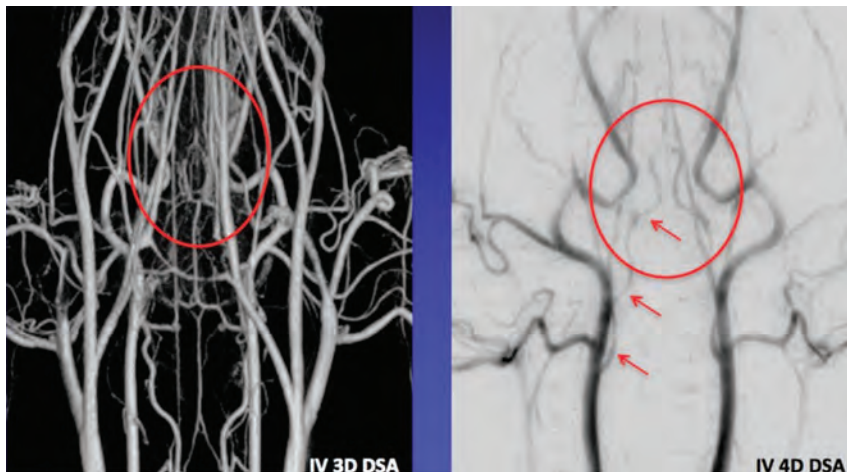


FIG 5. Comparison of intravenous 3D-DSA and early arterial phase time from a 4D-DSA reconstruction. In the standard 3D-DSA on the left, the overlap of both arteries and veins obscures visualization of the internal carotid arteries. In this example, there is no viewing angle that will eliminate this overlap in the 3D-DSA. The image on the right is an early arterial timeframe from a 4D-DSA reconstruction viewed from the same angle as the 3D-DSA on the left. In this 4D image, the full course the right internal carotid artery is clearly visualized (*red arrows*). The red ellipse shows the position of the distal segments of the internal carotid arteries in both images.

straining image. With the use of this method, the similarity of the reconstructed signal curves to those of the input signal curves is satisfactory. This technique effectively helps to weight deposition of the attenuation coefficient in voxels along a ray, resulting in

more accurate 4D-DSA raw 3D temporal volume when a normalized projection is back-projected.

Anatomic Display

Imparting temporal resolution to an already reconstructed 3D vascular volume requires far fewer multiplicative projections than if the goal were to reconstruct a vascular (anatomic) volume itself by summing a limited number of projections. In our technique, the anatomic structures in those voxels have already been reconstructed. Time dependence can then be effectively performed with the use of a small number of multiplicative projections.^{10,11}

Figure 4 shows a series of 4D-DSA arterial phase images from a study performed for evaluation of an unruptured aneurysm. These illustrate the ability to view the time-resolved 4D series from any desired viewing angle. This ability to retrospectively view a dynamic angio-

graphic sequence from any arbitrary view angle can potentially result in a significant reduction in radiation exposure because, in our experience, to obtain optimal views, it is not unusual to require multiple 2D acquisitions even when performing a “tar-

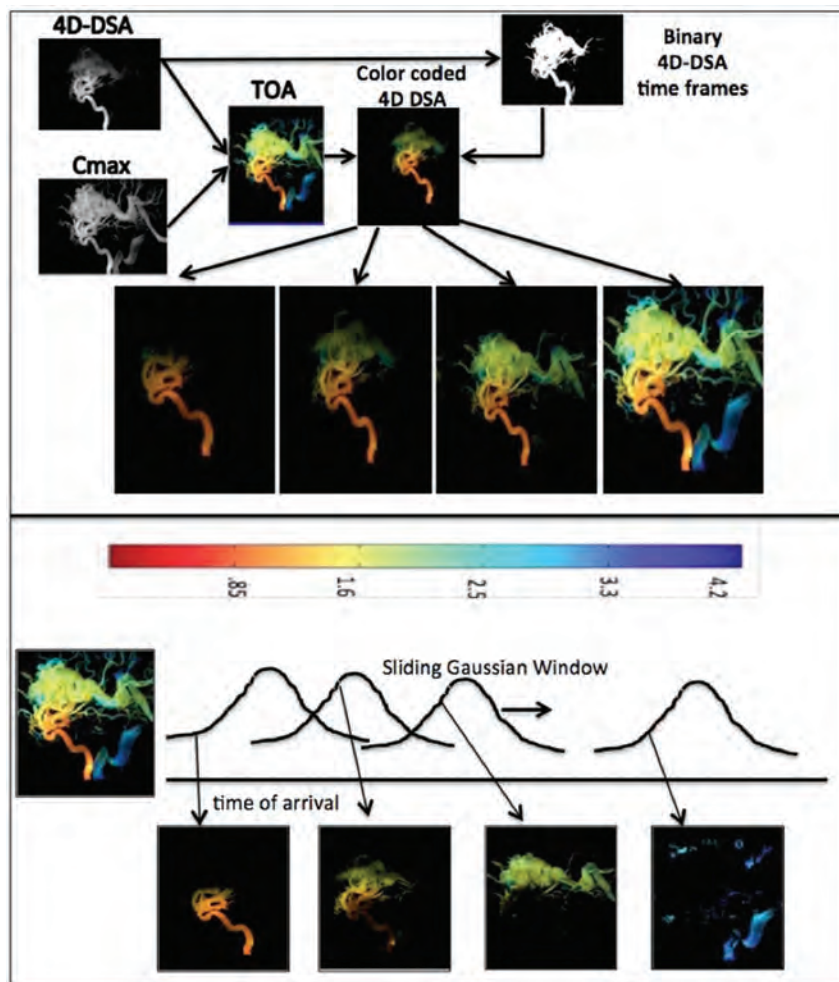


FIG 6. Color-coded 4D-DSA and bolus arrival images. The sequence was displayed at a rate of 6 frames per second for visualization of arrival times between 1 and 4.5 seconds. On the top of the figure, binarized 4D-DSA timeframes multiply a time-of-arrival map providing a dynamic display in which each pixel in each timeframe is represented by a quantitative time of arrival value. In the bottom half of the figure, a sliding Gaussian display window is used to show the passage of the bolus through the AVM. The 4D-DSA TOA volume (static) and 4D-DSA TOA (dynamic) 3D timeframes can be viewed from any angle. The 4D-DSA TOA (dynamic) 3D timeframes allow viewing of the temporal dynamics of the 4D-DSA TOA from any angle at any point in time for which data were acquired. These images were obtained by use of an IA injection of contrast medium.

geted” (single vessel) diagnostic examination. This ability also removes the need to obtain extreme cranial-caudal views that require passing x-rays through a highly attenuating path. With 4D-DSA, such views can be achieved with the use of a reconstruction acquired from data acquired such that rays traverse a much less attenuating trajectory.

Our initial efforts to use intravenous injections of contrast in conjunction with DSA were hampered by the overlap of vascular structures on the 2D images. With 4D-DSA, this limitation is largely overcome because optimal views, which avoid overlap, can be chosen and viewed at any stage of vascular filling (any view angle at any timeframe and any timeframe at any view angle). This is illustrated in Fig 5, in which the course of the right internal carotid artery can be clearly seen in the early arterial phase 4D-DSA timeframe.

SNR and Vessel Profiles

Figure 2 shows a comparison of SNR values measured in the regions of interest indicated by the yellow arrows. The apparent

SNR of the acquired projection may have been decreased because of anatomic variations during gantry rotation. Also shown are normalized vessel profiles along the red lines indicated. The profile across these 2 arteries on the acquired projection is noisy. Determination of the exact 4D-DSA spatial resolution requires more careful experiments with the use of well-defined phantoms. These studies are ongoing.

Figure 6 illustrates the ability to color-code a 4D-DSA image such that quantitative information about blood flow can be extracted. This example shows a 4D reconstruction of a study performed for evaluation of an AVM.

DISCUSSION

In this report, we have demonstrated the feasibility of generating time-resolved 3D-DSA vascular volumes with the use of commercially available flat detector angiographic systems and clinically practical injection protocols. A review of other angiographic methods (both time-resolved and non-time-resolved) indicates that 4D-DSA can provide spatial and temporal resolution that exceeds that of these competing techniques, for example, MRA and CTA. In particular, 4D-DSA thus provides a new imaging technique with spatial and temporal resolution exceeding competing time-resolved angiographic techniques. Figure 7 shows the relative voxel volume and frame duration for existing time-resolved angiographic methods. We emphasize that this was a feasibility study with implementation of the technique

with the use of a prototype environment. Studies to understand the trade-offs of various acquisition and injection protocols are underway. Full understanding and optimization of these protocols will require significantly more experience and use of the technology.

Validation studies will be required to establish the reconstructed matrix size and radiation dose that would be required to provide the highest-resolution 4D-DSA volumes. It is interesting to note that despite recent research developments in MR, the dominant commercial method is still time-resolved imaging of contrast kinetics (TRICKS), which has spatial and temporal resolution 2 orders of magnitude below that of 4D-DSA.¹²

The availability of 4D-DSA provides the user with a technique that, from a single contrast injection and rotational acquisition (provided an acceptable constraining volume can be obtained), provides a library of time-resolved images that may be viewed from any desired angle at any time during contrast filling and

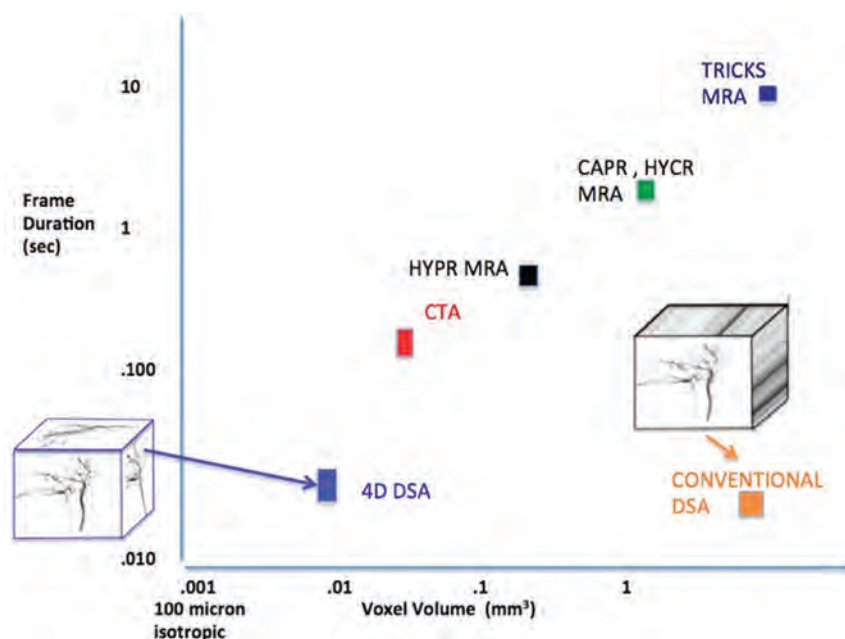


FIG 7. Relative spatial and temporal resolution for competing time-resolved angiography methods. The MRA values are based on the hybrid MRA method reported by Wu et al¹² and provide 0.69-mm pixel dimensions, leading to a voxel volume of 0.33 mm³. Typical frame times are 0.3 seconds. The CTA estimate is based on the large area Aquilion system (Toshiba Medical Systems, Tokyo, Japan)¹⁴ with a pixel dimension of 0.625 and frame rate of approximately 3/s. The 4D-DSA ultimate spatial resolution assuming a magnification factor of 1.5 and a pixel dimension 100 should easily support 200- μ pixel dimensions in a patient, leading to a voxel volume of 0.008 mm³.

emptying. Although conventional 3D-DSA reconstructions are viewable at any angle, they do not allow viewing of the vasculature during different stages of filling and emptying, for example, a pure arterial phase or pure venous phase. Because 4D-DSA allows this, it should, in our opinion, allow the performance of many procedures requiring the use of x-ray angiography with significantly less x-ray exposure and contrast medium dose because it would reduce the need to obtain multiple 2D-DSA acquisitions. We also believe that because the time-resolved volume viewable from any angle at any time will largely eliminate the impact of vascular overlap, that 4D-DSA will provide a method that will again make the use of intravenous injections for angiographic studies an attractive alternative to conventional IA studies, thus potentially increasing the safety (less invasive) and efficacy (obtaining images of all relevant vasculature with a single injection and acquisition) of interventional and diagnostic procedures.

It should be emphasized that 4D-DSA is a purely angiographic technique and as such only indirectly provides perfusion information, that is, it provides information about blood flow to tissue. This is because it is not possible to reconstruct the tissue surrounding vessels from only a single projection. Although the constraining volume is reconstructed from a large number of projections, the tissue perfusion represented by that volume is an average, over time, and thus cannot provide dynamic perfusion information. It is possible, however, that 4D-DSA could provide valuable arterial input function information for alternate schemes of measuring perfusion with a C-arm angiographic system.¹³

All of the images shown in this report were reconstructed retrospectively and were not available at the time of the actual examinations. The reconstruction time per 4D-DSA frame is presently

less than 1 second. Clinical validation of the anatomic and temporal accuracy as well as documentation regarding the value of the technique in reducing procedure times, x-ray exposure, and contrast medium dose will start once the technique is developed to a point at which it may be transferred to a clinical angiographic system.

Four-dimensional DSA will ultimately be used along with 4D fluoroscopy, a technique that will provide real-time fluoroscopic roadmap views from any arbitrary direction without a need for gantry movement. Together, 4D-DSA and 4D fluoroscopy should increase diagnostic capabilities and improve the safety and efficacy of endovascular interventions.

CONCLUSIONS

It is feasible to generate time-resolved 3D-DSA vascular volumes with the use of commercially available flat detector angiographic systems and clinically practical injection protocols. The spatial resolution and SNR of the timeframes are largely determined by that of the conventional 3D-DSA constraining image

and not by that of the projections used to generate the 3D reconstruction. The voxel volume and temporal resolution are theoretically almost 10 times that of CTA and MRA, and the small-vessel contrast is increased relative to that of conventional 2D-DSA as the result of the ability to use MIP renderings. The availability of 4D-DSA should greatly reduce the need to acquire multiple 2D series during examinations. The availability of 4D-DSA volumes viewable from any angle at any time completes the transition of DSA to a full 4D angiographic technique.^{12,13}

ACKNOWLEDGMENTS

We dedicate this work to the memory of our colleague Dr Jan Bose, who recently passed away. Although Jan was not an author of this manuscript, his insights and guidance were invaluable as we worked to bring this technology from a concept to a reality. Jan was a dear friend and colleague; his memory will never leave us.

Disclosures: Brian Davis—*RELATED: Grant:* Siemens Medical Sponsored Research Grant; * *Support for Travel to Meetings for the Study or Other Purposes:* Siemens Medical Sponsored Research Grant; * *OTHER RELATIONSHIPS:* We have a sponsored research agreement between UW Madison and Siemens Medical. Kevin Royalty—*RELATED: Grant:* Siemens Medical Solutions, USA; * *Comments:* Project was at least partially funded by Siemens Medical Solutions, USA; *UNRELATED: Employment:* Siemens Medical Solutions, USA; *Comments:* Full-time employee of Siemens Medical Solutions, USA; * *OTHER RELATIONSHIPS:* I am also a graduate student at the University of Wisconsin (Department of BioMedical Engineering). Markus Kowarschik—*UNRELATED: Employment:* Full-time employee at Siemens Healthcare; *Comments:* Part of this research was funded by Siemens Healthcare. Erick Oberstar—*RELATED: Grant:* Siemens Medical Sponsored Research Grant; * *Support for Travel to Meetings for the Study or Other Purposes:* Siemens Medical Sponsored Research Grant; * *OTHER RELATIONSHIPS:* We have a sponsored research agreement between UW Madison and Siemens

Medical. David Niemann—*RELATED*: Siemens Healthcare,* Comments: Master Research Agreement between University of Wisconsin and Siemens Health Care. Charles Strother—*RELATED*: Grant: Siemens Healthcare* Comments: Sponsored research agreement between Siemens HealthCare and UW Madison; *Support for Travel to Meetings for the Study or Other Purposes*: Siemens Healthcare* Comments: Money for travel to scientific meetings included in budget of research grant; *OTHER*: License of Intellectual Property; *UNRELATED*: *Consultancy*: Siemens Healthcare, Comments: I am an unpaid advisor; *Grants/Grants Pending*: Siemens Healthcare;* *Patents (planned, pending or issued)*: Siemens Healthcare, Comments: License of IP. Charles Mistretta—*RELATED*: Grant: Siemens Imaging Solutions,* Comments: Siemens/UW sponsored research grant; *Support for Travel to Meetings for the Study or Other Purposes*: The Siemens grant provides some travel money; *UNRELATED*: *Patents (planned, pending or issued)*: Siemens has been licensed to develop 4D-DSA (*money paid to institution).

REFERENCES

- Mistretta CA, Kruger RA, Houk TL, et al. **Computerized fluoroscopy techniques for noninvasive cardiovascular imaging: SPIE.** *Appl Opt Instr Med* 1978;152:65–71
- Kruger RA, Mistretta CA, Houk TL, et al. **Computerized fluoroscopy in real time for noninvasive visualization of the cardiovascular system: preliminary studies.** *Radiology* 1979;130:49–57
- Strother CM, Sackett JF, Crummy AB, et al. **Clinical applications of computerized fluoroscopy: the extracranial carotid arteries.** *Radiology* 1980;136:781–83
- Ning R, Kruger RA. **Computer simulation of image intensifier-based computed tomography detector: vascular application.** *Med Phys* 1988;15:188–92
- Ning R, Kruger RA. **Image intensifier-based computed tomography volume scanner for angiography.** *Acad Radiol* 1996;3:344–50
- Fahrig R, Fox AJ, Lownie S, et al. **Use of a C-arm system to generate true three-dimensional computed rotational angiograms: preliminary in vitro and in vivo results.** *AJNR Am J Neuroradiol* 1997;18:1507–14
- Fahrig R, Moreau M, Holdsworth DW. **Three-dimensional computed tomographic reconstruction using a C-arm mounted XRII: correction of image intensifier distortion.** *Med Phys* 1997;24:1097–106
- Strother CM, Bender F, Deuerling-Zheng Y, et al. **Parametric color coding of digital subtraction angiography.** *AJNR Am J Neuroradiol* 2010;31:919–24
- Lin CJ, Hung SC, Guo WY, et al. **Monitoring peri-therapeutic cerebral circulation time: a feasibility study using color-coded quantitative DSA in patients with steno-occlusive arterial disease.** *AJNR Am J Neuroradiol* 2012;33:1685–90
- Mistretta CA, Oberstar E, Davis B, et al. **4D-DSA and 4D fluoroscopy: preliminary implementation.** *Proceedings of SPIE Conference on Medical Imaging.* San Diego, California, February 2010
- Davis B, Kowarschik M, Royalty K, et al. **Progress in 4D digital subtraction angiography implementation: technical aspects.** *Presented at Annual Meeting of the American Society of Neuroradiology,* New York. April 23–26, 2012
- Wu Y, Johnson K, Kecskemeti SR, et al. **Time resolved contrast enhanced intracranial MRA using a single-dose delivered as sequential injections and highly constrained projection reconstruction (HYPR CE).** *Magn Reson Med* 2011;65:536–63
- Ganguly A, Fieselmann A, Marks M, et al. **Cerebral CT perfusion using an interventional C-arm imaging system: cerebral blood flow measurements.** *AJNR Am J Neuroradiol* 2011;32:1525–31
- Geleijns J, Salvado AM, de Bruin PW, et al. **Computed tomography dose assessment for a 160 mm wide, 320 detector row, cone beam CT scanner.** *Phys Med Biol* 2009;54:3141–59

Intracranial 4D Flow MRI: Toward Individualized Assessment of Arteriovenous Malformation Hemodynamics and Treatment-Induced Changes

S.A. Ansari, S. Schnell, T. Carroll, P. Vakil, M.C. Hurley, C. Wu, J. Carr, B.R. Bendok, H. Batjer, and M. Markl



ABSTRACT

BACKGROUND AND PURPOSE: Arteriovenous malformations are an important etiology of hemorrhagic stroke. However, current imaging modalities and risk do not provide insights into individual AVM hemodynamics and its role in pathophysiology. The aims of this study are to determine whether intracranial 4D flow MR imaging can provide insights into arteriovenous malformation hemodynamics independent of the Spetzler-Martin grade and to report the changes in flow observed during staged embolization.

MATERIALS AND METHODS: Intracranial 3D blood flow was assessed in 20 patients with AVM (age = 39 ± 15 years, Spetzler-Martin grade ranging from 1–4) with the use of 4D flow MR imaging (temporal resolution = 45 ms, spatial resolution = $[1.2\text{--}1.6\text{mm}]^3$). AVM hemodynamics were visualized by means of time-integrated 3D pathlines depicting the AVM arterial feeding and venous draining patterns over the cardiac cycle. Analysis included the grading of feeding and draining velocities on a 3-point scale (0 = low <25 cm/s, 1 = medium <50 cm/s, 2 = high >50 cm/s). For 4 of 20 patients undergoing 4D flow MR imaging follow-up after staged embolization, peak velocities were quantified in arterial feeders, draining veins, the sagittal sinus, and contralateral arteries.

RESULTS: In 50% of the cases with Spetzler-Martin grade >2 , heterogeneous flow (velocity grade differences >1) was found across arteries and veins. Velocities in draining veins increased from Spetzler-Martin grade = 1 (grading = 0.5 ± 0.6) to Spetzler-Martin grade ≥ 3 (1.1 ± 0.6), whereas arterial velocities were similar (1.7 ± 0.6 versus 1.5 ± 0.6). In the postembolization subgroup of 4 patients, 4D flow MR imaging demonstrated successively more compact AVM and redistribution of velocities. Changes in arterial and venous velocities during treatment were highly different among individuals.

CONCLUSIONS: Spetzler-Martin grade does not reflect differences in 3D AVM arterial and venous hemodynamics, and an individual assessment of AVM hemodynamics may be needed for improved lesion characterization. Four-dimensional flow MR imaging may have the potential to monitor and guide embolization treatment planning.

ABBREVIATIONS: SMG = Spetzler-Martin grade; PC = phase-contrast, FA = feeding artery

Arteriovenous malformations are composed of a tangled network of feeding arteries directly connected to abnormal “arterialized” draining veins and are an important etiology of hemorrhagic stroke.^{1,2} The Spetzler-Martin grade, combining information

of AVM size, location, and venous drainage patterns, was originally proposed for AVM risk stratification.³ A high SMG, flow-induced aneurysms, and history of hemorrhagic rupture are widely accepted as major risk factors. However, these parameters represent empiric measures and do not provide insights into individual AVM hemodynamics and their role in pathophysiology and clinical presentations (eg, hemorrhage, ischemia, seizures).^{4,5} In addition, the predictive value of SMG is limited to the surgical morbidity of resection, and there is currently no risk score for AVM rupture itself.

Digital subtraction angiography combined with selective intra-arterial iodine contrast injections provides excellent AVM vascular imaging, angioarchitecture, and flow distribution. In addition, DSA guides AVM treatment via staged embolization procedures (endovascular superselective occlusion of AVM feeding arteries with nidus penetration).^{6,7} However, DSA procedures are associated with high cumulative contrast and radiation doses.

Received October 22, 2012; accepted after revision January 21, 2013.

From the Department of Radiology (S.A.A., S.S., T.C., P.V., M.C.H., J.C., B.R.B., M.M.) and Department of Neurological Surgery (S.A.A., M.C.H., B.R.B., H.B.), Feinberg School of Medicine; and Department of Biomedical Engineering (T.C., P.V., C.W., M.M.), McCormick School of Engineering, Northwestern University, Chicago, Illinois.

Grant support was provided by NIH-T32-EB005170, NIH-R01-HL088437, and NIMH Excellence in Academic Medicine (EAM) Program, Advanced Cardiovascular MRI Research Center.

Please address correspondence to Michael Markl, PhD, Departments of Radiology and Biomedical Engineering, Northwestern University, 737 N Michigan Ave, Suite 1600, Chicago, IL 60611; e-mail: mmarkl@northwestern.edu

Indicates open access to non-subscribers at www.ajnr.org

<http://dx.doi.org/10.3174/ajnr.A3537>

Table 1: Demographics of 20 patients with AVM included in the study

AVM No.	Age, y	Sex	History	Venous Drainage		Location		AVM Size, cm	SMG
				Deep/Superficial	Eloquent	Superficial/Deep			
1 ^a	43	M		d+s	0	s	5.6 × 4.1 × 5.1	3	
2	22	M	Ruptured	d+s	0	s	2.5 × 2.3 × 2.4	2	
3	68	F		d+s	1	d	4.0 × 3.0 × 2.5	4	
4	44	M		d+s	1	d	1.0 × 1.0 × 1.0	3	
5 ^a	29	M		d+s	0	d	4.0 × 3.5 × 3.4	3	
6	48	F		s	0	s	3.5 × 3.5 × 3.0	2	
7	34	M	Ruptured	s	0	s	3.3 × 2.3 × 2.5	1	
8	22	F		s	1	s	1.3 × 1.6 × 1.3	2	
9	40	F		d+s	0	s	3.0 × 2.0 × 4.0	2	
10 ^a	43	M	Ruptured	d+s	1	d	2.7 × 3.1 × 3.1	3	
11	35	F		d+s	0	s	3.1 × 1.6 × 1.0	2	
12	25	F		d+s	0	s	2.3 × 2.3 × 1.7	2	
13 ^a	21	F		d+s	1	s	4.0 × 3.4 × 3.8	4	
14	52	F		s	0	s	2.4 × 2.1 × 2.6	1	
15	16	F		s	1	d	2.3 × 2.8 × 2.8	2	
16	66	M		s	0	s	0.8 × 1.0 × 0.8	1	
17	49	M		s	0	s	1.9 × 2.4 × 2.0	1	
18	22	F		s	0	s	1.0 × 2.5 × 0.6	1	
19	41	F		d+s	1	s	6.6 × 3.7 × 5.2	4	
20	55	M		s	0	s	2.1 × 3.6 × 2.6	2	

^a Patients for whom follow-up 4D flow MRI was obtained during staged embolization.

Note:—d indicates deep; s, superficial.

Moreover, noninvasive monitoring of embolization-induced changes has been limited by the lack of modalities to quantitatively assess AVM hemodynamics.

A number of studies reported the use of noninvasive 4D (3D + time) MR angiography for the evaluation of the MR contrast agent dynamics in the cerebral vasculature and AVM.^{8–13} More recently, 4D flow MR imaging, which adds a new dimension (quantitative 3-directional blood flow velocities) has been used for the in vivo measurement and visualization of intracranial arterial and venous 3D blood flow^{14–18} and to assess complex 3D flow patterns in AVMs in a small number of cases.^{19,20} It was the aim of this study to apply 4D flow MR imaging in patients with AVM to assess AVM 3D hemodynamics and to monitor changes during treatment by staged embolization. We hypothesize that intracranial 4D flow MR imaging can provide further insights into AVM hemodynamics independent of SMG and can identify changes in arterial feeding and venous draining blood flow velocities during staged embolization.

MATERIALS AND METHODS

Study Population

Intracranial 4D flow MR imaging was obtained in 20 patients with AVM (age = 39 ± 15 years, 11 female). Patient demographics and AVM characteristics are outlined in Table 1. The patient cohort included 3 ruptured and 17 unruptured AVMs with Spetzler-Martin grades ranging from 1–4. DSA confirmed deep AVM location in 5 of 20 patients and deep venous drainage in 11 of 20 patients. In 4 of 20 patients with AVM, follow-up 4D flow MRI was obtained during interventional treatment by staged embolization. For all patients included in this study, liquid Onyx (ethylene-vinyl alcohol copolymer; ev3, Irvine, California) was used as embolic material. The study was carried out in accordance with an institutional review board protocol, which permitted retrospective chart review.

MR Imaging

All measurements were performed with the use of 1.5T and 3T MR systems (Avanto & Trio; Siemens, Erlangen, Germany), with a standard 12-channel head coil. MR imaging included time-of-flight MR angiography and 3D T1-weighted MPRAGE for the localization of the AVM. Cerebral 3D blood flow was measured by using electrocardiographic gated and time-resolved (cine) 3D phase-contrast (PC) MR imaging with 3-directional velocity encoding (also termed “4D flow MR imaging”).^{15,21} Data were acquired in an axial oblique 3D volume covering the AVM. Pulse sequence parameters for 4D flow MR imaging were as follows: velocity sensitivity = 100–120 cm/s, flip angle = 15°, temporal resolution = 45 ms, section thickness = 1.2–1.6 mm, slab thickness = 52.8–70.4 mm, spatial resolution = (1.2–1.6)³ mm³. Total acquisition times for 4D flow MR imaging were heart rate–dependent and ranged between 15–20 minutes.

Data Analysis

All 4D flow data underwent preprocessing to correct for Maxwell terms, eddy currents, and velocity aliasing with the use of in-house software programmed in Matlab (MathWorks, Natick, Massachusetts), as described previously.²² In addition, a 3D phase-contrast MR angiogram was calculated from the 4D flow data.^{23,24} Anatomy, blood flow, and vascular geometry included in the resulting data were then further analyzed by means of a 3D visualization software package (EnSight; CEI, Apex, North Carolina). Three-dimensional blood flow visualization was based on the calculation of time-resolved 3D pathlines to depict the temporal evolution of blood flow in intracranial vessels. Three-dimensional pathlines were emitted within the entire intracranial vasculature, that is, all arteries and veins depicted by the 3D PC-MRA data that defined the vascular lumen; 15,000–25,000 emitter points were equally distributed within the 3D-PC-MRA vessel lumen and used to initiate the calculation of time-resolved 3D

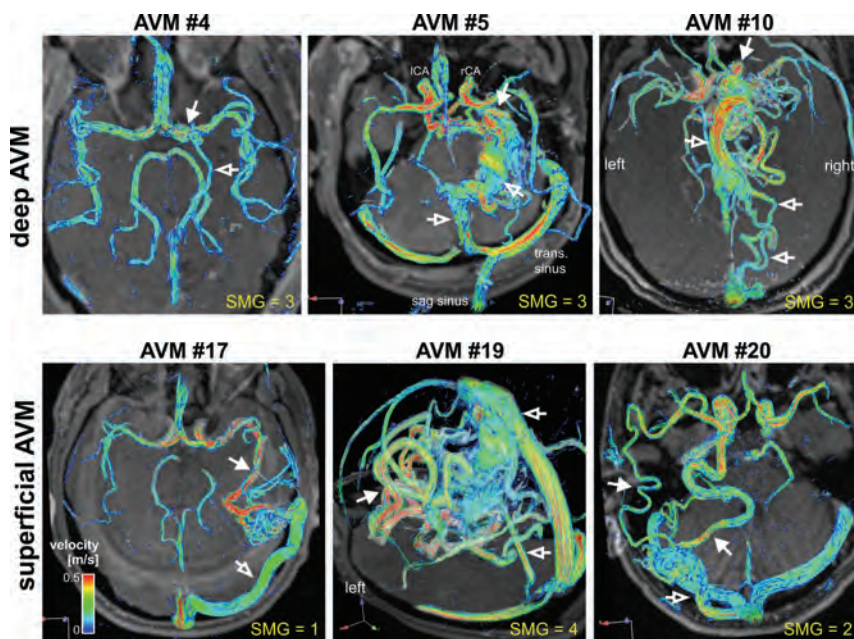


FIG 1. AVM hemodynamics visualized by time-integrated 3D pathlines in 6 of 20 patients. Color-coding shows the local velocity of blood traveling along the traces during 1 cardiac cycle. Different AVM sizes as well as feeding artery (solid white arrows) and draining vein patterns (white open arrows) can clearly be appreciated. AVM 4, 5, and 10: Deep AVM location and deep venous drainage resulting in with high SMG. AVM 17, 19, and 20: Superficial AVM location with superficial and deep venous drainage.

pathlines. Time-integrated pathlines were derived from the time-resolved pathlines by depicting the collective pathline traces over 1 cardiac cycle, that is, the cumulative path of blood flow over 1 cardiac cycle (Figs 1–3).

In contrast to alternative visualization options such as streamlines (traces along the 3D velocity field at 1 instance in time) or vector graphs (depiction of the 2D velocity field at a selected location and 1 point in time), time-intergraded 3D pathlines were chosen to provide an overview over the spatial and temporal distribution of 3D blood flow within a single image. In addition, pathline emission from the entire intracranial vasculature provided by the 3D PC-MRA data provided the advantage of visualizing 3D blood flow in all MR visible arteries and veins inside the entire 3D data volume.

The color coding of the time-integrated traces reflects the velocities of blood traveling along the pathlines during 1 cardiac cycle and was used to estimate the range and magnitude of blood flow velocities with the cardiac cycle. Previous studies have used similar approaches to analyze 3D blood flow distributions within patients with high-risk aortic plaques.²⁵ In consensus reading, 2 observers identified the number of arterial feeders and draining veins visible in the 4D flow data. Feeding/draining velocities in each vessel were visually graded as 0 (low flow <25 cm/s), 1 (medium flow <50 cm/s), and 2 (high flow >50 cm/s). The grading relied on the identification of clearly visible regions within individual arteries with velocity <25 cm/s or >50 cm/s. AVM velocity distribution was labeled as heterogeneous if velocity grades varied across vessels. For patients with follow-up 4D flow MR imaging after embolization, peak velocities were quantified in arterial feeders, draining veins, the sagittal sinus, and contralateral arteries. In addition, diameters of arterial feeders were measured and classified as homogeneous (maximum vessel diameter differences

<20%) or heterogeneous (maximum vessel diameter differences >20%).

Time needed for data analysis included approximately 10–15 minutes for preprocessing, 40–60 minutes for 3D blood flow visualization by use of time-integrated pathlines, and 15–20 minutes for placement of analysis planes and flow quantification.

Three-Dimensional Flow Connectivity Mapping

In a subset of 2 patients with SMG = 4, large and highly complex AVMs, 3D pathlines that originated from emitter planes in individual feeding arteries or draining veins were used to visualize different flow pathways inside the AVM. Traces emitted from each of the emitter planes were color-coded according to their anatomic origin to identify the blood flow paths with respect to their vascular source (3D flow connectivity mapping), as described previously.²⁶

RESULTS

Twenty-seven 4D flow MR imaging scans were performed in the 20 patients. Four patients who were undergoing treatment with staged embolization received additional follow-up 4D flow MRI after embolization procedures: 2 follow-up examinations in 3 patients (AVM 1, 5, and 13) and 1 follow-up examination in 1 patient (AVM 10). Three-dimensional visualization of AVM hemodynamics was successfully performed in 18 of 20 patients. Two patients were excluded from the analysis because of motion artifacts (AVM 11) or small AVM size <1 cm (AVM 16). In all remaining cases, the 4D flow MR imaging volume encompassed the entire AVM including the arterial supply and the venous drainage.

Three-Dimensional AVM Hemodynamics

Time-integrated pathlines in Fig 1 illustrate the complex distribution of blood flow inside the AVM and surrounding vessels for 6 patients with different AVM sizes, location, and draining patterns. Dominant arterial feeders and large deep and superficial draining veins were clearly identified in all cases. Note that blood flow characteristics, presence of high velocities (yellow/red colors) and distribution of velocities in AVM feeding arteries and draining veins were highly variable despite identical SMG. Particularly, venous blood flow velocities were substantially different and often unusually high (>30–50 cm/s) compared with normal venous flow (15–25 cm/s)²⁷ in the sagittal and transverse sinuses (Table 2).

Visual grading of time-integrated 3D particle traces confirmed considerable heterogeneity in 3D arterial feeding and venous draining patterns even for patients with identical SMG (Table 2). The number of feeding arteries (1–4), draining veins (1–3), and velocity distribution was highly variable. In 50% of the cases with

Table 2: Summary of the results of visual flow pattern grading in patients with AVM (n = 18)

	SMG 1 (n = 4)	SMG 2 (n = 7)	SMG ≥3 (n = 7)
Arterial feeders			
No. of arteries	Single	Single and multiple (1–3)	Single and multiple (1–4)
Flow across arteries	Homogeneous	Heterogeneous n = 4	Heterogeneous n = 3
Velocity grading	1.7 ± 0.6 Range = 1–2 Median = 2	1.4 ± 0.5 Range = 1–2 Median = 1	1.5 ± 0.6 Range = 0–2 Median = 1
Venous drainage			
No. of veins	Superficial only (1–2)	Superficial/deep (1–3)	Superficial/deep (1–3)
Flow across veins	Heterogeneous n = 2	Heterogeneous n = 3	Heterogeneous n = 4
Velocity grading	0.5 ± 0.6 Range = 0–1 Median = 0.5	0.8 ± 0.8 Range = 0–2 Median = 1	1.1 ± 0.6 Range = 0–2 Median = 1

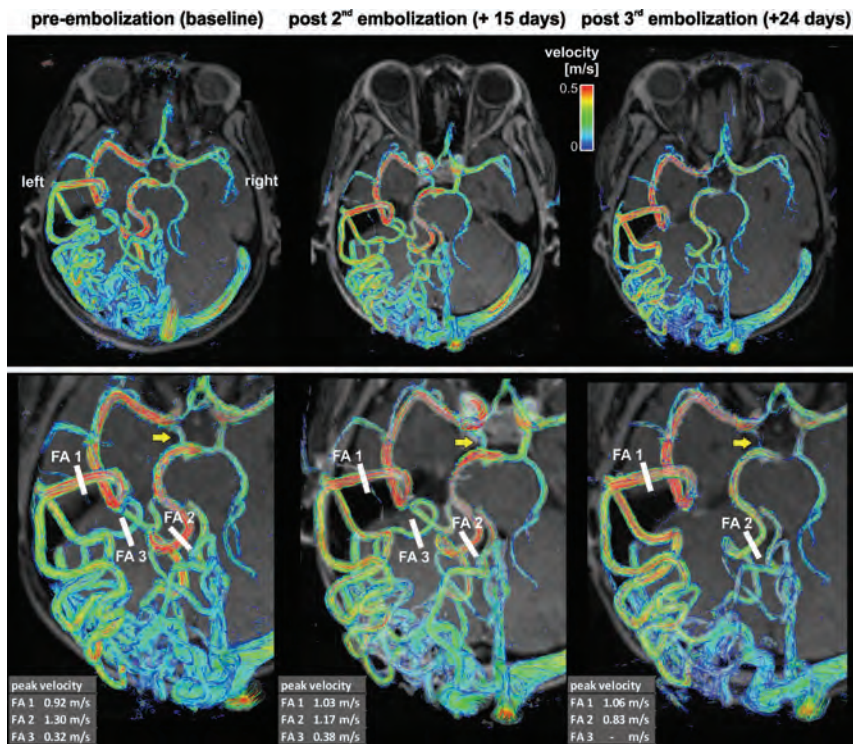


FIG 2. Three-dimensional blood flow visualization and quantification in a patient with a large unruptured temporo-occipital AVM (AVM 13, SMG = 4). Complex arterial feeding and convoluted hemodynamics as well as differences in pre-embolization and postembolization vascularization and hemodynamics are clearly visible. Flow quantification in 3 feeding arteries (FA 1–3) revealed substantial changes and redistribution of peak velocities during the course of staged embolization. Note that FA 3 was embolized during the third procedure. Note that embolization resulted in reduced flow in the right posterior communicating artery (yellow arrows). As evident from the changes in peak velocity in feeding arteries FA1 and FA2, the final embolization stage resulted in a substantial decrease in peak velocity in the FA2 systems. As a result, shunting to the FA2 system through the right posterior communicating artery was reduced, which resulted in its diminished appearance.

>1 feeding artery (SMG ≥2) or draining vein (SMG ≥1) heterogeneous flow was found, whereas the remaining patients showed homogeneous flow across arteries and veins. Overall, increased SMG corresponded to higher venous velocities (velocity grading increased by 120% from SMG = 1 to SMG ≥3), whereas arterial velocities were similar (decrease by 13% from SMG = 1 to SMG ≥3). Interestingly, for the 7 AVMs with heterogeneous velocity distribution across arterial feeders, only 2 showed a heterogeneous distribution of vessel diameters.

Follow-Up During Staged Embolization

As has been shown previously,²⁸ the embolization material (Onyx) appeared to be hypointense on MR images, did not interfere with MR images, and we did not observe artifacts related to embolic material in our study cohort.

As illustrated for a large temporo-occipital AVM (AVM 13, SMG = 4) in Fig 2, multiple embolization procedures resulted in a more compact AVM and altered velocity distribution as visualized by a reduced nidus network and changes in color-coding (reduction in velocities). Peak velocities in the 3 main feeding arteries (FA 1–3) underwent redistribution during treatment. Initially, the highest peak velocity in feeding artery FA 2 was reduced during the course of staged embolization. Moreover, the peak velocity ratio in FA 1 versus FA 2 (pre-embolization: FA 2 40% higher compared with FA 1) was inverted after the third embolization procedure (28% higher in FA 1 compared with FA 2).

Similar results (successively more compact AVM, redistribution of velocities) were found in all 4 cases undergoing staged embolization. Quantitative analysis (Fig 3B) revealed marked alterations during treatment in peak velocities in all vascular territories. Changes in velocities also occurred in locations distant to the site of arterial embolization such as the sagittal sinus and contralateral arteries (large artery in hemisphere not affected by the AVM).

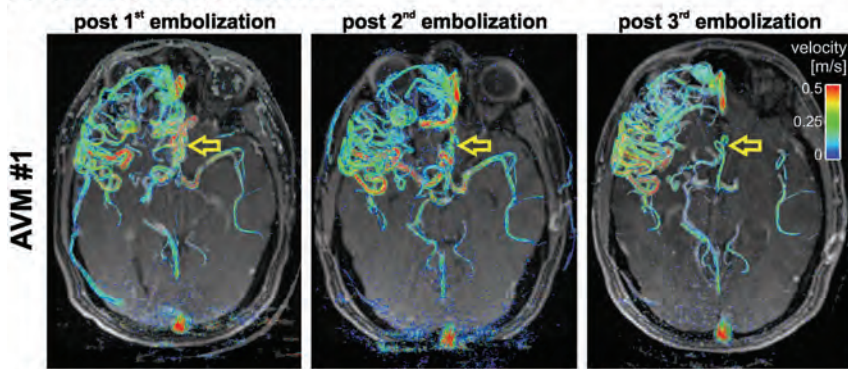
Three-Dimensional Flow Connectivity Mapping

Figure 4 demonstrates the use of flow connectivity mapping in 2 large AVMs. In comparison, velocity color-coded time-integrated pathlines for the same AVMs as shown in Fig 1 (AVM 19) and Fig 2 (AVM 13) provide an overview of AVM vascularization and velocity distribution. However, individual feeding and draining pathways are difficult to identify because of the complexity of the lesion. In these cases, flow connectivity mapping mimicking superselective iodine contrast injections provides a noninvasive method to selectively identify and delineate compartmentalized AVM feeding and draining pathways.

DISCUSSION

The findings of this study demonstrate the potential of 4D flow MR imaging for the 3D visualization of complex flow patterns

A 3D flow visualization



B Flow velocity quantification

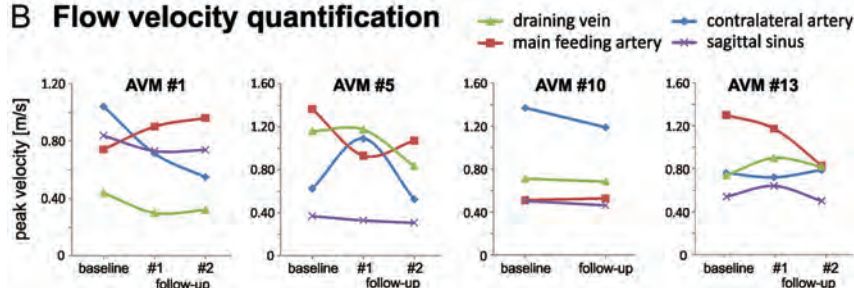


FIG 3. A, Three-dimensional blood flow in a large frontal AVM (AVM1, SMG = 3). Staged embolization resulted in compaction of the AVM with reduced blood flow velocities (yellow arrows). B, Quantification of postinterventional changes in AVM hemodynamics on the basis of 4D flow MR imaging after multiple embolization procedures in all 4 patients who underwent MR imaging follow-up.

within AVMs and its interconnections with the surrounding arterial and venous vascular system. Despite similar SMG, AVMs demonstrated heterogeneous and divergent arterial/venous patterns and flow velocity distributions, indicating the potential of *in vivo* 3D flow measurements to further characterize AVMs beyond the traditional empiric measures used for SMG.

In a subgroup of patients, 4D flow MR imaging was used for AVM treatment monitoring during multiple staged embolizations. Marked changes in velocities in all territories including sagittal sinus and contralateral arteries during follow-up demonstrate the potential of 4D flow MR imaging to evaluate the systemic impact of embolization on cerebral flow in multiple vascular territories.

Intracranial AVMs are highly complex and diverse lesions. Each AVM can consist of several types of tissues, compact or diffuse clusters of true nidus arteriovenous vessels, and areas of direct arteriovenous fistula in which a large arterial channel directly drains into the venous system.²⁹ Current preoperative noninvasive imaging methods often require assessment with invasive DSA and even superselective intra-arterial injections before embolization.³⁰ DSA is also routinely performed in the preoperative evaluation to more accurately map the anatomy or angioarchitecture of the lesion (feeding arteries, nidus, draining veins, venous outflow/stenoses, and flow-induced aneurysms) but provides only rudimentary information on flow dynamics.^{31,32} However, the impact of altered feeding patterns on the hemodynamics in AVMs with complex vascularization and flow patterns is difficult to predict even if feeding arteries can be clearly identified. Incomplete information on altered AVM hemodynamics may contribute to

the risk of hemorrhage postembolization, which is estimated at approximately 3–5%.^{33–36}

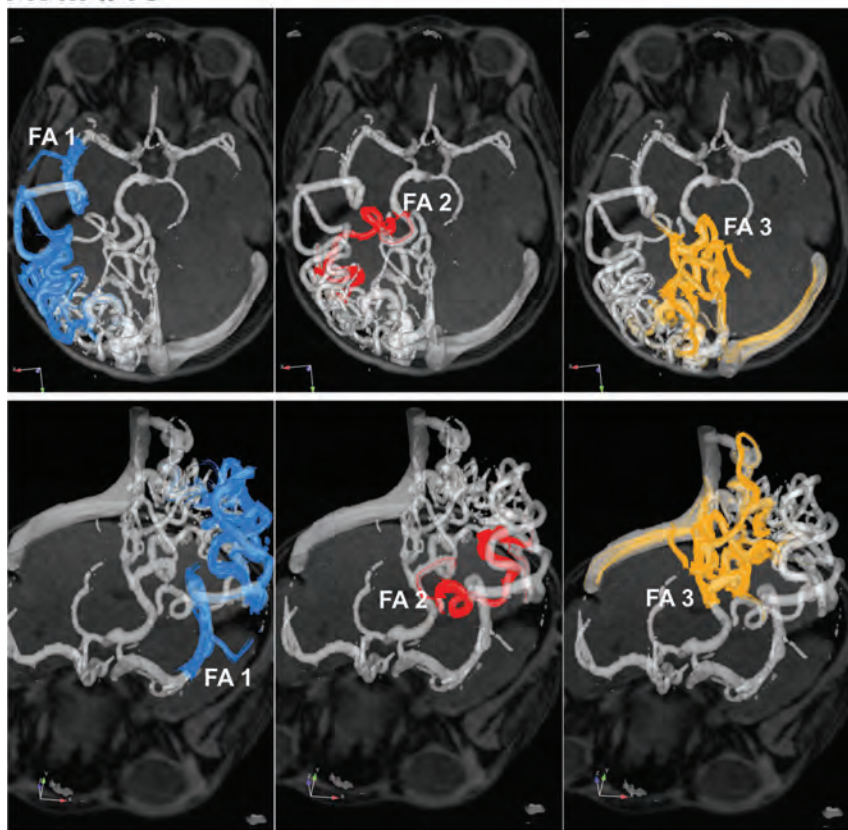
In the small cohort of patients included in our study, 4D flow MR imaging revealed intricate vascularization and heterogeneous flow patterns of AVMs independent of size, location, and severity of grade as specified by the SMG classification system. Different patterns of venous drainage with high variability in regional blood flow velocities indicate the complex nature of AVMs and the need for individual evaluation of flow characteristics. For example, in AVMs with heterogeneous peak velocity distribution across arterial feeders, only a small fraction showed differences in vessel diameters. This finding indicates that AVM hemodynamic parameters are not simply determined by vessel size but show a complex behavior that can in general not be directly linked to simple geometric markers.

The results of this study confirm the limited value of SMG for AVM risk stratification beyond the surgical morbidity of resection. New quantitative markers of AVM hemodynamics such as distribution of peak velocities across feeders or changes in feeding and draining velocities during treatment may thus have the potential to provide contributing factors to new and improved risk assessment for AVMs. Additional information that could be obtained during the same MR imaging examination, such as cerebral microvascular perfusion (cerebral blood flow and volume), could be incorporated into the hemodynamics analysis to offer a better multi-parametric functional assessment of AVMs. In this context, a detailed assessment of AVM blood flow distribution by 4D flow MR imaging in combination with parameters of microvascular perfusion may help to better understand the often controversial topic of vascular steal associated with AVMs. Four-dimensional flow MR imaging may offer the opportunity to study these effects and the impact of therapy and intervention (eg, reversal of hypoperfusion by removal of shunting) on vascular steal. Future studies in larger cohorts and long-term follow-up are needed to evaluate the diagnostic value of such parameter combinations as potential future risk scores for AVM characterization.

A previous 4D flow study by Hope et al¹⁹ reported findings in 1 patient with a large left frontoparietal AVM compared with 2 healthy volunteers. Similar to our findings, the AVM patient showed increased venous flow and high flow in arterial feeders (3.3 times faster flow was noted in the 3 largest arterial feeders supplying the AVM via the ipsilateral internal carotid artery in comparison to the healthy controls).

In a recent study, Chang et al²⁰ investigated 10 patients with AVM with 4D flow MR imaging to primarily assess wall shear stress in AVM feeding and contralateral normal arteries. Patients were divided into 2 subgroups, with the first group harboring

AVM #13



AVM #19

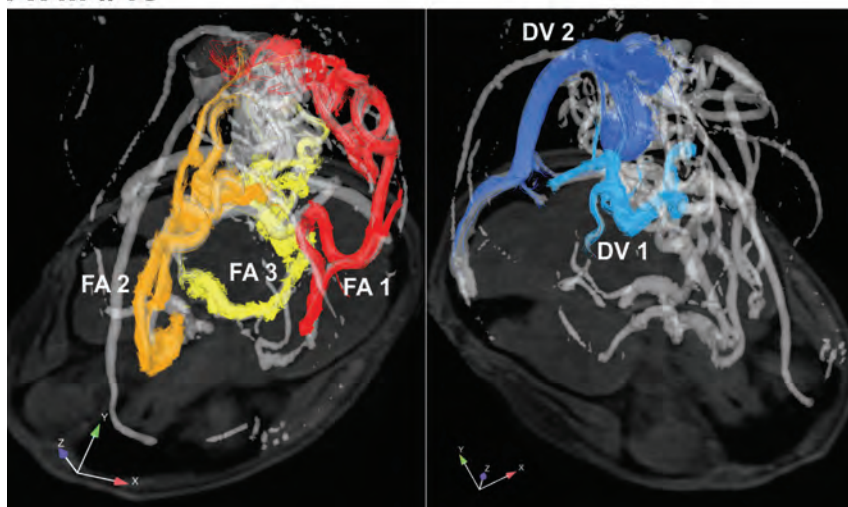


FIG 4. Flow connectivity mapping of AVM feeding and draining patterns in 2 large AVMs with complex vascularization (both SMG = 4). The gray shaded iso-surfaces show 3D-PC-MRA that was calculated from the 4D flow MR data. FA = feeding artery; DV = draining vein.

asymptomatic AVMs of SMG = 3 and the second group with ruptured AVMs of SMG 1–4, presenting with hemorrhage and neurologic deficits. In the first group, wall shear stress was similar for AVM feeding and contralateral normal arteries, as opposed to group 2, which exhibited a significant decrease of wall shear stress in normal vessels. An increased time-averaged velocity and flow in the feeding arteries compared with the contralateral arteries was found in both groups.

To our knowledge, these studies constitute the only reports of the application of 4D flow MR imaging to AVMs to date. Our study investigated a larger cohort of patients with AVM and clearly demonstrated the ability of 4D flow MR imaging to assess qualitative and quantitative changes in AVM hemodynamics during staged embolization. We were able to identify highly variable alterations in arterial or venous flow velocities that could be caused by compensatory flow after parallel feeder occlusion, aggressive intranidal embolization, or venous outflow penetration or obstruction. In this context, 4D flow MR imaging may identify subtleties and nuances of AVM angioarchitecture that supplement other modalities such as DSA. As such, the technique may offer a new tool for pre-interventional and post-interventional monitoring of intracranial hemodynamics and provide additional information on regional blood flow velocities and flow patterns. A particular advantage of the presented technique is related to the fact that imaging can easily and noninvasively be performed at multiple instances in conjunction with routine MR imaging without the need for ionizing radiation.

Limitations

A major limitation of our study is the small number of patients investigated. Although this is the largest series to date studying AVMs with 4D flow MR imaging for specific flow patterns, it remains a feasibility study and the conclusions are limited with respect to the clinical utility of the findings. Correlation of hemodynamic findings with either risk stratification or patient outcomes is unclear, possibly because of heterogeneous flow architecture of AVMs, inadequate power, and the paucity of ruptured AVMs. Another limitation is the limited spatial resolution resulting from the need to cover the entire intracranial vasculature for the AVM investigation, which also must be acquired in a reasonable scan time. These technical issues may be solved with advanced acceleration techniques and a dual-velocity encoding approach in future investigations. Further studies are warranted, including serial 4D flow imaging to evaluate its potential for improving interventional planning and postinterventional monitoring.

CONCLUSIONS

Four-dimensional flow MR imaging provides the opportunity for noninvasive assessment and visualization of complex feeding and draining patterns in cerebral AVMs. Phase-contrast MRA techniques allow the qualitative and quantitative evaluation of AVM hemodynamics and may offer the potential for risk stratification, more precise monitoring during staged embolization, and/or improved treatment planning.

Disclosures: Timothy Carroll—RELATED: Grant: NIH/NHLBI; * UNRELATED: Grants/Grants Pending: NIH/NIBIB; Patents (planned, pending or issued): Several, unrelated to work. Parmede Vakil—RELATED: Grant: NIH; * UNRELATED: Grants/Grants Pending: NIH; * James Carr—UNRELATED: Grant/Grants Pending: Siemens; * Comments: Research support. Michael Markl—UNRELATED: Grant: NIH; * Comments: NIH-T32-EB005170, NIH-R01-HL088437 (*money paid to institution).

REFERENCES

1. Rigamonti D, Hadley MN, Drayer BP, et al. **Cerebral cavernous malformations: incidence and familial occurrence.** *N Engl J Med* 1988;319:343–47
2. **Arteriovenous malformations of the brain in adults.** *N Engl J Med* 1999;340:1812–18
3. Spetzler RF, Martin NA. **A proposed grading system for arteriovenous malformations.** *J Neurosurg* 1986;65:476–83
4. Batjer HH, Devous MD Sr, Seibert GB, et al. **Intracranial arteriovenous malformation: relationships between clinical and radiographic factors and ipsilateral steal severity.** *Neurosurgery* 1988;23:322–28
5. Stapf C, Mast H, Sciacca RR, et al. **Predictors of hemorrhage in patients with untreated brain arteriovenous malformation.** *Neurology* 2006;66:1350–55
6. Ogilvy CS, Stieg PE, Awad I, et al. **Recommendations for the management of intracranial arteriovenous malformations: a statement for healthcare professionals from a special writing group of the Stroke Council, American Stroke Association.** *Circulation* 2001;103:2644–57
7. Andrews BT, Wilson CB. **Staged treatment of arteriovenous malformations of the brain.** *Neurosurgery* 1987;21:314–23
8. Unlu E, Temizoz O, Albayram S, et al. **Contrast-enhanced MR 3D angiography in the assessment of brain AVMs.** *Eur J Radiol* 2006;60:367–78
9. Hadizadeh DR, von Falkenhausen M, Gieseke J, et al. **Cerebral arteriovenous malformation: Spetzler-Martin classification at subsecond-temporal-resolution four-dimensional MR angiography compared with that at DSA.** *Radiology* 2008;246:205–13
10. Eddleman CS, Jeong HJ, Hurley MC, et al. **4D radial acquisition contrast-enhanced MR angiography and intracranial arteriovenous malformations: quickly approaching digital subtraction angiography.** *Stroke* 2009;40:2749–53
11. Nishimura S, Hirai T, Sasao A, et al. **Evaluation of dural arteriovenous fistulas with 4D contrast-enhanced MR angiography at 3T.** *AJNR Am J Neuroradiol* 2010;31:80–85
12. Illies T, Forkert ND, Ries T, et al. **Classification of cerebral arteriovenous malformations and intranidal flow patterns by color-encoded 4D-hybrid-MRA.** *AJNR Am J Neuroradiol* 2013;34:46–53
13. Forkert ND, Fiehler J, Illies T, et al. **4D blood flow visualization fusing 3D and 4D MRA image sequences.** *J Magn Reson Imaging* 2012;36:443–53
14. Bammer R, Hope TA, Aksoy M, et al. **Time-resolved 3D quantitative flow MRI of the major intracranial vessels: initial experience and comparative evaluation at 1.5T and 3.0T in combination with parallel imaging.** *Magn Reson Med* 2007;57:127–40
15. Wetzel S, Meckel S, Frydrychowicz A, et al. **In vivo assessment and visualization of intracranial arterial hemodynamics with flow-sensitized 4D MR imaging at 3T.** *AJNR Am J Neuroradiol* 2007;28:433–38
16. Hope TA, Hope MD, Purcell DD, et al. **Evaluation of intracranial stenoses and aneurysms with accelerated 4D flow.** *Magn Reson Imaging* 2010;28:41–46
17. Isoda H, Ohkura Y, Kosugi T, et al. **In vivo hemodynamic analysis of intracranial aneurysms obtained by magnetic resonance fluid dynamics (MRFD) based on time-resolved three-dimensional phase-contrast MRI.** *Neuroradiology* 2010;52:921–28
18. Rayz VL, Boussel L, Ge L, et al. **Flow residence time and regions of intraluminal thrombus deposition in intracranial aneurysms.** *Ann Biomed Eng* 2010;38:3058–69
19. Hope MD, Purcell DD, Hope TA, et al. **Complete intracranial arterial and venous blood flow evaluation with 4D flow MR imaging.** *AJNR Am J Neuroradiol* 2009;30:362–66
20. Chang W, Loecher MW, Wu Y, et al. **Hemodynamic changes in patients with arteriovenous malformations assessed using high-resolution 3D radial phase-contrast magnetic resonance angiography.** *AJNR Am J Neuroradiol* 2012;33:1565–72
21. Meckel S, Stalder AF, Santini F, et al. **In vivo visualization and analysis of 3-D hemodynamics in cerebral aneurysms with flow-sensitized 4-D MR imaging at 3 T.** *Neuroradiology* 2008;50:473–84
22. Bock J, Kreher BW, Hennig J, et al. **Optimized pre-processing of time-resolved 2D and 3D phase contrast MRI data.** In Proceedings: 15th Scientific Meeting of the International Society for Magnetic Resonance in Medicine 2007:3138
23. Bock J, Frydrychowicz A, Stalder AF, et al. **4D phase contrast MRI at 3 T: effect of standard and blood-pool contrast agents on SNR, PC-MRA, and blood flow visualization.** *Magn Reson Med* 2010;63:330–38
24. Markl M, Harloff A, Bley TA, et al. **Time-resolved 3D MR velocity mapping at 3T: improved navigator-gated assessment of vascular anatomy and blood flow.** *J Magn Reson Imaging* 2007;25:824–31
25. Harloff A, Simon J, Bredecke S, et al. **Complex plaques in the proximal descending aorta: an underestimated embolic source of stroke.** *Stroke* 2010;41:1145–50
26. Markl M, Geiger J, Kilner PJ, et al. **Time-resolved three-dimensional magnetic resonance velocity mapping of cardiovascular flow paths in volunteers and patients with Fontan circulation.** *Eur J Cardiothorac Surg* 2011;39:206–12
27. Fera F, Bono F, Messina D, et al. **Comparison of different MR venography techniques for detecting transverse sinus stenosis in idiopathic intracranial hypertension.** *J Neurol* 2005;252:1021–25
28. Saatci I, Cekirge HS, Ciceri EF, et al. **CT and MR imaging findings and their implications in the follow-up of patients with intracranial aneurysms treated with endosaccular occlusion with Onyx.** *AJNR Am J Neuroradiol* 2003;24:567–78
29. da Costa L, Wallace MC, Ter Brugge KG, et al. **The natural history and predictive features of hemorrhage from brain arteriovenous malformations.** *Stroke* 2009;40:100–05
30. Anzalone N, Scomazzoni F, Strada L, et al. **Intracranial vascular malformations.** *Eur Radiol* 1998;8:685–90
31. See AP, Raza S, Tamargo RJ, et al. **Stereotactic radiosurgery of cranial arteriovenous malformations and dural arteriovenous fistulas.** *Neurosurg Clin N Am* 2012;23:133–46
32. Hamm KD, Klisch J, Surber G, et al. **Special aspects of diagnostic imaging for radiosurgery of arteriovenous malformations.** *Neurosurgery* 2008;62:A44–52
33. Lv X, Wu Z, Li Y, et al. **Hemorrhage risk after partial endovascular NBCA and Onyx embolization for brain arteriovenous malformation.** *Neurol Res* 2012;34:552–56
34. Lv X, Wu Z, Jiang C, et al. **Complication risk of endovascular embolization for cerebral arteriovenous malformation.** *Eur J Radiol* 2011;80:776–79
35. Ogilvy CS, Stieg PE, Awad I, et al. **AHA scientific statement: recommendations for the management of intracranial arteriovenous malformations: a statement for healthcare professionals from a special writing group of the Stroke Council, American Stroke Association.** *Stroke* 2001;32:1458–71
36. Hartmann A, Mast H, Mohr JP, et al. **Determinants of staged endovascular and surgical treatment outcome of brain arteriovenous malformations.** *Stroke* 2005;36:2431–35

Fast 4D Flow MRI Re-Emerges as a Potential Clinical Tool for Neuroradiology

Shortly after the introduction of clinical MR imaging, Moran¹ demonstrated that velocity and flow could be measured non-invasively by using flow-encoding gradients integrated into conventional MR imaging techniques. This innovation was quickly implemented, resulting in 2D and 3D phase-contrast MRA.² The value of 4D flow MR imaging for the evaluation of brain AVMs was recognized by early investigators.³ However, initial excitement in 4D flow MR imaging was dampened by low resolution, loss of signal due to complex flow, difficulty selecting the velocity encoding, and the long scanning times for 4D acquisition. Fortunately, many of these limitations have been overcome, and we are entering a new era of fast high-resolution 4D flow MR imaging. Acquisition times have been reduced by using strategies such as compressed sensing⁴ and radial *k*-space trajectories.⁵ Shorter TEs have reduced signal loss, and new encoding strategies improve the dynamic range of velocities that are detected.⁶ 3T scanners and 32-channel coils provide substantial increases in signal and signal detection, enabling higher spatial resolution examinations.⁷ These improvements have already enabled 4D flow MR imaging to become a viable clinical tool in the assessment of a variety of non-neurologic conditions such as diseases of the aortic arch,⁸ congenital heart disease,⁹ portal venous hypertension,¹⁰ and renal arterial stenosis.¹¹

In this issue of *AJNR*, Ansari et al¹² have demonstrated that 4D flow MR imaging may play an important role in neurovascular diseases such as brain AVMs. The report demonstrated that cardiac-gated 4D flow MR imaging of the entire brain can be performed with excellent spatial and temporal resolution. The power of 4D flow MR imaging is that it allows simultaneous measurement of flow in the entire cerebrovascular system throughout the cardiac cycle, encompassing both arteries and veins.¹³ The 4D flow examination provides magnitude images that display the vascular anatomy and 3D velocity flow fields that can be used to derive flow-path¹⁴ and to estimate important parameters such as wall shear stress¹⁵ and pressure gradients.¹⁶ Ansari et al showed how 4D flow MR imaging can be used to improve the characterization of brain AVMs by incorporating physiologic information into the imaging assessment. It is now possible to extend the characterization to not only include important anatomic features such as size, location, and vascular components of arterial supply and drainage patterns, but also the flow conditions

within each major arterial feeder, arteries near the AVM, and contralateral arteries permitting a global assessment of flow across the entire cerebrovascular network.

The flow network can be further defined by generating velocity-derived flow-path lines providing an overview of the dominant flow channels. Future applications will likely provide quantitative measurements of flow, estimates of wall shear stress, and pressure gradients. The vascular anatomy can be eloquently displayed by using the velocity data within each voxel to derive streamlines weighted by the distance traveled per second. Virtual MR cartography requires segmentation of vessel boundaries followed by manual positioning of the plane emitter by using vessel cross-sections and blood-flow tracking within these vessels by generating velocity-based selective streamlines. A selective cartography of the vascular malformation can be displayed by choosing the starting point of the flow-tracking. The virtual selective cartography has the potential to improve the anatomic characterization and aid in pretreatment planning.¹⁷

Ansari et al showed the ability of 4D flow MR imaging to assist in the selection of vessels to treat and to monitor flow conditions during staged embolization. The arterial components are differentiated by the size, flow volume, velocity profile, and flow features and can be compared to relatively normal contralateral vessels. The alterations in flow during staged embolization are easily appreciated and in some instances may improve targeting of vessels for treatment.

However, although the flow information is very relevant, it is yet to be determined whether it can significantly contribute to the selection of patients for open surgical resection, endovascular surgery, radiosurgery, and combined therapy or provide information regarding risk stratification. The challenges for future work are how to apply this technology to enhance treatment and improve outcomes. Targets for the technology might include better definitions of steal phenomenon, the influence of the AVM on global brain flow, and the impact of steal on autoregulation. A somewhat less explored component is venous drainage; 4D flow MR imaging can show high-velocity flow in arterialized veins, identify venous stenosis, measure pressure gradients, and quantitate arteriovenous shunts. Another application may be the detection of high-

risk flow conditions that may promote aneurysm formation in arteries that supply the AVM.¹⁸

Currently, a significant limitation in the development of 4D flow MR imaging is the lack of easy-to-use postprocessing software tools that are readily available in a clinical environment. Most groups engaged in 4D flow MR imaging have elaborate in-house software libraries that require substantial time and effort to create meaningful flow data. Although there are many avenues to explore based on derivatives of the velocity vector fields (eg, streamlines, path lines, particle path traces, relative wall shear stress, pressure gradients), without appropriate software tools, these will remain in the research domain.

Combining time-resolved contrast-enhanced MRA (4D tr CE MRA) and 4D flow MR imaging into 1 acquisition is also possible when highly undersampled radial acquisition is used to dramatically reduce the imaging time.^{19,20} This approach, called HYPRFlow, provides time-resolved contrast-enhanced whole-brain serial images that display the vascular anatomy with good temporal and spatial resolution and also generate cardiac-synchronized 3D velocity flow fields. The entire highly accelerated examination takes slightly >5 minutes. Recently, investigators have shown that 4D tr CE MRA can also be analyzed to generate color-coded time-of-arrival maps that improve delineation of the AVM arterial supply and reveal variable intranidal flow patterns.²¹

Finally, although highly controversial, 4D flow MR imaging can, in fact, assist in the characterization of intracranial aneurysms based on flow features such as a compact inflow jet, a small focal impingement zone, high vorticity, and wall shear stress, which have been identified as possibly contributing to aneurysm rupture.²² There is still a great deal of debate on which flow features are important and how they contribute to aneurysm formation, growth, and rupture; however, it is likely that ultra-high-resolution 4D flow MR imaging will provide information similar to computational fluid dynamics and will contribute to the hemodynamic assessment of intracranial aneurysms.²³

4D flow MR imaging will have a role to play in the evaluation of neurovascular diseases. The challenge will be how to apply the technology to provide clinically useful information with well-defined applications.

REFERENCES

1. Moran PR. A flow velocity zeugmatographic interlace for NMR imaging in humans. *Magn Reson Imaging* 1982;1:197–203
2. Pelc NJ, Bernstein MA, Shimakawa A, et al. Encoding strategies for three-direction phase-contrast MR imaging of flow. *J Magn Reson Imaging* 1991;1:405–13
3. Marks M, Pelc N, Ross M, et al. Determination of cerebral blood flow with a phase contrast cine MR imaging technique: evaluation of normal subjects and patients with arteriovenous malformations. *Radiology* 1992;182:467–76
4. Stadlbauer A, van der Riet W, Creleir G, et al. Accelerated time resolve three dimensional MR velocity mapping of blood flow patterns in the aorta using SENSE and k-t BLAST. *Eur J Radiol* 2010;75:e15–21
5. Gu T, Korosec F, Block W, et al. PC VIPR: a high speed 3D phase contrast method for flow quantification and high resolution angiography. *AJNR Am J Neuroradiol* 2005;26:743–49
6. Johnson K, Markl M. Improved SNR in phase contrast velocimetry with five point balanced flow encoding. *Magn Reson Med* 2010;63:349–55

7. Wetzel S, Meckel S, Frydrychowicz A, et al. In vivo assessment and visualization of intracranial arterial hemodynamics with flow sensitized 4D MR imaging at 3T. *AJNR Am J Neuroradiol* 2007;28:433–38
8. Frydrychowicz A, François CJ, Turski PA. Four-dimensional phase contrast magnetic resonance angiography: potential clinical applications. *Eur J Radiol* 2011;80:24–35
9. Markl M, Geiger J, Kilner P, et al. Time resolved three-dimensional magnetic resonance velocity mapping of cardiovascular flow paths in volunteers and patients with Fontan circulation. *Eur J Cardiothorac Surg* 2011;39:206–12
10. Roldán-Alzate A, Frydrychowicz A, Niespodzany E, et al. In vivo validation of 4D flow MRI for assessing the hemodynamics of portal hypertension. *J Magn Reson Imaging* 2013;37:1100–08
11. François C, Lum D, Johnson K, et al. Renal arteries: isotropic, high-spatial-resolution, unenhanced MR angiography with three-dimensional radial phase contrast. *Radiology* 2011;258:254–60
12. Ansari SA, Schnell S, Carroll T, et al. Intracranial 4D flow MRI: toward individualized assessment of arteriovenous malformation hemodynamics and treatment-induced changes. *AJNR Am J Neuroradiol* 2013 May 2 [Epub ahead of print]
13. Hope M, Percell D, Hope T, et al. Complete intracranial arterial and venous blood flow evaluation with 4D flow MR Imaging. *AJNR Am J Neuroradiol* 2009;30:362–66
14. Markl M, Kilner P, Ebbers T. Comprehensive 4D velocity mapping of the heart and great vessels by cardiovascular magnetic resonance. *J Cardiovasc Magn Reson* 2011;13:7–12
15. Boussel L, Rayz v, McCulloch C, et al. Aneurysm growth occurs at region of low wall shear stress: patient-specific correlation of hemodynamics and growth in a longitudinal study. *Stroke* 2008;39:2997–3002
16. Lum DP, Johnson KM, Paul R, et al. Transstenotic pressure gradients: measurements in swine: ECG gated 3D phase contrast MRA versus endovascular pressure sensing guidewires. *Radiology* 2007;245:751–60
17. Roca P, Edjlali M, Rabrait C, et al. Selective MR flow cartography of brain vascular malformations. In: *Proceedings of the 21st Annual Meeting of the International Society for Magnetic Resonance in Medicine*, Salt Lake City, Utah. April 20–26, 2013
18. Chang W, Loecher MW, Wu Y, et al. Hemodynamic changes in patients with arteriovenous malformations assessed using high resolution 3D radial phase contrast MR angiography. *AJNR Am J Neuroradiol* 2012;33:1565–72
19. Velikina J, Johnson K, Wu Y, et al. PC HYPRFlow: a technique for rapid imaging of contrast dynamics. *J Magn Reson Imaging* 2010;31:447–56
20. Grist T, Mistretta C, Strother C, et al. Time-resolved angiography: past, present and future. *J Magn Reson Imaging* 2012;36:1273–86
21. Illies T, Forkert ND, Ries T, et al. Classification of cerebral arteriovenous malformations and intranidal flow patterns by color-encoded 4D hybrid MRA. *AJNR Am J Neuroradiol* 2013;34:46–53
22. Boussel L, Rayz V, Martin A, et al. Phase-contrast magnetic resonance imaging measurements in intracranial aneurysms in vivo of flow patterns, velocity fields, and wall shear stress: comparison with computational fluid dynamics. *Magn Reson Med* 2009;61:409–17
23. Kecskemeti S, Johnson KJ, Wu Y, et al. High resolution three dimensional cine phase contrast MRI of small intracranial aneurysms using a stack of stars k-space trajectory. *J Magn Reson Imaging* 2012;35:518–27

P. Turski

University of Wisconsin
School of Medicine
Madison Wisconsin

M. Edjlali

C. Oppenheim
Sainte-Anne Hospital Center
Paris, France

<http://dx.doi.org/10.3174/ajnr.A3664>

Evolution of Cortical and Thalamus Atrophy and Disability Progression in Early Relapsing-Remitting MS during 5 Years

R. Zivadinov, N. Bergsland, O. Dolezal, S. Hussein, Z. Seidl, M.G. Dwyer, M. Vaneckova, J. Krasensky, J.A. Potts, T. Kalincik, E. Havrdová, and D. Horáková



ABSTRACT

BACKGROUND AND PURPOSE: Pathologic changes in GM have an important role in MS. We investigated the association between SDGM and cortical volume changes and disability progression in early RRMS.

MATERIALS AND METHODS: One hundred eighty patients with RRMS had clinical assessment during 5 years and were divided into those with or without SDP at 5 years by the usual definition in treatment trials. The number of available MR imaging scans at various time points was the following: at baseline, 178; and at 6 months, 172; at 12 months, 175; at 24 months, 155; at 36 months, 160; at 48 months, 158; and at 60 months, 162, respectively. Longitudinal changes in cortical, GM, and WM volume were calculated by using the direct method.

RESULTS: At 5 years, 90 patients with RRMS experienced SDP and 90 had stable disease. At baseline, patients with SDP had longer disease duration, greater T2-lesion volume, and smaller whole-brain, WM, cortical, and SDGM volume ($P < .01$). At 5 years, patients with SDP had significantly greater percentage decreases from baseline compared with those without SDP in the volume of the whole brain ($P < .0001$), cortex ($P = .001$), GM ($P = .003$), and thalamus ($P = .01$). In patients who developed SDP at 5 years and those who did not, mixed-effect models, adjusted for age, disease duration, and change of the treatment status, showed significant interactions between SDP status at 5 years and changes with time in whole-brain, cortical, lateral ventricle (all $P < .001$), thalamus ($P = .006$), and total SDGM ($P = .0095$) volume.

CONCLUSIONS: SDP is associated with progression of cortical, central, and thalamic atrophy in early RRMS during 5 years.

ABBREVIATIONS: ASA = Avonex-Steroid-Azathioprine; EDSS = Expanded Disability Status Scale; GM = gray matter; RR = relapsing-remitting; SDGM = subcortical deep gray matter; SDP = sustained disability progression; SIENA = structural image evaluation with normalization of atrophy.

Historically, MS has been classified as a disease predominantly affecting the WM of the central nervous system.^{1,2} Nevertheless, pathologic changes in GM are increasingly recognized as an important component of the MS disease process.³⁻⁸ Advances in

MR imaging have enabled detection of changes in GM volume.^{9,10} However, the available imaging techniques are still unable to adequately detect GM lesions, especially in the cortex,^{2,7} probably due to these lesions having a different underlying pathology compared with WM lesions: those in the GM appear to have minimal infiltration of immune cells and are of a less inflammatory nature.^{7,8,11}

Studies in patients with RRMS showed that GM atrophy is a meaningful indicator of neurodegeneration and occurs more rapidly than WM atrophy during both the early and advanced stages of MS.^{4-6,12} Moreover, GM atrophy is a better indicator of disability progression than WM atrophy or accumulation of lesion burden.^{4-6,13} Cognitive impairment in patients with RRMS is thought to be associated with MS-related GM pathology, particularly in the cortex,¹⁴ with variability in disability progression among patients with RRMS possibly arising from differences in GM injury.¹⁵

It is likely that GM pathology reflects increased cortical and SDGM damage and atrophy, which may also underlie other aspects of MS-associated disability.^{1-3,7,8} Several case-control studies have established that SDGM but not cortical atrophy is present

Received August 22, 2012; accepted after revision December 5.

From the Buffalo Neuroimaging Analysis Center (R.Z., N.B., S.H., M.G.D.) and Jacobs Neurological Institute (R.Z.), University at Buffalo SUNY, Buffalo, New York; Department of Neurology and Center of Clinical Neuroscience (O.D., T.K., E.H., D.H.) and Department of Radiology (Z.S., M.V., J.K.), Charles University in Prague, First Faculty of Medicine and General University Hospital, Prague, Czech Republic; Melbourne Brain Centre (T.K.), Department of Medicine, University of Melbourne, Australia; and Biogen Idec Inc. (J.A.P.), Weston, Massachusetts.

Writing support was provided by Infusion Communications and was funded by Biogen Idec Inc. The authors were not compensated and retained full editorial control. The Avonex-Steroids-Azathioprine study is an investigator-initiated study that was supported by Czech Ministries of Education and Health (NT13237-4/2012, MSM 0021620849, PRVOUK-P26/LFI/4, RVO-VFN64165/2012). The MR imaging acquisition part of the study was supported by Gedeon Richter and Biogen Idec.

Please address correspondence to Robert Zivadinov, MD, PhD, FAAN, Department of Neurology, Buffalo Neuroimaging Analysis Center, Jacobs Neurological Institute, University at Buffalo, State University of New York, 100 High St, Buffalo, NY 14203; e-mail: rzivadinov@bnac.net

Indicates open access to non-subscribers at www.ajnr.org

<http://dx.doi.org/10.3174/ajnr.A3503>

at the earliest clinical stages of the disease.¹⁶⁻²⁰ Other studies indicate that damage to the SDGM is associated with memory impairment.^{21,22} However, to date, there have been no long-term longitudinal studies investigating possible associations among SDGM, cortical atrophy, and disability progression in RRMS.

Clinical trials on the therapeutic use of intramuscular interferon β -1a in patients with RRMS have validated measures of whole-brain atrophy as clinically significant markers of future disease progression and therapeutic response.²³⁻²⁵ Most important, intramuscular interferon β -1a has been shown to significantly slow the progression of brain atrophy in patients with RRMS, primarily through a reduction in GM atrophy.^{25,26}

The aim of the current study was to monitor the temporal dynamics of SDGM and cortical atrophy in patients with early RRMS who participated in an intramuscular interferon β -1a study during 5 years and to determine any association with disability progression.

MATERIALS AND METHODS

MR imaging data were obtained from patients who were initially enrolled in the 2-year, double-blind, placebo-controlled Avonex-Steroid-Azathioprine study.²⁷ In this study, patients were randomized to treatment with intramuscular interferon β -1a (30 μ g/week) alone or in combination with azathioprine (50 mg/day) or azathioprine plus prednisone (10 mg every other day). At the end of the ASA study, patients with MS were eligible to enter a 3-year extension study during which they were able to continue to receive monotherapy with intramuscular interferon β -1a, add other therapies to intramuscular interferon β -1a, or switch to new therapies. All patients were clinically assessed by using the EDSS every 2 months during the first 12 months and then every 3 months until month 60. MR imaging assessments were performed at baseline and at yearly intervals at least 14 days after the last administration of any steroid treatment. Full details of the design and results of the 2-year ASA study (by randomized treatment group) and preliminary results from the 5-year extension period (by disability progression) were reported.^{12,27}

The study was approved by the Medical Ethics Committee (Charles University of Prague and University of Buffalo).

MR Imaging and Analysis. All MR imaging assessments were performed by using the same Gyroscan 1.5T scanner (Philips Healthcare, Best, the Netherlands). Axial images of the brain were obtained by using FLAIR with 1.5-mm section thickness and axial T1-weighted 3D spoiled gradient-recalled images with 1-mm section thickness. Both images had an in-plane resolution of 1×1 mm. All images were nongapped. MR imaging assessment protocols were conducted as reported.^{12,27} Investigators performing the image analyses were blinded to subject characteristics and clinical status.

Lesion Volume. T2-lesion volume was calculated by using a reliable semiautomated edge-detection contouring/thresholding technique previously described.²⁸ With FMRIB's Linear Image Registration Tool software (FMRIB; <http://www.fmrib.ox.ac.uk/>),²⁹ all follow-up FLAIR images for a given subject were coregistered to his or her baseline FLAIR image by using a 6 *df* rigid-body model. All subsequent lesion analyses were performed

by using the coregistered images. For each follow-up time point, T2-lesion volume was performed via the aid of a "subtraction image." Briefly, the FLAIR image from the previous time point was subtracted from the corresponding current FLAIR image. The result was then smoothed with a Gaussian kernel of $\sigma = 0.5$ mm. Cross-sectional ROIs were overlaid on the subtraction image to facilitate the identification of a new T2-lesion volume.

Global and Tissue-Specific Atrophy Measures. For baseline analyses, SIENAX software from the FMRIB package was used (Version 2.6), with corrections for T1-hypointensity misclassification by using an in-house-developed in-painting program on T1WI 3D spoiled gradient-recalled images. Normalized whole-brain, normalized GM, normalized WM volume, normalized cortical, and normalized lesion volume were measured as previously described.³⁰

For longitudinal changes of the whole-brain volume, we applied the SIENA method³¹ to calculate the percentage brain volume change. To quantify longitudinal GM, WM, and cortical and lateral ventricle percentage volume changes, we used a modified hybrid of SIENA and SIENAX in FMRIB. We used a brain- and skull-constrained coregistration technique to place both baseline and follow-up images into a position half-way between the two. As in the original SIENA method,³¹ this helps minimize a potential bias by subjecting both images to the effects of coregistration. Next, we combined baseline and follow-up intracranial volume masks via union and valid voxel masks via intersection, ensuring that the same imaging volume was analyzed at both time points. Finally, we segmented the resulting images with a modified longitudinal version of FMRIB's Automated Segmentation Tool (FAST),³² which uses a 4D joint hidden random Markov field to prevent misclassification between time points when longitudinal intensity changes are lacking (or minimal). Total tissue volume was calculated for both baseline and follow-up for each tissue compartment from partial volume maps, and percentage volume change was derived directly from the images.

Absolute tissue volumes for the thalamus, caudate, putamen, globus pallidus, hippocampus, amygdala, and nucleus accumbens at each time point were estimated from in-painted T1WI 3D spoiled gradient-recalled images with FMRIB's Integrated Registration and Segmentation Tool (FIRST, version 1.2), a model-based segmentation/registration tool.³³ Normalized SDGM volumes were obtained by multiplying the estimated volumes from this tool by the volumetric scaling factor from SIENAX.³⁰

Statistical Analyses. The 5-year evaluation of the associations between SDGM, cortical atrophy measures, and disability progression was preplanned. Because neither the 2-year²⁷ nor the 5-year^{6,12} nor the 6-year³⁴ results showed any statistically significant differences between the treatment groups, the groups were merged for the purpose of the current analysis.

For the present analyses, patients were divided into 2 groups based on disability progression. The first group contained patients who, at the end of the 5-year period, had SDP. This was defined as any 1.0-point sustained (24-week) increase in the EDSS score in patients who had a baseline EDSS score of ≥ 1.0 or any ≥ 1.5 -point sustained (24-week) increase in the EDSS score in pa-

Table 1: Baseline demographics and clinical characteristics for all patients, split by progression status at 5 years^a

	Sustained Disease Progression (n = 90)	Stable Disease (n = 90)	P Value
Female (No.) (%)	68 (75.6)	73 (81.1)	.4
Age (yr) (mean) (SD) (median)	31.9 (7.9) 31.5	29.5 (7.8) 28.5	.04
Disease duration (yr) (mean) (SD) (median)	6.0 (5.8) 4.0	4.0 (4.3) 3.0	.01
EDSS (mean) (SD)	2.0 (1.0)	1.8 (0.8)	.2
Median (range)	2.0 (0–3.5)	2.0 (0–3.5)	
Treatment assignment (No.) (%)			
IFN-β 1a monotherapy	25 (27.8%)	34 (37.8%)	.3
IFN-β 1a + AZA	32 (35.6%)	26 (28.9%)	
IFN-β 1a + AZA + Steroids	33 (36.7%)	30 (33.3%)	
Treatment switch ^b			
Did not switch	34 (38%)	62 (69%)	<.0001
Switched	56 (62%)	26 (29%)	

Note:—IFN-β indicates interferon-β; AZA, azathioprine.

^a The difference of the means between the groups was calculated using the Student *t* test, Pearson χ^2 test, or Mann-Whitney rank sum test, as appropriate.

^b Treatment switch was defined on the basis of a derived yes/no variable as to whether patients changed treatment status during the 5-year follow-up.

Table 2: Baseline MRI characteristics for all patients, split by progression status at 5 years^a

	Sustained Disease Progression (n = 90) (mean) (SD) (median)	Stable Disease (n = 90) (mean) (SD) (median)	P Value
T2-LV	11.2 (12.9) 6.3	4.7 (5.5) 2.8	<.0001
NWBV	1488.8 (84.4) 1485.6	1524.4 (74.1) 1520.6	.003
NGMV	797.9 (53.1) 800.2	815.5 (50) 822.7	.02
NWMV	690.9 (49.9) 689.5	708.9 (37.4) 704.5	.007
NLTV	42.6 (15.1) 39.7	40 (11.8) 38.9	.3
NCV	623.6 (43.3) 627	639.7 (41.3) 643.6	.01
Total NSDGMV	44.5 (4.5) 44.5	46.6 (3.9) 46.4	.002
NSDGMV structures			
Caudate nucleus	6.4 (0.8) 6.4	6.8 (0.8) 6.8	.0009
Putamen	9.4 (1.1) 9.3	9.8 (1) 9.9	.015
Globus pallidus	3.4 (0.4) 3.4	3.5 (0.4) 3.5	.05
Thalamus	14.6 (1.8) 14.6	15.4 (1.5) 15.2	.002
Hippocampus	7.2 (0.8) 7.2	7.5 (0.8) 7.6	.015
Nucleus accumbens	0.9 (0.2) 0.9	1 (0.2) 1	.018
Amygdala	2.6 (0.4) 2.6	2.6 (0.3) 2.6	.14

Note:—LV indicates lesion volume; NWBV, normalized whole-brain volume; NGMV, normalized gray matter volume; NWMV, normalized white matter volume; NLTV, normalized lateral ventricle volume; NCV, normalized cortical volume; NSDGMV, normalized subcortical deep gray matter volume.

^a The difference of the means between the groups was calculated using Student *t* test. The MRI volumes are presented in milliliters.

tients who had a baseline EDSS score of 0.0. The second group contained subjects without SDP who were patients with stable disease.

Patients who completed the 2-year study and did not enter the 3-year extension period or who had discontinued treatment for reasons other than disability progression underwent scheduled follow-up evaluations. Because early study enrollment resulted in a total observation period of >5 years for some patients, data were not censored at 5 years; therefore, any patient reaching sustained progression after 5 years was categorized as having “progressed” at year 5.

Comparisons were made between SDP and stable MS. Comparisons at baseline were performed by using the Pearson χ^2 test for categorical values and the Student *t* test or Wilcoxon rank sum test for continuous variables with a skewed distribution. Regression analysis at 5 years for absolute and percentage change from baseline variables was used to adjust for differences in baseline age, disease duration, and change of treatment status during the 5-year follow-up.

Temporal changes in global, tissue-specific, and deep gray matter MR imaging measures by disability-progression status at different time points of the study are shown as mean \pm 95% confidence intervals and median \pm interquartile range, as appropriate. Longitudinal linear or quadratic random-intercept mixed-effect models,³⁵ adjusted for baseline age, disease duration, and change of treatment status during the 5-year follow-up, were used to describe the temporal associations between SDGM and cortical atrophy along with other MR imaging measures and disability progression. Variables violating normality assumptions were transformed by using Box-Cox transformations for modeling purposes.

To avoid too many spurious findings due to multiple comparisons, we have not reported anything as statistically significant unless the nominal *P* value was \leq .01 by using 2-tailed tests.

RESULTS

Subjects. In total, 180 patients with RRMS (90 patients each in the SDP and stable disease groups, according to the 5-year classification) were included in the study. The disability progression status was captured for all 180 patients at 5 years. The number of available MR imaging scans at various time points was the following: at baseline, 178, and at 6 months, 172; at 12 months, 175; at 24 months, 155; at 36 months, 160; at 48 months, 158; and at 60 months, 162, respectively. The missing scans at various time points were due to the unavailability of MR imaging scans or failure of accurate quantitative analysis

(data not shown). The observed patient populations with MR imaging data at 5 years exhibited no statistically significant differences in baseline demographics or clinical or MR imaging characteristics compared with those with missing MR imaging data at 5 years, except for a trend toward a treatment switch (*P* = .019, data not shown). Tables 1 and 2 present baseline characteristics for the 180 evaluable patients.

Clinical and MR Imaging Outcomes at Baseline. Comparisons between the MS groups showed that patients in the SDP group had a longer disease duration (*P* = .01) than patients with stable disease (Table 1). Additionally, patients with SDP had a greater T2-lesion volume (*P* < .001) as well as a smaller total SDGM volume (*P* = .002), whole-brain volume (*P* = .003), normalized WM volume (*P* = .007), and normalized cortical volume (*P* = .01) (Table 2). There were no significant differences between the 2 patient groups in baseline EDSS score and normalized lateral ven-

Table 3: Evolution of whole-brain and tissue-specific MRI measures during 5 years, split by progression status at 5 years^a

	Sustained Disease		P Value
	Progression (mean) (SD) (median)	Stable Disease (mean) (SD) (median)	
T2-LV (No. patients)	80	78	
Absolute change	2.8 (6.3) 1.6	2.3 (3.8) 1.0	
% Change	53.9 (66.7) 36.3	79.1 (156.4) 40.5	.4
Whole-brain (No. patients)	82	80	
% Change	-4.8 (3.4) -3.9	-2.6 (2) -2.2	<.0001
Gray matter (No. patients)	82	79	
% Change	-5.3 (3.1) -4.5	-3.8 (2.3) -4.1	.003
White matter (No. patients)	82	79	
% Change	-0.9 (3.4) -0.5	0.4 (3.1) 0.8	.06
Lateral ventricle volume, (No. patients)	82	79	
% Change	26.7 (24.8) 22.6	14.9 (11.3) 13.4	.02
Cortical volume (No. patients)	80	78	
% Change	-5.4 (3.1) -4.9	-3.8 (2.2) -4	.001

Note:—T2-LV indicates T2-lesion volume.

^a The difference between the groups was calculated using regression analysis adjusting for age, disease duration, and change of treatment status during the 5-year follow-up. The absolute volume changes are presented in milliliters. Variables with skewed distributions (% change in T2-LV and % change in LV) were transformed using Box-Cox transformations. The changes between baseline and follow-up scans for whole-brain, gray matter, white matter, lateral ventricle, and cortical volume were calculated using the direct-measurement technique; hence, no absolute but only percentage volume changes are available.

Table 4: Evolution of tissue-specific subcortical deep gray matter structures during 5 years, split by progression status at 5 years^a

	Sustained Disease		P Value
	Progression (mean) (SD) (median)	Stable Disease (mean) (SD) (median)	
Total SDGMV (No. patients)	81	78	
Absolute change	-2.5 (1.6) -2.5	-2 (1.1) -1.9	
% Change	-5.7 (3.8) -5.3	-4.4 (2.5) -4	.03
SDGMV structures			
Caudate nucleus (No. patients)	80	79	
Absolute change	-0.4 (0.4) -0.3	-0.3 (0.3) -0.3	
% Change	-5.9 (7) -5.1	-4.5 (4.6) -4.5	.3
Putamen (No. patients)	80	79	
Absolute change	-0.5 (0.4) -0.5	-0.4 (0.4) -0.5	
% Change	-5.8 (4.2) -5.7	-4.3 (3.7) -4.5	.02
Globus pallidus (No. patients)	80	79	
Absolute change	-0.06 (0.02) -0.07	-0.02 (0.02) -0.02	
% Change	-1.8 (5.1) -2.1	-0.5 (4.5) -0.7	.99
Thalamus (No. patients)	80	79	
Absolute change	-0.9 (0.6) -0.8	-0.7 (0.5) -0.6	
% Change	-6.2 (4.4) -5.5	-4.5 (3.2) -3.9	.01
Hippocampus (No. patients)	80	79	
Absolute change	-0.4 (0.4) -0.4	-0.4 (0.4) -0.4	
% Change	-5.5 (5.5) -5.7	-5.6 (5.6) -4.8	.9
Nucleus accumbens (No. patients)	80	79	
Absolute change	-0.08 (0.1) -0.08	-0.09 (0.1) -0.1	
% Change	-7.6 (14.8) -9.1	-8.7 (11.8) -10	.1
Amygdala (No. patients)	80	79	
Absolute change	-0.1 (0.2) -0.2	-0.1 (0.3) -0.2	
% Change	-5.1 (8.3) -6.2	-4.6 (9.7) -5.8	.95

Note:—SDGMV indicates subcortical deep gray matter volume.

^a The difference between the groups was calculated using regression analysis adjusting for age, disease duration, and change of treatment status during the 5-year follow-up. The absolute volume changes are presented in milliliters. Variables with skewed distributions (% change in globus pallidus and % change in amygdala) were transformed using Box-Cox transformations.

tricle or normalized GM volume. With the exception of the caudate ($P = .001$) and thalamus ($P = .002$), the SDGM brain structures measured were not significantly different at baseline between the 2 groups (Table 2).

atrophy accumulation with disability progression in patients with early RRMS. At the end of the 5-year observation period, retrospective analyses of baseline characteristics and MR imaging assessments were performed to compare patients who

Clinical and MR Imaging Outcomes at Year 5. At 5 years, the mean EDSS was 3.2 in the SDP group and 1.6 in the stable group ($P < .001$). Comparisons of percentage change from baseline to 5 years in MR imaging outcomes are shown in Tables 3 and 4.

The percentage change in whole-brain volume was greater in patients with SDP than in stable patients (-4.8% versus -2.6%; $P < .001$; Fig 1). Additionally, there was a significant interaction effect in the mixed-effect model analysis with disability progression and percentage change in whole-brain volume with time (interaction P value $< .001$) showing patients with disability progression having a steeper decline (Fig 2).

Significantly greater percentage volume change in the cortex (-5.4% versus -3.8%, $P = .001$) and GM (-5.3% versus -3.8%, $P = .003$) was detected in patients with SDP than in stable patients (Table 3 and Fig 2). There was a significant interaction effect in the mixed-effect model analysis, with disability progression and percentage change in cortical (interaction P value $< .001$) but not total GM volume with time, showing patients with disability progression having a steeper decline (Fig 2).

At 5 years, a significantly greater decrease in thalamus volume (-6.2% versus -4.5%, $P = .01$) was detected in patients with SDP than in stable patients (Fig 3). When we detected changes in slope over the entire study period, thalamus and total SDGM volume showed significant decreases with time in patients with SDP compared with stable patients (thalamus interaction P value = .0006 and total SDGM volume interaction P value = .0095; Fig 4).

The SDP group exhibited a significant increase with time in lateral ventricle volume (interaction P value $< .001$) compared with stable patients (Figs 1 and 2).

During 5 years, no significant difference in accumulation of T2-lesion volume was detected between stable patients and those with SDP (Figs 1 and 2).

DISCUSSION

This study is the first prospective, longitudinal, long-term investigation of the association between the SDGM and cortical

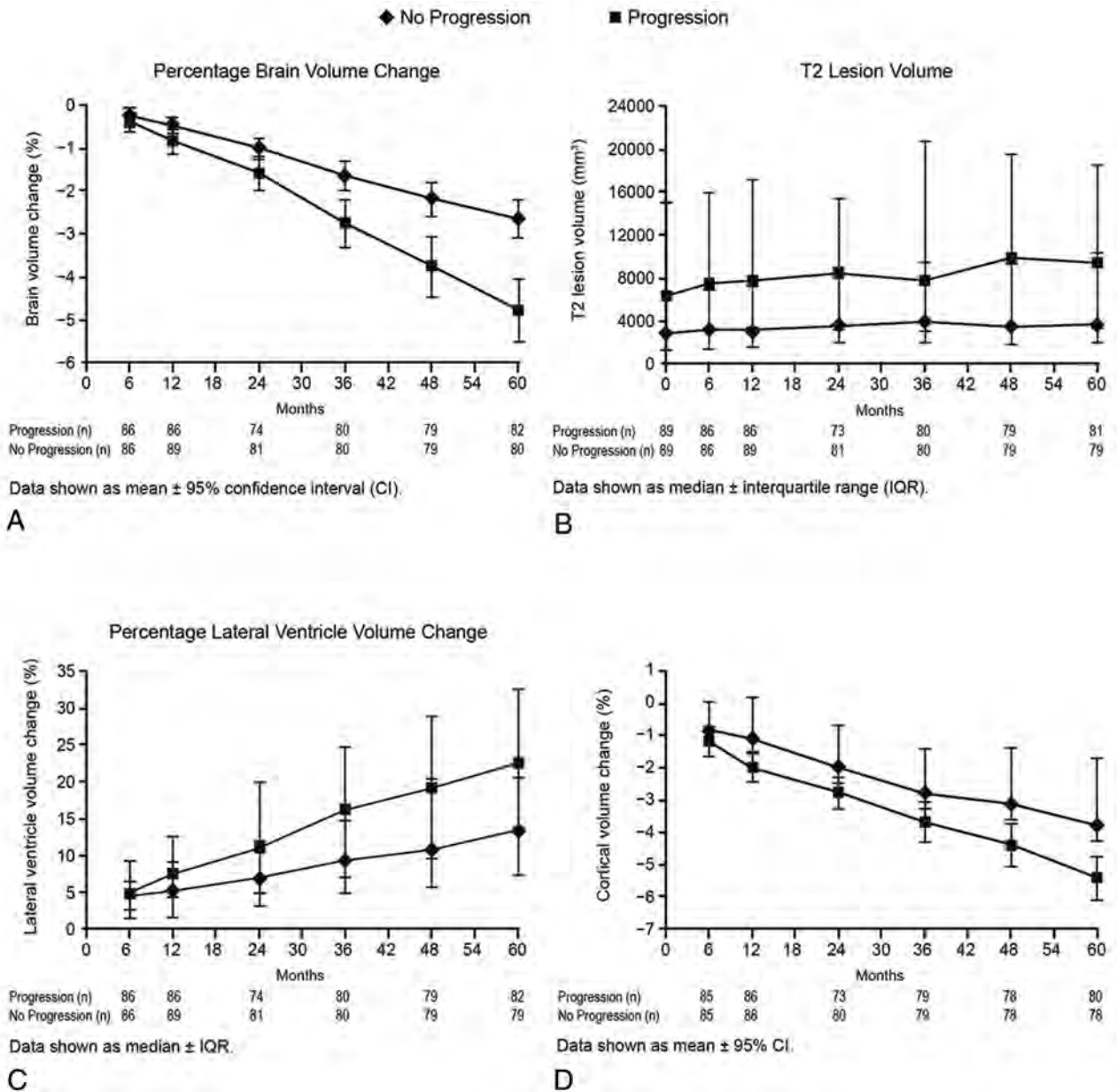


FIG 1. Temporal changes in global and tissue-specific MR imaging measures by disability-progression status at different time points of the study are shown as mean \pm 95% confidence intervals and median \pm interquartile range, as appropriate. A, Percentage change in whole-brain volume. B, T2-lesion volume. C, Percentage change in lateral ventricular volume. D, Percentage change in cortical volume.

developed disability progression with patients whose disease remained stable. Most interesting, the baseline MR imaging assessments gave an indication of patients who would progress because these patients had significantly greater T2-lesion volume and significantly smaller whole brain, WM, total SDGM, caudate, and thalamus volume. In the previous preliminary analysis of the 5-year data,¹² no difference in baseline whole-brain volume or normalized WM volume was found between patients who progressed or those who remained stable after 5 years. This could have been related to the fewer patients and the shorter time period used for the definition of the SDP group in the previous study.¹² In addition, a newer version of the SIENAX (2.6) and an improved in-painting method were applied in the current study, which could have contributed to

better accuracy of the results. After adjusting for age, disease duration at baseline, and change of treatment status during 5 years, we saw significant interactions with time and disability progression with whole-brain volume and cortex, lateral ventricles, thalamus, and total SDGM volume, suggesting that the association with disability progression and deterioration on these MR imaging structures is predictive and time-dependent.

We performed this study as an exploratory one, and given the paucity of data, we did not know how many comparisons we would make a priori; thus, we did not adjust the significance tests for multiple comparisons. Potential associations identified in the current study may drive future research with preplanned analyses to validate the results of this exploratory research.

As expected, MS patient groups exhibited substantial de-

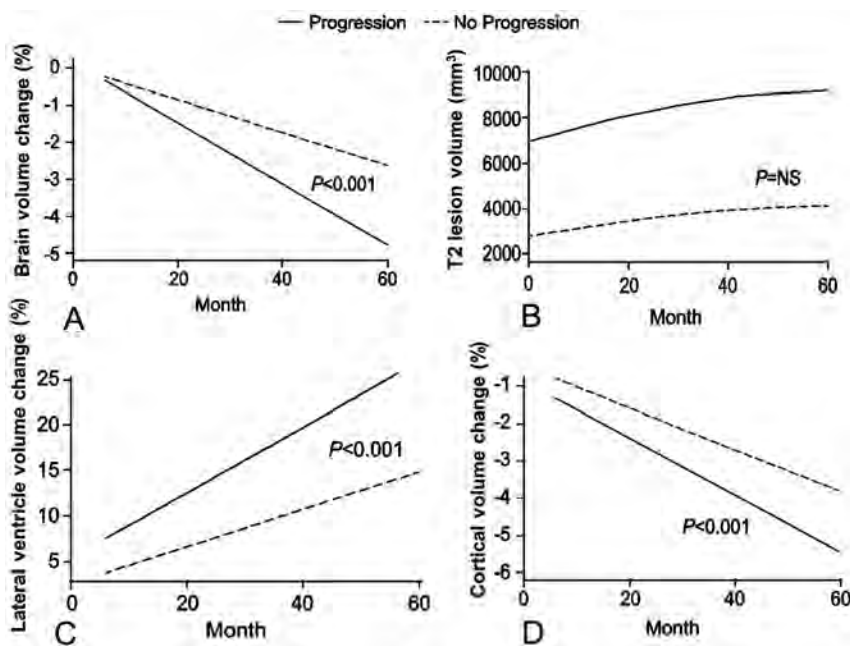


FIG 2. Changes in global and tissue-specific MR imaging measures (fitted values–intercept model) by disability-progression status with time. Percentage change in whole-brain volume: interaction $P < .001$ (A); and T2-lesion volume: interaction $P =$ not significant (B). C, Percentage change in lateral ventricular volume: interaction $P < .001$. D, Percentage change in cortical volume: interaction $P < .001$.

increases in whole-brain volume and corresponding increases in lateral ventricle volume during 5 years. This finding is in line with those of previous studies.³⁶ Previous clinical studies in MS have shown an association between whole-brain atrophy and an increase in lateral ventricle volume and have found that both measurements were associated with increased disability.^{37,38} This association was confirmed in an earlier analysis of data from part of this cohort,¹² which showed that whole-brain volume was predictive of disability progression. Of particular note in the present study was the increase in lateral ventricle volume during 5 years, which was $>10\%$ greater in patients with SDP than in stable patients.

Among the patients with MS, more SDGM atrophy was seen in patients with SDP than in stable patients, most likely as a result of the significantly greater decreases in thalamus volumes in the former group. Because previous study showed age-dependent atrophy in the thalamus in healthy subjects,³⁹ age was retained in all analyses, as a covariate. The findings from the current study suggest that SDGM structures are severely affected in the first 10 years of disease after clinical onset. The potential relevance of SDGM atrophy to the development of disability progression was shown by the significantly smaller volumes at baseline in patients with SDP. The largest longitudinal difference during 5 years between the SDP and stable MS groups was detected in the thalamus (1.7 percentage points), which has a role in regulating a wide variety of functions, including receiving input from other SDGM structures and relaying neural signals to the motor cortex.⁴⁰ The results from our study suggest that SDGM and, in particular, thalamus atrophy in MS may affect areas of the brain that are important for the control of motor functions.

Patients with SDP showed more advanced cortical atrophy at 5 years compared with stable patients. This was confirmed by the

mixed-effect-model analysis, which found an interaction with time. These findings are in agreement with those in previous studies that have suggested differential patterns of GM and WM atrophy during 2 years for patients with MS versus healthy controls⁶ and that the rate of GM, but not WM, atrophy increased with advancing disease stage and was correlated with disability.^{4,5,12,24,25} Fundamentally cross-sectional approaches like SIENAX are still widely used to measure GM and WM changes,²⁵ leading to potentially less accurate results and more analysis failures. Direct measures of cortical, GM, and WM volume changes with advantages similar to those of SIENA have been lacking. We built on the basic half-way-registration and scaling-factor estimation components of SIENA. In addition, we modified FAST to incorporate a fourth dimension in its hidden Markov random field model, to directly represent time. Like SIENAX, the output provides individual cortical, GM, WM, and lateral ventricle volume but with significantly reduced classification errors between time

points. The SDs of longitudinal percentage-volume changes with our approach (Table 3) are substantially lower than those found in previous studies measuring GM and WM changes with time.^{4,6,12} Therefore the robust findings between patients with SDP and stable patients for 5 years in the present study may be related to the new longitudinal direct way of performing calculations for the evolution of cortical, GM, and WM volume changes.

Albeit not significantly different, of interest were changes in WM volumes between patients with SDP and stable patients during 5 years (Table 3). There was almost a 1% WM volume decrease in the SDP group and a 0.4 increase in the stable group. This finding suggests that development of WM atrophy may also play an important role in disease progression. The proposed direct measurement approach of brain tissue compartments in this study improves on the standard SIENAX technique and may provide more precise data and additional statistical power for studies evaluating cortical, GM, and WM atrophy changes with time.

Placebo-controlled clinical studies have shown that intramuscular interferon β -1a slows disability progression,⁴¹ reduces T2-lesion volume,⁴² and prevents atrophy.^{23-26,43} Despite these known effects of treatment with intramuscular interferon β -1a, both patients with SDP and those with stable MS exhibited loss of brain tissue during the course of this study. The extent of atrophy in untreated patients with MS is likely to be greater than that observed in the treated patients in this study, though it is not known whether the differential pattern of WM and GM atrophy would be as evident.

Our study confirmed previous reports from this cohort that showed that accumulation of T2-lesion volume did not influence disability progression during the long term.^{6,12,44} During the

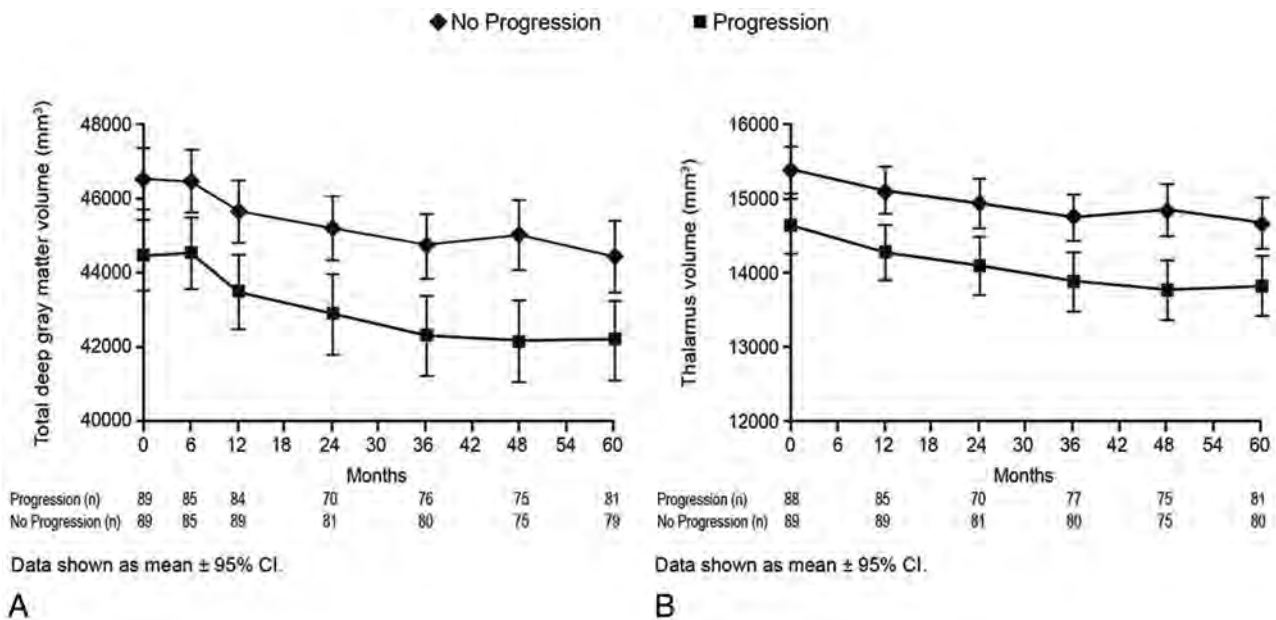


FIG 3. Temporal changes in deep gray matter MR imaging measures by disability-progression status at different time points of the study are shown as mean \pm 95% confidence intervals and median \pm interquartile range, as appropriate. Total deep gray matter volume (A) and thalamus volume (B).

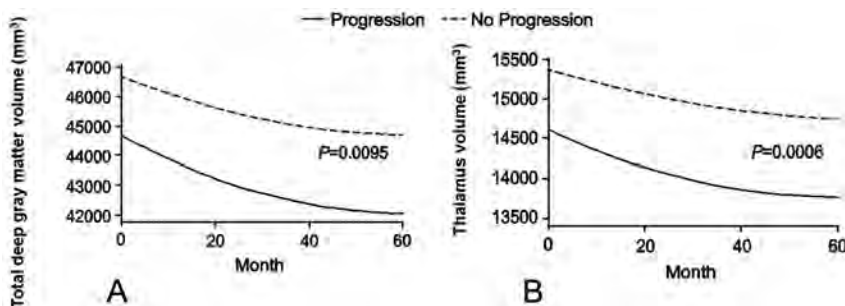


FIG 4. Changes in deep gray matter MR imaging measures (fitted values—intercept model) by disability-progression status with time. Total deep gray matter volume: interaction $P = .0095$ (A); and thalamus volume: $P = .0006$ (B).

course of the study, no significant difference in the evolution of T2-lesion volume was seen in the stable group compared with the SDP group. However, the baseline T2-lesion volume was substantially larger in the SDP group. In the original 2-year ASA study, the percentage of T2-lesion volume change at 2 years was significantly lower for the combination (+14.5%) versus interferon β -1a alone (+30.3%) group.²⁷ However, in a most recent 6-year follow-up evaluation of the ASA study by the original treatment arm,³⁴ it was reported that no significant difference in the absolute T2-lesion volume and its changes during 6 years was seen between the original treatment groups. These additional data suggest that the original percentage changes of T2-lesion volume differences were probably inflated by the lower baseline T2-lesion volume in the interferon β -1a-alone group.

CONCLUSIONS

Our findings suggest that changes in cortical, thalamus, and central atrophy occur early in the MS disease course, particularly in patients who are likely to have more rapid disease progression.

Greater decrease of thalamus and cortical percentage volume change during the first 10 years of the disease influenced disability progression as measured by the EDSS, in addition to being evident already early in the disease process. Although it is currently not possible to accurately identify patients who will have a more aggressive disease course before the manifestation of clinical symptoms, our findings indicate that measurement of thalamus and cortical atrophy, even in early-stage patients, may have future potential in predicting the disease course. Further studies are required to expand on these findings, particularly in those patients who have progressive disability associated with cognition, either with or without ambulatory problems.

ACKNOWLEDGMENTS

The authors thank all patients who participated in this study and Eve Salczynski for technical assistance in the preparation of this manuscript.

Disclosures: Robert Zivadinov—RELATED: Grant: Biogen Idec,* Czech Ministry of Education,* Provision of Writing Assistance, Medicines, Equipment, or Administrative Support: Writing support was provided by Infusion Communications and was funded by Biogen Idec Inc. The authors were not compensated and retained full editorial control. UNRELATED: BMC Neurology, Consultancy: Teva Neuroscience, Biogen Idec, EMD Serono, and Questcor Pharmaceuticals, Grants/Grants Pending: Biogen Idec,* Teva Neuroscience,* Genzyme,* Bracco,* Questcor Pharmaceuticals,* EMD Serono,* Payment for Lectures (including service on Speakers Bureaus): Teva Neuroscience, Biogen Idec, EMD Serono, and Questcor Pharmaceuticals. Niels Bergsland—RELATED: Grant: Czech Ministry of Education,* Biogen Idec,* Comments: This study was supported by the Czech Ministry of Education, Research Program MSM0021620849, PRV0UK-P26/LF1/4, RVO-VFN64165/2012, and Biogen Idec Inc. Provision of Writing Assistance, Medicines, Equipment, or Administrative Support: Writing support was provided by Infusion Communications and was funded by Bio-

gen Idec Inc. The authors were not compensated and retained full editorial control. Ondrej Dolezal—RELATED: Grant: Biogen Idec,* Czech Ministry of Education,* UNRELATED: Consultancy: Sanofi Aventis, Grants/Grants Pending: Biogen Idec, Travel/Accommodations/Meeting Expenses Unrelated to Activities Listed: Biogen Idec. Zdenek Seidl—RELATED: Grant: Czech Ministry of Education (RVO-VFN64165/2012),* Other: Biogen Idec, Comments: financial support for research activities. Michael G. Dwyer—RELATED: Grant: Czech Ministry of Education,* Biogen Idec,* Manuela Vaneckova—RELATED: Grant: Czech Ministry of Education (RVO-VFN64165/2012),* Other: Biogen Idec, Comments: support for research activities. Jan Krasensky—UNRELATED: Support for Travel/Accommodations/Meeting Expenses Unrelated to Activities Listed: Biogen Idec. James A. Potts—UNRELATED: Employment: I am a full-time employee of Biogen Idec. Tomas Kalincik—RELATED: Grant: Czech Ministry of Education (MSM0021620849),* Fees for Participation in Review Activities such as Data Monitoring Boards, Statistical Analysis, Endpoint Committees, and the Like: Biogen Idec, Provision of Writing Assistance, Medicines, Equipment, or Administrative Support: Biogen Idec,* UNRELATED: Employment: Multiple Sclerosis Research Australia, MSBase Foundation, Comments: postdoctoral fellowship, Grants/Grants Pending: Czech Ministry of Health,* Travel/Accommodations/Meeting Expenses Unrelated to Activities Listed: Novartis, Biogen Idec, Sanofi Aventis, Teva, Merck Serono. Eva Havrdová—RELATED: Grant: Czech Ministry of Education,* Biogen Idec,* Comments: Projects of Czech Ministry of Education: MSM0021620849, PRVOUK-P26/LFI/4, RVO-VFN64165/2012; MRI acquisition: Biogen Idec, UNRELATED: Consultancy: Biogen Idec, Merck Serono, Novartis, Genzyme, Teva, Grants/Grants Pending: Biogen Idec,* Merck Serono,* Payment for Lectures (including service on Speakers Bureaus): Biogen Idec, Merck Serono, Novartis, Genzyme, Teva. Dana Horáková—RELATED: Grant: Czech Ministry of Education,* Comments: Research Program MSM0021620849, PRVOUK-P26/LFI/4, RVO-VFN64165/2012, Consulting Fee or Honorarium: Biogen Idec, Other: Biogen Idec, Comments: support for research activities, UNRELATED: Consultancy: Biogen Idec, Novartis, Merck Serono, Bayer Shering. *Money paid to the institution.

REFERENCES

- Geurts JJ, Stys PK, Minagar A, et al. **Gray matter pathology in (chronic) MS: modern views on an early observation.** *J Neurol Sci* 2009;282:12–20
- Zivadinov R, Pirko I. **Advances in understanding gray matter pathology in multiple sclerosis: are we ready to redefine disease pathogenesis?** *BMC Neurol* 2012;12:9
- Pirko I, Lucchinetti CF, Sriram S, et al. **Gray matter involvement in multiple sclerosis.** *Neurology* 2007;68:634–42
- Fisher E, Lee JC, Nakamura K, et al. **Gray matter atrophy in multiple sclerosis: a longitudinal study.** *Ann Neurol* 2008;64:255–65
- Fisniku LK, Chard DT, Jackson JS, et al. **Gray matter atrophy is related to long-term disability in multiple sclerosis.** *Ann Neurol* 2008;64:247–54
- Horáková D, Cox JL, Havrdova E, et al. **Evolution of different MRI measures in patients with active relapsing-remitting multiple sclerosis over 2 and 5 years: a case-control study.** *J Neurol Neurosurg Psychiatry* 2008;79:407–14
- Hulst HE, Geurts JJ. **Gray matter imaging in multiple sclerosis: what have we learned?** *BMC Neurol* 2011;11:153
- Popescu BF, Lucchinetti CF. **Meningeal and cortical grey matter pathology in multiple sclerosis.** *BMC Neurol* 2012;12:11
- Bozzali M, Cercignani M, Sormani MP, et al. **Quantification of brain gray matter damage in different MS phenotypes by use of diffusion tensor MR imaging.** *AJNR Am J Neuroradiol* 2002;23:985–88
- Audoain B, Ranjeva JP, Duong MV, et al. **Voxel-based analysis of MTR images: a method to locate gray matter abnormalities in patients at the earliest stage of multiple sclerosis.** *J Magn Reson Imaging* 2004;20:765–71
- Bö L, Geurts JJ, Mork SJ, et al. **Grey matter pathology in multiple sclerosis.** *Acta Neurol Scand Suppl* 2006;183:48–50
- Horáková D, Dwyer MG, Havrdova E, et al. **Gray matter atrophy and disability progression in patients with early relapsing-remitting multiple sclerosis: a 5-year longitudinal study.** *J Neurol Sci* 2009;282:112–19
- Tedeschi G, Dinacci D, Comerci M, et al. **Brain atrophy evolution and lesion load accrual in multiple sclerosis: a 2-year follow-up study.** *Mult Scler* 2009;15:204–11
- Calabrese M, Agosta F, Rinaldi F, et al. **Cortical lesions and atrophy associated with cognitive impairment in relapsing-remitting multiple sclerosis.** *Arch Neurol* 2009;66:1144–50
- Jure L, Zaaraoui W, Rousseau C, et al. **Individual voxel-based analysis of brain magnetization transfer maps shows great variability of gray matter injury in the first stage of multiple sclerosis.** *J Magn Reson Imaging* 2010;32:424–28
- Calabrese M, Atzori M, Bernardi V, et al. **Cortical atrophy is relevant in multiple sclerosis at clinical onset.** *J Neurol* 2007;254:1212–20
- Henry RG, Shieh M, Okuda DT, et al. **Regional grey matter atrophy in clinically isolated syndromes at presentation.** *J Neurol Neurosurg Psychiatry* 2008;79:1236–44
- Roosendaal SD, Bendfeldt K, Vrenken H, et al. **Grey matter volume in a large cohort of MS patients: relation to MRI parameters and disability.** *Mult Scler* 2011;17:1098–106
- Calabrese M, Rinaldi F, Mattisi I, et al. **The predictive value of gray matter atrophy in clinically isolated syndromes.** *Neurology* 2011;77:257–63
- Bergsland N, Horáková D, Dwyer MG, et al. **Subcortical and cortical gray matter atrophy in a large sample of patients with clinically isolated syndrome and early relapsing-remitting multiple sclerosis.** *AJNR Am J Neuroradiol* 2012;33:1573–78
- Benedict RH, Ramasamy D, Munschauer F, et al. **Memory impairment in multiple sclerosis: correlation with deep grey matter and mesial temporal atrophy.** *J Neurol Neurosurg Psychiatry* 2009;80:201–06
- Benedict R, Bruce J, Dwyer M, et al. **Neocortical atrophy, third ventricular width, and cognitive dysfunction in multiple sclerosis.** *Arch Neurol* 2006;63:1301–06
- Rudick RA, Fisher E, Lee JC, et al. **Use of the brain parenchymal fraction to measure whole brain atrophy in relapsing-remitting MS: Multiple Sclerosis Collaborative Research Group.** *Neurology* 1999;53:1698–704
- Hardmeier M, Wagenpfeil S, Freitag P, et al. **Rate of brain atrophy in relapsing MS decreases during treatment with IFN-beta-1a.** *Neurology* 2005;64:236–40
- Zivadinov R, Locatelli L, Cookfair D, et al. **Interferon beta-1a slows progression of brain atrophy in relapsing-remitting multiple sclerosis predominantly by reducing gray matter atrophy.** *Mult Scler* 2007;13:490–501
- Nakamura K, Rudick RA, Lee JC, et al. **Effect of intramuscular interferon beta-1a on gray matter atrophy in relapsing-remitting multiple sclerosis.** *Neurology* 2010;74:A407 (abstract)
- Havrdova E, Zivadinov R, Krasensky J, et al. **Randomized study of interferon beta-1a, low-dose azathioprine, and low-dose corticosteroids in multiple sclerosis.** *Mult Scler* 2009;15:965–76
- Zivadinov R, Rudick RA, De Masi R, et al. **Effects of IV methylprednisolone on brain atrophy in relapsing-remitting MS.** *Neurology* 2001;57:1239–47
- Jenkinson M, Bannister P, Brady M, et al. **Improved optimization for the robust and accurate linear registration and motion correction of brain images.** *Neuroimage* 2002;17:825–41
- Zivadinov R, Heininen-Brown M, Schirda CV, et al. **Abnormal subcortical deep-gray matter susceptibility-weighted imaging filtered phase measurements in patients with multiple sclerosis: a case-control study.** *Neuroimage* 2012;59:331–39
- Smith SM, Zhang Y, Jenkinson M, et al. **Accurate, robust, and automated longitudinal and cross-sectional brain change analysis.** *Neuroimage* 2002;17:479–89
- Zhang Y, Brady M, Smith S. **Segmentation of brain MR images through a hidden Markov random field model and the expectation-maximization algorithm.** *IEEE Trans Med Imaging* 2001;20:45–57
- Patenaude B, Smith SM, Kennedy DN, et al. **A Bayesian model of shape and appearance for subcortical brain segmentation.** *Neuroimage* 2011;56:907–22
- Kalincik T, Horáková D, Dolezal O, et al. **Interferon, azathioprine and corticosteroids in multiple sclerosis: 6-year follow-up of the ASA cohort.** *Clin Neurol Neurosurg* 2012;114:940–46

35. Fitzmaurice GM, Laird N, Ware JH. *Applied Longitudinal Analysis*. Hoboken, New Jersey: John Wiley and Sons; 2004
36. Zivadinov R, Reeder A, Filippi M, et al. **Mechanisms of action of disease-modifying agents and brain volume changes in multiple sclerosis.** *Neurology* 2008;71:136–44
37. Turner B, Lin X, Calmon G, et al. **Cerebral atrophy and disability in relapsing-remitting and secondary progressive multiple sclerosis over four years.** *Mult Scler* 2003;9:21–27
38. Martola J, Bergstrom J, Fredrikson S, et al. **A longitudinal observational study of brain atrophy rate reflecting four decades of multiple sclerosis: a comparison of serial 1D, 2D, and volumetric measurements from MRI images.** *Neuroradiology* 2010;52:109–17
39. Cherubini A, Peran P, Caltagirone C, et al. **Aging of subcortical nuclei: microstructural, mineralization and atrophy modifications measured in vivo using MRI.** *Neuroimage* 2009;48:29–36
40. Minagar A, Barnett M, Benedict R, et al. **The thalamus and multiple sclerosis: modern views on pathologic, imaging and clinical aspects.** *Neurology* 2013;80:210–19
41. Jacobs LD, Cookfair DL, Rudick RA, et al. **Intramuscular interferon beta-1a for disease progression in relapsing multiple sclerosis: the Multiple Sclerosis Collaborative Research Group (MSCRG).** *Ann Neurol* 1996;39:285–94
42. Simon JH, Jacobs LD, Campion M, et al. **Magnetic resonance studies of intramuscular interferon beta-1a for relapsing multiple sclerosis: the Multiple Sclerosis Collaborative Research Group.** *Ann Neurol* 1998;43:79–87
43. Rudick RA, Fisher E, Lee JC, et al. **Brain atrophy in relapsing multiple sclerosis: relationship to relapses, EDSS, and treatment with interferon beta-1a.** *Mult Scler* 2000;6:365–72
44. Horáková D, Kalincik T, Dolezal O, et al. **Early predictors of non-response to interferon in multiple sclerosis.** *Acta Neurol Scand* 2012; 126:390–97

Parenchymal Hypointense Foci Associated with Developmental Venous Anomalies: Evaluation by Phase-Sensitive MR Imaging at 3T

M. Takasugi, S. Fujii, Y. Shinohara, T. Kaminou, T. Watanabe, and T. Ogawa



ABSTRACT

BACKGROUND AND PURPOSE: The risk of hemorrhage in the context of developmental venous anomaly is considered to be very low, but it has never been evaluated by susceptibility-weighted MR imaging at 3T. The goal of the present study was to evaluate the prevalence of hypointense foci (ie, microhemorrhage or cavernous malformation) associated with DVA on phase-sensitive MR imaging, on the basis of principles similar to those of susceptibility-weighted MR imaging, and to evaluate the relationship between the hypointense foci and several factors, such as white matter hyperintense lesions adjacent to DVA on T2-weighted imaging, DVA morphology, and clinical symptoms.

MATERIALS AND METHODS: This study retrospectively evaluated 61 lesions in 59 consecutive patients with DVA who underwent MR imaging including phase-sensitive MR imaging. Two neuroradiologists independently assessed for the presence of hypointense foci and other factors such as DVA location, depth, size, direction of draining vein on phase-sensitive MR imaging, and white matter hyperintense lesion on T2-weighted imaging. Clinical symptoms were also assessed.

RESULTS: Hypointense foci were observed in 62.3% (38/61) of lesions. White matter hyperintense lesion was more frequently observed in patients with hypointense foci (26/38) than in patients without hypointense foci (7/23) ($P < .01$). There was no significant association between hypointense foci and other factors.

CONCLUSIONS: Our results support the hypothesis that microhemorrhage or cavernous malformation can be related to venous congestion caused by abnormal venous drainage. We conclude that phase-sensitive MR imaging is useful for the detection of microhemorrhage or cavernous malformation in patients with DVA, especially when associated with white matter hyperintense lesion.

ABBREVIATIONS: CM = cavernous malformation; DVA = developmental venous anomaly; ICH = intracranial hemorrhage; PSI = phase-sensitive MR imaging; WMH = white matter hyperintense lesion

Developmental venous anomaly, also called venous angioma, is the most common type of vascular malformation. The embryogenesis of DVAs is not well understood, but it is hypothesized that they result from a focal arrest of venous development and retention of primitive medullary veins.¹ Mullan et al^{2,3} suggested that early occlusion of normal developing veins may lead to absence of normal cortical venous vasculature and compensatory formation of collateral dilated veins. Okudera et al⁴ concluded that DVAs arose from aplasia, hypoplasia, or occlusion of the various segments of the su-

perficial or deep drainage medullary veins or distal pial vein immediately before opening into the dural sinus from the evaluation of microangiograms of postmortem-injected brain specimens.

Before the advent of MR imaging, DVAs were thought to be rare lesions that were associated with intracranial hemorrhage. However, the increasing use of MR imaging revealed that DVAs were relatively prevalent and were associated with a low risk of hemorrhage (reported prevalence of hematoma, 2.4–3.0%; ICH annual risk, 0.15–0.68%).^{5–8} MR imaging sometimes reveals hypointense foci that can be regarded as microhemorrhage or CM in the territory of the DVA. Several studies have characterized the prevalence of hemorrhage or CM associated with DVA.^{5–10} However, this phenomenon has not yet been assessed by susceptibility-weighted MR imaging at 3T. Thus, the first goal of this study was to assess the prevalence of hypointense foci by using phase-sensitive MR imaging on the basis of principles similar to those of susceptibility-weighted MR imaging at 3T.

Several types of brain parenchymal abnormalities within the

Received September 3, 2012; accepted after revision November 1.

From the Division of Radiology (M.T., S.F., Y.S., T.K., T.O.), Department of Pathophysiological and Therapeutic Science, and Division of Neurosurgery (T.W.), Department of Brain and Neurosciences, Faculty of Medicine, Tottori University, Yonago, Tottori, Japan.

Please address correspondence to Dr Marie Takasugi, Division of Radiology, Department of Pathophysiological and Therapeutic Science, Faculty of Medicine, Tottori University, 36-1, Nishi-cho, Yonago, Tottori 683-8504, Japan; e-mail: mtakasugi@med.tottori-u.ac.jp

<http://dx.doi.org/10.3174/ajnr.A3495>

drainage territory of DVA have been identified; these include WMH on T2-weighted imaging and FLAIR imaging, atrophy, and dystrophic calcification.^{7,11,12} WMHs sometimes coexist with hypointense foci. Although the pathologic correlation and etiology of WMH in the drainage territory of DVA remains unknown, it has been speculated that WMH reflects leukoaraiosis, which histopathologically includes edema, demyelination, and gliosis resulting from chronic venous hypertension caused by anomalous venous drainage.^{7,11} Meanwhile, the relationship between WMH and hypointense foci has not yet been studied. Therefore, the secondary goal of this study was to evaluate the relationship between hypointense foci and other factors, such as WMH.

MATERIALS AND METHODS

Patient Population

We searched a computer data base of all radiologic results that were obtained at our hospital from January 2006 to December 2011 for MR imaging reports containing the terms “developmental venous anomaly” “venous angioma,” or “medullary venous malformation.” From these search results, patients who underwent MR imaging including PSI were selected. The criteria used to establish the diagnosis of DVA are based on MR imaging findings, especially on PSI. DVAs are characterized by a cluster of venous radicles that converge into a collecting vein, resulting in the typical caput medusae appearance. If the characteristic morphology is seen on MR imaging, DVA is strongly suspected. One patient was excluded because of susceptibility artifacts caused by postoperative changes around the DVA, and another 5 patients were excluded because the DVA region was not sufficiently included on PSI. One patient had 3 DVAs. Thus, 61 lesions in 59 consecutive patients (age range, 2–83 years; mean age, 54 years) were included in the final analysis.

This study was approved by the ethics committee of our university, and the requirement for written informed consent was waived because of the retrospective nature of this study.

MR Technique

All brain MR imaging was obtained with a 3T MR system (Signa Excite HD; GE Healthcare, Milwaukee, Wisconsin) by means of an 8-channel phased array coil.

Axial T2-weighted fast spin-echo images was obtained with the following imaging parameters: TR/TE, 4000/95 msec; 512 × 320 matrix, 21-cm field of view, and section thickness/intersection gap, 5/1.5 mm. For susceptibility-weighted MR imaging, PSI was performed with a 3D spoiled gradient-recalled acquisition in steady state sequence with flow compensation, by use of the following imaging parameters: TR/TE, 45/30 msec; flip angle, 20°; FOV, 21 cm; matrix, 512 × 192; section thickness, 1.5 mm; acquisition time, 7 minutes, 50 seconds. Phase-sensitive MR images were postprocessed by the use of a high-pass filter, and the images were converted into negative phase masks that were multiplied 4 times into the corresponding magnitude images by use of research software (PSIRecon: GE Yokogawa Medical Systems, Tokyo, Japan). A minimum intensity projection was used to display the processed data as PSI by use of contiguous 10.5-mm-thick sections with 7-mm overlap in the transverse plane (Advantage Workstation Version 4.1; GE HealthCare).

Image Reading

Two neuroradiologists (M.T., S.F.) who were blinded to the patient clinical information independently reviewed images on PSI and T2-weighted imaging. Assessments included the presence of hypointense foci around DVA on PSI and the presence of WMH in the drainage territory of the DVA on T2-weighted images. The drainage territory was defined as the brain parenchyma directly adjacent to the visualized radicles of the DVA. We also assessed the location of hypointense foci on PSI according to a previous study. Location of CM was classified into “central” or “peripheral,” according to whether the main location was a portion of the DVA where abnormal small tributaries of medullary veins gathered.¹³ Additionally, we evaluated DVA location, depth, and the size and direction of draining vein. The DVAs were classified by depth as juxtacortical, subcortical, and periventricular, according to previous studies.^{11,14} “Juxtacortical” (or superficial) was defined as within the gray matter or at the gray-white junction. “Subcortical” was defined as below the juxtacortical region but not adjacent to the ventricular wall. “Periventricular” (or deep) was defined as adjacent to the lateral, third, or fourth ventricle or within the center of the structure, such as the pons. The terminal or draining vein to which the caput medusae join was classified as either a deep (toward the ventricle) or superficial (toward the brain surface) draining vein. Concerning the distance of draining vein, the draining vein is “long” if the depth is juxtacortical and the direction is deep or if the depth is periventricular and the direction is superficial. The draining vein is “short” if the depth is juxtacortical and the direction is superficial or if the depth is periventricular and the direction is deep. All others are categorized as “median” draining vein.

Discordance between the 2 radiologists was resolved by consensus. To minimize bias, T2-weighted imaging assessments were performed 3 months after PSI assessments.

Furthermore, one neuroradiologist (M.T.) also assessed the presence of calcifications in patients with hypointense foci on CT images, which were performed within 1 year of MR imaging. Among 38 patients with hypointense foci, 14 patients underwent CT within 1 year from MR imaging.

Clinical and Imaging Finding Correlation

We retrospectively reviewed their clinical records, clinical indications for the examinations, and symptoms. Clinical indications and symptoms were tabulated for each case and assessed for correlation with the presence of hypointense foci.

Statistical Analysis

The relationship between hypointense foci and WMH, DVA location, depth, size and direction of draining vein, and the presence of symptoms was assessed by χ^2 testing. A difference with a value of $P < .05$ was considered statistically significant.

RESULTS

A total of 61 lesions in 59 patients with DVA were evaluated. Hypointense foci were observed on PSI in 62.3% (38/61 sides); WMH was observed on T2-weighted imaging in 54.1% (33/61 sides).

Table 1 shows the location of hypointense foci. The main location of hypointense foci was the peripheral portion of medullary veins.

Table 2 outlines the presence or absence of WMH, DVA location, depth, and the size and direction of draining vein on the basis of

Table 1: Location of cavernous malformation

	<i>n</i>
Peripheral	18
Central	11
Both	6

Note:—Total *n* = 35. Three patients were excluded because the hypointense foci were too large to assess.

Table 2: Associations between hypointense foci and other factors

		Hypointense Foci (+) (<i>n</i> = 38)		Hypointense Foci (-) (<i>n</i> = 23)	
		<i>n</i>	%	<i>n</i>	%
WMH	Yes	26	68.4	7	30.4
	No	12	31.6	16	69.6
Location	Basal ganglia/ thalamus	6	15.8	0	0
	Lobe	19	50.0	15	65.2
	Cerebellum	10	26.3	5	21.7
	Pons	3	7.9	3	13.0
Depth	Periventricular	16	42.1	13	56.5
	Juxtacortical	8	21.1	5	21.7
	Subcortical	14	36.8	5	21.7
Draining vein	Long	15	39.5	16	69.6
	Medium	14	36.8	5	21.7
	Short	9	23.7	2	8.7
Direction	Deep	11	28.9	4	17.4
	Superficial	27	71.1	19	82.6

Note:—Total *n* = 61.

hypointense foci. WMH was more frequently observed in DVAs with hypointense foci (68.4%) than in those without hypointense foci (30.4%) ($P < .01$) (Figs 1–3). There was no significant association between hypointense foci and other factors.

Table 3 outlines clinical indications and symptoms on the basis of hypointense foci. We evaluated the association between the presence of symptoms and hypointense foci. Although patients with hypointensities had higher rates of being symptomatic (71%) than those without (52%), no significant association was identified.

Among 38 patients with hypointense foci, 14 patients underwent CT within 1 year from MR imaging. Apparent calcification within the drainage territory of DVA was observed in 1 patient on CT images, but hypointense foci were also observed in other regions distant to the calcification.

DISCUSSION

Our results demonstrated that the prevalence of hypointense foci, indicating microhemorrhage or CM, was higher (62.3%) than previously reported. According to previous studies, CM occurs in up to 18% of patients with DVA,^{7,9} whereas DVA is present in 8–33% of patients with CM.^{5,8–10} The discrepancy in the prevalence of hemorrhage and CM between this study and previous studies may be related to several factors. First, susceptibility-weighted MR imaging was used in the present study but not in prior studies. Susceptibility-weighted MR imaging is a high-resolution 3D gradient-echo MR imaging technique with phase post-processing that accentuates the paramagnetic properties of blood products, such as deoxyhemoglobin, intracellular methemoglobin, and hemosiderin. As a result, it is quite sensitive to the presence of even small amounts of hemorrhage. Previous studies have reported susceptibility-weighted MR imaging is more sensitive in

detecting CM than T2*, which in turn is much better than T1 or T2.^{15,16} Susceptibility-weighted MR imaging has also been specifically recommended when imaging DVAs because of their association with CM.¹⁷ Second, 3T MR was used in the present study but not in prior studies, and the susceptibility effect in higher field strength increases the conspicuity of paramagnetic substances. Additionally, we could detect hypointense foci more frequently in the peripheral regions of medullary veins in comparison to a previous study that used T2-weighted imaging and T1-weighted spoiled gradient-recalled acquisition in steady state imaging with gadobutrol enhancement at 3T.¹³ This may result from the increased detectability of minute hemorrhage and CM in the peripheral region of medullary veins in response to the increased conspicuity of paramagnetic substances with PSI at 3T.

The incidence of WMH in the drainage territory of DVA in this study was >50%, whereas reported WMH rates on MR imaging were 12.5% and 28.3%.^{7,11} Although we have no good explanation for this discrepancy, variations in the imaging parameters and the scanners themselves could produce different results. For example, we used a 3T MR system, whereas both previous studies were mainly investigated by 1.5T MR systems. Moreover, the discrepancy may be due to the differences in the populations and readers among these reports.

This study also demonstrated a significant relationship between hypointense foci and WMH, which may reflect leukoariosis that histopathologically includes edema, demyelination, and gliosis resulting from chronic venous hypertension caused by anomalous venous drainage. That supposition is based on several reports of stenosis of the draining vein, which leads to chronic venous congestion,^{7,18,19} and on a report of reduced cerebral blood flow in the drainage territory of the DVA, which suggests the presence of altered hemodynamics.^{20–22} Alternatively, some case reports have described de novo formation of CM in the drainage territory of DVA.^{23–25} Although the exact events leading to de novo formation of CM in patients with DVA is unclear, some investigators have speculated that development of venous hypertension and resultant microhemorrhages from the fragile vessel wall of the DVA may induce reactive angiogenesis.^{26,27} Relative ischemia can result in production of angiogenic factors and stimulation of growth of new vessels.²⁸ However, the neovasculature lacks vasoregulatory capacity, and its fragility makes it susceptible to bleeding. This leads to repeated hemorrhage and formation of abnormal vessels, which eventually results in CM formation.^{13,29} Hong et al¹³ reported that the angio-architectural factors of DVA cause disturbances in blood flow and may lead to CM within the territory of DVA by increasing venous pressure. Taken together, these data suggest that venous congestion caused by angioarchitectural or other factors leads to WMH and subsequent CM formation. Hence, these 2 phenomena are likely to occur simultaneously.

In the present study, there was no significant association between the presence of hypointense foci and the presence of clinical symptoms. However, CM is generally considered to be an active lesion characterized by dynamic behaviors, including enlargement, regression, and de novo formation. Furthermore, several studies have reported that clinical presentation of patients with both DVA and CM is nearly always related to CM, reflecting its potential for epileptogenesis and symptomatic hemorrhage.^{5,9,29,30} Although no associ-

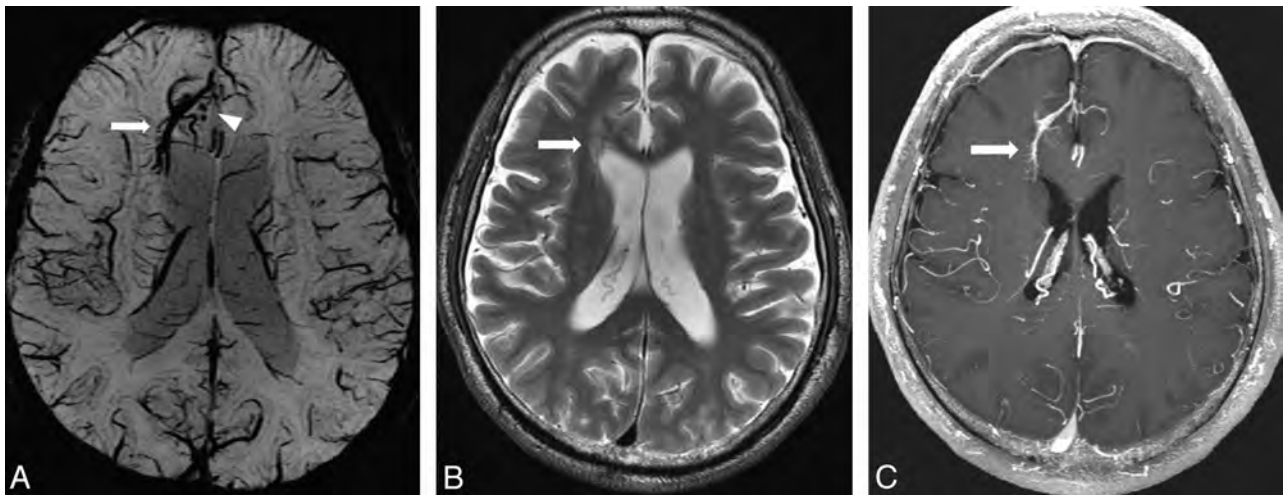


FIG 1. A 64-year-old man with DVA in the right frontal lobe. A, PSI shows DVA in the right frontal lobe (arrow) and hypointense foci around the DVA (arrowhead). B, T2-weighted image shows WMH around the DVA (arrow). C, DVA is enhanced by contrast agent administration, whereas hypointense foci are not enhanced on T1-weighted image.

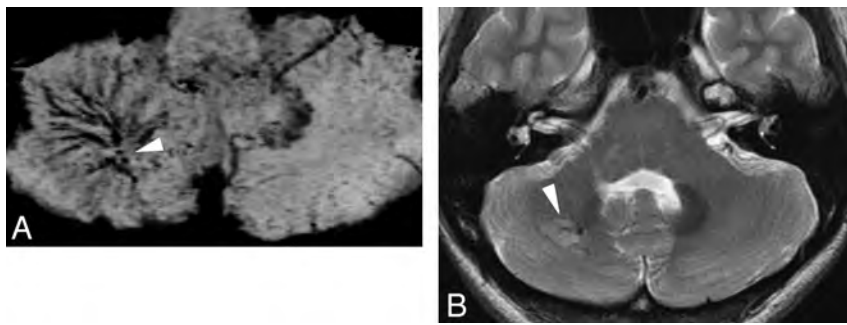


FIG 2. A 25-year-old woman with DVA in the right cerebellum. A, PSI shows DVA in the right cerebellum and hypointense foci around the medullary veins (arrowhead). B, T2-weighted image shows WMH around the DVA (arrowhead).

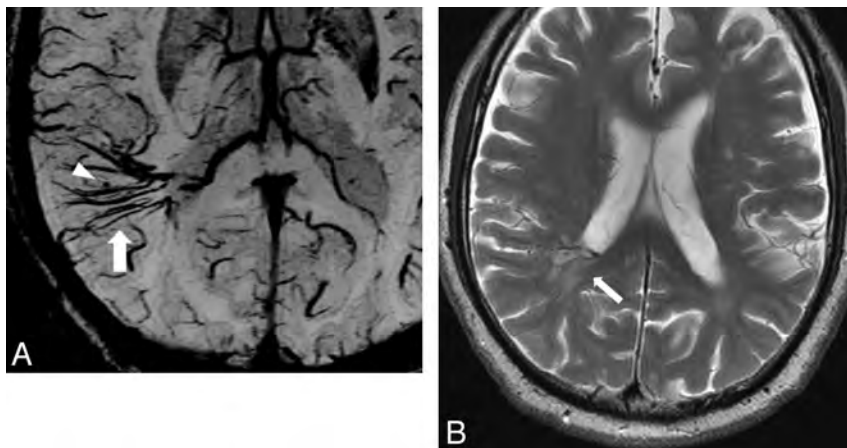


FIG 3. A 75-year-old man with DVA in the right parieto-temporal lobe. A, PSI shows DVA in the right parieto-temporal lobe (arrow) and minute hypointense foci around the DVA (arrowhead). B, T2-weighted image shows WMH around the DVA (arrow).

ation was found between hypointensities and presence of clinical symptoms or indications, patients with hypointensities had higher rates of being symptomatic than those without (71% versus 52%) in the present study. This result shows a tendency that supports previous assumptions of CM being a dynamic lesion with the potential to

cause bleeding and other symptoms. If analyzed with a larger population, there may be a significant association. Therefore, careful follow-up examination with the use of susceptibility-weighted MR imaging should be performed to assess whether there is a change in size of the hypointense foci, and further follow-up survey is needed to predict symptomatic ICH.

This study has several limitations. First, the study population was relatively small, and further studies in a large population are required to validate the present results. Second, hypointense foci may have represented dystrophic calcification or thrombosis rather than microhemorrhage and CM. However, only 1 among 14 patients with hypointense foci on PSI showed calcification on CT. Therefore, it is unlikely that calcification around the DVA plays a major role in the hypointensity on PSI, though minute calcification can coexist with hemorrhage.

CONCLUSIONS

The prevalence of hypointense foci, indicating microhemorrhage or CM, is higher than previously reported in patients with DVA. These hypointense foci may be related to WMH. PSI is useful for the detection of these hypointense foci in patients with DVA, especially when associated with WMH.

ACKNOWLEDGMENTS

We thank Eijirou Yamashita, PhD; Takuro Tanaka, BS; Nobuo Hashimoto, BS; and Shota Sakimoto, BS, for technical support in obtaining the high-quality MR images used in this study.

Table 3: Patient symptoms and indications for examinations in the 2 groups based on hypointense foci

		Hypointense Foci (+) (n = 38)		Hypointense Foci (-) (n = 21)		n
		n	%	n	%	
Symptoms or clinical indications for examinations	No/follow-up of primary disease	11	52.4	10	47.6	21
	Seizures	5	83.3	1	16.7	6
	Transient ischemic attack/stroke	5	83.3	1	16.7	6
	Dizziness, vertigo	1	25	3	75	4
	Headache	4	100	0	0	4
	Sensory disturbance	2	66.7	1	33.3	3
	Double vision	2	100	0	0	2
	Dysarthria	2	100	0	0	2
	Nerve palsy	1	50	1	50	2
	SDH	1	50	1	50	2
	Consciousness disturbance	1	100	0	0	1
	ICH	1	100	0	0	1
	Visual field disturbance	1	100	0	0	1
	SAH	0	0	1	100	1
	Syncope	0	0	1	100	1
	Trauma	0	0	1	100	1
	Unknown	1		0		1

Note:—SDH indicates subdural hematoma.

REFERENCES

- Saito Y, Kobayashi N. Cerebral venous angiomas: clinical evaluation and possible etiology. *Radiology* 1981;139:87–94
- Mullan S, Mojtahedi S, Johnson DL, et al. Cerebral venous malformation-arteriovenous malformation transition forms. *J Neurosurg* 1996;85:9–13
- Mullan S, Mojtahedi S, Johnson DL, et al. Embryological basis of some aspects of cerebral vascular fistulas and malformations. *J Neurosurg* 1996;85:1–84
- Okudera T, Huang YP, Fukusumi A, et al. Micro-angiographical studies of the medullary venous system of the cerebral hemisphere. *Neuropathology* 1999;19:93–111
- McLaughlin MR, Kondziolka D, Flickinger JC, et al. The prospective natural history of cerebral venous malformations. *Neurosurgery* 1998;43:195–200
- Naff NJ, Wemmer J, Hoenig-Rigamonti K, et al. A longitudinal study of patients with venous malformations: documentation of a negligible hemorrhage risk and benign natural history. *Neurology* 1998;50:1709–14
- San Millán Ruíz D, Delavelle J, Yilmaz H, et al. Parenchymal abnormalities associated with developmental venous anomalies. *Neuroradiology* 2007;49:987–95
- Buhl R, Hempelmann RG, Stark AM, et al. Therapeutical considerations in patients with intracranial venous angiomas. *Eur J Neurol* 2002;9:165–69
- Töpper R, Jürgens E, Ruel J, et al. Clinical significance of intracranial developmental venous anomalies. *J Neurol Neurosurg Psychiatry* 1999;67:234–38
- Rabinov JD. Diagnostic imaging of angiographically occult vascular malformations. *Neurosurg Clin North Am* 1999;10:419–32
- Santucci GM, Leach JL, Ying J, et al. Brain parenchymal signal abnormalities associated with developmental venous anomalies: detailed MR imaging assessment. *AJNR Am J Neuroradiol* 2008;29:1317–23
- Augustyn GT, Scott JA, Olson E, et al. Cerebral venous angiomas: MR imaging. *Radiology* 1985;156:391–95
- Hong YJ, Chung TS, Suh SH, et al. The angioarchitectural factors of the cerebral developmental venous anomaly: can they be the causes of concurrent sporadic cavernous malformation? *Neuroradiology* 2010;52:883–91
- Lee C, Pennington MA, Kenney CM III. MR evaluation of DVAs: medullary venous anatomy of venous angiomas. *AJNR Am J Neuroradiol* 1996;17:61–70
- De Champfleur NM, Langlois C, Ankenbrandt WJ, et al. Magnetic resonance imaging evaluation of cerebral cavernous malformations with susceptibility-weighted imaging. *Neurosurgery* 2011;68:641–48
- De Souza JM, Dominiques RC, Cruz LC Jr, et al. Susceptibility-weighted imaging for the evaluation of patients with familial cerebral cavernous malformations: a comparison with T2-weighted fast spin-echo and gradient-echo sequences. *AJNR Am J Neuroradiol* 2008;29:154–58
- Ruiz DS, Yilmaz H, Gailloud P. Cerebral developmental venous anomalies: current concepts. *Ann Neurol* 2009;66:271–83
- Truwit CL. Venous angioma of the brain: history, significance, and imaging findings. *AJR Am J Roentgenol* 1992;159:1299–307
- Dillon WP. Cryptic vascular malformations: controversies in terminology, diagnosis, pathophysiology, and treatment. *AJNR Am J Neuroradiol* 1997;18:1839–46
- Uchida K, Tamura K, Takayama H, et al. Xenon-enhanced CT CBF measurements in intracranial vascular malformations. *No Shinkei Geka* 1989;17:239–46
- Matsuda H, Terada T, Katoh M, et al. Brain perfusion SPECT in a patient with a subtle venous angioma. *Clin Nucl Med* 1994;19:785–88
- Tomura N, Inagumi A, Uemura K, et al. Multiple medullary venous malformations decreasing cerebral blood flow: case report. *Surg Neurol* 1991;35:131–35
- Maeder P, Gudinchet F, Meuli R, et al. Development of a cavernous malformation of the brain. *AJNR Am J Neuroradiol* 1998;19:1141–45
- Cakirer S. De novo formation of a cavernous malformation of the brain in the presence of a developmental venous anomaly. *Clin Radiol* 2003;58:251–56
- Campeau N, Lane J. De novo development of a lesion with the appearance of a cavernous malformation adjacent to an existing developmental venous anomaly. *AJNR Am J Neuroradiol* 2005;26:156–59
- Perrini P, Lanzino G. The association of venous developmental anomalies and cavernous malformations: pathophysiological, diagnostic, and surgical considerations. *Neurosurg Focus* 2006;21:e5
- Awad IA, Robinson JR Jr, Mohanty S, et al. Mixed vascular malformations of the brain: clinical and pathogenetic considerations. *Neurosurgery* 1993;33:179–88
- Circillo SF, Dillon WP, Fink ME, et al. Progression of multiple cryptic vascular malformations associated with anomalous venous drainage: case report. *J Neurosurg* 1994;81:477–81
- Ramos SK, Maina R, Lanzino G. Developmental venous anomalies: current concepts and implications for management. *Neurosurgery* 2009;65:20–30
- Rigamonti D, Spetzler RF, Medina M, et al. Cerebral venous malformations. *J Neurosurg* 1990;73:560–64

Widespread White Matter Alterations in Patients with End-Stage Renal Disease: A Voxelwise Diffusion Tensor Imaging Study

M.-C. Chou, T.-J. Hsieh, Y.-L. Lin, Y.-T. Hsieh, W.-Z. Li, J.-M. Chang, C.-H. Ko, E.-F. Kao, T.-S. Jaw, and G.-C. Liu



ABSTRACT

BACKGROUND AND PURPOSE: ESRD results in excessive accumulation of urea and toxic metabolites. Hemodialysis is usually performed to maintain health in patients with ESRD; however, it may cause silent white matter alterations in the earlier stages. Hence, this study aimed to perform voxelwise diffusion tensor analysis for global detection of subtle white matter alterations in patients with ESRD.

MATERIALS AND METHODS: Twenty-eight patients with ESRD and 25 age-matched control subjects were enrolled in this study. Each subject underwent CASI assessment and DTI. After spatial normalization of DTI images, voxelwise statistical analyses were performed to compare DTI parameters between the 2 groups.

RESULTS: In patients with ESRD, AD, RD, and MD values were significantly increased, whereas the FA value was significantly decreased, mostly in the corpus callosum, bilateral sagittal stratum, and pons. Multiple regression analysis further revealed that both RD and MD were positively correlated with the duration of hemodialysis in the pons; however, no significant correlation was observed with FA. Negative correlations of RD and MD and a positive correlation of FA with the CASI score were observed in the corona radiata.

CONCLUSIONS: We concluded that voxelwise DTI analysis is helpful in the detection of white matter alterations caused by hemodialysis.

ABBREVIATIONS: AD = axial diffusivity; CASI = Cognitive Abilities Screening Instrument; ESRD = end-stage renal disease; FA = fractional anisotropy; MD = mean diffusivity; RD = radial diffusivity

ESRD has become an increasing problem, with a growing number of patients undergoing hemodialysis in the United States in recent years.¹ ESRD has been characterized as the failure of renal functions, which permanently decrease to <10% of the normal status, and is accompanied by multiple organ dysfunction.¹ To maintain their health, patients with ESRD usually undergo regular hemodialysis 3 times per week to remove excess urea and other toxic metabolites from the body. However, uremic neurop-

athy has been reported in patients with ESRD undergoing hemodialysis. These neurologic complications may be related to ESRD itself or to dialysis. These neurologic complications include acute reactions such as dialysis disequilibrium syndrome and osmotic myelinolysis and chronic changes such as encephalopathy, dementia, and stroke.^{2,3} These acute complications are presumably related to brain swelling or tissue edema caused by the osmotic gradient between plasma and brain tissue during hemodialysis.^{2,4} Excessive edema may gradually lead to damaged brain tissue.

For direct measurement of water diffusion, in a previous animal MR imaging study, DWI was performed in nephrectomized rats.⁵ The results showed that ADC was significantly increased in the rat brain immediately after hemodialysis. Similar results were also observed in a human brain study in which ADC measurement was performed in multiple regions of the brain of patients with ESRD by using region-of-interest analysis.⁶ That study found that before hemodialysis, ADC values were significantly higher for both the gray and white matter in patients with ESRD than in control subjects. After the initial hemodialysis, ADC values were further increased in the frontal white matter; this change implied that immediate hemodialysis led to increased water diffusion in brain tissue.

Because hemodialysis may cause white matter alterations, another previous study used the DTI technique to investigate

Received October 13, 2012; accepted after revision December 25.

From the Departments of Medical Imaging and Radiological Sciences, College of Health Sciences; (M.-C.C., T.-J.H., Y.-L.L., Y.-T.H., W.Z.L., E.-F.K.), and Departments of Radiology (T.-J.H., T.-S.J., G.-C.L.), Renal Care (J.-M.C.), and Psychiatry (C.-H.K.), College of Medicine, Kaohsiung Medical University, Kaohsiung, Taiwan; Departments of Medical Imaging (T.-J.H., T.-S.J., G.-C.L.), Internal Medicine (J.-M.C.), and Psychiatry (C.-H.K.), Kaohsiung Medical University Hospital, Kaohsiung Medical University, Kaohsiung, Taiwan; Department of Medical Imaging (T.-J.H.), Kaohsiung Municipal Ta-Tong Hospital, Kaohsiung Medical University, Kaohsiung, Taiwan; and Departments of Internal Medicine (J.-M.C.) and Psychiatry (C.-H.K.), Kaohsiung Municipal Hsiao-Kang Hospital, Kaohsiung Medical University, Kaohsiung, Taiwan.

This work was supported in part by grant NSC-99-2314-B-037-070-MY2 from the National Science Council of Taiwan.

Please address correspondence to Tsyh-Jyi Hsieh, MD, Department of Medical Imaging, Kaohsiung Medical University, 100 Shih-Chuan 1st Rd, Kaohsiung 80708, Taiwan; e-mail: tsyhjyi.hsieh@gmail.com

Indicates open access to non-subscribers at www.ajnr.org

<http://dx.doi.org/10.3174/ajnr.A3511>

Table 1: Demographic characteristics of enrolled subjects^a

	Patients with ESRD	Control Subjects
Age (yr)	39 ± 8	39 ± 7
Sex (M/F)	14/14	11/14
Dialysis duration (yr)	7 ± 5	N/A
CASI score	93.5 ± 7.2 ^b	96.8 ± 3.7 ^b

Note:—N/A indicates not applicable.

^aData are means.

^bStatistically significant difference ($P < .05$).

the effects of long-term hemodialysis on white matter integrity by comparing FA values between patients with ESRD and healthy subjects by using manual region-of-interest analysis.⁷ The results showed that FA values were significantly reduced in many white matter regions and that negative correlations were evident between reduction in FA values and the duration of hemodialysis. Recently, a DTI tractography study further showed an association between abnormalities of fiber tracts and cognitive function.⁸

However, manual region-of-interest analysis has been used in the studies in which diffusion measurements of the brain tissue of patients with ESRD were performed. This method is known to be effort-intensive, and the results are dependent on the locus and size of the region of interest drawn by the operators.⁹ In contrast, voxel-based analysis is an automatic method that normalizes whole-brain DTI to a standard coordinate system in which 2 datasets are compared on a voxel-by-voxel basis.¹⁰ This approach has been widely used to detect disease-, drug-, or age-related white matter alterations in the human brain¹¹⁻¹³; however, no study has used this technique in patients with ESRD, to our knowledge. Recently, better registration accuracy was demonstrated with diffeomorphic image registration.^{14,15} Combining voxel-based analysis with diffeomorphic registration may provide more accurate results than conventional methods.¹⁶ Moreover, in DTI, AD and RD represent the diffusivity in directions parallel and perpendicular to fiber orientations, respectively. Both can provide in-depth insight into underlying biophysical changes in the axon and myelin. Thus, white matter alterations may be better characterized in patients with ESRD by using AD, RD, and MD values together with FA values.

This study aimed to perform voxelwise DTI analysis with diffeomorphic registration for accurate characterization of white matter alterations in patients with ESRD. AD, RD, and MD values were combined with FA values in this study, and the relationships of these values with the duration of hemodialysis and cognitive function in subjects with ESRD were explored.

MATERIALS AND METHODS

Subjects

This study was approved by the institutional review board of Hsiao-Kang Municipal Hospital. Twenty-eight patients with ESRD (male/female ratio = 14:14; 39 ± 8 years of age) and 25 age-matched control subjects (male/female ratio = 11:14; 39 ± 7 years of age) were enrolled in this study. Patients who had undergone hemodialysis for >1 year were regarded as long-term dialysis subjects. The mean of their duration of dialysis was 7 ± 5 years, and their last hemodialysis was conducted 2 days before MR imaging. Table 1 shows the demographic characteristics of the en-

rolled subjects. All participants completed an informed consent form. Subjects who had a history of diabetes, alcoholism, drug abuse, psychiatric disorders, and major neurologic disorders or who had claustrophobia were excluded from this study. All participants completed the overall evaluation of cognitive functions in approximately 30 minutes, by using the CASI assessment.¹⁷ The CASI covers a broad range of cognitive domains and is usually used in evaluating cognitive changes clinically.

Data Acquisition

All brain MR imaging data were acquired from a 1.5T MR imaging scanner (Signa Excite; GE Healthcare, Milwaukee, Wisconsin). After triplanar scans and acquisition of calibration data for array spatial sensitivity encoding technique parallel imaging, 20 axial T1WI, T2WI, and T2-FLAIR images were sequentially acquired from each subject. Those anatomic images were used to diagnose pre-existing lesions in patients, and those who had lesions diagnosed were excluded from this study.

DTI acquisitions were performed by using single-shot twice-refocused spin-echo echo-planar diffusion-weighted sequences with an 8-channel phased array neurovascular coil. Thirty axial sections were placed to cover the whole-brain region with orientation parallel to the anterior/posterior commissure line. Other imaging parameters were as follows: TR/TE = 8000/82.8 ms, matrix size = 128 × 128, $b = 1000$ s/mm², number of noncollinear diffusion directions = 33, $B_0 = 1$, FOV = 240 × 240 mm, NEX = 1, array spatial sensitivity encoding technique factor = 2.0, section thickness = 4.4 mm, and no gap between sections. The scanning time for the DTI acquisition was 4 minutes 48 seconds.

DTI Analysis

All data were transferred to a stand-alone workstation and were processed by using the fMRI of the Brain Software Library (<http://www.fmrib.ox.ac.uk/>) to obtain diffusion tensor maps. First, the eddy-current distortions were corrected by using affine registration to minimize the diffusion gradient-induced eddy-current distortions in 33 DWIs with $b = 0$ as the reference image. Subsequently, a diffusion tensor was fitted with least-squares estimation on a voxel-by-voxel basis to obtain 3 eigenvalues, from which AD, RD, MD, and FA values were calculated.

Voxel-Based DTI Analysis

In voxel-based analysis, whole-brain FA maps were spatially normalized to an International Consortium for Brain Mapping FA template¹⁸ by using affine registration to minimize global differences, followed by nonparametric diffeomorphic demon registration¹⁴ to further minimize local differences between individual and template images. The displacement maps generated from the affine and demon registrations were used to spatially normalize the corresponding AD, RD, and MD maps, respectively. Subsequently, the voxel-based analysis was conducted by using SPM5 (Wellcome Department of Imaging Neuroscience, London, UK) on a Matlab platform (MathWorks, Natick, Massachusetts). The statistical comparisons of DTI indices between patients with ESRD and healthy subjects were performed by using a 2-sample t test. In addition, multiple regression analysis was used to reveal the associations of DTI indices with the duration of hemodialysis

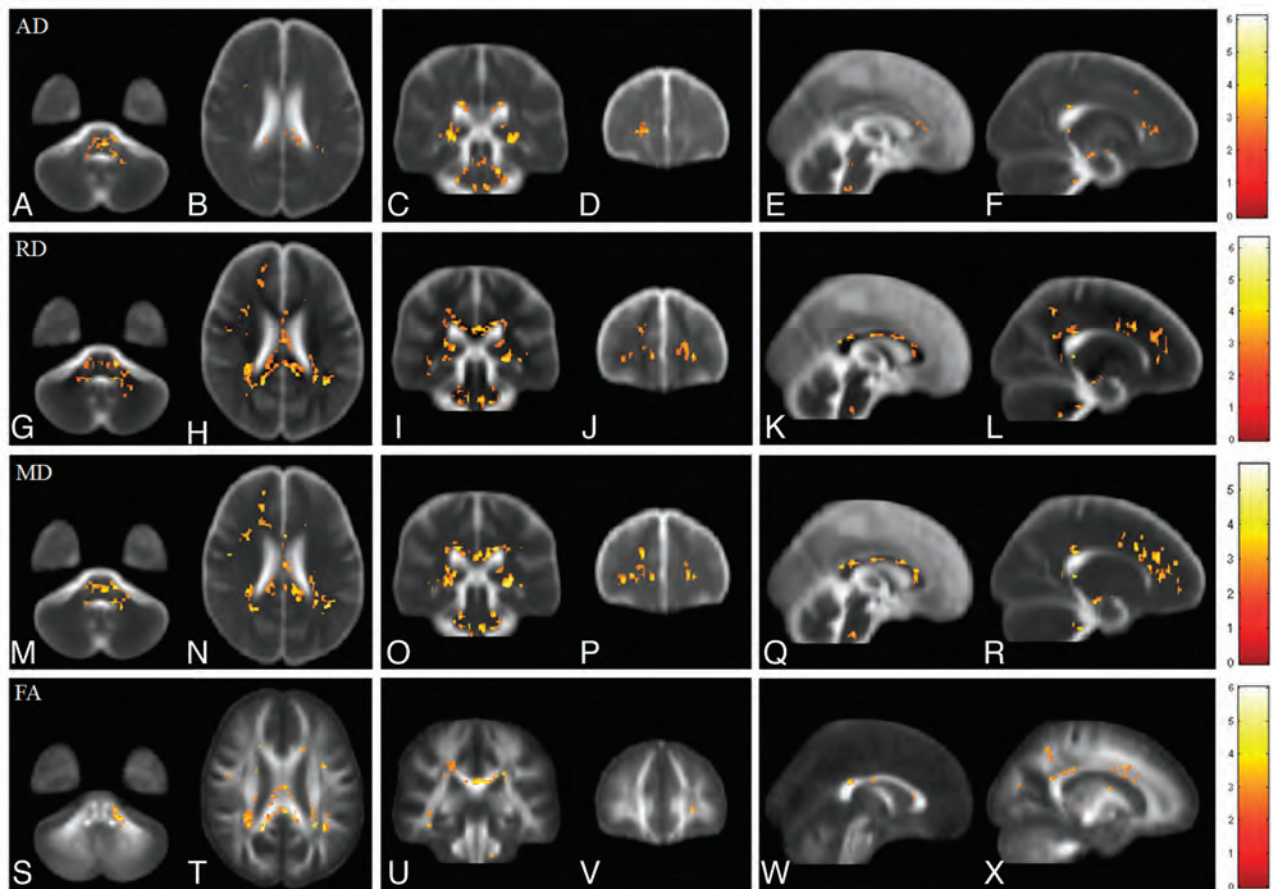


FIG 1. Voxelwise comparisons of AD, RD, MD, and FA between patients with ESRD and healthy subjects. Red-yellow colors indicate significant increases of AD (A–F), RD (G–L), and MD (M–R) and significant decreases of FA (S–X) in patients with ESRD. Color bars show the ranges of *t*-scores.

and the CASI score, respectively, whose net effects were extracted by nulling the age and sex influences. In this study, the areas with statistically significant differences (uncorrected $P < .01$ and cluster of > 50 voxels) were displayed as red-yellow colors superimposed on the averaged AD, RD, MD, and FA maps, respectively.

RESULTS

Age, Sex, CASI Score, and Duration of Hemodialysis

In this study, the sex distributions of patients with ESRD and healthy subjects were not well-matched but did not have a significant difference. The results of 2-sample *t* tests revealed significantly lower CASI scores in patients with ESRD than in healthy subjects ($P < .05$). Correlation testing found no significant correlations between CASI scores and age, sex, or duration of hemodialysis in patients with ESRD or healthy subjects.

Axial Diffusivity

In patients with ESRD, AD values were significantly higher than those in control subjects in the bilateral stria terminalis extending laterally to the retrolenticular part of the internal capsule, left anterior forceps minor, and pons, as shown in Fig 1A–F. Montreal Neurological Institute coordinates of areas with significant AD differences are shown in Table 2. No significant correlation was observed among AD values, the duration of dialysis, and CASI scores in patients with ESRD.

Table 2: MNI coordinates of major areas with significant AD differences along with means of AD values

Brain Regions	MNI Coordinate (mm)			AD (mean) $\times 10^{-3}$ mm ² /s	
	X	Y	Z	ESRD	Healthy
Rt RLIC	25	-16	-12	1.43 \pm 0.17	1.39 \pm 0.14
Lt RLIC	-27	-14	-14	1.66 \pm 0.21	1.57 \pm 0.13
Lt Fminor	-21	52	-12	1.43 \pm 0.07	1.33 \pm 0.07
Pons	1	-14	-56	1.85 \pm 0.18	1.73 \pm 0.11

Note:—Fminor indicates forceps minor; RLIC, retrolenticular part of the internal capsule; MNI, Montreal Neurological Institute; Rt, right; Lt, left.

Radial Diffusivity

Compared with control subjects, significant increases in RD values were observed in multiple white matter areas in patients with ESRD, including the genu, splenium, and body of the corpus callosum; the bilateral retrolenticular part of the internal capsule; the bilateral forceps major; the bilateral anterior corona radiata; the bilateral posterior corona radiata; the pontine region; and the bilateral cerebellum, as shown in Fig 1G–L. Montreal Neurological Institute coordinates of areas with significant RD differences are shown in Table 3. Multiple regression analysis revealed a positive correlation between RD and the duration of hemodialysis in the pontine region and a negative correlation between RD and the CASI score in the left anterior corona radiata and right superior corona radiata in patients with ESRD, as shown in Figs 2A–C and 3 A–C, respectively.

Table 3: MNI coordinates of major areas with significant RD differences along with means of RD values

Brain Regions	MNI Coordinate (mm)			RD (mean) $\times 10^{-3} \text{ mm}^2/\text{s}$	
	X	Y	Z	ESRD	Healthy
GCC	1	39	-1	0.94 \pm 0.2	0.86 \pm 0.14
SCC	1	-14	5	0.65 \pm 0.15	0.56 \pm 0.08
Rt. Fmajor	24	-54	-8	0.66 \pm 0.11	0.62 \pm 0.09
Lt. Fmajor	-28	-42	-8	0.67 \pm 0.09	0.61 \pm 0.11
Rt. PCR	25	-23	7	0.64 \pm 0.09	0.63 \pm 0.04
Lt. PCR	-28	-20	7	0.66 \pm 0.09	0.65 \pm 0.04
Rt. ACR	17	51	-6	0.64 \pm 0.06	0.62 \pm 0.05
Lt. ACR	-20	56	-8	0.63 \pm 0.06	0.59 \pm 0.05
Pons	3	-13	-54	0.82 \pm 0.19	0.71 \pm 0.12

Note:—ACR indicates anterior corona radiata; Fmajor, forceps major; PCR, posterior corona radiata; SCC, splenium of the corpus callosum; MNI, Montreal Neurological Institute; GCC, genu of the corpus callosum; Rt, right; Lt, left.

Mean Diffusivity

In patients with ESRD, widespread significant increases in MD were observed in the white matter regions, including the genu, splenium, and body of the corpus callosum; the bilateral posterior corona radiata; the bilateral anterior corona radiata; the bilateral forceps major; and the bilateral retrolenticular part of the internal capsule. These increases extended to the bilateral sagittal stratum, pontine crossing tracts, and middle cerebellar peduncle, as shown in Fig 1M–R. Montreal Neurological Institute coordinates of areas with significant MD differences are shown in Table 4. Multiple regression analysis revealed a positive correlation between MD and the duration of hemodialysis in the pons, the right retrolenticular part of the internal capsule, and the left anterior frontal white matter, as shown in Fig 2D–I. A significant negative corre-

lation between MD and the CASI score was also observed in the left anterior corona radiata and right superior corona radiata, as shown in Fig 3D–F.

Fractional Anisotropy

Similarly, FA values were significantly decreased in multiple areas of the brain in patients with ESRD. Major differences between patients with ESRD and healthy subjects were found in clusters in the genu and splenium of the corpus callosum and the bilateral retrolenticular part of the internal capsule extending to the bilateral sagittal stratum. Some scattered clusters were found in the middle cerebellar peduncle, as shown in Fig 1S–X. Montreal Neurological Institute coordinates of areas with significant FA differences are listed in Table 5. Multiple regression analysis revealed a positive correlation between FA values and the CASI score in the left anterior corona radiata, left posterior corona radiata, and right superior corona radiata in patients with ESRD, as shown in Fig 3G–I. However, no significant correlations were observed between FA and the duration of hemodialysis. Montreal Neurological Institute coordinates of areas with significant correlations of RD, MD, and FA values to the duration of hemodialysis and CASI score are shown in Table 6.

DISCUSSION

In this study, voxelwise analysis of DTI was performed in patients with ESRD on long-term hemodialysis to reveal global white matter alterations not only in the cerebrum but also in the infratentorial structures. In general, AD, RD, and MD values increased significantly, whereas FA decreased significantly in multiple white matter areas in patients with ESRD. Significant increases in MD were observed in many white matter regions in patients with ESRD that are similar to those of a previous DWI study⁶; however, in this study, increases in AD, RD, and MD and a decrease in FA that were not mentioned previously were also observed in the pons and cerebellum. Although these changes were observed in patients with ESRD who underwent an MR imaging 2 days after the last weekly hemodialysis, part of these results may very likely be attributed to the immediate effects of hemodialysis, which were shown to impact cognitive functions longer than 2 days.¹⁹

Unlike cognitive function, white matter alterations in the infratentorial regions after hemodialysis were only discussed in a few studies using conventional MR imaging.^{20–22} Dialysis disequilibrium syndrome, first described in 1962 by Kennedy et al,³ is commonly described as an acute neurologic disorder that occurs in patients undergoing hemodialysis. In addition, osmotic demyelination syndrome, which has been

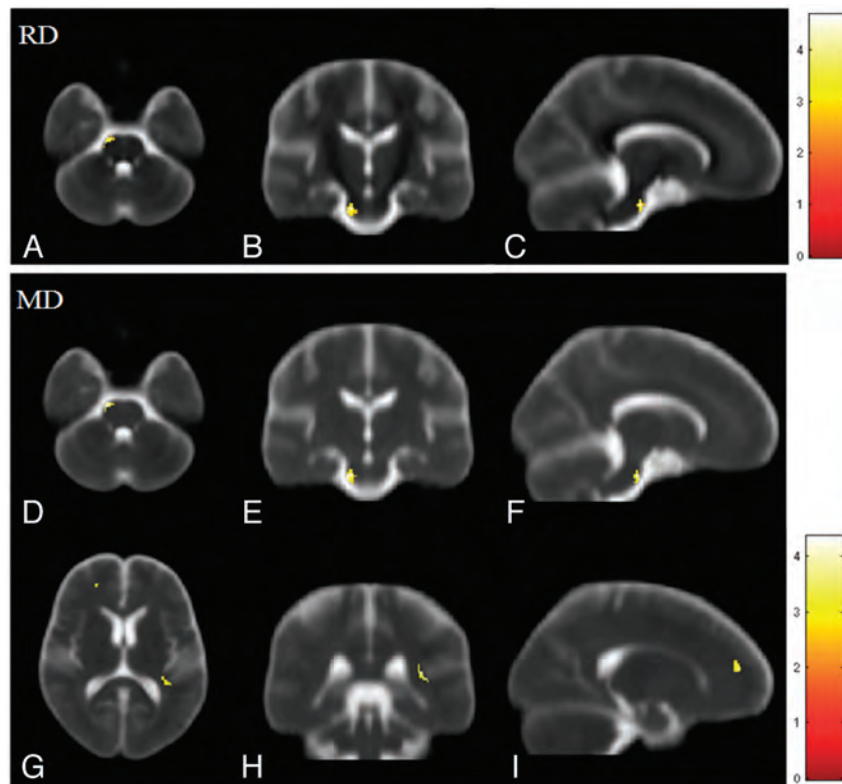


FIG 2. Voxelwise multiple regression analysis of DTI indices and the duration of hemodialysis in patients with ESRD. Red-yellow colors indicate the significant positive correlation in RD (A–C) and MD (D–I). Color bars show the ranges of *t*-scores.

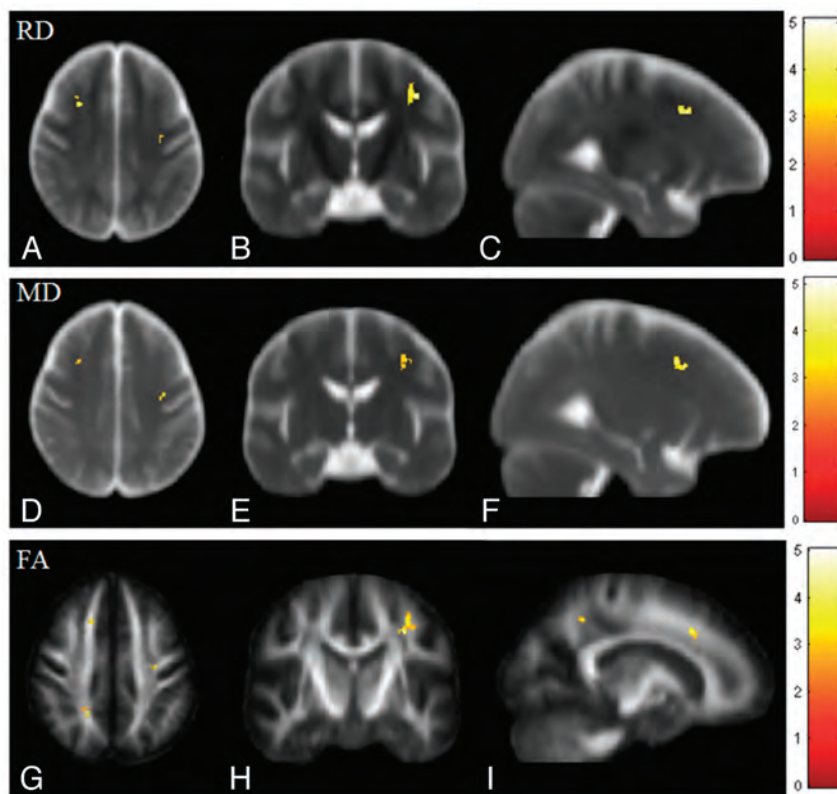


FIG 3. Voxelwise multiple regression analysis of DTI indices and CASI scores in patients with ESRD. Red-yellow colors indicate the significant negative correlations in RD (A–C) and MD (D–F) and a positive correlation in FA (G–I). Color bars show the ranges of *t*-scores.

observed in patients with ESRD, is characterized by transient edema and demyelination in the pons and extrapontine regions after hemodialysis.²¹ Although both syndromes occur less often in patients on long-term dialysis, the results of this study suggest that dialysis-associated changes may occur not only in cerebral white matter but also in cerebellar and brain stem regions. These changes may have been associated with both syndromes.

In analyses of diffusivity, AD and RD were associated with white matter changes in patients with ESRD. In most regions with increased MD, significant increases in RD but not AD were found. Similar findings have been reported in previous animal and human studies in which defective myelin was shown to increase RD

Table 4: MNI coordinates of major areas with significant MD differences along with means of MD values

Brain Regions	MNI Coordinate (mm)			MD (mean) × 10 ⁻³ mm ² /s	
	X	Y	Z	ESRD	Healthy
GCC	1	39	-8	1.16 ± 0.07	1.08 ± 0.05
SCC	1	-13	5	1.12 ± 0.13	1.02 ± 0.06
Rt. SS	31	-31	-9	1.27 ± 0.22	1.21 ± 0.15
Lt. SS	-39	-24	-15	1.07 ± 0.12	1.04 ± 0.08
Rt. Fmajor	25	-42	-3	0.96 ± 0.11	0.89 ± 0.04
Lt. Fmajor	-30	-34	-3	1.15 ± 0.11	0.99 ± 0.09
Rt. PCR	27	-25	4	1.07 ± 0.12	0.92 ± 0.06
Lt. PCR	-29	-25	1	1.21 ± 0.18	1.11 ± 0.15
Pons	2	-14	-56	1.28 ± 0.13	1.13 ± 0.09

Note:—Fmajor indicates forceps major; PCR, posterior corona radiata; SCC, splenium of the corpus callosum; SS, sagittal stratum; MNI, Montreal Neurological Institute; GCC, genu of the corpus callosum; Rt, right; Lt, left.

more than AD.^{23,24} Although the mechanisms of uremic neuropathy are complex, the results of this study suggest that demyelination of white matter is the major neuropathy in patients with ESRD with long-term hemodialysis. Furthermore, a positive correlation of MD and RD with the duration of hemodialysis was found. These findings may reflect progressive changes of demyelination, which is the subsequent change in uremic neuropathy. Because a previous study demonstrated that neurologic complications, whether due to the uremic state or its treatment, play an important role in the morbidity and mortality of patients with ESRD,²⁵ monitoring the damage to brain microstructures is important in these patients. The results of this study suggest that MD and RD may be good indices for monitoring changes in demyelination in patients with ESRD.

Similar to our previous study, this study identified significant decreases in FA in multiple areas of the brains of patients with ESRD.⁷ However, these decreases were observed not only in the cerebral white matter but also in the middle cerebellar peduncle. Similar to

that in previous studies, a decrease in diffusion anisotropy is recommended as a good index for neural degeneration.^{23,26} In patients with ESRD, decreases in FA and increases in MD were caused by reduced microstructural integrity with macroscopic tissue loss or interstitial edema, whereas decreases in FA and normal MD were attributed to microstructural changes without gross tissue loss or with the occurrence of gliosis. However, decreases in FA and increases in RD occurred because of demyelination of white matter tissue. In multiple regression analysis, though no significant correlation was observed between FA and the duration of hemodialysis, a trend of negative correlations was observed when the statistical criteria were lowered ($P < .05$), suggesting that long-term hemodialysis slightly and gradually compromised the integrity of white matter tissue in these patients.

Two-sample *t* test analysis revealed significantly lower CASI scores in patients with ESRD than in healthy subjects. Multiple regression analysis further revealed significant correlations of RD, MD, and FA values with CASI scores in the frontal and parietal white matter that are likely responsible for cognitive function of the brain. The increases in RD and MD values and decreases in FA values may highlight microstructural nerve damage, including axon injury and demyelination, which generally parallel the degree of clinical and pathologic impairment. Previous studies demonstrated that DTI can detect early neurodegenerative changes and subtle changes in clinical function.^{27,28} The results of this study suggested that DTI can detect uremic neuropathy, which is associated with cognitive function.

Table 5: MNI coordinates of major areas with significant FA differences along with means of FA values

Brain Regions	MNI Coordinate (mm)			FA (mean)	
	X	Y	Z	ESRD	Healthy
GCC	3	40	-8	0.6 ± 0.06	0.67 ± 0.04
SCC	3	-14	5	0.65 ± 0.05	0.72 ± 0.05
Rt. SS	31	-28	-6	0.50 ± 0.04	0.56 ± 0.04
Lt. SS	-27	-39	-6	0.46 ± 0.05	0.56 ± 0.07
Rt. MCP	13	-18	-58	0.45 ± 0.03	0.53 ± 0.04

Note:—MCP indicates middle cerebellar peduncle; SCC, splenium of the corpus callosum; SS, sagittal stratum; MNI, Montreal Neurological Institute; GCC, genu of the corpus callosum; Rt, right; Lt, left.

Table 6: MNI coordinates of areas with significant correlations along with their correlation coefficients

Brain Regions	MNI Coordinate (mm)			Correlation Coefficient
	X	Y	Z	
RD and duration				
Lt. Pons	-16	-3	-46	0.7093
RD and CASI				
Lt. ACR	-28	33	19	-0.7442
Rt. SCR	31	7	21	-0.6154
MD and duration				
Rt. RLIC	33	-20	-6	0.6009
Lt. FWM	-21	63	-5	0.6287
Lt. Pons	-12	-3	-46	0.6675
MD and CASI				
Lt. ACR	-28	33	19	-0.7657
Rt. SCR	31	7	21	-0.5463
FA and CASI				
Lt. ACR	-17	40	18	0.7067
Lt. PCR	-20	-29	24	0.6117
Rt. SCR	33	6	26	0.6815

Note:—ACR indicates anterior corona radiata; PCR, posterior corona radiata; RLIC, retrolenticular part of the internal capsule; SCR, superior corona radiata; MNI, Montreal Neurological Institute; FWM, frontal white matter; Rt, right; Lt, left.

The small number of participants with ESRD is a limitation of this study. The inclusion criteria that patients had to be young and undergoing hemodialysis may have been responsible for the small sample size. An extended study with a larger sample size and inclusion of those undergoing peritoneal dialysis, which led to higher mortality rates than hemodialysis in a previous study,²⁹ may provide more information about the effects of different factors. A further follow-up study would be helpful for understanding the long-term effects of dialysis methods. In terms of data acquisition, this study acquired DTI data with a section thickness of 4.4 mm, which is larger than the in-plane resolution and has more partial volume averaging in the through-plane direction. Hence, the results of this study may have been affected by the partial volume effects of imaging in the through-plane direction. In cognitive assessment, this study did not record the subject's education level. Because the CASI score is associated with education,³⁰ the results of this study may also have been affected by the educational difference between the 2 groups.

CONCLUSIONS

The voxel-based analysis method was used in this study for global detection of white matter alterations in patients with ESRD on long-term hemodialysis. The results showed that AD, RD, and MD were significantly increased, whereas FA was significantly decreased in many white matter regions of the brain of patients

with ESRD. The interpretation of these white matter alterations by using all DTI indices led to the conclusion that long-term hemodialysis caused increased interstitial edema in both the supra- and infratentorial regions and gradually led to axonal demyelination in the pons. Finally, voxel-based DTI analysis was helpful in characterizing white matter alterations in patients with ESRD on long-term hemodialysis.

REFERENCES

- Foley RN, Collins AJ. End-stage renal disease in the United States: an update from the United States renal data system. *J Am Soc Nephrol* 2007;18:2644–48
- Arief AI. Dialysis disequilibrium syndrome: current concepts on pathogenesis and prevention. *Kidney Int* 1994;45:629–35
- Kennedy AC, Eaton JC, Linton AL. Urea levels in cerebrospinal fluid after haemodialysis. *Lancet* 1962;1:410–11
- Pappius HM, Oh JH, Dossetor JB. The effects of rapid hemodialysis on brain tissues and cerebrospinal fluid of dogs. *Can J Physiol Pharmacol* 1967;45:129–47
- Galons JP, Trouard T, Gmitro AF, et al. Hemodialysis increases apparent diffusion coefficient of brain water in nephrectomized rats measured by isotropic diffusion-weighted magnetic resonance imaging. *J Clin Invest* 1996;98:750–55
- Chen CL, Lai PH. A preliminary report of brain edema in patients with uremia at first hemodialysis: evaluation by diffusion-weighted MR imaging. *AJNR Am J Neuroradiol* 2007;28:68–71
- Hsieh TJ, Chang JM, Chuang HY, et al. End-stage renal disease: in vivo diffusion-tensor imaging of silent white matter damage. *Radiology* 2009;252:518–25
- Kim H, Park J, Bai D, et al. Diffusion tensor imaging findings in neurologically asymptomatic patients with end stage renal disease. *NeuroRehabilitation* 2011;29:111–16
- Snook L, Plewes C, Beaulieu C. Voxel based versus region of interest analysis in diffusion tensor imaging of neurodevelopment. *Neuroimage* 2007;34:243–52
- Ashburner J, Friston KJ. Voxel-based morphometry: the methods. *Neuroimage* 2000;11:805–21
- Della Nave R, Foresti S, Pratesi A, et al. Whole-brain histogram and voxel-based analyses of diffusion tensor imaging in patients with leukoaraiosis: correlation with motor and cognitive impairment. *AJNR Am J Neuroradiol* 2007;28:1313–19
- Liu HS, Chou MC, Chung HW, et al. Potential long-term effects of MDMA on the basal ganglia-thalamocortical circuit: a proton MR spectroscopy and diffusion-tensor imaging study. *Radiology* 2011;260:531–40
- Grieve SM, Williams LM, Paul RH, et al. Cognitive aging, executive function, and fractional anisotropy: a diffusion tensor MR imaging study. *AJNR Am J Neuroradiol* 2007;28:226–35
- Vercauteren T, Pennec X, Perchant A, et al. Diffeomorphic demons: Efficient non-parametric image registration. *Neuroimage* 2009;45:S61–72
- Ashburner J. A fast diffeomorphic image registration algorithm. *Neuroimage* 2007;38:95–113
- Takahashi R, Ishii K, Miyamoto N, et al. Measurement of gray and white matter atrophy in dementia with Lewy bodies using diffeomorphic anatomic registration through exponentiated lie algebra: a comparison with conventional voxel-based morphometry. *AJNR Am J Neuroradiol* 2010;31:1873–78
- Teng EL, Hasegawa K, A. H., et al. The Cognitive Abilities Screening Instrument (CASI): a practical test for cross-cultural epidemiological studies of dementia. *Int Psychogeriatr* 1994;6:45–58
- Mori S, Oishi K, Jiang HY, et al. Stereotaxic white matter atlas based on diffusion tensor imaging in an ICBM template. *Neuroimage* 2008;40:570–82
- Williams MA, Sklar AH, Burrighat RG, et al. Temporal effects of dial-

- ysis on cognitive functioning in patients with ESRD. *Am J Kidney Dis* 2004;43:705–11
20. Lakadamyali H, Ergun T. MRI for acute neurologic complications in end-stage renal disease patients on hemodialysis. *Diagn Interv Radiol* 2011;17:112–17
 21. Tarhan NC, Agildere AM, Benli US, et al. Osmotic demyelination syndrome in end-stage renal disease after recent hemodialysis: MRI of the brain. *AJR Am J Roentgenol* 2004;182:809–16
 22. Ağildere AM, Benli S, Erten Y, et al. Osmotic demyelination syndrome with a disequilibrium syndrome: reversible MRI findings. *Neuroradiology* 1998;40:228–32
 23. Song SK, Sun SW, Ramsbottom MJ, et al. Demyelination revealed through MRI as increased radial (but unchanged axial) diffusion of water. *Neuroimage* 2002;17:1429–36
 24. Metwalli NS, Benatar M, Nair G, et al. Utility of axial and radial diffusivity from diffusion tensor MRI as markers of neurodegeneration in amyotrophic lateral sclerosis. *Brain Res* 2010;1348:156–64
 25. Brouns R, De Deyn PP. Neurological complications in renal failure: a review. *Clin Neurol Neurosurg* 2004;107:1–16
 26. Filippi M, Cercignani M, Inglese M, et al. Diffusion tensor magnetic resonance imaging in multiple sclerosis. *Neurology* 2001;56:304–11
 27. Huang J, Friedland RP, Auchus AP. Diffusion tensor imaging of normal-appearing white matter in mild cognitive impairment and early Alzheimer disease: preliminary evidence of axonal degeneration in the temporal lobe. *AJNR Am J Neuroradiol* 2007;28:1943–48
 28. Kantarci K, Senjem ML, Avula R, et al. Diffusion tensor imaging and cognitive function in older adults with no dementia. *Neurology* 2011;77:26–34
 29. Bloembergen WE, Port FK, Mauger EA, et al. A comparison of mortality between patients treated with hemodialysis and peritoneal dialysis. *J Am Soc Nephrol* 1995;6:177–83
 30. McCurry SM, Edland SD, Teri L, et al. The Cognitive Abilities Screening Instrument (CASI): data from a cohort of 2524 cognitively intact elderly. *Int J Geriatr Psychiatry* 1999;14:882–88

Assessment of Whole-Brain White Matter by DTI in Autosomal Recessive Spastic Ataxia of Charlevoix-Saguenay

K.K. Oguz, G. Haliloglu, C. Temucin, R. Gocmen, A.C. Has, K. Doerschner, A. Dolgun and M. Alikasifoglu



ABSTRACT

BACKGROUND AND PURPOSE: Extension and characteristics of WM involvement other than the brain stem remain inadequately investigated in ARSACS. The aim of this study was to investigate whole-brain WM alterations in patients with ARSACS.

MATERIALS AND METHODS: Nine Turkish unrelated patients with ARSACS and 9 sex- and age-matched healthy control participants underwent neurologic examination, molecular studies, electrophysiologic studies, and DTI of the brain. TBSS was used for whole-brain voxelwise analysis of FA, AD, RD, mean diffusivity of WM. Tractographies for the CST and TPF were also computed.

RESULTS: Molecular studies revealed 8 novel mutations (3 nonsense, 4 missense, and 1 frameshift insertion) and a missense variation in the SACS gene. Thick TPF displaced and compressed the CST in the pons. The TPF had increased FA, decreased RD, and increased AD, which may be attributed to hypertrophy and/or hypermyelination. Widespread decreased FA and increased RD, suggesting demyelination, was found in the limbic, commissural, and projection fibers. In addition to demyelination, CST coursing cranial and caudal to the pons also showed a marked decrease in AD, suggesting axonal degeneration. Electrophysiologic studies revealed findings that concur with demyelination and axonal involvement.

CONCLUSIONS: In addition to developmental changes of the TPF and their effects on the CST in the brain stem, axonal degeneration mainly along the pyramidal tracts and widespread demyelination in WM also occur in patients with ARSACS. Widespread tissue damage may be associated with extensive loss of saccin protein in the brain and may explain a wide range of progressive neurologic abnormalities in patients with ARSACS.

ABBREVIATIONS: AD = axial diffusivity; ARSACS = autosomal recessive spastic ataxia of Charlevoix-Saguenay; CST = corticospinal tracts; FA = fractional anisotropy; RD = radial diffusivity; TBSS = tract-based spatial statistics; TPF = transverse pontine fibers

ARSACS (MIM 270550) is a distinctive form of hereditary, early-onset spastic ataxia, which manifests mainly by early-onset pyramidal tract and cerebellar involvement, peripheral neuropathy, and hypermyelination of the retinal nerve fibers. Clinical variations including later-onset mental retardation, ophthalmoplegia, skeletal deformities, and biochemical abnormalities have been reported.^{1,2}

Since the first description of patients in the Charlevoix-Saguenay region of Quebec in 1978, the disease has been increas-

ingly defined worldwide, with numerous mutations and diverse phenotypes.² The responsible gene (SACS, MIM 604490) was located on chromosome 13q and encodes the saccin protein, which is widely expressed throughout the brain with a predilection for pyramidal neurons, Purkinje cells, thalamic and pontine nuclei, and reticular formation.³ Confusion with cerebral palsy and secondary spastic diplegia, and variations in the phenotype lead to underdiagnosis of ARSACS.^{4,5}

Neuroimaging findings include slowly progressive atrophy of the superior vermis, and atrophy of the cerebellar hemispheres, cervical spinal cord, and cerebral cortex.^{5,6} The description of characteristic bilateral, parallel, paramedian, T2 hypointense stripes on MR imaging contributed to an increased diagnosis of ARSACS.⁷

By measuring anisotropic diffusion of water in the WM, DTI detects abnormalities in the myelin, axon, or orientation of fibers within the bundle.^{8,9} Gazulla et al^{10,11} described nonquantitative abnormalities of the TPF and CST by DTI in 2 studies with 5 patients. These authors suggested a developmental basis for

Received November 1, 2012; accepted after revision December 7.

From the National Magnetic Resonance Research Center (UMRAM) (K.K.O., A.C.H., K.D.), Bilkent University, Bilkent, Ankara, Turkey; and Departments of Radiology (K.K.O., R.G.), Pediatric Neurology (G.H.), Neurology (C.T.), Biostatistics (A.D.), and Medical Genetics (M.A.), Faculty of Medicine, Hacettepe University, Sıhhiye, Ankara, Turkey.

Please address correspondence to Kader K. Oguz, National Magnetic Resonance Research Centre (UMRAM), Bilkent University, Cyberplaza, CBlock Level 2, Bilkent-Ankara, Turkey; e-mail:karlioguz@yahoo.com

Indicates article with supplemental on-line tables.

<http://dx.doi.org/10.3174/ajnr.A3488>

ARSACS by showing interruption of the CST in the pons by large TPF. More recently, Prodi et al¹² showed involvement of several additional structures such as the forceps minor and major, superior longitudinal fasciculus, and cingulum by using an ROI approach for these predetermined areas. None of these studies investigated whole-brain WM changes in ARSACS by multiple diffusion indices.

TBSS enables an unbiased whole-brain voxelwise analysis of multi-subject FA data by using a nonlinear registration algorithm, projection of the individual data onto a mean alignment-invariant tract representation, and stringent statistical analysis. It has been increasingly used for the depiction of WM abnormalities, especially in patient groups with diseases in which alterations in WM fibers cannot be precisely predicted.¹³

Given the high expression of the saccin protein in the brain, we hypothesized that WM alterations are not limited to the brain stem and the cerebellum, and TBSS would show more widespread abnormality in patients with ARSACS. We also aimed to seek electrophysiologic correlates of DTI findings.

MATERIALS AND METHODS

Participants

The local institutional review board approved the study, and all participants gave written informed consent. Patients were asked to participate in this prospective study on observation of MR imaging findings and confirmation of ARSACS by genetic studies.

Nine Turkish patients with ARSACS (male/female, 6/3; age range, 5–42 years; mean age, 23.67 ± 13.28 years) and 9 sex- and age-matched control participants (male/female, 6/3; age range, 5–41 years; mean age, 23.78 ± 12.43 years) were included in the study.

All patients underwent neurologic and ophthalmologic examinations, molecular studies, electrophysiologic studies, structural MR imaging, and DTI of the brain.

Healthy volunteers without previous neuropsychological or systemic disease served as control participants. They had normal findings on structural MR imaging.

Molecular Studies

The method for molecular studies is given in the On-line Appendix, Part 1.

Electrophysiologic Studies

Nerve conduction studies and motor-evoked potential studies from the tibialis anterior muscle and somatosensory-evoked potential by stimulation of the posterior tibial nerve were performed. Technical details are given in the On-line Appendix, Part 2.

Image Acquisition

Imaging studies were performed on a 1.5T MR imaging scanner (Symphony TIM; Siemens, Erlangen, Germany) equipped with an 8-channel head coil. Brain MR imaging included sagittal and axial T1-weighted imaging, axial T2-weighted imaging, and T2* gradient recalled-echo. DTI applied axial single-shot echo-planar imaging (TR, 5814 ms; TE, 98 ms; maximal b factor, 1000 s/mm²; 30 independent directions; field of view, 230 × 230 mm; matrix,

128 × 128; number of sections, 50, with 3-mm thickness without gap).

Image Processing and Analysis

Two experienced neuroradiologists (K.K.O., R.G.) evaluated brain MR imaging for the presence of atrophy of the infratentorial structures and the cerebrum, T2 hypointense stripes in the pons, T2 hyperintense stripes in the lateral thalami, and susceptibility on T2* GRE images in consensus.

DTI data were analyzed by use of TBSS. All scans were corrected for head motion and eddy currents by use of the affine registration. B0 volumes of each participant were extracted and averaged. The main diffusion tensor was fitted in each voxel with the FSL DTIFit tool (http://fsl.fmrib.ox.ac.uk/fsl/fsl-4.1.9/fdt/fdt_dtifit.html), and the FA, RD, AD, and mean diffusivity maps were calculated. After registration and alignment of individual maps to the average space as input for TBSS, the mean FA map and then the thinned mean FA skeleton (which represents the centers of all tracts common to the group) were computed. Then voxelwise statistics on FA, RD, AD, and mean diffusivity were performed by use of 500 permutations. The results were corrected for multiple comparisons, and family-wise error–corrected maps at *P* values < .05 were considered significant.

Because the TPF and CST in the brain stem were reported to be morphologically altered, we first recognized and evaluated these structures on a directionally encoded color FA map of each participant, and we then outlined and calculated corresponding ROIs. Supratentorial WM clusters with significant change on the resulting TBSS maps were extracted as ROIs and registered and overlaid onto an anatomic Montreal Neurological Institute template. These ROIs were labeled according to Johns Hopkins University WM tractography and the International Consortium for Brain Mapping DTI-81 WM atlases in FSL, and the mean diffusion indices of the ROIs were calculated.

3D fiber tractographies of the CST and TPF were obtained by MedINRIA (<http://www-sop.inria.fr/asclepios/software/MedINRIA>). The threshold for stopping fiber propagation was FA < 0.2 and angle < 70°. Seed points were located at the level of the corona radiata and medulla oblongata for the CST and central pons for the TPF.

Statistical Analysis

Statistical analyses were done with a specific software package (SPSS for Windows, version 15.0; SSPS, Chicago, Illinois). Age and sex differences between patients and control participants were tested by use of the independent-sample Student *t* test and the Fisher exact test, respectively. The independent Student *t* test was used for testing diffusion measures between patients and control participants. *P* values < .05 were considered significant.

RESULTS

Patient Demographics and Clinical Assessment

Demographic and clinical data for patients are summarized in On-line Table 1. Delays in motor skills (*n* = 7), ataxic gait (*n* = 4), dystonia (*n* = 1), and frequent falls (*n* = 1) were presenting symptoms. Initial diagnoses of the patients were cerebral

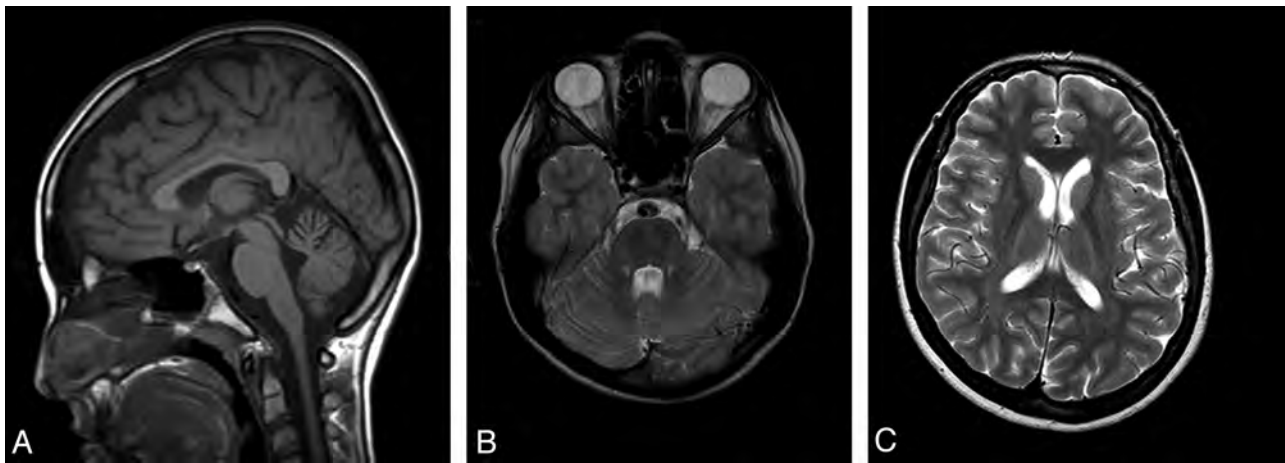


FIG 1. Sagittal T1-weighted spin-echo (A), axial T2-weighted fast spin-echo (B,C) images of a 14-year-old patient show atrophy of the superior vermis (A) and bilateral, paramedian, T2-hypointense stripes (B) and bilateral, linear T2 hyperintensities in the lateral thalamus (C).

palsy ($n = 4$), hereditary spastic paraparesis ($n = 4$), and static cerebellar ataxia ($n = 1$). The parents were first cousins in 4 families. None of the patients had a family history of similar clinical features. Neurologic and ophthalmologic examination revealed spasticity ($n = 7$), extremity deformity ($n = 2$), cerebellar ataxia ($n = 4$), dysarthria ($n = 4$), nystagmus ($n = 1$), peripheral neuropathy ($n = 7$), and myelinated retinal fibers ($n = 2$) or thickening of the peripapillary retinal fibers ($n = 1$).

Molecular Findings

Molecular results are summarized in On-line Table 1 (detailed results in On-line Appendix, Part 3, and On-line Table 2). Eight never-reported different mutations (3 nonsense, 4 missense, and 1 frameshift insertion) and a missense variation were identified in 9 patients from unrelated families.

Electrophysiologic Studies

Results of electrophysiologic studies are given in On-line Table 3. Nerve conduction studies were obtained in patients; somatosensory-evoked potential and motor-evoked potential studies were obtained in 5 patients. Decreased nerve conduction velocities of the motor nerves and prolonged motor distal latencies were found in patients with ARSACS. F waves were either prolonged or absent. Sensory nerve action potentials were absent bilaterally in the sural nerves. When sensory conduction velocities could be obtained, they were reduced in the sensory nerve action potentials. Although central motor conduction times were significantly prolonged, cortical motor-evoked potential responses were remarkably low in patients without spinal and cortical somatosensory-evoked potential responses. Compound muscle action potential of the motor nerves was also low, especially in the lower extremities.

Structural MR Imaging

All patients showed superior vermian atrophy (Fig 1A) and bilateral parallel and paramedian T2-hypointense stripes in the pons (Fig 1B). Atrophy of the brain stem ($n = 4$), the cerebellar and cerebral hemispheres ($n = 3$), and bilateral T2 hyperintensities in the lateral thalami ($n = 4$) were observed (Fig 1C). On T2*gradient recalled-echo imaging, no patient had susceptibility signal change.

DTI

Visual evaluation of color FA maps revealed bilaterally smaller and displaced CSTs in the pons (Fig 2A, -B) in patients with ARSACS compared with control participants. The pyramids and CSTs in the midbrain were normal in location. The pons was mostly occupied by “left-to-right” direction-coded fibers of the TPF (Fig 2A). Tractography showed thickening of the TPF and interruption of the CST in the pons with relative thinning in the midbrain and medulla oblongata in the patients (Fig 2C, -D).

The WM structures with significant change and their mean quantitative values are summarized in On-line Table 4. The TPF in patients with ARSACS had higher FA, lower RD, higher AD ($P < .05$), and a comparable mean diffusivity ($P > .05$) compared with control participants. In the patients, CST in the brain stem revealed significantly lower FA, increased RD, increased mean diffusivity ($P < .05$), and no remarkable change in AD ($P > .05$). TBSS maps showed consistent results with these measurements of ROIs outlined from color FA maps (Fig 3).

TBSS revealed extensive reductions in FA, accompanied by increased RD in the supratentorial WM, including the entire corpus callosum, both cingula, fornices, superior and inferior longitudinal fasciculi, the inferior fronto-occipital fasciculi, corona radiata, internal capsules, and thalami. Bilateral superior cerebellar WM and vermis and CST in the medulla oblongata and midbrain showed a similar pattern of FA and RD changes. The extent of increased mean diffusivity and AD followed that of FA and RD changes in decreasing order. However, reduced AD was present along the internal capsules and midbrain, medulla oblongata, the splenium of the corpus callosum, and bilateral frontoparietal WM. No remarkable decrease in mean diffusivity was present except for a few small clusters in the subcortical temporal WM (Fig 3).

DISCUSSION

Three major results, which confirm and add to previous findings¹⁰⁻¹², can be derived from our data: 1) Large TPF with increased FA and AD and decreased RD squeezed and displaced the pontine CST with decreased FA, increased RD, and increased mean diffusivity, as was also observed on tractography. 2) The

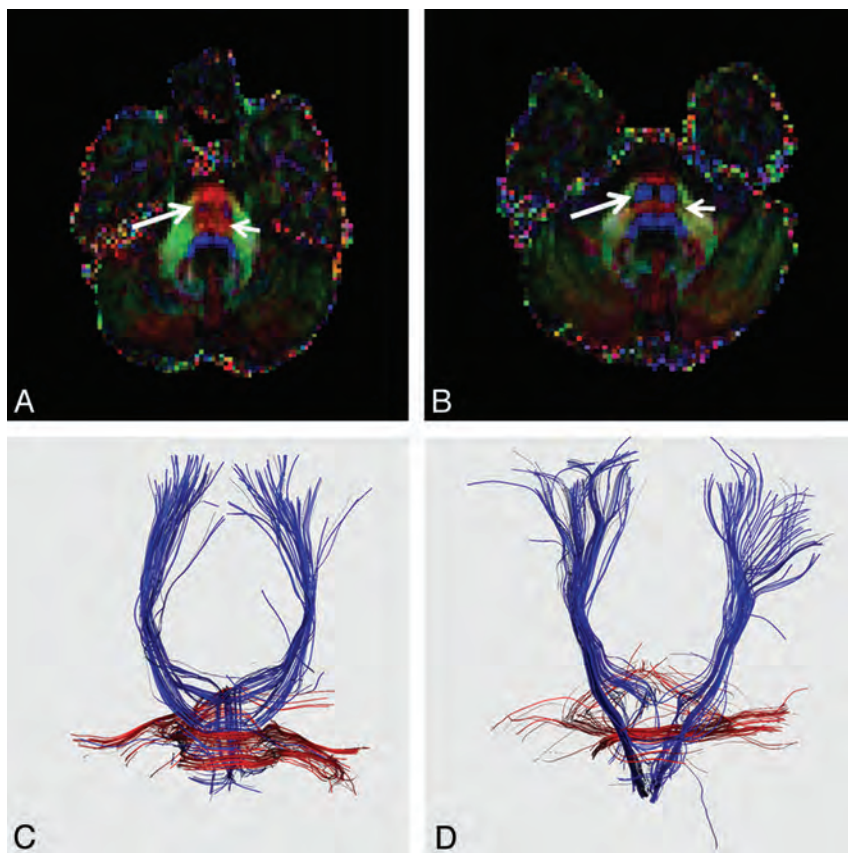


FIG 2. Directionally encoded color FA image of the same patient as in Fig 1 (A) shows that the CST (blue, long arrow) is smaller and displaced in the pons by “left-to-right” direction-encoded TPF (red, short arrow). Tractographies of CST (blue) and TPF (red) depict interruption of CST by thick TPF (C). Corresponding FA image (B) and tractography (D) of a sex- and age-matched control participant are also given.

CST cranial and caudal to the pons showed an apparent reduction in AD, suggestive of axonal degeneration. 3) The supratentorial WM, including the limbic, commissural, and projection fibers, was markedly involved, as demonstrated by reduced FA, increased RD, and increased mean diffusivity, suggestive of demyelination.

In agreement with Gazulla et al,^{10,11} the pontine CST was not only engulfed by the TPF (TPF was thick because of hypermyelination and/or axonal hypertrophy), but was also dislocated on directionally encoded FA images. The presence of hypermyelinated or thickened peripapillary retinal fibers has been considered a pathognomonic feature of ARSACS for quite some time.¹⁴ We cannot confidently consider the thickening of the TPF and hypermyelination/peripapillary nerve thickening a result of identical pathogenesis, given the rarity of patients with abnormal fundoscopic findings in our study, similar to other non-Quebec patient populations. Furthermore, to our knowledge, no evidence has been available regarding a relationship between retinal nerve fiber layer thickening and SACS mutation and the duration and severity of ARSACS.¹⁵

AD (diffusion parallel to WM fibers) and RD (diffusion perpendicular to WM fibers) have been demonstrated to be sensitive measures in the characterization of tissue abnormalities. Experimental studies with immunohistostaining of phosphorylated neurofilament and myelin basic protein have proven that reduced

AD and increased RD correlated with axonal and myelin damage, respectively.^{16,17} Our finding of decreased AD in the pyramidal pathways suggests anterograde and retrograde Wallerian degeneration secondary to damage to the CST by the TPF at the pons, very similar to that observed after a pontine infarct or a spinal cord injury.^{18,19} However, because there was accompanying reduced FA and increased RD in the CST, one can suggest that both axonal degeneration and demyelination occur along the pyramidal tracts.

We also observed symmetric, linear, and mild T2 hyperintensities in the lateral thalami of 4 patients, which was recently suggested as reflecting degeneration of fibers of the external lamina consisting of afferent and efferent fibers between the cortex and reticular thalamic nuclei.^{12,20} TBSS analysis was able to detect supratentorial abnormalities beyond the thalami and motor pathways and showed widespread demyelination. Supporting our nerve conduction studies and DTI findings, previous nerve conduction studies and sural nerve biopsy examinations also revealed demyelinating neuropathy with superimposed axonal involvement in patients with ARSACS.^{11,21-23} Severe CST involvement, as assessed by motor-evoked

potential abnormalities, was attributed to the demyelination of the CST in an autopsy study.²⁴ Our current TBSS study, on the contrary, points out both axonal and myelin damage in the CST. These features can also contribute to differentiation of ARSACS from other degenerative diseases of mainly axonal neuropathy, such as Friedreich ataxia.²⁵ In our study, a widespread WM abnormality is being documented first in ARSACS, in contrast to more localized involvement of WM in the superior cerebellar peduncles and peridentate area in Friedreich ataxia.^{26,27}

Iron deposition in the basal ganglia and thalami and lipofuscin-like dens material within the lysosomes of swollen thalamic and cerebellar cortical neurons were suggested to cause T2 hypointensity in the pons and middle cerebellar peduncles.^{5,28,29} Our data do not support these suggestions because of lack of paramagnetic susceptibility; T2 signal loss in the thalami or middle cerebellar peduncles; and DTI findings of material storage in swollen neurons, such as reduced mean diffusivity.

Clinical variations such as mental retardation, ophthalmoplegia, and lack of retinal nerve hypermyelination have been reported more frequently in non-Quebec patients.² In addition to developmental abnormalities in the TPF and their mechanical effects on the CST, axonal degeneration and, more extensively, demyelination in cerebral WM may explain a wide range of neurologic abnormalities other

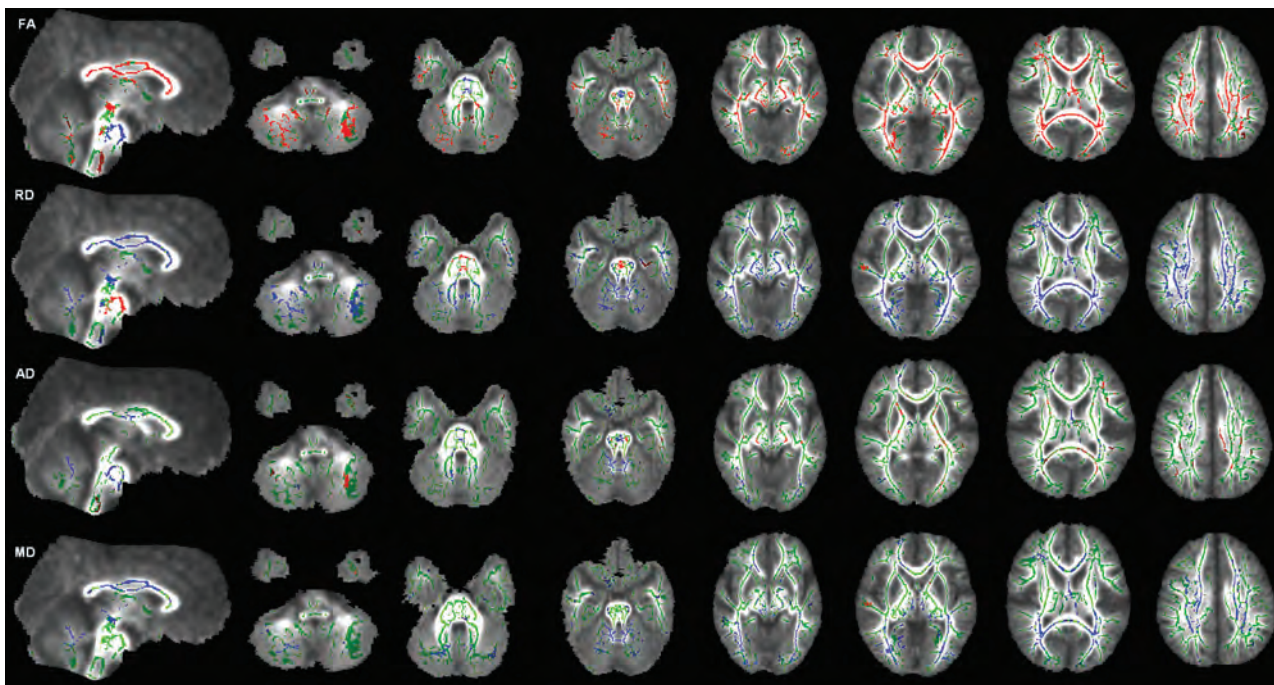


FIG 3. TBSS (family-wise error–corrected threshold-cluster extend voxel p maps) display clusters with significantly different FA, RD, AD, and mean diffusivity compared with sex- and age-matched control participants at $P < .05$. For all diffusion measures, blue shows increased values and red shows decreased values. FA skeleton projected on a mean FA map is shown in green.

than spasticity and the progressive nature of the disease. Recently, Girard et al³⁰ showed localization of sarsin to mitochondria and a cascade of detrimental effects resulting in neuronal cell death by loss of sarsin function in knockout mice. These authors further suggested the presence of some common pathophysiologic features between ARSACS and some other neurodegenerative diseases with mitochondrial impairment such as Alzheimer, Parkinson, and Huntington disease.^{30,31} Herein, by using TBSS, we present another common feature of ARSACS with these diseases: extensive WM alterations in the brain.^{32,33}

Our current study was distinguished in several ways: First, to the best of our knowledge, our study was the first that investigated whole-brain WM in patients with ARSACS. Second, it quantified the abnormal pattern of diffusion indices, including RD and AD, indicating widespread WM disintegration. Last, although the number of patients was limited, our patient cohort constituted the largest population of patients with ARSACS in Turkey.^{34,35} In our study, 8 different SACS mutations have been identified in 9 unrelated families referred to a single tertiary-care center. We believe that recognition of imaging features, as well as the identification of new mutations, will increase the rate of diagnosis of ARSACS in Turkey and other countries.

We did not measure the number of TPF and the CST because changing DTI parameters can significantly alter the results, and DTI has not been considered a precise way of measuring the length and number of fibers.³⁶ The small CST was not found to have a significant change in the pons on TBSS maps. Because only the major WM tracts are included in the skeleton, assessment of small fiber tracts is difficult by TBSS. We overcame this problem by outlining ROIs from directionally encoded FA images after recognition of the morphologically altered structures.

CONCLUSIONS

In 9 Turkish patients with 8 new mutations, diffusion alterations suggestive of widespread demyelination and axonal involvement, mainly of the pyramidal tracts, have been demonstrated in addition to thickening of TPF and interruption of the CST in the pons. These abnormalities may reflect tissue damage related to extensive alterations in mitochondrial dynamics because of loss of sarsin function and may explain a wide range of neurologic abnormalities in patients with ARSACS.

ACKNOWLEDGMENTS

The authors thank Damagen personnel for their support in the molecular studies, Sueda Turk (Bilkent University, Department of Electronics and Electronics Engineering) for contribution in data collection, Prof. Dr. Meral Topcu (Hacettepe University, Department of Pediatric Neurology) and Prof. Dr. Ersin Tan (Hacettepe University, Department of Neurology) for their contribution of patients.

REFERENCES

1. Van de Warrenburg BP, Sinke RJ, Kremer B. Recent advances in hereditary spinocerebellar ataxias. *J Neuropathol Exp Neurol* 2005;64:171–80
2. Bouhhal Y, Amouri R, El Euch-Fayeche G, et al. Autosomal recessive spastic ataxia of Charlevoix-Saguenay: an overview. *Parkinsonism Relat Disord* 2011;17:418–22
3. Parfitt DA, Michael GJ, Vermeulen EG, et al. The ataxia protein sarsin is a functional co-chaperone that protects against polyglutamine-expanded ataxin-1. *Hum Mol Genet* 2009;18:1556–65
4. Bouchard JP, Barbeau A, Bouchard R, et al. Autosomal recessive spastic ataxia of Charlevoix-Saguenay. *Can J Neurol Sci* 1978;5:61–69
5. Bouchard JP, Richter A, Mathieu J, et al. Autosomal recessive spastic ataxia of Charlevoix-Saguenay. *Neuromuscul Disord* 1998;8:474–79

6. Anheim M, Fleury M, Monga B, et al. **Epidemiological, clinical, paraclinical and molecular study of a cohort of 102 patients affected with autosomal recessive progressive cerebellar ataxia from Alsace, Eastern France: implications for clinical management.** *Neurogenetics* 2010;11:1–12
7. Martin MH, Bouchard JP, Sylvain M, et al. **Autosomal recessive spastic ataxia of Charlevoix-Saguenay: a report of MR imaging in 5 patients.** *AJNR Am J Neuroradiol* 2007;28:1606–08
8. Le Bihan D. **Looking into the functional architecture of the brain with diffusion MRI.** *Nat Rev Neurosci* 2003;4:469–80
9. Mori S, Zhang J. **Principles of diffusion tensor imaging and its applications to basic neuroscience research.** *Neuron* 2006;51:527–39
10. Gazulla J, Vela AC, Marin MA, et al. **Is the ataxia of Charlevoix-Saguenay a developmental disease?** *Med Hypotheses* 2011;77:347–52
11. Gazulla J, Benavente I, Vela AC, et al. **New findings in the ataxia of Charlevoix-Saguenay.** *J Neurol* 2012;259:869–78
12. Prodi E, Grisoli M, Panzeri M, et al. **Supratentorial and pontine MRI abnormalities characterize recessive spastic ataxia of Charlevoix-Saguenay. A comprehensive study of an Italian series.** *Eur J Neurol* 2013;20:138–46
13. Smith SM, Jenkinson M, Johansen-Berg H, et al. **Tract-based spatial statistics: voxelwise analysis of multi-subject diffusion data.** *Neuroimage* 2006;31:1487–505
14. Desserre J, Devos D, Sautière BG, et al. **Thickening of peripapillary retinal fibers for the diagnosis of autosomal recessive spastic ataxia of Charlevoix-Saguenay.** *Cerebellum* 2011;10:758–62
15. Vingolo EM, Di Fabio R, Salvatore S, et al. **Myelinated retinal fibers in autosomal recessive spastic ataxia of Charlevoix-Saguenay.** *Eur J Neurol* 2011;18:1187–90
16. Xie M, Wang Q, Wu TH, et al. **Delayed axonal degeneration in slow Wallerian degeneration mutant mice detected using diffusion tensor imaging.** *Neuroscience* 2011;197:339–47
17. Kim JH, Wu TH, Budde MD, et al. **Noninvasive detection of brainstem and spinal cord axonal degeneration in an amyotrophic lateral sclerosis mouse model.** *NMR Biomed* 2011;24:163–69
18. Gupta RK, Saksena S, Chandra A, et al. **Retrograde Wallerian degeneration of cranial corticospinal tracts in cervical spinal cord injury patients using diffusion tensor imaging.** *J Neurosci Res* 2008;86:2271–80
19. Liang Z, Zeng J, Zhang C, et al. **Longitudinal investigations on the anterograde and retrograde degeneration in the pyramidal tract following pontine infarction with diffusion tensor imaging.** *Cerebrovasc Dis* 2008;25:209–16
20. Guillery RW, Harting JK. **Structure and connections of the thalamic reticular nucleus: advancing views over half a century.** *J Comp Neurol* 2003;463:360–71
21. Takiyama Y. **Autosomal recessive spastic ataxia of Charlevoix-Saguenay.** *Neuropathology* 2006;26:368–75
22. Vermeer S, Meijer RP, Pijl BJ, et al. **ARSACS in the Dutch population: a frequent cause of early-onset cerebellar ataxia.** *Neurogenetics* 2008;9:207–14
23. Peyronnard JM, Charron L, Barbeau A. **The neuropathy of Charlevoix-Saguenay ataxia: an electrophysiological and pathological study.** *Can J Neurol Sci* 1979;6:199–203
24. García A, Criscuolo C, de Michele G, et al. **Neurophysiological study in a Spanish family with recessive spastic ataxia of Charlevoix-Saguenay.** *Muscle Nerve* 2008;37:107–10
25. Pandolfo M. **Friedreich's ataxia: clinical aspects and pathogenesis.** *Semin Neurol* 1999;19:311–21
26. Della Nave R, Ginestroni A, Tessa C, et al. **Brain white matter tracts degeneration in Friedreich ataxia. An in vivo MRI study using tract-based spatial statistics and voxel-based morphometry.** *Neuroimage* 2008;40:19–25
27. Pagani E, Ginestroni A, Della Nave R, et al. **Assessment of brain white matter fiber bundle atrophy in patients with Friedreich ataxia.** *Radiology* 2010;255:882–89
28. Melberg A, Dahl N, Hetta J, et al. **Neuroimaging study in autosomal dominant cerebellar ataxia, deafness, and narcolepsy.** *Neurology* 1999;53:2190–92
29. Shimazaki H, Takiyama Y, Honda J, et al. **Middle cerebellar peduncles and pontine T2 hypointensities in ARSACS.** *J Neuroimaging* 2013;23:82–85
30. Girard M, Larivière R, Parfitt DA, et al. **Mitochondrial dysfunction and Purkinje cell loss in autosomal recessive spastic ataxia of Charlevoix-Saguenay (ARSACS).** *Proc Natl Acad Sci U S A* 2012;109:1661–66
31. Johri A, Beal MF. **Mitochondrial dysfunction in neurodegenerative diseases.** *J Pharmacol Exp Ther* 2012;342:619–30
32. Bohanna I, Georgiou-Karistianis N, Sritharan A, et al. **Diffusion tensor imaging in Huntington's disease reveals distinct patterns of white matter degeneration associated with motor and cognitive deficits.** *Brain Imaging Behav* 2011;5:171–80
33. Stebbins GT, Murphy CM. **Diffusion tensor imaging in Alzheimer's disease and mild cognitive impairment.** *Behav Neurol* 2009;21:39–49
34. Richter AM, Ozgul RK, Poisson VC, et al. **Private SACS mutations in autosomal recessive spastic ataxia of Charlevoix-Saguenay (ARSACS) families from Turkey.** *Neurogenetics* 2004;5:165–70
35. Gücüyener K, Ozgül K, Paternotte C, et al. **Autosomal recessive spastic ataxia of Charlevoix-Saguenay in two unrelated Turkish families.** *Neuropediatrics* 2001;32:142–46
36. Mukherjee P, Chung SW, Berman JL, et al. **Diffusion tensor MR imaging and fiber tractography: technical considerations.** *AJNR Am J Neuroradiol* 2008;29:843–52

MR Imaging Features of Amyloid-Related Imaging Abnormalities

J. Barakos, R. Sperling, S. Salloway, C. Jack, A. Gass, J.B. Fiebach, D. Tampieri, D. Melançon, Y. Miaux, G. Rippon, R. Black, Y. Lu, H.R. Brashear, H.M. Arrighi, K.A. Morris, and M. Grundman



ABSTRACT

BACKGROUND AND PURPOSE: AD is one of the few leading causes of death without a disease-modifying drug; however, hopeful agents are in various phases of development. MR imaging abnormalities, collectively referred to as amyloid-related imaging abnormalities, have been reported for several agents that target cerebral A β burden. ARIA includes ARIA-E, parenchymal or sulcal hyperintensities on FLAIR indicative of parenchymal edema or sulcal effusions, and ARIA-H, hypointense regions on gradient recalled-echo/T2* indicative of hemosiderin deposition. This report describes imaging characteristics of ARIA-E and ARIA-H identified during studies of bapineuzumab, a humanized monoclonal antibody against A β .

MATERIALS AND METHODS: Two neuroradiologists with knowledge of imaging changes reflective of ARIA reviewed MR imaging scans from 210 bapineuzumab-treated patients derived from 3 phase 2 studies. Each central reader interpreted the studies independently, and discrepancies were resolved by consensus. The inter-reader κ was 0.76, with 94% agreement between neuroradiologists regarding the presence or absence of ARIA-E in individual patients.

RESULTS: Thirty-six patients were identified with incident ARIA-E (17.1%, 36/210) and 26 with incident ARIA-H (12.4%, 26/210); of those with incident ARIA-H, 24 had incident microhemorrhages and 2 had incident large superficial hemosiderin deposits.

CONCLUSIONS: In 49% of cases of ARIA-E, there was the associated appearance of ARIA-H. In treated patients without ARIA-E, the risk for incident blood products was 4%. This association between ARIA-E and ARIA-H may suggest a common pathophysiologic mechanism. Familiarity with ARIA should permit radiologists and clinicians to recognize and communicate ARIA findings more reliably for optimal patient management.

ABBREVIATIONS: A β = amyloid- β ; AD = Alzheimer disease; ARIA = amyloid-related imaging abnormalities; ARIA-E = amyloid-related imaging abnormalities associated with edema or effusion/exudate; ARIA-H = amyloid-related imaging abnormalities associated with hemosiderin deposition

AD remains a leading cause of morbidity and mortality without the availability of a disease-modifying agent. Although the cause of AD remains unclear, the amyloid hypothesis has been a leading postulate on which many therapies have been developed and are now in various phases of clinical evaluation. Several agents specifically designed to lower cerebral A β burden

have been associated with MR imaging abnormalities of the brain.¹⁻⁴ Reported MR imaging findings appear similar among various drugs, despite differences in the proposed mechanisms of action, indicating some commonality in effect. In this report, we specifically describe the imaging abnormalities associated with bapineuzumab, a humanized monoclonal antibody against cerebral A β .

Imaging findings reported with bapineuzumab have occurred in both phase 1 and 2 clinical studies and have typically been identified in asymptomatic patients undergoing routine scheduled MR imaging surveillance.^{1,5} These MR imaging findings

Received August 9, 2012; accepted after revision December 2.

From the California Pacific Medical Center (J.B.), San Francisco, California; Synarc (J.B., Y.M.), Newark, California; Brigham and Women's Hospital (R.S.), Massachusetts General Hospital, Harvard Medical School, Boston, Massachusetts; Warren Alpert Medical School of Brown University (S.S.), Providence, Rhode Island; Mayo Clinic (C.J.), Rochester, Minnesota; University Hospital Mannheim (A.G.), University of Heidelberg, Mannheim, Germany; Center for Stroke Research (J.B.F.), Charité, Berlin, Germany; NeuroRx Research (D.T., D.M.), Montreal, Quebec, Canada; Pfizer Inc (G.R., R.B.), Collegeville, Pennsylvania; Janssen Alzheimer Immunotherapy Research & Development, LLC (H.R.B., H.M.A., K.A.M., M.G.), South San Francisco, California; and Global Partners Inc (M.G.), Cambridge, Massachusetts.

This work was supported by Janssen Alzheimer Immunotherapy Research & Development, LLC, and Pfizer Inc. Michael Grundman was a paid consultant to Janssen Alzheimer Immunotherapy Research & Development, LLC, in the development of this article. Editorial support was provided by Lisette T. Arnaud, PhD, at Phase Five Communications Inc and was funded by Pfizer Inc and Janssen Alzheimer Immunotherapy Research & Development, LLC.

Paper previously presented at: Annual Meeting of the American Society of Neuroradiology and the Foundation of the ASNR Symposium, April 21–26, 2012; New York, New York; 12th International Stockholm/Springfield Symposium on Advances in Alzheimer Therapy, May 9–12, 2012; Stockholm, Sweden; and 36th European Society of Neuroradiology Annual Meeting, September 20–23, 2012; Edinburgh, Scotland.

Please address correspondence to Jerome Barakos, MD, California Pacific Medical Center, 2333 Buchanan St, San Francisco, CA 94115; e-mail: barakosmd@gmail.com

<http://dx.doi.org/10.3174/ajnr.A3500>

Table 1: Clinical characteristics of ARIA

ARIA Component	Primary Diagnostic Imaging Sequence	Nature of Leakage Products	Location of Increased Vascular Permeability	
			Parenchyma	Leptomeninges
ARIA-E	FLAIR	Proteinaceous fluid	Vasogenic edema	Sulcal effusion/exudate
ARIA-H	GRE/T2*	Heme products	Microhemorrhage (hemosiderin deposits <10 mm or large hemosiderin deposits ≥10 mm)	Superficial hemosiderin deposits

Note:—GRE indicates gradient recalled-echo.

were characteristic of transiently extravasated fluid within the brain parenchyma and were initially described as vasogenic edema among AD clinical specialists.⁵ With time, a more diverse set of imaging changes was noted that could not be accurately described by the term “vasogenic edema.” This spectrum of imaging findings included parenchymal edema and ranged from sulcal effusions to the appearance of associated blood-degradation products. In response to this spectrum of observations, a recent expert workgroup suggested the comprehensive term “ARIA,” because the imaging findings encountered are thought to be pathophysiologically related to leakage of intravascular contents due to shifts in amyloid.⁶ The designation “ARIA” has been further subdivided into ARIA-E and ARIA-H (Table 1). ARIA-E has been applied to FLAIR signal abnormalities thought to represent parenchymal edema and/or sulcal effusions (ie, exudates), whereas ARIA-H refers to hemosiderin deposition detected on gradient recalled-echo/T2*-weighted sequences believed to represent blood-degradation products, including microhemorrhages (<10 mm) and larger superficial hemosiderin deposits (≥10 mm). The purpose of this report was to describe the imaging characteristics of ARIA.

MATERIALS AND METHODS

This imaging report is derived from the source population of 210 patients with AD treated with bapineuzumab from 3 phase 2 studies, the methodology of which has been published.⁷ In brief, 2 studies were blinded, randomized clinical trials, whereas the third was an open-label trial in which all patients were eligible for bapineuzumab. Key inclusion criteria consisted of a diagnosis of probable AD with a Mini-Mental State Examination score of 16–26. Key exclusion criteria were clinically significant neurologic diseases other than AD. Patients were additionally excluded if they had a screening-visit brain MR imaging scan indicative of >1 microhemorrhage or any significant abnormality including but not limited to evidence of a single prior hemorrhage of >1 cm³, multiple lacunar infarcts, or evidence of a single prior infarct of >1 cm³. There were no specific exclusionary criteria regarding baseline senescent white matter disease. At initial study enrollment, patients were randomized to bapineuzumab or placebo and received the study drug every 13 weeks for 18 months. Per study protocol, safety MR imaging was performed at baseline and at 13-week intervals, 6 weeks after each infusion. A uniform MR imaging protocol was used in this multisite study and included FLAIR, gradient recalled-echo/T2*, DWI, T2, and 3D T1-weighted sequences on 1.5T systems. All MR imaging machines were calibrated using the American College of Radiology phantom at baseline and at 4-month intervals according to specifications made by the American College of Radiology MRI Accreditation Program. Unscheduled imaging was also performed as

dictated by any significant change in clinical symptoms or as follow-up to monitor and assess ongoing ARIA-E; 2572 MR imaging scans were obtained on the 210 bapineuzumab-treated study participants.

All scans were reviewed and interpreted contemporaneously by local MR imaging readers at each of the 30 clinical study sites in the United States. Subsequently, all examinations were centrally reviewed by 2 neuroradiologists with specific knowledge of the range and spectrum of imaging changes reflective of ARIA. Central readers, blinded with respect to the study arm, placebo or drug, and *Apolipoprotein ε4* status, reviewed all imaging studies in serial order, having baseline and serial imaging available for comparison. Patients were identified as having incident ARIA-E by the detection of new areas of either parenchymal or sulcal FLAIR hyperintensity, in the absence of imaging features that would suggest other pathologies such as ischemia and neoplasm. Readers recorded lesion location (cerebrum versus cerebellum) by hemisphere (right or left) and by lobe involved (frontal, parietal, occipital, and/or temporal). Incident ARIA-H was determined by the detection of any blood products noted as new hypointense lesions on the blood-sensitive gradient recalled-echo/T2*-weighted imaging sequence. Incident hypointense lesions were characterized by size and location, namely, whether they were microhemorrhages (<10 mm in diameter) or large hemosiderin deposits (≥10 mm). ARIA-H lesion localization was recorded by using a similar map as outlined above. Each central reader interpreted the studies independently, and discrepancies were resolved by consensus. The inter-reader κ was 0.76, with 94% agreement between neuroradiologists regarding the presence or absence of ARIA-E in individual patients.

RESULTS

Thirty-six patients were identified with incident ARIA-E (17.1%, 36/210), and 26, with incident ARIA-H (12.4%, 26/210); of those with incident ARIA-H, 24 had incident microhemorrhages and 2 had incident large superficial hemosiderin deposits (Table 2). The most commonly encountered MR imaging feature of ARIA-E at detection was a region of sulcal FLAIR hyperintensity in 78% (28/36) of cases, referred to as ARIA-E effusion/exudate (Fig 1). Of these, 13 also had some degree of adjacent parenchymal FLAIR hyperintensity, with parenchymal involvement described as ARIA-E edema (Fig 2). Parenchymal hyperintensity without sulcal hyperintensity was observed in 8 patients. Parenchymal involvement ($n = 21$) was always coupled with negative findings on a DWI scan, with resolution of the FLAIR signal on serial imaging (Fig 3). Of the 36 cases of ARIA-E identified by the central readers, 15 (42%) were not identified by the local readers.

Gadolinium was administered in 5 of the 36 patients in whom ARIA-E was detected. In most cases, there was no significant pa-

Table 2: Results

ARIA Type: Incidence	Location: Isolated Leptomeningeal	Location: Isolated Parenchymal	Location: Combined
ARIA-E: 36/210 (17%)	ARIA-E: sulcal effusion: 15/36 (42%)	ARIA-E: parenchymal edema: 8/36 (22%)	ARIA-E: effusion and edema combined: 13/36 (36%)
ARIA-H: 26/210 (12.4%)	ARIA-H: superficial hemosiderin deposit: 2/26 (8%)	ARIA-H: parenchymal microhemorrhage: 24/26 (92%)	

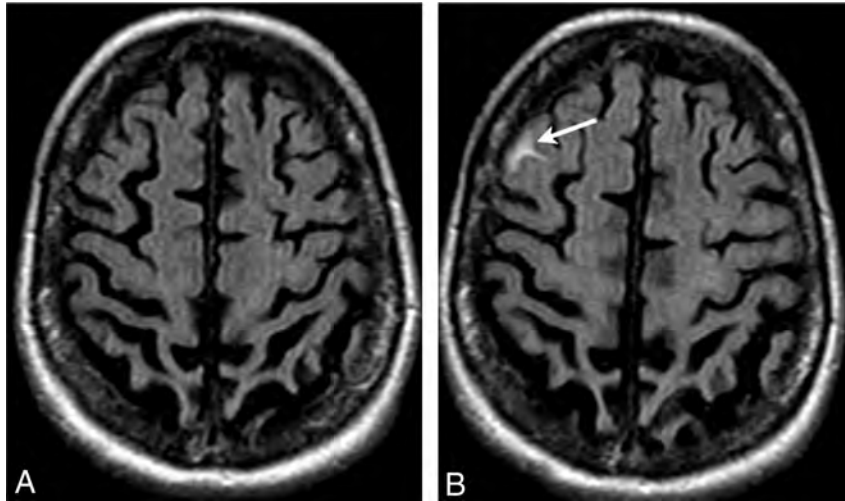


FIG 1. ARIA-E (effusion); sulcal FLAIR hyperintensity. FLAIR MR imaging at baseline (A) and week 19 (B). On the follow-up surveillance scan (week 19), sulcal FLAIR hyperintensity developed in the right frontal region (arrow). No associated signal abnormality was identified on other imaging sequences, including T1 and gradient recalled-echo/T2* imaging (not shown). Because the imaging appearance mimicked that of a subarachnoid hemorrhage, CT and lumbar puncture were performed, both of which had normal findings, revealing no evidence of blood products.

parenchymal enhancement other than a mild prominence in cortical vascular enhancement, as would be expected in any nonspecific parenchymal or leptomeningeal edematous process. Of the patients with ARIA-E, 35 had acceptable gradient recalled-echo/T2* images at study enrollment for the assessment of incident ARIA-H; of these, 49% (17/35) had incident ARIA-H microhemorrhages (Fig 4). One patient with ARIA-E did not have an acceptable pretreatment baseline gradient recalled-echo/T2*. However, timing was not always simultaneous, with 24% (4/17) of incident ARIA-H microhemorrhages identified on an image before first identification of ARIA-E and 29% (5/17) of incident ARIA-H microhemorrhages identified on an image after the first identification. Seven patients developed incident ARIA-H microhemorrhages without ARIA-E (4%, 7/174). In 2 other patients with ARIA-E, ARIA-H, as large superficial hemosiderin deposits, also developed during follow-up (Fig 5). Two-thirds (69%, 25/36) of ARIA-E cases were identified after the first or second bapineuzumab infusion, corresponding to the imaging at study weeks 6 and 19, respectively. Before identification of ARIA-E, the mean number of infusions was 2.4 (range, 1–7; median, 1.7). The actual duration of ARIA-E was difficult to accurately define because imaging was routinely performed at 13-week intervals. However, occasional unscheduled examinations were performed at shorter intervals to monitor ARIA-E evolution for cases detected during the clinical study. Given these limitations, follow-up imaging revealed ARIA-E at a median duration of 16 weeks.

With ARIA-E edema ($n = 21$), cerebral parenchymal involvement was unilateral in 67% (14/21) and bilateral in 33% (7/21) of

patients. ARIA-E edema was noted in the cerebellum in 4 patients, of whom 2 also had cerebral involvement and involvement in 2 was isolated to the posterior fossa. Lesion severity ranged from subtle to nearly holohemispheric involvement (Fig 4) and, as reported in Sperling et al,⁷ was associated with both *Apolipoprotein ε4* allele status and increasing drug dosage. However, no specific baseline clinical or imaging features were predictive of the development of ARIA. In particular, no correlation was identified between patients with microhemorrhage at baseline and subsequent development of ARIA.

When tabulated by regions of lobar involvement, ARIA-E edema was distributed as follows: occipital lobe, 48% ($n = 10$); frontal lobe, 43% ($n = 9$); temporal lobe, 29% ($n = 6$); cerebellum, 19% ($n = 4$); and parietal lobe, 14% ($n = 3$). (Total was $>100%$ [$n = 21$] because a single case may have contributed to multiple regions depending on the extent of involvement.)

DISCUSSION

In several clinical AD studies with agents directed at modifying cerebral A β burden, including bapineuzumab studies, hyperintense FLAIR signal abnormalities have been detected on brain MR imaging and are often associated with the development of blood products.^{1,5} This constellation of imaging features is in keeping with the hypothesis of altered vascular permeability,^{6,8} which is now recognized as part of the ARIA spectrum. ARIA-E specifically refers to associated parenchymal edema and sulcal effusions, whereas ARIA-H refers to hemosiderin deposits from blood products within the parenchyma or leptomeninges. Although the focus of this report is on imaging features of ARIA associated with therapeutic amyloid-modifying agents, similar imaging findings have been noted to occur spontaneously, such as in cerebral amyloid angiopathy.^{9–15}

Therapy-related ARIA should be a diagnostic consideration when specific imaging findings are encountered in the appropriate clinical setting—namely, a patient being treated with an amyloid-modifying agent with exclusion of other underlying pathologies. For the most part, clinical history will be of value as the patient will typically be asymptomatic, imaged as part of routine drug study surveillance (ie, safety scan).

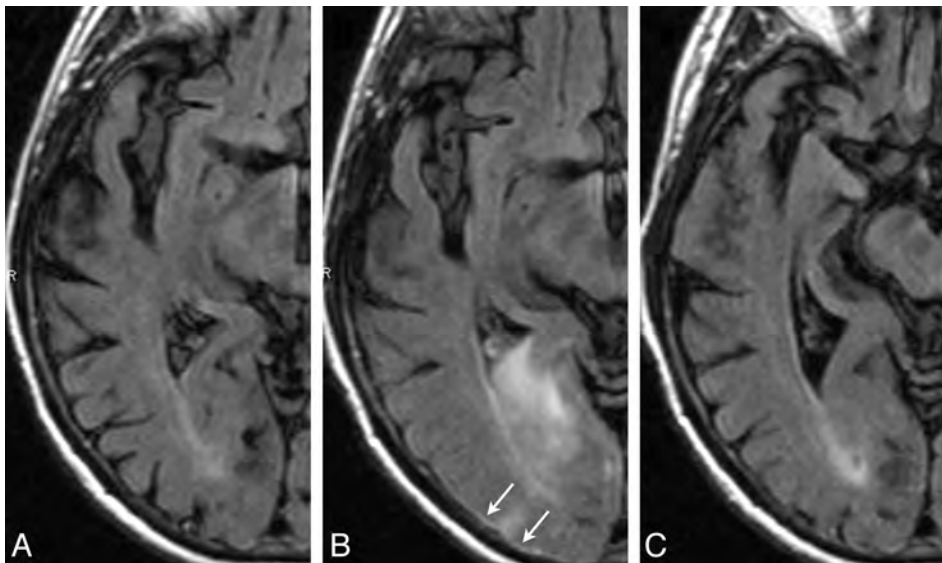


FIG 2. ARIA-E (edema and effusion); parenchymal and sulcal FLAIR hyperintensity. FLAIR sequences at baseline (A), week 19 (B), and week 32 (C). By week 19 (6 weeks after the second dose of bapineuzumab), a zone of cortical swelling, sulcal effacement, and parenchymal hyperintensity has developed in the right temporal-occipital lobe. A small sulcal effusion and faint overlying linear leptomeningeal hyperintensity (arrows) help define the area of abnormality. By week 32, these findings have largely resolved. As is typically the case with bapineuzumab-related ARIA, the patient remained asymptomatic throughout all imaging time points.

Pathophysiology

Potential mechanisms giving rise to ARIA in association with agents that target amyloid removal, including immunotherapy agents such as bapineuzumab, remain to be fully explained. However, both imaging and histopathologic studies have demonstrated that immunotherapies may reduce amyloid burden and are associated with the development of ARIA-type changes.¹⁶ Additionally, prior reports indicate that the risk for ARIA-E is increased in *Apolipoprotein ε4* allele carriers and is also associated with an increasing dose of bapineuzumab.⁵ These findings are supported by studies indicating that vascular $A\beta$ accumulation and clearance are involved.^{8,17} Studies in PDAPP mice have shown that the murine version of bapineuzumab (3D6) binds and clears vascular $A\beta$ in a dose-dependent manner and is associated with a transient increase in vascular permeability.¹⁸ Hypothetically, bapineuzumab may have a similar action on vascular $A\beta$ in some patients, resulting in transient vascular leakage of fluid, protein, and/or red cells. The suggestion that ARIA is related to increases in vascular permeability is also supported by the frequent co-occurrence of ARIA-E and ARIA-H, albeit not always with simultaneous onset, which indicates that these are likely related phenomena. Specifically, in review of the phase 2 bapineuzumab data, incident ARIA-H was detected in association with 49% of patients with ARIA-E but in only 4% of patients without ARIA-E.

Vascular $A\beta$ burden is highest in the cerebral cortex and leptomeninges,¹⁹ which may account for the predilection of ARIA to occur in these areas. Also of note are reports of spontaneous ARIA-like phenomena in patients with cerebral amyloid angiopathy, described as cerebral amyloid angiopathy-related inflammation, and in AD patients without identifiable underlying cerebral amyloid angiopathy on MR imaging.⁹⁻¹⁵ An underlying endovascular inflammatory component has been described in

this condition and may provide an additional potential mechanism involved with the ARIA phenomenon. Nevertheless, these findings indicate that shifts in cerebral amyloid accumulation may occur naturally, occasionally resulting in increased vascular permeability or in overwhelmed transport systems and leading to edema and sulcal effusions.

ARIA-E (Edema versus Effusions)

The parenchymal and sulcal forms of ARIA-E are distinguished by differences in anatomic location (intra-axial versus extra-axial, respectively) but are similar in that both are transient in nature and not associated with restricted (reduced) diffusion abnormalities. The imaging features of ARIA-E edema are consistent with parenchymal edema and presumably reflect leakage of intravascular fluid and proteins into the parenchymal interstitial compartment due to the compromise of vessel-wall integrity.

In contrast to the parenchymal pattern of ARIA-E edema, sulcal FLAIR hyperintensities representing extra-axial effusions/exudate were referred to as ARIA-E effusions. In these cases, findings were consistent with proteinaceous fluid confined to the subarachnoid/leptomeningeal space, with the resulting effect on T1 and T2 relaxation yielding a corresponding hyperintensity on FLAIR imaging. Although isolated effusions were noted, especially in the early phases of ARIA-E, progression of these effusions commonly was associated with some degree of contiguous parenchymal FLAIR hyperintensity (ARIA-E edema).

Imaging Considerations

Given that imaging features of ARIA-E comprised parenchymal edema and/or sulcal proteinaceous effusions, identification was most conspicuous on MR imaging when one used a T2-weighted FLAIR sequence. In addition, sulcal effusions were entirely obscured with proton-attenuation or T2-weighted imaging due to the T2 hyperintensity of CSF. As such, FLAIR imaging is essential in detecting ARIA-E effusions. As expected, even the parenchymal form of ARIA-E was routinely visualized with improved conspicuity by using FLAIR sequences in contrast to proton-attenuation or T2-weighted imaging.

Differentiating ARIA-E from Other Pathologies

As with routinely encountered parenchymal or sulcal FLAIR hyperintensities occurring in clinical practice, the MR imaging features of ARIA-E are nonspecific and may reflect a wide variety of pathologic conditions. Thus, in the setting of a patient being

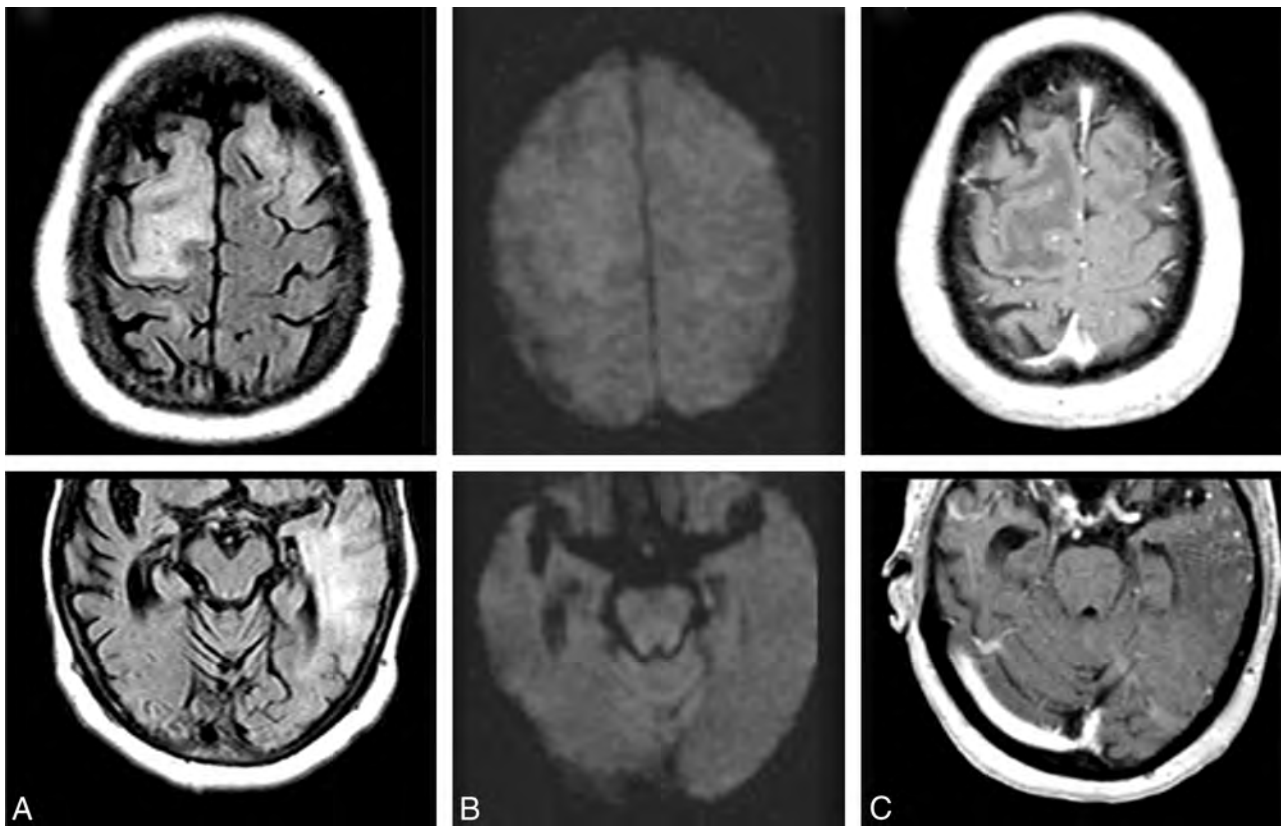


FIG 3. ARIA-E (edema); week 19 parenchymal FLAIR hyperintensity. Week 19 FLAIR (A) and corresponding DWI (B) and week 19 gadolinium (C). On the surveillance scan for week 19 (A), several large regions of parenchymal edema develop, principally in the bifrontal and left temporal regions, which resolve on follow-up (not shown). Week 19 DWI reveals minimal T2 shine-through (B), but no ADC abnormality (not shown). With gadolinium, there is no frank enhancement with only mild prominence of overlying cortical vasculature, in keeping with nonspecific cerebral swelling (C).

treated with an amyloid-modifying agent, any newly detected region of FLAIR hyperintensity must be fully characterized to exclude other potential pathologies. The parenchymal FLAIR hyperintensity of ARIA-E edema may be mimicked by ischemia, neoplasm/metastatic disease, cerebritis, and so forth. As such, DWI is essential to evaluate ischemia, and gadolinium administration is important in excluding an underlying source of parenchymal edema such as malignancy and infection/cerebritis. In contrast, the leptomeningeal FLAIR hyperintensity of ARIA-E effusion may be mimicked by various conditions including subarachnoid hemorrhage, meningitis, and even inadequate CSF-nulling artifacts.^{20,21} In fact, in the first few patients in whom sulcal effusions were encountered, because the appearance of the effusion precisely mimics imaging features of a subarachnoid hemorrhage, CT and lumbar puncture were performed. Such testing consistently confirmed lack of subarachnoid hemorrhage as a source of these imaging findings. Additionally, in several of the initial cases of ARIA-E, gadolinium was administered. These contrast-enhanced MR images typically revealed little to no enhancement, with mild overlying vascular congestion, as expected in any edematous cortical process.

MR imaging abnormalities characteristic of ARIA-E are very similar to posterior reversible encephalopathy syndrome. Both conditions are usually reversible, demonstrating parenchymal and leptomeningeal involvement, with potential for development of blood products. Additionally, both conditions reveal a predi-

lection for the occipital lobes, often more symmetric with posterior reversible encephalopathy syndrome. Although isolated leptomeningeal involvement and milder cases seem more common with ARIA-E than in posterior reversible encephalopathy syndrome, this difference is most likely due to matters of timing. Specifically, cases of ARIA-E were detected early in the disease course due to routine surveillance imaging. During this early phase of ARIA-E, leptomeningeal involvement predominates. In contrast, patients identified with posterior reversible encephalopathy syndrome often come to attention because of frank neurologic symptoms and dysfunction, including seizures and coma and thus are at a more severe phase of their disease, with parenchymal involvement overshadowing the leptomeningeal disease. Pathophysiologic underpinnings of increased vascular permeability of both ARIA-E and posterior reversible encephalopathy syndrome are thought to be very similar, thus explaining the parallel imaging features of these conditions.

In summary, ARIA-E should be a highly likely diagnostic consideration when there is evidence of parenchymal edema and/or sulcal FLAIR hyperintensity, identified in patients recently exposed to an amyloid-modifying agent and in whom no evidence of any other inciting cause or underlying lesion can be found.

ARIA-H

In 49% of cases of ARIA-E detected on MR imaging, there was the associated appearance of small amounts of blood degradation prod-

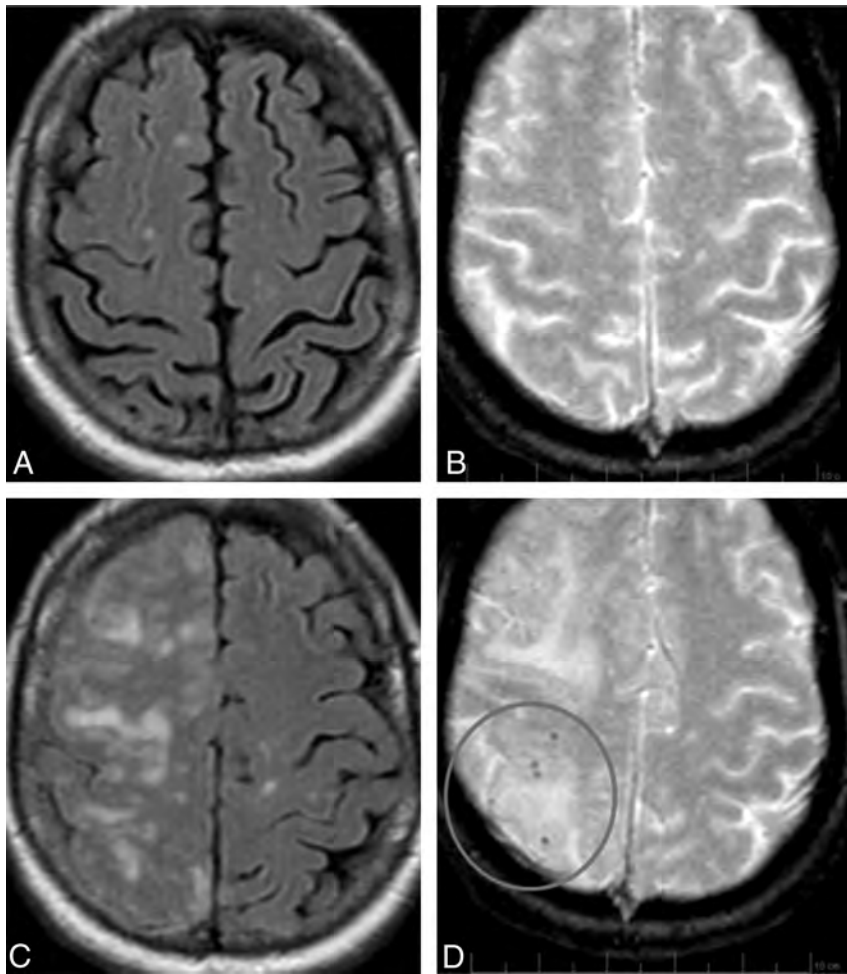


FIG 4. ARIA-E (edema) with incident ARIA-H (microhemorrhages). FLAIR and corresponding gradient recalled-echo/T2* sequences of the same patient, at baseline (A and B) and week 19 (C and D). By week 19 (6 weeks after the second dose of bapineuzumab), significant right-hemispheric edema has developed. As is characteristic of ARIA-E, despite the extensive parenchymal changes, DWI and ADC findings remained normal (not shown), confirming these findings as reflecting vasogenic as opposed to cytotoxic edema. On the corresponding gradient recalled-echo/T2* images, there is concomitant development of several punctate microhemorrhages in the right parietal region (circle). On subsequent imaging, the cerebral edema resolved while the microhemorrhages remained stable (not shown). In general, the severity of ARIA changes was associated with both *Apolipoprotein ε4* allele status and drug dosage. As such, this patient was an *Apolipoprotein ε4* homozygote and in the highest drug-dose arm.

ucts (ARIA-H). In treated patients without ARIA-E, the risk for incident blood products was 4%. Association between ARIA-E and ARIA-H may suggest a common pathophysiologic mechanism—namely, increased vascular permeability to the point at which both fluid and red blood cells cross the vessel wall. These blood products were most commonly microhemorrhages, defined as punctate parenchymal foci of signal void on gradient recalled-echo/T2*-weighted images, measuring <10 mm in diameter. Less commonly, larger superficial foci of blood products were detected measuring ≥ 10 mm in diameter (ie, superficial hemosiderin deposits).

Overall, these blood-degradation products were petechial in nature and, as with microhemorrhages, only identifiable as signal voids on gradient recalled-echo/T2*-weighted images. Without such sequences, these minute amounts of blood product cannot be detected because they are invisible on T1, T2, and FLAIR imaging due to use of rephasing pulse gradients. This feature

highlights the importance of using gradient recalled-echo/T2*-weighted sequences for surveillance of ARIA-H.

A review of the phase 2 bapineuzumab data did not identify an associated risk of the presence of microhemorrhages from the pretreatment baseline image with the subsequent development of ARIA-E. However, lack of an association may reflect study enrollment criteria, whereby patients with ≥ 2 microhemorrhages were excluded. As such, the hypothesis of such a risk requires further evaluation because the observed association of ARIA-E with an increasing *Apolipoprotein ε4* allele number suggests that an increased amyloid burden relating to cerebral amyloid angiopathy underlies various proposed mechanisms in the development of ARIA-E. Both AD and cerebral amyloid angiopathy share a common neuropathology relating to the deposition of $A\beta$, which affects arterial wall integrity and interference with perivascular drainage pathways. In this regard, it is interesting to note the imaging similarities between cerebral amyloid angiopathy-related inflammation¹²⁻¹⁵ and ARIA-E associated with amyloid-modifying agents. Both conditions may reveal asymmetric, patchy, or confluent FLAIR hyperintense lesions with little or no enhancement after gadolinium administration and with imaging features suggesting noncytotoxic edema on DWI sequences. Additionally, in both conditions, gradient recalled-echo/T2*-weighted images may show associated foci of parenchymal and leptomeningeal microhemorrhages, more consistently in cerebral amyloid angiopathy-related inflammation though a case without microhemorrhages has been proposed.¹¹

Given that compromise of both arterial wall integrity and perivascular pathways is a proposed mechanism in the development of ARIA, eliminating patients with frank imaging features of cerebral amyloid angiopathy (eg, evidence of numerous parenchymal or leptomeningeal microhemorrhages) is prudent. Current FDA guidelines for enrolling patients in studies assessing amyloid-modifying agents recommend excluding patients with ≥ 5 microhemorrhages and any evidence of siderosis or prior parenchymal hemorrhage, all of which are potential imaging features that may be reflective of underlying cerebral amyloid angiopathy.

Given the ARIA imaging features outlined, an ARIA surveillance scanning protocol is recommended. Minimum surveillance imaging for ARIA should consist of FLAIR, gradient recalled-echo/T2*, and DWI. FLAIR and gradient recalled-echo/T2*

Given the ARIA imaging features outlined, an ARIA surveillance scanning protocol is recommended. Minimum surveillance imaging for ARIA should consist of FLAIR, gradient recalled-echo/T2*, and DWI. FLAIR and gradient recalled-echo/T2*

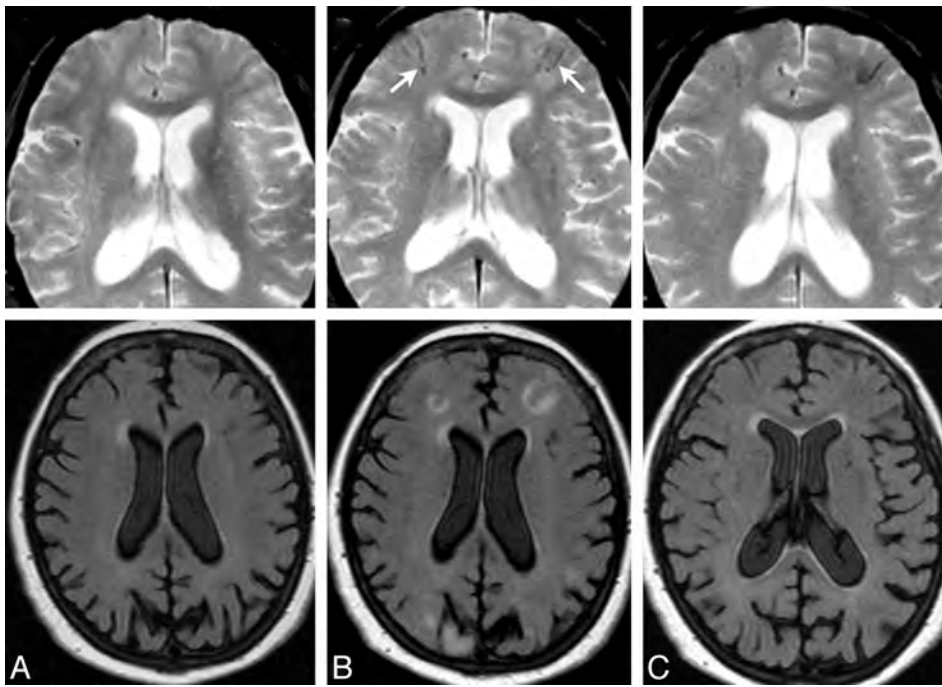


FIG 5. ARIA-E (edema) with incident ARIA-H (superficial hemosiderin deposits). Gradient recalled-echo/T2* and corresponding FLAIR sequences from the same patient, at baseline (A), week 19 (B), and week 28 (C). By week 19 (B), several regions of parenchymal edema have developed, including bifrontal regions and the right parieto-occipital lobe. On the corresponding gradient recalled-echo/T2* images, by week 19, there is concomitant development of several superficial linear areas of blood-degradation products (arrows) in the bifrontal regions (≥ 10 mm). By week 28, the FLAIR changes relating to ARIA-E have resolved, with blood products re-demonstrated.

provide optimal detection of ARIA-E and ARIA-H, respectively. When a new area of parenchymal FLAIR hyperintensity is detected, DWI allows the evaluation of cytotoxic edema. T1 has a limited role, but in clinical trials when acquired by using 3D technique, it allows hippocampal volumetric calculations. Finally, additional imaging sequences such as gadolinium enhancement should be performed at the discretion of the radiologist when further lesion characterization is needed.

CONCLUSIONS

A spectrum of MR imaging features has been described and designated as ARIA, with 2 subtypes, ARIA-E and ARIA-H, which are associated with several therapeutic agents directed at modification of amyloid burden in the treatment of AD. Familiarity with these findings will allow MR imaging readers to approach such imaging studies with increased diagnostic sensitivity and specificity, ensuring that treating clinicians are aware of potential changes reflected on imaging studies and allowing them to properly manage drug administration.

ACKNOWLEDGMENTS

We acknowledge and thank all participating patients and their caregivers, as well as investigators. Additionally, we thank Lorna Fang, Janssen Alzheimer Immunotherapy Research & Development, LLC, for help in statistical programming.

Disclosures: Jerome Barakos—UNRELATED: Consultancy: Synarc, Janssen, Pfizer, Comments: consultant to Synarc, an imaging clinical research organization that helps manage the imaging aspect of clinical trials for pharmaceutical companies including Elan, Janssen, and Pfizer, Payment for Development of Educational Presentations:

Janssen, Pfizer, Comments: helped in developing educational materials for Medscape on behalf of Janssen and Pfizer. Reisa Sperling—RELATED: Grant: Janssen,* Comments: This work was conducted as part of a phase 2 study; we were a clinical site, Consulting Fee or Honorarium: Janssen, Pfizer, Comments: a paid consultant in the past for Janssen and Pfizer, but not in 2012, Support for Travel to Meetings for the Study or Other Purposes: Janssen, Pfizer, Comments: I have been paid to speak at meetings in 2011, UNRELATED: Consultancy: Merck, Eisai, Satori, Kirin, Roche, Janssen, Pfizer, Comments: consulted for multiple companies developing drugs for AD, Payment for Lectures (including service on Speakers Bureaus): Janssen, Pfizer, Lilly, Comments: in 2011, Payment for Development of Educational Presentations: Janssen, Comments: in 2011, I was paid to help develop educational materials. Stephen Salloway—RELATED: Grant: Janssen Alzheimer Immunotherapy,* Pfizer,* Consulting Fee or Honorarium: Janssen Alzheimer Immunotherapy, Pfizer, Elan, Support for Travel to Meetings for the Study or Other Purposes: Janssen Alzheimer Immunotherapy, Pfizer, Elan, UNRELATED: Consultancy: Bristol-Myers Squibb (BMS), Avid, Baxter, Bayer, Sanofi, Lilly, Grants/Grants Pending: BMS,* Avid,* Genentech,* Baxter,* GE Healthcare,* Merck,* Payment for Development of Educational Presentations: Janssen Alzheimer Immunotherapy, Travel/Accommodations/Meeting Expenses Unrelated to Activities Listed: BMS, Baxter, Bayer, Sanofi. Clifford Jack—RELATED: Grant: National Institutes of Health,* Consulting Fee or Honorarium: Janssen,* Bristol-Meyer-Squibb,* Johnson & Johnson.* Achim Gass—RELATED: Consulting Fee or Honorarium: Pfizer/Janssen Advisory Board member, Payment for Lectures (including service on Speakers Bureau): Bayer Schering, Biogen Idec, Merck Serono, Novartis, Teva Neurosciences. Jochen B. Fiebach—UNRELATED: Consultancy: Wyeth, Novartis, BMS, Comments: central assessment of cerebral MRI examinations, Payment for Development of Educational Presentations: Biolumaging, Comments: introduction in neuroimaging. Donatella Tampieri—RELATED: Consulting Fee or Honorarium: NeuroRx, Comments: consulting in MRI. Yves Miaux—UNRELATED: Consultancy: Synarc. Gregory Rippon—UNRELATED: Employment: Pfizer, Comments: paid employee of Pfizer Inc, Stock/Stock Options: Pfizer, Comments: presently own stock and have received stock options as an employee of Pfizer Inc. Ronald Black—Employment: Pfizer, Comments: full-time employee of Pfizer, a sponsor of this study, Stock/Stock Options: Pfizer, Comments: stock and stock options in Pfizer. Yuan Lu—Employment: Janssen Alzheimer Immunotherapy. H. Robert Brashear—RELATED: Other: Janssen Alzheimer Immunotherapy, UNRELATED: Employment, Stock/Stock Options, Other: Janssen Alzheimer Immunotherapy, Comments: I am an employee of Janssen Alzheimer Immunotherapy, the cosponsor company who conducted the clinical research studies for which the MR images in the manuscript were obtained and assessed (I also received stock and stock options as an employee). H. Michael Arrighi—RELATED: Other: Janssen Alzheimer Immunotherapy, Comments: employee of Janssen Alzheimer Immunotherapy, a sponsor of the work, UNRELATED: Employment: Janssen Alzheimer Immunotherapy, Stock/Stock Options: Elan Pharmaceuticals, Comments: Elan owns 49.9% of Janssen Alzheimer Immunotherapy, Travel/Accommodations/Meeting Expenses Unrelated to Activities Listed: Janssen Alzheimer Immunotherapy, Other: Janssen Alzheimer Immunotherapy. Kristen A. Morris—UNRELATED: Employment: I am a Janssen Alzheimer Immunotherapy employee. Michael Grundman—RELATED: Consulting Fee or Honorarium, Payment for Writing or Reviewing the Manuscript: Janssen Alzheimer Immunotherapy, UNRELATED: Consultancy, Employment: Janssen Alzheimer Immunotherapy. *Money paid to the institution.

REFERENCES

- Black RS, Sperling RA, Safirstein B, et al. A single ascending dose study of bapineuzumab in patients with Alzheimer disease. *Alzheimer Dis Assoc Disord* 2010;24:198–203

2. Sperling R, Bronen R, Greenberg S, et al. **Three cases of apparent vasogenic edema (VE) from a phase 2 clinical trial of the gamma secretase inhibitor BMS-708163 in patients with mild-to-moderate AD.** *Alzheimers Dement* 2011;7(suppl):S377
3. Doody R. **Results from independent analyses of the EXPEDITION (solanezumab) study data conducted by the Alzheimer's Disease Cooperative Study (ADCS).** In: *Proceedings of the Annual Meeting of The American Neurological Association*, Boston, Massachusetts. October 7–9, 2012
4. Ostrowitzki S, Deptula D, Thurffjell L, et al. **Mechanism of amyloid removal in patients with Alzheimer disease treated with gantenezumab.** *Arch Neurol* 2012;69:198–207
5. Salloway S, Sperling R, Gilman S, et al. **A phase 2 multiple ascending dose trial of bapineuzumab in mild to moderate Alzheimer disease.** *Neurology* 2009;73:2061–70
6. Sperling RA, Jack CR Jr, Black SE, et al. **Amyloid-related imaging abnormalities in amyloid-modifying therapeutic trials: recommendations from the Alzheimer's Association Research Roundtable Workgroup.** *Alzheimers Dement* 2011;7:367–85
7. Sperling R, Salloway S, Brooks DJ, et al. **Amyloid-related imaging abnormalities in patients with Alzheimer's disease treated with bapineuzumab: a retrospective analysis.** *Lancet Neurol* 2012;11:241–49
8. Boche D, Zotova E, Weller RO, et al. **Consequence of Abeta immunization on the vasculature of human Alzheimer's disease brain.** *Brain* 2008;131(pt 12):3299–310
9. Eng JA, Frosch MP, Choi K, et al. **Clinical manifestations of cerebral amyloid angiopathy-related inflammation.** *Ann Neurol* 2004;55:250–56
10. Scolding NJ, Joseph F, Kirby PA, et al. **Abeta-related angiitis: primary angiitis of the central nervous system associated with cerebral amyloid angiopathy.** *Brain* 2005;128(pt 3):500–15
11. Carlson C, Estergard W, Oh J, et al. **Prevalence of asymptomatic vasogenic edema in pretreatment Alzheimer's disease cohorts from phase 3 trials of semagacestat and solanezumab.** *Alzheimers Dement* 2011;7:396–401
12. Oh U, Gupta R, Krakauer JW, et al. **Reversible leukoencephalopathy associated with cerebral amyloid angiopathy.** *Neurology* 2004;62:494–97
13. Kinnecom C, Lev MH, Wendell L, et al. **Course of cerebral amyloid angiopathy-related inflammation.** *Neurology* 2007;68:1411–16
14. Savoiardo M, Erbetta A, Storchi G, et al. **Case 159: cerebral amyloid angiopathy-related inflammation.** *Radiology* 2010;256:323–27
15. Sakaguchi H, Ueda A, Kosaka T, et al. **Cerebral amyloid angiopathy-related inflammation presenting with steroid-responsive higher brain dysfunction: case report and review of the literature.** *J Neuroinflammation* 2011;8:116
16. Rinne JO, Brooks DJ, Rossor MN, et al. **11C-PiB PET assessment of change in fibrillar amyloid-beta load in patients with Alzheimer's disease treated with bapineuzumab: a phase 2, double-blind, placebo-controlled, ascending-dose study.** *Lancet Neurol* 2010;9:363–72
17. Weller RO, Subash M, Preston SD, et al. **Perivascular drainage of amyloid-beta peptides from the brain and its failure in cerebral amyloid angiopathy and Alzheimer's disease.** *Brain Pathol* 2008;18:253–66
18. Schroeter S, Khan K, Barbour R, et al. **Immunotherapy reduces vascular amyloid-beta in PDAPP mice.** *J Neurosci* 2008;28:6787–93
19. Vinters HV. **Cerebral amyloid angiopathy: a critical review.** *Stroke* 1987;18:311–24
20. Filippi CG, Ulug AM, Lin D, et al. **Hyperintense signal abnormality in subarachnoid spaces and basal cisterns on MR images of children anesthetized with propofol: new fluid-attenuated inversion recovery finding.** *AJNR Am J Neuroradiol.* 2001;22:394–99
21. Stuckey SL, Goh TD, Heffernan T, et al. **Hyperintensity in the subarachnoid space on FLAIR MRI.** *AJR Am J Roentgenol* 2007;189:913–21

Role of Semantic Paradigms for Optimization of Language Mapping in Clinical fMRI Studies

D. Zacà, S. Jarso, and J.J. Pillai

ABSTRACT

BACKGROUND AND PURPOSE: The optimal paradigm choice for language mapping in clinical fMRI studies is challenging due to the variability in activation among different paradigms, the contribution to activation of cognitive processes other than language, and the difficulties in monitoring patient performance. In this study, we compared language localization and lateralization between 2 commonly used clinical language paradigms and 3 newly designed dual-choice semantic paradigms to define a streamlined and adequate language-mapping protocol.

MATERIALS AND METHODS: Twelve healthy volunteers performed 5 language paradigms: Silent Word Generation, Sentence Completion, Visual Antonym Pair, Auditory Antonym Pair, and Noun-Verb Association. Group analysis was performed to assess statistically significant differences in fMRI percentage signal change and lateralization index among these paradigms in 5 ROIs: inferior frontal gyrus, superior frontal gyrus, middle frontal gyrus for expressive language activation, middle temporal gyrus, and superior temporal gyrus for receptive language activation.

RESULTS: In the expressive ROIs, Silent Word Generation was the most robust and best lateralizing paradigm (greater percentage signal change and lateralization index than semantic paradigms at $P < .01$ and $P < .05$ levels, respectively). In the receptive region of interest, Sentence Completion and Noun-Verb Association were the most robust activators (greater percentage signal change than other paradigms, $P < .01$). All except Auditory Antonym Pair were good lateralizing tasks (the lateralization index was significantly lower than other paradigms, $P < .05$).

CONCLUSIONS: The combination of Silent Word Generation and ≥ 1 visual semantic paradigm, such as Sentence Completion and Noun-Verb Association, is adequate to determine language localization and lateralization; Noun-Verb Association has the additional advantage of objective monitoring of patient performance.

ABBREVIATIONS: BOLD = blood oxygen level–dependent; IFG = inferior frontal gyrus; MFG = middle frontal gyrus; LI = lateralization index; MNI = Montreal Neurological Institute; MTG = middle temporal gyrus; PSC = percentage signal change; SFG = superior frontal gyrus; STG = superior temporal gyrus

The 2-fold aim of presurgical language mapping is to localize eloquent language cortical tissue and determine hemispheric language lateralization for surgical planning. To date, presurgical

language mapping is challenged by the inability to a priori define an individual's language network.¹ The classically accepted model of language representation, describing expressive language (speech production) in the left inferior frontal gyrus (IFG) (Broca area) and language comprehension (receptive language processing) in the Wernicke area, in the posterior aspect of the left superior temporal gyrus (STG), is inadequate to fully describe the entire language network. A newer framework, validated by both functional and structural MR imaging, proposes that language processing occurs through a ventral and dorsal pathway.²

Other limitations of clinical language blood oxygen level–dependent (BOLD) fMRI include both variability in activation patterns among different language paradigms and the variable specificity of activation for the delineation of the essential language cortex. Cognitive processes such as decision-making, attention, and working memory are also involved in language processing, thereby making it more difficult to explicitly use language mapping to distinguish essential and nonessential regions of the language network.

Received November 21, 2012; accepted after revision January 26, 2013.

From the Division of Neuroradiology (D.Z., J.J.P.), Russell H. Morgan Department of Radiology and Radiological Science, Johns Hopkins University School of Medicine, Baltimore, Maryland; Center for Mind/Brain Sciences (D.Z.), University of Trento, Trento, Italy; and F.M. Kirby Research Center for Functional Brain Imaging (S.J.), The Kennedy-Krieger Institute, Baltimore, Maryland.

This work was supported in part by a research grant from Siemens Medical Solutions (Dr Pillai is the Principal Investigator). Siemens was not involved in the study design, data collection, analysis, or manuscript preparation but did provide salary support for Dr Zacà.

Paper previously presented in part at: 50th Annual Meeting of the American Society of Neuroradiology, April 21–26, 2012; New York, New York.

Please address correspondence to Jay J. Pillai, MD, Division of Neuroradiology, Russell H. Morgan Department of Radiology and Radiological Science, The Johns Hopkins Hospital, Phipps B-100, 1800 Orleans St, Baltimore, MD 21287; e-mail: jpillai@jhmi.edu

<http://dx.doi.org/10.3174/ajnr.A3628>

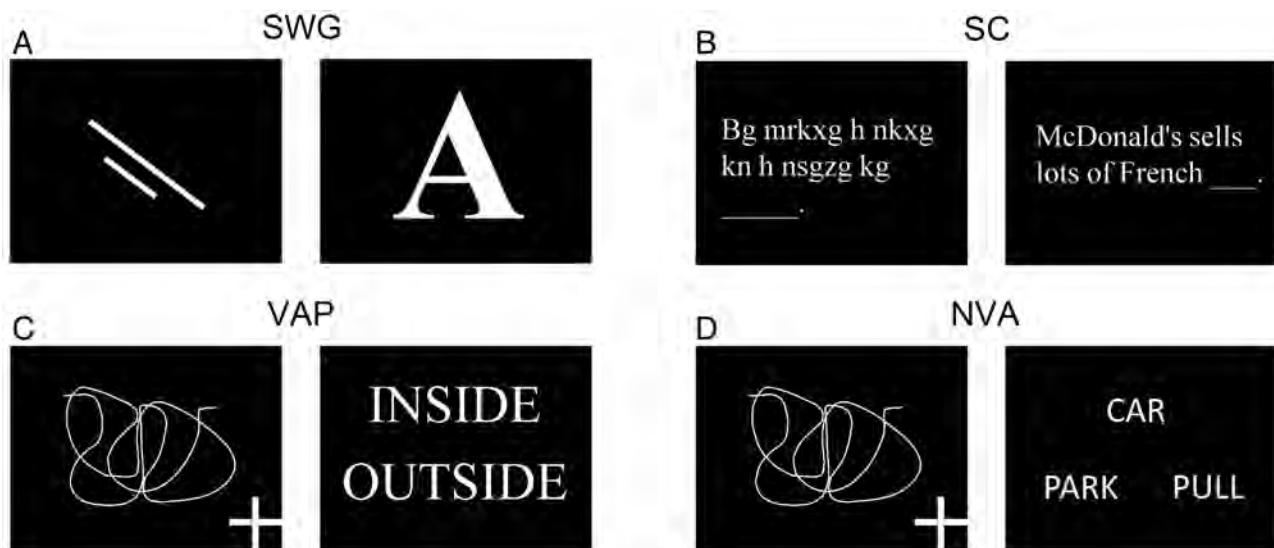


FIG 1. Examples of the stimuli in the control (first and third columns) and active (second and fourth columns) tasks in the 4 visually delivered paradigms used in the study: A, Silent Word Generation; B, Sentence Completion; C, Visual Antonym Pair; D, Noun-Verb Association.

Additionally, monitoring patient compliance during task performance is important to assess the task-activation pattern. Covert verbal fluency tasks have been shown to be the best for determination of expressive language regions and hemispheric lateralization, but they do not allow adequate monitoring of task performance inside the scanner.³

Determination of language lateralization is, in many cases, as important as language localization for surgical planning. The risk of postoperative deficits is generally thought to be higher in surgical procedures in which the lesion is located in the language-dominant hemisphere. However, the assessment of language lateralization by fMRI can be affected by many factors, including task selection, ROIs used for lateralization index (LI) computation, and statistical thresholding.^{4,5}

For all of the above-mentioned reasons, fMRI for language mapping is still not universally accepted as a standard of care for presurgical planning. In light of the recently developed language models and to contribute to the effort to establish effective protocols for language fMRI, we designed this study to determine which paradigm or combination of paradigms provides an adequate and streamlined protocol for comprehensive language mapping in clinical fMRI studies. This was carried out by comparing patterns of activation between 2 commonly used clinical language fMRI paradigms and 3 newly designed semantic language tasks that allow objective monitoring of patient task performance.

MATERIALS AND METHODS

Study Design

Twelve right-handed (6 men/6 women; range, 21–45 years of age) primarily English-speaking healthy volunteers participated in this study approved by the institutional review board. Two commonly used clinical language paradigms—Silent Word Generation and Sentence Completion—and 3 newly designed semantic paradigms—Visual Antonym Pair, Auditory Antonym Pair, and Noun-Verb Association—were performed by all the participating subjects (Fig 1). All paradigms were block design with alternating active and control blocks lasting 20 seconds each for a total of 4

minutes. The paradigms were implemented by using Prism Acquire (Prism Clinical Imaging Inc, Elm Grove, Wisconsin). See below for a description of each paradigm:

Silent Word Generation

Control Block. Visual fixation on 2 consecutive nonsense drawings, each for 10 seconds.

Active Block. Covert generation of words for 2 consecutively presented letters, each for 10 seconds.

Sentence Completion

Control Block. Scan through 5 consecutive samples of scrambled letters arranged to resemble words in a sentence.

Active Block. Covert reading of 5 consecutive real sentences with the last word missing and covert generation of a word to complete each sentence.

Visual Antonym Pair

Control Block. Visual fixation of 5 consecutive drawings with a cross placed in 1 of the 4 corners of the screen. Keypad button press was required if the cross location was in the upper or lower right corner.

Active Block. Reading of 5 consecutive pairs of words. Keypad button press was required if the 2 words were antonyms.

Auditory Antonym Pair

Control Block. Listening to 5 consecutive pairs of tones. Keypad button press was required if the 2 tones were identical.

Active Block. Listening to 5 consecutive pairs of words. Keypad button press was required if the 2 words were antonyms.

Noun-Verb Association

Control Block. Same as “Visual Antonym Pair.”

Active Block. Visual presentation of 5 samples of a noun on the top row and a pair of verbs on the bottom row. Keypad button

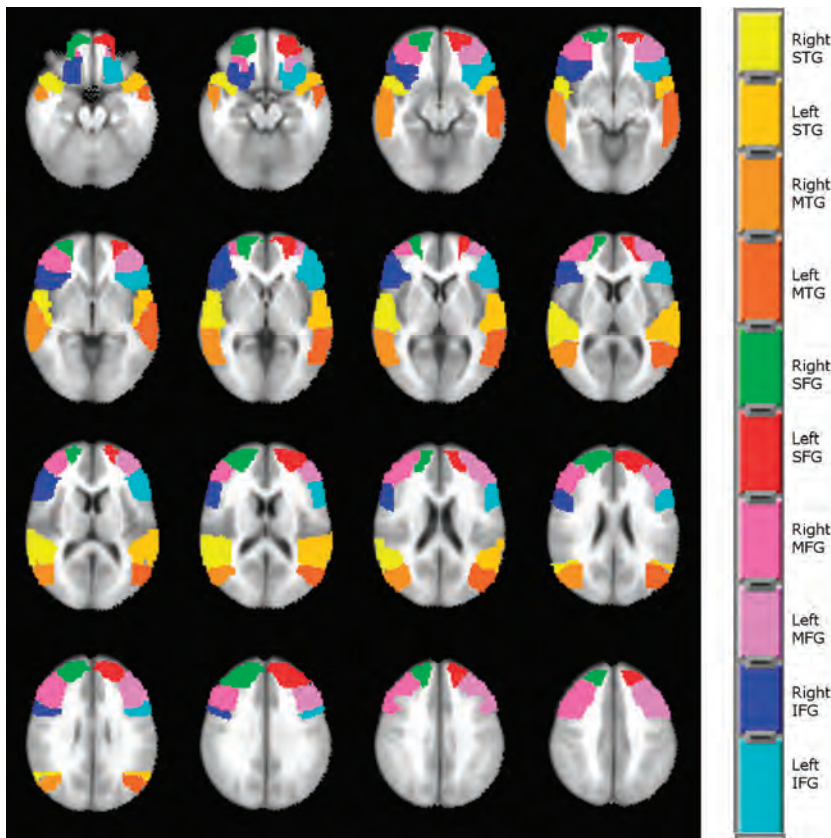


FIG 2. Regions of interest defined on the MNI-152 atlas, where language localization (PSC) and lateralization (LI) were compared among the 5 language paradigms adopted in this study.

press was required if the verb presented on the right of the bottom row was more closely semantically associated with the presented noun than the verb on the bottom left (eg, Fig 1D; the verb “park” on the bottom left was more closely associated with the noun “car” than the verb “pull” located on the bottom right; therefore, a button response was not required in this case; vice versa, if the verb “park” was on the bottom right and the verb “pull,” on the bottom left, a button response would have been required).

For the dual-choice tasks, the number of expected button presses in the control and active blocks was balanced. A training and practice session was performed outside the MR imaging scanner with each participant to provide task instructions and opportunity to practice the tasks by using similar but different stimuli from those that were included in the actual examination.

Imaging

Images were acquired by using a 3T Magnetom Trio scanner (Siemens, Erlangen, Germany) equipped with a 12-channel head matrix coil.

BOLD images were acquired by using a single-shot T2*WI gradient-echo EPI sequence. Imaging parameters were the following: TR = 2000 ms; TE = 30 ms; flip angle = 90°; FOV = 24 cm; 80 × 80 matrix acquisition; section thickness = 3 mm with a 1-mm gap between sections.

Structural images for coregistration and overlay of functional activation maps were acquired by using a standard 3D T1WI gra-

dient-echo sequence (TR = 2300 ms; TI = 900 ms; TE = 3.5 ms; flip angle = 9°; FOV = 256 cm²; 256 × 256 matrix acquisition; section thickness = 1 mm).

Image Analysis

AFNI software (<http://afni.nimh.nih.gov/afni>) was used for image processing. Preprocessing included section timing, motion correction, spatial smoothing, and registration in a stereotactic space, the Montreal Neurological Institute (MNI)-152 atlas. Regression analysis was then performed by fitting each voxel time-series, divided by the mean and multiplied by 100, to a theoretic expected time-series (ideal TS) generated by convoluting each paradigm timing with a hemodynamic impulse response function. Percentage signal change (PSC) maps from the baseline were calculated for each paradigm as

$$PSC = 100 \times \frac{a \times PP(\text{ideal TS})}{\text{Baseline}}$$

where PP indicates peak to peak; PP (ideal TS), maximum (ideal TS) to minimum (ideal TS); and Baseline = $b_0 + b_1 \times (\text{average polynomial grade } 1) + a \times \text{minimum (ideal TS)}$, where b_0 is the

baseline constant, b_1 a linear trend slope, and a the regression coefficient.

Statistical Analysis

Language localization and lateralization were compared among the 5 paradigms in 5 ROIs (IFG, superior frontal gyrus [SFG], middle frontal gyrus [MFG], middle temporal gyrus [MTG] and STG) automatically defined for the left and right hemispheres on the MNI atlas available in AFNI (Fig 2). To assess statistically significant differences in language localization, we performed a nonparametric analysis with statistical significance considered at the $P < .01$ level. A Friedman test was run voxelwise in each region of interest followed by Wilcoxon signed rank tests between each pair of paradigms in the voxels where the Friedman test score achieved statistical significance. Multiple comparison correction was applied on the results of the Wilcoxon tests by using a combination of probability and clustering thresholding obtained by using the AlphaSim simulation program available in AFNI.

Lateralization was expressed by calculating, in each region of interest for each paradigm, the LI by using a threshold-independent method⁶:

$$LI = \frac{LH - RH}{LH + RH}$$

where LH and RH are the weighted sum of all voxel t values in the left and right hemisphere portion, respectively, of each region of interest.

Table 1: Summary of Wilcoxon test results in PSC for language localization in the 5 ROIs included in the analysis

IFG	MFG	SFG	MTG	STG
AAP<NVA	AAP<NVA	AAP<NVA	AAP>NVA	AAP>NVA
Left	Left	Left	Right	Right
SC>AAP	AAP>NVA	AAP>NVA	SC>AAP	SC>NVA
Left	Right	Right	Left	Right
SC>NVA	SC>AAP	SC>AAP	SC>VAP	SC>VAP
Left	Left	Left	Right and Left	Right
SC>VAP	SC>NVA	SC>VAP	SWG<AAP	SWG<AAP
Left	Left	Left	Right and Left	Right and Left
SWG>AAP	SC>VAP	SWG>AAP	SWG<NVA	SWG<NVA
Left	Left	Left	Right and Left	Right and Left
SWG>NVA	SWG>AAP	SWG>NVA	SWG<SC	SWG<SC
Left	Left	Left	Right and Left	Right and Left
SWG>VAP	SWG>VAP	SWG>VAP	SWG<VAP	SWG<VAP
Left	Left	Left	Right and Left	Right and Left
VAP>AAP	SWG<VAP	VAP>AAP	VAP<AAP	VAP<AAP
Left	Right	Left	Right	Right and Left
SC>AAP	VAP>AAP	VAP<AAP	SC>NVA	
Left	Left	Right		

Note:—AAP indicates Auditory Antonym Pair; NVA, Noun-Verb Association; SC, Sentence Completion; SWG, Silent Word Generation; VAP, Visual Antonym Pair.

Table 2: Summary of Wilcoxon test results in the LI for lateralization analysis

IFG	MFG	SFG	MTG
SWG>SC	SWG>SC	SWG>AAP	SWG>AAP
SWG>AAP	SWG>VAP	SWG>NVA	SC>AAP
NVA>AAP	SWG>NVA	SC>NVA	VAP>AAP
NVA>VAP	SWG>AAP		NVA>AAP
	NVA>AAP (trend)		

Note:—AAP indicates Auditory Antonym Pair; NVA, Noun-Verb Association; SC, Sentence Completion; SWG, Silent Word Generation; VAP, Visual Antonym Pair.

The same nonparametric tests used for language localization analysis were performed to assess differences in LI among the paradigms in the 5 ROIs. Statistical significance was considered at the $P < .05$ level.

RESULTS

Language Localization

All 5 ROIs showed voxels with χ scores above the threshold associated with statistical significance ($P < .01$). Table 1 summarizes the significant results of the Wilcoxon tests comparing the PSC between pairs of paradigms in each region of interest. The results of the simulation run in AlphaSim determined a cluster size of 9 voxels to apply multiple comparison correction on the Wilcoxon test χ score maps at the $P < .01$ level. The verbal fluency paradigm Silent Word Generation and Sentence Completion were demonstrated to be more robust activators than the semantic paradigms in frontal gyri ROIs (IFG, MFG, SFG) in the dominant left hemisphere, with Auditory Antonym Pair showing the weakest activation in the left IFG, MFG, and SFG but stronger than Visual Antonym Pair and Noun-Verb Association in the right IFG, MFG, and SFG. Silent Word Generation provided the weakest activation in both the right and left MTG and STG. Sentence Completion was more robust than Auditory Antonym Pair and Visual Antonym Pair in the left MTG and STG, but not more robust than Noun-Verb Association. Auditory Antonym Pair and Sentence Completion were the strongest activators of the right MTG and STG.

Language Lateralization

In Table 2, the results of the Wilcoxon tests demonstrating a significant difference at $P < .05$ in LI between each pair of paradigms

in each region of interest are reported. Silent Word Generation was the best lateralizing task in the expressive ROIs, whereas Sentence Completion did not outperform, in general, Noun-Verb Association and Visual Antonym Pair as a lateralizing task, except for Noun-Verb Association in the SFG. Auditory Antonym Pair provided the most bilateral

activation both in the frontal regions and in the MTG. The other 4 paradigms did not demonstrate statistically significant differences in LI in the MTG. No significant differences in LI between the paradigms were found in the STG.

DISCUSSION

In this study, we compared the localization (as locally detectable statistically significant PSC) and lateralization (via the LI) provided by 2 clinically used covert language tasks, Silent Word Generation and Sentence Completion, with those provided by 3 newly designed dual-choice block-design semantic language paradigms, Visual Antonym Pair, Auditory Antonym Pair, and Noun-Verb Association in a group of right-handed healthy volunteers. We made this comparison to determine which paradigm or set of paradigms would be most useful for presurgical mapping of the eloquent language cortex. The analyzed ROIs included more than just the classic Broca and Wernicke areas (left IFG and left STG, respectively), because it is well-recognized that language activation extends well beyond these 2 areas.² Language is not a unitary process but rather a collection of processes operating at distinct levels, such as phonetics, phonology, orthography, and semantics. Therefore, the representation areas related to these processes deserve attention in presurgical planning because their inadvertent resection may also cause postoperative language deficits. We adopted a nonparametric statistical approach because the variables that we compared among the different tasks in the different ROIs for localization (PSC) and lateralization (LI) are defined as ratios of Gaussian variables, and in general, the distribution of a quotient of 2 normal variables can be multimodal.

The results demonstrate that Silent Word Generation is the most robust task for language localization and the most effective for determining language lateralization in the frontal gyri (IFG, MFG, and SFG) of the dominant (left) language hemisphere (Tables 1 and 2). A verbal fluency task, such as Silent Word Generation, requires phonologic access, verbal working memory, and lexical search activity, and these functions are localized in the left inferior frontal gyrus as demonstrated in multiple studies.^{7,8} In addition, the MFG and SFG are regions of the brain involved in speech production because of the activation of the middle frontal cortex in word retrieval⁹ and the presupplementary motor area for initiation and execution.¹⁰ Sentence Completion activates the dominant hemisphere frontal gyri as robustly as Silent Word Generation because of the word-generation component present in this paradigm (a word required to complete each sentence). However, its pattern of activation is significantly less lateralized than Silent Word Generation in the IFG and MFG because of the contribution of the right hemisphere homologous areas in speech comprehension tasks involving executive processing.¹¹ Semantic decision tasks also elicit activation in the IFG, MFG, and SFG,¹² but the lack of word retrieval, initiation, and execution components of the Noun-Verb Association, Visual Antonym Pair, and Auditory Antonym Pair tasks explains their weaker activation in these gyri compared with our 2 tasks with a verbal fluency component. In addition, the auditory semantic task Auditory Antonym Pair showed weaker activation than Visual Antonym Pair and Noun-Verb Association. This result is consistent with the findings of multiple studies reporting activation of the pars triangularis and pars opercularis both for speech and nonspeech sounds when they had to be held in auditory working memory, as in both the control and active blocks of the Auditory Antonym Pair task.^{13,14}

The requirement of working memory and articulatory recording activity both in the control and active tasks for Auditory Antonym Pair justifies the same findings in the MFG and SFG.^{15,16} The analysis of patterns of activation in the temporal gyri demonstrated a weaker BOLD PSC for the purely verbal fluency task Silent Word Generation both in the left and right hemispheres compared with the other 4 paradigms, all of which are associated with semantic processing localized in the middle temporal and angular gyri.¹⁷ The relative strength of activation among Sentence Completion, Noun-Verb Association, Visual Antonym Pair, and Auditory Antonym Pair was somewhat variable depending also on the considered hemisphere. In particular, as reported in Table 1, Auditory Antonym Pair was the most robust activator task in the right MTG and STG because its PSC in these 2 regions of interest was greater than Silent Word Generation, Noun-Verb Association, and Visual Antonym Pair in both regions. Auditory Antonym Pair activation results are also highly bilateral in the STG (average LI = 0.20 ± 0.20) and in the MTG (average LI = 0.15 ± 0.20), where it was also significantly lower in comparison with the other 4 paradigms ($P < .05$).

Results from the literature indicate a bilateral superior temporal activation for both speech and nonspeech sounds.¹⁸ However, the reason for bilateral STG activation even after the subtraction of the speech (tones) control task from the speech (antonyms) active task may be that more demand is placed on short-term

auditory memory during the speech task than during the tone task. Furthermore, contrary to phonologic processing studies reporting lateralized activation in receptive language areas, the semantic component of the active task (antonym versus nonantonym) explains the bilateral pattern of activation in our group of volunteers.⁴ We found, in our study, greater activation for Sentence Completion in the left MTG compared with Visual Antonym Pair and Auditory Antonym Pair but not compared with Noun-Verb Association, and these findings could be attributed to the higher level of lexical-semantic processing required for Sentence Completion and Noun-Verb Association.¹⁹ Instead Sentence Completion activation was stronger than Noun-Verb Association and Visual Antonym Pair in the right MTG and STG, confirming the role of the right hemisphere in semantic tasks involving executive processing.¹¹

The Silent Word Generation group LI was not significantly different from either Sentence Completion or the semantic paradigms but was higher than that of Auditory Antonym Pair. Therefore one could consider using only Silent Word Generation in a clinical language fMRI examination because of its capability to determine language lateralization in both the frontal and temporal lobes. However its PSC is weaker in both the left and right temporal gyri compared with the other 4 paradigms that include language comprehension in the active blocks of the paradigms; therefore, the semantic tasks are more adequate to map the temporal regions involved in the language network because they elicit a stronger BOLD response than a verbal fluency task. Furthermore, it has been demonstrated that the combination of multiple tasks, a language-specific region of interest approach and implementation of statistical threshold-independent approaches for determination of hemispheric lateralization, provides more reliable lateralization that correlates better with the criterion standard Wada test.^{20,21}

One limitation of this study includes the exclusion of the cerebellum from region-of-interest analysis. The cerebellum has demonstrated fMRI activation during silent articulation.²² Cases of cognitive deficits in association with cerebellar damage have been reported,²³ yet frank aphasic disturbances are rare. Multiple cognitive studies performed on a group of healthy volunteers have demonstrated a further parceling out of language functions in each of the 5 ROIs considered in our work.^{24,25} However, since this study aimed to improve language presurgical mapping, where analysis is conducted at the single subject level, such parcellation would not be practical and it most likely would not add any critical information for patient surgical management. Finally, no Wada testing was performed to actually confirm language lateralization in these subjects, but this would not be ethical in a group of healthy volunteers.

CONCLUSIONS

In this study, we demonstrated that the combination of a fluency task such as Silent Word Generation and ≥ 1 visually delivered semantic task provides an adequate protocol for determination of language localization and lateralization. The newly designed Noun-Verb Association paradigm is potentially very effective because its forced dual-choice paradigm design allows effective patient monitoring of task performance. Nevertheless, it is always

advisable in clinical studies to have a variety of available paradigms because if a patient finds a particular task too challenging because of neurologic impairment, it will rarely produce meaningful fMRI results.

ACKNOWLEDGMENTS

The authors thank Gayane Yenokyan, MD, PhD, for assistance with data analysis.

Disclosures: Domenico Zacà—RELATED: Grant: Siemens Medical Solutions,* Comments: Siemens provided support for my postdoctoral fellowship salary at Johns Hopkins University. Jay J. Pillai—RELATED: Grant: Siemens Medical Solutions,* Comments: This research grant paid for Dr Zacà's (my former postdoctoral fellow) salary. However, Siemens was not involved in the study design, analysis, reporting of results, or writing of the manuscript in any way. OTHER RELATIONSHIPS: I am an unpaid member of the Medical Advisory Board of Prism Clinical Imaging. *Money paid to the institution.

REFERENCES

1. Seghier ML, Lazeyras F, Pegna AJ, et al. **Variability of fMRI activation during a phonological and semantic language task in healthy subjects.** *Hum Brain Mapp* 2004;23:140–55
2. Saur D, Kreher BW, Schnell S, et al. **Ventral and dorsal pathways for language.** *Proc Natl Acad Sci U S A* 2008;105:18035–40
3. Partovi S, Konrad F, Karimi S, et al. **Effects of covert and overt paradigms in clinical language fMRI.** *Acad Radiol* 2012;19:518–25
4. Zacà D, Nickerson JP, Deib G, et al. **Effectiveness of four different clinical fMRI paradigms for preoperative regional determination of language lateralization in patients with brain tumors.** *Neuroradiology* 2012;54:1015–25
5. Ruff IM, Petrovich Brennan NM, Peck KK, et al. **Assessment of the language laterality index in patients with brain tumor using functional MR imaging: effects of thresholding, task selection, and prior surgery.** *AJNR Am J Neuroradiol* 2008;29:528–35
6. Branco DM, Suarez RO, Whalen S, et al. **Functional MRI of memory in the hippocampus: laterality indices may be more meaningful if calculated from whole voxel distributions.** *Neuroimage* 2006;32:592–602
7. Palmer ED, Rosen HJ, Ojemann JG, et al. **An event-related fMRI study of overt and covert word stem completion.** *Neuroimage* 2001; 14(1 pt 1):182–93
8. Eulitz C, Elbert T, Bartenstein P, et al. **Comparison of magnetic and metabolic brain activity during a verb generation task.** *Neuroreport* 1994;6:97–100
9. Paulesu E, Goldacre B, Scifo P, et al. **Functional heterogeneity of left inferior frontal cortex as revealed by fMRI.** *Neuroreport* 1997;8:2011–17
10. Kawashima R, Okuda J, Umetsu A, et al. **Human cerebellum plays an important role in memory-timed finger movement: an fMRI study.** *J Neurophysiol* 2000;83:1079–87
11. Vigneau M, Beaucousin V, Herve PY, et al. **What is right-hemisphere contribution to phonological, lexico-semantic, and sentence processing? Insights from a meta-analysis.** *Neuroimage* 2011;54:577–93
12. Binder JR, Desai RH, Graves WW, et al. **Where is the semantic system? A critical review and meta-analysis of 120 functional neuroimaging studies.** *Cereb Cortex* 2009;19:2767–96
13. Burton MW, Small SL, Blumstein SE. **The role of segmentation in phonological processing: an fMRI investigation.** *J Cogn Neurosci* 2000;12:679–90
14. Hsieh L, Gandour J, Wong D, et al. **Functional heterogeneity of inferior frontal gyrus is shaped by linguistic experience.** *Brain Lang* 2001;76:227–52
15. Wilson SM, Iacoboni M. **Neural responses to non-native phonemes varying in producibility: evidence for the sensorimotor nature of speech perception.** *Neuroimage* 2006;33:316–25
16. Wilson SM, Saygin AP, Sereno MI, et al. **Listening to speech activates motor areas involved in speech production.** *Nat Neurosci* 2004;7:701–02
17. Vandenberghe R, Price C, Wise R, et al. **Functional anatomy of a common semantic system for words and pictures.** *Nature* 1996;383:254–56
18. Booth JR, Burman DD, Meyer JR, et al. **Functional anatomy of intra- and cross-modal lexical tasks.** *Neuroimage* 2002;16:7–22
19. Démonet JF, Chollet F, Ramsay S, et al. **The anatomy of phonological and semantic processing in normal subjects.** *Brain* 1992;115(pt 6):1753–68
20. Niskanen E, Kononen M, Villberg V, et al. **The effect of fMRI task combinations on determining the hemispheric dominance of language functions.** *Neuroradiology* 2012;54:393–405
21. Suarez RO, Whalen S, Nelson AP, et al. **Threshold-independent functional MRI determination of language dominance: a validation study against clinical gold standards.** *Epilepsy Behav* 2009;16:288–97
22. Ackermann H. **Cerebellar contributions to speech production and speech perception: psycholinguistic and neurobiological perspectives.** *Trends Neurosci* 2008;31:265–72
23. Fiez JA, Petersen SE, Cheney MK, et al. **Impaired non-motor learning and error detection associated with cerebellar damage: a single case study.** *Brain* 1992;115(pt 1):155–78
24. Specht K, Reul J. **Functional segregation of the temporal lobes into highly differentiated subsystems for auditory perception: an auditory rapid event-related fMRI-task.** *Neuroimage* 2003;20:1944–54
25. Thierry G, Giraud AL, Price C. **Hemispheric dissociation in access to the human semantic system.** *Neuron* 2003;38:499–506

Improving Clinical fMRI: Better Paradigms or Higher Field Strength?

The clinical significance of functional MR imaging is steadily increasing. At the latest annual meeting of the Organization for Human Brain Mapping (www.humanbrainmapping.org) in Seattle this year, the largest group of contributions concerned the category “Disorders of the Nervous System.” In addition, specialized clinical associations have been founded in recent years (eg, www.asfnr.org and www.oegfmrt.org); and at clinical centers with dedicated expertise, the demand for clinical fMRI reports is steadily growing (exact quantifications are difficult due to the absence of international statistics). The most important tasks for clinical fMRI are the generation of noninvasive biomarkers for the classification and prognosis of patients with brain disease and the presurgical localization of essential motor, language, or memory areas. Research concerning possible improvements of current clinical fMRI techniques is highly topical. Two distinctive features render this research difficult: First, the techniques need to generate reliable data in individual patients. Second, the techniques need to work with atypical morphology and functionality (ie, pathologic brains).

The consequence of these features is that clinical fMRI has to struggle with several issues that are less problematic in research with healthy subjects. Among these are patient compliance, performance monitoring, recognition of neuroplastic changes, and evaluation of compensatory activations that may result in a changed lateralization index. The latter is particularly problematic because a clinically valid interpretation of lateralized activation in pathologic brains is not trivial. Recent neuroimaging research indicates that there are 2 types of contralateral activation increase after ipsilateral brain damage. If much of the functional capacity is lost in the damaged hemisphere, contralateral activations may be essential and inhibition of this activity may be deleterious. In contrast, if sufficient functional capacity is left in the damaged hemisphere, contralateral activations may represent maladaptations and their inhibition improves patient performance.^{1,2} Differentiating these 2 types of compensatory activation is not straightforward. Important issues in this context are the patient’s clinical performance and the time elapsed since brain damage. Particular caution is required when results indicate an atypical functional lateralization. Evidently this situation requires

a comprehensive evaluation of the individual case but also highly reliable functional data.

Considerable research within the past decade has focused on improving the reliability of clinical fMRI data. Much of it concerns the important issue of how to optimize experimental paradigms. Especially for localization of essential language areas, many different paradigms have already been suggested. However, only a few comprise the most important issues of performance monitoring and comprehensive testing of the various subcomponents of language processing. A nice example is included in the present issue of the *American Journal of Neuroradiology* in the article by Zacà et al.³ This study—like most paradigm research—is based on healthy subjects, and unfortunately, much less data are available from pathologic brains or typical clinical fMRI populations. Even worse is the situation with research on the issue of how to optimize signal strength when a well-functioning paradigm is already in place. Given that functional signals within pathologic tissue may be rather weak and given the clinical implications of defining a brain area as functionally “dead” as opposed to functionally “compromised,” the issue of optimizing signal strength is highly important. This is particularly true for the clinical demands that require a diagnosis in an individual without the possibility of averaging over a group. Due to the approximately linear increase of the signal-to-noise ratio from 1.5T to 7T, increasing the magnetic field strength of MR imaging systems is one of the key issues in this regard. If one considers MR imaging history, approximately 1 decade ago, 1.5T was the maximum field strength used for clinical applications. Currently 3T clinical systems are widely available and quasistandard for fMRI investigations. The cutting edge technology, however, is 7T ultra-high-field systems, with approximately 60 installations worldwide.

Besides an increased signal-to-noise ratio, theoretic expectations also include benefits for the typical fMRI blood oxygen level–dependent contrasts, summarized as contrast-to-noise improvements. Detailed theoretic predictions are difficult, however, because several factors influence possible clinical benefits (eg, increased artifacts level, scaling of physiologic noise with field strength, dependence of effects on the voxel size). Therefore, experimental investigations on how much functional signals in-

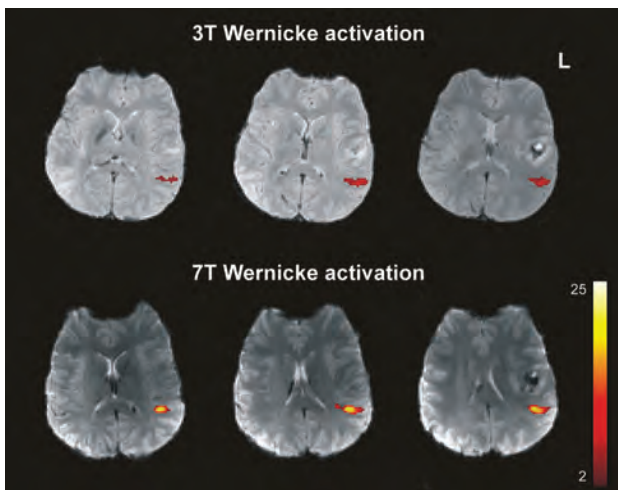


FIG 1. Improved functional signal strength in a patient with tumor generated by a 7T (Siemens Magnetom) ultra-high-field system within the Wernicke language area (overt speech design, Study Group Clinical fMRI⁴).

crease with field strength are urgently needed. A first study comparing 3T and 7T motor cortex signals in patients with brain tumors provided promising results: Five of 6 functional parameters indicated improved sensitivity for 7T, even at a standard resolution ($1.8 \times 1.8 \times 3$ mm voxel size) and with standard clinical procedures.⁴ Corresponding language data (work in progress) achieved with an overt response paradigm that includes various subcomponents of language processing⁵ indicate a similar 7T benefit, provided that the artifacts situation can be controlled (Fig 1).

Although the current reliability of fMRI is adequate for most clinical demands, there is still the potential for further improvement.⁶ Given that a number of high-quality paradigms have been published by several expert clinical groups for the most important tasks in the interim, significant further progress is most likely to be achieved by new techniques that improve functional signal strength, such as clinical 7T systems. Research into this issue is of the utmost importance. If initial results can be confirmed, there is

a good chance that such studies will fuel a hardware revolution similar to the general shift of clinical work from 1.5T to 3T during the past 10 years.

ACKNOWLEDGMENTS

I am grateful to M. Wurnig, F. Fischmeister, E. Matt, E. Auff, A. Geißler (Study Group Clinical fMRI, Department of Neurology, High Field MR Center, Medical University of Vienna, Austria), and S. Trattnig and S. Robinson (Department of Radiology, High Field MR Center, Medical University of Vienna, Austria) for contributions to the clinical fMRI data. Generation of the data was supported by the Vienna Spots of Excellence Program of the Center of Innovation and Technology, City of Vienna (ZIT), Austria, and the Austrian Science Fund (FWF) grants KLI264 and P23611.

REFERENCES

1. O'Shea J, Boudrias MH, Stagg CJ, et al. **Predicting behavioural response to TDCS in chronic motor stroke.** *Neuroimage* 2013; pii:S1053-8119(13)00598-603
2. Szaflarski JP, Allendorfer JB, Banks C, et al. **Recovered vs. not-recovered from post-stroke aphasia: the contributions from the dominant and non-dominant hemispheres.** *Restor Neurol Neurosci* 2013;31:347-60
3. Zacà D, Jarso S, Pillai JJ. **Role of semantic paradigms for optimization of language mapping in clinical fMRI studies.** *AJNR Am J Neuroradiol* 2013;34:1963-68
4. Beisteiner R, Robinson S, Wurnig M, et al. **Clinical fMRI: evidence for a 7 T benefit over 3 T.** *Neuroimage* 2011;57:1015-21
5. Gartus A, Foki T, Geissler A, et al. **Improvement of clinical language localization with an overt semantic and syntactic language functional MR imaging paradigm.** *AJNR Am J Neuroradiol* 2009; 30:1977-85
6. Wurnig MC, Rath J, Klinger N, et al. **Variability of clinical functional MR imaging results: a multicenter study.** *Radiology* 2013;268: 521-31

R. Beisteiner
Study Group Clinical fMRI
Department of Neurology
High Field MR Center
Medical University of Vienna
Vienna, Austria

<http://dx.doi.org/10.3174/ajnr.A3722>

Spinal Dural Arteriovenous Fistulas: Clinical Experience with Endovascular Treatment as a Primary Therapy at 2 Academic Referral Centers

JJ. Gemmete, N. Chaudhary, A.E. Elias, A.K. Toma, A.S. Pandey, R.A. Parker, I. Davagnanam, C.O. Maher, S. Brew, and F. Robertson



ABSTRACT

BACKGROUND AND PURPOSE: Spinal dural arteriovenous fistulas are a rare entity that, if left untreated, can lead to considerable morbidity with progressive spinal cord symptoms. The aim of this study was to evaluate the clinical outcome of patients with spinal dural arteriovenous fistulas that were primarily treated with endovascular embolization.

MATERIALS AND METHODS: A retrospective review was performed of all patients from 1997–2010 who underwent treatment at 2 academic referral centers for a spinal dural arteriovenous fistula. Follow-up was performed by clinical examination, and functional status was measured by use of the Aminoff-Logue Disability Scale, McCormick classification grading, and mRS scores. The nonparametric Wilcoxon signed rank test was used to compare pretreatment and posttreatment Aminoff-Logue Disability Scale gait and micturition scores, McCormick classification grading, and mRS scores. *P* values < .05 were considered significant.

RESULTS: A total of 38 patients were included. Five patients (2 endovascular, 3 surgical) were lost to follow-up and therefore were excluded from the analysis, 29 patients were initially treated from an endovascular approach (9 Onyx, 20 cyanoacrylate), and 4 patients were treated from a standard surgical approach. Five patients in the endovascular group subsequently underwent surgery for various reasons. The clinical improvements in the Aminoff-Logue Disability Scale gait and micturition scores, McCormick classification grading, and the mRS scores were statistically significant (*P* < .05, Wilcoxon signed rank test).

CONCLUSIONS: We conclude that endovascular treatment of spinal dural arteriovenous fistulas can result in good clinical outcomes. Surgery remains the treatment of choice when safe embolization of the proximal radicular draining vein cannot be obtained or because the shunting artery of the spinal dural arteriovenous fistula also supplies the anterior spinal, posterior spinal, or a radiculomedullary artery.

ABBREVIATIONS: ALS = Aminoff-Logue Disability Scale; MC = McCormick classification; mRS = modified Rankin Scale; SDAVF = spinal dural arteriovenous fistula

SDAVFs are the most common spinal vascular malformations accounting for 70% of the vascular lesions involving the spinal cord.^{1,2} The time between the onset of symptoms and diagnosis of the lesion is usually late in the disease course. This is because of the nonspecific clinical presentation.^{3,4} Patients may present with gait

disturbances, difficulty climbing stairs, sensory symptoms, and even radicular pain that may affect 1 or both extremities. The neurologic symptoms show progression with time.⁵ Bowel and bladder incontinence, erectile dysfunction, and urinary retention are seen late in the course of the disease process.⁶ If the lesion is not treated, 50% of patients will become severely disabled and < 10% will be able to walk independently after 3 years.⁷ The lesion is thought to be an acquired fistula of the dural branch of a segmental artery draining into a radicular vein at the dural sleeve of the nerve root.⁸ SDAVFs can be treated by surgery with clip placement or coagulation of the vein from a posterior spinal laminectomy approach.⁹ Endovascular embolization is an effective therapy in the treatment of SDAVFs and can be used as a definitive intervention in most patients.¹⁰ The success of endovascular treatment is believed to be dependent on complete occlusion of the proximal radicular draining vein and the site of the fistula itself.¹⁰ The goal of treatment, regardless of the type of intervention, is to eliminate the abnormal arteriovenous communication to avoid progression or

Received October 17, 2012; accepted after revision December 27, 2012.

From the Departments of Radiology (JJ.G., N.C., A.E.E.) and Neurosurgery (JJ.G., N.C., A.S.P., C.O.M.), University of Michigan Health Systems, Ann Arbor, Michigan; Departments of Neuroradiology (I.D., S.B., F.R.) and Neurosurgery (A.K.T.), National Hospital for Neurology & Neurosurgery, University College London Hospitals, London, United Kingdom; and Department of Biostatistics (R.A.P.), School of Public Health, University of Michigan, Ann Arbor, Michigan.

Paper previously presented at: World Federation of Interventional & Therapeutic Neuroradiology (WFITN) Congress, November 8–11, 2011; Cape Town, South Africa.

Please address correspondence to Joseph J. Gemmete, MD, Department of Radiology, Neurosurgery, Otolaryngology, Division of Neurointerventional Surgery, University of Michigan Health Systems, UH BID 328, 1500 E. Medical Center Dr, Ann Arbor, MI 48109; e-mail: gemmete@med.umich.edu

Indicates article with supplemental on-line tables

<http://dx.doi.org/10.3174/ajnr.A3522>

worsening of the neurologic symptoms. The aim of our study was to evaluate the clinical outcome of patients with an SDAVF primarily treated with endovascular embolization.

MATERIALS AND METHODS

A retrospective chart review was performed to identify all cases of patients with SDAVFs seen at 2 tertiary academic medical institutions from 1997–2010. The institutional review board of both academic referral centers granted approval of the study.

The medical records of these patients were retrospectively reviewed, and clinical history, neurologic examination, and diagnostic work-up were obtained. Patients were evaluated in clinics attended by neurosurgeons, neurologists, and interventional neurologists. Information collected included patient demographics, clinical presentation, location of the fistula, years of symptoms before diagnosis, treatment, duration of follow-up, and the functional status (preoperative and postoperative). Functional status (gait and micturition) was measured by use of the ALS, MC, and mRS, calculated retrospectively from the preoperative and postoperative clinical notes. The interval between the onset of initial symptoms and diagnosis of SDAVF by angiography was calculated as the time of diagnosis. All suspected lesions on MR imaging were confirmed by digital subtraction angiography. Preoperative MR imaging was performed in all patients. Postoperative MR imaging was available for 15 patients at 1 institution; at the other institution, we could not obtain the posttreatment MR imaging reports.

If available, pre- and posttreatment imaging characteristics were compared. The treatment strategy was identical for all patients; an attempt at endovascular obliteration was the first choice of treatment. Surgery was offered whenever embolization failed or was abandoned for technical reasons.

Technique of Endovascular Embolization

All spinal angiograms were performed with the patients under general endotracheal anesthesia (with somatosensory- and motor-evoked potentials in some instances) to avoid patient discomfort and minimize motion artifacts. Both angiographic suites are composed of a biplane angiographic unit with conebeam CT capability (Axiom Artis; Siemens, Erlangen, Germany). Patients were placed supine on the angiographic table, and transfemoral access and sheath placement was obtained by use of a modified Seldinger technique. All patients were given intravenous heparin (70 U/kg–100 U/kg) to maintain an activated coagulation between 250 and 300 s. Spinal angiography was performed in all patients to identify the anterior and posterior spinal arteries and the site of the fistula. After the diagnostic portion of the procedure, a 4F or 5F catheter was placed in the segmental artery supplying the SDAVF.

Coaxially, through the catheter, depending on the liquid embolic agent used, a Prowler 10 (Codman Neurovascular, Raynham, Massachusetts), Magic (Balt, Montmorency, France), Echelon 10 (ev3 Neurovascular, Irvine, California), or Marathon (ev3 Neurovascular) microcatheter was advanced under road-mapping over a microwire to reach the most distal aspect of the segmental artery supplying the SDAVF. Microcatheter angiography was performed to determine microcatheter position and if there was filling of the anterior spinal, posterior spinal, or a radiculom-

edullary artery. If a question arose about the safety of the selective microcatheter position for those cases performed with Onyx, a provocative test was performed with 1 mg of methohexital sodium (Brevital) and 15 mg of preservative-free 2% lidocaine hydrochloride. Embolization was not performed if a 50% reduction in amplitude of the motor-evoked potential on monitoring was demonstrated.

Endovascular embolization of the SDAVF was performed with Onyx (ev3 Neurovascular) or with cyanoacrylate glue (*n*-BCA; Codman Neurovascular), Glubran 2 (GEM, Viareggio, Italy), or Histoacryl (Braun, Melsungen, Germany). The aim of the embolization was to penetrate the liquid embolic agent into the proximal draining vein while occluding the fistula site and feeding arterial vessels. Repeated segmental angiography after embolization was performed bilaterally at the level of the arterial feeder and the adjacent 2 segmental levels above and below the site of the fistula.

After the procedure, the patient was admitted to the neurointensive care unit for close monitoring for 24–48 hours. If the patient's condition deteriorated in the immediate postoperative period, the patient was given heparin and a subsequent angiogram was performed.

Surgical Technique

Surgery was uniform throughout the study period. A midline laminectomy was performed 1 level above and 1 level below the fistula. The dura was opened in the midline, the fistula identified, and the draining radicular vein coagulated and divided. The dural nidus at the nerve root was coagulated whenever possible.

In patients harboring a common segmental artery supplying the fistula and an anterior spinal artery, endovascular embolization was not attempted, and those patients were referred for surgery. Embolization was considered a failure if the liquid embolic agent did not penetrate the proximal shunting radicular vein. If embolization failed to occlude the fistula as shown by postembolization angiography, surgery was performed immediately. Furthermore, surgery was performed in those patients with severe atheromatous disease or a tortuous feeding artery where catheter navigation near the site of the fistula could not be obtained.

Follow-Up

Occlusion of the fistula was confirmed by repeated spinal angiography in all patients before discharge from the hospital. Depending on the treatment approach, neurologists, neurosurgeons, and/or interventional neuroradiologists obtained clinical follow-up. Spinal angiogram and MR imaging were obtained at 6 months after treatment in all patients; however, we were only able to review the follow-up MR imaging results in 15 patients at 1 institution. If there was a delay in recovery or a clinical concern for residual or recurrent disease, MR imaging and angiography studies were repeated.

Statistical Analysis

Data were summarized by descriptive statistics, including percentages and counts for categorical data and means and SDs for continuous data. Statistical analysis was performed by use of the software program SAS 8.02 (SAS Institute, Cary, North Carolina). All statistical tests were 2-tailed. The nonparametric



FIG 1. Patient 15, a 66-year-old man with a history of bilateral lower extremity weakness. A, Sagittal T2-weighted MR image shows multiple serpiginous flow voids (arrow) within the sacrum and lower lumbar spine. B, Left anterior oblique right lateral sacral angiogram shows site of SDAVF (arrow). C, Frontal spot fluoroscopic image shows glue cast within the arterial feeder, site of the fistula, and outflow vein (arrow). D, Sagittal T2-weighted MR image 6 months after treatment shows some interval resolution of the multiple serpiginous flow voids (arrow) within the sacrum and lower lumbar spine.

Wilcoxon signed rank test was used to compare pre- and post-treatment ALS gait and micturition scores, MC grading, and mRS scores. *P* values < .05 were considered significant. Because of the retrospective design and the small surgical sample size, no statistical comparison between the 2 treatment techniques was performed.

RESULTS

Between 1997 and 2010, a total of 38 patients were treated for an SDAVF. Our study population included 33 patients (26 men and 7 women; average age, 64.6 years; age range, 39–81 years) who were available for long-term follow-up. Twenty-nine patients were treated from an endovascular approach (9 Onyx, 20 *n*-BCA) (Figs 1 and 2), 5 patients from an endovascular followed by a surgical approach, and 4 patients from a surgical approach. Five patients were lost to follow-up (2 endovascular, 3 surgical) and therefore were not included

in the analysis. Diagnosis of SDAVF was confirmed by spinal angiography. Clinical presentation included the following: of the 33 patients, lower extremity weakness was seen in 29 (88%), patchy dermatomal symptoms in 25 (76%), nonspecific back pain in 17 (52%), and urinary symptoms in 9 (27%). The average duration of symptoms before treatment was 24.6 months (range, 1–84 months). In this series, there were 5 sacral, 9 lumbar, 12 low thoracic (T8–T12), and 6 midthoracic fistulas (T4–T7); and 1 cervical fistula (Fig 3). Most of the fistulas had a single segmental arterial feeding artery; however, there were 2 fistulas that demonstrated multiple feeding arteries. There was 1 treatment-related complication. One patient had clinical deterioration of clinical symptoms after penetration of the embolic material too far into the venous system; however, this improved after administration of heparin. The mean interval follow-up was 13 months (range, 1–120 months).

According to preprocedure and postprocedure ALS, improvement in gait was seen in 15 of 33 patients, and improvement in micturition was seen in 6 of 33 patients (On-Line Table 1). Gait and micturition stabilized in 17 of 33 patients and in 27 of 33 patients, respectively. One patient (Patient 30) experienced worsening of gait ALS and had been treated for an SDAVF at S2. This patient's symptoms probably worsened because of penetration of embolic material too far into the venous system. In the 9 patients treated with Onyx, improvement in ALS gait was seen in 5 (56%) of 9 patients and ALS micturition in 3 (33%) of 9 patients, respectively.

On MC grading, 15 (45%) of 33 patients had improvement and 18 (55%) had no change. No patient showed worsening of MC grading (On-Line Table 1). On assessment by mRS score, 14 (42%) of 33 patients had improvement and 18 (55%) had no change. One patient (3%) showed worsening of the mRS score (On-Line Table 1). This patient was treated from an endovascular approach with *n*-BCA with the fistula at T12.

Two of the 20 patients in the cyanoacrylate group underwent repeated embolization. In these 2 patients, clinical deterioration at initial follow-up prompted a repeated diagnostic angiography study revealing a persistent SDAVF, which was treated with subsequent embolization. On final follow-up, both patients improved clinically based on ALS gait and micturition scores.

In the group who underwent embolization followed by surgery (*n*=5), 2 patients were initially treated with cyanoacrylate and 3 with Onyx. The first patient (Patient 2) was successfully treated with cyanoacrylate for an SDAVF at L4; however, clinical examination revealed worsening of this patient's condition, and a second angiographic examination was obtained. Results demonstrated formation of a collateral vessel. The patient was surgically treated because no safe position for embolization was available. The second patient (Patient 5) was treated for an SDAVF at L1; there was poor penetration of Onyx into the draining radicular vein. Patient 5 remained neurologically stable, but a repeated angiographic study showed persistent filling of the fistula. At surgical exploration, the arterialized vein could not be identified. The third patient (Patient 9) had 2 discrete SDAVFs with supply from T7 and T12, with the anterior spinal artery arising from T12. The T7 level was successfully treated with excellent penetration of cyanoacrylate into the draining radicular vein. Given the additional supply to the fistula from T12 (where the anterior spinal artery arose), surgery was performed. The fourth patient (Patient 13) had an SDAVF at C5. Onyx



FIG 2. Patient 1, a 59-year-old man with inability to stand and persistent retention. *A*, Sagittal T2-weighted MR image shows high signal within the conus medullaris, lower and midthoracic spinal cord (arrow). *B*, Right T12 angiogram shows filling of an SDAVF (small arrow) with initial filling of the epidural venous plexus (small arrow), which then fills the radicular veins (large arrow). *C*, Frontal spot fluoroscopic images showing Onyx cast. *D*, Sagittal T2-weighted MR image 3 months after treatment shows interval resolution of the high signal within the conus medullaris, lower and midthoracic spinal cord.

embolization was attempted; however, there was poor penetration into the draining radicular vein and we were concerned about non-target embolization into the main vertebral artery, necessitating surgery. The fifth patient (Patient 16) had an SDAVF at L2 that was successfully treated with Onyx, with good penetration into the draining radicular vein. However, follow-up angiogram at 6 months demonstrated development of a collateral vessel to the fistula at L3, and surgery was therefore performed. One patient had improvement in motor strength on the ALS scale, and 4 (80%) of 5 patients demonstrated stable motor strength. According to MC grading, 2 (40%) of 5 patients had improvement and 3 (60%) of 5 had no change. On mRS assessment, 1 (20%) of 5 patients had improvement and 4 (80%) of 5 had no change.

The improvements seen after treatment in the ALS gait and micturition scores, MC grading, and the mRS scores were statis-

tically significant ($P < .05$, Wilcoxon signed rank test) (Tables 1 and 2). Eight patients in the ALS micturition analysis and 3 patients in the MC grading analysis were excluded because their preintervention examination results were normal.

A total of 33 preoperative and postprocedure MR imaging scans were performed; however, we were able to only obtain such scans in 15 patients (On-Line Tables 2–4). Five patients had cord edema within the midthoracic region on preoperative MR imaging; in this group, 3 had no improvement on follow-up imaging, 1 had mild improvement, and 1 had moderate improvement. In the midthoracic group, 3 patients had improvement in the ALS gait score, but this score remained unchanged in 2 patients. The ALS micturition score remained the same in all 5 patients. Seven patients had cord edema in the low thoracic region on preoperative MR imaging; in this group, 2 had no change, 1 had mild improvement, and 4 had marked improvement. ALS gait score in this group improved in 5 and remained the same in 2 patients. ALS micturition score improved in 3 patients and remained the same in 4. Only 2 patients had cord edema isolated to the conus medullaris on preoperative MR imaging; in this group, 1 had mild improvement and 1 had marked improvement in the extent of the edema. ALS gait and micturition scores improved in 1 patient and remained unchanged in the other patient.

DISCUSSION

SDAVFs arise from a spontaneous or acquired abnormal communication between a segmental radicular artery and the corresponding radicular vein at its site of dural penetration. SDAVFs are relatively rare, and their diagnosis is often missed because of nonspecific clinical symptoms at presentation.^{11–13} The delay to diagnosis in our patients (mean, 24.6 months) is comparable to other series.^{13–15} At the time of diagnosis 14 of 33 patients were severely disabled (mRS > 4). This finding is also comparable to other reports.^{13–15} We did not correlate the severity of the clinical presentation with the time of diagnosis.

Most of our patients in our study were men (26/33), with an average age of 64.6 years. This finding also correlates with the demographics seen in several other large studies.^{11,14,15} We had only 1 patient younger than 40 years in our study, which illustrates the rarity of this diagnosis in the younger patient population.

Presenting symptoms in our patient population included the following: of our 33 patients, lower extremity weakness was seen in 29 (87%), patchy dermatomal symptoms in 25 (75%), nonspecific back pain in 17 (51%), and urinary symptoms in 9 (27%). These symptoms at clinical presentation are similar to those reported in other large series.^{3,14,15} Development of upper motor neuron signs with gait and micturition impairment is usually seen late in the course of the disease process. Early diagnosis and successful treatment of the fistula correlates with improvement in clinical symptoms.¹⁶ Even with successful treatment, late presentation is associated with poor clinical and functional outcomes.

Also in accordance with previous studies, most SDAVFs in our series originated from the thoracic and lumbar levels,^{14,15,17} as demonstrated in Fig 3. Most of the fistulas had a single segmental arterial feeding artery; however, there were 2 fistulas that demonstrated multiple feeding arteries.

Several prior studies have reported results after endovascular

Fistulae distribution

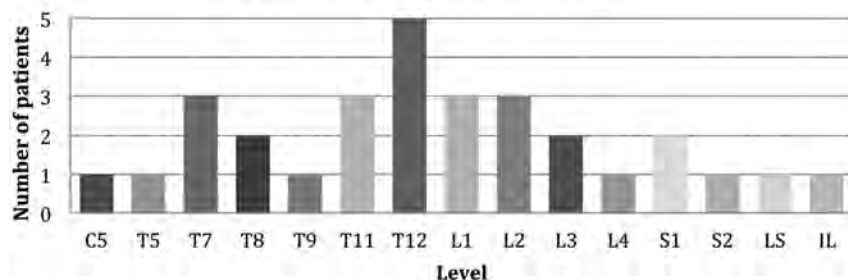


FIG 3. Site of fistulas. LS indicates lateral sacral; IL, ileolumbar.

Table 1: ALS functional grades before and after intervention

	Before Treatment (Avg ± SD)	Last Follow-Up (Avg ± SD)	P Values
Gait (n=33)	3.09 ± 1.48	2.51 ± 1.46	*.0021
Micturition (n=25)	2.24 ± 0.77	1.50 ± 1.09	*.025

* Values were statistically significant ($P < .05$; Wilcoxon signed rank test).

Table 2: MC and mRS scores before and after intervention

	Before Treatment (Avg ± SD)	Last Follow-Up (Avg ± SD)	P Values
MC (n=30)	2.96 ± 0.88	2.36 ± 1.06	*.0003
mRS (n=33)	3.15 ± 1.48	2.60 ± 1.51	*.0034

* Values were statistically significant ($P < .05$; Wilcoxon signed rank test).

treatment of SDAVFs. Niimi et al¹⁸ reported 49 patients who were primarily treated with *n*-BCA, but isobutyl-2-cyanoacrylate and polyvinyl alcohol were also used. According to these authors, adequate embolization was achieved in 39 patients (80%); however, angiographic recurrence was seen in 8 (23%) of the 35 patients.¹⁸ Westphal and Koch¹⁹ found recurrent fistulas in 20 (57%) of 35 patients treated with embolization at a mean follow-up time of 7.5 months. In another reported series of 27 SDAVFs, Song et al²⁰ showed a 25% failure rate in patients treated with *n*-BCA.

Furthermore, several studies have reported outcomes after embolization of SDAVFs. Eskander et al²¹ reported on their experience in 26 consecutive patients who were treated for a 6-year period. Nine (39%) of the 23 patients in whom liquid acrylic embolization was performed or attempted ultimately required surgery.²¹ All patients were stabilized or their condition improved after definitive treatment, as assessed by the ALS.²¹ Van Dijk et al⁶ reported a cure rate of only 25% (11/44 patients) after treatment with *n*-BCA embolization. After failed endovascular treatment, 31 patients were cured surgically; the 2 other patients refused surgery.⁶ Motor and bladder function scores were significantly improved in 35 patients who had long-term follow-up (both $P < .005$).⁶ Sherif et al,²² in their study of 26 patients in which embolization with Histoacryl was performed in 19 patients (73.1%) and direct surgery in 7 patients (26.9%), reported a statistically significant improvement was seen in both the mRS score and the ALS gait scale score ($P < .05$). In addition, Andres et al²³ in a group of 21 patients showed that surgical and endovascular treatment resulted in significant improvement in ALS scores (−62.5% and −31.4%, respectively; $P < .05$) and a tendency toward improved mRS (−50% and −32%, respectively) scores. Furthermore, Narvid et al,³ in a group of 63 patients in whom 39 were treated by an endovascular approach and 24 by a surgical approach, reported a signifi-

cant improvement was observed in ALS scores in both the endovascular and surgery groups (gait, $P < .001$; micturition, $P = .005$). In our study, the improvements seen after treatment in the ALS gait and micturition scores were statistically significant ($P < .05$, Wilcoxon signed rank test). The clinical improvements in the MC grading and the mRS score seen after treatment were also statistically significant ($P < .05$, Wilcoxon signed rank test). Our study compares favorably with the other reports described above. In our study, the time from symptom onset to diagnosis of

the SDAVF was 24.6 months. This finding may have influenced our results because, even with proper treatment, a long duration of initial neurologic symptoms is associated with poor clinical and functional outcomes.⁹ In our study, there was only a 17% (5/29) failure rate after embolization, which is an improvement for endovascular treatment compared with the studies described above. Such a rate may be the result of improvements in diagnostic imaging, a better understanding of the pathophysiology of SDAVF, further developments in microcatheter and microwire technology, or the technical experience of the operators regarding use of liquid embolic agents.

Ethylene vinyl alcohol (Onyx) is a relatively new liquid embolic agent used to treat cerebral arteriovenous malformations and fistulas.^{24–26} Because of the physical properties of the agent, this may allow a longer, more controlled injection with better penetration of the vascular bed (ie, venous aspect of the fistula) compared with conventional liquid agents, which polymerize immediately on contact with blood (Fig 2). However, in our series there was a 10% (2/20) failure rate with cyanoacrylate glue and a 33.3% (3/9) failure rate with Onyx. This finding may be related to the experience the authors have with the injection of glue. Since 2003, a total of 3 small case series have described the use of Onyx in the treatment of SDAVFs.^{24,27,28} To the best of our knowledge, our series of 9 patients, in whom SDAVF was treated with Onyx, is the largest to date.

The goal of treatment of SDAVF is to arrest neurologic deterioration. Studies have shown no significant correlation with duration of symptom onset and the extent of cord edema on MR imaging.²⁹ A trend has suggested that earlier exclusion of the fistula correlates with improved motor function.¹⁰ In general, studies suggest that bladder function, if affected, does not recover.^{16,30,31} In our series, we found a similar correlation with the duration of symptoms and treatment outcome. Improvement in motor function after treatment was more likely to occur than improvement in micturition dysfunction. Patients should be monitored with clinical examination and MR imaging after treatment; however, at present no statistical data have suggested correlation between resolution of T2-weighted cord hyperintensity and clinical outcome.^{29,31–33} The persistence of flow voids despite treatment should prompt further spinal angiography to exclude persistent fistula from the same or adjacent level with collateral flow.

In our series, 14 of 15 patients demonstrated increased T2-weighted medullary signal alterations on diagnostic MR imaging, and 6 of 15 patients showed cord expansion, most compatible with edema or venous congestion. Only a small portion of pa-

tients showed an association between clinical improvement and a decrease in signal alterations and cord expansion (On-Line Tables 2–4). Furthermore, only 42% of our patients experienced complete resolution of flow voids/vessels within the spinal canal, whereas Song et al²⁰ reported a 73% resolution of flow voids/vessels within the spinal canal after successful treatment in their series. Our imaging findings are similar to those reported in the previous literature.^{29,32,33}

Limitations of our study were the relatively small sample size (particularly the surgery group) and the retrospective, nonrandomized design. Another weakness of our study was that the delayed time of diagnosis was calculated on the basis of the time of symptom onset reported by the patient on evaluation in the clinic, often many months after symptoms had started. Thus, a possibility of recall bias exists. Furthermore, pre- and post-MR imaging studies were not available in more than 50% of our patients; therefore, the sensitivity of this imaging technique in this study was limited.

CONCLUSIONS

Endovascular treatment of SDAVFs can result in good clinical outcomes. Surgery remains the treatment of choice when safe embolization of the proximal radicular draining vein cannot be obtained or because the shunting artery of the SDAVF also supplies the anterior spinal, posterior spinal, or radioculomedullary artery.

Disclosures: James Robertson—UNRELATED: Payment for Development of Educational Presentations: Codman Endovascular, Comments: Nurse Radiographer Course 2012, departmental grant provided.

REFERENCES

1. Lv X, Li Y, Yang X, et al. Endovascular embolization for symptomatic perimedullary AVF and intramedullary AVM: a series and a literature review. *Neuroradiology* 2012;54:349–59
2. Takai K, Taniguchi M. Comparative analysis of spinal extradural arteriovenous fistulas with or without intradural venous drainage: a systematic literature review. *Neurosurg Focus* 2012;32:E8
3. Narvid J, Hetts SW, Larsen D, et al. Spinal dural arteriovenous fistulae: clinical features and long-term results. *Neurosurgery* 2008; 62:159–66; discussion 166–67
4. Jellema K, Tijssen CC, van Gijn J. Spinal dural arteriovenous fistulas: a congestive myelopathy that initially mimics a peripheral nerve disorder. *Brain* 2006;129:3150–64
5. Koenig E, Thron A, Schrader V, et al. Spinal arteriovenous malformations and fistulae: clinical, neuroradiological and neurophysiological findings. *J Neurol* 1989;236:260–66
6. Van Dijk JM, TerBrugge KG, Willinsky RA, et al. Multidisciplinary management of spinal dural arteriovenous fistulas: clinical presentation and long-term follow-up in 49 patients. *Stroke* 2002;33:1578–83
7. da Costa L, Dehdashti AR, terBrugge KG. Spinal cord vascular shunts: spinal cord vascular malformations and dural arteriovenous fistulas. *Neurosurg Focus* 2009;26:E6
8. McCutcheon IE, Doppman JL, Oldfield EH. Microvascular anatomy of dural arteriovenous abnormalities of the spine: a microangiographic study. *J Neurosurg* 1996;84:215–20
9. Steinmetz MP, Chow MM, Krishnaney AA, et al. Outcome after the treatment of spinal dural arteriovenous fistulae: a contemporary single-institution series and meta-analysis. *Neurosurgery* 2004;55: 77–87; discussion 87–88
10. Sivakumar W, Zada G, Yashar P, et al. Endovascular management of spinal dural arteriovenous fistulas. A review. *Neurosurg Focus* 2009;26:E15
11. Krings T, Geibprasert S. Spinal dural arteriovenous fistulas. *AJNR Am J Neuroradiol* 2009;30:639–48
12. Houdart E, Redondo A, Saint-Maurice JP, et al. Natural history of an incidentally discovered spinal dural arteriovenous fistula. *Neurology* 2001;57:742–43
13. Hurst RW, Kenyon LC, Lavi E, et al. Spinal dural arteriovenous fistula: the pathology of venous hypertensive myelopathy. *Neurology* 1995;45:1309–13
14. Jellema K, Canta LR, Tijssen CC, et al. Spinal dural arteriovenous fistulas: clinical features in 80 patients. *J Neurol Neurosurg Psychiatry* 2003;74:1438–40
15. Muralidharan R, Saladino A, Lanzino G, et al. The clinical and radiological presentation of spinal dural arteriovenous fistula. *Spine* 2011;36:E1641–47
16. Behrens S, Thron A. Long-term follow-up and outcome in patients treated for spinal dural arteriovenous fistula. *J Neurol* 1999;246:181–85
17. Mourier KL, Gelbert F, Rey A, et al. Spinal dural arteriovenous malformations with perimedullary drainage. Indications and results of surgery in 30 cases. *Acta Neurochirurg* 1989;100:136–41
18. Niimi Y, Berenstein A, Setton A, et al. Embolization of spinal dural arteriovenous fistulae: results and follow-up. *Neurosurgery* 1997;40: 675–82, discussion 82–83
19. Westphal M, Koch C. Management of spinal dural arteriovenous fistulae using an interdisciplinary neuroradiological/neurosurgical approach: experience with 47 cases. *Neurosurgery* 1999;45:451–57, discussion 457–58
20. Song JK, Gobin YP, Duckwiler GR, et al. N-butyl 2-cyanoacrylate embolization of spinal dural arteriovenous fistulae. *AJNR Am J Neuroradiol* 2001;22:40–47
21. Eskandar EN, Borges LF, Budzik RF Jr, et al. Spinal dural arteriovenous fistulas: experience with endovascular and surgical therapy. *J Neurosurg* 2002;96:162–67
22. Sherif C, Gruber A, Bavinszki G, et al. Long-term outcome of a multidisciplinary concept of spinal dural arteriovenous fistulae treatment. *Neuroradiology* 2008;50:67–74
23. Andreas RH, Barth A, Guzman R, et al. Endovascular and surgical treatment of spinal dural arteriovenous fistulas. *Neuroradiology* 2008;50:869–76
24. Corkill RA, Mitsos AP, Molyneux AJ. Embolization of spinal intramedullary arteriovenous malformations using the liquid embolic agent, Onyx: a single-center experience in a series of 17 patients. *J Neurosurg Spine* 2007;7:478–85
25. Nogueira RG, Dabus G, Rabinov JD, et al. Preliminary experience with Onyx embolization for the treatment of intracranial dural arteriovenous fistulas. *AJNR Am J Neuroradiol* 2008;29:91–97
26. Weber W, Kis B, Siekmann R, et al. Endovascular treatment of intracranial arteriovenous malformations with Onyx: technical aspects. *AJNR Am J Neuroradiol* 2007;28:371–77
27. Warakaulle DR, Aviv RI, Niemann D, et al. Embolisation of spinal dural arteriovenous fistulae with Onyx. *Neuroradiology* 2003;45:110–12
28. Nogueira RG, Dabus G, Rabinov JD, et al. Onyx embolization for the treatment of spinal dural arteriovenous fistulae: initial experience with long-term follow-up. Technical case report. *Neurosurgery* 2009;64:E197–98; discussion E8
29. Aghakhani N, Parker F, David P, et al. Curable cause of paraplegia: spinal dural arteriovenous fistulae. *Stroke* 2008;39:2756–59
30. Jellema K, Tijssen CC, van Rooij WJ, et al. Spinal dural arteriovenous fistulas: long-term follow-up of 44 treated patients. *Neurology* 2004;62:1839–41
31. Song JK, Vinuela F, Gobin YP, et al. Surgical and endovascular treatment of spinal dural arteriovenous fistulas: long-term disability assessment and prognostic factors. *J Neurosurg* 2001; 94:199–204
32. Cenzato M, Versari P, Righi C, et al. Spinal dural arteriovenous fistulae: analysis of outcome in relation to pretreatment indicators. *Neurosurgery* 2004;55:815–22, discussion 22–23
33. Atkinson JL, Miller GM, Krauss WE, et al. Clinical and radiographic features of dural arteriovenous fistula, a treatable cause of myelopathy. *Mayo Clin Proc* 2001;76:1120–30

Hemodynamics of 8 Different Configurations of Stenting for Bifurcation Aneurysms

K. Kono and T. Terada



ABSTRACT

BACKGROUND AND PURPOSE: SACE is performed for complex aneurysms. There are several configurations of stent placement for bifurcation aneurysms. We investigated hemodynamics among 8 different configurations of stent placement, which may relate to the recanalization rate.

MATERIALS AND METHODS: We created a silicone block model of a patient-specific asymmetric bifurcation aneurysm. Enterprise closed-cell stents were deployed in the model as various configurations. 3D images of these stents were obtained by micro-CT. We performed CFD simulations for a no-stent model and 8 stent models: a single stent from a proximal vessel to a right or left distal vessel, a horizontal stent, a kissing-Y stent with a uniformly narrowed structure, a nonoverlapping-Y stent, a virtual-Y stent with no narrowed structure (fusion of 2 single stents), and 2 different crossing-Y stents with a focally narrowed structure. Hemodynamic parameters were evaluated.

RESULTS: Cycle-averaged velocity and WSS in the aneurysm were reduced because of stent placement in the following order: single stent (19% reduction in cycle-averaged velocity) < nonoverlapping-Y stent (29%) < virtual-Y stent (32%) < horizontal stent (39%) < kissing-Y stent (48%) < crossing-Y stent (54%). Kissing- and crossing-Y stents redirected impingement flow into the distal vessels because of lowered porosity of stents due to narrowed structures.

CONCLUSIONS: Among 8 different configurations of stent placement, kissing- and crossing-Y stents showed the strongest reduction in flow velocity in the aneurysm because of lowered porosity of stents and redirection of impingement flow. This may be a desirable reconstruction of flow hemodynamics and may decrease recanalization rates in SACE.

ABBREVIATIONS: CFD = computational fluid dynamics; L = left; PCA = posterior cerebral artery; R = right; SACE = stent-assisted coil embolization; WSS = wall shear stress

SACE is widely accepted for endovascular treatment of wide-neck or complex aneurysms. Several recent reports have demonstrated that SACE promotes occlusion of incompletely coiled aneurysms and lowers recanalization rates compared with non-stenting embolization, probably because of the hemodynamic effects of stents.¹⁻⁵ However, recanalization rates of SACE are 8.1%–17.2%^{2,4,5}; therefore, these rates still need to be improved. In addition, various configurations of stentings have been proposed and performed for bifurcation aneurysms, including a sin-

gle stent from a proximal to a distal vessel; a waffle-cone stent⁶; a horizontal stent⁷⁻⁹; a nonoverlapping-Y stent¹⁰; a kissing (double-barrel) Y stent, in which both stents are deployed in a parallel fashion^{11,12}; and a crossing-Y stent, in which the second stent is deployed through the interstices of the first stent.¹²⁻¹⁸ The differences in hemodynamics among these various configurations of stent placement are unclear, and this may be important for the recanalization rate. In crossing-Y stents, use of double closed-cell stents causes narrowing of the second stent through the interstices of the first stent,¹⁷ while using an open-cell stent as the first stent can avoid this effect of narrowing.¹⁶ Whether the narrowed structure is beneficial or harmful is unknown. Using micro-CT, we obtained 3D images of various configurations of stent placement in a silicone block model of a bifurcation aneurysm. We performed CFD simulations to clarify differences in hemodynamics among 8 different configurations of stent placement. We also investigated hemodynamics unique to the narrowed structure in the crossing-Y stent with closed-cell stents.

Received October 1, 2012; accepted after revision December 2.

From the Department of Neurosurgery, Wakayama Rosai Hospital, Wakayama, Japan.

Please address correspondence to Kenichi Kono, MD, Department of Neurosurgery, Wakayama Rosai Hospital, 93-1 Kinomoto, Wakayama, 640-8505, Japan; e-mail: vyr01450@gmail.com

Indicates open access to non-subscribers at www.ajnr.org

Indicates article with supplemental on-line figures.

<http://dx.doi.org/10.3174/ajnr.A3479>

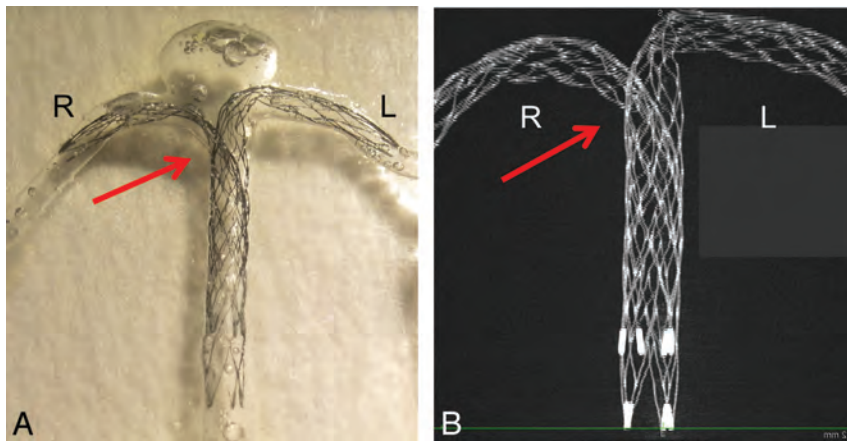


FIG 1. An example of stent placement in a silicone model and an image of stents by micro-CT are shown. A, Double Enterprise stents are deployed as a crossing-Y stent in a silicone block model of the basilar tip aneurysm. The second stent shows narrowing (*arrow*) at the interstices of the first stent. B, A 3D image of the stents was obtained by micro-CT. A maximum-intensity-projection image shows a narrowed structure (*arrow*).

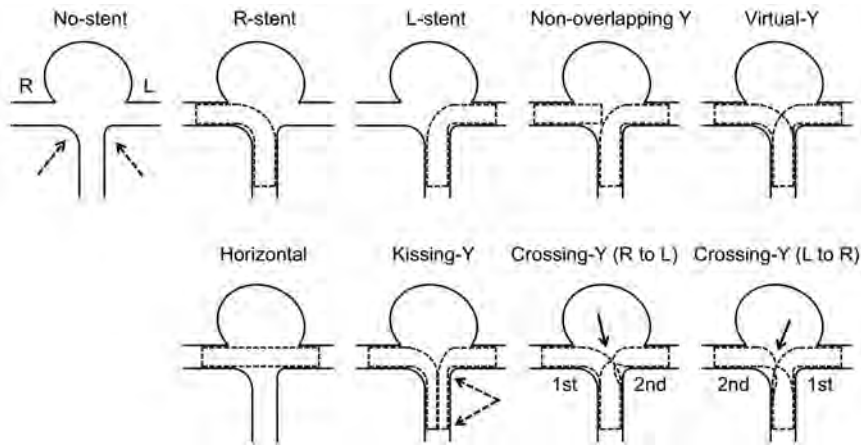


FIG 2. Schematic illustrations of various configurations of stent placement are shown. “No-stent” shows an asymmetric (*dashed arrows*) bifurcation aneurysm without stents. Single-stent placement into a right or a left distal vessel is shown in the R-stent or L-stent, respectively. The dashed lines show shapes of the deployed stents. “Nonoverlapping-Y” shows placement of 1 stent from the proximal to the left distal vessel and placement of another stent within the right distal vessel without overlapping of the 2 stents. “Virtual-Y” shows fusion of the R-stent and L-stent, which does not exist in reality because stent struts have to interact with each other. “Horizontal” shows a single stent placement from the right to the left distal vessel. “Kissing-Y” shows double-stent placement into the right and the left distal vessels in a parallel fashion. In a proximal artery, both stents have uniformly narrowed structures (between the dashed arrows), which lower porosity of the stents. In crossing-Y (R to L), the first stent is deployed into the right distal vessel and the second stent is deployed into the left distal vessel through the interstices of the first stent, which causes narrowing and focally lowered porosity of the second stent (*solid arrow*). “Crossing-Y” (L to R) shows stent placement in the opposite order, which also causes narrowing and focally lowered porosity of the second stent (*solid arrow*).

MATERIALS AND METHODS

Stent Geometry

A rigid silicone block model of a bifurcation aneurysm was created on the basis of an asymmetric basilar tip aneurysm with a maximum diameter of 8 mm in a patient. The diameter of the basilar artery was 2.3 mm. We have previously described detailed methods of creating patient-specific silicone models.¹⁹ Briefly, on the basis of the 3D image obtained by a rotational angiogram, a 3D real-scale model of the aneurysm was created with acrylate photopolymer by using a rapid prototyping system (Vision Realizer RVS-G1; Real Vision Systems, Kanagawa, Japan). The aneurysm

model was placed in a rectangular solid box, and the box was filled with silicone. After the silicone solidified, the acryl inside the silicone block was removed. The aneurysm and vessels formed a cavity in the silicone model (Fig 1A). We deployed closed-cell stents, 28-mm Enterprise (Cordis Neurovascular, Miami Lakes, Florida), in the silicone model in the following 7 different configurations (Fig 2): a single-stent placement from the basilar artery to the right or left PCA, a nonoverlapping-Y stent,¹⁰ a horizontal stent,⁷⁻⁹ a kissing-Y stent (double-stent placement in a parallel fashion),^{11,12} and 2 different crossing-Y stents with a narrowed structure.^{13,14,17} In 1 crossing-Y stent, crossing-Y (R to L), the first stent was deployed into the right PCA and the second stent was placed into the left PCA through the interstices of the first stent. The narrowed structure focally lowered the porosity of the stent (Fig 2). In another crossing-Y stent, crossing-Y (L to R), the order of stent placement was the opposite. In the kissing-Y stent, the narrowed structure of both stents was observed in the basilar artery and uniformly lowered porosity was found in both stents (Fig 2).

Stents in the silicone model were scanned by micro-CT, by using the TOSCANER-30900 μ C3 (Toshiba IT & Control Systems, Tokyo, Japan). The resolution of the micro-CT scanner is 5 μ m. The images were obtained in the standard triangulated language format. The maximum-intensity-projection image of the crossing-Y stent revealed narrowing of the second stent (Fig 1B). Using an engineering design software, 3-matic (Version 6.1; Materialise n.v., Leuven, Belgium), we constructed 9 models, including the no-stent and 8 different configurations of stents (7 stents plus 1 virtual stent): no-stent, R-stent, L-stent, nonoverlapping-Y, virtual-Y, horizontal, kissing-Y, crossing-Y (R to L), and crossing-Y (L to R) (Fig 2). We created the virtual-Y stent by fusion of 2 single stents, the R-stent and L-stent. The virtual-Y stent did not have a narrowed structure. The virtual-Y stent does not exist in reality because stent struts have to interact with each other. We created this model to compare it with the crossing-Y stent with narrowing to evaluate the hemodynamic effects unique to this narrowing.

We could not obtain a clear 3D aneurysm image from the silicone model with stents by micro-CT because of an unclear boundary surface between the silicone and air. Therefore, we

merged the image of the aneurysm obtained by rotational angiography with the image of the stents obtained by micro-CT. The stents slightly overlapped with the wall of the distal portion of the PCAs because of limitations of resolution. We trimmed the overlapped region because we considered that the distal portion of the stent would not significantly alter hemodynamic flow around the aneurysm. We determined the neck orifice by a flat plane, which divided the aneurysm from the parental artery.

CFD Simulations

We performed CFD simulations in a similar manner as we described previously.^{20,21} The fluid domains were extruded at the inlet to allow fully developed flow and were meshed by using ICEM CFD software (Version 14.0, ANSYS, Canonsburg, Pennsylvania) to create finite-volume tetrahedral elements. The smallest grid size was 0.03 mm. Small meshes were generated near the stent struts, and large meshes were generated far from the stent struts to enhance local resolution while keeping the total number of elements within reasonable bounds. The number of elements in each model ranged from approximately 1.8 million to 2.5 million, which was confirmed to be adequate to calculate the velocity and WSS by creating meshes of finer grid densities. Approximately doubled grid densities showed <3% differences in velocity and WSS in the aneurysm, and grid independence was confirmed. Blood was modeled as a Newtonian fluid with an attenuation of 1056 kg/m³ and a viscosity of 0.0035 kg/m/s. A rigid-wall no-slip boundary condition was implemented at the vessel walls.

We performed pulsatile flow simulations with an implicit solver, CFX (Version 14.0, ANSYS), the accuracy of which had been validated previously.²¹ For the inlet flow conditions, we used the volumetric flow rate waveform of the basilar artery of healthy subjects given by Gwilliam et al.²² The flow rate was scaled so that cycle-averaged WSS at the parental artery would be 2.5 Pa, because a WSS of 1.5–7 Pa is considered physiologic.²³ The mean flow velocity at the basilar artery was approximately 0.3 m/s in all 9 models, which is within physiologic levels.²⁴ Zero pressure was imposed at the outlets. The width of the time-step for calculation was set at 0.005 seconds. Calculations were performed for 3 cardiac cycles, and the result of the last cycle was used for analysis. We examined the following hemodynamic parameters: area-averaged velocity on the neck orifice, volume-averaged velocity in the aneurysm, and area-averaged WSS on the dome.

RESULTS

The width of each strut of the stent obtained by micro-CT was measured. This width was a mean of 0.0752 ± 0.0015 mm (*n* = 60; 95% confidence interval, 0.0713–0.0790 mm). The accuracy of micro-CT was sufficient because the width of the strut of the Enterprise stent is 0.078 mm.²⁵

Figure 3A shows reconstructed 3D images of vessels with 8 different configurations of stent placement. Although there were concerns about whether 2 stents could sufficiently open in the kissing-Y stent, the cross-section of the image showed good opening of both stents (data not shown). Figure 3B shows the contours of flow velocity on a coronal plane at peak systole. The strongest impingement flow into the aneurysm was observed in the no-stent. The impingement flow was largely disturbed in the horizon-

tal, kissing-Y, and crossing-Y (both R to L and L to R) models. Redirection of the impingement flow into the PCAs was observed in the kissing-Y and crossing-Y models.

To quantify these redirection effects, we drew 100 streamlines at diastole from the inlet in each model. The streamlines were classified into 3 groups: those entering the aneurysm and those directly entering the right or left PCA without entering the aneurysm. The number of streamlines in each group was counted (Fig 4A). The R-stent or L-stent showed slight redirection effects into each side compared with the no-stent. While the horizontal stent showed few redirection effects, the kissing-Y and crossing-Y stents showed the largest flow redirection effects. Although measurements based on streamlines are not definitive for evaluating flow-redirection effects, they represent semiquantitative analysis.

We speculate that flow-redirection effects depend on the porosity of stents, which varies in each stent configuration. Because it was difficult to measure the porosity of stents owing to skewed stent struts, we measured the mean pore size (area) of stents around the neck orifice responsible for redirection of the impingement flow (Fig 4B). In the crossing-Y stent, we measured the mean pore size of a narrowed stent (ie, the second deployed stent). We did not measure this pore size in the nonoverlapping-Y and virtual-Y stents because these models did not contain narrowed structures and the 2 stents did not interfere with each other. The horizontal stent showed the largest pore size because of swelling of stents across the neck (Fig 3A). The kissing-Y and crossing-Y stents had the smallest pore size (Fig 4B), which was caused by the narrowed structure. In the kissing-Y stent, stent pores were narrowed because 2 stents were deployed in parallel in the parent artery. In the crossing-Y stent, stent pores were narrowed because the second stent was deployed through the closed-cell strut of the first stent. Therefore, we demonstrated that the narrowed structure results in a decrease in the pore size of stents and lowers the porosity of stents, which will redirect the impingement flow into the distal vessels.

To visualize these redirection effects, we selected 4 models: the virtual-Y, horizontal, kissing-Y, and crossing-Y (L to R) (Fig 5). Although all 4 models, except for the virtual-Y, strongly disturbed the impingement flow into the aneurysm, only the kissing-Y and crossing-Y (L to R) redirected impingement flow. The kissing-Y redirected impingement flow into both PCAs because of lowered porosity due to the uniformly narrowed structures of both stents in the basilar artery. The crossing-Y (L to R) also redirected impingement flow into the right PCA because of lowered porosity due to the focally narrowed structure of the second stent through the interstices of the first stent. These results clarify the unique differences between a crossing-Y stent with narrowing (crossing-Y) and a Y-stent without narrowing (virtual-Y). Namely, the narrowed structure produces strong hemodynamic effects by reducing flow velocity in aneurysms. Streamlines and contours of WSS in all 9 models are shown in On-line Figs 1 and 2.

Figure 6 shows quantitative results of cycle-averaged velocity and WSS of the aneurysm (volume-averaged velocity in the aneurysm, area-averaged velocity on the neck, and area-averaged WSS on the dome). Volume-averaged velocity in the aneurysm was reduced in the models in the following order: a single stent (R-stent or L-stent) (mean, 19%) < nonoverlapping-Y (29%) <

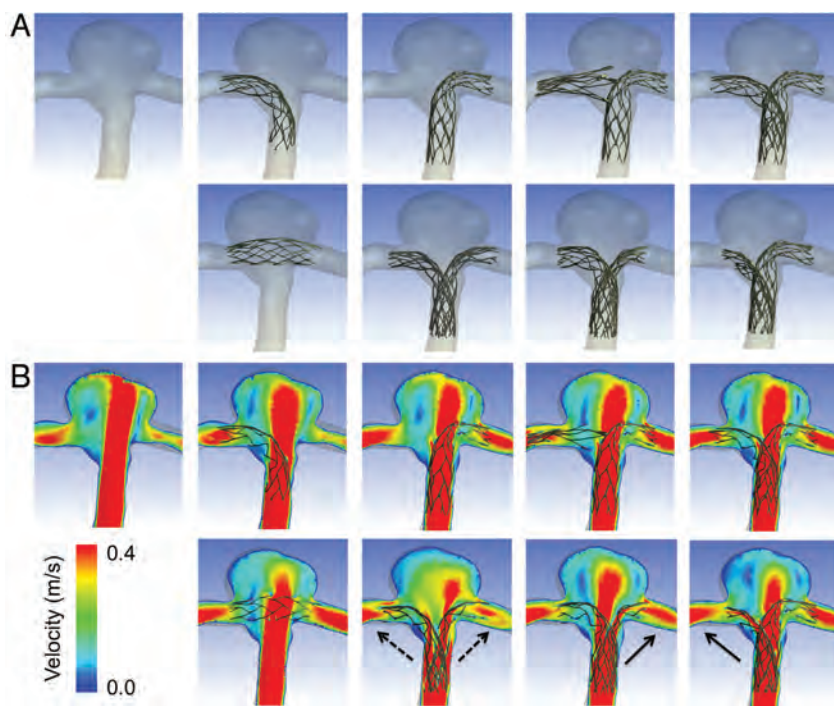


FIG 3. A, Reconstructed images of 8 different configurations of stent placement and no-stent are shown. The arrangement of panels is the same as in Fig 2. In the first row, from left to right, no-stent, R-stent, L-stent, nonoverlapping-Y, and virtual-Y models are shown. In the second row, from left to right, horizontal, kissing-Y, crossing-Y (R to L), and crossing-Y (L to R) models are shown. B, Contours of flow velocity on a coronal plane at peak systole are shown in the same arrangement as in A. The strongest jet flow into the aneurysm can be seen in no-stent. The jet flow is largely disturbed in the horizontal, kissing-Y, and crossing-Y models. Redirection of flow into the right or the left distal vessel is observed in the kissing-Y (dashed arrows) and crossing-Y (solid arrows) models.

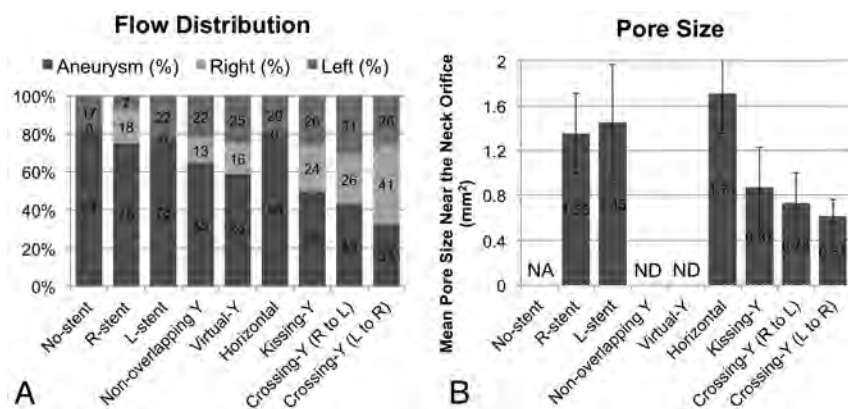


FIG 4. A, Evaluation of flow distribution. In each model, 100 streamlines at diastole are drawn from the inlet. The streamlines are classified into 3 groups: those entering the aneurysm (labeled as "aneurysm") and those directly entering the right or left PCA without entering the aneurysm (labeled as "right" or "left"). The number of streamlines in each group was counted. While the horizontal model shows no flow-redirection effects, the kissing-Y and crossing-Y models show the largest flow redirection effects. B, The mean pore size (area) of stents around the neck orifice in 6 models. The kissing-Y and crossing-Y models have the smallest pore size. Bars show SDs. NA indicates not applicable; ND, not determined.

virtual-Y (32%) < horizontal (39%) < kissing-Y (48%) < crossing-Y (R to L) or crossing-Y (L to R) (mean, 54%). Most of the reduction in velocity or WSS was observed in the kissing-Y and crossing-Y models. The virtual-Y model showed less reduction in velocity compared with the kissing-Y and crossing-Y models, because the kissing-Y and crossing-Y models redirect impingement

flow into the PCAs because of their narrow structures, while the virtual-Y model does not have such an effect because of the lack of a narrow structure. Peak systolic and diastolic hemodynamic values showed the same trends as cycle-averaged values (data not shown).

DISCUSSION

Clinical Aspects of Stents

An important issue of coil embolization of aneurysms is how to decrease recanalization rates because recanalization may require retreatment or even cause subarachnoid hemorrhage. Several recent reports have demonstrated that SACE promotes occlusion of incompletely coiled aneurysms³⁻⁵ and significantly lowers recanalization rates compared with those in nonstenting coil embolization (14.9% versus 33.5%,⁵ 8.1% versus 37.5%,⁴ and 17.2% versus 38.9%²), probably because of the hemodynamic effects of stents. Although thromboembolic complications are a concern of SACE, assessment of antiplatelet activity before treatments decreases these complications.^{2,5} Chalouhi et al² recently reported that thromboembolic complications occurred in 6.8% of patients in both the nonstented ($n = 147$) and stented ($n = 88$) groups. They also demonstrated that crossing-Y stents showed lower recanalization rates compared with those in a single stent (8.3% versus 19.2%).² Several reports mainly focusing on crossing-Y stents showed 0%–33.3% recanalization rates.^{12,13,16,26} Most interesting, only crossing-Y stents using open-cell stents showed recanalization.

Although these previous reports^{12,13,16,26} consist of a small number of case series, these results are consistent with our conclusions that the narrowed structure of Y-stents using closed-cell stents may decrease recanalization rates by reducing flow velocity in aneurysms.²⁷ With regard to concerns of thromboembolic complications of crossing-Y stents using double closed-cell stents with a narrowed structure, assessment of antiplatelet activity before treatment decreases these complications to acceptable levels, as well as using nonstented coil embolization or SACE with a single stent.¹⁴ In clinical practice, in addition to the recanalization rate, properties of open- or closed-cell stents, such as ease of delivery, stability, and vessel wall apposition, should be considered.³

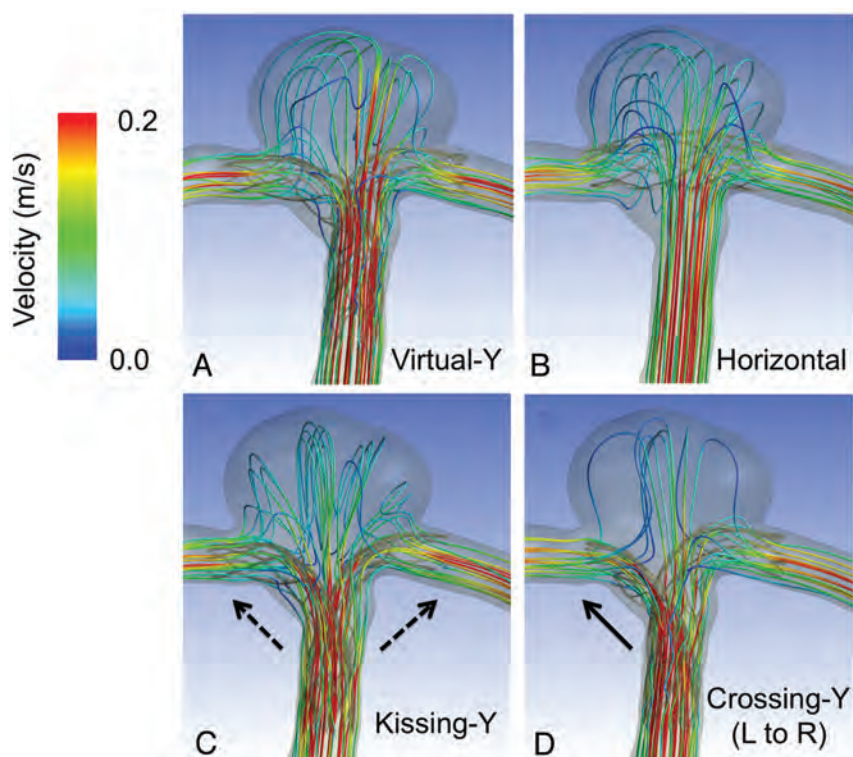


FIG 5. Streamlines colored according to flow velocity at diastole are shown in virtual-Y (A), horizontal (B), kissing-Y (C), and crossing-Y (L to R) stents (D). Stents are transparent so that streamlines can be clearly seen. Horizontal, kissing-Y, and crossing-Y (L to R) models more strongly disturb impingement flow than the virtual-Y model. The kissing-Y model redirects impingement flow into the right and left distal vessels (*dashed arrows*). The crossing-Y (L to R) model also redirects impingement flow into the right distal vessel (*solid arrow*).

Cekirge et al¹⁴ showed that crossing-Y stents by using Enterprise stents without coils can occlude aneurysms, and they considered that the Enterprise stent has stronger hemodynamic effects than an open-cell stent because of its narrow interstices. Our study supports the results of Cekirge et al because we found that a crossing-Y stent with narrowing, the crossing-Y, reduced flow velocity in aneurysms more than a Y-stent without narrowing, the virtual-Y. Therefore, crossing-Y stents by using double closed-cell stents may be superior to open-cell stents for reducing the recanalization rate.

There are 2 other configurations of Y-stent: the nonoverlapping-Y stent¹⁰ and the kissing-Y stent.^{11,12} Nonoverlapping-Y stents are the least effective in reducing the velocity in aneurysms among all configurations of Y-stents. The kissing-Y stent and crossing-Y stent reduce velocity by redirecting impingement flow (Fig 6). Although there are a few reported cases of using kissing-Y stents,^{11,12} the kissing-Y stent may also reduce recanalization rates and occlude aneurysms without coils as in cases of crossing-Y stents using Enterprise stents.¹⁴

Other than Y-stents, single-stent placement, horizontal stent placement,⁷⁻⁹ or waffle-cone-configuration stent placement⁶ are alternative methods for SACE of bifurcation aneurysms. We did not include a waffle-cone-configuration stent placement in this study. However, this omission does not change our conclusions because waffle-cone-configuration stent placement will not disturb impingement flow and it will probably reduce flow velocity in aneurysms less than in a single-stent placement (ie, R-stent or

L-stent). Considering hemodynamic effects, our study demonstrated that the kissing-Y or crossing-Y stent is preferable. In clinical practice, consideration of other issues, such as the technical problems of each configuration of stent placement, selection of stents on the basis of stent properties and profiles, and vascular geometries, should be taken into consideration.^{3,13,14}

Hemodynamics of Stents

Hemodynamics of several configurations of stent placement for aneurysms has been previously studied.²⁸⁻³¹ However, most studies compared hemodynamics between nonstenting and stent-placement models, or among different designs of stents or multiple stentings of stent-in-stent configurations. They did not investigate hemodynamic differences among different configurations of stent placement. While we used vascular-specific conformed stent geometry obtained by micro-CT, in most of the previous studies,^{28,31} stents were virtually conformed to fit into a parent vessel lumen and were deployed across an aneurysm neck. Because the geometry and porosity of stents change by the vascular geometry and the radius of vessels, virtual deployment is not appropriate for reproducing the real geometry of stents deployed in vessels. Our study shows that changes in the porosity of stents are important for hemodynamics due to stent placement. Among the 8 different configurations used in our study, kissing-Y and crossing-Y stents showed the strongest reduction in flow because of the narrowed structures, which lowered the porosity of stents and redirected flow.

A few studies have investigated the flow dynamics of Y-stents.^{30,31} Cantón et al³⁰ and Babiker et al³¹ performed in vitro flow studies of crossing-Y stents with double open-cell stents by using particle image velocimetry. They showed that the crossing-Y stent reduced flow velocity in an aneurysm by 11%³⁰ or 22.0%–42.9%.³¹ Both studies used open-cell stents, and there was no narrowed structure in the Y-stent. Babiker et al³¹ also performed CFD simulations, but only for single-stent-placement models, which correspond to the L-stent and horizontal stents in our models. In our study, because we created a silicone model and used micro-CT, we were able to obtain 3D images of various configurations of stent placement, including a crossing-Y stent with a narrowed structure, and showed that its narrowed structure has a unique function of redirection of impingement flow into distal vessels.

Most CFD studies on stents for aneurysms, including this study, did not include coils in simulations because of technical difficulties. While flow-diverter stents can be used without coils, high-porosity stents, such as Enterprise stents, are generally used with coils because they usually cannot occlude aneurysms without coils. In this study, our intention was not to show that the Enterprise

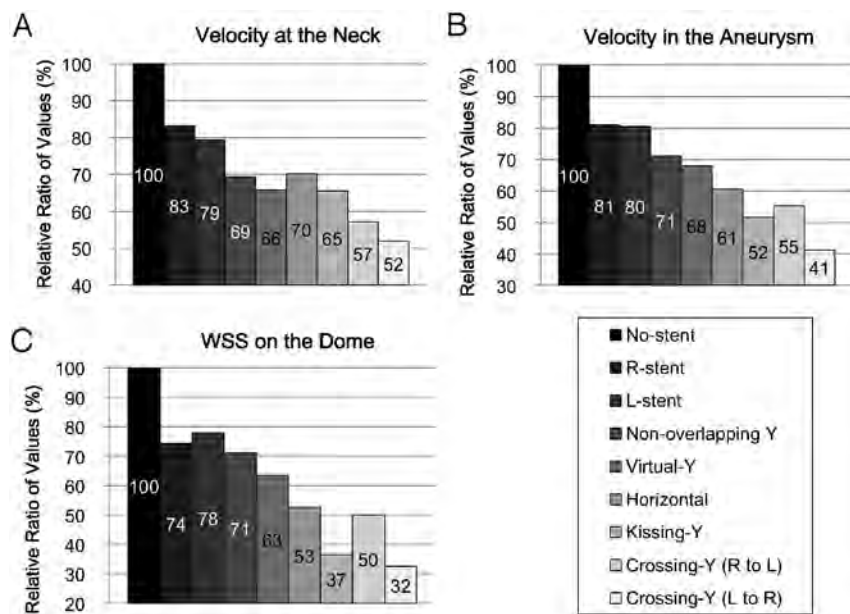


FIG 6. Relative ratios of area-averaged velocity at the neck orifice (A), volume-averaged velocity in the aneurysm (B), and area-averaged WSS on the dome (C), shown as cycle averages for the 9 models. Most of the reduction in velocity or WSS was observed in the kissing-Y, crossing-Y (R to L), and crossing-Y (L to R) models.

stent works as a flow diverter or to recommend stent-only therapy, but to demonstrate that the crossing-Y or kissing-Y stent with coils may reduce recanalization rates. In aneurysm treatments, we should first consider a simple strategy, such as coil embolization with no stent or a single stent. In case of complex or recanalized aneurysms, the results in this study may be helpful and the crossing-Y or kissing-Y stent with coils may be considered.

Limitations of the Study

In our CFD study, we simplified several properties, such as the viscoelasticity of the vessel wall and the non-Newtonian property of the blood for technical reasons. Although the main hemodynamic features are thought to be preserved,³² these simplifications may cause differences between the results of CFD simulation and the in vivo state. Specifically, the present CFD study has the following limitations: First, single vascular geometry was examined. Different vascular geometries may cause different CFD results. The aneurysm model is relatively symmetric, and the size of the aneurysm is not large. Some stent configurations may be unnecessary or unrealistic in this model. Second, the geometry of stents slightly changes each time with stent placement, which may lead to different hemodynamic results. Third, we extruded the fluid domain at the inlet to allow fully developed flow, which neglected the shape of the proximal artery. A curvature could lead to a velocity profile that is not parabolic.³³ Fourth, we did not include coils in the CFD simulations because of technical difficulties, while we basically assumed SACE in this study. Fifth, the number of elements for the CFD simulations may be insufficient to calculate absolute hemodynamic values, though we consider that they are sufficient to show global flow patterns and compare them among the models.

Despite these 5 limitations, we consider that our conclu-

sions are still valid because a narrow structure is an important factor for redirecting flow, which is maintained in other vascular geometries or slightly different stent geometries in the same configurations. In addition, because our conclusions do not depend on the absolute values of hemodynamic parameters but on comparison among the models, our conclusions are relatively robust. Therefore, we consider that the reduction in flow in aneurysms among the 8 different configurations of stent placement (Fig 6) would not substantially change, even if we took these 5 limitations into consideration.

CONCLUSIONS

Among 8 different configurations of stent placement for a bifurcation aneurysm, kissing- and crossing-Y stents show the strongest effects on flow reduction because of their narrowed structures, which lower the porosity of stents

and redirect impingement flow into distal vessels. This may be a desirable reconstruction of flow hemodynamics and may decrease the recanalization rate in SACE. Although this study uses only single vascular geometry, these results may be applicable to other shapes of bifurcation aneurysms because narrowed structures do not depend on vascular geometry but on configurations of stent placement instead.

REFERENCES

1. Wakhloo AK, Linfante I, Silva CF, et al. Closed-cell stent for coil embolization of intracranial aneurysms: clinical and angiographic results. *AJNR Am J Neuroradiol* 2012;33:1651–56
2. Chalouhi N, Jabbour P, Gonzalez LF, et al. Safety and efficacy of endovascular treatment of basilar tip aneurysms by coiling with and without stent-assistance: a review of 235 cases. *Neurosurgery* 2012;71:785–94
3. Izar B, Rai A, Raghuram K, et al. Comparison of devices used for stent-assisted coiling of intracranial aneurysms. *PLoS One* 2011;6:e24875
4. Lawson MF, Newman WC, Chi YY, et al. Stent-associated flow remodeling causes further occlusion of incompletely coiled aneurysms. *Neurosurgery* 2011;69:598–603
5. Piotin M, Blanc R, Spelle L, et al. Stent-assisted coiling of intracranial aneurysms: clinical and angiographic results in 216 consecutive aneurysms. *Stroke* 2010;41:110–15
6. Horowitz M, Levy E, Sauvageau E, et al. Intra/extra-aneurysmal stent placement for management of complex and wide-necked-bifurcation aneurysms: eight cases using the waffle cone technique. *Neurosurgery* 2006;58(4 suppl 2):ONS-258–62, discussion ONS-262
7. Wanke I, Gizewski E, Forsting M. Horizontal stent placement plus coiling in a broad-based basilar-tip aneurysm: an alternative to the Y-stent technique. *Neuroradiology* 2006;48:817–20
8. Siddiqui MA, J Bhattacharya J, Lindsay KW, et al. Horizontal stent-assisted coil embolisation of wide-necked intracranial aneurysms with the Enterprise stent: a case series with early angiographic follow-up. *Neuroradiology* 2009;51:411–18

9. Yashar P, Kan PT, Levy EI. **Horizontal deployment of an intracranial stent via an antegrade approach for coil embolization of a basilar apex aneurysm: technical note.** *J Neurointerv Surg* 2011;3:355–57
10. Cho YD, Park SW, Lee JY, et al. **Nonoverlapping Y-configuration stenting technique with dual closed-cell stents in wide-neck basilar tip aneurysms.** *Neurosurgery* 2012;70:244–49
11. Bain M, Hussain MS, Spiotta A, et al. **“Double-barrel” stent reconstruction of a symptomatic fusiform basilar artery aneurysm: case report.** *Neurosurgery* 2011;68:E1491–96
12. Zhao KJ, Yang PF, Huang QH, et al. **Y-configuration stent placement (crossing and kissing) for endovascular treatment of wide-neck cerebral aneurysms located at 4 different bifurcation sites.** *AJNR Am J Neuroradiol* 2012;33:1310–16
13. Akgul E, Aksungur E, Balli T, et al. **Y-stent-assisted coil embolization of wide-neck intracranial aneurysms: a single center experience.** *Interv Neuroradiol* 2011;17:36–48
14. Cekirge HS, Yavuz K, Geyik S, et al. **A novel “Y” stent flow diversion technique for the endovascular treatment of bifurcation aneurysms without endosaccular coiling.** *AJNR Am J Neuroradiol* 2011;32:1262–68
15. Spiotta AM, Gupta R, Fiorella D, et al. **Mid-term results of endovascular coiling of wide-necked aneurysms using double stents in a Y configuration.** *Neurosurgery* 2011;69:421–29
16. Lozen A, Manjila S, Rhiew R, et al. **Y-stent-assisted coil embolization for the management of unruptured cerebral aneurysms: report of six cases.** *Acta Neurochir (Wien)* 2009;151:1663–72
17. Rohde S, Bendszus M, Hartmann M, et al. **Treatment of a wide-necked aneurysm of the anterior cerebral artery using two Enterprise stents in “Y”-configuration stenting technique and coil embolization: a technical note.** *Neuroradiology* 2010;52:231–35
18. Chow MM, Woo HH, Masaryk TJ, et al. **A novel endovascular treatment of a wide-necked basilar apex aneurysm by using a Y-configuration, double-stent technique.** *AJNR Am J Neuroradiol* 2004;25:509–12
19. Kono K, Shintani A, Okada H, et al. **Preoperative simulations of endovascular treatment for a cerebral aneurysm using a patient-specific vascular silicone model.** *Neurol Med Chir (Tokyo)* 2013;53:347–51
20. Kono K, Fujimoto T, Shintani A, et al. **Hemodynamic characteristics at the rupture site of cerebral aneurysms: a case study.** *Neurosurgery* 2012;71:E1202–29
21. Kono K, Shintani A, Fujimoto T, et al. **Stent-assisted coil embolization and computational fluid dynamics simulations of bilateral vertebral artery dissecting aneurysms presenting with subarachnoid hemorrhage: case report.** *Neurosurgery* 2012;71:E1192–201
22. Gwilliam MN, Hoggard N, Capener D, et al. **MR derived volumetric flow rate waveforms at locations within the common carotid, internal carotid, and basilar arteries.** *J Cereb Blood Flow Metab* 2009;29:1975–82
23. Malek AM, Alper SL, Izumo S. **Hemodynamic shear stress and its role in atherosclerosis.** *JAMA* 1999;282:2035–42
24. Lupetin AR, Davis DA, Beckman I, et al. **Transcranial Doppler sonography. Part 1. Principles, technique, and normal appearances.** *Radiographics* 1995;15:179–91
25. Patel NV, Gounis MJ, Wakhloo AK, et al. **Contrast-enhanced angiographic cone-beam CT of cerebrovascular stents: experimental optimization and clinical application.** *AJNR Am J Neuroradiol* 2011;32:137–44
26. Thorell WE, Chow MM, Woo HH, et al. **Y-configured dual intracranial stent-assisted coil embolization for the treatment of wide-necked basilar tip aneurysms.** *Neurosurgery* 2005;56:1035–40
27. Luo B, Yang X, Wang S, et al. **High shear stress and flow velocity in partially occluded aneurysms prone to recanalization.** *Stroke* 2011;42:745–53
28. Tremmel M, Xiang J, Natarajan SK, et al. **Alteration of intra-aneurysmal hemodynamics for flow diversion using Enterprise and Vision stents.** *World Neurosurg* 2010;74:306–15
29. Kim M, Levy EI, Meng H, et al. **Quantification of hemodynamic changes induced by virtual placement of multiple stents across a wide-necked basilar trunk aneurysm.** *Neurosurgery* 2007;61:1305–12
30. Cantón G, Levy DI, Lasheras JC. **Hemodynamic changes due to stent placement in bifurcating intracranial aneurysms.** *J Neurosurg* 2005;103:146–55
31. Babiker MH, Gonzalez LF, Ryan J, et al. **Influence of stent configuration on cerebral aneurysm fluid dynamics.** *J Biomech* 2012;45:440–47
32. Ford MD, Nikolov HN, Milner JS, et al. **PIV-measured versus CFD-predicted flow dynamics in anatomically realistic cerebral aneurysm models.** *J Biomech Eng* 2008;130:021015
33. Castro MA, Putman CM, Cebal JR. **Computational fluid dynamics modeling of intracranial aneurysms: effects of parent artery segmentation on intra-aneurysmal hemodynamics.** *AJNR Am J Neuroradiol* 2006;27:1703–09

Stent-Assisted Coiling Versus Balloon Remodeling of Wide-Neck Aneurysms: Comparison of Angiographic Outcomes

N. Chalouhi, R.M. Starke, M.T. Koltz, P.M. Jabbour, S.I. Tjoumakaris, A.S. Dumont, R.H. Rosenwasser, S. Singhal, and L.F. Gonzalez

ABSTRACT

BACKGROUND AND PURPOSE: Stent-assisted coiling and balloon-assisted coiling are 2 well-established techniques for treatment of wide-neck intracranial aneurysms. A direct comparative analysis of angiographic outcomes with the 2 techniques has not been available. We compare the angiographic outcomes of wide-neck aneurysms treated with stent-assisted coiling versus balloon-assisted coiling.

MATERIALS AND METHODS: A retrospective review was conducted on 101 consecutive patients treated at our institution, 69 with stent-assisted coiling and 32 with balloon-assisted coiling. Two multivariate logistic regression analyses were performed to determine predictors of aneurysm obliteration and predictors of progressive aneurysm thrombosis at follow-up.

RESULTS: The 2 groups were comparable with respect to all baseline characteristics with the exception of a higher proportion of ruptured aneurysms in the balloon-assisted coiling group (65.6%) than in the stent-assisted coiling group (11.5%, $P < .001$). Procedural complications did not differ between the stent-assisted coiling group (6%) and the balloon-assisted coiling group (9%, $P = .5$). The rates of complete aneurysm occlusion (Raymond score 1) at the most recent follow-up were significantly higher for the stent-assisted coiling group (75.4%) compared with the balloon-assisted coiling group (50%, $P = .01$). Progressive occlusion of incompletely coiled aneurysms was noted in 76.6% of aneurysms in the stent-assisted coiling group versus 42.8% in the balloon-assisted coiling group ($P = .02$). Retreatment rates were significantly lower with stent-assisted coiling (4.3%) versus balloon-assisted coiling (15.6%, $P = .05$). In multivariate analysis, stented aneurysms independently predicted both complete aneurysm obliteration and progression of occlusion.

CONCLUSIONS: Stent-assisted coiling may yield lower rates of retreatment and higher rates of aneurysm obliteration and progression of occlusion at follow-up than balloon-assisted coiling with a similar morbidity rate.

ABBREVIATIONS: SAC = stent-assisted coiling; BAC = balloon-assisted coiling; PED = Pipeline Embolization Device

Wide-neck intracranial aneurysms were classically considered unsuitable for endovascular treatment and were typically managed by surgical clipping. Recent advancements in endovascular devices and techniques have placed such aneurysms within the range of endovascular therapy. Specifically, stent-assisted coiling and balloon-assisted coiling (also known as the balloon remodeling technique) have emerged as safe and efficient treatment modalities for complex and wide-neck aneurysms. Both techniques have improved

the long-term durability of endovascular coiling.^{1,2} By preventing coil herniation into the parent vessel and helping the coil to assume the 3D shape of the aneurysm, the use of a balloon allows denser aneurysm packing than does conventional coiling.^{3,4} On the other hand, a stent acts as a scaffold for coils and improves neck coverage, thus allowing optimal aneurysm coiling.⁵ A growing but currently incomplete body of evidence also suggests that self-expanding stents may have flow-remodeling effects that lead to more durable aneurysm obliteration.^{2,6,7} Although the safety and efficacy of SAC and BAC have been studied in several series, to our knowledge a direct comparative analysis of angiographic outcomes with the 2 techniques has not been available.

We present the results of the first study comparing the angiographic outcomes of BAC and SAC in wide-neck intracranial aneurysms. Two multivariate logistic regression analyses were conducted to determine predictors of aneurysm obliteration and predictors of progressive aneurysm thrombosis at follow-up.

Received October 26, 2012; accepted after revision January 20, 2013.

From the Department of Neurological Surgery (N.C., R.M.S., M.T.K., P.M.J., S.I.T., A.S.D., R.H.R., S.S., L.F.G.), Thomas Jefferson University and Jefferson Hospital for Neuroscience, Philadelphia, Pennsylvania; and Department of Neurological Surgery (R.M.S.), University of Virginia, Charlottesville, Virginia.

Please address correspondence to L. Fernando Gonzalez, MD, Department of Neurological Surgery, Division of Neurovascular Surgery and Endovascular Neurosurgery, Thomas Jefferson University Hospital, 901 Walnut St, 3rd Floor, Philadelphia, PA 19107; e-mail: fernando.gonzalez@jefferson.edu

<http://dx.doi.org/10.3174/ajnr.A3538>

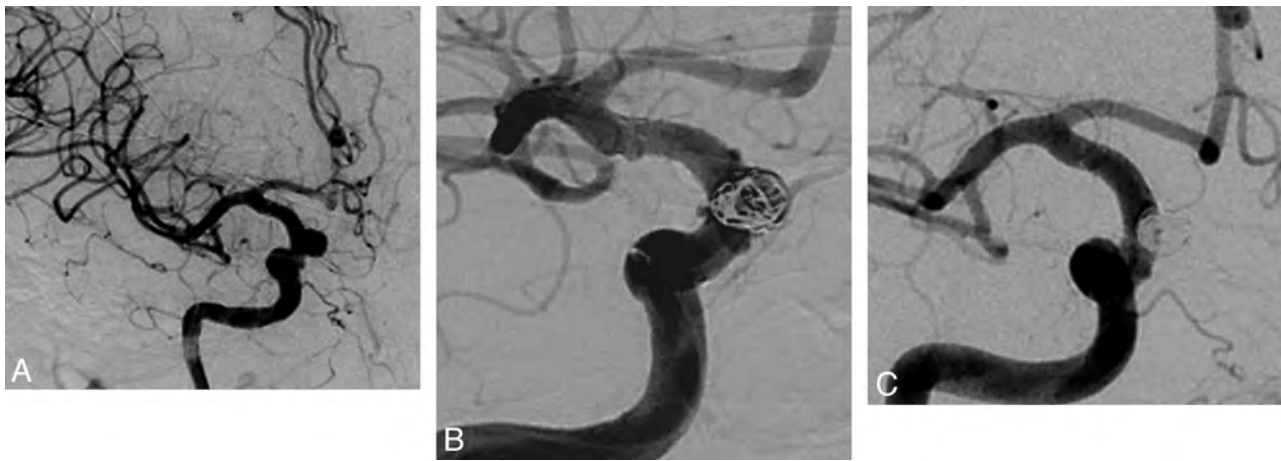


FIG 1. Frontal views of DSA. *A*, Unruptured wide-neck superior hypophyseal artery aneurysm before treatment. *B*, Angiogram obtained immediately after SAC with residual filling of the aneurysm. *C*, Twelve-month follow-up angiogram shows progression of the aneurysm to complete occlusion.

MATERIALS AND METHODS

Institutional review board approval was obtained before data collection. Nine hundred fifty-nine aneurysms were treated (779 with endovascular means, 180 with surgical clipping) at Jefferson Hospital for Neuroscience between 2009–2010. Consecutive patients with wide-neck aneurysms treated by SAC during a 1-year period (2009) or BAC during a 2-year period (2009–2010) at our institution were identified. Wide-neck aneurysms were defined as aneurysms with a fundus-to-neck ratio of <2 or a neck diameter of ≥ 4 mm. One hundred twenty-three patients with wide-neck aneurysms were treated with SAC and 57 patients were treated with BAC. Patients with at least 1 available DSA follow-up were included in the study. Previously treated aneurysms were excluded from the analysis. Fifty patients had only MRA/CTA follow-up, 16 patients had previously treated aneurysms, and 13 patients were lost to follow-up. Thus, a total of 101 patients, 69 treated with SAC and 32 treated with BAC, met our criteria and constituted our study population (Fig 1).

Demographic data on patient age, sex, aneurysm location, ruptured or unruptured aneurysm status, aneurysm size, and type of procedure were recorded. Aneurysm volume and packing density were calculated by use of Angiocalc software (<http://www.angiocalc.com>) on the basis of the angiographic shape and size of the aneurysm as well as the type and size of coils. Initial and follow-up angiograms were reviewed by an independent observer. Aneurysm occlusion was categorized based on the Raymond scale as complete occlusion (Raymond class 1), residual neck (Raymond class 2), and dome filling (Raymond class 3). The incidence of progression of occlusion with BAC versus SAC was determined in aneurysms with an initial Raymond class of 2 or 3.

Procedures were performed under general anesthesia; continuous neurophysiologic monitoring including somatosensory evoked potentials, brain stem auditory-evoked responses, and electroencephalography. Patients with unruptured aneurysms treated with BAC were heparinized, and activated clotting time was maintained intraoperatively at twice the baseline. Patients presenting with SAH received 35 U/kg of heparin after deployment of the first coil. Access was obtained with a single 7F sheath and a 6F guide catheter. A 3-way rotatory hemostatic valve was

used in all cases; 3D reconstruction was obtained to best demonstrate the aneurysm neck and the parent vessel. The balloon was advanced through the center port of the rotatory hemostatic valve and left spanning the neck of the aneurysm. Subsequently, a microcatheter was introduced to the aneurysm and an attempt was made initially to place the coils with the balloon deflated. If the coils compromised the lumen of the parent vessel, the balloon was inflated to provide assistance. Multiple coils were deployed during a single inflation. Once coiling had been completed, the balloon was deflated on a blank roadmap to determine the stability of the coil mass. If coil displacement occurred, the balloon was re-inflated and more coils were deployed. Antiplatelet therapy was not given in any of these patients either during or after surgery. A HyperGlide (ev3, Irvine, California) balloon was used in 30 patients and a HyperForm (ev3) balloon in 2 patients.

SAC procedures were either staged ($n = 35$) or performed during a single session ($n = 34$) at the operator's discretion. In staged procedures, the stent was placed first across the aneurysm neck and left to endothelialize for 6–12 weeks before the patient was brought back for coil embolization. This usually allowed greater stability and less movement of the stent during coil deployment. Single-stage SAC was performed by use of the microcatheter “jailing” technique. Neuroform stents were sized on the basis of the largest diameter of the target vessel and were usually slightly oversized. When the use of a stent was anticipated, patients were pretreated with 81 mg of aspirin and 75 mg of clopidogrel 10 days before the procedure. Platelet function tests were performed with aspirin assay and P2Y₁₂ assay (VerifyNow; Accumetrics, San Diego, California). Patients treated in the setting of SAH were loaded intraoperatively with 600 mg of clopidogrel via a nasogastric tube immediately after stent deployment. During the procedure, they also received boluses of intravenous heparin to maintain an activated clotting time of 2 to 3 times their baseline. All patients were maintained on daily doses of 75 mg of clopidogrel and 81 mg of aspirin for 2 months, followed by aspirin 81 mg daily indefinitely. The Neuroform stent (Stryker Neurovascular, Fremont, California) was used in 49 patients and the Enterprise stent (Codman & Shurtleff, Raynham, Massachusetts) in 20

Table 1: Baseline characteristics of the 2 groups

	Stent Group	Balloon Group	P Values
Age, y	54.2	53.7	.4
Female sex, n (%)	57/69 (82.6)	26/32 (81.2)	.9
Ruptured aneurysms, n (%)	8/69 (11.5)	21/32 (65.6)	<.001
Anterior circulation aneurysms, n (%)	58/69 (84.1)	26/32 (81.3)	.8
Mean aneurysm size, mm	6.8	6.4	.3

patients. The choice between Neuroform and Enterprise stent placement was mainly based on operator preference.

Bare platinum coils were used for aneurysm embolization. In BAC, coiling was interrupted when the aneurysm was completely occluded or when the microcatheter was pulled out of the aneurysm. Because of the potential flow-remodeling effects of self-expanding stents, we may tend to achieve lower packing densities in SAC than in BAC at the operator's discretion. Angiographic follow-up is scheduled at 6 months, 1 year, 2 years, and 5 years after treatment with BAC or SAC at our institution.

Statistical Analysis

Data are presented as mean and range for continuous variables and as frequency for categorical variables. Analysis was carried out with the use of unpaired *t* test, χ^2 , and Fisher exact tests as appropriate.

Univariable analysis was used to test covariates predictive of aneurysm obliteration at follow-up: Raymond score 1 versus 2–3 and Raymond score 1–2 versus 3. Interaction and confounding was assessed through stratification and relevant expansion covariates. Factors predictive in univariable analysis ($P < .15$)⁸ were entered into a multivariable logistic regression analysis. *P* values of $\leq .05$ were considered statistically significant. Statistical analysis was carried out with STATA 10.0 (StataCorp, College Station, Texas).

A similar statistical analysis was conducted to determine predictors of progression of occlusion. Only aneurysms that were initially incompletely occluded (Raymond score of 2 or 3) were included in this analysis: 47 in the SAC group and 21 in the BAC group (Fig 1).

RESULTS

Anatomic Results

The 2 groups were comparable with respect to all baseline characteristics (Table 1) with the exception of a higher proportion of ruptured aneurysms in the BAC group (65.6%) than in the SAC group (11.5%, $P < .001$).

In the SAC group, Raymond scores were 1 in 22 (31.9%) patients, 2 in 44 (63.8%) patients, and 3 in 3 (4.3%) patients. In the BAC group, Raymond scores were 1 in 11 (34.4%) patients and 2 in 21 (65.6%) patients ($P = .8$). Packing density was significantly higher in the BAC (29.4%) versus the SAC group (17.5%, $P < .001$). Of note, in the SAC group, mean packing density was 23.4% in ruptured aneurysms and 16.7% in unruptured aneurysms ($P = .3$). Mean angiographic follow-up was 10.2 ± 7.0 months in the entire cohort (median, 8; range, 3–48), 10.7 ± 7.5 months in the SAC group (median, 8; range, 5–48), and 8.9 ± 5.7 months (median, 6.5; range, 3–36) in the BAC group ($P = .2$). At follow-up, in

the SAC group, Raymond scores were 1 in 52 (75.4%) patients, 2 in 13 (18.8%) patients, and 3 in 4 (5.8%) patients. In the BAC group, Raymond scores were 1 in 16 (50%) patients, 2 in 11 (34.4%) patients, and 3 in 5 (15.6%) patients. The rates of complete aneurysm occlusion (Raymond 1) at follow-up were significantly higher for the SAC group (75.4%) compared with the BAC group (50%, $P = .01$). The rates of adequate aneurysm occlusion (Raymond 1–2) at follow-up, however, did not differ significantly between the SAC group (94.2%) and the BAC group (84.4%, $P = .1$). In univariate analysis, the following factors were tested for as predictors of complete obliteration (Raymond 1): age ($P = .7$), sex ($P = .5$), ruptured/unruptured aneurysm status ($P = .8$), aneurysm location ($P = .005$), aneurysm size ($P = .03$), packing density ($P = .2$), follow-up duration ($P = .5$), initial aneurysm occlusion ($P = .6$), and type of treatment ($P = .01$). Aneurysm location, aneurysm size, and type of treatment were subsequently entered into a multivariate model. In multivariate analysis, smaller (<7 mm) aneurysms (OR = 0.83; 95% CI, 0.68–0.98; $P = .01$) and stented aneurysms (OR = 0.3; 95% CI, 0.12–0.81; $P = .02$) were independent predictors of complete obliteration at follow-up. Posterior communicating artery–carotid cavernous–carotid terminus–middle cerebral artery–posterior carotid wall aneurysms (ie, aneurysm locations with rates of complete occlusion below 60%) (OR = 3.3; 95% CI, 1.3–8.6; $P = .01$) were negative predictors of obliteration. These 3 factors remained statistically significant even after controlling for packing density and ruptured aneurysm status. The same factors as above were tested for as predictors of adequate aneurysm occlusion (Raymond 1–2). Aneurysm size ($P = .01$) and stented aneurysms ($P = .1$) were the only predictors in univariate analysis. In multivariate analysis, smaller (<7 mm) aneurysms (OR = 0.2; 95% CI, 0.06–0.6; $P = .004$) were predictive of adequate aneurysm occlusion. There was also a trend for stented aneurysms (OR = 0.2; 95% CI, 0.05–1.2; $P = .08$) to predict adequate aneurysm occlusion.

The rates of retreatment were 4.3% (3/69) in the SAC group versus 15.6% (5/32) in the BAC group ($P = .05$). No patient in the SAC group had evidence of in-stent stenosis or occlusion on follow-up angiograms.

Of 47 aneurysms in the SAC group and 21 aneurysms in the BAC group that were initially incompletely occluded, progressive occlusion at follow-up was noted in 36 (76.6%) aneurysms in the SAC group and 9 (42.8%) aneurysms in the BAC group ($P = .02$). In univariate analysis, the following factors were tested for as predictors of progression of occlusion: age ($P = .8$), sex ($P = .2$), ruptured/unruptured aneurysm status ($P = .4$), aneurysm location ($P = .06$), aneurysm size ($P = .02$), packing density ($P = .04$), follow-up duration ($P = .7$), and type of treatment ($P = .02$). Aneurysm location, aneurysm size, packing density, and type of treatment were subsequently entered into a multivariate model. In multivariate analysis, decreasing packing density (OR = 1.03; 95% CI, 0.9–1.12; $P = .382$) and decreasing aneurysm size (OR = 0.9; 95% CI, 0.7–1.1; $P = .2$) were no longer predictive of progression of occlusion. Stented aneurysms (OR = 0.08; 95% CI, 0.02–0.3; $P < .001$) positively predicted progression of occlusion, whereas anterior communicating artery–carotid cavernous–carotid terminus aneurysms (ie, aneurysm locations with incidence of progressive occlusion below 50%) were negative predictors

(OR = 11.5; 95% CI, 2.2–59; $P = .004$). These 2 factors remained statistically significant even after controlling for packing density and ruptured aneurysms.

Procedural Outcomes

Procedural complications occurred in 4 (6%) patients of the SAC group and resulted in permanent morbidity in 2 (3%): Intraoperative aneurysm rupture causing intraparenchymal hemorrhage; new infarct in the posterior limb of right internal capsule; new frontal and parietal infarcts; and small clinically silent parietal infarcts. In the BAC group, there were 3 (9%, $P = .5$) procedural complications, leaving permanent morbidity in 1 (3%): intraoperative aneurysm rupture rapidly controlled by balloon inflation and coil packing; thrombus visualized intraprocedurally treated by intra-arterial infusion of abciximab; and hemiparesis caused by a frontal paramedian infarct.

Favorable outcomes (mRS 0–2) at the most recent follow-up visit (mean, 7.3 months) were noted in 66 of 69 patients (95%) of the SAC group and 29 of 32 patients (91%) of the BAC group ($P = .9$).

DISCUSSION

The most important findings of the present study are the following: 1) SAC of wide-neck aneurysms provides higher rates of complete obliteration (Raymond 1) at follow-up than does BAC. The rates of adequate aneurysm occlusion (Raymond 1–2), however, did not significantly differ between the 2 techniques. 2) Lower retreatment rates were observed with SAC versus BAC in wide-neck aneurysms. 3) SAC causes delayed occlusion of incompletely coiled wide-neck aneurysms at a significantly higher rate than does BAC. 4) Both treatment strategies are associated with low rates of morbidity and excellent clinical outcomes.

The high rate of aneurysm recanalization is considered the major drawback of endovascular therapy. Raymond et al⁹ found some degree of recurrence in as many as 33.6% of coiled aneurysms and identified aneurysm size ≥ 10 mm, treatment during the acute phase of subarachnoid hemorrhage, incomplete initial occlusion, and duration of follow-up as significant predictors of recurrence. In the International Subarachnoid Aneurysm Trial retreatment was done 4.6 times more commonly after endovascular therapy (17.4%) than after microsurgical clipping (3.8%).^{10,11} The risk of late rebleeding was also higher after endovascular repair (2.9%) than after open surgery (0.9%). In a systematic review of the literature that included 8161 coiled aneurysms, Ferns et al¹² reported aneurysm reopening in 20.8% of cases and retreatment in 10.3% and identified location in the posterior circulation and size > 10 mm as risk factors for aneurysm reopening. The adjunctive use of endovascular devices such as nondetachable balloons or self-expanding stents has notably improved the long-term durability of endovascular treatment. As such, in a large study, Piotin et al² found remarkably lower angiographic recurrence rates with stent-assisted coiling compared with conventional coiling (14.9% versus 33.5%, respectively). In a recent large multicenter French study (CLARITY), Pierot et al¹ identified 3 factors associated with the quality of midterm aneurysm occlusion after endovascular therapy, namely, neck size, the use of the balloon remodeling technique, and the quality of postoperative

occlusion. The authors concluded that future treatment strategies should be focused on reinforcement and neointimalization at the level of the neck, especially for wide-necked aneurysms.

Initial patient comparability is a significant limitation of studies comparing SAC or BAC with conventional coiling, because aneurysms treated with SAC or BAC tend to be wide-neck, larger, and typically more complex than those treated with conventional coiling. In contrast to previous studies, the present study has the advantage of comparing 2 homogeneous groups of patients harboring wide-neck aneurysms treated by BAC or SAC. Our results are in line with the findings of recent reports showing that stented aneurysms have better angiographic outcomes than nonstented aneurysms coiled with or without balloon assistance. Lawson et al¹³ compared the follow-up angiographic outcomes of 37 stented versus 72 nonstented (with or without balloon assistance) incompletely coiled aneurysms and found that the odds of progression of occlusion of stent-coiled aneurysms were 18.5 times that of nonstented aneurysms. The authors attributed their results, at least in part, to the “flow remodeling” effects of self-expanding stents. In fact, stents may elicit a neointimal response that leads to endovascular vessel reconstruction and ultimately excludes the aneurysm from the circulation. Lopes and Sani¹⁴ described complete endothelialization of a Neuroform stent 4 months after its placement in an explanted human aneurysm specimen, with significant de novo fibroelastic tissue formation along the neck of the aneurysm. Such in-growth of endothelial tissue over the stented segment may potentially alter intra-aneurysmal flow dynamics causing stasis and thrombosis inside the aneurysm. This could explain why SAC yields higher rates of aneurysm occlusion and progressive thrombosis than conventional coiling or even BAC. Because of this potential flow-remodeling effect of self-expanding stents, we generally avoid overpacking stented aneurysms and may settle for more modest packing densities. At most neurovascular centers, however, the same range of packing density is achieved in aneurysms coiled with or without stent assistance. In vitro studies have also shown that higher packing densities are associated with significant flow reduction at the neck of the aneurysm.¹⁵ In addition, obtaining high packing densities remains a priority in ruptured aneurysms treated with SAC to minimize the risk of rebleeding. As such, packing density was 23.4% on average in ruptured aneurysms versus 16.7% in unruptured aneurysms.

The main limitation of BAC remains the inability to pack the neck of the aneurysm, because 65% of aneurysms initially and 35% at follow-up showed a neck remnant in the present series. This translated into significantly lower rates of complete aneurysm occlusion (Raymond 1) and higher rates of retreatment with BAC versus SAC. The difference between the 2 groups, however, was less prominent when comparing the rates of adequate aneurysm occlusion (Raymond 1–2 versus 3), with only a trend favoring SAC in multivariate analysis. Both techniques appear to have high efficacy with respect to adequate aneurysm occlusion at follow-up (94.2% with SAC and 84.4% with BAC).

Assessment of procedural safety and clinical outcomes are essential to determine the best therapeutic approach for wide-neck aneurysms. In our study, both techniques were associated with low morbidity rates (3%) and excellent clinical outcomes ($> 90\%$). It is worth noting that the significantly higher propor-

tion of patients treated in the setting of subarachnoid hemorrhage in the BAC group has probably favored the stent group. In fact, the rate of procedural complications with BAC is reportedly 11.7% in unruptured aneurysms versus 17% in ruptured aneurysms.^{4,16} Likewise, stent procedures in ruptured aneurysms carry a higher rate of morbidity than in unruptured aneurysms.¹⁷ For many neurointerventionalists, BAC is preferred over SAC for treatment of ruptured wide-necked aneurysms because the patient is spared the initiation of an antiplatelet regimen and its potential hemorrhagic complications.¹⁷ Mocco et al¹⁷ reported a 12% procedural mortality rate with SAC of acutely ruptured aneurysms and concluded that extreme caution should be exercised when considering stent deployment in patients with subarachnoid hemorrhage. Amenta et al¹⁸ treated 65 patients with acutely ruptured aneurysms with a 15.4% major complication rate including bleeding secondary to antiplatelet therapy in 7.7% and intraoperative in-stent thrombosis in 7.7%. In a systematic review of the literature of acutely ruptured intracranial aneurysms (339 patients) treated with stents, Bodily et al¹⁹ found that intracranial hemorrhagic and thromboembolic complications occurred in 8% and 6% of patients, respectively, and concluded that adverse outcomes were more common with SAC compared with conventional coiling. The use of a stent may also have considerable influence on flow in perforating vessels near treated cerebral aneurysms.¹⁵ On the other hand, a balloon may protect a side-branch from coil herniation and, in the event of intraprocedural aneurysm rupture, provide proximal control thus preventing devastating consequences for the patient. In a critical review of the literature, Pierot et al²⁰ noted that all except 1 publication showed a similar safety profile between BAC and conventional coiling, with better initial and follow-up anatomic results in aneurysms treated by BAC. On the basis of these data, they recommended wide use of BAC for treatment of wide-neck aneurysms and cautioned against wide use of stents given the potential associated morbidity.

Some operators advocate staging the stent-coil procedure to allow endothelialization of the stent. This may allow for greater stability and less movement of the stent and may also avoid endothelial damage and platelet activation during coil deployment. Accordingly, Lodi et al²¹ compared single-stage ($n = 37$) and multistage ($n = 50$) SAC and found higher complication rates with single-stage SAC. On the other hand, staging the stent-coil procedure may carry a theoretic risk of interval aneurysm rupture and loss to follow-up with an increased procedural cost. Currently, both techniques are widely applied in clinical practice.

Flow diversion and flow disruption are potential alternatives in the treatment of wide-neck intracranial aneurysms. In a large series of 191 patients with 251 aneurysms treated with the Pipeline Embolization Device (PED) (Covidien, Irvine, California), Saatci et al²² reported an event rate of 14.1%, with a permanent morbidity rate of 1% and mortality rate of 0.5%. The rate of aneurysm occlusion was 91.2% at 6 months and further increased to 94.6% with longer follow-up. In a prospective study from Hong Kong that included 143 patients with 178 aneurysms treated with the PED, Yu et al²³ noted periprocedural death or major stroke in 3.5% of cases with complete aneurysm occlusion in 84% at 18 months. The authors concluded that PED therapy was safe and effective and should be considered a first choice for treating un-

ruptured aneurysms and recurrent aneurysms after previous treatments. Flow disruption with the WEB device (Sequent Medical, Palo Alto, California) is a new technique that has shown promising results for treatment of wide-neck aneurysms. Lubicz et al²⁴ have recently treated 19 patients with 20 unruptured wide-neck bifurcation aneurysms by WEB placement and reported symptomatic complications in 2 patients. Although additional stent placement and/or coiling was necessary in 3 cases at the acute phase and in 1 case at follow-up, complete or near-complete aneurysm occlusion was achieved in 89% of cases at 6 months. The results of this series showing feasibility of treatment of wide-neck aneurysms with the WEB require confirmation in larger studies.

The limitations of the present study are related to its retrospective design, the relatively short angiographic follow-up time (10.2 months), and the relatively small sample size, especially in the BAC group. Follow-up time was slightly longer in the SAC group, which may have influenced the anatomic results, especially the rate of progression of occlusion. Ruptured aneurysms were also more common in the BAC group, which may have favored better results in the SAC group, because it is well known that recurrences are more common when treatment is undertaken in the acute setting of subarachnoid hemorrhage. As such, ruptured aneurysms were strongly predictive of aneurysm recurrence in the studies by Piotin et al² and Raymond et al.⁹ Likewise, Cognard et al²⁵ found that unruptured aneurysms of <9 mm have a recanalization rate of 7% as opposed to ruptured aneurysms of the same size, which had a recurrence rate of 17%. Also, stent-assisted coiling of ruptured aneurysms has been shown to be associated with lower angiographic obliteration rates at follow-up compared with unruptured aneurysms.⁷ Nevertheless, a multivariate analysis was conducted to account for such differences in baseline characteristics and identify independent predictors of occlusion. Prospective, randomized trials will be needed to provide definitive information on the best therapeutic approach for wide-neck aneurysms.

CONCLUSIONS

In this study, we found that SAC yields lower rates of retreatment and higher rates of complete aneurysm obliteration and progression of occlusion at follow-up than does BAC. The rates of adequate aneurysm occlusion, however, did not differ significantly between the 2 groups. Both techniques appear to have a favorable safety-efficacy profile and may be applied for treatment of wide-neck aneurysms. The findings of this retrospective study require confirmation by larger prospective studies.

Disclosures: Pascal Jabbour—UNRELATED: Consultancy; ev3, CNV. Stavropoula Tjournakaris—UNRELATED: Consultancy; Stryker. Aaron Dumont—UNRELATED: Consultancy; ev3.

REFERENCES

1. Pierot L, Cognard C, Anxionnat R, et al. **Endovascular treatment of ruptured intracranial aneurysms: factors affecting midterm quality anatomic results: analysis in a prospective, multicenter series of patients (CLARITY).** *AJNR Am J Neuroradiol* 2012;33:1475–80
2. Piotin M, Blanc R, Spelle L, et al. **Stent-assisted coiling of intracranial aneurysms: clinical and angiographic results in 216 consecutive aneurysms.** *Stroke* 2010;41:110–15
3. Pierot L, Cognard C, Anxionnat R, et al. **Ruptured intracranial**

- aneurysms: factors affecting the rate and outcome of endovascular treatment complications in a series of 782 patients (CLARITY study). *Radiology* 2010;256:916–23
4. Pierot L, Cognard C, Anxionnat R, et al. Remodeling technique for endovascular treatment of ruptured intracranial aneurysms had a higher rate of adequate postoperative occlusion than did conventional coil embolization with comparable safety. *Radiology* 2011; 258:546–53
 5. Bendok BR, Parkinson RJ, Hage ZA, et al. The effect of vascular reconstruction device-assisted coiling on packing density, effective neck coverage, and angiographic outcome: an in vitro study. *Neurosurgery* 2007;61:835–40
 6. Izar B, Rai A, Raghuram K, et al. Comparison of devices used for stent-assisted coiling of intracranial aneurysms. *PLoS One* 2011; 6:e24875
 7. Chalouhi N, Dumont AS, Hasan D, et al. Is packing density important in stent-assisted coiling? *Neurosurgery* 2012;71:381–87
 8. Altman D. *Practical Statistics for Medical Research*. Boca Raton, Florida: Chapman & Hall/CRC; 1999
 9. Raymond J, Guilbert F, Weill A, et al. Long-term angiographic recurrences after selective endovascular treatment of aneurysms with detachable coils. *Stroke* 2003;34:1398–403
 10. Molyneux A, Kerr R, Stratton I, et al. International Subarachnoid Aneurysm Trial (ISAT) of neurosurgical clipping versus endovascular coiling in 2143 patients with ruptured intracranial aneurysms: a randomised trial. *Lancet* 2002;360:1267–74
 11. Molyneux AJ, Kerr RS, Yu LM, et al. International Subarachnoid Aneurysm Trial (ISAT) of neurosurgical clipping versus endovascular coiling in 2143 patients with ruptured intracranial aneurysms: a randomised comparison of effects on survival, dependency, seizures, rebleeding, subgroups, and aneurysm occlusion. *Lancet* 2005;366:809–17
 12. Ferns SP, Sprengers ME, van Rooij WJ, et al. Coiling of intracranial aneurysms: a systematic review on initial occlusion and reopening and retreatment rates. *Stroke* 2009;40:e523–29
 13. Lawson MF, Newman WC, Chi YY, et al. Stent-associated flow remodeling causes further occlusion of incompletely coiled aneurysms. *Neurosurgery* 2011;69:598–603
 14. Lopes D, Sani S. Histological postmortem study of an internal carotid artery aneurysm treated with the Neuroform stent. *Neurosurgery* 2005;56:E416
 15. Roszelle BN, Babiker MH, Hafner W, et al. In vitro and in silico study of intracranial stent treatments for cerebral aneurysms: effects on perforating vessel flows. *J Neurointerv Surg* 2013;5:354–60
 16. Pierot L, Spelle L, Leclerc X, et al. Endovascular treatment of unruptured intracranial aneurysms: comparison of safety of remodeling technique and standard treatment with coils. *Radiology* 2009;251: 846–55
 17. Mocco J, Snyder KV, Albuquerque FC, et al. Treatment of intracranial aneurysms with the Enterprise stent: a multicenter registry. *J Neurosurg* 2009;110:35–39
 18. Amenta PS, Dalyai RT, Kung D, et al. Stent-assisted coiling of wide-necked aneurysms in the setting of acute subarachnoid hemorrhage: experience in 65 patients. *Neurosurgery* 2012;70:1415–29
 19. Bodily KD, Cloft HJ, Lanzino G, et al. Stent-assisted coiling in acutely ruptured intracranial aneurysms: a qualitative, systematic review of the literature. *AJNR Am J Neuroradiol* 2011;32:1232–36
 20. Pierot L, Cognard C, Spelle L, et al. Safety and efficacy of balloon remodeling technique during endovascular treatment of intracranial aneurysms: critical review of the literature. *AJNR Am J Neuroradiol* 2012;33:12–15
 21. Lodi Y, Latorre J, El-Zammar Z, et al. Single stage versus multi-staged stent-assisted endovascular repair of intracranial aneurysms. *J Vasc Interv Neurol* 2011;4:24–28
 22. Saatci I, Yavuz K, Ozer C, et al. Treatment of intracranial aneurysms using the Pipeline flow-diverter embolization device: a single-center experience with long-term follow-up results. *AJNR Am J Neuroradiol* 2012;33:1436–46
 23. Yu SC, Kwok CK, Cheng PW, et al. Intracranial aneurysms: midterm outcome of Pipeline embolization device: a prospective study in 143 patients with 178 aneurysms. *Radiology* 2012;265:893–901
 24. Lubicz B, Mine B, Collignon L, et al. WEB device for endovascular treatment of wide-neck bifurcation aneurysms. *AJNR Am J Neuroradiol* 2013;34:1209–14
 25. Cognard C, Weill A, Spelle L, et al. Long-term angiographic follow-up of 169 intracranial berry aneurysms occluded with detachable coils. *Radiology* 1999;212:348–56

Does Stent-Assisted Coiling Still Have a Place in the Management of Intracranial Aneurysms?

The article by Chalouhi et al¹ in this issue of the *American Journal of Neuroradiology* is an interesting contribution to the debate about the present place of stent-assisted coiling (SAC) in the management of intracranial aneurysms.

Endovascular treatment plays an important role in the management of intracranial aneurysms but still has some limitations, including complex aneurysms (wide-neck, fusiform, large, and giant) and the risk of aneurysm recanalization.²⁻⁵ Stabilization of the coils in wide-neck aneurysms can be difficult; therefore balloon-assisted coiling (BAC) was developed to overcome this technical limitation of coiling.^{6,7} BAC is not associated with a higher rate of complications as compared with standard coiling, and some studies have even shown better anatomic outcome after BAC.^{8,9}

Initially, SAC was introduced into the armamentarium for aneurysm treatment 10 years ago, for the treatment of wide-neck aneurysms. Clinical evaluation of this technique is mostly limited to single-center retrospective series with a limited number of patients. However, Shapiro et al¹⁰ provided a literature review in 2012 showing that the overall complication incidence was 19%, with an overall death incidence of 2.1%. Thromboembolic and hemorrhagic complications were observed in 10% and 2.2%, respectively, and stent-related technical complications in 9%. At the first treatment session, 45% of aneurysms were completely occluded, but this increased to 61% on the follow-up imaging. In-stent stenosis was seen in 3.5% of cases and stent occlusion was observed in 0.6% of cases at angiographic follow-up. A learning curve was also clearly demonstrated. These results were disappointing because the morbidity of SAC was somewhat higher as compared with standard coiling, and complete occlusion rates were low.

Similar results were reported in large recent series.^{11,12} Lee et al,¹¹ in a series of 289 patients, demonstrated a procedure-related complication rate of 13.8%, with permanent neurologic sequelae in 1.5% of patients. Follow-up imaging of 229 patients' aneurysms demonstrated a minor recanalization rate of 7.4% and major recanalization of 12.7%. In-stent stenosis was observed in 12.7% of cases, stent migration in 4.5% of cases, and late delayed infarction in 4.2% of patients. Gao et

al,¹² in a large series of 232 patients with 239 wide-neck aneurysms treated with Neuroform SAC, also reported a high rate of procedural complications (14.7%), with a high procedure-related morbidity of 4.2% and a mortality rate of 1.3%. The overall recanalization was also relatively high, at 14.5%.

Recent multicenter studies show contradictory results, including a retrospective study involving 9 US neurointerventional centers.¹³ There were 229 patients with 229 aneurysms, which included 32 ruptured aneurysms. The death rate was 3.5% of patients (16% for all patients with SAH and 1.5% for elective patients). Nonfatal intracranial hemorrhage was seen in 1.0% of patients, and immediate or delayed thromboembolic events were seen in 4.4% of patients.¹³ In the ruptured aneurysm group, 3 of 5 deaths were related to the treatment. In patients with angiographic follow-up data, complete occlusion was observed in 59%. Nineteen patients (8.3%) had retreatment of their aneurysms, and in-stent stenosis was observed in 3.4%.

In the French multicenter registry, treatment of 107 patients with 107 aneurysms with SAC was performed.¹⁴ The postprocedure rate for complete occlusion was 66.4%. The rate of progressive occlusion at 12–18 months was 14%, and the rate of recurrence was 9.7%. The rate of subsequent treatment was 4%. The thromboembolic rate in the periprocedural period was 3.7%, and the rate of delayed thromboembolic events was 3%. Overall, the mortality rate at 12–18 months was 1%, and the permanent morbidity rate was 1%.

The most important point is to have a direct comparison between patients treated with SAC and standard coiling (or BAC). Few series are available for this comparison, and most are single-center, retrospective series with a limited number of patients and significant differences regarding the aneurysms treated with both techniques. Piotin et al¹⁵ reported a large, retrospective, single-center series of 1137 patients with 1325 aneurysms treated without (1109 aneurysms) and with stents (216 aneurysms). Aneurysms were different in the nonstented and stented groups, according to anatomic characteristics (bifurcation/sidewall, aneurysm size, neck size), making the comparison of clinical and anatomic results of limited value. Per-

manent neurologic procedure-related complications occurred in 7.4% of the procedures in the stent placement group versus 3.8% in the nonstented group ($P = .644$). Procedure-related death occurred in 4.6% in the stent placement group and 1.2% in nonstented group ($P = .006$). Follow-up was available in only 52.7% of the patients, and angiographic recurrence was observed in 14.9% in the stent placement group versus 33.5% in the nonstented group.

Jahshan et al¹⁶ reported different results in a single-center series dealing with 489 aneurysms in 459 patients with similar permanent event-related morbidity in nonstented and stent placement groups, with higher rates of complete occlusion in stented aneurysms.

On the contrary, in a retrospective, single-center series by Hwang et al,¹⁷ in a relatively small group of 86 aneurysms treated with coils alone and 40 aneurysms treated with stent and coils, the rates of progressive occlusion at 2-year follow-up (42.5% in the stent placement group and 39.5% in the nonstented group) and recanalization (17.5% in the stent placement group and 21.0% in the non-stented group) did not statistically demonstrate any significant difference.

In the current article, in their single-center, retrospective series, Chalouhi et al¹ compare 69 patients treated with SAC and 32 patients treated with BAC. The 2 groups were comparable except for aneurysm status; in the BAC group, 65.6% of the aneurysms were ruptured, and in the SAC group, 11.5% of the aneurysms were ruptured ($P < .001$). The rates of complete aneurysm occlusion were significantly higher in the SAC group (75.4%) versus the BAC group (50%; $P = .001$). In the incompletely coiled group, progressive aneurysm occlusion occurred more frequently in the SAC group (76.6%) than in the BAC group (42.8%, $P = .02$). The retreatment rates were significantly lower with SAC (4.3%) than with BAC (15.6%, $P = .05$). The aneurysm rupture status plays an important role in recanalization, and as the BAC and SAC groups are different regarding this status, it is difficult to know the true significance of these results.

SAC has been used for more than 10 years, and the data are lacking to know precisely whether the safety and efficacy are different between SAC and standard coiling. The only way to answer these important questions is to build a randomized, controlled trial comparing stent placement versus nonstenting in a large group of patients to determine whether the addition of a stent to standard coiling can decrease the recurrence rate without increasing morbidity and mortality.¹⁸

The development of new techniques such as flow diversion and flow disruption will also modify the global strategy of aneurysm treatment, and the respective places of stenting, flow diversion, and flow disruption must be defined according to their safety and efficacy profile.^{19,20} Currently, flow diverters are indicated and recommended in sidewall, unruptured aneurysms, singularly those located on the ICA, but these aneurysms are also a good indication for stent placement. Flow disrupters are used in wide-neck bifurcation aneurysms (ruptured and unruptured). Aneurysm locations treated with flow disruption are the MCA, basilar tip, ICA bifurcation, and the anterior communicating artery. For these locations, stent

placement can also be used (singularly for unruptured aneurysms), including more complex techniques such as Y and X stent placement. A direct comparison of stent placement and coiling versus flow diversion or flow disruption will be mandatory in the future to directly compare the safety and efficacy of these techniques and to specify their respective place in aneurysm management.

Disclosures: Laurent Pierot—RELATED: Consultancy: Codman, Covidien/ev3, MicroVention, Penumbra, and Sequent. Christophe Cognard—RELATED: Consultancy: Codman, Covidien/ev3, MicroVention, Sequent, and Stryker.

REFERENCES

1. Chalouhi N, Starke RM, Koltz MT, et al. **Stent-assisted coiling versus balloon remodeling of wide-neck aneurysms: comparison of angiographic outcomes.** *AJNR Am J Neuroradiol* 2013;34:1984–89
2. Molyneux A, Kerr R, Stratton I, et al. **International Subarachnoid Aneurysm Trial (ISAT) of neurosurgical clipping versus endovascular coiling in 2143 patients with ruptured intracranial aneurysms: a randomised trial.** *Lancet* 2002;360:1262–63
3. Pierot L, Spelle L, Vitry F, ATENA Investigators. **Immediate clinical outcome of patients harbouring unruptured intracranial aneurysms treated by endovascular approach: results of the ATENA Trial.** *Stroke* 2008;39:2497–504
4. Cognard C, Pierot L, Anxionnat R, et al, CLARITY Investigators. **Results of embolization used as the first treatment choice in a consecutive non selected population of ruptured aneurysms: clinical results of the Clarity GDC study.** *Neurosurgery* 2011;69:837–41
5. Ferns SP, Sprengers MES, von Rooij WJ, et al. **Coiling of intracranial aneurysms: a systematic review on initial occlusion and reopening and retreatment rates.** *Stroke* 2009;40:e523–29
6. Moret J, Cognard C, Weill A, et al. **The “remodelling technique” in the treatment of wide neck intracranial aneurysms.** *Intervent Neuroradiol* 1997;3:21–35
7. Pierot L, Cognard C, Spelle L, et al. **Safety and efficacy of balloon remodelling technique during endovascular treatment of intracranial aneurysms: critical review of the literature.** *AJNR Am J Neuroradiol* 2012;33:12–15
8. Pierot L, Spelle L, Leclerc C, et al. **Endovascular treatment of unruptured intracranial aneurysms: comparison of safety of remodeling technique and standard treatment with coils.** *Radiology* 2009;251:846–55
9. Pierot L, Cognard C, Anxionnat R, et al, for the CLARITY Group. **The remodelling technique for endovascular treatment of ruptured intracranial aneurysms is more efficacious than standard coiling with a similar safety.** *Radiology* 2011;258:546–53
10. Shapiro M, Beckske T, Sahlein D, et al. **Stent-supported aneurysm coiling: a literature survey of treatment and follow-up.** *AJNR Am J Neuroradiol* 2012;33:159–63
11. Lee SJ, Cho YD, Kang HS, et al. **Coil embolization using the self-expandable closed cell stent for intracranial saccular aneurysm: a single center experience of 289 consecutive aneurysms.** *Clin Radiol* 2013;68:256–63
12. Gao X, Liang G, Li Z, et al. **Complications and adverse events associated with Neuroform stent-assisted coiling of wide-neck intracranial aneurysms.** *Neurol Res* 2011;33:841–52
13. Fargen KM, Hoh BL, Welch BG, et al. **Long-term results of Enterprize stent-assisted coiling of cerebral aneurysms.** *Neurosurgery* 2012;71:239–42
14. Gentric JC, Biondi A, Piotin M, et al. **Safety and efficacy of Neuroform for treatment of intracranial aneurysms: a prospective, consecutive, French multicentric study.** *AJNR Am J Neuroradiol* 2013;34:1203–08

15. Piotin M, Blanc R, Spelle L, et al. **Stent-assisted coiling of intracranial aneurysm: clinical and angiographic results in 216 consecutive aneurysms.** *Stroke* 2010;41:110–15
16. Jahshan S, Abla AA, Natarajan SK, et al. **Results of stent-assisted vs non-stent-assisted endovascular therapies in 489 cerebral aneurysms: single-center experience.** *Neurosurgery* 2013;72:232–39
17. Hwang G, Park H, Bang JS, et al. **Comparison of 2-year angiographic outcomes of stent- and nonstent-assisted coil embolization in unruptured aneurysms with unfavorable configuration for coiling.** *AJNR Am J Neuroradiol* 2011;32:1707–10
18. Darsault TE, Raymond J, for the STAT Collaborative Group. **The design of the Stenting in Aneurysm Treatments (STAT) trial.** *J Neurointervent Surg* 2012;4:178–81
19. Pierot L. **Flow diverter stents in the treatment of intracranial aneurysms: where are we?** *J Neuroradiol* 2011;38:40–46
20. Pierot L, Liebig T, Sychra V, et al. **Intrasaccular flow-disruption treatment of intracranial aneurysms: preliminary results of a multicenter clinical study.** *AJNR Am J Neuroradiol* 2012;33:1232–38

L. Pierot

Department of Neuroradiology,
Hôpital Maison-Blanche,
CHU Reims,
Reims University, Reims, France

C. Cognard

Department of Neuroradiology,
CHU Toulouse, Toulouse University,
Toulouse, France

<http://dx.doi.org/10.3174/ajnr.A3614>

Stent Retriever Use for Retrieval of Displaced Microcoils: A Consecutive Case Series

T.M. Leslie-Mazwi, M. Heddier, H. Nordmeyer, M. Stauder, A. Velasco, P.J. Mosimann, and R. Chapot

ABSTRACT

SUMMARY: Coil displacement during endovascular coiling procedures may require coil retrieval in the context of flow limitation or thromboembolic risk. No standard recommended method of coil retrieval exists. We present a consecutive series of 14 patients with displaced coil during aneurysm coiling in whom the complication was effectively managed with the use of a stent retriever system. Two illustrative cases from the 14 are described, and technical notes are detailed regarding use of the technique. The use of stent retrievers presents a simple, safe, and effective choice for removal of prolapsed coils during aneurysm coiling.

ABBREVIATION: ACA = anterior cerebral artery

Endovascular occlusion of intracranial aneurysms is now widely practiced, with positive results in direct comparisons to open surgery.¹ However, the occurrence of coil displacement and migration carries the risk for thromboembolic complications² Therefore, if present during a case, coil displacement often requires either retrieval or fixation of the errant coil.

Stent retrievers have been introduced recently for the treatment of ischemic stroke, enabling rapid and reliable extraction of thrombus.³ We present a consecutive series of 14 cases in which off-label application of a stent retriever allowed retrieval of displaced intracranial aneurysm coils.

MATERIALS AND METHODS

We reviewed our prospectively collected data base of combined symptomatic and incidental aneurysm coiling cases, from January 2009 to August 2012. A total of 1125 consecutive aneurysms were treated during this time in our institution. Technique was similar for all, involving dual antiplatelet therapy in unruptured aneurysms, anticoagulation with heparin, use of MicroVention, (Aliso Viejo, California) coils, and systematic balloon assistance when necessary. Thirteen consecutive cases were prospectively identi-

fied in which intraprocedural coil displacement or migration occurred that required intervention. In all cases, the intervention chosen was application of a stent retriever, either the Solitaire retrievable stent (Covidien, Dublin, Ireland), or the Catch Plus device (Balt Extrusion, Montmorency, France).

Patients

A total of 14 patients (12/14 women), ranging in age from 29–73 years, met inclusion criteria. Aneurysms were of various sizes (4–28 mm) in various locations (ICA, MCA M1, anterior cerebral artery [ACA] A2, and basilar artery). In every case, retrieval was successful, without a change in the stability of the aneurysm or in the patient's baseline neurologic examination. Six cases had retrieval with a single pass. One patient required a maximum of 7 passes, with a median of 2 and mean of 2.3 passes per patient.

A brief description of 2 illustrative cases follows.

Case 1. A 2–3 HyperSoft coil (MicroVention) dislodged and migrated into the pericallosal artery during placement at the neck in a patient with a ruptured anterior communicating artery aneurysm (Fig 1). A Rebar 18 microcatheter (ev3, Irvine, California) was navigated beyond the coil to enable a stent retriever (Solitaire 4 × 20, Covidien) to be delivered at the level of the coil. After partial resheathing of the stent retriever, the coil was trapped and the system progressively withdrawn, enabling retrieval of the coil.

Case 2. A single loop of coil prolapsed into the main trunk of the MCA after coiling of an unruptured MCA aneurysm. Despite effective dual antiplatelet therapy, a TIA occurred 2 days later related to clot formation on, and subsequent embolization from, the prolapsed coil loop. A decision was made to attempt coil removal. A stent retriever (Solitaire 4 × 15, Covidien) was delivered

Received October 18, 2012; accepted after revision January 6, 2013.

From the Department of Interventional Neuroradiology (T.M.L.-M., M.H., H.N., M.S., A.V., P.J.M., R.C.) Alfried-Krupp-Krankenhaus, Essen, Germany; Department of Interventional Neuroradiology/Endovascular Neurosurgery (T.M.L.-M.), Massachusetts General Hospital, Boston, Massachusetts; and Department of Radiology and Neuroradiology (P.J.M.), Centre Hospitalier Universitaire Vaudois and University of Lausanne, Lausanne, Switzerland.

Please address correspondence to R. Chapot, MD, Department of Intracranial Endovascular Therapy, Alfried-Krupp-Str. 21, 45131 Essen, Germany; e-mail: rene.chapot@krupp-krankenhaus.de

<http://dx.doi.org/10.3174/ajnr.A3552>

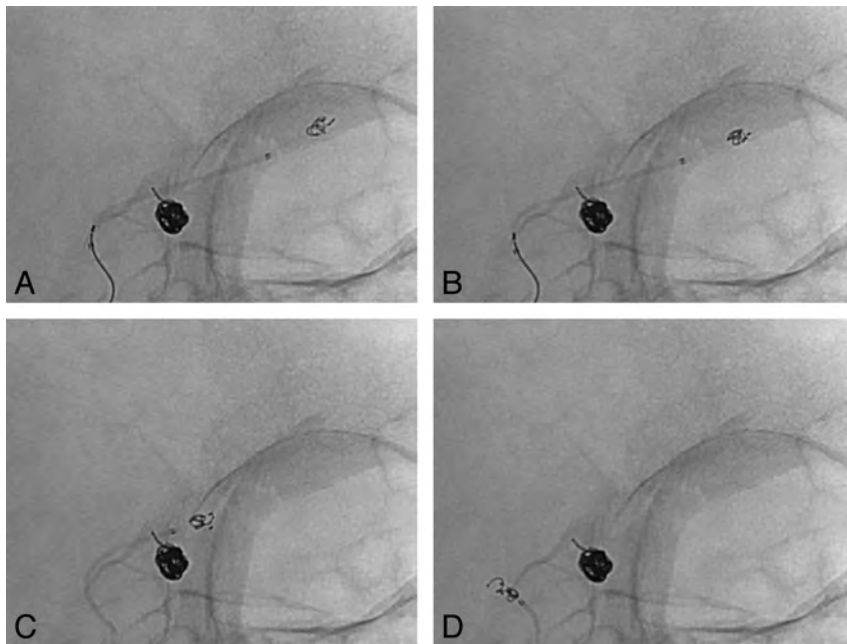


FIG 1. Coil retrieval. A, Displaced coil is visible in the more distal ACA, distinct from the coil mass within the anterior communicating artery aneurysm. The coiling microcatheter has been removed. The stent retriever delivery catheter is seen traversing the aneurysm neck, and the stent retriever has been deployed adjacent to the errant coil. B, Retraction of the stent shows capture of the displaced coil. Note the conformational change to the displaced coil mass. C, The stent retriever is pulled from the intracranial circulation with coil engaged, past the existing coil mass. D, The coil is successfully removed, without disruption of the remaining coil within the aneurysm. Additional coils were subsequently placed in the aneurysm to complete the procedure.

in the region of the coil by use of the technique described below, and gently withdrawn while only partially resheathed. The coil was then retrieved without dislocation of the other coils (Fig 2). The patient's symptoms resolved.

DISCUSSION

Aneurysm coiling seals the aneurysm from blood flow by inducing thrombosis within the lumen of the aneurysm.⁴ Thromboembolic complications remain the greatest risk in treatment of an endovascular aneurysm, with displaced coil material contributing significantly to this risk.² In addition, the coil may migrate with blood flow into smaller-branch vessels or lodge at a vessel bifurcation, producing flow limitation. The risk for coil displacement and migration is influenced by a combination of anatomic and technical factors. Both undersized and/or unstable long coils can result in distal coil migration, especially in wide-neck aneurysms.⁵ Use of balloon or stent assistance minimizes the risks for coil displacement and migration; careful coil delivery to avoid prolapse of the catheter tip, and deployment of new coils within a stable coil basket additionally aim to minimize the risk for coil displacement.

In the absence of flow limitation or thrombus accumulation, many single loops of herniated coil are best left alone, and short infusions of intravenous glycoprotein IIb/IIIa antagonists provide protection from potential thrombus formation until fibrin coating makes the coil loops less thrombogenic. However, if displaced coil does require intervention, available options vary: broadly divisible into either stent placement to pin the coil down or active retrieval of the displaced coil loops. Fixation with a stent is an

efficient technique⁶ that potentially avoids displacement of other coils during a retraction maneuver. Stent placement additionally requires less manipulation within the lumen of the affected vessel. However, as a salvage technique, it is often less attractive because of the concern of placing another thrombogenic intravascular implant, the need for dual antiplatelet therapy, and the possibility of multiple stents being required. The placement of a stent may also limit the ability to continue the definitive endovascular procedure. These concerns become particularly significant in the context of a ruptured aneurysm.

Hence, attempts at coil retrieval are often the primary strategy. Various methods to retrieve the loosened coil have been described. These include the use of microsnares,^{7,8} the Alligator retrieval device (Covidien),⁹ use of the Merci retriever (Concentric Medical, Mountain View, California),¹⁰ microwire manipulation,¹¹ and even microsurgery in the event of acute parent artery occlusion without the possibility of endovascular coil retrieval.¹² The use

of a stent for this role was first reported by Wakhloo and Gounis,¹³ who used a retrievable closed-cell intracranial stent to successfully extract coil material in an *in vivo* aneurysm model. Our initial experience with this technique was an attempt to fix an errant coil with a Solitaire AB stent. During this maneuver, we noted that the coil was engaged in the stent during stent movement, and therefore proceeded to retract it until it was cleared from the circulation. This was previously published by our group.¹⁴ We have since used the technique with success in a variety of scenarios. Use of a stent retriever in this role, as with many of the other techniques proposed, represents an off-label indication for the device.

We would make the following technical observations regarding use of a stent retriever device for coil retrieval:

1. Always decide whether the herniated coil requires intervention. Single loops of coil are usually best left undisturbed. Longer or unstable coil loops require definitive therapy. It is clear that any evidence of embolic phenomena or thrombus aggregation related to the coil requires intervention.
2. On identification of the complication, the patient should receive a loading dose of antiplatelet medication (preferably IV glycoprotein IIb/IIIa antagonists) if not already receiving these agents, and a heparin bolus should be administered if no strong contraindication exists. In the context of flow limitation, collateral augmentation should be pursued through fluid bolus and induced hypertension, if tolerated.
3. We have used stent retrievers comfortably in more proximal vessels, with coil retrieval from vessels the diameter of M2 MCA and A2 ACA vessels. In vessels < 2 mm, the combination

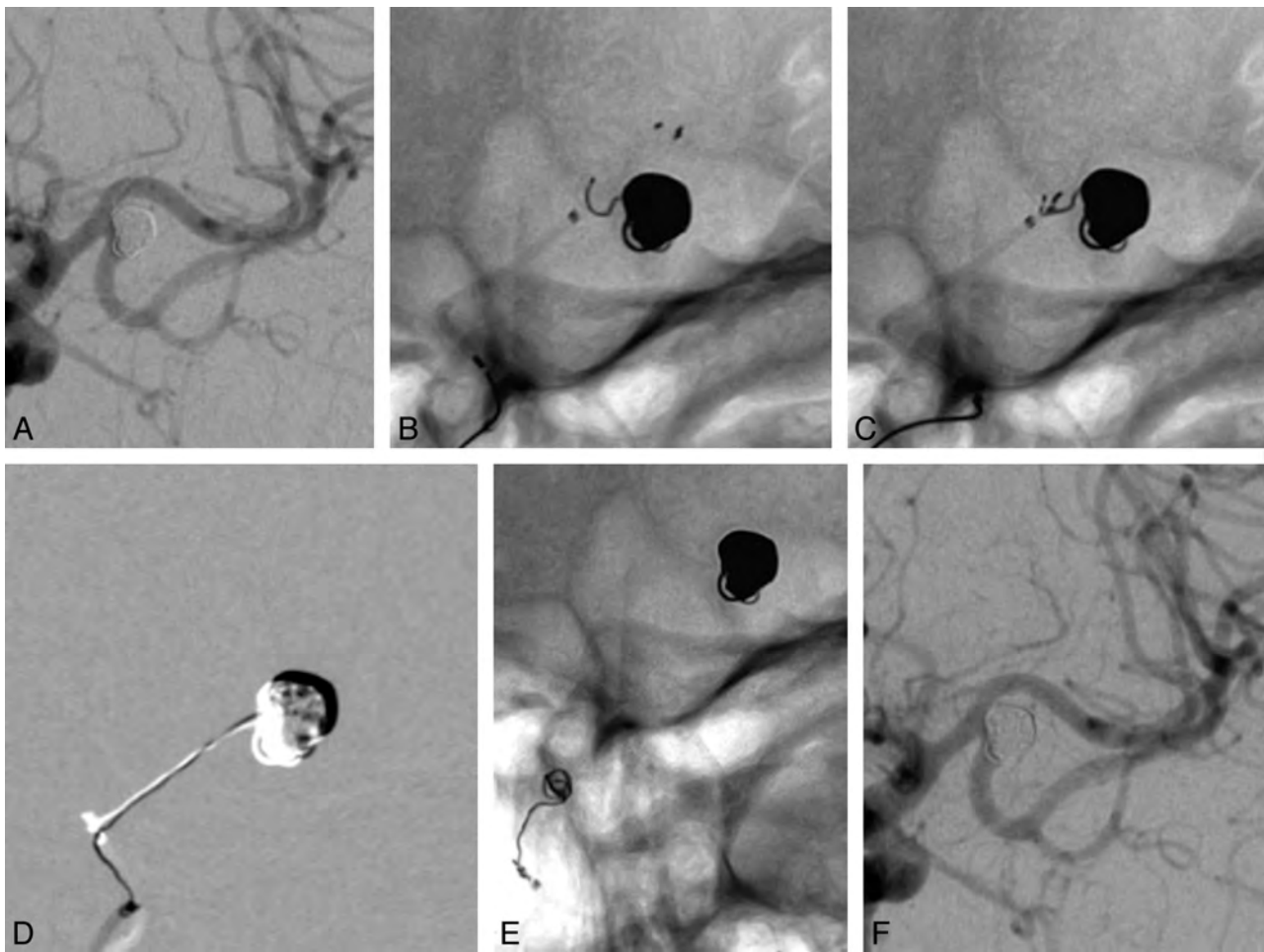


FIG 2. Delayed coil retrieval. *A*, Final coiling result, with coil loop protruding into the postbifurcation M1 segment of the MCA. The initial intention was to manage this conservatively. However, the patient had subsequent embolic events and required definitive treatment of the prolapsed coil. *B*, Deployment of the stent retriever, starting immediately distal to the prolapsed coil. *C*, Engagement of the coil, as evidenced by the conformational change in the coil loop appearance. *D*, Subtracted image showing traction on the coil loop during extraction from the aneurysm lumen. *E*, Successful removal of the offending coil from the circulation. *F*, Final result, with the aneurysm secured and unchanged in morphologic features after the removal of the prolapsed coil. The ischemic events in this patient did not recur.

of a small microcatheter (eg, 0.017 inner diameter) with dedicated distal access stent retrievers (eg, the Capture stent [MindFrame, Irvine, California] or the Catch Mini [Balt Extrusion]) may be preferred.

4. The intention should be unsheathing of the stent retriever immediately distal to the displaced coil (in our experience, within 5 mm of the distal coil). The stent retriever delivery catheter should be carefully navigated over a microwire until the tip is in the desired location for stent exposure. During this maneuver, minor movement of the displaced coil, including possible further distal migration, is not uncommon and should be expected. The ability to navigate the microcatheter distal to the coil may be a limiting factor, particularly when a significant coil mass is displaced and is potentially obstructive.
5. Delivery of the stent retriever is similar to the technique for thrombectomy in stroke. The stent retriever is partially unsheathed in the region of coil displacement, with just enough stent retriever exposed to completely cover the coil. This should be factored into catheter positioning before deployment. Coil-stent interaction should be maximized by slight

forward pressure on the stent pusher wire to increase the potential for optimal stent deployment.

6. An attempt should then be made to resheath the stent retriever by advancing the microcatheter back over the device. Typically, this maneuver will trap the coil within the interstices of the stent retriever and pull the coil loops into the microcatheter with the stent retriever. Constant tension must be applied to the stent retriever to maintain the resheathed position, minimizing the likelihood of the coil working loose by securing it tightly in the retracted device.
7. Once the coil is successfully engaged, the system should be slowly withdrawn into the guide catheter with attention to potential movement of the rest of the coil mass. We had no patient in whom the coil mass within the aneurysm was displaced during this process. Anticipate that the coil will be extracted from the aneurysm intact.
8. Examine the coil retained within the stent retriever on removal. If the aneurysm and patient have remained stable, proceed with further coiling as indicated to complete the case.
9. Caution should be exercised in the context of previous place-

ment of a stent, which may not prevent coils prolapse but inhibits the ability to safely remove coils with this method, as pulling a stent retriever through a pre-existing stent carries the risk for stent dislodgement. The main technical limitation is placement of the catheter tip distal to the coil, which may be especially challenging in smaller distal vessels (<2-mm diameter).

Previously, our preferred device for this clinical scenario was a microsnare, with 15 cases in the 13 years before January 2009 in which the snare-and-lasso technique was used. We were successful in 13 cases but failed to retrieve coils in 2 of the cases, and found the technical aspects significantly more challenging, with more vasospasm encountered and more attempts required to trap the coil. We also have experience with the Alligator retrieval device and have found that the progressive straightening of the teeth of the device limits the number of attempts that can be performed with each device (in our experience, no more than 2 or 3 attempts). In addition, the relative stiffness of the distal tip reduces the ability to orient the device well in a curved segment. Our experience with stent retrievers has proved much more consistent and reliable. Our current report includes consecutive patients, and it is noteworthy that the stent retriever device was successful in every case, with less technical manipulation than is required in many of the other techniques to retrieve stray coil. Despite prospective and consecutive collection of cases, it is important to note that our report had the limitations inherent in any limited, single-center case series. Although our findings relate to 2 specific stent retrievers, it seems reasonable, based on similar existing technology, that the principles described here would apply to any of the stent retrievers currently on the market. We cannot, however, comment on other systems with the data available at this time.

CONCLUSIONS

Stent retrievers are our first option in cases of coil displacement, presenting a simple, safe, and effective alternative for removal of a prolapsed coil during aneurysm coiling.

Disclosures: René Chapot—UNRELATED: Consultancy: ev3/Covidien,* Microvention;* Payment for Lectures (including service on speaker bureaus): ev3,* Microvention,* Balt.* *Money paid to institution.

REFERENCES

1. Molyneux A, Kerr R; International Subarachnoid Aneurysm Trial (ISAT) Collaborative Group, et al. **International Subarachnoid Aneurysm Trial (ISAT) of neurosurgical clipping versus endovascular coiling in 2143 patients with ruptured intracranial aneurysms: a randomized trial.** *J Stroke Cerebrovasc Dis* 2002;11:304–14
2. Derdeyn CP, Cross DT 3rd, Moran CJ, et al. **Postprocedure ischemic events after treatment of intracranial aneurysms with Guglielmi detachable coils.** *J Neurosurg* 2002;96:837–43
3. Pereira VM, Narata AP, Gonzalez AM, et al. **Use of stentrievers in acute stroke: tips, tricks, and current results.** *Tech Vasc Interv Radiol* 2012;15:68–77
4. Bavinszki G, Talazoglu V, Killer M, et al. **Gross and microscopic histopathological findings in aneurysms of the human brain treated with Guglielmi detachable coils.** *J Neurosurg* 1999;91:284–93
5. Eddleman CS, Welch BG, Vance AZ, et al. **Endovascular coils: properties, technical complications and salvage techniques.** *J Neurointerv Surg* 2013;5:104–09.
6. Schutz A, Solymosi L, Vince GH, et al. **Proximal stent fixation of fractured coils: technical note.** *Neuroradiology* 2005;47:874–78
7. Koseoglu K, Parildar M, Oran I, et al. **Retrieval of intravascular foreign bodies with goose neck snare.** *Eur J Radiol* 2004;49:281–85
8. Fiorella D, Albuquerque FC, Deshmukh VR, et al. **Monorail snare technique for the recovery of stretched platinum coils: technical case report.** *Neurosurgery* 2005;57(1 Suppl): E210; discussion E210
9. Henkes H, Lowens S, Preiss H, et al. **A new device for endovascular coil retrieval from intracranial vessels: Alligator retrieval device.** *AJNR Am J Neuroradiol* 2006;27:327–29
10. Kung DK, Abel TJ, Madhavan KH, et al. **Treatment of endovascular coil and stent migration using the Merci retriever: report of three cases.** *Case Report Med* 2012;2012:242101
11. Lee CY. **Use of wire as a snare for endovascular retrieval of displaced or stretched coils: rescue from a technical complication.** *Neuroradiology* 2011;53:31–35
12. Kim YB, Lee KC, Lee JW, et al. **Rescue microsurgery in coil herniation causing thromboembolic occlusion of parent artery.** *Acta Neurochir (Wien)* 2009;151:1609–16
13. Wakhloo AK, Gounis MJ. **Retrievable closed cell intracranial stent for foreign body and clot removal.** *Neurosurgery* 2008;62(5 Suppl 2):ONS390–93; discussion ONS393–94
14. O'Hare AM, Rogopoulos AM, Stracke PC, et al. **Retrieval of displaced coil using a Solitaire((R)) stent.** *Clin Neuroradiol* 2010;20: 251–54

Differences between Internal Jugular Vein and Vertebral Vein Flow Examined in Real Time with the Use of Multigate Ultrasound Color Doppler

G. Ciuti, D. Righi, L. Forzoni, A. Fabbri, and A. Moggi Pignone

ABSTRACT

BACKGROUND AND PURPOSE: The hypothesis that MS could be provoked by a derangement of the blood outflow from the brain has been largely discredited. In part, it was because data on the normal pattern of outflow are scarce and obtained with different methods. The aim of this study was to evaluate the normal pattern of outflow for the vertebral and internal jugular veins in healthy subjects with multigate color Doppler.

MATERIALS AND METHODS: Twenty-five volunteers were studied to assess vessel area, mean velocity, and flow for the vertebral and internal jugular veins in the supine and sitting positions.

RESULTS: In the sitting position, flow decreases, both in vertebral veins and internal jugular veins, as the total vessel area decreases (from 0.46 ± 0.57 to 0.09 ± 0.08 cm²), even if the mean velocity increases (from 12.58 ± 10.19 to 24.14 ± 17.60 cm/s). Contrary to what happens to the blood inflow, outflow in the supine position, through vertebral and internal jugular veins, is more than twice the outflow in the sitting position (739.80 ± 326.32 versus 278.24 ± 207.94 mL/min). In the sitting position, on application of very low pressure to the skin with the sonography probe, internal jugular veins rarely appear to occlude. A pronounced difference of diameter between internal jugular veins was present in approximately one-third of subjects.

CONCLUSIONS: Our results support the view that other outflow pathways, like the vertebral plexus, play a major role in the normal physiology of brain circulation and must be assessed to obtain a complete picture of blood outflow.

ABBREVIATIONS: VV = vertebral vein; IJV = internal jugular vein; BF = blood flow; QDP = Quality Doppler Profiles

Some authors have found that MS is associated with chronic cerebrospinal venous insufficiency syndrome, characterized by stenoses or obstructions of the internal jugular vein (IJV) and/or azygos veins, with disturbed flow and formation of collaterals.^{1,2}

Received November 21, 2012; accepted after revision January 28, 2013.

From SOD Medicina Interna ad Orientamento all'Alta Complessità Assistenziale 3 (G.C., A.M.P., A.F.), Dipartimento di Medicina Interna e di Urgenza, and SOD Valutazione Cardiologica (D.R.), Dipartimento del Cuore e dei Vasi, Azienda Ospedaliero-Universitaria Careggi, Firenze, Italy; and Esaote S.p.A. (L.F.), Firenze, Italy.

Authorship details: G.C., concept and design of the study, analysis and interpretation of data, critical writing and revising of the intellectual content, final approval of the version to be published; D.R., concept and design of the study, analysis and interpretation of data, critical writing and revising of the intellectual content, final approval of the version to be published; L.F., concept and design of the study, analysis and interpretation of data, critical writing and revising of the intellectual content, final approval of the version to be published; A.F., analysis and interpretation of data, critical writing and revising of the intellectual content, final approval of the version to be published; A.M.P., critical writing and revising of the intellectual content, final approval of the version to be published.

Please address correspondence to Gabriele Ciuti, MD, SOD Medicina Interna Orientamento all'Alta Complessità Assistenziale 3, AOU Careggi, 50134 Firenze, Italy; e-mail: gabriele.ciuti@gmail.com

<http://dx.doi.org/10.3174/ajnr.A3557>

However, the blood flow in IJVs is received from the superior sagittal sinus and the straight sinus via the transverse and sigmoid sinuses as well as from the cavernous sinus via the inferior petrosal sinus. After that, the IJV flow returns in the vena cava through the brachiocephalic trunk.

The extrajugular venous system is more complex, and it can be divided into intraspinal and extraspinal compartments. Vertebral veins (VVs) are part of this system and can be considered as potential collectors of these compartments.³

According to some studies, the extrajugular venous system is fundamental for cerebral outflow drainage because it can be sufficient alone to take over the entire venous drainage of the brain.⁴⁻⁸

With body position change, the outflow in IJVs appears to be mostly present in the supine position, whereas it is markedly reduced during standing position, with a tendency of IJVs to collapse⁹⁻¹¹; at the same time, a concomitant flow rise in the VVs was seen.

According to the study by Shreiber et al⁷, the magnitude of flow increase in the VVs did not match the decrease measured in the IJVs;

therefore, a more complex extrajugular drainage must be considered.⁷

On this basis, most authors think that chronic cerebrospinal venous insufficiency simply does not exist,^{3,12} that findings previously reported in some patients can be a normal variant, and that other important drainage pathways such as the VVs and the vertebral plexus^{6,7} must be assessed.

Moreover, outflow through IVJs and VVs is often asymmetric between the 2 sides of the neck, even in healthy subjects.²

Because physiologic data on the cerebral venous outflow are scarce and obtained by the use of different techniques, we performed a study to evaluate the normal physiology of both the VVs and IJVs in healthy subjects by use of multigate color Doppler.

MATERIALS AND METHODS

Research Design

The aim of this study is to investigate the physiology of IJVs and VVs in a cohort of healthy subjects with multigate echo color Doppler ultrasonography in the supine and sitting positions.

Subjects and Materials

In this study, 25 young, healthy volunteers were enrolled [12 men and 13 women; mean age, 27 years (range, 24–52)]. In all subjects, no IJV and/or VV lesions or previous catheter insertions in the IJV were reported, nor was a disease involving neck organs present. All patients underwent echo color Doppler ultrasonography examination of IJVs and VVs on both sides. Ultrasound examinations were performed by an expert vascular sonographer on all subjects' IJVs, and VVs were examined bilaterally from their distal part, connected to the subclavian and brachiocephalic veins, to the proximal part, represented by the presence of the mandible. Vessel area of the IJV was measured in the horizontal plane in the B-mode image at cricoid cartilage level. In the VVs, diameter measurements were obtained in the sagittal plane in the V1 segment, between the origin of VV and the intervertebral foramina, and the area was calculated by $[(\text{diameter of vessel}/2) \times \pi]$.

Venous blood volume flow (BF) (cm^3/min) for IJVs and VVs was calculated as $[(\text{average velocity} \times \text{area of vessel}) \times 60]$.

Morphologic and functional characteristics of both IJVs and VVs were investigated in the supine (0°) and upright sitting (90°) positions. Image acquisitions were performed by use of a MyLab 50 Gold sonography system (Esaote S.p.A., Firenze, Italy) equipped with a linear array transducer probe (LA332, Esaote S.p.A.; operating bandwidth, 3–11 MHz; imaging frequencies, 3.5–5.0–6.6–10.0 MHz; Doppler frequencies, 3.3–5.0 MHz).

Each session started with the subject in supine position, and it then shifted to sitting position. A sufficient level of hydration of the subject during the 12 hours before the examination was recommended. A proper rigid head support was used to prevent hypo-extension or hyperextension of the neck and turning to the left or right side.

A thick layer of ultrasound gel (Aquasonic 100; Parker Laboratories, Fairfield, New Jersey) was used to ensure a complete coupling between the transducer and the examined subject's skin to avoid black cones and dark areas on the ultrasound image and to prevent excessive pressure on the examined neck to preserve the IJV shape and dimension.

Quality Doppler Profiles Technology

Quality Doppler Profiles (QDP) is an innovative multigate spectral Doppler technology that processes the echo signals backscattered from multiple depths along the ultrasound beam, producing and displaying in real-time the so-called spectral profile.¹³ This is a matrix of power spectral densities corresponding to the simultaneously investigated depths.^{14,15} The spectral profile is obtained by calculating, through the classic Fast Fourier Transform algorithm, the Doppler spectrum of 128 samples, gathered from 1 depth and by repeating the procedure over 128 or 256 consecutive depths (covering a total length of 5 cm). As a result, the QDP approach extends the known benefits of spectral analysis¹⁶ to a large depth range without sacrificing the axial resolution. QDP technology investigates the “third dimension of Doppler” in a graphical form, in which spatial distribution is on the vertical axis and velocity on the horizontal one; the brightness of any pixel describes the power of the corresponding spectral attenuation. In this way, QDP enables the simultaneous analysis of different vessels (and different blood flow components within the same vessel) in real time without frame rate loss.

Transducer Design

The shape and the weight of the transducer are ergonomically important to preserve the sonographer's comfort and musculoskeletal integrity while scanning. The linear probe used for the above examinations was designed to be gripped in different ways to release the muscular effort on the wrist and on the hand during the scanning session. The longer the duration of the examination, the more useful was the possibility of changing the probe grip: the average time for the performed scanning was 40 minutes.

Furthermore, the so called “palm-hold” eased the correct orientation of the probe during transverse scanning to avoid the Doppler spectrum mirroring effect obtained when the transducer was perpendicular to the blood flow. Vein compression had to be completely avoided to preserve vein dimensions and hemodynamic characteristics: even a small external pressure can cause a huge collapse of the IJV.

This was facilitated by the low probe weight (80 g plus 170 g for the entire cable).

The probe used in the examinations had a tip dimension of 33×8 mm, with an externally mounted soft silicon acoustical lens without sharp angles to avoid uncomfortable contact in the scanning area for the examined subjects.

The optimized probe design allowed an easier scan; when the subject had a fat or short neck, or when venous valves assessment forced the operator to work in the neck area close to the clavicle, the narrow probe tip ensured the desired field of view.¹⁷

Statistical Analysis

For statistical analysis, we used the Student *t* test for paired samples to compare differences of area and BF between supine and standing positions. A *P* value of $<.05$ was considered significant.

RESULTS

Mean and standard deviation (SD) of cross-sectional area and BF of both IJVs and VVs in supine and standing positions are shown in Tables 1 and 2. The area ratio between the right and left sides, in

Table 1: Velocity and flow analysis in internal jugular vein and vertebral vein in supine and standing positions

	Velocity, cm/s ^a		Flow, mL/min ^a	
	Supine Position	Standing Position	Supine Position	Standing Position
IJV right	20.58 ± 12.6	27.33 ± 21.24	357.03 ± 230.6	108.5 ± 117.0
IJV left	12.71 ± 9.23	29.32 ± 20.35	309.06 ± 233.31	126.97 ± 135.25
Total	16.65 ± 11.63	28.33 ± 20.61	666.10 ± 270.45 ^b	235.49 ± 202.35 ^b
VV right	9.60 ± 7.00	19.76 ± 12.34	41.25 ± 150.03	21.81 ± 24.02
VV left	7.45 ± 5.64	20.17 ± 16.61	32.45 ± 136.65	20.94 ± 26.45
Total	9.60 ± 7.01	19.64 ± 12.86	73.70 ± 197.31	42.75 ± 38.13
IJV + VV total	12.58 ± 10.19	24.14 ± 17.60	739.80 ± 326.32 ^b	278.24 ± 207.94 ^b

^a Mean ± SD.^b *P* < .01.**Table 2: Differences of area between internal jugular vein and vertebral vein in supine and standing positions**

	Area, cm ^{2a}	
	Supine Position	Standing Position
IJV right	0.42 ± 0.40	0.07 ± 0.06
IJV left	0.41 ± 0.25	0.07 ± 0.06
Total	0.83 ± 0.56	0.14 ± 0.09
VV right	0.02 ± 0.01	0.02 ± 0.01
VV left	0.06 ± 0.25	0.02 ± 0.01
Total	0.08 ± 0.25	0.03 ± 0.02
IJV + VV total	0.91 ± 0.61	0.17 ± 0.09

^a Mean ± SD.**Table 3: Side area differences in internal jugular vein and vertebral vein**

	Ratio >2	Right Smaller
IJV supine	9/25 (36%)	6/9 (67%)
VV supine	15/25 (60%)	5/15 (34%)

supine position, was ≥ 2 in 9 subjects (36%) for IJV and in 15 (60%) for VV (Table 3). There was no significant side difference between the cross-sectional area and blood flow either in the supine position ($P = .9$ for IJV, $P = .8$ for VV) or the sitting position ($P = .9$ for IJV, $P = .7$ for VV). Instead, body position influenced both the cross-sectional area and BF: in fact, a reduction of 430.61 (64.6%) and 30.25 (41.0%) mL/min was present in both IJVs and VVs, respectively; however, the difference of BF was statistically significant ($P < .01$) only for IJVs. The reduction of total BF (IJVs + VVs) between the 2 body positions was 461.56 (62.4%) and was significantly different ($P < .01$). BF in both IJVs and VVs was more modulated in the supine position than in the sitting position ($P < .01$) (Fig 1).

DISCUSSION

In this study, we have shown that the BF in both IJVs and VVs is significantly reduced between supine and sitting positions, confirming the data of other studies.^{11,18}

Because the arterial BF passing from the supine to the sitting position is slightly reduced¹⁹ or increased,²⁰ additional paths of cerebral outflow should be strongly considered.

The reduction in total venous outflow that we found in the sitting position was approximately 60%, which is inferior to some studies¹¹ but comparable to another study that used the MR imaging technique.¹⁸

We found that the area of IJVs and even VVs is different between the 2 sides of the neck, that the BF is asymmetric in many

patients, and that the BF in IJVs is more modulated in sitting than supine position.

In a similar study conducted by Valdueza et al,^{11,21} who examined the postural dependence of cerebral venous outflow through IJVs and VVs in 23 young healthy adults by use of color-coded duplex sonography, measurements were taken with the body at 0°, +15°, +30°, +45°, and +90°.

The authors found that in IJVs, BF was reduced, whereas in VVs, it was increased when the subjects moved from a 0° to a 90° position; however, this increase was not sufficient to compensate for the drop in jugular flow, therefore, total BF was significantly reduced.

In the sitting position, half of the IJVs collapsed completely and had no flow visible (23 of 46 vessels); in 9 (39%) subjects, the flow was absent in both IJVs.

These last data are not confirmed by our study; we think it is because of the increased accuracy and sensibility of modern machines as compared with the ones used in the previous study and in the technique that we used to avoid compression of the partially collapsed jugular veins.

Moreover, we found that BF in VVs was reduced with the body at 90°; we think it could be explained by the different point of BF sampling because we recorded VV BF in V1, between the origin of the VV and the intervertebral foramina, where the vein diameter is more likely to change than in the rigid V2 section. Moreover, a different regulation of the pulsed Doppler filter could in part explain these differences.

Alperin et al¹⁸ conducted a study on 10 volunteers by use of an MR imaging technique to assess effects of posture on intracranial physiology.

The study showed that a shift of the venous outflow from the IJVs to secondary venous pathways occurred in the upright posture and was also less pulsatile (57%).

Our study confirms variations of pulsatility of BF in the 0–90° body position by use of the echo color Doppler ultrasonography technique, and our BF measurements are similar to those obtained in this study.

We found considerable side differences of IJV BF, in agreement with other studies by use of different techniques, including MR imaging, PET, and echo color Doppler ultrasonography,²² and this can be explained by a frequent side dominance of venous drainage.²³ Again, in accordance with the previous studies, we found a right IJV outflow dominance.

A large intersubject variability was also seen in cerebral blood outflow, as has been reported in other studies.^{7,11,18,22}

The reasons for these differences are not completely understood and are probably due to many factors such as age²⁴ and a wide range of global arterial inflow.^{25–27}

The existence of different outflow pathways can also play a role because they can have a different effect in different subjects.

Echo color Doppler ultrasonography can easily be used to evaluate not only the IJV diameter differences but also the flow and flow patterns and probably can be used as a sophisticated

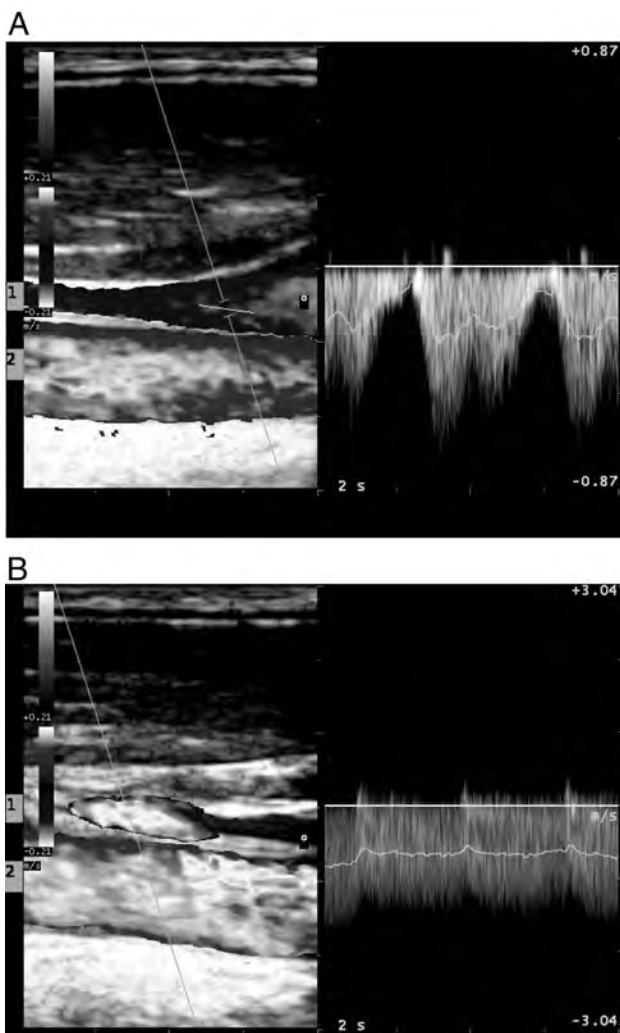


FIG 1. The pulse wave analysis shows how signal in internal jugular vein is more modulated in supine position (A) than in standing position (B). In each frame, both the internal jugular vein (1) and the external carotid artery (2) are shown.

guide to evaluate which IJV can be used for intravenous infusion devices.

In contrast to other studies, we verified that the IJV rarely occludes during the sitting position: it is not simple in this position to examine the neck, and in particular, the IJVs; it is easy to compress the IJV under the probe, so it is important to be careful and to have adequate support and an abundant quantity of ultrasonic gel to avoid the IJV collapse.

We found that QDP technology, which is able to elaborate the Doppler spectrum along all the vessel lumen, showing the spatial distribution, the velocity, and the power spectral attenuation in real time, was useful to give us a qualitative idea of how the diameter of the vessel and the velocity inside it varied with time and with the position of our subjects (Fig 2).

CONCLUSIONS

According to our data, cerebral outflow changes with body position, diminishing to less than half in the IJVs and in the VVs, and the increase in mean flow velocity is not sufficient to compensate

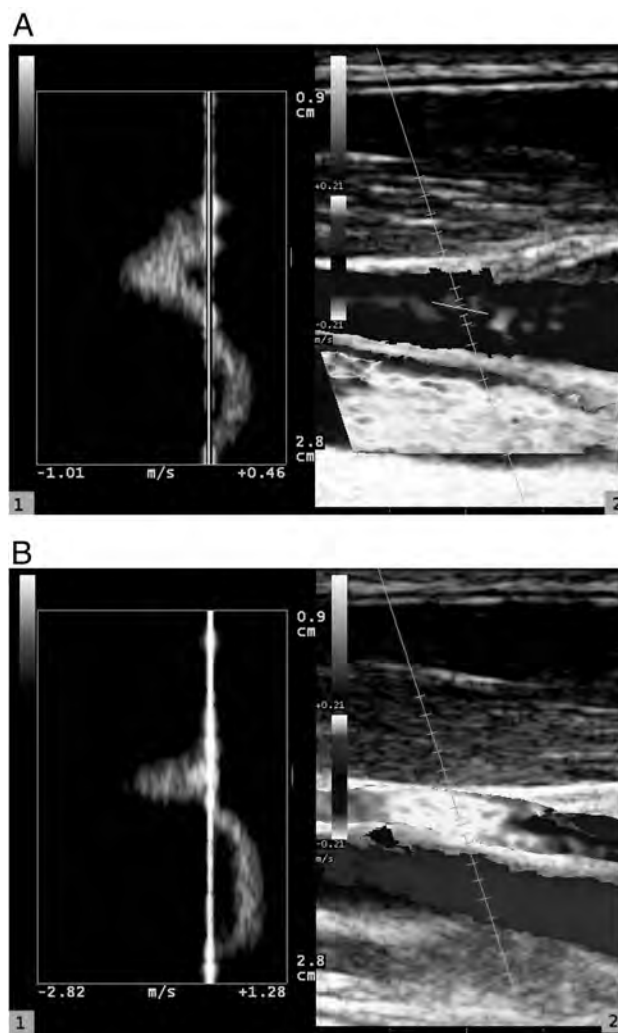


FIG 2. Blood flow in internal jugular vein analyzed by use of QDP technology (1); reference image shows internal jugular vein and common carotid artery (2). Internal jugular vein is analyzed both in supine position (A) and in standing position (B).

for the decrease of the cross-section of these vessels in the upright position.

Because arterial inflow is not so dramatically diminished, alternative outflow pathways must play a role and must be studied if any conclusion must be drawn from cerebral outflow impairment.

Because the suspected pathway is the venous plexus, which is situated inside the vertebral channel, sonography methods that are impervious to thick bone are probably inadequate to study such an anatomic structure.

The large difference that exists in a large number of subjects between the IJV area in the 2 sides of the neck makes the study of only 1 side poorly suited to draw firm conclusions and suggests that a sonography study of both veins could be useful to choose which side to use for the insertion of intravenous devices.

Disclosures: Leonardo Forzoni—UNRELATED: Employment: Esaote S.p.A., Comments: I am an employee of Esaote S.p.A., the company that implemented the QDP technology used in the study.

REFERENCES

1. Zamboni P. **The big idea: iron-dependent inflammation in venous disease and proposed parallels in multiple sclerosis.** *J R Soc Med* 2006;9911:589–93
2. Zamboni P, Morovic S, Menegatti E, et al. **Screening for chronic cerebrospinal venous insufficiency (CCSVI) using ultrasound: recommendations for a protocol.** *Int Angiol* 2011;306:571–97
3. Doepp F, Paul F, Valdueza JM, et al. **No cerebrocervical venous congestion in patients with multiple sclerosis.** *Ann Neurol* 2010;682:173–83
4. Gius JA, Grier DH. **Venous adaptation following bilateral radical neck dissection with excision of the jugular veins.** *Surgery* 1950;282:305–21
5. Fitz-Hugh GS, Robins RB, Craddock WD. **Increased intracranial pressure complicating unilateral neck dissection.** *Laryngoscope* 1966;765:893–906
6. Batson OV. **The vertebral vein system: Caldwell lecture, 1956.** *Am J Roentgenol Radium Ther Nucl Med* 1957;782:195–212
7. Schreiber SJ, Lurtzing F, Gotze R, et al. **Extrajugular pathways of human cerebral venous blood drainage assessed by duplex ultrasound.** *J Appl Physiol* 2003;945:1802–05
8. San Millán Ruíz D, Gailloud P, Rüfenacht DA, et al. **The craniocervical venous system in relation to cerebral venous drainage.** *AJNR Am J Neuroradiol* 2002;239:1500–08
9. Holt JP. **The collapse factor in the measurement of venous pressure: the flow of fluid through collapsible tubes.** *Am J Physiol* 1941;134:292–99
10. Cirovic S, Walsh C, Fraser WD, et al. **The effect of posture and positive pressure breathing on the hemodynamics of the internal jugular vein.** *Aviat Space Environ Med* 2003;742:125–31
11. Valdueza JM, Von Münster T, Hoffman O, et al. **Postural dependency of the cerebral venous outflow.** *Lancet* 2000;3559199:200–01
12. **FDA issues alert on potential dangers of unproven treatment for multiple sclerosis.** <http://www.fda.gov/NewsEvents/Newsroom/PressAnnouncements/ucm303538.htm>. Accessed Jan 20, 2013
13. Tortoli P, Guidi G, Berti P, et al. **An FFT-based flow profiler for high-resolution in vivo investigations.** *Ultrasound Med Biol* 1997;236:899–910
14. Tortoli P, Ricci S, Andreuccetti F, et al. **Detection of chronic cerebrospinal venous insufficiency through multigate quality Doppler profiles.** In: *Ultrasonics Symposium (IUS), 2010 IEEE* 2010:1190–93
15. Forzoni L, Morovic S, Semplici P, et al. **Detection of reflux in jugular and vertebral veins through directional multigate quality Doppler profiles.** In: Nowicki A, Litniewski J, Kujawska T, eds. *Acoustical Imaging*. Vol 31. Berlin, Germany: Springer-Verlag; 2012:55–67
16. Evans DH, McDicken WN. *Doppler Ultrasound: Physics Instrumentation and Signal Processing*. New York: Wiley; 2000
17. Forzoni L, D'Onofrio S, Farina M, et al. *Combined Ultrasound Technologies and Optimized Probe Design for Neck Veins Examination*. Proceedings of the IASTED Biomedical Engineering BioMed Congress 2012. Calgary, Canada: Actapress; pp. 252–59
18. Alperin N, Lee SH, Sivaramakrishnan A, et al. **Quantifying the effect of posture on intracranial physiology in humans by MRI flow studies.** *J Magn Reson Imaging* 2005;225:591–96
19. Scheinberg P, Stead EA. **The cerebral blood flow in male subjects as measured by the nitrous oxide technique. Normal values for blood flow, oxygen utilization, glucose utilization, and peripheral resistance, with observations on the effect of tilting and anxiety.** *J Clin Invest* 1949;285(Pt 2):1163–71
20. Nelson RJ, Lovick AH, Pickard JD, et al. **Changes in cerebral blood flow during anaesthesia and surgery in the sitting position.** *J Neurol Neurosurg Psychiatry* 1987;508:971–75
21. Von Münster T. [Einfluss der Körperposition auf die zerebrale venöse Drainage. Eine duplexsonographische Untersuchung der Vena jugularis interna und Vena vertebralis]. <https://edoc.hu-berlin.de/docviews/abstract.php?id=10508>. Accessed Jan 20, 2013. edoc-Server der Humboldt-Universität zu Berlin
22. Stoquart-Elsankari S, Lehmann P, Villette A, et al. **A phase-contrast MRI study of physiologic cerebral venous flow.** *J Cereb Blood Flow Metab* 2009;296:1208–15
23. Durgun B, Ilglt ET, Cizmeli MO, et al. **Evaluation by angiography of the lateral dominance of the drainage of the dural venous sinuses.** *Surg Radiol Anat* 1993;152:125–30
24. Scheel P, Ruge C, Petruch UR, et al. **Color duplex measurement of cerebral blood flow volume in healthy adults.** *Stroke* 2000;311:147–50
25. Scheel P, Ruge C, Schöning M. **Flow velocity and flow volume measurements in the extracranial carotid and vertebral arteries in healthy adults: reference data and the effects of age.** *Ultrasound Med Biol* 2000;268:1261–66
26. Schöning M, Scheel P. **Color duplex measurement of cerebral blood flow volume: intra- and interobserver reproducibility and habituation to serial measurements in normal subjects.** *J Cereb Blood Flow Metab* 1996;163:523–31
27. Schöning M, Walter J, Scheel P. **Estimation of cerebral blood flow through color duplex sonography of the carotid and vertebral arteries in healthy adults.** *Stroke* 1994;251:17–22

Differences in Imaging Characteristics of HPV-Positive and HPV-Negative Oropharyngeal Cancers: A Blinded Matched-Pair Analysis

S.C. Cantrell, B.W. Peck, G. Li, Q. Wei, E.M. Sturgis, and L.E. Ginsberg



ABSTRACT

BACKGROUND AND PURPOSE: Human papillomavirus–positive oropharyngeal cancers typically have younger age of onset, limited tobacco exposure, and more favorable prognosis than HPV-negative oropharyngeal cancers. We assessed whether HPV-positive and HPV-negative oropharyngeal cancers have consistent differences in pretreatment imaging characteristics.

MATERIALS AND METHODS: A retrospective review of 136 pretreatment CT examinations of paired HPV-positive and HPV-negative oropharyngeal cancers matched for T stage, tumor subsite, and smoking status was performed with the reviewing radiologist blinded to HPV status and clinical stage. Demographic/clinical characteristics and imaging characteristics of primary lesions and metastatic nodal disease were compared by use of Fisher exact testing. The McNemar χ^2 test was used for the matched-pair analysis.

RESULTS: By imaging, HPV-negative tumors were more likely to demonstrate invasion of adjacent muscle (26% versus 6%, $P = .013$). HPV-positive primary tumors were more likely to be enhancing and exophytic with well-defined borders, whereas HPV-negative primary tumors were more likely to be isoattenuated and demonstrate ill-defined borders, though these results were not statistically significant. HPV-positive tumors were more likely to demonstrate cystic nodal metastases than HPV-negative tumors (36% versus 9%, $P = .002$).

CONCLUSIONS: In this matched and blinded analysis of the imaging differences between HPV-positive and HPV-negative oropharyngeal cancers, HPV-positive carcinomas often had primary lesions with well-defined borders and cystic nodal metastases, whereas HPV-negative primaries more often had poorly defined borders and invasion of adjacent muscle.

ABBREVIATIONS: HPV = human papillomavirus; SCCOP = squamous cell carcinomas of the oropharynx; EGFR = epidermal growth factor

Whereas age-adjusted incidence of oral cavity, laryngeal, and hypopharyngeal carcinomas has predictably declined with decreased smoking prevalence, there has been a paradoxical increase in the age-adjusted incidence of oropharyngeal carcinomas

secondary to the emergence of an epidemic of HPV-related squamous cell carcinomas of the oropharynx (SCCOP).^{1–5} HPV-positive SCCOP represents a unique demographic, molecular, and clinical entity with typically younger age of onset, limited tobacco exposure, and more favorable prognosis than HPV-negative SCCOP.^{6–10} The favorable prognosis among patients with HPV-positive SCCOP may be attributed in part to fewer somatic molecular alterations in HPV-positive cancers; HPV-positive smokers, however, appear to have a worse prognosis than HPV-positive nonsmokers, which may also be secondary to somatic molecular alterations in these cancers in smokers.^{6,11} It also appears that HPV-positive oropharyngeal carcinomas are a distinct histologic entity exhibiting basaloid, lymphoepithelial, and poorly differentiated histology as opposed to the keratinizing histologies seen in HPV-negative SCCOP.¹²

Although differences in the clinical characteristics, risk factors such as smoking and sexual behaviors, tumor pathways, and patient prognosis of HPV-positive versus HPV-negative SCCOP have been reported, distinctions between pretreatment imaging characteristics of HPV-positive and negative SCCOP have not

Received November 9, 2012; accepted after revision January 9, 2013.

From the Departments of Diagnostic Imaging (S.C.C., L.E.G.), Epidemiology (G.L., Q.W., E.M.S.), and Head and Neck Surgery (G.L., E.M.S.), University of Texas MD Anderson Cancer Center, Houston, Texas; Department of Radiology (S.C.C.), University of Texas Health Science Center, Houston, Texas; and Department of Otorhinolaryngology (B.W.P.), Mayo Clinic, Rochester, Minnesota.

This work was funded in part by start-up funds from University of Texas MD Anderson Cancer Center (E.M.S.); NIH Head and Neck SPORE grant P50CA097007 Career Development Award (E.M.S.); University of Texas MD Anderson Cancer Center Institutional Research Grant (E.M.S.); NIH grant K-12 88084 (E.M.S., faculty trainee; R.C. Bast, P.I.); NIH grant R03CA128110-01A1 (E.M.S.); NIH grant R01ES011740 (Q.W.); NIH grant R01CA131274 (Q.W.); and an NIH Cancer Center Support grant P30CA016672 (to John Mendelsohn).

Please address correspondence to Dr Lawrence E. Ginsberg, Department of Diagnostic Imaging, Unit 1482, University of Texas MD Anderson Cancer Center, 1400 Pressler St, Houston, TX 77030; e-mail: lginsberg@mdanderson.org

Indicates open access to non-subscribers at www.ajnr.org

Indicates article with supplemental on-line tables.

<http://dx.doi.org/10.3174/ajnr.A3524>

been thoroughly investigated.⁷ The most comprehensive examination of the imaging characteristics of HPV SCCOP was performed by Goldenberg et al,¹³ whose retrospective review of pretreatment CT examinations of SCCOP demonstrated an association of cystic nodal metastases with base of tongue and tonsillar primary cancers and an association of cystic nodal metastases with HPV-positive cancers. Furthermore, Goldenberg et al made a distinction between cystic and necrotic nodal metastases, suggesting that they are distinct imaging and pathophysiologic entities. Cystic nodal metastases were defined as having homogeneous fluid content without internal complex, irregular, or solid areas and an enhancing capsule <2 mm in thickness, whereas necrotic nodal metastases were defined as having thicker or more irregular walls with complex central low attenuation.¹³ Although the association of cystic nodal metastases with squamous cell carcinomas of the Waldeyer ring has been well established,¹⁴⁻¹⁷ our objective was to explore differences in the pretreatment imaging characteristics of HPV-positive and -negative oropharyngeal cancers.

MATERIALS AND METHODS

Patients with newly diagnosed oropharyngeal cancer who had been prospectively enrolled in a molecular epidemiology study conducted between May 1995 and June 2008 were matched on T-category, tumor subsite (base of tongue or tonsil), and smoking status (never, former, or current smoker). This research was approved by the institutional review board. Patients eligible for the current study met the following criteria: newly diagnosed, previously untreated SCCOP (base of tongue or tonsil), resident of the United States, and age 18 years or older. Exclusion criteria included treatment of head and neck malignancy (conventional surgical management, radiation therapy, or chemoradiation) before CT examination. Patients were also excluded if contrast-enhanced pretreatment CT imaging was not available for review in PACS. Each pair's HPV status was determined by HPV in situ hybridization or HPV16 polymerase chain reaction testing. "Never-smokers" were defined as having smoked fewer than 100 cigarettes in their lifetime, with "former smokers" having quit smoking at least 1 year before their cancer diagnosis. "Current drinkers" were defined as having at least 1 alcoholic drink per week for at least 1 year and who were still drinking in this manner at the time of their presentation, whereas "former drinkers" were defined as those who had drunk alcoholic beverages in this manner in the past but had begun drinking less or stopped drinking at least 1 year before presentation.

Retrospective review of pretreatment CT examinations of paired patients with HPV-positive or HPV-negative SCCOP matched for T-category, tumor subsite, and smoking status was performed by a single neuroradiologist blinded to HPV status and clinical stage. T-category was determined clinically with clinical examination, direct laryngoscopy, and pretreatment imaging. All CT examinations were performed on 16- and 64-channel scanner systems (various software platforms; GE Healthcare, Milwaukee, Wisconsin). Images were obtained after administration of intravenous contrast, (125 mL, 60-second delay) from the aortic arch to the orbital roof with the following imaging parameters (tube current 100–600 mA, tube voltage 120 kVp, gantry rotation time 0.5–1 second, pitch

0.9, 1.25-mm image thickness). All patients with dental fillings had an additional stack of axial images obtained to angle away from the fillings. Although contrast bolus timing and volume of contrast may modify conspicuity of the interface between the primary lesion and surrounding soft tissues, in all cases contrast enhancement was sufficient to identify and adequately evaluate the primary tumor.

Demographic and clinical characteristics, imaging characteristics of primary lesion, and imaging characteristics of metastatic nodal disease were compared by means of Fisher exact testing. The McNemar χ^2 test was used for the matched-pair analysis. Variables compared for the primary lesion included visibility, well-defined versus ill-defined border, submucosal spread, invasion of adjacent muscle, enhancement, necrosis, and exophytic margins. Submucosal spread was defined as extension of mucosal lesion >1 cm in depth with infiltration of the submucosal fat plane and spread parallel to the mucosal surface. Variables compared for nodal metastases included radiologic N stage, presence of cystic nodes, necrotic nodes, metastatic spread to node of Rouvier (lateral retropharyngeal lymph node), nodal enhancement, and extracapsular spread. Extracapsular spread was recognized by indistinct nodal margins, irregular nodal capsular enhancement, and infiltration into the adjacent perinodal fat or muscle. Cystic lymph nodes were defined as having a thin (<2 mm) enhancing capsule and homogeneous fluid content (>70% with HU <20), with no internal complexity.

RESULTS

Of 102 matched pairs (204 patients) initially identified, 34 matched pairs were excluded because for one or both members of the matched pair no pretreatment CT was available for review, yielding 68 matched pairs. Each pair's HPV status had been determined by HPV in situ hybridization (38 pairs) or HPV16 polymerase chain reaction (30 pairs) testing.

The demographic and clinical characteristics of the patients with HPV-positive or HPV-negative SCCOP are presented in On-line Table 1. Patients with HPV-positive and HPV-negative SCCOP were similar in demographics and clinical characteristics; however, there was a higher proportion of males in the group with HPV-positive SCCOP ($P = .02$, On-line Table 1). Patients were excluded from analysis of the primary lesion (Table 1) if one or both members of the matched pair had a primary tonsillar tumor subsite with tonsillectomy before CT examination (7 matched pairs). Small primary tumors could not be visualized on CT imaging in 14 patients with HPV-positive SCCOP and in 10 patients with HPV-negative SCCOP (Table 1), and these patients were also excluded from further comparison of primary tumor imaging characteristics. HPV-negative tumors were more likely to demonstrate invasion of adjacent muscle (26% versus 6%, $P = .013$; Table 1) (Fig 1). HPV-positive tumors were more likely to have enhancing, exophytic primary lesions with well-defined borders by CT imaging (Fig 2), whereas HPV-negative tumors were more likely to have isoattenuated primary lesions that demonstrated ill-defined borders, though these results did not reach statistical significance (Fig 3).

Patients were excluded from analysis of the metastatic nodal imaging (Table 2) if one or both members of the matched pair had prior excisional lymph node biopsy (9 matched pairs). In 6 pa-

Table 1: Imaging characteristics of patients with primary tumor among those with HPV+ oropharynx cancer and matched patients with HPV- oropharynx cancer

Imaging Characteristic	HPV+ (n = 61)		HPV- (n = 61)		P Value
	N	%	N	%	
Primary lesion is visible					.362
Yes	47	77.0	51	83.6	
No	14	23.0	10	16.4	
Primary lesion is enhancing					.182
Yes	37	78.7	34	66.7	
No	10	21.3	17	33.3	
Primary lesion demonstrates necrosis					.651
Yes	39	83.0	44	86.3	
No					
Primary lesion demonstrates well-defined border					.067
Yes	35	74.5	29	56.9	
No	12	25.5	22	43.1	
Primary lesion is exophytic					.095
Yes	14	29.8	8	15.7	
No	33	70.2	43	84.3	
Primary lesion demonstrates submucosal spread					.667
Yes	26	55.3	26	51.0	
No	21	44.7	25	49.0	
Primary lesion invades adjacent muscle					.013
Yes	3	6.4	13	25.5	
No	44	93.6	38	74.5	



FIG 1. HPV-negative SCCOP demonstrating deep muscular invasion involving the extrinsic muscles of the tongue with submucosal spread. Axial contrast-enhanced CT image shows a large and deeply invasive T4 base of tongue lesion, extending anteriorly into the oral tongue.

tients with HPV-positive SCCOP and 9 patients with HPV-negative SCCOP, nodal metastases were not visible (Table 2). HPV-positive tumors were more likely to demonstrate cystic nodal metastases than HPV-negative tumors (36% versus 9%, $P = .002$; Table 2) (Fig 4).

In matched-pair analysis (On-line Table 2), 18 matched pairs were excluded from primary lesion subgroup analysis because one or both members of the matched pair had prior tonsillectomy or radiologic T0 category, and 14 matched pairs were excluded from nodal subgroup analysis secondary to one or both members having prior excisional lymph node biopsy or radiologic N0 category. In matched-

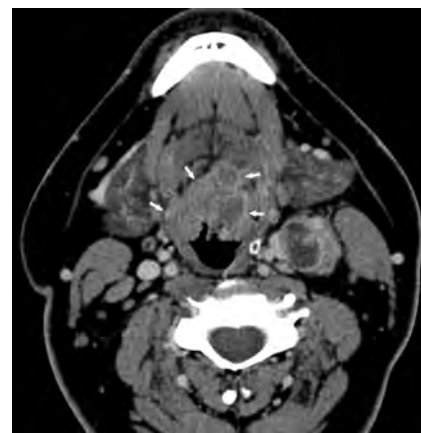


FIG 2. HPV-positive SCCOP with typically well-defined borders. Axial contrast-enhanced CT image shows a midline T2 base of tongue mass with well-defined margins (arrows). Level II left lymph node metastasis demonstrates extracapsular extension.

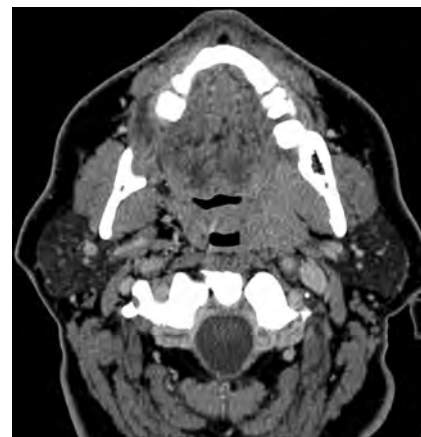


FIG 3. HPV-negative SCCOP demonstrating ill-defined borders. Axial contrast-enhanced CT image shows a mass in the left tonsil, with poorly defined borders, especially anteriorly.

pair analysis, cystic nodal metastases were associated with HPV-positive tumors (>5-fold; $P = .013$; On-line Table 2). Invasion of adjacent muscle was associated with HPV-negative tumors ($P = .002$; On-line Table 2).

DISCUSSION

In this blinded analysis of the CT imaging differences between HPV-positive and HPV-negative SCCOP, a greater percentage of HPV-positive SCCOP demonstrated primary tumors with well-defined borders whereas HPV-negative primary tumors demonstrated ill-defined borders and increased invasion of adjacent muscle. Despite the overall improved prognosis of HPV-positive SCCOP relative to HPV-negative SCCOP, we found no significant difference in incidence of extracapsular spread of nodal metastases, a well-established predictor of poor prognosis in squamous cell carcinoma of the head and neck.¹⁸⁻²¹ Our data are consistent with the findings of Goldenberg et al,¹³ which demonstrated increased incidence of cystic nodal metastases in HPV-positive SCCOP. These imaging differences between HPV-positive SCCOP compared with HPV-negative SCCOP are congruent with an understanding that HPV-positive SCCOP represent a

Table 2: Imaging characteristics of nodal metastases among patients with HPV+ oropharynx cancer and matched patients with HPV- oropharyngeal cancer

Imaging Characteristic	HPV+ (n = 59)		HPV- (n = 59)		P Value
	N	%	N	%	
Radiologic N stage					.754
N0	6	10.2	9	15.3	
N1	7	11.9	8	13.6	
N2	45	76.3	42	71.2	
N3	1	1.6	0	0	
Nodal metastases demonstrate extracapsular spread					.983
Yes	16	30.2	15	30.0	
No	37	69.8	35	70.0	
Nodal metastases demonstrate cystic morphology					.002
Yes	19	35.8	5	10.0	
No	34	64.2	45	90.0	
Nodal metastases demonstrate necrosis					.149
Yes	37	69.8	41	82.0	
No	16	30.2	9	18.0	
Nodal metastases demonstrate enhancement					.693
Yes	33	62.2	33	66.0	
No	20	37.8	17	34.0	
Nodal metastases include node of Rouvier					.474
Yes	9	17.0	6	12.0	
No	44	83.0	44	88.0	



FIG 4. HPV-positive SCCOP demonstrating a cystic nodal metastasis. Axial contrast-enhanced CT image shows an obvious bulky midline left-sided base of tongue cancer (with characteristically well-defined borders) and a predominantly cystic mass in level IIa.

separate clinical entity, driven by different somatic molecular events and with a different clinical phenotype.^{11,22}

Although HPV-positive SCCOP has a reliably better prognosis than HPV-negative SCCOP, deleterious somatic alterations resulting from tobacco exposure worsen the prognosis of HPV-positive smokers relative to HPV-positive nonsmokers.⁴ HPV infection ultimately results *E6* and *E7* oncogene-mediated degradation of p53 and retinoblastoma (Rb) tumor suppressors.²³ Overexpression of p16 protein, which functions as a tumor suppressor, is closely correlated with HPV positivity.⁴ HPV-positive nonsmokers are more likely to harbor an HPV-driven tumor phenotype characterized by high HPV titer,

increased p16 expression, wild-type p53, and low epidermal growth factor (EGFR) expression.²⁴ This molecular profile resulting from HPV positivity and limited or no smoking history results in favorable tumor phenotype and increased overall survival.⁴ Smokers are more likely to have tumors with adverse somatic alterations related to tobacco exposure, including mutated p53 and EGFR overexpression, concurrent with decreased HPV titer, and decreased p16 expression.²⁴

The most significant limitation of our study was our sample size. Several results lacking statistical significance in matched-pair analysis, including primary tumor borders and the presence of cystic lymph node metastases, are probably limited by a relatively small sample size. Despite limitations imposed by small sample size, matched-pair analysis provides a controlled and homogeneous setting and is a well-established means of controlling for confounding. Furthermore, all images were reviewed specifically for this study by a single radiologist without knowledge of the HPV status of the individual cases. Additional limitations of our study included retrospective review.

Finally, a common imaging finding in HPV-positive SCCOP, cystic metastases caused by small or poorly visualized primary, highlights a common clinical/radiologic pitfall that is of particular concern, given the rapidly rising incidence of SCCOP attributable to HPV. Because HPV-positive SCCOP is commonly clinically and radiologically occult at the primary site, radiologists must recognize that cystic neck masses in adult patients should be considered cystic metastases until proved otherwise; a brachial cleft cyst in an adult should be considered the exception rather than the rule for an adult with a cystic neck mass. Because HPV-positive SCCOP commonly arises in nonsmokers, a lack of significant tobacco or alcohol exposure does not provide evidence against malignancy.^{12,25} Such patients must be evaluated thoroughly by an otolaryngologist or head and neck surgeon, and the index of suspicion for carcinoma must be high.

CONCLUSIONS

HPV-negative primary tumors demonstrated ill-defined borders and increased invasion of adjacent muscle, whereas HPV-positive SCCOP more frequently demonstrated primary tumors with well-defined borders and cystic nodal metastases. Given the rising incidence of HPV-positive SCCOP, radiologists should maintain a high index of suspicion for underlying malignancy when evaluating cystic neck lesions in adult patients without significant tobacco or alcohol exposure.

REFERENCES

1. Chaturvedi AK, Engels EA, Anderson WF, et al. **Incidence trends for human papillomavirus-related and -unrelated oral squamous cell carcinomas in the United States.** *J Clin Oncol* 2008;26:612–19
2. Carvalho AL, Nishimoto IN, Califano JA, et al. **Trends in incidence and prognosis for head and neck cancer in the United States: a site-specific analysis of the SEER database.** *Int J Cancer* 2005;114:806–16
3. Shiboski CH, Schmidt BL, Jordan RC. **Tongue and tonsil carcinoma: increasing trends in the US population ages 20–44 years.** *Cancer* 2005;103:1843–49
4. Sturgis EM, Ang KK. **The epidemic of HPV-associated oropharyngeal cancer is here: is it time to change our treatment paradigms?** *J Natl Compr Canc Netw* 2011;9:665–73
5. Sturgis EM, Cinciripini PM. **Trends in head and neck cancer incidence in**

- relation to smoking prevalence: an emerging epidemic of human papillomavirus-associated cancers? *Cancer* 2007;110:1429–35
6. Ang KK, Harris J, Wheeler R, et al. **Human papillomavirus and survival of patients with oropharyngeal cancer.** *N Engl J Med* 2010;363:24–35
 7. Dahlstrom KR, Li G, Tortolero-Luna G, et al. **Differences in history of sexual behavior between patients with oropharyngeal squamous cell carcinoma and patients with squamous cell carcinoma at other head and neck sites.** *Head Neck* 2011;33:847–55
 8. D'Souza G, Kreimer AR, Viscidi R, et al. **Case-control study of human papillomavirus and oropharyngeal cancer.** *N Engl J Med* 2007;356:1944–56
 9. Gillison ML, D'Souza G, Westra W, et al. **Distinct risk factor profiles for human papillomavirus type 16-positive and human papillomavirus type 16-negative head and neck cancers.** *J Natl Cancer Inst* 2008;100:407–20
 10. Ji X, Neumann AS, Sturgis EM, et al. **p53 codon 72 polymorphism associated with risk of human papillomavirus-associated squamous cell carcinoma of the oropharynx in never-smokers.** *Carcinogenesis* 2008;29:875–79
 11. Klussmann JP, Mooren JJ, Lehnen M, et al. **Genetic signatures of HPV-related and unrelated oropharyngeal carcinoma and their prognostic implications.** *Clin Cancer Res* 2009;15:1779–86
 12. Marur S, D'Souza G, Westra WH, et al. **HPV-associated head and neck cancer: a virus-related cancer epidemic.** *Lancet Oncol* 2010;11:781–89
 13. Goldenberg D, Begum S, Westra WH, et al. **Cystic lymph node metastasis in patients with head and neck cancer: an HPV-associated phenomenon.** *Head Neck* 2008;30:898–903
 14. Flanagan PM, Roland NJ, Jones AS. **Cervical node metastases presenting with features of branchial cysts.** *J Laryngol Otol* 1994;108:1068–71
 15. Gourin CG, Johnson JT. **Incidence of unsuspected metastases in lateral cervical cysts.** *Laryngoscope* 2000;110:1637–41
 16. Regauer S, Mannweiler S, Anderhuber W, et al. **Cystic lymph node metastases of squamous cell carcinoma of Waldeyer's ring origin.** *Br J Cancer* 1999;79:1437–42
 17. Thompson LD, Heffner DK. **The clinical importance of cystic squamous cell carcinomas in the neck: a study of 136 cases.** *Cancer* 1998;82:944–56
 18. Myers JN, Greenberg JS, Mo V, et al. **Extracapsular spread: a significant predictor of treatment failure in patients with squamous cell carcinoma of the tongue.** *Cancer* 2001;92:3030–36
 19. Wenzel S, Sagowski C, Kehrl W, et al. **The prognostic impact of metastatic pattern of lymph nodes in patients with oral and oropharyngeal squamous cell carcinomas.** *Eur Arch Otorhinolaryngol* 2004;261:270–75
 20. Iyer NG, Kim L, Nixon IJ, et al. **Outcome of patients with early T1 and T2 squamous cell carcinoma of the base of tongue managed by conventional surgery with adjuvant postoperative radiation.** *Head Neck* 2012 doi: 10.1002/hed.23071
 21. Olsen KD, Caruso M, Foote RL, et al. **Primary head and neck cancer: histopathologic predictors of recurrence after neck dissection in patients with lymph node involvement.** *Arch Otolaryngol Head Neck Surg* 1994;120:1370–74
 22. Martinez I, Wang J, Hobson KF, et al. **Identification of differentially expressed genes in HPV-positive and HPV-negative oropharyngeal squamous cell carcinomas.** *Eur J Cancer* 2007;43:415–32
 23. Weinberger PM, Yu Z, Haffty BG, et al. **Molecular classification identifies a subset of human papillomavirus-associated oropharyngeal cancers with favorable prognosis.** *J Clin Oncol* 2006;24:736–47
 24. Kumar B, Cordell KG, Lee JS, et al. **EGFR, p16, HPV titer, Bcl-xL and p53, sex, and smoking as indicators of response to therapy and survival in oropharyngeal cancer.** *J Clin Oncol* 2008;26:3128–37
 25. Hudgins PA, Gillison M. **Second branchial cleft cyst: not!!** *AJNR Am J Neuroradiol* 2009;9:1628–29

Morning Glory Disc Anomaly: Characteristic MR Imaging Findings

S. Ellika, C.D. Robson, G. Heidary, and M.J. Paldino

ABSTRACT

SUMMARY: Establishing the diagnosis of morning glory disc anomaly is crucial to appropriate patient treatment. Although typically made clinically, the diagnosis is not always straightforward, especially in circumstances where physical examination is limited. The goal of this study was to define the spectrum and frequency of orbital findings in a series of patients with funduscopically-confirmed morning glory disc anomaly by using MR imaging. MR imaging demonstrated 3 findings in all patients: 1) funnel-shaped morphologic pattern of the posterior optic disc with elevation of the adjacent retinal surface; 2) abnormal tissue associated with the distal intraorbital segment of the ipsilateral optic nerve, with effacement of the regional subarachnoid spaces; and 3) discontinuity of the uveoscleral coat. These findings were not observed in any of the unaffected globes of the study patients. In summary, these consistent and characteristic findings of morning glory disc anomaly should allow for accurate differentiation from other ocular anomalies and have the potential to guide appropriate management of this patient population.

ABBREVIATIONS: MGDA = morning glory disc anomaly

Morning glory disc anomaly (MGDA) is a congenital optic nerve anomaly characterized by a funnel-shaped excavation of the posterior globe that incorporates the optic disc.¹ The term was first coined in 1970 by Kindler,² who noted the resemblance of the malformed optic nerve to the morning glory flower. The fundusoscopic appearance of the MGDA includes 3 primary features: an enlarged, funnel-shaped excavation in the optic disc; an annulus of chorioretinal pigmentary changes that surrounds the optic disc excavation; and a central glial tuft overlying the optic disc.³ A radial orientation of unusually straight and narrow retinal blood vessels emerging from the periphery of the abnormal disc is an additional diagnostic feature.⁴ MGDA has been reported to be associated with other ocular anomalies and numerous intracranial abnormalities including midline craniofacial and skull base defects, vascular abnormalities, and cerebral malformations.^{1,3,5-14}

Establishing the correct diagnosis of MGDA guides appropriate ophthalmic management and should also prompt a search for associated intracranial abnormalities.⁴ Although the diagnosis of MGDA is typically made clinically, imaging may provide added

value in several ways. First, when the clinical picture is not definitive, identification of specific features on imaging may serve to establish the diagnosis and reveal the extent and character of associated ocular abnormalities. For example, confusion often arises in distinguishing MGDA from optic nerve coloboma clinically. This distinction is important because of the implications for genetics and family counseling; MGDA is almost universally a sporadic condition whereas optic nerve coloboma is commonly familial and may occur in association with multisystem congenital malformation syndromes.^{7,15,16} Second, cross-sectional imaging allows for evaluation of the globe in the setting of associated opacities of the refractive media, including persistent hyperplastic primary vitreous, which may mitigate the capacity to make this diagnosis on the basis of the fundusoscopic examination alone.¹⁷ Finally, these patients may undergo imaging for unrelated clinical issues, and identification of the MGDA at imaging may be the only indicator to search for known associated intracranial abnormalities.

Findings in MGDA at cross-sectional imaging have been reported in several case studies. In particular, several groups have reported a defect in the posterior aspect of the globe, presumed to reflect the optic disc excavation observed clinically.¹⁷⁻¹⁹ Auber and O'Hara³ have expanded this work by identifying fluffy hyperintense tissue on T1-weighted MR images immediately adjacent to the "funnel-shaped" abnormality of the optic disc, a finding that may represent an imaging correlate of the chorioretinal pigmentary disturbance.³ Unfortunately, these previous reports of at

Received December 18, 2012; accepted after revision January 23, 2013.

From the Departments of Radiology (S.E., C.D.R., M.J.P.) and Ophthalmology (G.H.), Children's Hospital Boston and Harvard Medical School, Boston, Massachusetts.

Please address correspondence to Michael J. Paldino, MD, Children's Hospital Boston, 300 Longwood Ave, Boston, MA 02115; e-mail: Michael.paldino@gmail.com

<http://dx.doi.org/10.3174/ajnr.A3542>

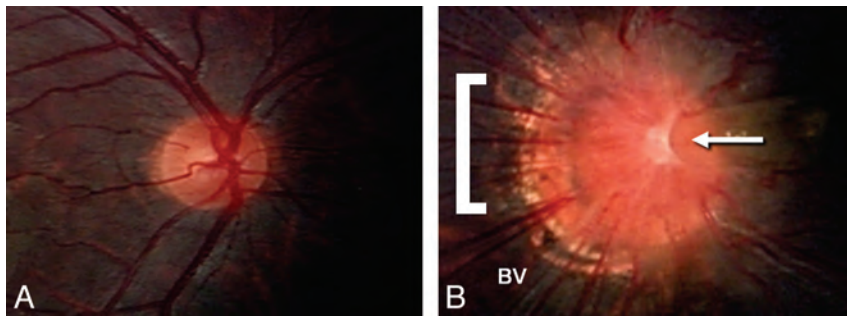


FIG 1. Fundus photos illustrating normal right optic nerve (A) and morning glory optic nerve anomaly (B). Note the larger overall size, central glial tuft (arrow), halo of pigmentary changes surrounding the nerve (bracket), and the radial orientation of the blood vessels (BV) emanating from the anomalous optic nerve.

most 2 patients make it difficult to determine the consistency with which individual findings occur in this clinical setting. Furthermore, in our experience, the orbital findings of MGDA at high-quality imaging are not only highly characteristic for this entity but are also of greater breadth than what has been previously reported. The goal of our study was to characterize the spectrum and frequency of orbital findings in a series of patients with MGDA by using MR imaging and to explore the pathogenesis of this optic nerve anomaly on the basis of these radiographic features.

CASE SERIES

Patients

This study was compliant with the Health Insurance Portability and Accountability Act and was approved by the local institutional review board. Patients were identified retrospectively from a search of existing patient data. Inclusion in this study was based on the following criteria: 1) pediatric age group (≤ 18 years); 2) confirmed diagnosis of MGDA, based on ophthalmologic examination; and 3) an MR imaging examination of the brain and orbits. A total of 6 patients (age range, 8 months–2 years; 3 boys, 3 girls) with a diagnosis of MGDA at funduscopic examination (Fig 1) comprised the final study group.

MR Imaging

Patients underwent MR imaging with a 3T Tim Trio MR scanner (Siemens, Erlangen, Germany) or a 1.5T Signa TwinSpeed MR scanner (GE Healthcare, Milwaukee, Wisconsin). Representative imaging protocols are as follows:

3T system: 1) Sagittal magnetization-prepared rapid acquisition of gradient echo of the brain (TR, 2530 ms; TE, 3.39 ms; number of acquisitions, 1; flip angle, 7° ; TI, 1450 ms; FOV, 22 cm; acceleration factor, 2; voxel size, $1 \times 1 \times 1$ mm). 2) Axial FSE T2-weighted imaging of the brain (TR, 11,730 ms; TE, 89 ms; number of acquisitions, 2; flip angle, 120° ; FOV, 20 cm; acceleration factor, 2; voxel size, $0.6 \times 0.4 \times 2.5$ mm). 3) Axial FLAIR imaging of the brain (TR, 9000 ms; TE, 137 ms; TI, 2500 ms; number of acquisitions, 1; flip angle, 150° ; FOV, 20 cm; acceleration factor, 2; voxel size, $0.6 \times 0.6 \times 4$ mm). 4) Axial and coronal high-resolution fat-saturated T2WI of the orbits (TR, 6000 ms; TE, 94 ms; number of acquisitions, 3; flip angle, 120° ; FOV, 16 cm; acceleration factor, 2; voxel size, $0.6 \times 0.4 \times 2$ mm). 5) Axial and coronal high-resolution T1WI (TR, 605 ms; TE, 10 ms; number of

acquisitions, 2; flip angle, 90° ; FOV, 16 cm; voxel size, $0.4 \times 0.3 \times 2$ mm).

1.5T system: 1) Sagittal T1WI of the brain (TR, 459 ms; TE, 10 ms; number of acquisitions, 2; flip angle, 90° ; FOV, 16 cm; voxel size, $0.7 \times 0.6 \times 4$ mm). 2) Axial FSE T2WI of the brain (TR, 4050 ms; TE, 102 ms; FOV, 20 cm; voxel size, $0.6 \times 0.4 \times 4$ mm). 3) Axial FLAIR imaging of the brain (TR, 10,000 ms; TE, 160 ms; TI, 2200 ms; FOV, 20 cm; voxel size, $0.6 \times 0.4 \times 2.5$ mm). 4) Axial and coronal high-resolution fat-saturated T2WI (TR, 5230 ms; TE, 118 ms; number of acquisitions, 3; flip angle, 150° ; FOV, 16 cm; acceleration factor, 2; voxel size, $0.5 \times 0.4 \times 3$ mm). 5) Axial and coronal T1WI (TR, 400 ms; TE, 10 ms; number of acquisitions, 2; flip angle, 90° ; FOV, 16 cm; voxel size, $0.6 \times 0.6 \times 3$ mm).

All images were acquired with standard phased array coils: a 32-channel head coil for 3T and an 18-channel head-and-spine coil for 1.5T.

Image Review and Analysis

All imaging examinations were reviewed by 2 pediatric neuroradiologists (M.J.P. and S.E.), each with a minimum of 5 years of dedicated subspecialty experience in neuroradiology. Specifically, the presence or absence of the following orbital findings was evaluated and tabulated: 1) funnel-shaped morphologic pattern of the optic disc; 2) elevation of the adjacent retinal surface; 3) dehiscence and abnormal morphologic features of the uveoscleral coat at the optic nerve insertion, manifest as discontinuity of the normal ring of T2 hypointensity (and enhancement) that reflects the sclera, choroid, and lamina cribrosa²⁰; 4) abnormal tissue associated with the distal intraorbital segment of the optic nerve (ipsilateral to the MGDA); 5) effacement of the subarachnoid spaces of the distal optic nerve sheath (ipsilateral to the MGDA) resulting from this abnormal tissue; 6) fat within the distal optic nerve sheath; 7) enhancement within the distal optic nerve; and 8) size of the globe. Associated intracranial findings were also noted, with particular attention to the following features: 1) skull base abnormalities, including cephaloceles; 2) evidence of Moyamoya disease; 3) callosal dysgenesis; and 4) midline facial defects.^{5-7,11,13,18,21,22}

Imaging Findings

Orbital Findings. Although most patients had unilateral retinal abnormalities at funduscopy ($n=5$), 1 patient was diagnosed with bilateral MGDA. MR imaging results demonstrated a funnel-shaped morphologic pattern of the optic disc with elevation of the adjacent retinal surface in all patients (Fig 2A). This elevated region demonstrated hyperintensity in all patients on the T1WI (Fig 2B). Also observed in all patients was abnormal tissue associated with the distal intraorbital segment of the ipsilateral optic nerve; this tissue was associated with effacement of the subarachnoid spaces (Fig 2A). Posterior discontinuity of the uveoscleral coat

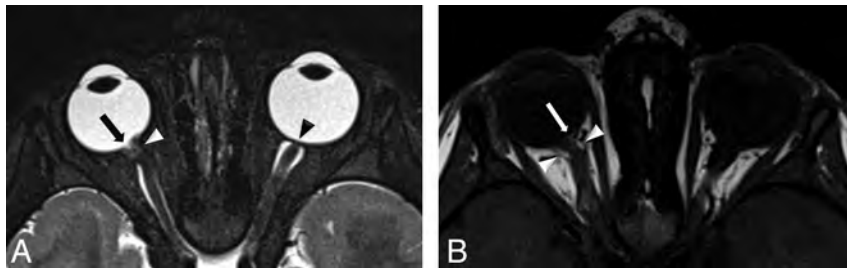


FIG 2. A, Axial fat-saturated T2WI through the orbits of a patient with right MGDA demonstrates a funnel-shaped morphologic pattern of the optic disc (*white arrow*) with elevation of the adjacent retinal surface. This image also demonstrates abnormal tissue associated with the distal intraorbital segment of the ipsilateral optic nerve and effacement of the subarachnoid space at that level (*white arrowheads*). Also note discontinuity of the uveoscleral coat at the optic nerve insertion (compare with normal left globe where the curvilinear hypointensity of the uveoscleral coat is continuous across the lamina cribrosa; *black arrowhead*). B, Axial T1WI demonstrates hyperintensity within the elevated region of the retina (*white arrow*) as well as fat within the distal optic nerve sheath (*white arrowheads*).

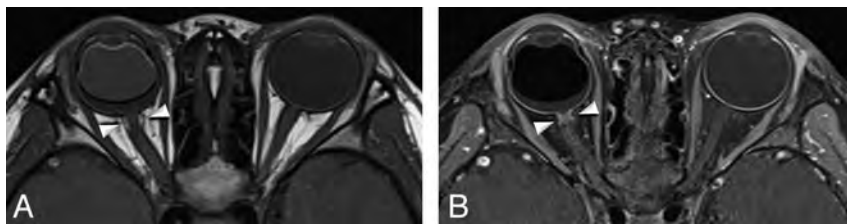


FIG 3. A, Axial T1WI through the orbits of a different patient with right-sided MGDA again demonstrates fat within the distal optic nerve sheath (*white arrowheads*). B, Axial gadolinium-enhanced fat-saturated T1WI through the orbits in the same patient demonstrates enhancement in the region of the distal optic nerve (*white arrowheads*), which is thought to represent displaced choroidal tissue, perhaps in concert with glial, fibrous, and pigment epithelial proliferation. Careful inspection and cross-correlation established the locale of enhancement to be immediately internal to the fat in the optic nerve sheath. Of note, the fat within the nerve sheath is saturated on this sequence, confirming its identity. These images also demonstrate an associated retinal detachment; the patient is status post a scleral banding procedure.

across the lamina cribrosa was also observed in all patients (Fig 2A). In a similar fashion, in patients who received gadolinium, there was discontinuity of the posterior choroidal–lamina cribrosa enhancement. These findings were not observed in any of the contralateral unaffected globes of the study patients (excluding the patient with bilateral MGDA). Less consistent orbital findings included the following features: 1) fatty infiltration of the distal optic nerve sheath ($n=3$; Fig 3A), 2) enhancement within the distal aspect of the optic nerve ($n=2$; Fig 3B), 3) small size of the globe containing the MGDA ($n=2$), and 4) retinal detachment ($n=1$) (Table).

Extraorbital Findings. Enlargement of the prechiasmatic segment of the ipsilateral optic nerve, consistent with optic nerve glioma, was observed in 1 patient. Asymmetry of the optic chiasm, abnormally small contralateral to the MGDA, was observed in 1 patient. One patient had evidence of internal carotid steno-occlusive vasculopathy with collaterals, consistent with Moyamoya disease. Finally, persistence of the craniopharyngeal canal was observed in 1 patient; in this case, there was mildly anomalous positioning of the pituitary gland within the proximal aspect of the canal. No evidence of midline facial defects, callosal dysgenesis, or basal cephaloceles was identified in the study population (Table).

DISCUSSION

Here we report the MR imaging findings in 6 patients with MGDA confirmed by funduscopic examination. Consistent orbital findings included the following features: 1) funnel-shaped morphologic pattern of the optic disc associated with elevation of the adjacent retinal margins, 2) abnormal tissue associated with the distal intraorbital segment of the ipsilateral (to the MGDA) optic nerve, 3) effacement of the regional subarachnoid spaces on the basis of this soft tissue, and 4) discontinuity of the normal uveoscleral coat at the optic nerve insertion. This constellation of findings has not been reported in other ocular abnormalities and may serve to establish the radiologic diagnosis of MGDA.

Our observations are consistent with the few previous imaging studies of MGDA. Hu¹⁷ reported protrusion of the vitreous through a defect in the posterior wall of the globe by using CT in 6 patients with MGDA and forebrain defects. Several studies have also used MR imaging to describe MGDA. Görbe et al¹⁸ reported a posterior excavation of the optic disc in 1 patient with MGDA associated with multiple cerebral malformations; in a similar fashion, Tonami et al¹⁹ reported a “colobomatous area” in the region of the optic disc associated with retinal detachment in 1 patient

with morning glory syndrome. Auber and O’Hara³ described intraorbital but extraocular findings in a report of 2 patients. In addition to an enlarged, funnel-shaped optic disc with overlying fluffy T1 hyperintense material, they observed enhancement at the distal aspect of the optic nerve in a very similar configuration to that observed in 2 of our patients. Of interest, this study also demonstrated an abnormal aggregate of fat within the optic nerve of 1 patient. In contradistinction to our observations, however, this fat was remote from the optic disc and was not clearly confined to the nerve sheath. Our observations broaden the constellation of ocular findings of the MGDA and, furthermore, establish a set of consistent and characteristic orbital imaging findings for this entity. It is worth noting that, although a detailed description of the MR imaging findings in optic nerve coloboma is beyond the scope of our methodology, retinal elevation, soft tissue in the distal aspect of the optic nerve, and optic nerve sheath fat have not been reported in association with this entity.^{23,24}

The embryologic basis for the development of MGDA has yet to be elucidated. In the minority of patients, MGDA may occur in association with midline facial defects, callosal dysgenesis, and basal encephalocele. On the basis of the overlapping critical periods of development for the frontonasal process, midfacial structures, and primordium of the eyes, this so-called morning glory

Patient characteristics and imaging findings in MGDA

Pt No.	Age (y)	Sex	Side	Funnel-Shaped Optic Disc	Retinal Elevation	Optic Nerve Soft Tissue	Uveoscleral Discontinuity	Nerve Sheath		Associated Abnormalities
								Fat	Enhancement	
1	2	M	R	Present	Present	Present	Present	Present	Present	Retinal detachment
2	1	F	L	Present	Present	Present	Present	Present	Absent	Small chiasm contralateral to MGDA
3	2	M	R	Present	Present	Present	Present	Absent	Absent	Persistent craniopharyngeal canal
4	0.67	F	B	Present	Present	Present	Present	Absent	Present	Moyamoya disease
5	1	M	L	Present	Present	Present	Present	Absent	Absent	N/A
6	1	F	L	Present	Present	Present	Present	Present	Absent	N/A

Note:—N/A indicates not applicable; R, right; L, left; B, bilateral.

syndrome is believed to emerge from a single insult occurring during induction of the forebrain. However, the nature of the embryologic defect that leads to the MGDA itself remains the subject of debate. Superficial similarities initially prompted consideration of MGDA as a part of the optic nerve coloboma spectrum, a disorder that results from incomplete closure of the embryonic fissure. However, most now consider MGDA to be a distinct entity that develops as a result of combined dysgenesis of both ectodermal and mesodermal elements.² On the basis of histopathologic analyses, it has been hypothesized that MGDA results from a defect in the maturation of the posterior sclera that results in a failure of normal fusion and allows the optic disc, lamina cribrosa, peripapillary retina, and choroid to herniate posteriorly.^{25,26} Also observed in these studies has been a marked lack of mature differentiation of the sclera, with the outer surface being replaced by disorganized spindle cells arranged in a coarse reticular form resembling that of embryonic mesenchyme.^{25,26} The optic nerve sheath may demonstrate similar findings and, in addition, contained localized aggregations of fat with a loose areolar appearance.^{25,26}

This theory, along with previously published pathologic images, closely parallels and informs our observed MR imaging findings. According to this theory, the consistently observed dehiscence of the posterior uveoscleral coat may, in fact, represent the primary abnormality of the MGDA. The abnormal tissue we observed at the distal optic nerve may then reflect evagination of the choroid and peripapillary retina into the perineural space with associated effacement of CSF. Enhancement in this region is presumably related to the displaced choroidal tissue, perhaps in concert with glial, fibrous, and pigment epithelial proliferation.^{25,26} The observed retinal depression, therefore, likely represents a “false physiologic pit, formed by the coapted internal surface of the prolapsed retina”.²⁵ Finally, elevation of the adjacent optic disc margins may result from some combination of retinal folding and redundancy; thickening of the retina because of pseudofibrotic metaplastic retinal pigment epithelium; and/or an annular glial mass overlying the scleral dehiscence, all of which have been observed histologically.^{25,26} Each of these findings could potentially demonstrate T1 hyperintensity and may therefore account for the observed signal intensity of this elevation in our study.³ Of note, imaging in 3 of our patients demonstrated fat within the distal optic nerve sheath, also consistent with previous histopathologic studies.^{25,26}

MGDA has been reported to be associated with a broad range of cranial abnormalities. Ocular associations are particularly numerous and include retinal detachment, persistent hyperplastic primary vitreous, congenital cataract, nanophthalmos, eyelid

hemangioma, drusen, and preretinal gliosis.^{2,8,21,27} Of these, we observed retinal detachment in 1 patient. Abnormal communication between the subretinal, subarachnoid, and vitreous spaces in MGDA may account for this frequent association.^{21,28} Abnormalities of the visual pathways have also been reported in MGDA, including atrophy/hypoplasia of the contralateral optic chiasm as well as optic nerve glioma.^{3,29} In our cohort, we observed each of these findings in 1 patient. The optic chiasm atrophy/hypoplasia in MGDA could result either from retrograde axonal degeneration in the setting of an intracranial lesion or from antegrade degeneration related to the ganglion cell deficit within the developing retina.⁸ The relationship between MGDA and optic nerve glioma remains largely unexplored.

MGDA is associated with intracranial vascular abnormalities, which range from static segmental aplasia of the circle of Willis to a progressive vasculopathy (Moyamoya disease), in up to 45% of patients.^{5,9,11-13,22} Indeed, one of our patients demonstrated the characteristic findings of Moyamoya, including steno-occlusive changes of the anterior circulation and extensive lenticulostriate collateralization. The association of MGDA with vascular abnormalities has been proposed to reflect the fact that, during the fourth week of gestation, the internal carotid arteries develop in close relationship to the optic vesicles.³⁰ However, the exact relationship between these 2 systems in patients with MGDA, particularly in the setting of a progressive disease such as Moyamoya disease, has yet to be elucidated. There has been at least 1 report suggesting that the coexistence of hemangioma, MGDA, and intracranial vascular abnormalities may reflect a manifestation of PHACES association.³¹

MGDA has also been associated with skull base abnormalities, including basal cephaloceles.^{1,13} It has been proposed that the incomplete fusion of the palates abrogates normal development of the optic nerves, potentially by drawing them into the defect.³² Although no cephaloceles were detected in our cohort, we observed in 1 patient a patent craniopharyngeal canal with herniation of the pituitary gland into its proximal aspect. The posterior pituitary bright spot was present, and the patient’s endocrine function was intact. The absence of a consistent association in our study sheds doubt on a causal relationship between skull base abnormalities and development of the MGDA.

CONCLUSIONS

We have demonstrated several consistent orbital features of MGDA with MR imaging in the largest series to date. These findings may allow for accurate differentiation from other optic nerve and associated ocular anomalies and have the potential to guide

appropriate management of this patient population, especially in situations where funduscopy examination is limited.

Disclosures: Caroline D. Robson—UNRELATED: Consultancy, Royalties: Amirsys, Comments: Content author and editor. Gena Heidary—UNRELATED: Grants/Grants Pending: Knights Templar Eye Foundation; Payment for Lectures (including service on speaker bureaus): I received honoraria from the Lancaster Course held at Colby College, where I teach a session on pediatric neuro-ophthalmology every year. I have been participating in the course for the past 3 years. I also, in 2011, taught a boards review course through the Osler Institute. The institute provided me with an honorarium for my time teaching the residents. Finally, I received an honorarium for speaking at St. Anne's Hospital on neuro-ophthalmic emergencies. Michael J. Paldino—UNRELATED: Grants/Grants Pending: Foundation of the American Society of Neuroradiology.* *Money paid to institution.

REFERENCES

1. Quah BL, Hamilton J, Blaser S, et al. **Morning glory disc anomaly, midline cranial defects and abnormal carotid circulation: an association worth looking for.** *Pediatr Radiol* 2005;35:525–28
2. Kindler P. **Morning glory syndrome: unusual congenital optic disk anomaly.** *Am J Ophthalmol* 1970;69:376–84
3. Auber AE, O'Hara M. **Morning glory syndrome. MR imaging.** *Clin Imaging* 1999;23:152–58
4. Lee BJ, Traboulsi EI. **Update on the morning glory disc anomaly.** *Ophthalmic Genet* 2008;29:47–52
5. Bakri SJ, Siker D, Masaryk T, et al. **Ocular malformations, Moyamoya disease, and midline cranial defects: a distinct syndrome.** *Am J Ophthalmol* 1999;127:356–57
6. Brodsky MC, Hoyt WF, Hoyt CS, et al. **Atypical retinohoroidal coloboma in patients with dysplastic optic discs and transsphenoidal encephalocele.** *Arch Ophthalmol* 1995;113:624–28
7. Eustis HS, Sanders MR, Zimmerman T. **Morning glory syndrome in children. Association with endocrine and central nervous system anomalies.** *Arch Ophthalmol* 1994;112:204–07
8. Steinkuller PG. **The morning glory disk anomaly: case report and literature review.** *J Pediatr Ophthalmol Strab* 1980;17:81–87
9. Krishnan C, Roy A, Traboulsi E. **Morning glory disk anomaly, choroidal coloboma, and congenital constrictive malformations of the internal carotid arteries (Moyamoya disease).** *Ophthalmic Genet* 2000;21:21–24
10. Lit ES, D'Amico DJ. **Retinal manifestations of morning glory disc syndrome.** *Int Ophthalmol Clin* 2001;41:131–38
11. Hanson MR, Price RL, Rothner AD, et al. **Developmental anomalies of the optic disc and carotid circulation. A new association.** *J Clin Neuroophthalmol* 1985;5:3–8
12. Massaro M, Thorarensen O, Liu GT, et al. **Morning glory disc anomaly and Moyamoya vessels.** *Arch Ophthalmol* 1998;116:253–54
13. Komiyama M, Yasui T, Sakamoto H, et al. **Basal meningoencephalocele, anomaly of optic disc and panhypopituitarism in association with Moyamoya disease.** *Pediatr Neurosurg* 2000;33:100–04
14. Morioka M, Marubayashi T, Masumitsu T, et al. **Basal encephaloceles with morning glory syndrome, and progressive hormonal and visual disturbances: case report and review of the literature.** *Brain Dev* 1995;17:196–201
15. Mafee MF, Jampol LM, Langer BG, et al. **Computed tomography of optic nerve colobomas, morning glory anomaly, and colobomatous cyst.** *Radiol Clin North Am* 1987;25:693–99
16. Traboulsi EI. **Morning glory disc anomaly or optic disc coloboma?** *Arch Ophthalmol* 1994;112:153
17. Hu J. **The clinical characteristics and imaging findings of morning glory syndrome.** *J Huazhong Univ Sci Technol Med Sci* 2008;28:465–68
18. Görbe E, Vamos R, Rudas G, et al. **Neuronal migration disorders, agenesis of corpus callosum, preauricular skin tag and bilateral morning glory syndrome in a term newborn infant.** *Clin Dysmorphol* 2008;17:123–25
19. Tonami H, Nakagawa T, Yamamoto I, et al. **MR imaging of morning glory syndrome.** *J Comput Assist Tomogr* 1987;11:529–30
20. Sadun AA, Carelli V, Bose S, et al. **First application of extremely high-resolution magnetic resonance imaging to study microscopic features of normal and LHON human optic nerve.** *Ophthalmology* 2002;109:1085–91
21. Bartz-Schmidt KU, Heimann K. **Pathogenesis of retinal detachment associated with morning glory disc.** *Int Ophthalmol* 1995;19:35–38
22. Lenhart PD, Lambert SR, Newman NJ, et al. **Intracranial vascular anomalies in patients with morning glory disk anomaly.** *Am J Ophthalmol* 2006;142:644–50
23. Pyhtinen J, Lindholm EL. **Imaging in optic nerve coloboma.** *Neuroradiology* 1996;38:171–74
24. Yagev R, Monos T, Shoham A, et al. **Microphthalmos and optic disc coloboma associated with a retrobulbar cyst.** *J AAPOS* 2000;4:381–82
25. Pedler C. **Unusual coloboma of the optic nerve entrance.** *Br J Ophthalmol* 1961;45:803–07
26. Manschot WA. **Morning glory syndrome: a histopathological study.** *Br J Ophthalmol* 1990;74:56–58
27. Chaudhuri Z, Grover AK, Bageja S, et al. **Morning glory anomaly with bilateral choroidal colobomas in a patient with Goldenhar's syndrome.** *J Pediatr Ophthalmol Strab* 2007;44:187–89
28. Coll GE, Chang S, Flynn TE, et al. **Communication between the subretinal space and the vitreous cavity in the morning glory syndrome.** *Graefes Arch Clin Exp Ophthalmol* 1995;233:441–43
29. Giampietro PF, Babu D, Koehn MA, et al. **New syndrome: focal dermal hypoplasia, morning glory anomaly, and polymicrogyria.** *Am J Med Genet A* 2004;124A:202–08
30. Dempster AG, Lee WR, Forrester JV, et al. **The 'morning glory syndrome' — a mesodermal defect?** *Ophthalmologica* 1983;187:222–30
31. Puvanachandra N, Heran MK, Lyons CJ. **Morning glory disk anomaly with ipsilateral capillary hemangioma, agenesis of the internal carotid artery, and Horner syndrome: a variant of PHACES syndrome?** *J AAPOS* 2008;12:528–30
32. Itakura T, Miyamoto K, Uematsu Y, et al. **Bilateral morning glory syndrome associated with sphenoid encephalocele. Case report.** *J Neurosurg* 1992;77:949–51

Early White Matter Changes in Childhood Multiple Sclerosis: A Diffusion Tensor Imaging Study

A. Blaschek, D. Keeser, S. Müller, I.K. Koerte, A. Sebastian Schröder, W. Müller-Felber, F. Heinen, and B. Ertl-Wagner



ABSTRACT

BACKGROUND AND PURPOSE: Loss of integrity in nonlesional white matter occurs as a fundamental feature of multiple sclerosis in adults. The purpose of our study was to evaluate DTI-derived measures of white matter microstructure in children with MS compared with age- and sex-matched controls by using tract-based spatial statistics.

MATERIALS AND METHODS: Fourteen consecutive pediatric patients with MS (11 female/3 male; mean age, 15.1 ± 1.6 years; age range, 12–17 years) and age- and sex-matched healthy subjects (11 female/3 male; mean age, 14.8 ± 1.7 years) were included in the study. After we obtained DTI sequences, data processing was performed by using tract-based spatial statistics.

RESULTS: Compared with healthy age- and sex-matched controls, children with multiple sclerosis showed a global decrease in mean fractional anisotropy ($P \leq .001$), with a concomitant increase in mean ($P < .001$), radial ($P < .05$), and axial diffusivity ($P < .001$). The most pronounced fractional anisotropy value decrease in patients with MS was found in the splenium of the corpus callosum ($P < .001$). An additional decrease in fractional anisotropy was identified in the right temporal and right and left parietal regions ($P < .001$). Fractional anisotropy of the white matter skeleton was related to disease duration and may, therefore, serve as a diagnostic marker.

CONCLUSIONS: The microstructure of white matter is altered early in the disease course in childhood multiple sclerosis.

ABBREVIATIONS: AD = axial diffusivity; FA = fractional anisotropy; MD = mean diffusivity; RD = radial diffusivity; TBSS = tract-based spatial statistics

MS most commonly occurs in adults in their late 20s and 30s, but early onset in childhood and adolescence is increasingly being diagnosed, with up to 10% of MS cases manifesting before adulthood. Conventional MR imaging has become an essential part of diagnostic decision making in MS. On MR imaging, children tend to have fewer white matter lesions and less enhance-

ment with gadolinium-based contrast agents.¹ Lesion load has been shown to correlate moderately with clinical outcome in longitudinal studies in children and adults.²

In addition to the above-mentioned localized lesions, white matter microstructure is known to be altered in the macroscopically normal-appearing white matter.³ Advanced MR imaging techniques such as DTI allow the evaluation of the microstructure of the cerebral white matter by detecting subtle changes in the magnitude and direction of water diffusion. White matter damage is mainly reflected by a decrease in fractional anisotropy (FA) and an increase in mean diffusivity (MD). MD consists of axial diffusivity (AD) and radial diffusivity (RD), measuring diffusivity parallel and perpendicular to the main axis of white matter tracts, respectively.⁴ Both parameters are purported to indicate myelin and axonal injury.⁵ Recently, DTI studies in adult patients with MS demonstrated axonal and myelin injury occurring much earlier in the course of the disease than previously assumed.^{6,7}

Physiologic myelination is known to expand well into early adulthood in conjunction with cognitive, behavioral, emotional, and motor development.⁸⁻¹⁰ Any pathology interfering with this process of myelination is likely to affect white matter integrity as has been shown in hypoxic-ischemic encephalopathy, former premature in-

Received November 15, 2012; accepted after revision January 3, 2013.

From the Department of Pediatric Neurology and Developmental Medicine (A.B., A.S.S., W.M.-F., F.H.), Hauner Children's Hospital, Ludwig-Maximilian-University, Munich, Germany; Department of Psychiatry and Psychotherapy (D.K.) and Institute for Clinical Radiology (D.K., S.M., I.K.K., B.E.-W.), Ludwig-Maximilian University, Munich, Germany; and Psychiatry Neuroimaging Laboratory (I.K.K.), Brigham and Women's Hospital, Harvard Medical School, Boston, Massachusetts.

A. Blaschek and D. Keeser contributed equally to the manuscript. F. Heinen and B. Ertl-Wagner shared senior authorship.

This work was supported by a research grant from Merck Serono. Inga Koerte was supported by the Else Kröner-Fresenius Stiftung, Bad Homburg, Germany.

Please address correspondence to Astrid Blaschek, MD, Department of Pediatric Neurology and Developmental Medicine, Hauner Children's Hospital, Ludwig-Maximilian-University Munich, Lindwurmstraße 4, 80337 Munich, Germany; e-mail: astrid.blaschek@med.uni-muenchen.de



Indicates article with supplemental on-line tables.



Indicates article with supplemental on-line figure.



Evidence-Based Medicine Level 2.

<http://dx.doi.org/10.3174/ajnr.A3581>

fants, and normal-pressure hydrocephalus.¹¹ The onset of childhood MS occurs within this vulnerable period of central nervous system maturation. To date, only a few MR imaging studies have investigated white matter microstructure in children with MS. These studies demonstrated decreased FA¹² or slightly increased mean diffusivity¹³ in the macroscopically unaffected white matter by using either summary measures of the entire brain or a region-of-interest approach. Most recently, a study assessing major white matter tracts in children with MS compared with children with a single demyelinating event showed a decrease in FA with a concomitant increase in MD in patients with MS only.^{14,15}

Tract-based spatial statistics (TBSS) allows a coregistration of likely white matter tracts to analyze multisubject diffusion tensor data. For this purpose, subject data are projected on a mean FA skeleton, which refers to the center of all tracts common to both groups, before applying voxelwise between-group comparisons.¹⁶ This technique permits an observer-independent voxelwise analysis of the main white matter tracts with a sensitivity to intergroup differences, considering less across-subject FA variability.¹⁶

The aim of our study was to evaluate DTI-derived measures of white matter microstructure in children with MS compared with age- and sex-matched controls by using TBSS.

MATERIALS AND METHODS

Subjects

This study was approved by the local institutional review board. Oral and written informed consent was obtained from all participants and their legal guardians.

Fourteen consecutive pediatric patients with MS (11 female/3 male; mean age, 15.1 ± 1.6 years; age range, 12–17 years) were included in the study. Inclusion criteria were an age younger than 18 years and a definite diagnosis of MS with a relapsing–remitting course. Exclusion criteria consisted of MR imaging–related contraindications (eg, cardiac pacemakers, ferromagnetic implants, or claustrophobia). All patients were clinically evaluated on the basis of the Kurtzke Expanded Disability Status Scale.

MR imaging of age- and sex-matched healthy subjects (11 female/3 male; mean age, 14.8 ± 1.7 years) was included from a local data base of healthy volunteers; all volunteers had been imaged with the identical MR imaging protocol on the same MR imaging scanner (Magnetom Verio; Siemens, Erlangen, Germany). All volunteers underwent MR imaging for scientific purposes only. Inclusion criteria were an age match to a patient included in the MS cohort of ± 6 months and a sex match to the respective patient. Exclusion criteria were any history of chronic or ongoing medical conditions, intake of medication, a history of traumatic brain injury (including mild traumatic brain injury), a history of headache disorders, a history of learning disorders, any history of other neurologic or psychiatric disorders, and structural brain abnormalities on conventional MR imaging sequences.

Clinical Tests

As part of the clinical work-up, selected elements of standardized tests were available for 13 of the 14 patients. Two parts of the Multiple Sclerosis Functional Composite score were administered: the right- and left-hand Nine-Hole Peg Test, to measure upper extremity fine motor skills, and the Timed 25-Foot Walk

Test, to assess the lower extremities. All values were compared with normative data.^{17,18} All clinical scores were converted to *z* scores. The *z* score indicates the deviation from the mean population score. A *z* score lying outside the 95% normal distribution is considered abnormal. Screening of cognitive function was performed with 2 subtests of widely used cognitive tests in 11 patients: the Trail-Making Test (subtests A and B)¹⁹ and the German Leistungsprüfungssystem (subtest 5) for verbal fluency.²⁰ All raw values were age-corrected for each patient according to Helmstaedter et al,²¹ to receive an age-independent measure.

MR Imaging Acquisition

MR imaging of the brain was performed on a 3T scanner (Magnetom Verio; Siemens Healthcare, Erlangen, Germany) by using a 12-element phased-array head coil for both the patient cohort and the healthy control subjects. The following structural sequences were acquired for all subjects: 3D magnetization-prepared rapid acquisition of gradient echo: TR, 11 ms; TE, 4.76 ms; FOV, 250 mm; voxel size, $1 \times 1 \times 1$ mm³; iPAT (Siemens syngo software) acceleration factor, 2; sagittal sections covering the entire brain, 160; and FLAIR: TR, 94 ms; TE, 7000 ms; FOV, 220 mm; voxel size, $0.9 \times 0.9 \times 3$ mm³; distance factor, 10%; fat saturation; axial sections, covering the entire brain, 45. A DTI sequence with 20 independent diffusion directions and 3 averages was applied with the following parameters: *b*=0 and 1000 s/mm²; matrix size, 128×128 mm²; FOV, 230×230 mm². The resulting voxel size was $1.8 \times 1.8 \times 4.0$ mm³. Thirty-six transverse sections were acquired.

Image Analysis and Postprocessing

Evaluation of Lesions. All structural sequences were visually assessed and graded by a board-certified neuroradiologist with >10 years' experience in MR imaging of the brain.

DTI Analysis. Image data processing was performed by using the TBSS approach implemented in FMRIB Software Library 4.19 (FSL; <http://www.fmrib.ox.ac.uk/fsl>). Images were corrected for eddy currents due to changing gradient fields and head motion.²² Brain masks were created by using the Brain Extraction Tool in FSL.²² FA and mean, axial, and radial diffusivity were calculated for each voxel. FA data of all subjects were aligned to a common space by using the FMRIB58 FA standard space with nonlinear registration.¹⁶ A mean FA image and a mean FA skeleton were created, which corresponded to the centers of all tracts common to the group (On-line Fig 1). The white matter skeleton is, therefore, a representation of white matter tract geometry, and fiber bundle centers are represented in the mean skeleton. The threshold of the mean FA skeleton white matter mask (shown as a green underlay) was set to an FA value between 0.2 and 0.8 to exclude voxels that consisted of gray matter or CSF. The voxel size was set to $1 \times 1 \times 1$ mm Montreal Neurological Institute space. The obtained binary skeleton mask determined all subsequent processing steps.

FA values of each subject were then projected onto the mean FA skeleton. A voxelwise cross-subject statistical analysis was performed to identify FA differences between patients and healthy control subjects. Group differences were determined by using Randomize, Version 2.9 (The Mathworks, Natick, Massachusetts) (permutation-based nonparametric testing, 5000 permuta-

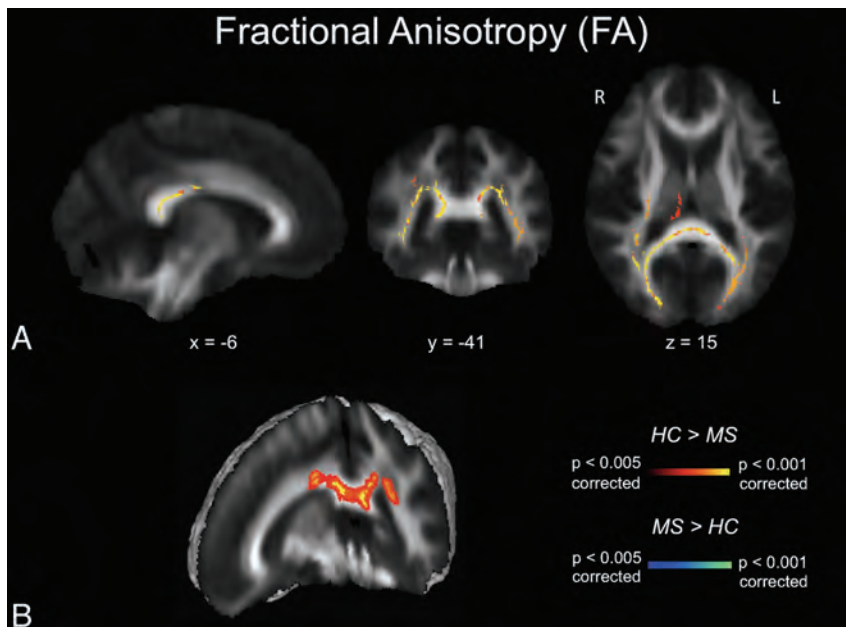


FIG 1. FA maps. *A*, TBSS FA results for healthy subjects compared with patients with MS. Significant clusters of decreased FA values in patients with MS compared with healthy controls are shown as corresponding *P* values in red-orange (scale ranging from red to yellow for the comparison HC > MS and scale ranging from blue to light blue for the comparison MS > HC) and have been thresholded at $P < .005$ for between-group comparisons (corrected for multiple comparisons). *B*, 3D visualization of significantly ($P < .01$, corrected for multiple comparisons) different white matter clusters between the 2 groups. Note that the results are thickened for visual purposes only. L indicates left; R, right (radiologic convention); HC, healthy controls.

tions).²³ We used threshold-free cluster enhancement to avoid choosing an arbitrary initial cluster-forming threshold. This method provides a voxelwise significance (*P* value) that is corrected for multiple comparisons.²⁴ The *P* values are fully corrected for multiple comparisons across voxels but only for each white matter mask and only as 1-tailed *P* values. Because we used 4 different white matter masks and investigated between-group increases and between-group decreases, a $P < .05$ equaled an adjusted $P < .00625$ [$0.05 / (4 \times 2)$], a P value $< .01$ corresponded to an adjusted $P < .00125$, a $P < .005$ corresponded to an adjusted $P < .000625$, and a $P < .001$ corresponded to an adjusted $P < .000125$. We considered a $P < .05$ statistically significant.

The same procedure was applied to MD, RD, and AD data.

Clinical Correlations

Within the patient group, clinical results were correlated with mean FA values and of 2 ROIs, which displayed the most significant group differences in the TBSS analysis. The defined ROIs had a diameter of 20 mm around the peak voxel on the FA skeleton. For all analyses, *P* values $< .05$ were considered statistically significant.

Statistical Analysis

All clinical scores were calculated as *z* scores. A *z* score lying outside the 95% normal distribution is conventionally considered abnormal.

The Pearson product moment correlation coefficient (*r*) was calculated for the correlation between clinical data and mean individual FA values. Correlations were calculated by using the Statistical Package for the Social Sciences, Version 19 (SPSS, Chicago,

Illinois), and a *P* value $< .05$ was considered statistically significant.

RESULTS

Demographic Data, Disease, and MR Imaging Characteristics

Fourteen consecutive pediatric patients with MS and age- and sex-matched healthy subjects were included in the study (On-line Table 1). Disease duration in patients ranged between 2 and 57 months (median, 16.5 months). Patients had a low level of neurologic impairment measured by the Kurtzke Expanded Disability Status Scale (mean, 0.75 ± 1.2) and the Timed 25-Foot Walk Test (3.73 ± 1.3 seconds), consistent with the relatively short disease duration. Cognitive screening with the Trail-Making Test A (mean, 5.9 ± 0.5), Trail-Making Test B (mean, 5.72 ± 0.6), and the Verbal Fluency test (mean, 4.18 ± 0.6) showed no differences in normative data (*z* scores < 2).²¹ Unusually high completion times (*z* score > 2) were only observed for the Nine-Hole Peg Test (dominant hand mean, 19.5 ± 2.6 seconds; nondominant hand mean, 19.7 ± 1.3 seconds) compared with normative

data.¹⁷ Mean lesion load for all patients was low in supratentorial (3.25 ± 0.96) and infratentorial (2.5 ± 0.76) regions.

Diffusion Parameters in TBSS Analysis

Mean FA values of the white matter skeleton were significantly decreased in patients with MS compared with age- and sex-matched controls ($P < .005$). MD ($P < .001$), RD ($P < .001$), and AD ($P < .05$) values were increased in patients with MS, with changes in RD being more extensive than those in AD. Detailed results of TBSS analysis can be found in On-line Table 2. The most pronounced decrease in FA was found in the splenium of the corpus callosum ($P < .001$) (Fig 1). This result remained stable after excluding 3 patients with lesions within the splenium and surrounding regions ($P < .001$). An additional reduction of FA values was identified in the right temporal and right and left parietal regions (Fig 1A). We did not detect any FA value increase in the patient group compared with the control group.

Diffusivity maps revealed a widespread increase in MD in most white matter tract regions, including the corpus callosum, superior longitudinal fasciculus, fornix, corona radiata, corticospinal tract, and uncinate fasciculus (Fig 2). Of the 2 components contributing to MD, AD increase (Fig 3) was less widespread than RD increase (Fig 4). Neither the anterior or posterior corpus callosum nor the internal capsules exhibited any AD alterations (Fig 3). The anterior internal capsule did not show any RD alterations. We did not detect any significant MD, RD, or AD decreases in the patient group.

Correlation between FA and Clinical Scores

We found a statistically significant correlation between mean skeletal FA and disease duration ($r = -0.57$; $P < .01$), right temporal ($r =$

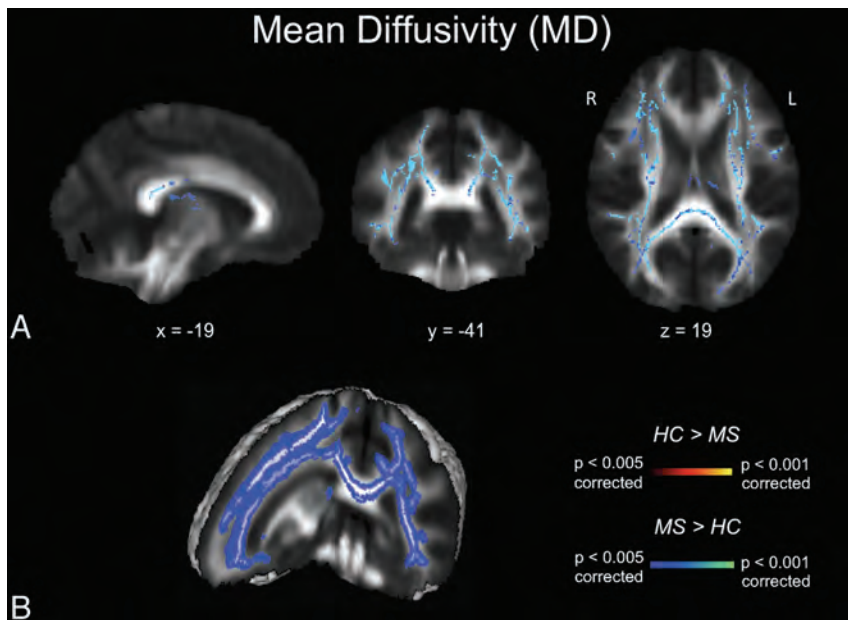


FIG 2. MD maps. A, TBSS MD results for healthy subjects compared with patients with MS. Significant clusters of increased MD values in patients with MS compared with healthy controls are shown as corresponding P values in red-orange (scale ranging from red to yellow for the comparison $HC > MS$ and scale ranging from blue to light blue for the comparison $MS > HC$) and have been thresholded at $P < .005$ for between-group comparisons (corrected for multiple comparisons). B, 3D visualization of significantly ($P < .01$, corrected for multiple comparisons) different white matter clusters between the 2 groups. Note that the results are thickened for visual purposes only. L indicates left; R, right (radiologic convention); HC, healthy controls.

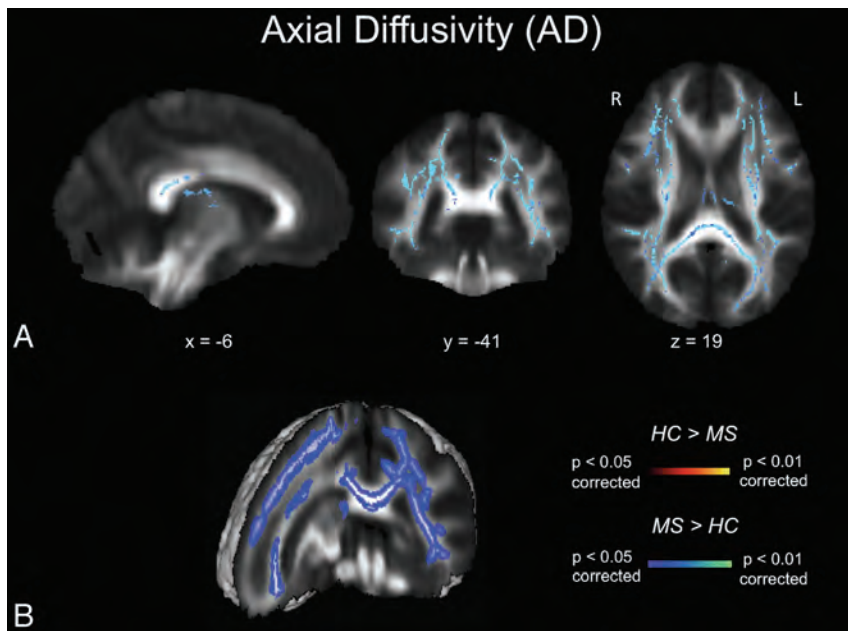


FIG 3. AD maps. A, TBSS AD results for healthy subjects compared with patients with MS. Significant clusters of increased AD values in patients with MS compared with healthy controls are shown as corresponding P values in red-orange (scale ranging from red to yellow for the comparison $HC > MS$ and scale ranging from blue to light blue for the comparison $MS > HC$) and have been thresholded at $P < .05$ for between-group comparisons (corrected for multiple comparisons). B, 3D visualization of significantly ($P < .01$, corrected for multiple comparisons) different white matter clusters between the 2 groups. Note that the results are thickened for visual purposes only. L indicates left; R, right (radiologic convention); HC, healthy controls.

-0.55 ; $P < .05$), and left parietal ($r = -0.54$; $P < .05$) regions. No significant correlations were found for the Kurtzke Expanded Disability Status Scale, annual relapse rate, number of total relapses, lesion load, Nine-Hole Peg Test, Timed 25-Foot Walk Test, or cognitive screening with FA values.

DISCUSSION

We investigated the white matter microstructure in children with MS. TBSS analysis revealed significantly decreased FA values along with a widespread increase in MD, RD, and AD in patients with MS. These findings provide evidence for the influence of MS in nonlesional macroscopically unaffected WM even at an early stage of the disease. Potential causes of these alterations are diverse and include direct disease effects such as axonal injury and demyelination or indirect effects such as protracted or inhibited maturation.

Our findings are in accordance with previously published data on the microstructure of white matter in childhood MS.^{12,13} Two recent studies of Vishwas et al^{14,15} demonstrated higher MD and lower mean FA values in all white matter pathways in pediatric patients with MS compared with controls. However, no changes were observed in 27 patients with a single demyelinating event,¹⁵ from which the authors concluded that there might be a window of opportunity to prevent further damage between the period of a single demyelination and the diagnosis of MS. This is in accordance with the significant negative correlation between mean FA of the white matter skeleton and disease duration that we observed in our study. In adults, conflicting data on the correlation of FA measures with the annual relapse rate, number of total relapses, and lesion load exist. Disease durations of >3 years have been reported to negatively correlate with FA,^{25,26} whereas in clinically isolated syndrome, no correlation was reported.⁶

It has been proposed that global changes in white matter occur to a lesser degree in childhood at the beginning of the disease compared with adult-onset MS.⁶ However, early changes in childhood MS are known to be characterized by pathologic MR imaging findings of gray

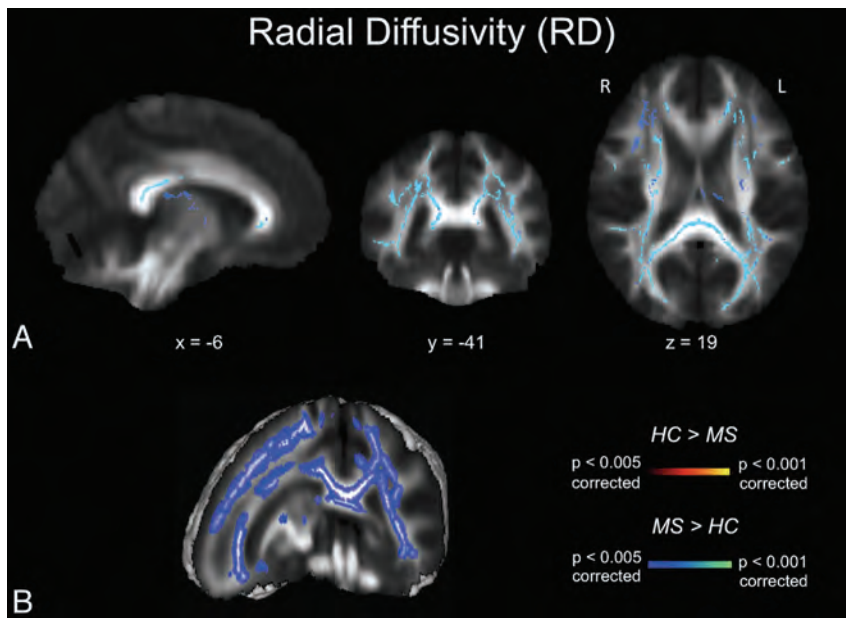


FIG 4. RD maps. A, TBSS RD results for healthy subjects compared with patients with MS. Significant clusters of increased RD values in patients with MS compared with healthy controls are shown as corresponding P values in red-orange (scale ranging from red to yellow for the comparison $HC > MS$ and scale ranging from blue to light blue for the comparison $MS > HC$) and have been thresholded at $P < .005$ for between-group comparisons (corrected for multiple comparisons). B, 3D visualization of significantly ($P < .01$, corrected for multiple comparisons) different white matter clusters between the 2 groups. Note that the results are thickened for visual purposes only. L indicates left; R, right (radiologic convention); HC, healthy controls.

and white matter structures that are generally more subtle compared with MR imaging findings in adult MS.^{12,13,27} This difference may explain why patients with early-onset MS tend to have a longer duration of illness before reaching a state of irreversible disability.²⁸ Considering the fact that myelination continues well into adolescence, it is conceivable that MS may interfere with this process of physiologic myelination in addition to the ongoing demyelination by the disease process itself.^{8,29} Longitudinal assessment might be a useful tool for gaining insight into the dynamics of the disease process, especially because established markers for disease activity such as lesion load correlate only moderately with clinical outcome in longitudinal studies in adults and children.²

The spatial extent and distribution of increase in diffusivity indices (MD/RD/AD) was far more widespread than the decrease in FA values in our patient cohort. Changes in diffusivity parameters are indicators of mainly extracellular diffusion and might be related to axon or myelin damage. Water diffusion in the white matter of the brain is highly sensitive to alterations in the microstructural integrity of cellular membranes; thus, water diffusion is a sensitive marker for early differences in tissue properties related to neuroinflammation, for example.^{4,5} An increase in RD is proposed to reflect myelin destruction as demonstrated in mouse models or human postmortem brain studies.³⁰⁻³² The relevance of AD as a marker of axonal damage is less well-understood. In our study, AD was increased but to a lesser extent than RD; these findings are in accordance with those in earlier studies in adults with MS.^{10,25} In contrast, Lin et al³³ showed a trend toward lower AD in the normal-appearing pyramidal tract in adult patients with MS. Recent pathologic studies in degenerative neurologic diseases indicate a topographic concordance between WM loss and AD changes in Huntington disease or Friedreich ataxia.^{34,35} Ro-

sas et al³⁴ suggested that the increase in AD might be due to reduced axonal diameters, resulting in increased extra-axonal space. Thus, interpretation of this diffusivity value is still controversial, with most studies in MS pointing toward an increase in AD. On the other hand, RD plays a predominant role in detecting subtle pathologic damage from very early on in MS, making it a potential marker for monitoring changes in the course of the disease.

In addition to the already-known global decrease in skeletal FA,¹² patients with MS displayed a regional FA reduction in the splenium of the corpus callosum and in the right temporal and left and right parietal regions. Reduction in FA was most profound in the splenium. These changes in FA may serve as an early indicator of MS white matter pathology in childhood MS. Our results are in accordance with DTI studies in adult-onset MS, which report that the earliest changes in white matter tracts occurred in the corpus callosum.⁶ A focal FA decrease in the splenium of the corpus callosum has furthermore been described in patients with isolated optic neuritis.³⁶ Our results suggest that the

corpus callosum is one of the most affected regions in early-onset MS. It may, therefore, be a potential target region for the early detection of disease processes by MR imaging. Special attention was drawn to this region by Hagmann et al,³⁷ who combined modern MR imaging techniques with network analyses. This publication presented evidence for the existence of a structural core of highly interconnected brain regions, located primarily in the posterior medial and parietal cortex. The splenium of the corpus callosum has been proposed as an integral part of this core, interconnecting both hemispheres.

In our relatively small patient cohort, we observed a significant negative correlation between mean FA of the white matter skeleton and disease duration, while no correlation was found for other clinical parameters. In adults, conflicting data on the correlation of FA measures with annual relapse rate, number of total relapses, and lesion load exist. Disease duration of >3 years is reported to negatively correlate with FA,^{25,26} whereas in clinically isolated syndrome, no correlation was reported.⁶

Study Limitations

There are several limitations to our study that need to be taken into account when interpreting the data. First, the sample sizes in our patient and control cohorts are relatively small due to the rare nature of MS in children. Nevertheless, the alterations in diffusivity parameters were highly significant and appear robust in light of the tests applied. In addition, the MR images of the age- and sex-matched healthy controls were recruited from a local data base, in which the clinical assessment did not include the Nine-Hole Peg Test and the Timed 25-Foot Walk Test. The study-related MR imaging protocol and the MR imaging scanner were identical in both cohorts, though.

CONCLUSIONS

Our study demonstrates the white matter microstructure of non-lesional tissue to be affected in childhood MS, even in early stages of the disease. Decreased FA values and increased diffusion parameters may indicate impaired myelination. The observed decrease in FA in the white matter correlated with disease duration.

ACKNOWLEDGMENTS

We thank all participants in this study.

Disclosures: Astrid Blaschek—RELATED: Grant: Research grant from Merck Serono GmbH;* UNRELATED: Payment for Lectures (including service on speaker bureaus); Speaker honoraria from Biogen Idec GmbH, Merck Serono GmbH, and Bayer Schering GmbH;* Travel/Accommodations/Meeting Expenses Unrelated to Activities Listed: Bayer Schering GmbH, Merck Serono GmbH. Sophia Mueller—UNRELATED: Travel/Accommodations/Meeting Expenses Unrelated to Activities Listed: I received a travel grant from the GlaxoSmithKline Foundation (2012) to travel to the Annual Meeting of the Organization for Human Brain Mapping. I presented work that is unrelated to the submitted study. Wolfgang Müller-Felber—UNRELATED: Board Membership: Pompe registry board. Florian Heinen—RELATED: Grant: Merck Serono GmbH;* Consulting Fee or Honorarium: Speakers honorarium from Merck Serono; UNRELATED: Payment for Lectures (including service on speaker bureaus): Merz Pharma, Pfizer Deutschland GmbH, and Allergan GmbH. Birgit Ertl-Wagner—RELATED: Grant: German Research Council; UNRELATED: Board Membership: Philips Healthcare, Bracco, Springer Medical Publisher; Consultancy: Munich Medical International, Philips Healthcare; Grants/Grants Pending: Eli Lilly,* Genentech,* Geurbet,* Merck Serono;* Payment for Lectures (including service on speaker bureaus): Siemens, Bayer Schering; Payment for Manuscript Preparation: Siemens, Springer Medical Publisher, Thieme Medical Publisher, Bracco; Royalties: Springer Medical Publisher, Thieme Medical Publisher; Payment for Development of Educational Presentations: Siemens, Bracco, Springer, Thieme; Stock/Stock Options: Siemens (stock owned by spouse); Travel/Accommodations/Meeting Expenses Unrelated to Activities Listed: Siemens. *Money paid to institution.

REFERENCES

- Banwell B, Shroff M, Ness JM, et al. MRI features of pediatric multiple sclerosis. *Neurology* 2007;68(16 suppl 2):S46–53
- Mikaeloff Y, Adamsbaum C, Husson B, et al. MRI prognostic factors for relapse after acute CNS inflammatory demyelination in childhood. *Brain* 2004;127(pt 9):1942–47
- van der Valk P, Amor S. Preactive lesions in multiple sclerosis. *Curr Opin Neurol* 2009;22:207–13
- Pierpaoli C, Basser PJ. Toward a quantitative assessment of diffusion anisotropy. *Magn Reson Med* 1996;36:893–906
- Song SK, Sun SW, Ju WK, et al. Diffusion tensor imaging detects and differentiates axon and myelin degeneration in mouse optic nerve after retinal ischemia. *Neuroimage* 2003;20:1714–22
- Raz E, Cercignani M, Sbardella E, et al. Clinically isolated syndrome suggestive of multiple sclerosis: voxelwise regional investigation of white and gray matter. *Radiology* 2010;254:227–34
- Bodini B, Cercignani M, Khaleeli Z, et al. Corpus callosum damage predicts disability progression and cognitive dysfunction in primary-progressive MS after five years. *Hum Brain Mapp* 2013;34:1163–72
- Barnea-Goraly N, Menon V, Eckert M, et al. White matter development during childhood and adolescence: a cross-sectional diffusion tensor imaging study. *Cereb Cortex* 2005;15:1848–54
- Koerte I, Heinen F, Fuchs T, et al. Anisotropy of callosal motor fibers in combination with transcranial magnetic stimulation in the course of motor development. *Invest Radiol* 2009;44:279–84
- Roosendaal SD, Geurts JJ, Vrenken H, et al. Regional DTI differences in multiple sclerosis patients. *Neuroimage* 2009;44:1397–403
- Utsunomiya H. Diffusion MRI abnormalities in pediatric neurological disorders. *Brain Dev* 2011;33:235–42
- Tortorella P, Rocca MA, Mezzapesa DM, et al. MRI quantification of gray and white matter damage in patients with early-onset multiple sclerosis. *J Neurol* 2006;253:903–07
- Mezzapesa DM, Rocca MA, Falini A, et al. A preliminary diffusion tensor and magnetization transfer magnetic resonance imaging study of early-onset multiple sclerosis. *Arch Neurol* 2004;61:366–68
- Vishwas MS, Chitnis T, Pienaar R, et al. Tract-based analysis of callosal, projection, and association pathways in pediatric patients with multiple sclerosis: a preliminary study. *AJNR Am J Neuroradiol* 2010;31:121–28
- Vishwas MS, Healy BC, Pienaar R, et al. Diffusion tensor analysis of pediatric multiple sclerosis and clinically isolated syndromes. *AJNR Am J Neuroradiol* 2013;34:417–23
- Smith SM, Jenkinson M, Johansen-Berg H, et al. Tract-based spatial statistics: voxelwise analysis of multi-subject diffusion data. *Neuroimage* 2006;31:1487–505
- Poole JL, Burtner PA, Torres TA, et al. Measuring dexterity in children using the nine-hole peg test. *J Hand Ther* 2005;18:348–51
- Nieuwenhuis MM, Van Tongeren H, Sorensen PS, et al. The six spot step test: a new measurement for walking ability in multiple sclerosis. *Mult Scler* 2006;12:495–500
- Reitan RM, Wolfson D. The trail making test as an initial screening procedure for neuropsychological impairment in older children. *Arch Clin Neuropsychol* 2004;19:281–88
- Horn W. *Leistungsprüfungssystem Manual*. Göttingen, Germany: Hogrefe; 1983
- Helmstaedter C, Schoof K, Rossmann T, et al. Introduction and first validation of EpiTrack Junior, a screening tool for the assessment of cognitive side effects of antiepileptic medication on attention and executive functions in children and adolescents with epilepsy. *Epilepsy Behav* 2010;19:55–64
- Smith SM. Fast robust automated brain extraction. *Hum Brain Mapp* 2002;17:143–55
- Nichols TE, Holmes AP. Nonparametric permutation tests for functional neuroimaging: a primer with examples. *Hum Brain Mapp* 2002;15:1–25
- Smith SM, Nichols TE. Threshold-free cluster enhancement: addressing problems of smoothing, threshold dependence and localisation in cluster inference. *Neuroimage* 2009;44:83–98
- Liu Y, Duan Y, He Y, et al. Whole brain white matter changes revealed by multiple diffusion metrics in multiple sclerosis: a TBSS study. *Eur J Radiol* 2012;81:2826–32
- Yu HJ, Christodoulou C, Bhise V, et al. Multiple white matter tract abnormalities underlie cognitive impairment in RRMS. *Neuroimage* 2012;59:3713–22
- Balássy C, Bernert G, Wober-Bingol C, et al. Long-term MRI observations of childhood-onset relapsing-remitting multiple sclerosis. *Neuropediatrics* 2001;32:28–37
- Renoux C, Vukusic S, Mikaeloff Y, et al. Natural history of multiple sclerosis with childhood onset. *N Engl J Med* 2007;356:2603–13
- Wilke M, Krageloh-Mann I, Holland SK. Global and local development of gray and white matter volume in normal children and adolescents. *Exp Brain Res* 2007;178:296–307
- Song SK, Yoshino J, Le TQ, et al. Demyelination increases radial diffusivity in corpus callosum of mouse brain. *Neuroimage* 2005;26: 132–40
- Schmierer K, Wheeler-Kingshott CA, Tozer DJ, et al. Quantitative magnetic resonance of postmortem multiple sclerosis brain before and after fixation. *Magn Reson Med* 2008;59:268–77
- Zollinger LV, Kim TH, Hill K, et al. Using diffusion tensor imaging and immunofluorescent assay to evaluate the pathology of multiple sclerosis. *J Magn Reson Imaging* 2011;33:557–64
- Lin F, Yu C, Jiang T, et al. Diffusion tensor tractography-based group mapping of the pyramidal tract in relapsing-remitting multiple sclerosis patients. *AJNR Am J Neuroradiol* 2007;28:278–82
- Rosas HD, Lee SY, Bender AC, et al. Altered white matter microstructure in the corpus callosum in Huntington's disease: implications for cortical "disconnection." *Neuroimage* 2010;49:2995–3004
- Pagani E, Ginestroni A, Della Nave R, et al. Assessment of brain white matter fiber bundle atrophy in patients with Friedreich ataxia. *Radiology* 2010;255:882–89
- Bester M, Heesen C, Schippling S, et al. Early anisotropy changes in the corpus callosum of patients with optic neuritis. *Neuroradiology* 2008;50:549–57
- Hagmann P, Cammoun L, Gigandet X, et al. Mapping the structural core of human cerebral cortex. *PLoS Biol* 2008;6:e159

Incidental Findings in Youths Volunteering for Brain MRI Research

R.E. Gur, D. Kaltman, E.R. Melhem, K. Ruparel, K. Prabhakaran, M. Riley, E. Yodh, H. Hakonarson, T. Satterthwaite, and R.C. Gur



ABSTRACT

BACKGROUND AND PURPOSE: MRIs are obtained in research in healthy and clinical populations, and incidental findings have been reported. Most studies have examined adults with variability in parameters of image acquisition and clinical measures available. We conducted a prospective study of youths and documented the frequency and concomitants of incidental findings.

MATERIALS AND METHODS: Youths ($n = 1400$) with an age range from 8–23 years were imaged on the same 3T scanner, with a standard acquisition protocol providing 1.0 mm³ isotropic resolution of anatomic scans. All scans were reviewed by an experienced board-certified neuroradiologist and were categorized into 3 groups: 1) normal: no incidental findings; 2) coincidental: incidental finding(s) were noted, further reviewed with an experienced pediatric neuroradiologist, but were of no clinical significance; 3) incidental findings that on further review were considered to have potential clinical significance and participants were referred for appropriate clinical follow-up.

RESULTS: Overall, 148 incidental findings (10.6% of sample) were noted, and of these, 12 required clinical follow-up. Incidental findings were not related to age. However, whites had a higher incidence of pineal cysts, and males had a higher incidence of cavum septum pellucidum, which was associated with psychosis-related symptoms.

CONCLUSIONS: Incidental findings, moderated by race and sex, occur in approximately one-tenth of participants volunteering for pediatric research, with few requiring follow-up. The incidence supports a 2-tiered approach of neuroradiologic reading and clinical input to determine the potential significance of incidental findings detected on research MR imaging scans.

The prevalence of incidental findings in nondiagnostic brain MR imaging research has been examined in empirical studies, case reports, reviews, and ethical commentaries.^{1–3} Empirical studies have reported the prevalence of incidental findings in various samples commonly including at least 100 subjects.⁴ Of approximately 35 such studies, 75% evaluated adults, 10% were conducted in autopsies, and a few in pediatric populations. Of those, even fewer applied high-field (3T) high-resolution sequences with 1.0-mm³ isotropic or smaller voxels, which may result in more incidental findings. Given the increasingly common use of high-resolution brain MR imaging in pediatric pop-

ulations, establishing both a baseline rate for incidental findings and a framework for evaluation is of importance.

Prior work provides data regarding a possible range of rates of incidental findings in heterogeneous populations, commonly adults. The first large-scale study of 1000 asymptomatic volunteers (age range, 3–83 years) reported an incidental findings prevalence of 4.8%.⁵ Most studies reported rates excluding sinus disease. Kim et al,¹ in a study of 225 neurologically healthy subjects (age, 0–18 years), established an incidental findings prevalence of approximately 11%, and males had twice the occurrence of incidental findings as females. Seki et al⁶ evaluated 110 healthy children (age, 5–8 years) in a single scanner (1.5T) with the same imaging sequence and found 11% with incidental findings. A meta-analysis of 16 studies including nearly 20,000 scans, mainly in adults, reported inconsistent incidental findings and found that the rate of incidental findings was related to image resolution.⁴ With sequences considered low-resolution by present standards, incidental findings prevalence was approximately 3–4%. Thus, relatively few studies have examined incidental findings in youths, and prior studies have been limited by both the effective resolution of the imaging sequence used and small sample size.

Received December 12, 2012; accepted after revision January 3, 2013.

From the Brain Behavior Laboratory (R.E.G., D.K., K.R., K.P., M.R., E.Y., T.S., R.C.G.), Department of Psychiatry, and Division of Neuroradiology (R.E.G., E.R.M., R.C.G.), Department of Radiology, Perelman School of Medicine, University of Pennsylvania, Philadelphia; and Center for Applied Genomics (H.H.), Children's Hospital of Philadelphia, University of Pennsylvania, Philadelphia, Pennsylvania.

Please address correspondence to Raquel E. Gur, MD, PhD, Neuropsychiatry, 10 Gates, 3400 Spruce, Philadelphia, PA 19104; e-mail: Raquel@upenn.edu

Indicates open access to non-subscribers at www.ajnr.org

Evidence-Based Medicine Level 2

<http://dx.doi.org/10.3174/ajnr.A3525>

Clinical correlates of incidental findings have received some attention because incidental findings may be indicative of underlying pathology. For example, children with developmental delay of unknown etiology, according to retrospective chart reviews, were more likely (1.8 odds ratio) to have incidental findings than healthy control subjects.⁷ In a recent meta-analysis, Trzesniak et al⁸ concluded that the presence of a large cavum septum pellucidum is associated with schizophrenia spectrum disorders. However, no study has examined whether a finding of cavum septum pellucidum in an epidemiologically accrued sample is associated with increased incidence of psychotic features.

The Philadelphia Neurodevelopment Cohort provides an opportunity to evaluate incidental findings in a population-based sample of 1400 young people, ages 8–21 years. This is the largest single-site, single-scanner, high-resolution pediatric MR imaging study with a similar representation of whites and African Americans. We conducted a prospective examination of incidental findings yielding the largest standardized sample to date of high-resolution brain MRI in pediatric research. Our goal was to determine the prevalence of incidental findings in this young population and to examine whether certain findings were associated with demographic characteristics or correlated with clinical measures.

MATERIALS AND METHODS

Subjects

Subjects were recruited as part of the Philadelphia Neurodevelopment Cohort, a collaborative National Institute of Mental Health–funded Grand Opportunity study between the Brain Behavior Laboratory at the University of Pennsylvania and the Center for Applied Genomics at Children’s Hospital of Philadelphia. The overall goal of the project is to examine a large sample of genotyped youths, ascertained through the Children’s Hospital of Philadelphia network, who provided consent/assent to be re-contacted for the study of complex pediatric disorders. The Children’s Hospital of Philadelphia network includes a mixture of urban and suburban clinics as well as a tertiary care hospital. Therefore, the sample is diverse and represents the range of health conditions found in youths. Inclusion criteria were age 8–21 years; general good health, as indicated by review of electronic medical records and telephone screen; the ability to provide signed informed consent or assent; English proficiency; and physical and cognitive capability to participate in a comprehensive assessment. More than 9000 eligible participants who met inclusion criteria underwent further direct neuropsychiatric assessment and computerized neurocognitive testing.⁹ The neuropsychiatric assessment consisted of evaluation of medical, neurologic, and psychiatric disorders,¹⁰ including psychotic symptoms.¹¹ The computerized neurocognitive battery included measures of executive functions, memory, reasoning, social cognition, and sensorimotor speed, as detailed by Gur et al.¹²

A randomly selected subsample of 1400 subjects, stratified by age and sex and meeting criteria for MR imaging compatibility, completed the MR imaging study and were included in the present analysis.¹³ Notably, subjects were not recruited on the basis of any pre-existing disorder or symptoms. There were 670 males (48%) and 730 females (52%); 627 whites (45%), 589 African

Table 1: Sample demographics by group

Participant Characteristic	Normal Finding Group (n = 1252)	Incidental Finding Group (n = 148)
Age, y	14.72 ± 3.59	14.85 ± 3.92
Education, y	7.64 ± 3.50	7.81 ± 3.77
Sex, %		
Male	48	49
Female	52	51
Race, %		
White	45	49
African American	42	40
Other	13	11

Americans (42%), and 184 (13%) subjects of other or mixed races. The age distribution is presented in Table 1.

MR Imaging Acquisition

All MRIs were acquired on the same 3T scanner (TIM Trio; Siemens, Erlangen, Germany), with a 32-channel head coil, located in the Department of Radiology at the Hospital of the University of Pennsylvania. All scans were conducted by a board-certified MR imaging technologist by use of a standard protocol. Foam cushions were used to stabilize the head; no sedation was used. The sequence used was an axial T1-weighted magnetization-prepared rapid acquisition of gradient echo, with parameters TR/TE, 1810/3.51 ms; TI, 1100 ms; FOV, 180 × 240 mm; effective voxel resolution, 1 × 1 × 1 mm³; scanning time, 3 minutes, 28 seconds. Before the study proper, participants were acclimated to the MR imaging environment by use of a mock scanning session in a de-commissioned MR imaging scanner.

Classification of Findings

All scans were reviewed in the neuroradiology reading room at the Hospital of the University of Pennsylvania according to standard clinical procedures. Twenty board-certified neuroradiologists read the images and provided a written clinical report. Five of them reviewed 60% of the scans. The scans and reports were electronically transferred to a data base, and one investigator (R.E.G.) reviewed all reports and classified each as normal or coincidental:

Normal. No incidental finding noted.

Coincidental. All incidental finding(s) that were noted in the clinical report were further reviewed by an experienced pediatric neuroradiologist (E.R.M.) to determine their clinical pertinence. Findings that were not clinically significant were not communicated to the subject (nor to their parent/guardian, if applicable).

Follow-up. Coincidental findings of potential clinical significance were communicated to the subjects and/or their parent or guardian, with appropriate referrals as indicated.

Incidental Finding Categorization

As in previous studies, 6 categories were created to further analyze common incidental findings: 1) pineal cyst, 2) other cyst, 3) cavum septum pellucidum, 4) other ventricular abnormalities (prominence or asymmetry of ventricle or CSF), 5) vascular abnormalities (asymmetric prominence of artery or vein, developmental venous anomaly, tortuous artery, possible infarct, possible aneurysm), and 6) cerebellar abnormalities (cerebellar tonsillar

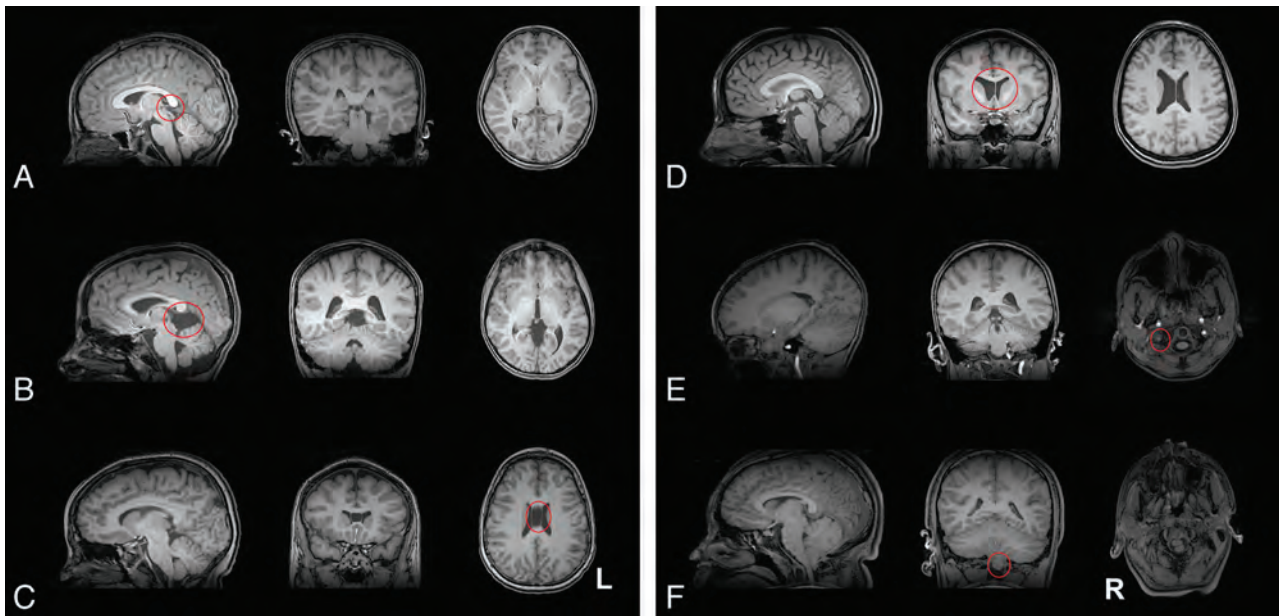


FIG 1. Examples of incidental findings categories. A, Pineal cyst; B, other cysts; C, cavum septum pellucidum; D, ventricular abnormalities; E, vascular abnormalities; F, cerebellar abnormalities.

ectopia, Chiari I malformation, prominent retrocerebellar space, low-lying cerebellar tonsils, mega cisterna magna, cerebellar cyst). Examples for these categories are provided in Fig 1A–F.

Two specific findings were excluded from the present analysis. As in prior work, findings outside the cranial vault were not considered in this report. This includes nasopharynx and sinus conditions, such as opacification of the sinus or sinus mucosal disease. Findings of dilated perivascular spaces were excluded from analysis because of inconsistent reporting.

Statistical Data Analysis

Statistical analysis comparing the demographic characteristics between groups was performed by use of the Student *t* test for age and the χ^2 test for proportions (sex and race). For each incidental finding category, logistic regression was performed to determine whether demographic characteristics (age, sex, race) predicted the odds of the incidental finding. Interactions within demographic variables were studied, but nonsignificant interactions were not included in the final models. All models were evaluated for lack of fit with the Hosmer-Lemeshow test. Analyses were implemented by use of R software (version 2.15.0, <http://www.r-project.org/>).¹⁴

To test the hypothesis of increased psychotic features in patients with cavum septum pellucidum,⁸ we compared individuals with this incidental finding with participants from the larger sample who matched most closely on age, sex, and race. Specifically, each subject was paired with all participants in the sample who had the same values on these demographics. The means of the 2 groups on the psychosis score¹¹ were compared by means of a Student *t* test. This part of the analysis was implemented in SAS, version 9.2 (SAS Institute, Cary, North Carolina).¹⁵

RESULTS

Incidental Findings

Of the 1400 scans, 1252 were read as normal (89.42%). There were 148 scans with incidental findings (10.57%), and of these, 12 in-

Table 2: Frequency of incidental findings

Finding	Count	Prevalence	Literature
Pineal cyst	34	2.43%	1–10%
Other cyst	19	1.36%	1–15%
Cavum septum pellucidum	16	1.14%	1–20+%
Other CSF abnormalities	33	2.36%	N/A
Vascular abnormalities	36	2.57%	N/A
Cerebellar abnormalities	33	2.36%	1–3% ectopia
Coincidental	136	9.71%	2–20%
All incidental	148	10.57%	3–85%

The literature values are mostly from adults. Counts do not add to 148 because some subjects have more than 1 finding.

dicated clinical follow-up. The age distribution of subjects with any incidental findings did not differ from those without incidental findings ($P = .69$). The sex distribution of those with incidental findings likewise did not differ from that of the total sample ($P = .52$), nor did racial distribution ($P = .41$). Table 2 shows the count and prevalence for each incidental finding category.

Association with Specific Incidental Findings

Multiple logistic regression analyses revealed several significant relationships between demographic indicators and the existence of a specific incidental finding. When controlling for age and sex in the model, whites were 195% more likely than African Americans to have a pineal cyst (OR = 2.95, CI = 1.20–7.22, $P = .02$); females were 76% less likely than males to have a cavum septum pellucidum (OR = 0.24, CI = 0.06–0.92, $P = .04$).

There was a significant age by race interaction for cerebellar abnormality ($P = .02$) and ventricular abnormality ($P = .04$). When controlling for sex, whites were more likely to have cerebellar abnormality than African Americans, and this effect of race on the odds of having cerebellar abnormality decreased with age. When controlling for sex, whites were less likely to have ventricular abnormality than African Americans, and this effect of race likewise decreased with age. All final multivariable adjusted mod-

els were reliable ($P > .2$) on the basis of the Hosmer-Lemeshow goodness-of-fit test.

Notably, the 16 cases with cavum septum pellucidum endorsed more psychotic symptoms than those with no incidental findings, matched for age and sex ($n = 459$, $t = 7.20$, $df = 471$, $P < .0001$).

DISCUSSION

In this prospective analysis of incidental findings in brain MR imaging of presumed healthy subjects, we established that incidental findings are common, with a prevalence of $>10\%$. Although the prevalence of such findings varies widely in the literature, from as low as 3% to $>80\%$, the meta-analysis by Morris et al⁴ reported a prevalence of approximately 4% . This value reflected a combination of studies with an effective voxel resolution of at best $2 \times 2 \times 2 \text{ mm}^3$ but typically $3 \times 3 \times 3 \text{ mm}^3$; this is referred to as “high resolution” but is in fact coarse by current standards. Despite our exclusion of sinus-related findings, which some studies in the meta-analysis included, we obtained a value more than twice as large as the Morris et al value.

There are several possible reasons for this finding. First and foremost, our study used a higher-field magnet (3T) and acquired higher-resolution (1-mm^3 isotropic voxels) images than any data set included in the Morris et al⁴ meta-analysis. This enhanced resolution probably allowed greater sensitivity to detect small cysts and vascular anomalies. In addition, the resolution and the sequence used allowed for a larger field of view than that used in many previous analyses of incidental findings.

This report represents the largest study to date of incidental findings in an adolescent population. Although no significant correlations were detected between age and the prevalence of incidental finding, the narrow age band under investigation limited our ability to detect any such differences; subjects were divided into age bins of only 2 years for this analysis, compared with the >10 -year age bins used in studies with more heterogeneous samples.

Analysis of specific incidental findings with logistic regression revealed several novel findings. Whites were more than twice as likely as African Americans to have any cyst and nearly 3 times more likely to have a pineal cyst. In addition, whites were more likely to have cerebellar findings, whereas African Americans had a greater incidence of ventricular findings. These latter effects became weaker with age. Earlier studies have been limited in their ability to examine the effects of race by smaller and more homogeneous samples.

Notably, males were approximately 5 times more likely than females to have a cavum septum pellucidum. Several studies suggest that the presence of a cavum septum pellucidum is significantly correlated with psychotic symptoms, also more prevalent in males. Whereas a recent meta-analysis by Trzesniak et al⁸ suggested that only a “large” cavum was associated with schizophrenia spectrum disorders, in our sample we found significantly greater incidence of reporting psychotic symptoms in the subsample with cavum septum pellucidum. However, the small sample size precludes establishing a correlation between symptom severity and septum size. Longitudinal studies are needed to ex-

amine whether individuals with cavum septum pellucidum are more likely to have psychotic illness.

The findings of this study can be used to better inform research participants about the potential risks and benefits of volunteering. As previously suggested,¹ further research on the prevalence of incidental findings could inform the risk/benefit calculus of informed consent for research participants if the anticipated prevalence of a finding becomes well established. The present study provides a highly standardized description of the prevalence of incidental findings in pediatric neuroimaging research at a resolution and magnetic field strength widely used by researchers today. Although ethics was not the primary focus of this study, our approach to handling incidental findings was commensurate with that recommended by bioethicists.¹⁶⁻¹⁸ Expert review of the research-grade images was performed routinely, with further review to determine the clinical significance. Despite an overall prevalence of roughly 11% , only 12 subjects were actually contacted for follow-up after expert consultation. The lack of involvement of a neuroradiology expert could cause unnecessary over-reporting of findings to research subjects.

Our study has several limitations. Although subjects were not recruited on the basis of any pre-existing condition, they were recruited through a children’s hospital network, and most were from the greater Philadelphia area. To compensate for the regional bias, we accounted for race, sex, and age in our model. All 3 factors were approximately balanced in the overall sample. In addition, several neuroradiologists conducted the initial image readings. Although standardized criteria are used to identify the various findings analyzed in this study, we cannot discount the potential variability in selective reporting of certain findings. To address this issue, a single investigator (R.E.G.) reviewed all of the neuroradiology reports and a single pediatric neuroradiologist (E.R.M.) reviewed all incidental findings. The 6 incidental finding categories were not determined a priori but were instead generated on the basis of their prevalence and are consistent with other reports.

Notwithstanding these limitations, our large-scale, prospective study has identified several common incidental findings in a pediatric population. A single high-field scanner and high-resolution imaging allow this study to establish a benchmark for the prevalence of incidental findings in an ethnically diverse population of male and female youths. The substantial prevalence of incidental findings indicates the utility of including a clinical reading of MR imaging scans performed on research participants. On the other hand, the small number of findings requiring follow-up support the use of further expert review so that participants are not unnecessarily alarmed. Our preliminary finding of increased reporting on psychotic symptoms in a subgroup of youths with cavum septum pellucidum supports longitudinal research on this group.

CONCLUSIONS

Our large-scale, population-based pediatric study with the use of high-resolution neuroimaging found a prevalence of approximately 10% incidental findings. This number is higher than the limited pediatric literature and supports the value of clinical reading of MR imaging performed as part of research studies. Notably,

some findings were moderated by race, with pineal cysts and cerebellar incidents more evident, whereas ventricular findings were less frequent in whites than in African Americans.

ACKNOWLEDGMENTS

This research was supported by National Institutes of Health grant MH089983. We thank the Division of Neuroradiology; MR imaging technologists Norman Butler, Doris Cain, and Tanya Kurtz; the Brain Behavior Laboratory MR imaging acquisition team, including Jeffrey Valdez, Ryan Hopson, Nicholas DeLeo, and Jack Keefe; and the participants and families.

Disclosures: Raquel Gur—RELATED: Grant: NIH/NIMH.* Comments: The work was supported by federal research grants acknowledged in the manuscript. David Kaltman—RELATED: Grant: National Institute of Mental Health.* Karthik Prabhakaran—RELATED: Grant: National Institute of Mental Health.* Marisa Riley—RELATED: Grant: NIH/NIMH.* Elliott Yodanis—RELATED: Grant: NIH/NIMH.* Hakon Hakonarson—RELATED: Grant: NIMH.* Comments: Support from NIMH to study Neurodevelopmental Genomics: Trajectories of Complex Phenotypes (IRC2MH089924–01). Theodore Satterthwaite—RELATED: Grant: NIMH.* Comments: MH089983, MH089924; UNRELATED: Grants/Grants Pending: NIMH.* APIRE.* NARSAD.* Ruben Gur—RELATED: Grant: NIMH.* Support for Travel to Meetings for the Study or Other Purposes: NIMH; UNRELATED: Expert Testimony: Courts and Federal Defenders, Comments: I have provided medical-legal expert testimony, mostly in capital cases, none related specifically to this manuscript or work; Grants/Grants Pending: NIMH* (*money paid to institution).

REFERENCES

1. Kim BS, Illes J, Kaplan RT, et al. **Incidental findings on pediatric MR images of the brain.** *AJNR Am J Neuroradiol* 2002;23:1674–77
2. Weber F, Knopf H. **Incidental findings in magnetic resonance imaging of the brains of healthy young men.** *J Neuro Sci* 2006;240:81–84
3. Vernooij MW, Ikram MA, Tanghe HL, et al. **Incidental findings on brain MRI in the general population.** *N Engl J Med* 2007;357:1821–28
4. Morris Z, Whiteley WN, Longstreth WT Jr, et al. **Incidental findings on brain magnetic resonance imaging: systematic review and meta-analysis.** *BMJ* 2009;339:b3016
5. Katzman GL, Dagher AP, Patronas NJ. **Incidental findings on brain magnetic resonance imaging from 1000 asymptomatic volunteers.** *JAMA* 1999;282:36–49
6. Seki A, Uchiyama H, Fukushi T, et al; Japan Children's Study Group. **Incidental findings of brain magnetic resonance imaging study in a pediatric cohort in Japan and recommendation for a model management protocol.** *J Epidemiol* 2010;20(Suppl 2):S498–504
7. Gupta S, Kanamalla U, Gupta V. **Are incidental findings on brain magnetic resonance images in children merely incidental?** *J Child Neurol* 2010;25:1511–16
8. Trzesniak C, Oliveira IR, Kempton MJ, et al. **Are cavum septum pellucidum abnormalities more common in schizophrenia spectrum disorders? A systematic review and meta-analysis.** *Schizophr Res* 2011;125:1–12
9. Gur RC, Richard J, Calkins ME, et al. **Age group and sex differences in performance on a computerized neurocognitive battery in children age 8–21.** *Neuropsychology* 2012;26:251–65
10. Kaufman J, Birmaher B, Brent D, et al. **Schedule for Affective Disorders and Schizophrenia for School-Age Children—Present and Lifetime Version (K-SADS-PL): initial reliability and validity data.** *J Am Acad Child Adolesc Psychiatry* 1997;36:980–88
11. Miller TJ, McGlashan TH, Rosen JL, et al. **Prodromal assessment with the structured interview for prodromal syndromes and the scale of prodromal symptoms: predictive validity, interrater reliability, and training to reliability.** *Schizophr Bull* 2003;29:703–15
12. Gur RC, Richard J, Huggett P, et al. **A cognitive neuroscience-based computerized battery for efficient measurement of individual differences: standardization and initial construct validation.** *J Neurosci Methods* 2010;187:254–62
13. Satterthwaite TD, Wolf DH, Loughhead J, et al. **Impact of in-scanner head motion on multiple measures of functional connectivity: relevance for studies of neurodevelopment in youth.** *Neuroimage* 2012;60:623–32
14. R Development Core Team. **R: a language and environment for statistical computing.** R version 2.12.0. Available at: <http://www.R-project.org>. Accessed October 15, 2010
15. SAS software, Version 9.2 of the SAS System for Linux, SAS Institute Inc, Cary, North Carolina; 2009
16. Illes J, Chin VN. **Bridging philosophical and practical implications of incidental findings in brain research.** *J Law Med Ethics* 2008;36:298–304
17. Wolf SM, Lawrenz FP, Nelson CA, et al. **Managing incidental findings in human subjects research: analysis and recommendations.** *J Law Med Ethics* 2008;36:219–48
18. Kumra S, Ashtari M, Anderson B, et al. **Ethical and practical considerations in the management of incidental findings in pediatric MRI studies.** *J Am Acad Child Adolesc Psychiatry* 2006;45:1000–06

Abnormal Cerebral Microstructure in Premature Neonates with Congenital Heart Disease

L.B. Paquette, J.L. Wisnowski, R. Ceschin, J.D. Pruetz, J.A. Detterich, S. Del Castillo, A.C. Nagasunder, R. Kim, M.J. Painter, F.H. Gilles, M.D. Nelson, R.G. Williams, S. Blüml, and A. Panigrahy



ABSTRACT

BACKGROUND AND PURPOSE: Abnormal cerebral microstructure has been documented in term neonates with congenital heart disease, portending risk for injury and poor neurodevelopmental outcome. Our hypothesis was that preterm neonates with congenital heart disease would demonstrate diffuse cerebral microstructural abnormalities when compared with critically ill neonates without congenital heart disease. A secondary aim was to identify any association between microstructural abnormalities, white matter injury (eg, punctate white matter lesions), and other clinical variables, including heart lesions.

MATERIALS AND METHODS: With the use of tract-based spatial statistics, an unbiased, voxelwise method for analyzing diffusion tensor imaging data, we compared 21 preterm neonates with congenital heart disease with 2 cohorts of neonates without congenital heart disease: 28 term and 27 preterm neonates, identified from the same neonatal intensive care unit.

RESULTS: Compared with term neonates without congenital heart disease, preterm neonates with congenital heart disease had microstructural abnormalities in widespread regions of the central white matter. However, 42% of the preterm neonates with congenital heart disease had punctate white matter lesions. When neonates with punctate white matter lesions were excluded, microstructural abnormalities remained only in the splenium. Preterm neonates with congenital heart disease had similar microstructure to preterm neonates without congenital heart disease.

CONCLUSIONS: Diffuse microstructural abnormalities were observed in preterm neonates with congenital heart disease, strongly associated with punctate white matter lesions. Independently, regional vulnerability of the splenium, a structure associated with visual spatial function, was observed in all preterm neonates with congenital heart disease.

ABBREVIATIONS: CHD = congenital heart disease; pWML = punctate white matter lesion; TBSS = tract-based spatial statistics; FA = fractional anisotropy

As the overall survival rate has improved for infants with congenital heart disease (CHD), there have been increased efforts made to improve long-term morbidity in the context of co-existing risk factors.¹ Approximately 16% of infants with CHD are

born prematurely, and CHD is twice as common in preterm compared with term neonates.² Multiple studies have documented higher rates of mortality and morbidity in neonates with CHD who are born prematurely or at lower birth weight,²⁻⁶ and it has been shown that lower gestational age at birth is associated with worse neurodevelopmental outcome among infants with CHD.^{7,8}

Prematurity and CHD are independent risk factors for adverse neurodevelopmental outcome, and it follows that having both further increases the risk. Prior studies of term neonates with CHD have also documented delayed brain maturation, particularly in term infants with single ventricle physiology, further increasing their risk for injury or adverse neurodevelopmental outcome.⁹⁻¹⁵ Thus, examining the cerebral microstructure of preterm infants with CHD in relation to prematurity and injury

Received December 10, 2012; accepted after revision January 8, 2013.

From the Division of Neonatology (L.B.P.); Department of Radiology (J.L.W., A.C.N., M.D.N., S.B., A.P.); Division of Cardiology (J.D.P., J.A.D.), Department of Pediatrics; Department of Anesthesiology and Critical Care Medicine (S.D.C.); Division of Cardio-Thoracic Surgery (R.K., R.G.W.), Department of Surgery; Division of Neuropathology (S.D.C.); and Department of Pathology (F.H.G.), Children's Hospital, Los Angeles, California; Brain and Creativity Institute (J.L.W.) and Department of Biomedical Engineering (S.B.), University of Southern California, Los Angeles, California; Departments of Pediatric Radiology (R.C., A.P.) and Pediatrics (M.J.P.), Division of Neurology, Children's Hospital of Pittsburgh of UPMC, and Department of Biomedical Informatics (R.C.), University of Pittsburgh, Pittsburgh, Pennsylvania.

L.B. Paquette and J.L. Wisnowski are co-first authors.

Support for this study is provided by the National Institutes of Health: K23NS063371 to A.P., P50NA019632 to J.L.W., 1UL1RR031986 to A.P., J.L.W., and L.B.P., K12HD052954 to J.A.D.; and Rudi Schulte Foundation to S.B.

Please address correspondence to Ashok Panigrahy, MD, Department of Pediatric Radiology, Children's Hospital of Pittsburgh of UPMC, 45th St and Penn Ave, Pittsburgh, PA 15201; e-mail: panigrahy@upmc.edu

Indicates open access to non-subscribers at www.ajnr.org

Indicates article with supplemental on-line appendix.

Indicates article with supplemental on-line figures.

<http://dx.doi.org/10.3174/ajnr.A3528>

may provide important insights into the complex combination of risks portending adverse neurodevelopment in infants with CHD. To date, few neonatal neuroimaging studies have been described in preterm infants with CHD.

On neuropathologic examination, periventricular leukomalacia is a commonly observed finding in neonates with CHD and neonates with a history of preterm birth.¹⁶⁻²¹ With advances in neonatal intensive care, there has been a trend away from observations of cavitated lesions toward smaller noncavitated lesions (often described as “microcysts”).²² The most widely recognized MR correlate of noncavitated periventricular leukomalacia are punctate T1-hyperintense lesions.²³

In the present study, we used DTI to investigate the microstructural integrity of the cerebral white matter and select gray matter regions in preterm neonates with CHD. Our hypothesis was that preterm neonates with CHD would demonstrate diffuse cerebral microstructural abnormalities at near term-equivalent age when compared with other critically ill neonates without CHD. Our secondary aim was to identify any association between microstructural abnormalities, documented patterns of white matter injury, and other pertinent clinical variables, including the complexity of the heart lesion. We included 2 separate comparison groups: term neonates without CHD and preterm neonates without CHD, both of which were identified from the same high-risk neonatal intensive care unit. The term neonates without CHD allowed us to determine whether the microstructure in our preterm neonates with CHD differed from “normal” at term-equivalent age. The preterm neonates without CHD allowed us to determine whether the presence of a congenital heart defect resulted in further microstructural abnormality than would be accounted for by prematurity alone. Finally, by separating our preterm neonates with CHD into the subset with punctate white matter lesions (pWMLs) and those without pWMLs, we were able to directly address whether the microstructural abnormalities were related to cerebral white matter injury.

MATERIALS AND METHODS

Subjects

Target Cohort of Preterm Neonates with CHD. Neonates undergoing clinically indicated brain MRI at near term-equivalent age during the period of 2005–2010 were recruited as part of ongoing longitudinal studies of neurodevelopment in neonates with prematurity and CHD at a single institution. In the preterm CHD group, we included neonates with any heart anomaly treated surgically, including atrial septal defect, ventricular septal defect, patent ductus arteriosus requiring surgery after term equivalency, hypoplastic left heart syndrome, Ebstein anomaly, coarctation of the aorta, truncus arteriosus, transposition of the great arteries, and double-outlet right ventricle (Table 1). Patients with CHD were excluded if 1) the heart anomaly did not require surgery; 2) they had a chromosomal abnormality; 3) the brain MR imaging did not include DTI data that were analyzable (ie, caused by motion artifact or technical factors); and 4) there was a congenital brain malformation or a significant brain abnormality/injury, which could distort subsequent DTI measurements. Given the diversity of heart lesions treated by surgery in the preterm CHD group, the clinical data (including fetal echocardiograms) for the

Table 1: Preterm CHD cases—frequency of diagnoses

Heart Defects	n
Hypoplastic left heart syndrome	5
Ebstein anomaly	2
Coarctation of the aorta	3
Transposition of the great arteries	2
Atrial septal defect, ventricular septal defect, patent ductus arteriosus requiring surgery	8
Double-outlet right ventricle	1

preterm CHD cases were reviewed by 3 pediatric cardiologists (J.D.P., R.G.W., J.A.D.) for determination of heart lesion complexity (see more details in On-line Appendix).

Comparison Cohorts of Critically Ill Term and Preterm Neonates without CHD. For comparison, we included data from 2 cohorts of neonates without CHD identified from the same high-risk neonatal intensive care unit—the first obtained as part of an internal review board–approved retrospective review of neonatal MRI conducted at the same institution as above between 2005–2010 and the second obtained as part of an ongoing longitudinal research program focused on prematurity. All near term-equivalent MRI was completed under clinical indications. The clinical indication for these studies included assessment of abnormal brain morphology (not confirmed), assessment of suspected brain injury or infection (not confirmed by imaging or relevant laboratory studies), assessment of possible seizure activity (including febrile seizures), and assessment of a nonintracranial abnormality, including a facial or orbital lesion. For all neonates, medical records were reviewed, including pertinent outpatient follow-up, by a neonatologist (L.B.P.) and a pediatric neuropsychologist (J.L.W.) (On-line Appendix). We also used region of interest measurements to validate this group against published healthy neonatal DTI data by using the same methods (On-line Appendix).²⁴

MR Imaging Protocol

All imaging was obtained in a 1.5T system (GE Healthcare Medical Systems, Milwaukee, Wisconsin) with a neonatal head coil and neonatal incubator (if clinically necessary). The following imaging sequences were acquired: T2WI FSE in axial and coronal planes (TE/TR = 85/5000 ms, FOV = 20 cm, matrix = 320 × 160 or 256 × 128, section thickness, 3 mm, spacing = 0) (5 minutes); coronal T1 3D spoiled gradient-recalled echo (TE/TR = 6/25 ms, FOV = 18 cm, matrix = 256 × 160, section thickness = 1 mm, spacing = 0) (10 minutes). The DTI protocol included an EPI sequence with the following parameters: TE/TR = 80/10,000 ms, FOV = 22 cm, matrix = 128 × 128, section thickness = 4.5 mm, spacing = 0, with an in-plane resolution of 1.7 mm applied along 25 noncolinear directions with a b-value of 700 seconds/mm² (6 minutes).

Evaluation of Conventional MR Imaging Data and Identification of pWMLs

All standard MR images were reviewed by 2 independent readers (J.L.W., A.P.) for the presence of pWMLs, used here as a MR imaging biomarker for noncystic periventricular leukomalacia (Fig 1). Consensus was achieved if there was disagreement.

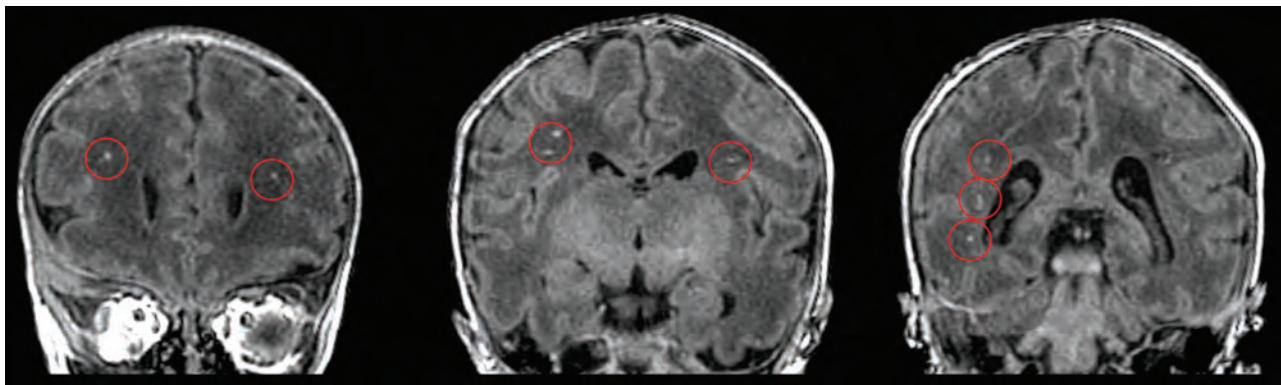


FIG 1. Infant with hypoplastic left heart syndrome born at 31 weeks postconceptional age and imaged at 35.5 weeks postconceptional age. Three coronal cuts from the 3D T1-weighted spoiled gradient recalled echo sequence demonstrating punctate T1-hyperintense lesions (circled in red) in the periventricular white matter and corona radiata just rostral to the genu of the corpus callosum (left), at the level of the pre- and post-central gyri (middle), and posterior to the trigone of the lateral ventricle (right), consistent with bilateral pWMLs or periventricular leukomalacia.

Table 2: Comparison of clinical variables between preterm neonates with CHD with pWMLs and preterm neonates without CHD

	CHD Preterm with pWMLs (n = 8)	Control Preterm (n = 27)	P Value ^a
PCA, weeks, mean (SD)	38.63 (3.36)	42.61 (6.51)	.13 ^a
GA, weeks, mean (SD)	33.29 (1.89)	30.67 (4.62)	.156 ^a
PNA MRI, weeks, mean (SD)	5.35 (4.38)	11.095 (8.24)	.087 ^a
PCA MRI, weeks, mean (SD)	38.63 (3.36)	42.61 (6.51)	.13 ^a
Apgar 1 minute, median (n)	6 (6)	6 (21)	.860 ^c
Apgar 5 minutes, median (n)	8.5 (6)	8 (21)	.878 ^c
Apgar 10 minutes, median (n)	6 (2)	7 (3)	.747 ^c
Size for GA	33	8	.216 ^b
Small, %	67	84	
Appropriate, %	0	8	
Large, %	6	25	
ISAM, % (n)	0 (5)	8.3 (24)	.763 ^d
Postnatal sepsis, % (n)	42.9 (7)	60.0 (25)	.706 ^d
Hydrocortisone for BP, % (n)	50 (6)	18.5 (27)	.271 ^d
Days on hydrocortisone, mean (SD)	0.5 (0.55)	1.741 (6.06)	.62 ^a
Inotropes, % (n)	100 (6)	46.2 (26)	.02 ^a
Days on dopamine, mean (SD)	4.33 (4.23)	3.81 (5.98)	.84 ^a

Note:—PCA indicates postconceptional age; GA, gestational age; PNA, postnatal age; ISAM, infant of substance abusing mom; BP, blood pressure.

^a ANOVA P values \leq .005.

^b Measurements are average left and right.

^c Mann-Whitney for testing difference in medians.

^d χ^2 for tests of homogeneity.

DTI Postprocessing: Tract-Based Spatial Statistics

DTI data analysis was performed by using FSL software (Version 4.1.4; <http://www.fmrib.ox.ac.uk/fsl>)²⁵. Our protocol for tract-based spatial statistics (TBSS) was similar to other published methods previously optimized for the neonates.²⁶ (Please refer to On-line Appendix for more detail about TBSS methodology).

Additional Statistical Analyses

Continuous clinical variables were compared by use of a 3-way ANOVA. Pair-wise comparisons were then made by means of Tukey analysis. Categorical clinical variables were compared by means of Kruskal-Wallis or χ^2 tests, as appropriate. Differences in perioperative variables were determined by nonparametric tests. R Developmental Core Team (<http://www.r-project.org/>) and SPSS (Version 19; SPSS, Chicago, Illinois) were used for all statistical analyses.

RESULTS

Characterization of the Clinical Population and Clinical Variable Data

There were 76 cases that met the inclusion criteria for this study: 21 preterm neonates with CHD, 28 neonates born at term (\geq 37 weeks; term comparison group), and 27 neonates born between 23–36 weeks gestational age (preterm comparison group). There were no significant differences in postconceptional age (defined as gestational age at birth plus postnatal age) at time of MR imaging among the 3 groups, including the subset of preterm CHD cases identified with pWMLs ($P = .58$, ANOVA). Information regarding diagnosis, clinical course, MR imaging, and surgical variables for preterm CHD cases are summarized in Tables 1–3.

Incidence of pWMLs in the Preterm CHD Group

On the basis of conventional MR imaging, pWMLs were found in approximately 42% of the preterm CHD cases (κ score = 1.0) (Fig 1). Of the CHD cases with pWMLs, 63% had MR imaging performed in the postoperative period. The most common heart lesion in the preterm neonates with CHD with pWMLs was hypoplastic left heart syndrome ($n = 4$; 1 preoperative; 3 postoperative). The other diagnoses associated with pWMLs included 1) Ebstein anomaly ($n = 1$, preoperative); coarctation ($n = 1$, postoperative); ventricular septal defect ($n = 1$, preoperative); and double-outlet right ventricle ($n = 1$, postoperative). The highest number of pWMLs was noted in 2 hypoplastic left heart syndrome cases and a coarctation case. We compared clinical variables between the preterm neonates with CHD and pWMLs and the preterm neonates without CHD, and the only statistically significant difference was the relatively increased use of inotropes ($P < .02$) (Table 2). We also compared multiple

Table 3: Preterm CHD group: comparison of perioperative variables between pWML versus non-pWML groups

Surgical Variables	CHD Preterm Group with pWML		CHD Preterm without pWML		P Value*
	Mean (SD)	n	Mean (SD)	n	
Birth weight	1963.5 (591.6)	8	1676.2 (566.6)	11	.341
Age at 1 st surgery, days	3.5 (2.8)	8	12.0 (12.7)	12	.05
PCA at 1 st surgery, weeks	37 (1.7)	8	43.1 (10.9)	12	.20
1 st ABG pH	7.24 (0.08)	5	7.29 (1.10)	5	.36
1 st ABG pO ₂	81.75 (74.82)	4	39 (—)	1	.64
Pre-op ABG pH	7.33 (0.1)	8	7.36 (0.05)	12	.41
Pre-op ABG pO ₂	62.2 (21.2)	8	69.75 (34.6)	8	.67
Post-op ABG pH	7.30 (0.07)	8	7.32 (0.05)	12	.38
Post-op ABG pO ₂	67.83 (48.3)	8	101 (83.52)	12	.37
Pre-op epi, no. of days	0 (0)	8	0.08 (0.3)	12	.49
Pre-op dobutamine, no. of days	0 (0)	8	0.08 (0.3)	12	.49
Pre-op dopamine, no. of days	1.167 (0.41)	8	0.417 (1.2)	12	.62
Pre-op hydrocortisone, no. of days	0.167 (0.41)	8	0.08 (0.3)	12	.61
Pre-op milirinone, no. of days	0 (0)	8	0.08 (0.3)	12	.49
Post-op epi, no. of days	1.67 (2.7)	8	1.5 (3)	12	.90
Post-op dobutamine, no. of days	0 (0)	8	0.25 (0.5)	12	.20
Post-op dopamine, no. of days	4.17 (4.4)	8	3.17 (4.3)	12	.64
Post-op hydrocortisone, no. of days	0.33 (0.5)	8	1.67 (5.5)	12	.50
Post-op milirinone, no. of days	3.33 (4.13)	8	3.5 (4.0)	12	.93
Post-op nitroprusside, no. of days	0.0 (0)	8	0.33 (0.9)	12	.37

Note:—PCA indicates postconceptional age; ABG, arterial blood gas; epi, epinephrine; Pre-op, preoperative; Post-op, postoperative.

perioperative variables between the preterm CHD cases with pWMLs and the preterm CHD cases without pWMLs and found that pWMLs were associated with earlier age at surgery ($P < .05$) (Table 3).

TBSS: Preterm Neonates with CHD Versus Term Neonates without CHD

Compared with the term neonates without CHD, the preterm neonates with CHD were found to have significantly reduced fractional anisotropy (FA) in focal regions of the posterior cerebral white matter. This included key regions caudally within the developing visual system (ie, optic radiations and the splenium of the corpus callosum) with relative sparing of the more rostral visual areas (ie, the inferior frontal-occipital fasciculus) (Fig 2, top row; and On-line Appendix Fig 2). There were fewer significantly reduced FA voxels seen in the developing limbic system (ie, fimbria and fornix) and the posterior body of the corpus callosum. There was relative sparing of the developing motor system (ie, posterior limb of the internal capsule and cerebral peduncle).

In contrast with the FA results, changes in diffusivity, including increases in both axial diffusivity and radial diffusivity, were observed in widespread cerebral white matter regions in the preterm neonates with CHD (Fig 2 and On-line Appendix Figs 3 and 4). There was involvement of all neural systems noted including both rostral and caudal visual areas, the limbic system, the motor system, and frontal lobe regions (Fig 2 and On-line Appendix Figs 3 and 4).

To examine whether the differences in the DTI metrics of brain microstructure above reflected maturational differences, we excluded the preterm CHD cases with pWMLs and compared the remaining preterm CHD cases ($n = 13$) to the term neonates without CHD. In this analysis, most of the diffuse microstructural differences disappeared except for persistent decreased FA and increased radial diffusivity in the splenium (On-line Fig 2, bottom row).

TBSS Analysis: Preterm Neonates with CHD Versus Preterm Neonates without CHD

In contrast to the results for the comparison between the patients with CHD and the term comparison group, there were far fewer differences in the white matter of the preterm patients with CHD relative to preterm neonates without CHD. In the analysis corrected for multiple comparisons, no significant differences were detected for FA or any of the diffusivity metrics.

To address whether there were maturation differences between the preterm neonates with CHD and the neonates without CHD, we repeated the above analyses while excluding the preterm neonates with CHD with pWMLs. Notably, no significant differences were detected in any brain region for any DTI metric in either the corrected or uncorrected data.

TBSS Analysis: Complex CHD Preterm Cases Compared with Other Heart Lesions. We compared complex preterm CHD cases (hypoplastic left heart syndrome, transposition of the great arteries, and Ebstein with significant valvular disturbance) with the other preterm CHD anomalies (atrial septal defect, ventricular septal defect, patent ductus arteriosus, coarctation, double-outlet right ventricle with subaortic ventricular septal defect). There were diffuse microstructural abnormalities, including decreased FA and increased axial diffusivity and radial diffusivity in widespread white matter regions, in the single-ventricle physiology cases compared with the other CHD cases (Fig 3, top row). However, when the analysis was corrected for the number of pWMLs, no differences were detected between these 2 groups (Fig 3, bottom row). Of note, there was relative sparing of the corpus callosum, including the splenium, suggesting that splenium was microstructurally similar between the 2 preterm CHD groups (Fig 3). Similar results were also obtained when the hypoplastic left heart syndrome and transposition cases were grouped together and compared with all of the other heart lesions (data not shown).

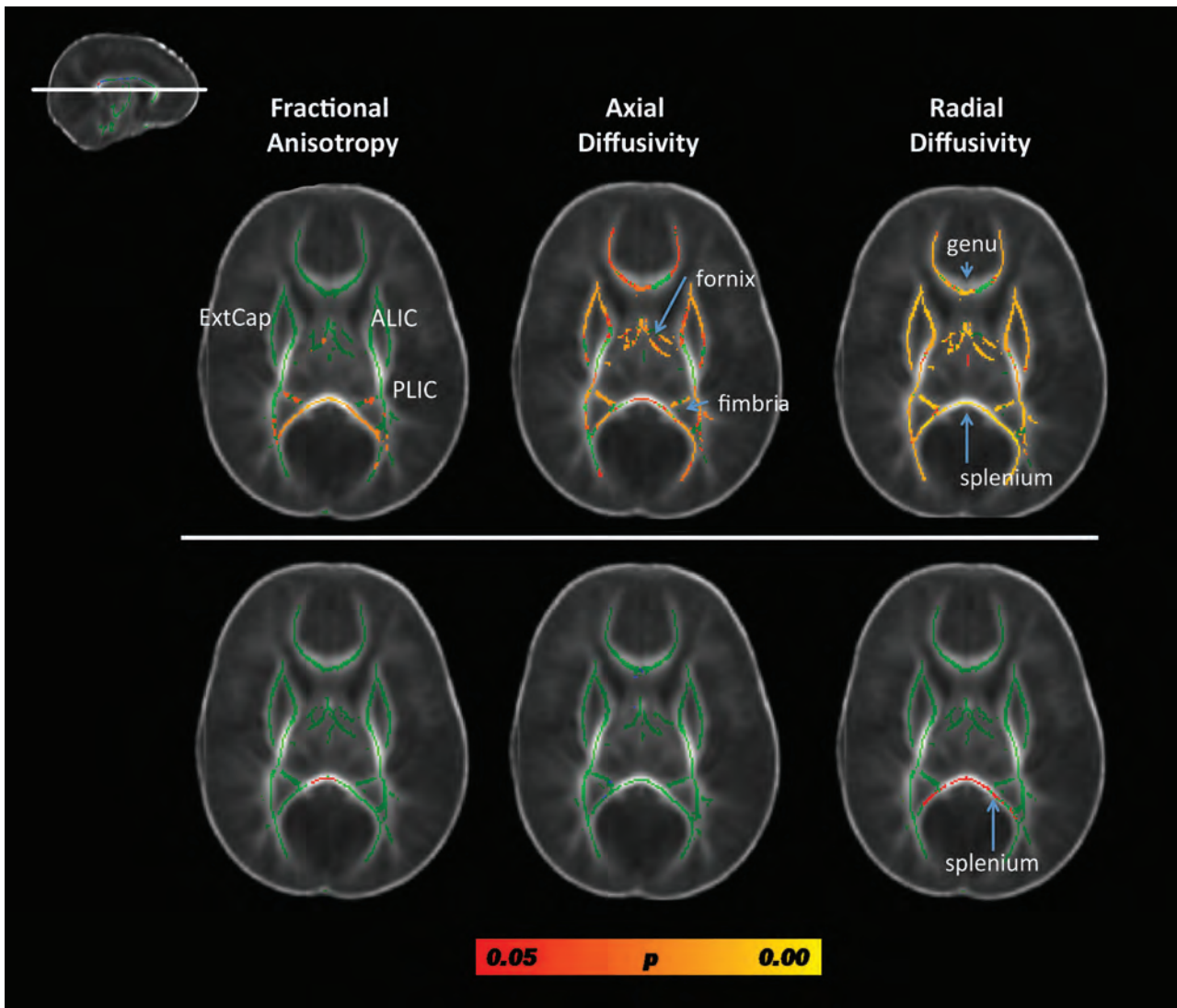


FIG 2. Results from the whole-brain, voxelwise TBSS analysis contrasting fractional anisotropy, axial diffusivity, and radial diffusivity metrics between preterm patients with CHD and term neonates without CHD, controlling for postconceptional age. Results from a single cut at the level of the genu and splenium of the corpus callosum are displayed (see *inlay in the upper left*). The *top row* includes data from comparing all preterm CHD cases to the term neonates without CHD. Diffuse microstructural abnormalities are seen in nearly all white matter regions. The *bottom row* includes data from comparing only the preterm CHD cases without pWMLs with the term neonates without CHD. The only structure showing microstructural abnormality is the splenium. Voxels showing a significant reduction in FA and axial diffusivity and a significant increase in radial diffusivity are shown in red-yellow, with the color bar denoting statistical significance, corrected for multiple comparisons. Note that most of the group differences are due to the cases with pWMLs or periventricular leukomalacia. ExtCap indicates external capsule; ALIC = anterior limb of the internal capsule; PLIC = posterior limb of the internal capsule.

DISCUSSION

Microstructural abnormalities and white matter injury, namely pWMLs, a putative MR imaging biomarker for noncavitary periventricular leukomalacia, have been well documented in previous studies of term neonates with CHD.^{9-12,16-19} This is the first study, to our knowledge, to use MR imaging and DTI to describe the occurrence of pWMLs and associated brain microstructural abnormalities in preterm neonates with CHD. Our most significant finding is that preterm neonates with CHD demonstrate diffuse microstructural changes in central white matter tracts (subserving visual, motor, limbic, and frontal executive functions) when compared with other critically ill neonates without CHD. However, these microstructural abnormalities were strongly associated with the presence of pWMLs. Importantly, we did not

observe many diffuse microstructural differences between preterm infants with CHD and preterm infants without CHD when the infants with pWMLs were excluded. Moreover, after correction for number of pWMLs, there was no difference in microstructure of complex CHD cases compared with other heart lesions. These findings support the hypothesis that there are diffuse microstructural abnormalities in preterm CHD cases and indicate that the microstructural abnormalities are most strongly associated with white matter injury. Of note, independent of white matter injury, we identified a microstructural abnormality in the splenium of the corpus callosum in all preterm infants with CHD. The splenium is composed of white matter pathways connecting visual regions, and these microstructural differences may be a biomarker for vulnerability for visual spatial dysfunction, which

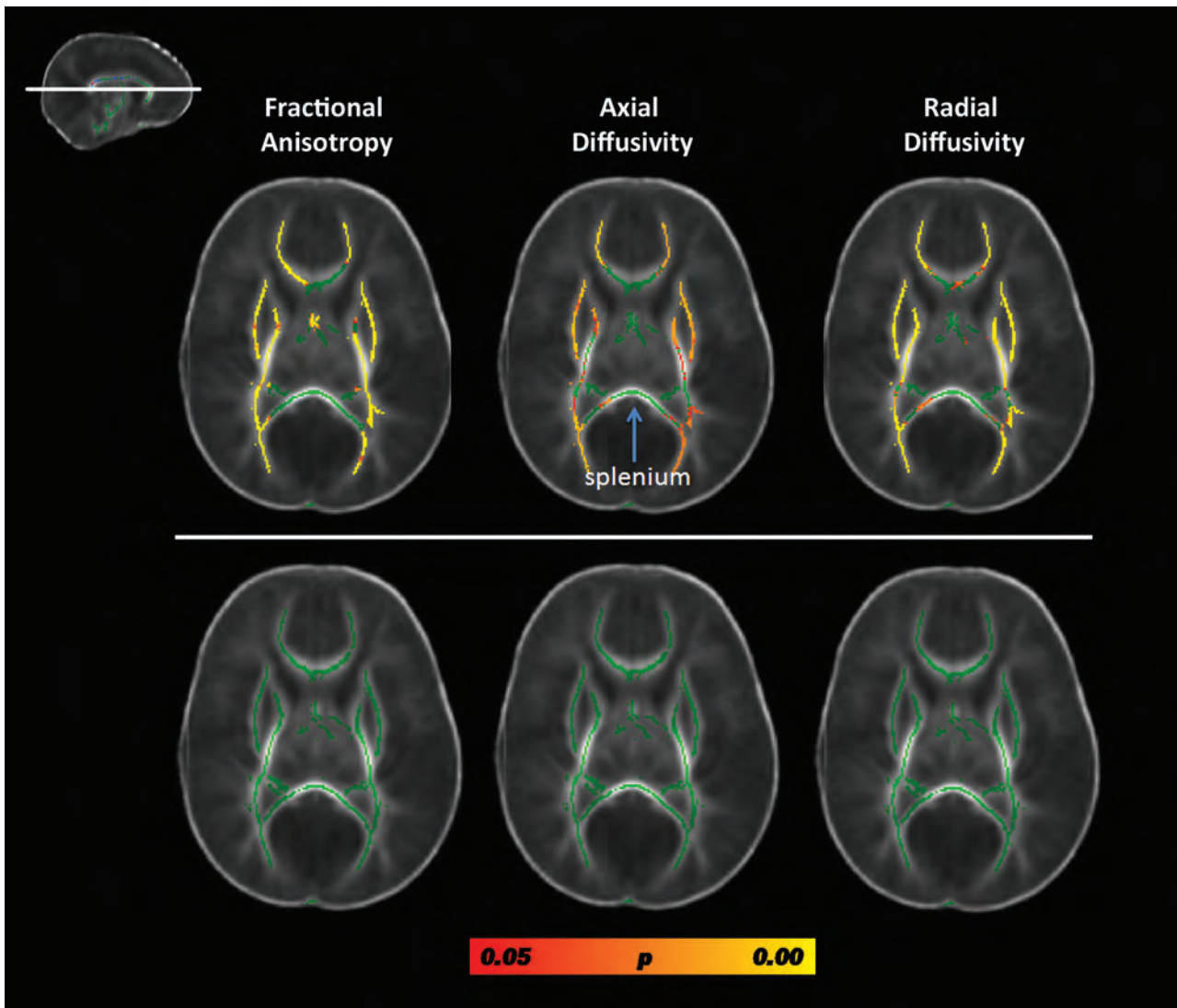


FIG 3. Results from the TBSS analysis contrasting FA, axial diffusivity (AD), and radial diffusivity (RD) in preterm patients with CHD with complex CHD lesions compared with preterm patients with CHD other heart lesions. Results from a single cut at the level of the genu and splenium of the corpus callosum are displayed (see *inlay*). The *top row* depicts the results of the contrasts between the preterm neonates with complex heart lesions relative to the preterm neonates with other heart lesions; the *bottom row* depicts the results from the contrasts of the same cases after correction for number of pWMLs. Both analyses are corrected for postconceptional age. Voxels showing a significant reduction in FA and AD and a significant increase in RD are shown in red-yellow, with the color bar denoting statistical significance, corrected for multiple comparisons. Of note, there is no difference in DTI metrics values in the splenium of the corpus callosum (*arrow*) between heart types.

is a well-described neurocognitive deficit observed in survivors of CHD.^{27–29}

Similar to prior studies of term infants with CHD,¹² we observed diffuse microstructural abnormalities in our preterm infants with CHD compared with term infants without CHD. However, in our study, these differences were largely attributable to the presence of pWMLs rather than maturational lag as had been suggested by Miller et al¹² in their analysis of term neonates with CHD. We did observe regional maturational differences (centered in the splenium); however, our widespread abnormalities in microstructure were only observed in the preterm neonates with CHD with pWMLs. This suggests that although the maturational state of the brain probably plays a role in the vulnerability to white matter injury, injury during the perinatal period and the associated microstructural abnormalities may best account for adverse

neurodevelopmental outcomes in the preterm neonates with CHD.³⁰

A maturational delay in fetal brain development has been described in term neonates with complex CHD.^{13,31} Importantly, the available data suggest that the maturational delay accelerates during the late third trimester.¹³ Thus, for a cohort of neonates with CHD born on average at 32 weeks gestational age, it would not necessarily be expected that we would observe global maturational delays on the microstructure of the cerebral white matter arising from delayed intrauterine development. Other techniques including structural imaging techniques may be more sensitive to detect maturational differences in this population, as demonstrated previously in term CHD cases.¹⁴

Consistent with prior studies of CHD, the highest incidence of pWMLs and concurrent microstructural abnormalities was

found in the infants with hypoplastic left heart syndrome. It is well established that these infants are at exceedingly high risk for maturational delay and perinatal brain injury owing to the complex factors associated with abnormal uterine brain development and abnormal cerebral perfusion.^{10,11,32} However, not all of the infants with hypoplastic left heart syndrome have significant long-term neurocognitive problems, and initial results from the multicenter single ventricle reconstruction trial indicate that early neurodevelopmental outcome is more highly associated with innate patient variables than with intraoperative management strategies.³³ In this analysis, there were no differences in microstructure between the neonates with complex CHD and neonates with other congenital heart lesions after correcting for the number of pWMLs. It is possible that pWMLs or associated microstructural abnormalities at the neonatal time period will be able to further distinguish among the infants with hypoplastic left heart syndrome, who are at highest risk for specific adverse neurodevelopmental outcomes.

Longitudinal studies of neonates with CHD have documented neurocognitive impairments across multiple cognitive domains, but most prominently in visual-spatial functions, executive functions, and language.^{27–29,34–38} In this study, widespread microstructural abnormalities involving neural systems subserving the visual system, motor system, limbic system, and frontoparietal executive system were identified in the preterm neonates with CHD with pWMLs. These results suggest that irrespective of heart lesion, this subpopulation of preterm neonates with CHD would be most at risk for long-term neurocognitive deficits involving visual functions, motor development, emotions/behavioral regulation, and attention/executive functions.³⁸

In contrast, the preterm neonates with CHD but without pWMLs were found to have microstructural abnormalities in the vicinity of the splenium—the posterior bundle of callosal crossing fibers. The splenium is one of the most rapidly developing white matter structures during the late fetal and early postnatal period.³⁹ The splenium contains fiber bundles crossing between temporal and occipital regions of the left and right hemispheres that are important for normal visual-spatial functions. Accordingly, the finding of a microstructural abnormality in the preterm CHD cases without PVL compared with term controls suggests that the infants with CHD may be at increased risk for visual-spatial dysfunction regardless of the presence of brain injury.^{27–29}

We found that younger age at surgery and increased use of inotropes were associated with pWMLs in the preterm CHD group, similar to previous studies of pWMLs in term patients with CHD, suggesting a similar pathogenesis or vulnerability to white matter injury in both the preterm and term CHD groups.³⁰ One remarkable clinical distinction between the preterm CHD group and both control groups was the high incidence of being small for gestational age in the preterm CHD group, suggesting that there could still be a prenatal influence on white matter vulnerability and injury in this group.⁴⁰

Limitations

It could be suggested that we should have focused on the major left-sided heart lesions and excluded infants with other lesions such as atrial septal defect or ventricular septal defect due to

marked differences in the hemodynamics in these neonates both in utero and postnatally.³² However, the incidence of hypoplastic left heart syndrome among preterm infants is relatively rare and we did not have sufficient sample size to include these lesions alone. A second limitation in this study is the inclusion of cases with MR imaging scans performed preoperatively and postoperatively. Third, there is the potential for sampling bias as we relied on clinical scans to identify our neonates before induction. Fourth, our study sample size was small and recruited from a single institution.

CONCLUSIONS

Our study provides evidence that preterm neonates with CHD demonstrate diffuse microstructural changes in central white matter tracts when compared with other critically ill neonates without CHD. However, these microstructural changes are highly associated with the occurrence of pWMLs, a biomarker for non-cavitary periventricular leukomalacia. Regardless of injury, a persistent microstructural abnormality was noted in the splenium, which could explain the high prevalence of visual-spatial neurocognitive dysfunction in surviving patients with CHD. This study suggests that MR imaging may not only have a beneficial role in identifying preterm infants with CHD who are at the greatest risk for adverse neurodevelopmental outcome, but also may be a clinical biomarker to help guide potential neuroprotective or rehabilitative therapies in this population.

ACKNOWLEDGMENTS

The authors thank Julie Castro, Anita Hamilton, and Hesham Mahmoud for their assistance with patient recruitment and data management. We also thank Drs Hannah Kinney and Dr Istvan Seri for careful review of the manuscript. We thank Melanie Gieraltowski for manuscript preparation.

Disclosures: *RELATED: Grant: NINDS (listed under grant funding)* (*money paid to institution).*

REFERENCES

1. Marino BS, Lipkin PH, Newburger JW, et al. **Neurodevelopmental outcomes in children with congenital heart disease: evaluation and management: a scientific statement from the American Heart Association.** *Circulation* 2012;126:1143–72
2. Tanner K, Sabrine N, Wren C. **Cardiovascular malformations among preterm infants.** *Pediatrics* 2005;116:e833–e838
3. Dees E, Lin H, Cotton RB, et al. **Outcome of preterm infants with congenital heart disease.** *J Pediatr* 2000;137:653–59
4. Cheng HH, Almodovar MC, Laussen PC, et al. **Outcomes and risk factors for mortality in premature neonates with critical congenital heart disease.** *Pediatr Cardiol* 2011;32:1139–46
5. Natarajan G, Anne SR, Aggarwal S. **Outcomes of congenital heart disease in late preterm infants: double jeopardy?** *Acta Paediatr* 2011;100:1104–07
6. Gelehrter S, Fifer CG, Armstrong A, et al. **Outcomes of hypoplastic left heart syndrome in low-birth-weight patients.** *Pediatr Cardiol* 2011;32:1175–81
7. Costello JM, Polito A, Brown DW, et al. **Birth before 39 weeks' gestation is associated with worse outcomes in neonates with heart disease.** *Pediatrics* 2010;126:277–84
8. Goff DA, Luan X, Gerdes M, et al. **Younger gestational age is associated with worse neurodevelopmental outcomes after cardiac surgery.** *J Thorac Cardiovasc Surg* 2012;143:535–42

9. Andropoulos DB, Hunter JV, Nelson DV, et al. **Brain immaturity is associated with brain injury before and after neonatal cardiac surgery with high-flow bypass and cerebral oxygenation monitoring.** *J Thorac Cardiovasc Surg* 2010;139:543–56
10. McQuillen PS, Miller SP. **Congenital heart disease and brain development.** *Ann N Y Acad Sci* 2010;1184:68–86
11. McQuillen PS, Goff DA, Licht DJ. **Effects of congenital heart disease on brain development.** *Prog Pediatr Cardiol* 2010;29:79–85
12. Miller SP, McQuillen PS, Hamrick S, et al. **Abnormal brain development in newborns with congenital heart disease.** *N Engl J Med* 2007;357:1928–38
13. Limperopoulos C, Tworetzky W, McElhinney DB, et al. **Brain volume and metabolism in fetuses with congenital heart disease: evaluation with quantitative magnetic resonance imaging and spectroscopy.** *Circulation* 2010;121:26–33
14. Licht DJ, Shera DM, Clancy RR, et al. **Brain maturation is delayed in infants with complex congenital heart defects.** *J Thorac Cardiovasc Surg* 2009;137:529–37
15. Watanabe K, Matsui M, Matsuzawa J, et al. **Impaired neuroanatomic development in infants with congenital heart disease.** *J Thorac Cardiovasc Surg* 2009;137:146–53
16. Galli KK, Zimmerman RA, Jarvik GP, et al. **Periventricular leukomalacia is common after neonatal cardiac surgery.** *J Thorac Cardiovasc Surg* 2004;127:692–704
17. Mahle WT, Tavani F, Zimmerman RA, et al. **An MRI study of neurological injury before and after congenital heart surgery.** *Circulation* 2002;106:1109–1114
18. Partridge SC, Vigneron DB, Charlton NN, et al. **Pyramidal tract maturation after brain injury in newborns with heart disease.** *Ann Neurol* 2006;59:640–51
19. Kinney HC, Panigrahy A, Newburger JW, et al. **Hypoxic-ischemic brain injury in infants with congenital heart disease dying after surgery.** *Acta Neuropathol* 2005;110:563–78
20. Miller SP, Ferriero DM, Leonard C, et al. **Early brain injury in premature newborns detected with magnetic resonance imaging is associated with adverse neurodevelopmental outcomes.** *J Pediatr* 2005;147:609–16
21. Nanba Y, Matsui K, Aida N, et al. **Magnetic resonance imaging regional T1 abnormalities at term accurately predicts motor outcome in preterm infants.** *Pediatrics* 2007;120:e10–e19
22. Buser JR, Maire J, Riddle A, et al. **Arrested preoligodendrocyte maturation contributes to myelination failure in premature infants.** *Ann Neurol* 2012;71:93–109
23. Miller SP, Ferriero DM. **From selective vulnerability to connectivity: insight from newborn brain imaging.** *Trends Neurosci* 2009;32:496–505
24. Bartha AI, Yap KR, Miller SP, et al. **The normal neonatal brain: MR imaging, diffusion tensor imaging, and 3D MR spectroscopy in healthy term neonates.** *AJNR Am J Neuroradiol* 2007;28:1015–21
25. Smith SM. **Tract-based spatial statistics: voxelwise analysis of multi-subject diffusion data.** *Neuroimage* 2006;31:1487–505
26. Ball G, Counsell SJ, Anjari M, et al. **An optimised tract-based spatial statistics protocol for neonates: applications to prematurity and chronic lung disease.** *Neuroimage* 2010;53:94–102
27. Bellinger DC, Newburger JW. **Neuropsychological, psychosocial, and quality-of-life outcomes in children and adolescents with congenital heart disease.** *Prog Pediatr Cardiol* 2010;29:87–92
28. Kravitz DJ, Saleem KS, Baker CI, et al. **A new neural framework for visuospatial processing.** *Nat Rev Neurosci* 2011;12:217–30
29. Bellinger DC, Bernstein JH, Kirkwood MW, et al. **Visual-spatial skills in children after open-heart surgery.** *J Dev Behav Pediatr* 2003;24:169–79
30. Ishibashi N, Scafidi J, Murata A, et al. **White matter protection in congenital heart surgery.** *Circulation* 2012;125:859–71
31. Clouchoux C, du Plessis AJ, Bouyssi-Kobar M, et al. **Delayed cortical development in fetuses with complex congenital heart disease.** *Cereb Cortex* 2012 Sep 12. [Epub ahead of print]
32. Kaltman JR, Di H, Tian Z, et al. **Impact of congenital heart disease on cerebrovascular blood flow dynamics in the fetus.** *Ultrasound Obstet Gynecol* 2005;25:32–36
33. Newburger JW, Sleeper LA, Bellinger DC, et al. **Early developmental outcome in children with hypoplastic left heart syndrome and related anomalies: the single ventricle reconstruction trial.** *Circulation* 2012;125:2081–91
34. Ballweg JA, Wernovsky G, Gaynor JW. **Neurodevelopmental outcomes following congenital heart surgery.** *Pediatr Cardiol* 2007;28:126–33
35. Bellinger DC, Wypij D, Rivkin MJ, et al. **Adolescents with d-transposition of the great arteries corrected with the arterial switch procedure: neuropsychological assessment and structural brain imaging.** *Circulation* 2011;124:1361–69
36. Mahle WT, Clancy RR, Moss EM, et al. **Neurodevelopmental outcome and lifestyle assessment in school-aged and adolescent children with hypoplastic left heart syndrome.** *Pediatrics* 2000;105:1082–89
37. Karsdorp PA, Everaerd W, Kindt M, et al. **Physiological and cognitive functioning in children and adolescents with congenital heart disease.** *Pediatr Psychol* 2007;32:527–41
38. Shillingford AJ, Glanzman MM, Ittenbach RF, et al. **Inattention, hyperactivity, and school performance in a population of school-age children with complex congenital heart disease.** *Pediatrics* 2008;121:e759–e767
39. Kasprian G, Brugger PC, Weber M, et al. **In utero tractography of fetal white matter development.** *Neuroimage* 2008;43:213–24
40. Padilla N, Falcón C, Sanz-Cortés M, et al. **Differential effects of intrauterine growth restriction on brain structure and development in preterm infants: a magnetic resonance imaging study.** *Brain Res* 2011;1382:98–108

Neuroradiologic Features in X-linked α -Thalassemia/Mental Retardation Syndrome

T. Wada, H. Ban, M. Matsufuji, N. Okamoto, K. Enomoto, K. Kurosawa, and N. Aida



ABSTRACT

BACKGROUND AND PURPOSE: X-linked α -thalassemia/mental retardation syndrome (Mendelian Inheritance in Man, 301040) is one of the X-linked intellectual disability syndromes caused by mutations of the *ATRX* gene and characterized by male predominance, central hypotonic facies, severe cognitive dysfunction, hemoglobin H disease (α -thalassemia), genital and skeletal abnormalities, and autistic and peculiar behavior. More than 200 patients in the world, including >70 Japanese patients, have been diagnosed with ATR-X syndrome.

MATERIALS AND METHODS: We reviewed the brain MRI and/or CT findings of 27 Japanese patients with ATR-X with *ATRX* mutations retrospectively.

RESULTS: The findings were categorized into 5 types: 1) nonspecific brain atrophy (17/27); 2) white matter abnormalities, especially around the trigones (11/27); 3) widespread and scattered white matter abnormalities (1/27); 4) delayed myelination (4/27); and 5) severe and rapidly progressive cortical brain atrophy (1/27).

CONCLUSIONS: This is the first report on a comprehensive study of brain MRI/CT findings of ATR-X syndrome. Our findings suggest that the *ATRX* protein seems to be involved in normal myelination. The classification will require revisions in the near future, but it will be helpful in establishing the relationship between *ATRX* mutation and brain development and understanding the *ATRX* protein function in the brain.

ABBREVIATIONS: ADD domain = *ATRX*-DNMT3-DNMT3L; ATR-X (*ATRX*) = X-linked α -thalassemia/mental retardation

X-linked α -thalassemia/mental retardation syndrome (Mendelian Inheritance in Man, 301040) is one of the X-linked intellectual disability syndromes and is due to mutations of the *ATRX* gene on Xq13.3, encoding a SWI/SNF-like chromatin remodeling protein.¹ The *ATRX* protein has 2 functionally important domains: the zinc-finger motif (ADD) and the highly conserved chromatin-remodeling domain, where the *ATRX* mu-

tations cluster.² Although the pathophysiologic mechanism of ATR-X syndrome is not yet completely known, ATR-X syndrome is one of the chromatin diseases (which include Rett, Coffin-Lowry, and Rubinstein-Taybi syndromes), and a disturbance of the epigenetic mechanism is suggested.³

More than 200 patients in the world, >70 of whom are Japanese, have been diagnosed with ATR-X syndrome.^{2,4} ATR-X syndrome seems to be a rare disease; however, we estimate that the prevalence of ATR-X syndrome is 1/30,000–40,000 neonate boys, which is much higher than previously reported estimations (K. Kurosawa, unpublished data 2012). Therefore, more patients remain to be diagnosed because 7–9 patients with ATR-X should be diagnosed every year based on the fact we have 1 million neonates born every year in Japan.

In 2010, we established the ATR-X Syndrome Network Japan (<http://kcmc.jp/ATR-X/index.html>) for patients and their families, and we have surveyed patients with ATR-X syndrome in Japan. The ultimate purpose of our clinical research is to establish diagnostic criteria, which would facilitate further clinical study of individuals with molecularly proved ATR-X, assist in the evaluation of those who appear to exhibit the clinical features of ATR-X with no *ATRX* mutations, and establish the management of ATR-X syndrome.

Received September 28, 2012; accepted after revision December 17.

From the Divisions of Neurology (T.W.), Genetics (K.E., K.K.), and Radiology (N.A.), Kanagawa Children's Medical Center, Yokohama, Japan; Department of Pediatrics (H.B.), Himeji Red Cross Hospital, Himeji, Japan; Department of Pediatrics (M.M.), Yanagawa Institute for Developmental Disabilities, Yanagawa, Japan; and Department of Molecular Medicine (N.O.), Osaka Medical Center and Research Institute for Maternal and Child Health, Osaka, Japan.

This work was supported by a research grant for Intractable Diseases from the Ministry of Health, Labour and Welfare of Japan (H22-nanchi-ippan-114).

Paper previously presented in the poster session at: American Society of Human Genetics hosting the 12th International Congress of Human Genetics, October 11–15, 2011; Montreal, Quebec, Canada.

Please address correspondence to Takahito Wada, MD, PhD, 2-138-4 Mutsukawa, Minami-ku, Yokohama, Kanagawa 232-8555, Japan; e-mail: takahito.wada0001@me.com

Indicates open access to non-subscribers at www.ajnr.org

Indicates article with supplemental on-line table

<http://dx.doi.org/10.3174/ajnr.A3560>

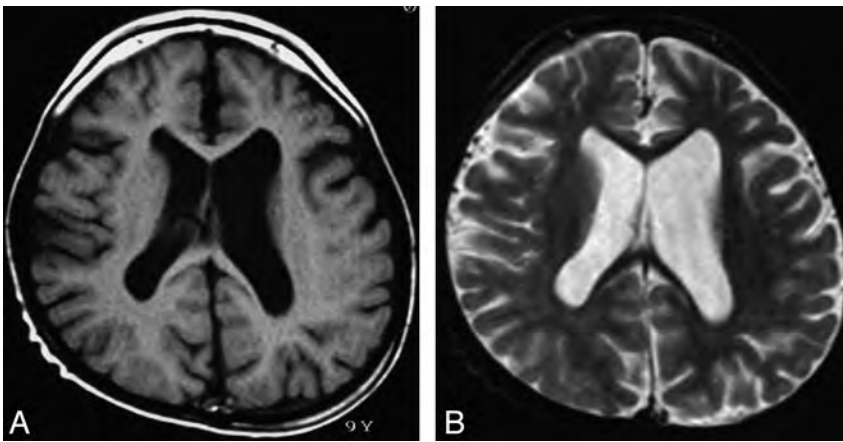


FIG 1. Type 1. Nonspecific brain atrophy. T1WI (A) and T2WI (B) of a 9-year-old patient (case 4) with an *ATRX* mutation of the ADD domain in exon 6 (c.390_391 ins A; E131fs). Nonprogressive diffuse cortical brain atrophy and ventricular enlargement due to loss of white matter volume are shown.

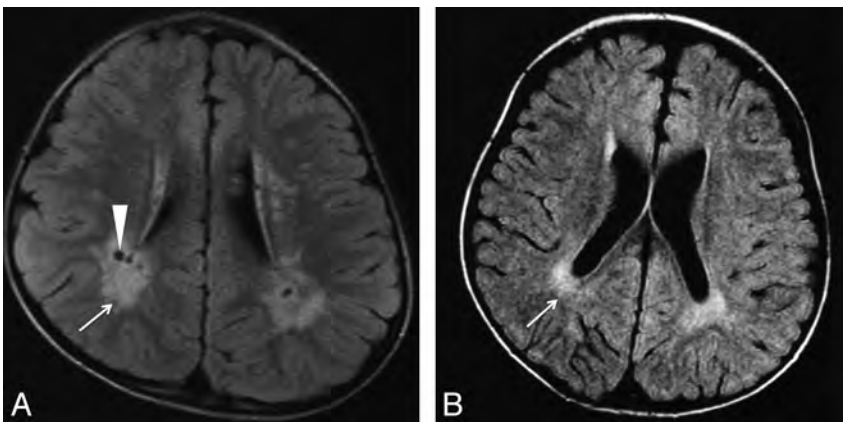


FIG 2. Type 2. White matter abnormalities, especially around the trigones. FLAIR image of a 4-year-old patient (case 22) (A) with an *ATRX* mutation of the chromatin-remodeling domain in exon 19 (p.V1624M), and a 35-month-old patient (case 21) (B) with an *ATRX* mutation of the chromatin-remodeling domain in exon 19 (p.A1622V). Increased signal intensity on T1WI/FLAIR in the periventricular region, especially around the peritrigonal area (arrow), and enlargement of perivascular space (arrowhead) are seen.

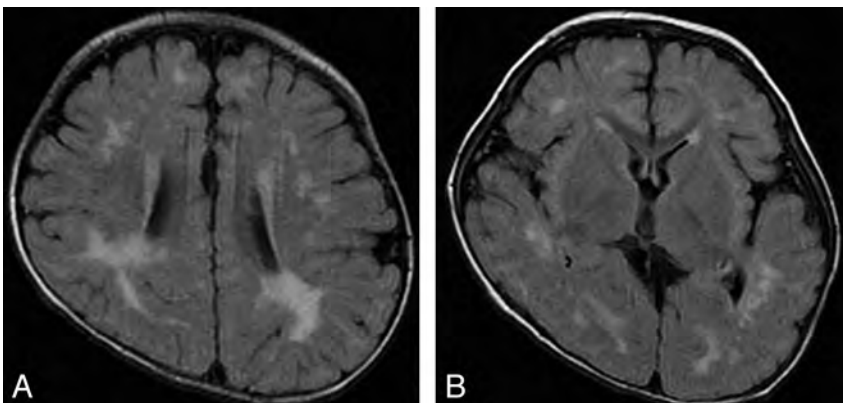


FIG 3. Type 3. Widespread and scattered white matter abnormalities. FLAIR image of a 12-month-old patient (case 1) with an *ATRX* mutation of a nucleotide substitution in 5'-UTR. Note high signal intensity on FLAIR/T2WI in the white matter, especially in the peritrigonal area and deep white matter, not in a diffuse but in a widespread and scattered pattern.

Because few comprehensive studies of brain MRI/CT of *ATRX*-X syndrome are available, we propose here the classification of brain MRI/CT findings in the case of *ATRX*-X syndrome.

MATERIALS AND METHODS

We reviewed the brain MRI/CT findings of 27 Japanese patients with *ATRX*-X who exhibited *ATRX* mutations retrospectively. The images came from our medical center and from referrals sent to our center for consultation and spanned 1994–2012. They were evaluated by a pediatric neuroradiologist, a pediatric radiologist, or pediatric neurologists. The mutations of patients 5–18 reside in the ADD domain; those of patients 20–24, in the chromatin-remodeling domain. Other mutations are outside these 2 domains, and all of these mutations cause loss-of-function mutations (On-line Table). Their ages at the time of the evaluated MRI/CT ranged from 4 months to 54 years of age. MR imaging of the brain was performed at 1.5T or 3T at multiple medical centers. Axial T1WI, T2WI, and FLAIR or CT scans were evaluated. DWI was examined in a limited number of patients. Patients with severe prematurity and clinical signs of neonatal hypoxic-ischemic injury that would result in white matter and/or cortex abnormalities on MRI or CT scans were excluded from this study.

RESULTS

The MRI/CT findings and *ATRX* mutations of 27 patients with *ATRX*-X are summarized in the On-line Table. The brain CT scans/MRI of all 27 patients whose scans were available showed some abnormal findings: Nonspecific brain atrophy (type 1, Fig 1) was shown in 17 of 27 patients (63%); a high intensity of white matter especially around the trigones, or the terminal zone, with/without multiple small spheric foci on FLAIR/T2WI (type 2, Fig 2) was seen in 11 patients (41%). Type 2 with hypoplasia of the cerebellar vermis was shown in 1 patient (case 22), and type 2 with hypoplasia of the corpus callosum and ventricular enlargement was seen in 1 patient (case 25). Compared with type 1, type 2 seemed more frequent in patients with mutations in the chromatin-remodeling domain. Four had hypoplasia of the corpus callosum. Furthermore, widespread and scattered white matter abnormalities on FLAIR (type 3, Fig 3) were seen in 1 patient (case 1). Delayed myelination (type 4, Fig 4) was shown in 4 (15%), and severe and rapidly progressive cortical brain atrophy with ventricular enlargement (type 5, Fig 5) was seen in 1 patient (case 27). No alterations of cerebral diffusion

could be observed on DWI in any patients with types 3, 4, and 5.

DISCUSSION

This is the first report on a comprehensive study of brain CT/MRI findings of patients with ATR-X syndrome, though some case reports or personal accounts mentioned some findings of brain MRI/CT, including mild cerebral atrophy, partial or complete agenesis of the corpus callosum, and hypoplasia of the white matter.^{5,6} Our results suggest that brain MRI/CT can present a broader spectrum of abnormalities in both white and gray matter than has been expected in ATR-X syndrome. Some of our patients with ATR-X were referred to our medical center because their MRI/CT scans showed white matter abnormalities, or myelination; and for some, leukodystrophy was suspected as their diagnosis. Therefore, we categorized the MRI/CT findings of 27 patients with ATR-X into 5 types from the point of view of white matter lesions, or myelination.

More patients showed nonspecific brain atrophy (type 1) on brain MRI/CT. This result agrees with the finding that, in a review of 168 patients with ATR-X syndrome, 77% presented with microcephaly.⁷ This brain atrophy in ATR-X syndrome is not pro-

gressive, and it seems to be due to the reduced production of neurons or glia in the perinatal period, not to some destructive process. This characterization was supported by a study by Bérubé et al⁸ by using a conditional targeting approach with mice, showing that *ATRX* is a critical mediator of cell survival during early neuronal differentiation and that increased neuronal loss may contribute to severe mental retardation.⁸

Types 2 and 3 suggest an abnormality of the white matter, or myelination. Type 2 includes white matter abnormalities, especially around the trigones, with increased signal intensity showing on T2WI/FLAIR in the periventricular region. Persistently high signal intensity in this peritrigonal area, or the terminal zones, is seen throughout the first decade of life, and it is sometimes very difficult to differentiate from white matter injury resulting from prematurity, which results in periventricular leukomalacia. Moreover, a layer of myelinated white matter is present between the trigones of the ventricle and the terminal zones in healthy patients.⁹ The findings shown in our patients with ATR-X differ from slow myelination in these areas or terminal zones, being normal variants in their distribution and signal intensity. Because these patients did not present clinically with apparent neonatal asphyxia and their findings do not show other signs suggesting periven-

tricular leukomalacia, these white matter abnormalities may be relatively frequent findings in CT/MRI of ATR-X syndrome.

Especially type 3, with its widespread and scattered white matter abnormalities, strongly suggests that normal expression of the *ATRX* protein is involved in normal myelination because the patient's mutation is a nucleotide substitution in 5'-UTR and *ATRX* expression should be reduced, though the *ATRX* protein structure is normal. Actually, red cells of case 1 had more hemoglobin H inclusions (5%) than those of other patients, and he had hypospadias. Most interesting, his development was much better than that of typical patients with ATR-X, and he can walk and speak a few words. This suggests that the quantity of the *ATRX* pro-

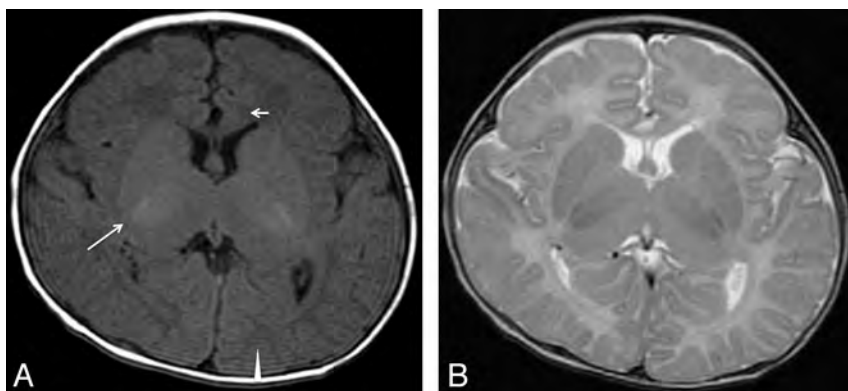


FIG 4. Type 4. Delayed myelination. T1WI (A) and T2WI (B) of a 4-month-old patient (case 26) with an *ATRX* mutation in exon 35 (c.7156C>T, p.Arg2386Stop). Myelination appears only at the posterior limb of the internal capsule (*long arrow*) on T1WI. At 4 months of age in a healthy infant, high intensity should extend from the junction of the anterior limb of the internal capsule at the callosal genu (*short arrow*) all the way back to the visual cortex (*arrowhead*) along the internal capsule and optic radiations.

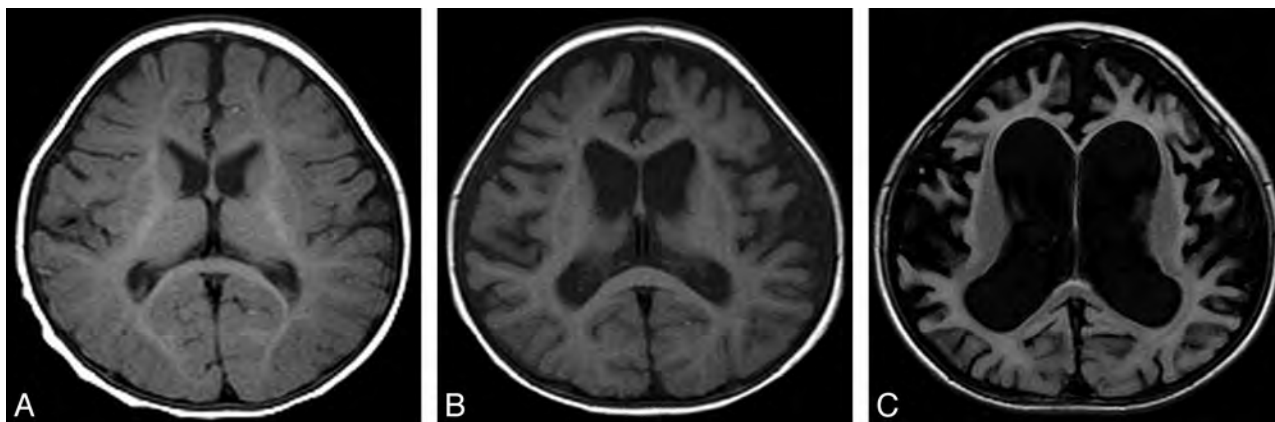


FIG 5. Type 5. Progressive brain atrophy. Sequential change of brain MR imaging of patient 27 with an *ATRX* mutation in int 35 (c.7200 + 4A>G, p.L2401fs) at 6 months (T1WI) (A), 14 months (T1WI) (B), and 34 months (FLAIR) (C).

tein can affect α -globin expression, genital development, and myelination, but the quality of the ATRX protein is more important for intellectual ability. Another possibility is that the site of the mutation may be more important for ATRX expression in the oligodendroglia, which is involved in myelination. The delayed myelination in type 4 also supports the idea that ATRX is important for normal myelination.

High signal on T2WI/FLAIR and no alteration on DWI in the white matter of these patients meaning that there is no cytotoxic edema but increased water content in the white matter region, and these findings may suggest the prematurity of the blood-brain barrier in ATR-X syndrome, though our data have limitations in that not all MRI/CT scans include diffusion imaging or contrast enhancement.

Most interesting, 2 patients with ATR-X with partial duplications of the ATRX gene, resulting a severe reduction of ATRX messenger RNA and absence of the ATRX protein, presented with normal brain MR imaging findings and agenesis of the corpus callosum, respectively.¹⁰ The former patient was evaluated before his death at 4.5 months of age, and it was difficult to detect white matter abnormalities. For the latter patient, although the age when the MR imaging was evaluated was 6 months, we cannot specify his age. He could have been too young for evaluation of myelination on MR imaging, and agenesis of the corpus callosum is the ultimate result of white matter abnormality. That finding does not contradict our theory that ATRX is important for normal myelination. However, more data should be forthcoming to clarify the relation between the ATRX protein and white matter or myelination.

Progressive brain atrophy in type 5 is an exceptional finding of CT/MRI in ATR-X syndrome. The patient with type 5 presented with a severe developmental delay and intractable epilepsy following West syndrome, which is rare in ATR-X syndrome. He had no episodes of hypoxic encephalopathy. Although it is possible that he may have had some other pathologic conditions, ATR-X syndrome should be considered in the differential diagnosis of patients with progressive brain atrophy on brain MRI/CT. His mutation was in int 35, or the last intron, resulting in skipping exon 35, which consists of 126 base pairs, and the introduction of a 43-amino-acid-deleted ATRX protein. This truncated protein may be related to his severe intellectual disability or epileptic condition.

A gray matter abnormality seems more frequent in those patients with ATRX mutation in the ADD domain, or exons 8, 9, and 10, and a white matter abnormality in the chromatin-remodeling domain, or exons 18 to 31. These results would indicate that mutations in the ADD domain produce more severe and permanent psychomotor deficiencies than those in chromatin-remodeling domains, though the clear phenotype-genotype correlation remains to be established.¹¹ However, conclusion may be too hasty because we have studied fewer cases with ATRX mutations in the chromatin-remodeling domains.

A number of intellectual disorders have been identified whose gene products regulate chromatin and chromosome architecture, and ATR-X syndrome is a disease of chromatin remodeling, as well as Rett syndrome (*MeCP2*) and Cornelia de Lange syndrome (*SMC1A*, *SMC3*, and *NIPBL*).^{3,12} These 3 diseases share clinical

manifestations, including severe intellectual disabilities, and ATRX, MeCP2, and cohesion proteins, respectively, indicating that these syndromes directly or indirectly interact with each other. Although these syndromes share a common final pathway to their pathogenesis, there are no common characteristic findings on brain MRI/CT among these diseases, except for brain hypoplasia or atrophy. These abnormal signals in the white matter on MR imaging seem to be relatively specific findings in ATR-X syndrome.

We propose that these findings should be included as associated (<50%) or supporting features of the diagnostic criteria for ATR-X syndrome. We will evaluate the brain MR imaging/CT of additional patients to validate these findings and update the consensus for the neuroradiologic features as a diagnostic criteria of ATR-X syndrome in the near future.

CONCLUSIONS

This is the first report on a comprehensive study of brain MRI/CT findings of ATR-X syndrome. We consider ATR-X syndrome a differential diagnosis in patients with intellectual disabilities whose brain MRI shows abnormal signals in the white matter. The ATRX protein seems to be involved in normal myelination. The classification will require revisions in the near future but will be helpful to establish the relationship between the ATRX gene mutation and brain development and to understand the ATRX protein function in the brain.

ACKNOWLEDGMENTS

We thank our patients and their families, their doctors, and the ATR-X Research Group in Japan: H. Osaka of the Kanagawa Children's Medical Center, Yokohama, Japan; S. Saitoh of the Nagoya City University Graduate School of Medical Science, Nagoya, Japan; N. Okamoto of the Osaka Medical Center and Research Institute for Maternal and Child Health, Osaka, Japan; Y. Fukushima of Shinshu University, Matsumoto, Japan; N. Matsumoto of Yokohama City University, Yokohama, Japan; H. Tanabe of The Graduate University for Advanced Studies, Hayama, Japan; and Y. Goto of the National Center of Neurology and Psychiatry, Kodaira, Japan. We appreciate Dr. Masahide Goto and Dr. Yoshiro Saito (National Center of Neurology and Psychiatry, Kodaira, Japan) for their useful information.

Disclosures: Takahito Wada—RELATED: Grant: This work is supported by a research grant for Intractable Diseases from the Ministry of Health, Labour and Welfare of Japan (H22-nanchi-ippan-114).

REFERENCES

1. Gibbons RJ, Picketts DJ, Villard L, et al. **Mutations in a putative global transcriptional regulator cause X-linked mental retardation with alpha-thalassemia (ATR-X syndrome).** *Cell* 1995;80:837–45
2. Gibbons RJ, Wada T, Fisher CA, et al. **Mutations in the chromatin-associated protein ATRX.** *Hum Mutat* 2008;29:796–802
3. Tsankova N, Renthal W, Kumar A, et al. **Epigenetic regulation in psychiatric disorders.** *Nat Rev Neurosci* 2007;8:355–67
4. Wada T, Kubota T, Fukushima Y, et al. **Molecular genetic study of Japanese patients with X-linked alpha-thalassemia/mental retardation syndrome (ATR-X).** *Am J Med Genet* 2000;94:242–48
5. Wada T, Nakamura M, Matsushita Y, et al. **Three Japanese children with X-linked alpha-thalassemia/mental retardation syndrome (ATR-X) [in Japanese].** *No To Hattatsu* 1998;30:283–89

6. Gibbons RJ. **ATR-X: a-thalassemia mental retardation-X-linked.** In: Cassidy SB, Allanson JE, eds. *Management of Genetic Syndromes*. Hoboken, New Jersey: John Wiley & Sons; 2010:97–109
7. Gibbons RJ, Wada T. **ATRX and the X-linked a-thalassemia mental retardation syndrome.** In: Epstein CJ, Erickson PP, Wynshaw-Boris A, eds. *Inborn Errors of Development*. 2nd ed. New York: Oxford University Press; 2008:943–54
8. Bérubé NG, Mangelsdorf M, Jagla M, et al. **The chromatin-remodeling protein ATRX is critical for neuronal survival during corticogenesis.** *J Clin Invest* 2005;115:258–67
9. Barkovich AJ, Raybaud C. **Normal development of the neonatal and infant brain, skull, and spine.** In: Barkovich AJ, Raybaud C. *Pediatric Neuroimaging*. 5th ed. Philadelphia: Lippincott Williams & Wilkins; 2012:20–80
10. Thienpont B, de Ravel T, Esch HV, et al. **Partial duplications of the ATRX gene cause the ATR-X syndrome.** *Eur J Hum Genet* 2007; 15:1094–97
11. Badens C, Lacoste C, Philip N, et al. **Mutations in PHD-like domain of the ATRX gene correlate with severe psychomotor impairment and severe urogenital abnormalities in patients with ATRX syndrome.** *Clin Genet* 2006;70:57–62
12. Kernohan KD, Jiang Y, Tremblay DC, et al. **ATRX partners with cohesion and MeCP2 and contributes to developmental silencing of imprinted genes in the brain.** *Dev Cell* 2010;18:191–202

Bone Involvement in Atypical Teratoid/Rhabdoid Tumors of the CNS

M. Warmuth-Metz, B. Bison, N.U. Gerber, T. Pietsch, M. Hasselblatt, and M.C. Frühwald



ABSTRACT

SUMMARY: Destruction of the bony structures of the skull is rare in primary tumors of the CNS. In low-grade gliomas, modeling of the skull is caused by slow growth and chronic pressure. Bony destruction is exceptional even in highly malignant gliomas. Atypical teratoid/rhabdoid tumors of the CNS are highly malignant neoplasms diagnosed with an increasing frequency, mainly in young children. On imaging, these tumors exhibit distinct though not specific morphologic features including peripheral cysts, bleeding residues, and a distinct bandlike, wavy pattern of enhancement. A combination of these single characteristics together with a predilection for young age is suggestive of an atypical teratoid/rhabdoid tumor. We present 5 children with an atypical teratoid/rhabdoid tumor affecting the adjacent bone. These 5 patients were collected in our imaging data base for childhood atypical teratoid/rhabdoid tumor consisting of 91 children at the time of this evaluation and thus representing 6.6%. The mean age of children with bone involvement (4.8 years) was above the average age (2 years) of all children in the data base. We add this rare feature to the list of typical features in MR imaging and CT morphology of atypical teratoid/rhabdoid tumor.

ABBREVIATION: AT/RT = atypical teratoid/rhabdoid tumor

Neuroepithelial tumors rarely demonstrate destruction of adjacent skull or skull base.¹⁻⁵ Atypical teratoid/rhabdoid tumors (AT/RT) are highly malignant primary tumors of the CNS, mostly occurring in very young infants.⁶ The incidence in children below the age of 1 year is nearly reaching the incidence of primitive neuroectodermal tumors/medulloblastomas (primitive neuroectodermal tumor/medulloblastoma). Indeed, in some series of children below 6 months of age, AT/RT has been shown to be the most common malignant CNS tumor.^{7,8} The genetic hallmark of rhabdoid tumors is mutation of the tumor suppressor gene *SMARCB1*; this results in loss of INI1 protein expression, which can be detected in most AT/RTs.⁹ A few cases showing

mutations of other chromatin remodeling complex members such as *SMARCA4* have also been described.¹⁰

MR imaging features of AT/RT are described as nonspecific.¹¹⁻¹³ However, a combination of nonspecific singular features including bleeding residues, peripherally localized cysts, high cellularity seen as low T2 and/or ADC signal, and a distinct bandlike enhancement in a brain tumor in an infant or young child is suggestive of an AT/RT.¹²

We report 5 children harboring an AT/RT with skull or skull base involvement. This rare phenomenon may add more specificity to the already present list of imaging characteristics of AT/RT.

MATERIALS AND METHODS

The patients presented in the current report were collected in the National Reference Center for Neuroradiology for the German Brain Tumor (HIT) Trials, conducted in German-speaking countries of Europe. At the time of evaluation, the data base contained 91 patients diagnosed with an AT/RT. Imaging files sent to our center come from more than 100 treating institutions and are collected within multicenter studies. According to this multicenter basis of data acquisition, no uniform MR imaging protocol was applied. With the consent to participate in the trials of the HIT network, parents or patients agree to the data transfer to reference institutions.

Received December 12, 2012; accepted after revision January 15, 2013.

From the National Reference Center for Neuroradiology (M.W.-M., B.B.), Department of Neuroradiology, University Hospital of Würzburg, Würzburg, Germany; Department of Pediatric Oncology (N.U.G.), Children's University Hospital of Zurich, Zurich, Switzerland; National Reference Center for Neuropathology (T.P.), Department of Neuropathology, University Hospital, Bonn, Germany; Institute of Neuropathology (M.H.), University Hospital Münster, Münster, Germany; and EURHAB Center of Competence for Rhabdoid Tumors (M.C.F.), Children's Hospital Augsburg, Suabian Children's Cancer Center, Augsburg, Germany, and Department of Pediatric Hematology and Oncology, University Children's Hospital Münster, Münster, Germany.

Please address correspondence to Monika Warmuth-Metz, MD, Abteilung für Neuroradiologie, Uniklinikum Würzburg, Josef-Schneider-Str 11, 97080 Würzburg, Germany; e-mail: warmuth@neuroradiologie.uni-wuerzburg.de

Indicates open access to non-subscribers at www.ajnr.org

<http://dx.doi.org/10.3174/ajnr.A3554>

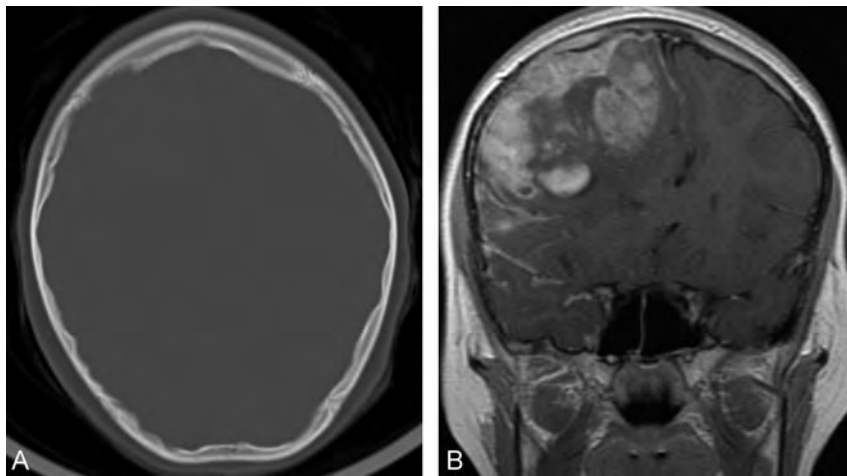


FIG 1. A, Circumscribed right frontal calvarial destruction on a CT in bone reconstruction mode. B, Inhomogeneously enhancing right frontal tumor showing a destruction of the inner table of the skull comparable to A.

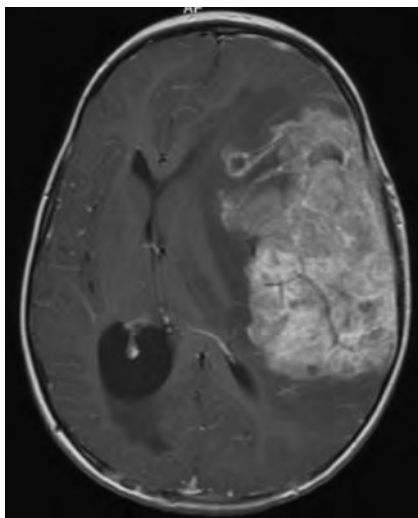


FIG 2. Contrast enhanced axial T1-weighted MRI showing a huge left hemispheric tumor with invasion of the skull and subfalcine herniation.

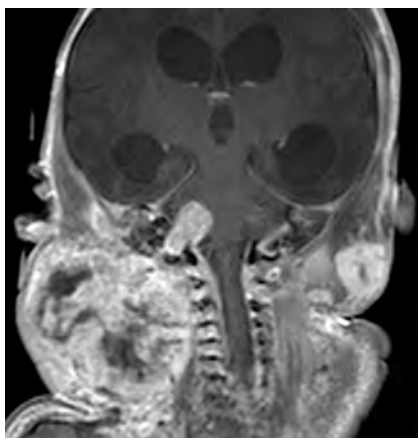


FIG 3. Coronal T1-weighted MRI after contrast showing a huge mass at the right side of the neck and an intracranial tumor with extension to the temporal bone. A smaller extracranial soft tissue tumor is seen in the left side of the neck.

Compared with the whole group of children with an AT/RT in our data base, the 5 children presented here were older (mean age of 2 years in general; our cases, mean age of 4.8 years).

Patient 1

The 9-year-old girl presented with double vision, abducens nerve paresis, and papilledema. On MR imaging, a large tumor in the right frontal lobe was detected. The tumor demonstrated a continuous spread into the local leptomeninges but no distant leptomeningeal dissemination. The CSF was positive for tumor cells. On MR imaging and on CT, an infiltration and erosion of the overlying skull was evident (Fig 1A, -B). The patient underwent intensive systemic

and intraventricular chemotherapy (Dana Farber Cancer Institute protocol¹⁴) and craniospinal irradiation. Six months after diagnosis, multiple brain lesions developed and an infectious complication was suspected. Biopsy of one such lesion remained inconclusive, and the patient died after local tumor progression 16 months after diagnosis.

Patient 2

The 3-year-old girl presented with a huge left hemispheric tumor without leptomeningeal dissemination (Fig 2). A partial resection was performed, and chemotherapy was started. After 3 blocs of chemotherapy and before a planned stem cell transplant, the tumor progressed locally, and, after palliative treatment, the child died 6 months after diagnosis.

Patient 3

On intrauterine MR imaging 2 days before delivery, hydrocephalic ventricles and a lesion in the right temporal lobe were seen (Fig 3). MR imaging was performed because high-risk sonography had demonstrated macrocephaly prenatally. At birth, the boy showed intracranial tumors and multiple nodules within the muscles and soft tissues of the neck, trunk, and extremities. The spleen, kidneys, pancreas, and adrenals were also affected. A biopsy of a mass affecting the upper extremity revealed a malignant rhabdoid tumor and the suspicion of synchronous rhabdoid tumors. A prognostically unfavorable rhabdoid tumor predisposition syndrome was diagnosed. After palliative chemotherapy the boy died at the age of 3 months.

Patient 4

The 5-year-old girl showed an extra-axially growing tumor in the cerebellopontine angle on the right side, with infiltration into the internal auditory canal (Fig 4). Preoperative hearing loss in the right ear remained unchanged after resection. The tumor was nearly totally removed, and treatment with chemotherapy and radiation therapy was completed. At the time of this evaluation, 2.5 years after diagnosis, the child is alive without disease.

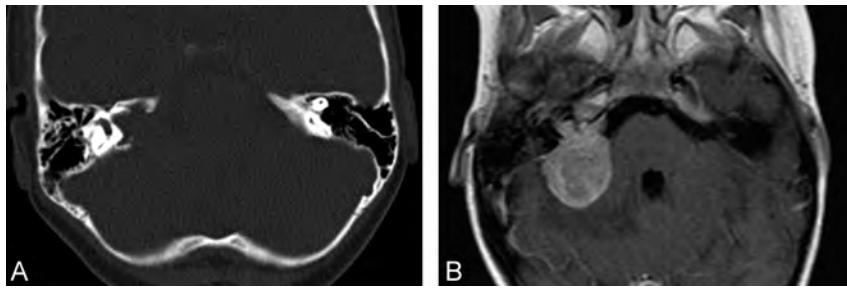


FIG 4. A, Bone CT shows destruction around the internal acoustic canal on the right side. B, This tumor would resemble a vestibular schwannoma if not for the bony destruction on axial post-contrast T1 and previous CT in A.



FIG 5. A, The tumor partially destroying the clivus has a relatively low T2-signal rendering a chordoma quite unlikely. B, T1-weighted contrast enhanced sagittal MRI with a lobulated solid tumor extending out of the clivus and the craniocervical junction.

Patient 5

The 7-year-old boy was diagnosed after development of nuchal pain, sickness, and general weakness. Because of destruction of the clivus and despite the low T2 signal of this tumor on initial MR imaging, a clivus chordoma was suspected (Fig 5). Biopsy revealed an AT/RT. He died 8 months after unsuccessful chemotherapy.

DISCUSSION

The dura is thought to be a natural barrier for glioma extension, rendering bone infiltration a rare event in primary brain tumors. There are only individual reports on highly malignant gliomas demonstrating growth through the untouched dura leading to calvarial destruction^{1,3-5} and tumor extension through the skull base into the orbit or the mouth.¹⁵ Although hematogeneous tumor spread, most frequently to the skeleton, is a rare but well-known finding mainly in the follow-up of medulloblastomas and very rarely in gliomas, virtually no reports on a destruction or invasion of the adjacent skull in medulloblastomas or CNS primitive neuroectodermal tumors exist.

AT/RTs are highly malignant tumors of childhood. After definition of this entity,⁶ this tumor has been diagnosed with increasing frequency. On histopathology, rhabdoid tumor cells exhibit typical morphologic features. However, these defining cells are not found in all tumor parts, leading to problems in the discrimination of AT/RT from other embryonal tumors, for example, CNS primitive neuroectodermal tumor and medulloblastoma.

The frequent loss of the nuclear protein INI1/*SMARCB1* has become state of the art for the diagnosis of intracranial rhabdoid tumor, AT/RT.^{16,17} Among the tumors in children below 1 year of age, AT/RT is now found nearly as frequently as CNS primitive neuroectodermal tumor/medulloblastoma.^{7,18} Rarely, adults are diagnosed with AT/RT, which in this age group are mainly supratentorial, in contrast to young children, in whom infratentorial tumor location predominates.^{18,19} In addition to the high cellularity of the tumor reflected by low signal on T2-weighted and ADC images,²⁰ bleeding residues, peripheral cysts, and a distinct pattern of contrast enhancement have been described as frequent findings.^{11-13,21} Rare reports of patients affected by AT/RT demonstrating involvement of the skull in children and adults exist.^{11,19} Two children with AT/RT of clival location (similar to our patient 5) have been described, whose radiologic appearance also led to the suspicion of chordoma despite very low signal on T2-weighted images.^{22,23} Indeed, in our patient, the possibility of “poorly differentiated chordoma”^{24,25} was also discussed during neuropathologic evaluation but rejected in favor of AT/RT, because the

tumor lacked any convincing chordoid differentiation. Patient 3 does not completely fit with the other cases because he probably had multifocal malignant rhabdoid tumors of the body in addition to the probable AT/RT. Histology was not performed on the intracerebral tumor but on a peripheral tumor and revealed malignant rhabdoid tumor. The tumor leading to destruction of the petrous bone also grew outside of the skull. Therefore, we cannot exclude the possibility that this was indeed a peripheral rhabdoid tumor extending through the skull base into the brain.

The differential diagnosis of bone-eroding gliomas and AT/RT may be impossible, especially when the more frequently observed features such as cysts, bleeding residues, and very low T2 or ADC values are missing. The frequency of 5 of 91 patients with AT/RT with involvement of the skull (6.6%) appears to be high enough to exclude the possibility of a random phenomenon and is in line with reports of AT/RT showing calvarial or skull base affection. We thus add another extraordinary imaging feature to the existing ones to facilitate the diagnosis of AT/RT.

ACKNOWLEDGMENTS

This work was supported by the Deutsche Kinderkrebsstiftung (German Childhood Cancer Foundation).

Disclosures: Monika Warmuth-Metz: *RELATED: Grant:* Deutsche Kinderkrebsstiftung German Childhood Cancer Foundation (Parents' association). * *Support for Travel to Meetings for the Study or Other Purposes:* Deutsche Kinderkrebsstiftung German

Childhood Cancer Foundation; UNRELATED: Board Membership: Roche, Grants/Grants Pending: Deutsche Kinderkrebsstiftung German Childhood Cancer Foundation*; Travel/Accommodations/Meeting Expenses Unrelated to Activities Listed: Deutsche Kinderkrebsstiftung German Childhood Cancer Foundation, Brigitte Bison: OTHER RELATIONSHIPS: My position is paid by the German Children's Cancer Foundation, which is a parents' association collecting money to support all scientific activities of the German HIT Studies. Martin Hasselblatt: RELATED: Grant: Interdisciplinary Centre for Clinical Research, University Munster,* (*money paid to institution).

REFERENCES

1. Gheyi V, Hui FK, Doppenberg EM, et al. **Glioblastoma multiforme causing calvarial destruction: an unusual manifestation revisited.** *AJNR Am J Neuroradiol* 2004;25:1533–37
2. Murphy MN, Korkis JA, Robson FC, et al. **Gliosarcoma with cranial penetration and extension to the maxillary sinus.** *J Otolaryngol* 1985;14:313–16
3. Osborn RE, Ley CE. **Astrocytoma with calvarial erosion.** *AJNR Am J Neuroradiol* 1986;7:178
4. Schuss P, Ulrich CT, Harter PN, et al. **Gliosarcoma with bone infiltration and extracranial growth: case report and review of literature.** *J Neuro-oncol* 2011;103:765–70
5. Woodruff WW Jr, Djang WT, Voorhees D, et al. **Calvarial destruction: an unusual manifestation of glioblastoma multiforme.** *AJNR Am J Neuroradiol* 1988;9:388–89
6. Rorke LB, Packer RJ, Biegel JA. **Central nervous system atypical teratoid/rhabdoid tumors of infancy and childhood: definition of an entity.** *J Neurosurg* 1996;85:56–65
7. von Hoff K, Hinkes B, Dannemann-Stern E, et al. **Frequency, risk factors and survival of children with atypical teratoid rhabdoid tumors (AT/RT) of the CNS diagnosed between 1988 and 2004, and registered to the German HIT database.** *Pediatr Blood Cancer* 2011;57:978–85
8. Woehrer A, Slavc I, Waldhoer T, et al. **Incidence of atypical teratoid/rhabdoid tumors in children: a population-based study by the Austrian Brain Tumor Registry, 1996–2006.** *Cancer* 2010;116:5725–32
9. Jackson EM, Sievert AJ, Gai X, et al. **Genomic analysis using high-density single nucleotide polymorphism-based oligonucleotide arrays and multiplex ligation-dependent probe amplification provides a comprehensive analysis of INI1/SMARCB1 in malignant rhabdoid tumors.** *Clin Cancer Res* 2009;15:1923–30
10. Schneppenheim R, Fruhwald MC, Gesk S, et al. **Germline nonsense mutation and somatic inactivation of SMARCA4/BRG1 in a family with rhabdoid tumor predisposition syndrome.** *Am J Hum Genet* 2010;86:279–84
11. Arslanoglu A, Aygun N, Tekhtani D, et al. **Imaging findings of CNS atypical teratoid/rhabdoid tumors.** *AJNR Am J Neuroradiol* 2004;25:476–80
12. Warmuth-Metz M, Bison B, Dannemann-Stern E, et al. **CT and MR imaging in atypical teratoid/rhabdoid tumors of the central nervous system.** *Neuroradiology* 2008;50:447–52
13. Cheng YC, Lirng JF, Chang FC, et al. **Neuroradiological findings in atypical teratoid/rhabdoid tumor of the central nervous system.** *Acta Radiologica* 2005;46:89–96
14. Chi SN, Zimmerman MA, Yao X, et al. **Intensive multimodality treatment for children with newly diagnosed CNS atypical teratoid rhabdoid tumor.** *J Clin Oncol* 2009;27:385–89
15. Horiuchi T, Osawa M, Itoh N, et al. **Extradural extension of glioblastoma multiforme into the oral cavity: case report.** *Surg Neurol* 1996;46:42–46
16. Judkins AR, Mauer J, Ht A, et al. **Immunohistochemical analysis of hSNF5/INI1 in pediatric CNS neoplasms.** *Am J Surg Pathol* 2004;28:644–50
17. Miller S, Ward JH, Rogers HA, et al. **Loss of INI1 protein expression defines a subgroup of aggressive central nervous system primitive neuroectodermal tumors.** *Brain Pathol* 2013;23:19–27
18. Takahashi K, Nishihara H, Katoh M, et al. **Case of atypical teratoid/rhabdoid tumor in an adult, with long survival.** *Brain Tumor Pathol* 2011;28:71–76
19. Han L, Qiu Y, Xie C, et al. **Atypical teratoid/rhabdoid tumors in adult patients: CT and MR imaging features.** *AJNR Am J Neuroradiol* 2011;32:103–08
20. Yamashita Y, Kumabe T, Higano S, et al. **Minimum apparent diffusion coefficient is significantly correlated with cellularity in medulloblastomas.** *Neurol Res* 2009;31:940–46
21. Parmar H, Hawkins C, Bouffet E, et al. **Imaging findings in primary intracranial atypical teratoid/rhabdoid tumors.** *Pediatr Radiol* 2006;36:126–32
22. Heuer GG, Kiefer H, Judkins AR, et al. **Surgical treatment of a clival-C2 atypical teratoid/rhabdoid tumor.** *J Neurosurg Pediatr* 2010;5:75–79
23. Kazan S, Goksu E, Mihci E, et al. **Primary atypical teratoid/rhabdoid tumor of the clival region: case report.** *J Neurosurg* 2007;106(4 Suppl):308–11
24. Mobley BC, McKenney JK, Bangs CD, et al. **Loss of SMARCB1/INI1 expression in poorly differentiated chordomas.** *Acta Neuropathol* 2010;120:745–53
25. Hoch BL, Nielsen GP, Liebsch NJ, et al. **Base of skull chordomas in children and adolescents: a clinicopathologic study of 73 cases.** *Am J Surg Pathol* 2006;30:811–18

Intramedullary Spinal Cord Metastases: MRI and Relevant Clinical Features from a 13-Year Institutional Case Series

J.B. Rykken, F.E. Diehn, C.H. Hunt, K.M. Schwartz, L.J. Eckel, C.P. Wood, T.J. Kaufmann, R.K. Lingineni, R.E. Carter, and J.T. Wald



ABSTRACT

BACKGROUND AND PURPOSE: Because intramedullary spinal cord metastasis is often a difficult diagnosis to make, our purpose was to perform a systematic review of the MR imaging and relevant baseline clinical features of intramedullary spinal cord metastases in a large series.

MATERIALS AND METHODS: Consecutive patients with intramedullary spinal cord metastasis with available pretreatment digital MR imaging examinations were identified. The MR imaging examination(s) for each patient was reviewed by 2 neuroradiologists for various imaging characteristics. Relevant clinical data were obtained.

RESULTS: Forty-nine patients had 70 intramedullary spinal cord metastases, with 10 (20%) having multiple intramedullary spinal cord metastases; 8% (4/49) were asymptomatic. Primary tumor diagnosis was preceded by intramedullary spinal cord metastasis presentation in 20% (10/49) and by intramedullary spinal cord metastasis diagnosis in 10% (5/49); 98% (63/64) of intramedullary spinal cord metastases enhanced. Cord edema was extensive: mean, 4.5 segments, 3.6-fold larger than enhancing lesion, and ≥ 3 segments in 54% (37/69). Intratumoral cystic change was seen in 3% (2/70) and hemorrhage in 1% (1/70); 59% (29/49) of reference MR imaging examinations displayed other CNS or spinal (non–spinal cord) metastases, and 59% (29/49) exhibited the primary tumor/non-CNS metastases, with 88% (43/49) displaying ≥ 1 finding and 31% (15/49) displaying both findings. Patients with solitary intramedullary spinal cord metastasis were less likely than those with multiple intramedullary spinal cord metastases to have other CNS or spinal (non–spinal cord) metastases on the reference MR imaging (20/39 [51%] versus 9/10 [90%], respectively; $P = .0263$).

CONCLUSIONS: Lack of known primary malignancy or spinal cord symptoms should not discourage consideration of intramedullary spinal cord metastasis. Enhancement and extensive edema for lesion size (often ≥ 3 segments) are typical for intramedullary spinal cord metastasis. Presence of cystic change/hemorrhage makes intramedullary spinal cord metastasis unlikely. Evidence for other CNS or spinal (non–spinal cord) metastases and the primary tumor/non-CNS metastases are common. The prevalence of other CNS or spinal (non–spinal cord) metastases in those with multiple intramedullary spinal cord metastases is especially high.

ABBREVIATIONS: ISCM = intramedullary spinal cord metastasis

Intramedullary spinal cord metastasis is uncommon, with a prevalence of up to 2.1% in autopsy series of patients with cancer.¹ Yet, ISCMs are being increasingly diagnosed, related to advances and increased use of imaging and therapies that prolong survival in patients with cancer.^{2–6} Prompt and accurate diagnosis of ISCM is necessary for effective treatment, and MR imaging is the preferred imaging technique.⁵ Despite this, large series sys-

tematically evaluating multiple MR imaging features of these masses have not been published. The literature on ISCM is limited to case reports, relatively small case series, literature reviews, and autopsy series. Because ISCM is often a difficult diagnosis to make, the purpose of this retrospective study was to perform a systematic review of the MR imaging and relevant baseline clinical features of ISCMs in a large series.

MATERIALS AND METHODS

Institutional review board approval with waived consent was obtained for this Health Insurance Portability and Accountability Act–compliant retrospective research study.

Subjects

The radiologic, clinical, surgical, and pathologic databases at a single institution were searched to identify a group of consecutive

Received December 14, 2012; accepted after revision January 12, 2013.

From the Division of Neuroradiology (J.B.R., F.E.D., C.H.H., K.M.S., L.J.E., C.P.W., T.J.K., J.T.W.), Department of Radiology, and Department of Health Sciences Research (R.K.L., R.E.C.), Mayo Clinic, Rochester, Minnesota.

Paper previously presented at: Annual Meeting of the American Society of Neuroradiology, the ASNR 50th Annual Meeting, April 2012; New York, New York.

Please address correspondence to Felix E. Diehn, MD, 200 1st St SW, Rochester, MN 55905; e-mail: Diehn.felix@mayo.edu

<http://dx.doi.org/10.3174/ajnr.A3526>

patients with ISCM ($n = 58$, 1999–2011). Patients without pretreatment digital MR imaging examination, patients in whom alternative diagnoses were suspected clinically, and patients in whom ISCM was never formally diagnosed were excluded. These 58 patients with ISCM also were the basis for a recent study, which described 2 specific enhancement features on postgadolinium MR imaging in ISCMs compared with primary cord masses.⁷ Five (9%) of these 58 patients were excluded for the current (and the prior) study because of the lack of available pretreatment MR imaging examination. Note that included in the current study but excluded in the prior study were 4 patients who lacked available postgadolinium pretreatment MR imaging. Several additional subject details were as reported in the prior study; specifically, 4 (8%) of the remaining 53 patients “were excluded because alternative diagnoses were being considered clinically and ISCM was never formally diagnosed.” Consequently, only patients with a clinical diagnosis of ISCM were included on the basis of review of all available clinical, pathologic, and imaging data. This yielded a final ISCM study population of 49 (92%) of the remaining 53 patients, with a total of 70 ISCMs. In 5 (10%) of these 49 patients with ISCM, the diagnosis of a solitary ISCM was confirmed by cord mass biopsy/resection. In an additional 44 (90%) of the 49 patients with ISCM, “pathologic proof of the systemic malignancy had been obtained from the primary site or a metastatic site outside of the spinal cord.” One (2%) of the 49 patients died “before any sampling but was clinically presumed to have an ISCM from lung carcinoma, given a classic radiographic pattern of dominant primary lung mass, with multiple pulmonary metastases, hilar and mediastinal adenopathy, distant metastases, a 50 pack-year smoking history, and a family history of lung cancer.”⁷

MR Imaging Review

Two radiologists reviewed all MR imaging examinations in consensus at an electronic workstation (one [F.E.D.] a neuroradiology faculty member with American Board of Radiology certification, a Certificate of Added Qualification in neuroradiology, and in full-time neuroradiology practice, and the other [J.B.R.] a neuroradiology fellow with American Board of Radiology certification). The MR imaging examinations were predominantly from our institution but did include some from outside facilities. All available pulse sequences were reviewed. The typical examination included sagittal T1- and T2-weighted, axial T2-weighted, and postgadolinium sagittal and axial T1-weighted images.

The presence or absence of the following imaging features was analyzed, by use of pregadolinium and postgadolinium T1-weighted images: 1) number of ISCMs per patient, and for each ISCM: 2) location (cervical, cervicothoracic, thoracic, thoracic-conus, conus), 3) position within the cord on axial images (central, eccentric, exophytic), 4) morphology (well-circumscribed versus ill-defined), and cord expansion (absent versus present), 5) T2 signal intensity (hyperintense, hypointense, or isointense to the spinal cord), 6) T1 signal intensity (hyperintense, hypointense, or isointense to the spinal cord), 7) convincing evidence of cystic change (nonenhancing fluid signal on T1- and T2-weighted images; rated as absent, or if present, intratumoral, peritumoral, or both), 8) convincing evidence of intratumoral hemorrhage (nonenhancing T1 hyperintensity and/or marked T1 hypointen-

sity and corresponding T2 hypointensity and/or “blooming” magnetic susceptibility artifact on gradient recalled-echo sequences, if available; rated as absent versus present), 9) gadolinium enhancement (absent or, if present, homogeneous versus heterogeneous versus peripheral [ring]), 10) maximal size of enhancing lesion in millimeters (measured anteroposterior, transverse [axial images required], and superior-inferior), 11) maximal longitudinal extent of enhancing lesion in number of vertebral segments, and 12) maximal longitudinal extent of spinal cord T2 hyperintensity in number of vertebral segments (sagittal T2 images required). The ratio of length of spinal cord T2 hyperintensity to length of ISCM was calculated for each lesion. For the per-patient T2 signal extent in patients with multiple ISCMs, the length of the longest lesion was considered. By including lesions that appeared eccentric or exophytic, it is possible that both primary intramedullary metastases and leptomeningeal metastasis invading the spinal cord would be included among ISCMs. Thus, eccentric/exophytic lesions were further characterized as either clearly intramedullary or possibly of leptomeningeal origin with spinal cord invasion, on the basis of which was dominant, the intramedullary or the cord surface component. In addition, for the exophytic lesions: 1) original MR imaging reports were reviewed to assess whether the interpreting radiologist described an intramedullary mass with exophytic extension or a leptomeningeal mass with invasion, and 2) previous categorization of “rim” and “flame” signs,⁷ two postgadolinium MR imaging findings specific for ISCM, was noted. Note also that leptomeningeal lesions without an apparent intramedullary component were not considered to be ISCMs.

For each patient, the reference spinal MR imaging was reviewed for evidence of the primary tumor and/or extraspinal, non-CNS metastases. The reference spinal MR imaging as well as any other electronically available MR imaging of the neuroaxis performed within 4 weeks before or 4 weeks after the reference MR imaging were reviewed by the 2 radiologists for any evidence of other spinal column or CNS metastases not involving the spinal cord (including vertebral column, leptomeningeal, and visualized intracranial contents). Leptomeningeal metastases were localized anatomically as involving the spinal cord/conus, the cauda equina, the cul-de-sac, or any combination of these. Any available spinal MR imaging examinations subsequent to the reference MR imaging were also reviewed for development of additional ISCMs.

Clinical Review

The electronic medical records of each patient with ISCM were reviewed. The primary tumor type for each patient was noted. The clinical presentation was recorded (asymptomatic or if symptomatic: weakness, sensory symptoms, pain, bowel and/or bladder dysfunction, and duration of these symptoms in weeks). Of these symptoms, when possible, the dominant presenting clinical symptom that led to the spine MR imaging was determined. The dates of the primary tumor diagnosis, ISCM clinical presentation, and ISCM diagnosis were identified. Two intervals were calculated: primary tumor diagnosis to ISCM clinical presentation and primary tumor diagnosis to ISCM diagnosis.

Table 1: Clinical features of ISCMs, per-patient basis (n = 49 patients)

Feature	Prevalence
Sex	
Female	26 (53%)
Primary malignancy	
Lung carcinoma	24 (49%)
Breast carcinoma	7 (14%)
Melanoma	5 (10%)
CNS origin	4 (8%)
Renal cell carcinoma	3 (6%)
Other	6 (12%)
Timing of primary tumor diagnosis	
ISCM presentation preceded primary tumor diagnosis	10 (20%)
ISCM diagnosis preceded primary tumor diagnosis	5 (10%)
Dominant presenting symptoms	
Weakness	28 (57%)
Sensory symptoms	8 (16%)
Bowel and/or bladder dysfunction	5 (10%)
Pain	4 (8%)
Asymptomatic	4 (8%)
Time interval, median (range)	
Duration of symptoms at clinical presentation (n = 44)	2 weeks (0.1–32)
Primary tumor diagnosis to ISCM presentation (n = 38)	1.8 years (0–19.3)
Primary tumor diagnosis to ISCM diagnosis (n = 44)	1.6 years (0–19.5)

Statistical Analysis

The association between solitary versus multiple ISCMs status and the following variables was analyzed by means of χ^2 test: primary tumor type and presence on reference MR imaging of 1) other CNS or spinal (non–spinal cord) metastases, 2) primary tumor/non-CNS metastases, or 3) specifically, leptomeningeal metastases. Descriptive statistics were obtained by use of Excel 2010 (Microsoft, Redmond, Washington). Additional analyses were conducted by using SAS version 9.3 (SAS Institute, Cary, North Carolina). Statistical significance was defined by a *P* value of <.05.

RESULTS

Patient and Histopathologic Characteristics of ISCM

Of the 49 patients with 70 ISCMs, 26 (53%) were female, with a median age of 57.7 years at diagnosis (range, 7–80 years). Histopathologies of the primary malignancies in the 49 patients are shown in Table 1. Regarding the category of “other,” 1 of each of the following primary tumor types were represented, for a total of 6 (12%) patients with 6 (9%) ISCMs: anaplastic thyroid carcinoma, salivary ductal carcinoma, neuroendocrine carcinoma, ovarian adenocarcinoma, lymphoma, and prostate carcinoma. The nature of the CNS-origin primaries in 4 patients is as described in the prior study.⁷ Solitary versus multiple ISCMs status did not correlate with tumor type (*P* = .1607), but the 10 cases of multiple ISCMs only occurred with the 2 most common primary malignancies: lung cancer (7/10, 70%) and breast cancer (3/10, 30%).

Clinical Characteristics

Table 1 includes additional relevant clinical features of the patients with ISCM. Patients had a median of 2 weeks of symptoms at clinical presentation. The most common presenting symptom



FIG 1. Multiple intramedullary spinal cord metastases in an asymptomatic patient. A 73-year-old man with a history of metastatic lung adenocarcinoma underwent a spine MR imaging after a PET-CT scan had demonstrated multifocal spinal hypermetabolism. He was asymptomatic with regard to the spinal cord. Postcontrast sagittal T1-weighted images of the cervical (A) and thoracic (B) spine are shown. Multiple intramedullary spinal cord metastases are demonstrated at the C2, T4, T4–5, and T11 levels (arrows in A, B). In this series, several other patients were asymptomatic.

was weakness (28/49, 57% of patients). However, several patients were asymptomatic with regard to the ISCM (4/49, 8% of patients); one-half (2/4) of these asymptomatic patients had multiple ISCMs (Fig 1). A diagnosis of primary malignancy was not always known at the time of reference MR imaging, as the clinical presentation of the ISCM preceded primary tumor diagnosis in 20% (10/49) of patients, with the actual diagnosis of ISCM preceding primary tumor diagnosis in 50% (5/10) of these patients. In all (10/10) of the patients with multiple ISCMs, the diagnosis of the primary malignancy preceded the ISCM diagnosis.

ISCM Imaging Characteristics on Reference MR Imaging

Thirty-nine (80%) of 49 patients had solitary ISCM on the reference MR imaging (Fig 2), whereas 10 (20%) of 49 had multiple ISCMs (31 additional ISCMs for a mean of 3 ISCMs per patient; Figs 1 and 3). The MR imaging features of the ISCMs on reference MR imaging on a per-lesion basis are detailed in Table 2. Note that most of the lesions were solitary (39/70, 56%), in the thoracic spinal cord (40/70, 57%), eccentrically located within the cord (35/62, 56%), expanding the cord (44/70, 63%), enhancing (63/64, 98%), T2-hyperintense relative to the cord (55/70, 79%), and T1-isointense relative to the cord (48/63, 76%). The length of cord T2 signal abnormality was often extensive (mean, 4.5 segments), on average 3.6-fold greater than the length of the enhancing lesion, extending ≥ 2 segments in 62% of lesions (43/69) and 75% of patients (36/48) and ≥ 3 segments in 54% of lesions (37/69) and 67% of patients (32/48).

Most lesions appeared convincingly of intramedullary origin rather than leptomeningeal with spinal cord invasion. Specifically, only 4 lesions were exophytic. One of these 4 cases demonstrated the “rim” sign and one both the “rim” and “flame” signs, specific signs previously described in ISCMs.⁷ In all 4 cases, the interpreting radiologist described an intramedullary mass with

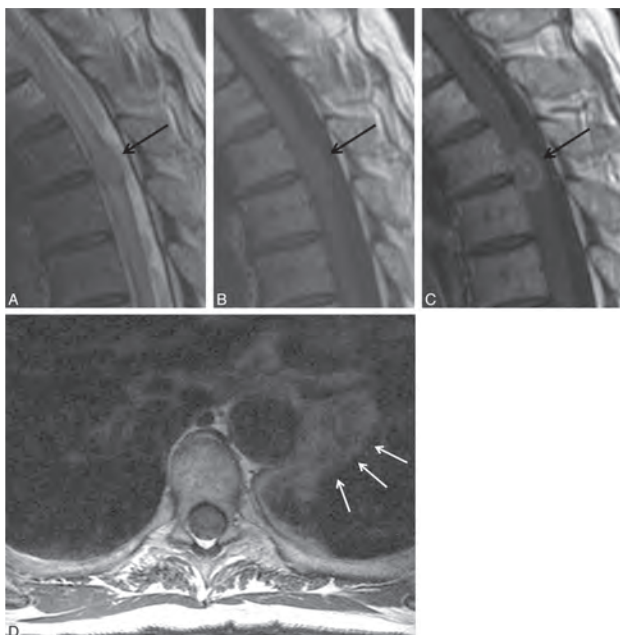


FIG 2. Typical solitary intramedullary spinal cord metastasis, with visualization of primary tumor. A 66-year-old man presented with 6 weeks of paresthesias, bladder dysfunction, lower extremity weakness, and pain. Thoracic spine sagittal T2-weighted (A), sagittal T1-weighted (B), postcontrast sagittal T1-weighted (C), and axial T1-weighted (D) images are shown. A T2 hyperintense, expansile intramedullary cord lesion (arrow) is associated with a large amount of cord T2 hyperintensity (A). The mass is isointense on T1-weighted images (arrow in B) and enhances heterogeneously (arrow in C). Also noted is a left hilar lung mass (arrows in D), which was further evaluated with chest CT imaging (not shown). This hilar mass was pathologically proved to be a grade 4 undifferentiated small-cell lung carcinoma. Visualization on MR imaging of the primary tumor/non-CNS metastases and/or other spinal/CNS (non-spinal cord) metastases was common in this series.

exophytic extension, not a leptomeningeal mass with parenchymal invasion. Of the 39 lesions that were characterized as being either eccentric in the spinal cord ($n = 35$) or exophytic ($n = 4$), only 3 lesions (4% of all 70 ISCMs, 6% of the 62 ISCMs for which axial images were available) appeared to potentially be of leptomeningeal origin, given a dominant surface component, rather than originating within the spinal cord. Two of these 3 lesions occurred in the same patient.

Two findings were rare. Central cystic or necrotic change was seen in only 2 of the ISCMs (2/70, 3%) (Fig 4), with only 1 of these 2 lesions demonstrating ring enhancement peripherally about the cystic change. Only 1 lesion demonstrated convincing evidence for associated hemorrhage (1/70, 1%) (Fig 5).

Visualization of Other Metastases, Primary Tumor on Reference MR Imaging

Table 3 includes additional findings on the reference MR imaging on a per-patient basis. Note that most patients (43/49, 88%) had additional CNS or spinal column metastasis(or metastases) not involving the spinal cord and/or the primary tumor or non-CNS metastasis(or metastases) visible on the reference MR imaging (Fig 2D; Fig 3C,-D). In other words, only in a minority of patients (6/49, 12%) did the MR imaging not demonstrate at least 1 of these associated findings. When leptomeningeal metastases were present (18/49, 37% of patients) on reference MR imaging, they



FIG 3. Multiple intramedullary spinal cord metastases, with visualization of other CNS metastases. A 60-year-old woman with a history of small-cell lung carcinoma, diagnosed 6.5 months prior, presented with several days of lower extremity weakness and urinary and stool incontinence. MR images of the cervical and thoracic spine with post-contrast fat-saturated consecutive sagittal T1-weighted images of the thoracic spine (A, B, C) and postcontrast sagittal T1-weighted image of the cervical spine (D) are shown. Several enhancing intramedullary lesions are present (white arrows in A, B, D). There is abnormal leptomeningeal enhancement with several small metastases studding the surface of the cord (arrows in C). Metastases are visualized in the lower pons and cerebellum (thick white arrows in D). Visualization on MR imaging of other CNS or spinal (non-spinal cord) metastases was common in this series, and more common in patients with multiple ISCMs.

most commonly manifested as diffuse involvement along the cord/conus, cauda equina and cul-de-sac (8/18, 44%); isolated involvement of the cul-de-sac did not occur. Patients with solitary compared with multiple ISCMs were less likely to have CNS/spinal (non-spinal cord) metastases on the reference MR imaging (20/39 [51%] versus 9/10 [90%], respectively; $P = .0263$). There was no correlation between solitary versus multiple ISCMs status and presence of either primary tumor/non-CNS metastasis or leptomeningeal metastases on reference MR imaging ($P = .3484$ and $P = .872$, respectively).

Findings on Prior and Subsequent Neurologic-MR Imaging

Forty-seven percent of patients (23/49) had evidence of other CNS/spinal metastases (non-spinal cord) on MR imaging examination(s) of the neuroaxis obtained within the 4 weeks preceding the reference MR imaging. An additional 16% of patients (8/49) demonstrated such other metastases within the 4 weeks subsequent to the reference MR imaging. The subsequent development of a new ISCM on follow-up MR imaging occurred in 22% (11/49) of patients.

DISCUSSION

The current study highlights several relevant clinical and MR imaging features of ISCMs in a large series of patients. The most salient clinical features of ISCM are 1) lung cancer is the most common primary tumor, 2) the primary malignancy has not always been diagnosed at the time of ISCM symptom onset or reference MR imaging, and 3) patients can be asymptomatic with

Table 2: MRI features of ISCMs, per-lesion basis, total of 70 lesions in 49 patients

Feature	Prevalence
Location (n = 70)	
Cervical	16 (23%)
Cervicothoracic	2 (3%)
Thoracic	40 (57%)
Thoracic-conus	1 (1%)
Conus	11 (16%)
Position (n = 62)	
Central	23 (37%)
Eccentric	35 (56%)
Exophytic	4 (6%)
Morphology (n = 66)	
Well-circumscribed	64 (97%)
Ill-defined	2 (3%)
Cord expansion (n = 70)	
Present	44 (63%)
Absent	26 (37%)
Enhancement (n = 64)	
Present	63 (98%)
Absent	1 (2%)
Enhancement pattern (n = 63)	
Homogeneous	31 (49%)
Heterogeneous	31 (49%)
Peripheral (ring)	1 (2%)
Size of enhancing lesion, mm, mean (range)	
Anterior-posterior (n = 63)	6.5 (1–16)
Transverse (n = 53)	7.3 (2–23)
Superior-inferior (n = 63)	19.9 (2–114)
Longitudinal extent, No. of vertebral segments, mean (range)	
Length of enhancement (n = 63)	1.4 (1–8)
Length of cord T2 signal hyperintensity (n = 69)	4.5 (1–15)
Ratio, T2 signal/enhancement (n = 63)	3.6 (1–14)
T2 signal intensity (n = 70)	
Hyperintense	55 (79%)
Hypointense	1 (1%)
Isointense	14 (20%)
T1 signal intensity (n = 63)	
Hyperintense	10 (16%)
Hypointense	5 (8%)
Isointense	48 (76%)
Cystic change (n = 70)	
Intratumoral	2 (3%)
Peritumoral	0 (0%)
Intratumoral hemorrhage (n = 70)	1 (1%)

regard to the ISCM, even in the case of multiple ISCMs. The 3 most pertinent imaging features of ISCMs are 1) almost all ISCMs enhance, 2) the associated spinal cord T2 hyperintensity is extensive, and 3) both intratumoral hemorrhage and intra-/peritumoral cystic/necrotic change are rare. An additional important imaging finding is that either additional CNS/spinal (non-spinal cord) metastases or the primary tumor/non-CNS metastases are extremely common, seen in nearly 90% of patients in this series on the reference MR imaging. The prevalence of other CNS/spinal (non-spinal cord) metastases in those with multiple ISCMs is especially high.

Knowledge of these relevant clinical and imaging features of ISCM and their significance is important for radiologists and the referring clinicians. When faced with a spinal cord mass, lack of a known primary malignancy and lack of symptoms related to the mass should not dissuade one from considering an ISCM. For any

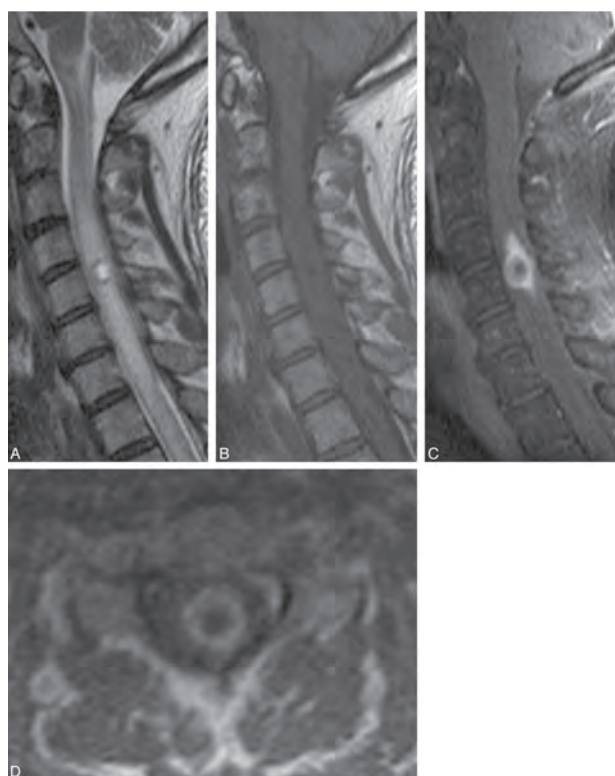


FIG 4. Atypical intramedullary spinal cord metastasis with central cystic change/necrosis. A 55-year-old man with recent nephrectomy of a renal cell carcinoma presented with 2 weeks of predominantly left upper extremity pain, paresthesias, and weakness, as well as global hyperreflexia. Cervical spine sagittal T2-weighted (A), T1-weighted (B), and postcontrast fat-saturated T1-weighted images (C), and postcontrast axial T1-weighted image are shown. A mass within the cord at the level of C5 has markedly hyperintense central signal on T2-weighted imaging (A) and corresponding T1 hypointensity (B) consistent with central cystic change/necrosis. The sagittal (C) and axial (D) T1-weighted postcontrast images demonstrate the peripheral enhancement with lack of central enhancement corresponding to the region of central cystic/necrotic change. This represents 1 of only 2 cases in the current series of intramedullary spinal cord metastasis demonstrating cystic/necrotic change. The primary tumor type in the other case (not shown) was lung carcinoma.

spinal cord mass, but particularly when ISCM is strongly considered, the visualized lungs should be scrutinized because lung cancer is the most common primary malignancy. Lack of enhancement and presence of cystic change and/or hemorrhage in an intramedullary mass should bring other etiologies of spinal cord masses higher in the differential diagnosis, such as primary cord neoplasms, in which such findings are not uncommon. The radiologist should scrutinize the MR imaging as well as other prior neuroaxis imaging studies for presence of other CNS/spinal (non-spinal cord) metastases and the primary tumor/non-CNS metastases. The presence of additional ISCMs should be specifically sought.

The current study contributes to the literature on ISCM. Recently, we described 2 postgadolinium MR imaging findings specific for ISCM compared with various primary cord masses, in 45 of the 49 ISCM patients from the current study.⁷ In the present study, we more fully characterize the MR imaging findings for these ISCMs. Other previous series of ISCMs have generally been smaller, with the largest of these consisting of 40 patients, 27 of

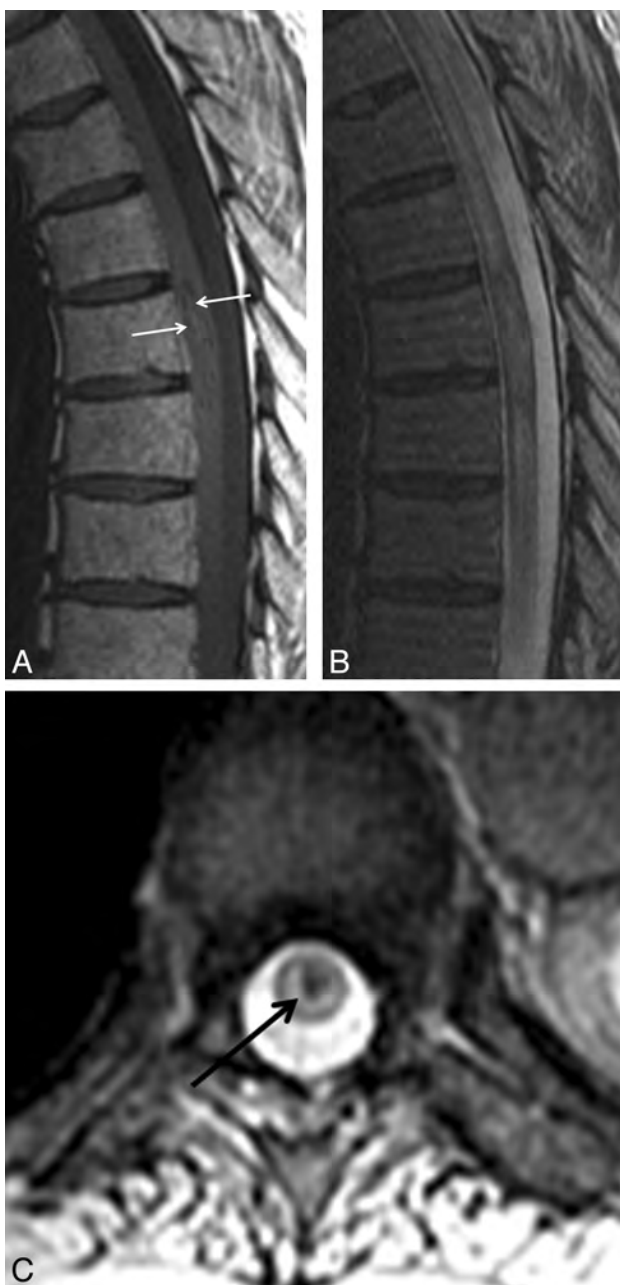


FIG 5. Atypical intramedullary spinal cord metastasis with associated hemorrhage. A 74-year-old man with squamous cell carcinoma of the lung diagnosed 2 years prior presented with 4 weeks of paraplegia. Thoracic spine shown with sagittal T1-weighted (A) and T2-weighted (B) and axial gradient recalled-echo (C) images. Heterogeneous mildly hyperintense central signal is present within the intramedullary spinal cord metastasis on T1-weighted imaging (arrows in A). There is corresponding heterogeneity on T2-weighted imaging (B). The axial gradient recalled-echo image demonstrates corresponding central hypointensity (“blooming,” arrow in C), typical of hemorrhage. This is the only intramedullary spinal cord metastasis in the current series demonstrating signal changes convincing for associated hemorrhage.

whom were imaged with MR imaging (25 with gadolinium).⁸ One recent small series of 8 ISCM patients reviewed the published literature of an additional 293 cases but did not specifically assess MR imaging findings.⁹

The large amount of spinal cord edema compared with the length of the enhancing ISCM has been known anecdotally and

Table 3: Additional MRI features of ISCMs on reference MRI, per-patient basis (n = 49 patients)

Feature	Prevalence
Solitary ISCM	39 (80%)
Multiple ISCMs	10 (20%)
Non-cord CNS and/or spinal metastasis	29 (59%)
Leptomeningeal metastasis	18 (37%)
Primary tumor and/or non-CNS metastasis	29 (59%)
Non-cord CNS/spinal metastasis OR primary tumor/non-CNS metastasis	43 (88%)
Both non-cord CNS/spinal metastasis AND primary tumor/non-CNS metastasis	15 (31%)

described in a smaller series with low field strength MR imaging examinations,¹⁰ as well as in other small series; for instance, in 3 patients in a study by Sze et al.¹¹ However, to our knowledge, this has not been systematically reported and quantified in a large series by use of modern MR imaging scanners.

The rarity of cystic change/necrosis demonstrated in our study conflicts with some existing literature. One review publication in the imaging literature does describe cysts to be rare in ISCM,¹² but specific references are not included. Other articles state that cystic change/necrosis is common.⁵ For instance, a study of 7 patients reported ring enhancement suggesting central necrosis in 4; note that no images demonstrating cystic change were provided and that the authors did not include a radiologist.¹³ A different study reported intratumoral cysts in 10 of 19 cases, but no representative image of such a case was provided.¹⁴

Other studies, including the recent comprehensive literature review by Sung et al,⁹ have also found that lung cancer accounts for approximately 50% of ISCM cases and that breast cancer is the second most common primary malignancy. The review by Sung et al also found a high frequency of systemic metastases, though our present study examined this specifically on the basis of what a radiologist might visualize on the reference MR imaging. Additional similarities between our series and the review by Sung et al, respectively, are: propensity for ISCM to be solitary (80% versus 88% prevalence), age (wide range, with median 58 years versus 56 years), weakness as the most common symptom (57% versus 88%), symptom duration (wide range, with median of 2 weeks versus 3 weeks), frequency of asymptomatic patients (8% versus 5%), ISCM preceding primary tumor diagnosis (“synchronous presentation”) (20% versus 26%), and interval between primary tumor diagnosis and ISCM diagnosis (wide range, with median of 19 months versus 16 months). Differences between our series and the review by Sung et al, respectively, are: prevalence of sensory symptoms (16% versus 73%) and prevalence of bowel/bladder dysfunction (10% versus 43%). These discrepancies may exist because we only assessed symptoms up to the time of the MR imaging, not for the remainder of the disease course. An additional difference between our series versus the comprehensive literature review by Sung et al, respectively, is the prevalence of thoracic ISCM (57% versus 34%). This discrepancy is probably multifactorial. For instance, our anatomic categorization was based exclusively on MR imaging (rather than autopsy) findings. Moreover, we did not include patients with “intramedullary” metastases exclusive to the cauda equina (not involving the spinal cord and presumably leptomeningeal), which may account for the rela-

tively higher proportion of “lumbar” spinal cord metastases (38%) seen in literature reviewed by Sung et al.

As for the development of ISCMs, several pathophysiologic mechanisms have been described, including arterial spread, retrograde venous spread (via Batson venous plexus), meningeal spread, perineural lymphatic spread, and direct invasion from a contiguous structure.^{4,8,13,15,16} Of these proposed mechanisms for the pathogenesis of ISCMs, spread via the arterial route is generally favored as the most common, though the mechanism may differ, depending on the primary tumor cell type. The preponderance of central and eccentric ISCMs in the present study and the relative lack of exophytic ISCMs also suggest that the arterial route is a more common means of spread, particularly given the robust arterial supply to the central gray matter of the cord. However, a case series encompassing all types of spinal cord metastases, ideally with microscopic pathologic correlation, would be needed to confidently achieve this conclusion. Inclusion of CSF analysis would also be potentially useful.

Limitations of this study include its retrospective nature, the use of consensus imaging review, and the lack of uniformity of MR imaging technique, because not all of the examinations were from our institution. Although our series is the largest published single institution study of patients with ISCM, the relatively small sample size remains a limitation. Only 10% of the 49 patients had pathologic confirmation. However, this is consistent with the other smaller published series of ISCM, because pathologic sampling from surgery/autopsy is typically not obtained. Moreover, the multiple aforementioned clinical features in the current study that were similar to published literature suggest that the patients in our series are indeed representative of patients with ISCMs. The most common reason for biopsy or resection of ISCM is for diagnostic purposes^{3,7,9}; knowledge of the results of the current study, as well as of the recently described enhancement characteristics specific for ISCM,⁷ is anticipated to decrease such diagnostic surgery rates.

CONCLUSIONS

We describe pertinent clinical and MR imaging features in a large series of patients with ISCM. When considering ISCM in the differential diagnosis of a spinal cord mass on MR imaging, the results of this study should be helpful to radiologists. Absence of clinical symptoms and lack of a known primary malignancy should not dissuade one from considering ISCM. Presence of cystic change or hemorrhage should cause one to entertain other diagnostic possibilities as more likely. Extensive edema compared with enhancing lesion size is typical. Evidence for other CNS or

spinal (non-spinal cord) metastases, the primary tumor, and non-CNS metastases should be sought because these features are common. The prevalence of other CNS or spinal (non-spinal cord) metastases in those with multiple ISCMs is especially high.

REFERENCES

1. Costigan DA, Winkelman MD. **Intramedullary spinal cord metastasis: a clinicopathological study of 13 cases.** *J Neurosurg* 1985;62:227–33
2. Mut M, Schiff D, Shaffrey ME. **Metastasis to nervous system: spinal epidural and intramedullary metastases.** *J Neurooncol* 2005; 75:43–56
3. Connolly ES Jr, Winfree CJ, McCormick PC, et al. **Intramedullary spinal cord metastasis: report of three cases and review of the literature.** *Surg Neurol* 1996;46:329–37
4. Kalayci M, Cagavi F, Gul S, et al. **Intramedullary spinal cord metastases: diagnosis and treatment—an illustrated review.** *Acta Neurochir (Wien)* 2004;146:1347–54
5. Kalita O. **Current insights into surgery for intramedullary spinal cord metastases: a literature review.** *Int J Surg Oncol* 2011; Epub; PMID:22312538
6. Zebrowski A, Wilson L, Lim A, et al. **Intramedullary spinal cord metastases in breast cancer are associated with improved longer-term systemic control.** *Future Oncol* 2010;6:1517–19
7. Rykken JB, Diehn FE, Hunt CH, et al. **Rim and flame signs: postgadolinium MRI findings specific for non-CNS intramedullary spinal cord metastases.** *AJNR Am J Neuroradiol* 2013;34:908–15
8. Schiff D, O’Neill BP. **Intramedullary spinal cord metastases: clinical features and treatment outcome.** *Neurology* 1996;47:906–12
9. Sung WS, Sung MJ, Chan JH, et al. **Intramedullary spinal cord metastases: a 20-year institutional experience with a comprehensive literature review.** *World Neurosurg* 2012; Epub; PMID: 22484768
10. Crasto S, Duca S, Davini O, et al. **MRI diagnosis of intramedullary metastases from extra-CNS tumors.** *Eur Radiol* 1997;7:732–36
11. Sze G, Krol G, Zimmerman RD, et al. **Intramedullary disease of the spine: diagnosis using gadolinium-DTPA-enhanced MR imaging.** *AJR Am J Roentgenol* 1988;151:1193–204
12. Koeller KK, Rosenblum RS, Morrison AL. **Neoplasms of the spinal cord and filum terminale: radiologic-pathologic correlation.** *Radiographics* 2000;20:1721–49
13. Watanabe M, Nomura T, Toh E, et al. **Intramedullary spinal cord metastasis: a clinical and imaging study of seven patients.** *J Spinal Disord Tech* 2006;19:43–47
14. Dam-Hieu P, Seizeur R, Mineo JF, et al. **Retrospective study of 19 patients with intramedullary spinal cord metastasis.** *Clin Neurol Neurosurg* 2009;111:10–17
15. Lee SS, Min KK, Sym SJ, et al. **Intramedullary spinal cord metastases: a single-institution experience.** *J Neurooncol* 2007; 84:85–89
16. Ishii T, Terao T, Komine K, et al. **Intramedullary spinal cord metastases of malignant melanoma: an autopsy case report and review of the literature.** *Clin Neuropathol* 2010;5:334–40



The First World Forum of Young Chinese Radiologists

**WFYCR
2014
TAIWAN**

March 23 (Sunday), 2014
Chung Shan Medical University, Taichung, Taiwan



A joint activity with the 63rd Annual Meeting
of the Chinese Taipei Society of Radiology

March 22-23, 2014

www.rsroc.org.tw

E-mail : rsroc.tw@gmail.com

FAX : +886-2-25865330

TEL : +886-2-25865332



AJNR CLASSIFIEDS

NEURORADIOLOGISTS AVAILABLE

Attract the best neuroradiologists
with an ad in the AJNR.

To place your ad,
contact Karen Halm at
(630) 522-6068

or
khalm@asnr.org

Academic Neuroradiologist

The Department of Diagnostic Radiology at Dartmouth-Hitchcock Medical Center and the Geisel School of Medicine at Dartmouth is seeking a fellowship-trained neuroradiologist who is an active clinician with a career interest in academic neuroradiology.

The full-time faculty position is for a clinician with strong interest in teaching and/or research. Responsibilities will include performance and interpretation of the full range of diagnostic neuroimaging studies, active clinical or translational research, and teaching of neuroradiology fellows, radiology residents and medical students. Dedicated research time is available for candidates with active research programs. Preferred candidates will have demonstrated leadership success, research productivity, and clinical experience.

The successful candidate will join an academic practice with five other neuroradiologists and more than 30 radiologists. Facilities include five state-of-the-art clinical MR scanners including two Siemens Skyra 3.0T systems and a GE Discovery750 3.0T system, an Advanced Imaging Center dedicated to MR imaging research, and the Center for Surgical Innovation with intraoperative 3T MR and CT capabilities.

Academic rank and compensation will be consistent with experience and medical center policies. Applicants must be eligible for licensure in New Hampshire. Candidates should submit a curriculum vitae and letter of interest electronically to:

Clifford J. Eskey, MD - Search Chair
Dartmouth-Hitchcock Medical Center
One Medical Center Drive
Lebanon, NH 03756
neuroradiology@dphysicians.org



Dartmouth-
Hitchcock



GEISEL
SCHOOL OF
MEDICINE
AT DARTMOUTH

Dartmouth-Hitchcock Clinic is an Equal Opportunity/Affirmative Action employer and encourages applications from women and members of minority groups.

www.dartmouth-hitchcock.org



Simplify the MOC Process



Manage your CME Credits Online

Available to Members of Participating Societies

American Board of Radiology (ABR)	Radiological Society of North America (RSNA)
American College of Radiology (ACR)	Society of Interventional Radiology (SIR)
American Roentgen Ray Society (ARRS)	SNM
American Society of Neuroradiology (ASNR)	The Society for Pediatric Radiology (SPR)
Commission on Accreditation of Medical Physics Educational Programs, Inc. (CAMPEP)	

CMEgateway.org

It's Easy and Free!

Log on to CME Gateway to:

- View or print reports of your CME credits from multiple societies from a single access point.
- Print an aggregated report or certificate from each participating organization.
- Link to SAMs and other tools to help with maintenance of certification.

American Board of Radiology (ABR) participation!

By activating ABR in your organizational profile, your MOC-fulfilling CME and SAM credits can be transferred to your own personalized database on the ABR Web site.

Sign Up Today!

go to CMEgateway.org

Go Green!

AJNR urges American Society of Neuroradiology members to reduce their environmental footprint by voluntarily suspending their print subscription.

The savings in paper, printing, transportation, and postage not only help members cut down on clutter, but go to fund new electronic enhancements and expanded content.

The digital edition of *AJNR* presents the print version in its entirety, along with extra features including:

- Publication Preview
- Case of the Week
- Podcasts
- Special Collections
- The *AJNR* Blog
- Weekly Poll

It also **reaches subscribers much faster than print**. An **electronic table of contents** will be sent directly to your mailbox to notify you as soon as it publishes.

Readers can **search, reference, and bookmark** current and archived content 24 hours a day on www.ajnr.org, rather than thumb through stacks of accumulated paper issues for articles and images they need.



<http://www.ajnr.org/cgi/feedback>

ASNR members who wish to opt out of print can do so by using the Feedback form on the *AJNR* Website (<http://www.ajnr.org/cgi/feedback>). Just type "Go Green" in the subject line to stop print and spare our ecosystem.



CALL FOR
APPLICATIONS

ARRS/ASNR Scholarship in Neuroradiology

Applications are being accepted in any area of research related to neuroradiology. Applications should describe the unique nature of the research effort independent of existing research efforts, and should have well-defined goals for the funding period of the grant. The two-year scholarship will provide \$150,000 (\$75,000 per year); it requires a minimum 50 percent time commitment.

Eligibility

- Applicant must be a member of both ARRS and ASNR at the time of application and for the duration of the award.
- Applicant must hold a full-time faculty position in a department of radiology, radiation oncology, or nuclear medicine within a North American educational institution at the time of application.
- Applicant must be within 5 years of initial faculty appointment with an academic rank of instructor or assistant professor, (or equivalent).
- Applicant must have completed advanced training and be certified by the American Board of Radiology (ABR) or on track for certification.
- Applicant must have completed neuroradiology training in an accredited ACGME neuroradiology fellowship program.

The deadline for receipt of applications is **January 15, 2014**.

Log onto www.arrs.org/RoentgenFund/Scholarships/ARRS_ASNR.aspx or foundation.asnr.org for more information.

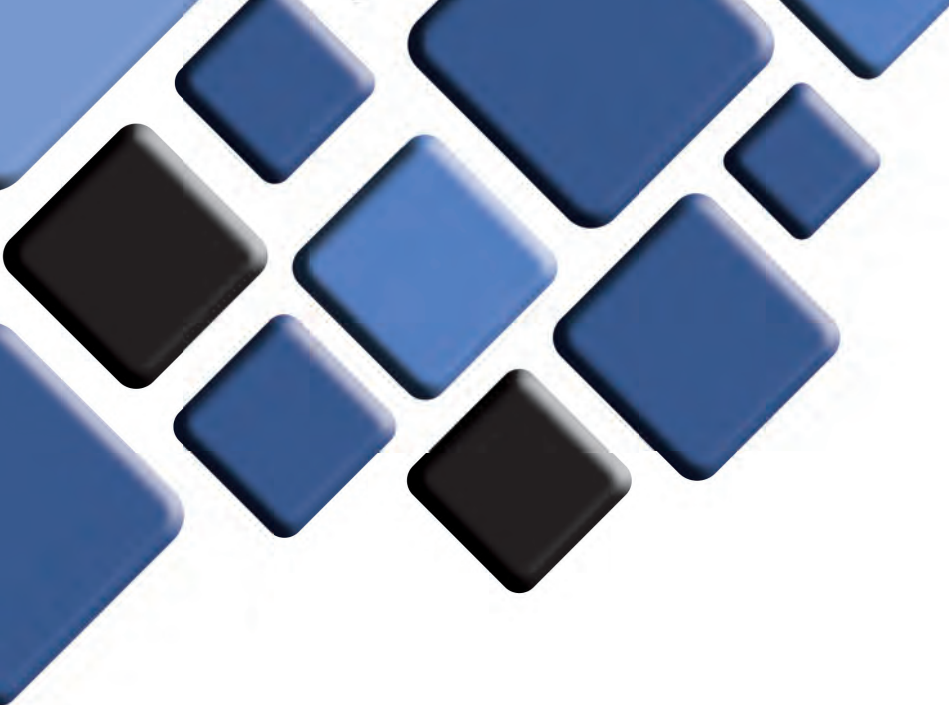
This scholarship is funded by The Foundation of the American Society of Neuroradiology in conjunction with The Roentgen Fund.® To support neuroradiology research and education with a generous tax-deductible contribution, visit foundation.asnr.org.

Application
Deadline:
**January
15**

www.asnr.org

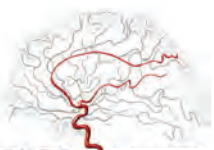
FOUNDATION OF THE ASNR





BARRICADE COIL SYSTEM™

COILING SIMPLIFIED, PERFORMANCE DELIVERED



BLOCKADE
M E D I C A L

18 TECHNOLOGY DRIVE #169, IRVINE CA 92618 | P 949.788.1443
WWW.BLOCKADEMEDICAL.COM



CE
0297
MKTG-020 REV. A

